

DEVELOPMENT OF A NEW TESTING PROCEDURE TO MEASURE  
THERMAL FATIGUE PERFORMANCE OF ASPHALT CONCRETE

A THESIS SUBMITTED TO  
THE GRADUATE SCHOOL OF NATURAL AND APPLIED SCIENCES  
OF  
MIDDLE EAST TECHNICAL UNIVERSITY

BY

REZA SHABANI

IN PARTIAL FULFILLMENT OF THE REQUIREMENTS  
FOR  
THE DEGREE OF DOCTOR OF PHILOSOPHY  
IN  
CIVIL ENGINEERING

September 2020



Approval of the thesis:

**DEVELOPMENT OF A NEW TESTING PROCEDURE TO MEASURE  
THERMAL FATIGUE PERFORMANCE OF ASPHALT CONCRETE**

submitted by **Reza Shabani** in partial fulfillment of the requirements for the degree of Doctor of Philosophy in Civil Engineering, **Middle East Technical University** by,

Prof. Dr. Halil Kalıpçılar  
Dean, Graduate School of **Natural and Applied Sciences**

\_\_\_\_\_

Prof. Dr. Ahmet Turer  
Head of the Department, **Civil Engineering**

\_\_\_\_\_

Prof. Dr. Murat Güler  
Supervisor, **Civil Engineering, METU**

\_\_\_\_\_

**Examining Committee Members:**

Prof. Dr. Mustafa Şahmaran  
Civil Engineering, Hacettepe University

\_\_\_\_\_

Prof. Dr. Murat Güler  
Civil Engineering, METU

\_\_\_\_\_

Prof. Dr. İsmail Özgür Yaman  
Civil Engineering, METU

\_\_\_\_\_

Assist. Prof. Dr. Hande Işık Öztürk  
Civil Engineering, METU

\_\_\_\_\_

Assoc. Prof. Dr. Mustafa Kürşat Cubuk  
Civil Engineering, Gazi University

\_\_\_\_\_

Date: 22.09.2020

**I hereby declare that all information in this document has been obtained and presented in accordance with academic rules and ethical conduct. I also declare that, as required by these rules and conduct, I have fully cited and referenced all material and results that are not original to this work.**

Name, Last name: Reza, Shabani

Signature:

## **ABSTRACT**

### **DEVELOPMENT OF A NEW TESTING PROCEDURE TO MEASURE THERMAL FATIGUE PERFORMANCE OF ASPHALT CONCRETE**

Shabani, Reza  
Doctor of Philosophy, Civil Engineering  
Supervisor: Prof. Dr. Murat Güler

September 2020, # 392 pages

In the scope of this study, a new test procedure is developed to investigate the thermal fatigue performance of asphalt concrete materials. To achieve this, test samples are compacted using different mixtures to be designed according to the Superpave mix design method. In the testing program, compacted samples are cut to produce beam specimens for thermal coefficient tests and semicircular specimens for thermal fatigue tests. Analysis of variance (ANOVA) and Multivariate analyses are both used to evaluate the effect of test variables on derived parameters characterizing the thermal coefficients and the thermal fatigue performance of the specimens. Results of ANOVA indicate that aggregate type is the most significant factor for the thermal coefficient of asphalt concrete. Asphalt type, aggregate type, gradation, frequency, aging and rest time are also significant design factors for thermal fatigue according to the results of multivariate analyses. However, among the test variables studied, loading frequency and asphalt type seem to be highly effective factors governing the behavior of asphalt concrete against thermal fatigue.

Keywords: Asphalt concrete, Thermal coefficient, Thermal fatigue, semicircular specimen

## ÖZ

### ASFALT BETONUN ISIL YORULMA PERFORMANSININ ÖLÇÜMÜ İÇİN YENİ BİR TEST YÖNTEMİNİN GELİŞTİRİLMESİ

Shabani, Reza  
Doktora, İnşaat Mühendisliği  
Tez Yöneticisi: Prof. Dr. Murat Güler

Eylül 2020, # 392 sayfa

Bu çalışma kapsamında, asfalt beton malzemelerinin ısı yorulma performansının araştırılması için yeni bir test prosedürü geliştirilmiştir. Bu amaçla, Superpave yöntemine göre hazırlanan asfalt karışımlar sıkıştırılarak deney numuneleri hazırlanmıştır. Deney programında kullanılmak üzere, sıkıştırılan numunelerden ısı genleşme katsayılarının ölçümü için prizmatik numuneler ve ısı yorulma deneyleri için yarım daire deney numuneleri kesilerek elde edilmiştir. Deney numunelerinin ısı genleşme ve ısı yorulma deneylerinden elde edilen parametreleri için etkin olan faktörler, varyans analizi ve çoklu varyans analiz yöntemleriyle belirlenmiştir. Varyans analiz sonuçları, agrega cinsinin asfalt betonun ısı genleşme katsayısı için en etkili parametre olduğunu göstermiştir. Çoklu varyans analizleri ise, asfalt cinsi, agrega cinsi ve gradasyonu, yükleme frekansı ve yük boşaltma süresi, ısı yorulma davranışı için önemli faktörler olduğunu göstermiştir. Bununla birlikte, araştırılan deney parametreleri arasında asfalt cinsi ve yükleme frekansının, asfalt betonun ısı yorulma davranışını belirleyen en etkili faktörler olduğu görülmektedir.

Anahtar Kelimeler: Asfalt betonu, ısı katsayısı, ısı yorulma, yarım daire şeklindeki numune

To my family

## ACKNOWLEDGMENTS

Firstly, I would like to express my sincere gratitude to my advisor Prof. Dr. Murat Güler. His guidance helped me in all the time of research and writing of this thesis. I could not have imagined having a better advisor and mentor for my Ph.D study.

Besides my advisor, I would like to thank the rest of my thesis committee: Prof. Dr. Ismail özgür yaman, Prof. Dr Mustafa Şahmaran, Assoc. Prof. Dr Mustafa Kürşat Cubuk, and Assist. Prof. Dr. Hande Işık Öztürk, for their insightful comments and encouragement, but also for the hard questions which incited me to widen my research from various perspectives.

I thank my fellow labmates, Dr Ayhan öner Yücel, Dr Başak Varli, Yalcin Karakaya, Farshad Kamran, Laleh Sorkhi for their friendship in the last eight years, and accepting nothing less than excellence from me.

My sincere thanks goes to Alan Feeley from Pavetest Pty. Ltd. who provided me technical support. Also I thank Mr. Ahmet Sağlam, laboratory technician for his support during my experiments.

Last but not the least, I would like to thank my parents (Vida Saedi and Enayatollah Shabani), and to my sister and brother (Raha and Rouzbeh) for supporting me spiritually throughout writing this thesis and my life in general.



## TABLE OF CONTENTS

ABSTRACT.....	v
ÖZ .....	vi
ACKNOWLEDGMENTS .....	viii
TABLE OF CONTENTS.....	ix
LIST OF TABLES .....	xiv
LIST OF FIGURES .....	xvi
LIST OF ABBREVIATIONS.....	xxiii
CHAPTERS	
1 INTRODUCTION .....	1
1.1 Background.....	1
1.2 Research objectives.....	2
1.3 Originality of the topic.....	3
1.4 Scope.....	4
1.5 Outline of the research .....	5
2 LITERATURE REVIEW .....	7
2.1 Introduction.....	7
2.2 Thermal cracking .....	7
2.3 Low temperature cracking .....	9
2.4 Thermal fatigue cracking .....	11
2.5 Factors affecting thermal fatigue cracking.....	12
2.5.1 Component material properties.....	13
2.5.2 Environmental factors .....	18

2.5.3	Asphalt mixture properties .....	21
2.6	Approaches to measuring the performance of asphalt concrete under thermal fatigue .....	24
2.6.1	Phenomenological approach.....	24
2.6.2	Mechanistic approach.....	24
2.7	Summary of previous researches on thermal fatigue cracking.....	25
2.8	General evaluation of previous thermal fatigue tests in the literature.....	26
2.8.1	Sample selection.....	26
2.8.2	Loading frequency.....	27
2.8.3	Type and shape of the loading.....	28
2.8.4	Rest time.....	30
3	METHODOLOGY AND MATERIALS .....	33
3.1	Introduction .....	33
3.2	Thermal coefficient test setup .....	33
3.2.1	Design and fabrication of thermal chamber .....	33
3.2.2	Programming .....	37
3.2.3	Measurement of thermal coefficient.....	38
3.2.4	Calibration of linear variable differential transformers (LVDT) .....	40
3.2.5	Preparation of beam specimens for thermal coefficient test .....	43
3.2.6	Sample preparation for thermal coefficient measurement tests .....	44
3.3	Thermal fatigue test setup .....	47
3.3.1	Test equipment .....	47
3.3.2	Programming for test protocol.....	48
3.4	The temperature difference for measuring thermal strain of asphalt concrete	63

3.5	Determination of thermal strains for applying cyclic haversine loading .....	63
3.6	Applying constant strain mode for semicircular bending geometry .....	64
3.7	Preparation of semicircular specimen for thermal fatigue test .....	65
3.8	Preparation of semicircular specimen for thermal fatigue test .....	66
3.9	Design of experiment .....	70
3.9.1	Multivariate analysis of design variables.....	76
3.10	Aggregate .....	77
3.10.1	Gradation and maximum density curve .....	77
3.10.2	Aggregate properties .....	79
3.11	Asphalt binder.....	80
3.12	Superpave method for mix design .....	82
3.13	Mixing and compacting temperature .....	82
3.13.1	Unmodified asphalt binder (50-70).....	82
3.13.2	Polymer modified asphalt binder .....	84
3.14	Asphalt mixture conditioning .....	86
3.15	Asphalt mixture compaction .....	87
3.15.1	Gyratory compaction parameters .....	88
3.16	Design aggregate structure.....	90
3.17	Optimum asphalt content for the design gradation .....	92
4	ANALYSIS OF TEST RESULTS AND DISCUSSION.....	95
4.1	Introduction.....	95
4.2	Results of measurement for thermal coefficient .....	95
4.3	Result of analysis for measured thermal coefficients .....	96
4.4	Stress analysis in semicircular bending test.....	100

4.4.1	Finite element analysis .....	100
4.4.2	Developing a viscoelastic material model .....	101
4.4.3	FEM analysis for stress distribution in semicircular bending test.....	106
4.5	Test results for the performance of asphalt concrete under thermal fatigue .	109
4.6	Determination of the slope of the line fitted to log-log scale data .....	111
4.7	Fatigue life extrapolation for reduced stiffness using the power model .....	112
4.8	Multivariate analysis for the number of loading cycles at different levels of reduced stiffness .....	114
4.8.1	Multivariate analysis for the number of loading cycles at 50% reduced stiffness.....	115
4.8.2	Multivariate analysis for the number of loading cycles at 25% reduced stiffness.....	132
4.8.3	Multivariate analysis for the number of loading cycles at 75% reduced stiffness.....	134
4.8.4	Multivariate analysis for stiffness modulus at 50% reduction .....	136
4.8.5	Multivariate analysis according to total dependent variables (number of loading cycles at 25%+50%+75%+reduced stiffness at 50%) .....	147
4.9	ANOVA results for rate of reduction in stiffness.....	148
4.10	Analysis of force – load line displacement (LLD) data .....	152
4.10.1	Determination of stiffness from load line displacement.....	152
4.10.2	Multivariate analysis for the number of loading cycles at different levels of reduced stiffness from load-line displacement curve.....	156
4.10.3	Statistical comparison of the results between two approaches.....	158
5	CONCLUSIONS AND RECOMMENDATIONS .....	161
5.1	Conclusions .....	161

5.2 Recommendation for future works .....	166
REFERENCES .....	167
APPENDICES	
A. Test designer code for thermal fatigue test .....	175
B. Programming code for Brookfield rotational viscometer .....	176
C. Stiffness calculated from bottom surface of the specimen (CMOD).....	181
D. Reduction in stiffness calculated from bottom surface of the specimen (CMOD).....	206
E. Bar charts and boxplots for cycle number at %25 reduced stiffness level (144 specimens).....	255
F. Bar charts and boxplots for cycle number at %75 reduced stiffness level (144 specimens).....	261
G. Stiffness reduction ratio calculated from bottom surface of the specimens ..	268
H. Reduction in stiffness, calculated from LLD-force curve.....	317
I. Stiffness from LLD .....	366
CURRICULUM VITAE .....	391

## LIST OF TABLES

### TABLES

Table 2.1. Selection of proper asphalt modifier for thermal fatigue experiment (Shell Bitumen Handbook- 2003) .....	16
Table 2.2. Measured coefficients of thermal expansion/contraction for AC in previous studies .....	23
Table 2.3. Recent laboratory studies on thermal fatigue cracking .....	26
Table 3.1. Thermal coefficients of LVDT and steel rod sample .....	43
Table 3.2. DTS16 test machine specifications .....	48
Table 3.3. Specifications for data acquisition system .....	48
Table 3.4. Input test parameters in Pre Test section .....	51
Table 3.5. Details of variables used in the design .....	71
Table 3.6. Standard matrix available for the fractional factorial design of <b>25 – 1</b> (NIST-Engineering Statistics Handbook) .....	72
Table 3.7. Design matrix for 1 Level 3 factor design.....	72
Table 3.8. Design matrix as a result of fractional factorial design <b>25 – 1 × 3</b> (3 replication).....	73
Table 3.9. Summary of specimen prepared for thermal coefficient measurement and thermal fatigue test .....	75
Table 3.10. Gradation type 1 .....	77
Table 3.11. Gradation type 2 .....	78
Table 3.12. Measured properties of coarse aggregates (larger than 4.75 mm).....	79
Table 3.13. Measured properties of fine aggregates (finer than 4.75 mm) .....	80
Table 3.14. Measured properties of asphalt 50-70 .....	80
Table 3.15. Measured properties of 50-70 polymer modified asphalt binder .....	81
Table 3.16. Design number of gyrations based on traffic levels according to Superpave method .....	89

Table 3.17. Design data at different asphalt contents (Mixture ID: BCM) .....	93
Table 3.18. Volumetric properties for different mixture .....	94
Table 4.1. Thermal coefficients of test specimens .....	96
Table 4.2. Statistic parameters and ANOVA results for thermal coefficient .....	97
Table 4.3. Prony series coefficients for asphalt mixture .....	103
Table 4.4. Multivariate analysis for number of loading cycles at 50 % reduced stiffness .....	117
Table 4.5. The average number of loading cycles at 50% reduced stiffness .....	118
Table 4.6. Multivariate analysis for number of loading cycles at 25% reduced stiffness .....	133
Table 4.7. The average number of loading cycles at 25% reduced stiffness .....	134
Table 4.8. Multivariate analysis for number of loading cycles at 75 % reduced stiffness .....	135
Table 4.9. The average number of loading cycles at 75% reduced stiffness .....	136
Table 4.10. Multivariate analysis for stiffness (50% reduction) .....	138
Table 4.11. Stiffness modulus of specimens at 50% reduction .....	139
Table 4.12. Multivariate test results for test variables (number of loading cycles at 25%+50%+75% reduced stiffness +reduced stiffness modulus at 50%) .....	147
Table 4.13. ANOVA results for slope of the fitted line .....	148
Table 4.14. The averaged measured slope for different specimens .....	149
Table 4.15. Multivariate analysis for number of loading cycles at different level of reduced stiffness calculated from LLD curve .....	157
Table 4.16. Comparison of statistical parameters for number of loading cycles at different levels of stiffness reductions for CMOD and LLD .....	160

## LIST OF FIGURES

### FIGURES

Figure 2.1. Thermal cracking plan view (Marasteanu et al. 2004).....	8
Figure 2.2. Fracture temperature of asphalt concrete .....	9
Figure 2.3. Example of low temperature cracking in asphalt concrete pavement (Minnesota department of transportation) .....	10
Figure 2.4. The mechanism for developing tensile stress by .....	11
Figure 2.5. Thermal stress versus temperature relationship for different test samples (Carpenter 1983).....	12
Figure 2.6. Diagram for components of asphalt concrete(Asphalt Institute 2014) .	13
Figure 2.7. Pavement distresses affected by asphalt binder (SHRP-A-410, 1994)	14
Figure 2.8. The acceptable range of asphalt content for different types of distresses(SHRP-A-410 1994).....	15
Figure 2.9. Air temperature and surface temperature as functions of time(Barber 1957).....	18
Figure 2.10. Pavement main distress modes in relation to rheological behavior of asphalt binders before and after aging (ASTM STP 1241, 1995) .....	20
Figure 2.11. Comparison between fatigue life of aged and unaged asphalt mixtures tested at 0.0004 Hz and different temperatures (Gerritsen and Jongeneel, 1999)...	20
Figure 2.12. Comparison between high frequency (40 Hz, 1) and low frequency (0.0004Hz, 2) fatigue test (A.h.Gerritsen and et.al 1989) .....	28
Figure 2.13. Variation of Measured strain under the wearing surface (Al-Qadi et al., 2005).....	29
Figure 2.14. Illustration of sinusoidal and haversine loading waveform .....	30
Figure 2.15. Number of cycles versus stiffness ratio with and without rest periods in load associated fatigue (Mamlouk et al. 2012a).....	31
Figure 3.1. Diagram for research methodology.....	34
Figure 3.2. Test set up for measuring the thermal coefficient of asphalt concrete..	35



Figure 3.3. General schematic of the thermal chamber for measuring thermal coefficient .....	35
Figure 3.4. Thermal chamber components: a) Heating resistor, b) Turbo fan & nitrogen nuzzle, c) Test set up .....	36
Figure 3.5. A view of the user interface program in the LabView program for measuring the thermal coefficient.....	39
Figure 3.6. LVDT installation for displacement measurement.....	40
Figure 3.7. Test setup for calibration of LVDT and steel rod using ceramic and steel beam.....	41
Figure 3.8. Deformation of steel and ceramic versus temperature variation .....	42
Figure 3.9. Gyrotory specimen section for cutting to obtain beam sample .....	43
Figure 3.10. <b>a)</b> Prepared beam specimens for thermal coefficient measurement, <b>b)</b> Beam specimens before and after aging according to (AASHTO R30 2006) .....	44
Figure 3.11. Mounting support pads on beam samples for thermal coefficient measurement .....	45
Figure 3.12. Mounting LVDT on beam specimen for measuring thermal coefficient .....	46
Figure 3.13. Thermal fatigue test setup.....	47
Figure 3.14. Schematic diagram of a) closed-loop diagram. b) PID controller.....	49
Figure 3.15. The loading section in the test navigation menu .....	52
Figure 3.16. A view of the Testlab program showing test data in the test navigation menu.....	53
Figure 3.17. A real-time tuning in the test navigation menu .....	54
Figure 3.18. A view of the Testlab program showing loading parameter in the test designer .....	56
Figure 3.19. A view of the Testlab program showing loading profile in the test designer .....	58
Figure 3.20. A view of the Test lab program showing test state sequence in the test designer .....	59

Figure 3.21. A view of the Testlab program showing calculations in the test designer.....	61
Figure 3.22. The waveform for applied force on the specimen.....	64
Figure 3.23. The waveform for strain at the bottom center of the specimen.....	65
Figure 3.24. <b>a)</b> Sliced SGC specimen 35mm from center, <b>b)</b> cutting cylinder sample to obtain semicircular specimen, <b>c)</b> cut semicircular samples. ....	66
Figure 3.25. <b>a)</b> Mounting steel knives to CMOD measurement using steel beam, <b>b)</b> Mounting point gauge for LLD using a template. ....	67
Figure 3.26. Attachment of gauges and LVDT to measure strains from CMOD and LLD .....	68
Figure 3.27. Schematic SCB test setup to measure thermal fatigue resistance .....	69
Figure 3.28. Diagram of the experimental design .....	70
Figure 3.29. Selected aggregate gradation type 1 (Coarse).....	78
Figure 3.30. Selected aggregate gradation type 2 (Fine).....	79
Figure 3.31. Comparison between measured viscosity of neat asphalt and polymer modified asphalt .....	81
Figure 3.32. Mixing and compaction temperature for 50-70 asphalt binder(ASTM D2493 2000).....	83
Figure 3.33. Frequency sweep test results at high temperatures .....	85
Figure 3.34. Binder master curve @ reduced frequency .....	85
Figure 3.35. Loose HMA conditioned samples in the oven at compaction temperature .....	86
Figure 3.36. Sample compaction by gyratory compactor for Superpave design method (AASHTO T 312 2019).....	87
Figure 3.37. Compacted mix design samples according to the Superpave method	88
Figure 3.38. Compaction curve of a design sample (Mixture ID: BCM).....	90
Figure 3.39. Densification curve obtained from a compacted sample (Mixture ID: BCM) .....	91
Figure 3.40. Plots of percent VMA, Percent air voids, Percent VFA, and density versus percent asphalt content (Mixture ID: BCM) .....	92

Figure 4.1. Thermal coefficient for different mixtures based on the aggregate type	98
Figure 4.2. Thermal strain versus temperature .....	99
Figure 4.3. Setup for semicircular bending test .....	100
Figure 4.4. Dynamic modulus versus reduced frequency at 4° C .....	102
Figure 4.5. Haversine loading according to target strain in the middle of the bottom surface of specimen at different frequencies (from FEM analysis).....	104
Figure 4.6. Stress versus strain in the middle of bottom surface of specimen at different frequencies (from FEM analysis) .....	105
Figure 4.7. Tensile strain components from FEM analysis in the middle of bottom surface of semicircular specimen at low frequency loading (0.01 Hz).....	105
Figure 4.8. Tensile strain components from FEM analysis in the middle of bottom surface of semicircular specimen at high frequency loading (0.1Hz).....	106
Figure 4.9. Finite element meshed model and horizontal stress contour.....	107
Figure 4.10. Finite element meshed model and horizontal strain contour.....	107
Figure 4.11. Horizontal stress and strain distribution at the bottom surface and along the X axis .....	108
Figure 4.12. Horizontal stress and strain distribution along the Y axis of the specimen .....	109
Figure 4.13. Applied thermal strain at the bottom of semicircular specimen (Specimen ID: BFMAH10).....	110
Figure 4.14. Stiffness versus number of loading cycles for test specimen (Specimen ID: BFMAH0).....	111
Figure 4.15. Slopes of fitted lines in a logarithmic scale for two different specimens .....	112
Figure 4.16. Power model fitted for stiffness versus number of loading cycles (Specimen ID:BFMAH0).....	113
Figure 4.17. Number of loading cycles versus stiffness (log scale) .....	114
Figure 4.18. Stiffness reduction versus number of loading cycles for two mixtures with similar ID and different asphalt types .....	119

Figure 4.19. The average number of loading cycles for different mixtures at 50% reduced stiffness, grouped based on the asphalt type.....	119
Figure 4.20. Box plot for number of loading cycles at 50% reduced stiffness, grouped based on the asphalt type.....	120
Figure 4.21. Stiffness reduction versus number of loading cycles for two mixtures with similar ID and different loading frequency .....	121
Figure 4.22. The average number of loading cycles for different mixtures at 50% reduced stiffness, grouped based on the loading frequency .....	122
Figure 4.23. Box plot for number of loading cycles at 50% reduced stiffness, grouped based on the loading frequency .....	122
Figure 4.24. Stiffness reduction versus number of loading cycles for two mixtures with similar ID and different aggregate type.....	123
Figure 4.25. The average number of loading cycles for different mixtures at 50% reduced stiffness, grouped based on the aggregate type.....	124
Figure 4.26. Box plot for number of loading cycles at 50% reduced stiffness, grouped based on the aggregate type.....	125
Figure 4.27. Stiffness reduction versus number of loading cycles for mixtures with similar ID and different gradations.....	126
Figure 4.28. The average number of loading cycles for different mixtures at 50% reduced stiffness, grouped based on the gradation .....	126
Figure 4.29. Box plot for number of loading cycles at 50% reduced stiffness, grouped based on the gradation.....	127
Figure 4.30. Stiffness reduction versus number of loading cycles for mixtures with similar ID and different rest times .....	128
Figure 4.31. The average number of loading cycles for different mixtures at 50% reduced stiffness, grouped based on the rest time .....	128
Figure 4.32. Box plot for number of loading cycles at 50% reduced stiffness, grouped based on the rest time .....	129
Figure 4.33. Stiffness versus number of loading cycles for mixtures with different aging condition .....	130

Figure 4.34. The average number of loading cycles for different mixtures at 50% reduced stiffness, grouped based on the rest time.....	131
Figure 4.35. Box plot for number of loading cycles at 50% reduced stiffness, grouped based on the aging.....	131
Figure 4.36. The average stiffness modulus at 50 % reduction grouped based on asphalt type .....	140
Figure 4.37. Box plot of average stiffness at 50% reduction grouped based on asphalt type .....	140
Figure 4.38. The average stiffness modulus at 50 % reduction grouped based on aggregate type .....	141
Figure 4.39. Box plot of average stiffness at 50% reduction grouped based on aggregate type .....	142
Figure 4.40. The average stiffness modulus at 50 % reduction grouped based on loading frequency.....	143
Figure 4.41. Box plot of average stiffness at 50% reduction grouped based on loading frequency.....	143
Figure 4.42. The average stiffness modulus at 50% reduction grouped based on aging.....	144
Figure 4.43. Box plot of average stiffness at 50% reduction grouped based on aging .....	145
Figure 4.44. The average stiffness modulus at 50 % reduction grouped based on gradation .....	146
Figure 4.45. Box plot of average stiffness at 50% reduction grouped based on gradation .....	146
Figure 4.46. The average slope for specimens grouped based on asphalt type ....	150
Figure 4.47. The average slope for specimens grouped based on aggregate type	150
Figure 4.48. The average slope for specimens grouped based on loading frequency .....	151
Figure 4.49. The average slope for specimens grouped based on gradation .....	151

Figure 4.50. Load versus load-line displacement relationship for a test specimen .....	153
Figure 4.51. Load versus LLD for two specimens with similar ID and different aging conditions.....	154
Figure 4.52. Stiffness and strain versus number of loading cycles calculated from LLD (specimen ID: LCMAH0).....	154
Figure 4.53. Stiffness versus number of loading cycles calculated from LLD and CMOD for specimens with similar ID and different asphalt type.....	155
Figure 4.54. Comparison of number of loading cycles at 25% reduced stiffness obtained from CMOD and LLD for all specimens.....	158
Figure 4.55. Comparison of number of loading cycles at 50% reduced stiffness obtained from CMOD and LLD for all specimens.....	159
Figure 4.56. Comparison of number of loading cycles at 75% reduced stiffness obtained from CMOD and LLD for all specimens.....	159

## LIST OF ABBREVIATIONS

### ABBREVIATIONS

**A:** Aged

**AASHTO:** American Association of State Highway and Transportation Officials

**ANOVA:** Analysis of Variance

**ASTM:** American Society for Testing and Materials

**$\alpha$ :** Thermal Coefficient

**B:** Basalt Aggregate

**C:** Coarse Aggregate

**CMOD:** Crack Mouth Opening Displacement

**F:** Fine Gradation

**FEM:** Finite Element Analysis

**FHWA:** Federal Highway Administration

**H:** High Frequency

**HMA:** Hot Mix Asphalt

**L:** Limestone Aggregate

**LLD:** Load Line Displacement

**LVDT:** Linear Variable Displacement Transducer

**M:** Modified Asphalt Binder

**MEPDG:** Mechanistic-Empirical Pavement Design Guide

**N:** Neat Asphalt Binder

**RTD:** Resistance Temperature Detector

**S:** Low Frequency

**SBS:** Styrene Butadiene Styrene

**Superpave:** Superior Performing Asphalt Pavements

**SHRP:** Strategic Highway Research Program

**TGDH:** Turkish General Directorate of Highways

**TSRST:** Thermal Stress Restrained Specimen Tests

**U:** Unaged



# CHAPTER 1

## INTRODUCTION

### 1.1 Background

In Turkey, asphalt pavements comprise around 95% of the entire roadway network, 28% percent of which is constructed by asphalt concrete pavements in motorways and intercity highways. In asphalt concrete pavements, distresses caused by the climatic and diurnal temperature changes are one of the most common reasons for deterioration after the traffic and moisture related distresses. The decrease in temperature as low as  $-20^{\circ}\text{C}$  in the East and West Interior Anatolian regions and the increase in the daytime-nighttime temperature cycles will eventually result in the development of thermally induced cracks, which reduce the useful service life of the pavements. As a consequence, the infiltration of rainfall and melting water into these cracks leads to serious structural damages in the subgrade, and also increase the potential for spalling in the crack regions by the effect of filling debris. As a result, thermal related distresses will eventually result in degradation in the driving comfort and traffic safety in addition to elevating the maintenance and rehabilitation costs of roadways.

Thermal fatigue cracks, as being one of the most important reasons for the thermally induced distresses in asphalt concrete pavements, becomes a crucial factor leading to serious structural problems. Thermal distresses in asphalt concrete can be assessed in two ways: Low temperature cracking and thermal fatigue cracking. Low temperature cracking occurs because of a drastic drop in pavement temperature in very cold environments. At low temperatures because of contraction, the induced tensile stress exceeds tensile strength of asphalt concrete and micro cracks appear in

the pavement. Thermal fatigue cracking is more common in regions with intermediate temperatures. This thermal distress, unlike low temperature cracking, does not occur immediately. The main mechanism responsible for the development of thermal fatigue cracks is the high temperature variations occurring during daytime and nighttime temperature cycles. When contracted under low temperature conditions, the wearing course is subject to high tensile stresses during these thermal changes due to generated restraint between the wearing course and the underlying layers. After a long cycle of these thermal changes, even if no visible cracks develop, the rigidity of the surface course will be reduced by the inception of micro cracks, and hence increasing the rate of crack growth under traffic loading. For instance, in Ankara, it is found that the maximum temperature differentials can increase up to 20 °C, and the maximum frequency of temperature differential is as high as 10°C, being enough to initiate thermal fatigue cracking in asphalt pavements. In the literature, it is discovered that only a limited study exists for thermal fatigue cracking phenomenon. In this research, a new methods has been proposed to develop the existing thermal fatigue testing procedure and the selection of test parameters representing the actual field conditions. In the initial step, previous research efforts regarding the thermal fatigue cracking have been investigated in detail. The fundamental parameters for the study are identified from two points of view; the results and the testing time for thermal fatigue tests. These fundamental parameters include specimen geometry, frequency of repeated loading, and computation of applied loading according to field conditions. This research aims at developing a new testing method for the thermal fatigue test and also investigating the behavior of various asphalt mixtures used in Turkey.

## **1.2 Research objectives**

Upon the completion of this proposed research, a new test method will be developed by selecting not only different specimen size and geometry but also loading condition

to represent the thermal fatigue phenomenon for asphalt concrete pavements. To achieve this, a semi-circular test specimen is proposed based on the results of finite element analysis as an alternative to the conventional beam specimen used in a four-point beam fatigue test. A new approach for loading pattern that simulates the thermal fatigue phenomenon of asphalt concrete is also developed. In the final phase of the study, important mixture properties for thermal fatigue performance of asphalt concrete is investigated using statistical analyses of variance methods. It is believed that the research outcomes will contribute to the national and international knowledge considering the fact that there is only a limited study available in the literature on the thermal fatigue phenomenon of asphalt concrete. The study outcomes will contribute to the existing knowledge on the thermal behavior of asphalt concrete pavements, which can help engineers conduct better design practices for long lasting pavements without frequent maintenance and rehabilitation.

### **1.3 Originality of the topic**

The originality of this research rests on using different specimen geometry and test method to investigate thermal fatigue behavior of asphalt concrete. In the literature, only a limited number of studies is available on thermal fatigue behavior of asphalt concrete. In the scope of this research, instead of using prismatic beam specimen, semicircular specimens are obtained directly from the Superpave compactor samples. Thus, the sample preparation process is simplified, and the problems associated with standard beam specimens are eliminated.

The other contribution is that the selection loading frequency and the amplitude of applied loading for thermal fatigue testing. In many of the reported studies in the literature, loading frequency is selected without any consideration of slow process of thermal fatigue, and the applied loading and its amplitude don't represent field conditions. In this study, however, loading magnitude is determined based on the maximum frequency of daily temperature variations ( $\Delta T$ ), This temperature

differential is used together with the thermal coefficient of asphalt concrete to calculate the loading amplitude, which is assumed to be reached in the field under daily temperature cycles.

#### **1.4 Scope**

The study for this research was started by preparing asphalt mixture samples to prepare test specimens. Various mixture samples with different gradations, aggregate type, asphalt modification, and aging condition were prepared according to the Superpave design method for this inquiry. Test specimens were obtained directly from cylindrical samples produced by the Superpave gyratory compactor. In this study, two types of specimens were used: the beam specimen for thermal coefficient measurements and semicircular specimen for the thermal fatigue tests.

To simulate the induced thermal strain by daily temperature fluctuations in asphalt concrete, a thermal coefficient measurement test was conducted. Due to special requirements of this test a thermal chamber was fabricated in the laboratory, which is insulated for high temperature range. The thermal coefficient of different mixtures was obtained by measuring displacements during the contraction of specimens inside the chamber.

Based on the thermal strain results from the thermal coefficient measurements, Three-point bending fatigue test in the strain control mode was conducted on semicircular specimens to assess asphalt concrete performance under thermal fatigue. Since the strain measurement was the main part of this test, FEM analysis was employed to investigate stress and strain distribution in the specimens. The length of strain gauge and required initial load to achieve target strain in the specimen under bending were determined based on the FEM analysis results.

The thermal fatigue tests were executed at 4°C to simulate an intermediate temperature environment. Thermal fatigue test included two stages: conditioning and main loading. The main loading was performed in the strain control mode (applied

load was modified over the test duration to achieve pre-defined strain and remain constant at that level) at two frequencies and three rest times.

Reduction in stiffness modulus was selected as a criterion to compare various specimens with different mix design variables. ANOVA and multivariate analysis were applied to the results of thermal coefficient measurement and thermal fatigue test, respectively. As a result of statistical analyses, the significance of different variables, including mix design variables and test loading variables, for the performance of asphalt concrete under thermal fatigue tests, were investigated.

## **1.5 Outline of the research**

The background overview, research objectives, scope, and outline of research are included in Chapter 1. Efforts for thermal fatigue cracking of asphalt concrete is presented in Chapter 2. The review includes a summary of research outcomes on the effect of mixture properties, climatic properties, test samples geometries, test set-up used to measure thermal fatigue cracking, and some modeling efforts to address the thermal fatigue cracking performance of asphalt concrete pavements.

In Chapter 3, methodology of research and sample preparation procedure in accordance with the related standards (including data collection tools and analysis methods) considering reference literature (and, if necessary preliminary studies) is explained in a consistent manner. Chapter 4 is dedicated to the statistical analysis of findings obtained from the thermal coefficient measurement and thermal fatigue test. In addition, significant mix design variables needed to address the thermal fatigue cracking are identified and incorporated in various statistical models. Chapter 5 highlights the derived conclusions from the study and future works to enhance the applicability of the proposed method.



## **CHAPTER 2**

### **LITERATURE REVIEW**

#### **2.1 Introduction**

This chapter delineates the concept and the mechanism for thermal fatigue cracking in asphalt concrete (AC) pavements. Also explained in this chapter is the factors important for thermal fatigue, different testing approaches, and general evaluation of previous studies based on the influential parameters for thermal fatigue tests, such as specimen geometry, loading frequency, loading wave shape, and rest time.

#### **2.2 Thermal cracking**

Asphalt concrete pavements are prone to thermal distresses when exposed to extreme variation of ambient temperatures. This form of distress is a common issue in northern climates, is called thermal cracking or transverse cracking. Thermal cracks generally occur at very cold ambient or under relatively cold thermal cycles. As shown in Figure 2.1, thermal cracks are revealed as groups of transverse cracks that spread across the AC pavement surface and are perpendicular to the longitudinal direction of the roadway. Some researchers noticed that thermal cracks appear at 6 m to 9 m intervals, but this range may change from 1m to 30m (Yoder and M. W. Witczak 1975); however, it was found that for any specific pavement, spacing of the cracks becomes consistent.

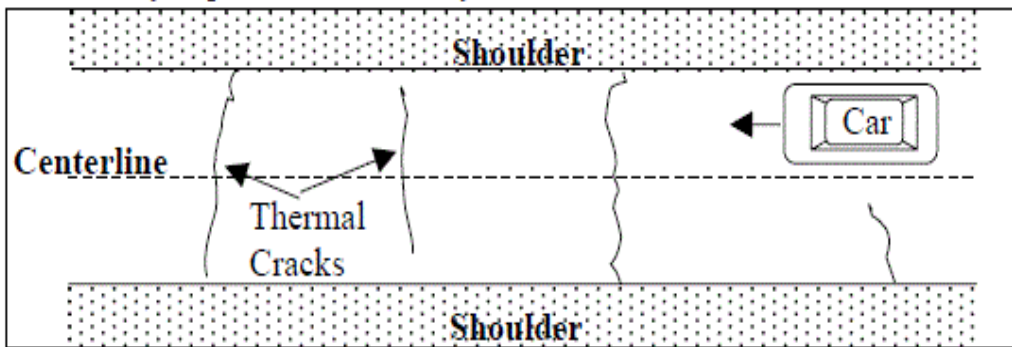


**Figure 2.1.** Thermal cracking plan view (Marasteanu et al. 2004)

After the thermal cracks expand throughout the pavement section, water and fines move into and out of the pavement structure. The first effect of water presence inside the pavement is separating the aggregate from the asphalt binder, which damages the pavement structure. During the cold season, penetration of defrosting solution into the base layer through the crack can result in thawing of the base layer and depression in the crack. Upward lipping at the crack edge because of ice formation beneath the crack is another problem generated by this type of distress, which affects riding quality. Many researchers consider two types of thermal cracking: low temperature cracking and thermal fatigue cracking. Low temperature cracking occurs when the induced thermal stress exceeds the asphalt concrete tensile strength (Figure 2.2). This mode of thermal distress appears at a cold temperatures like the northern regions. More details about low temperature cracking is presented in the next section of this chapter. Thermal fatigue cracking occurs when the daily temperature variations induce fatigue in asphalt concrete and eventually exceed asphalt concrete fatigue resistance. Thermal fatigue cracking is a common thermal distress mode in relatively low and moderate temperatures.



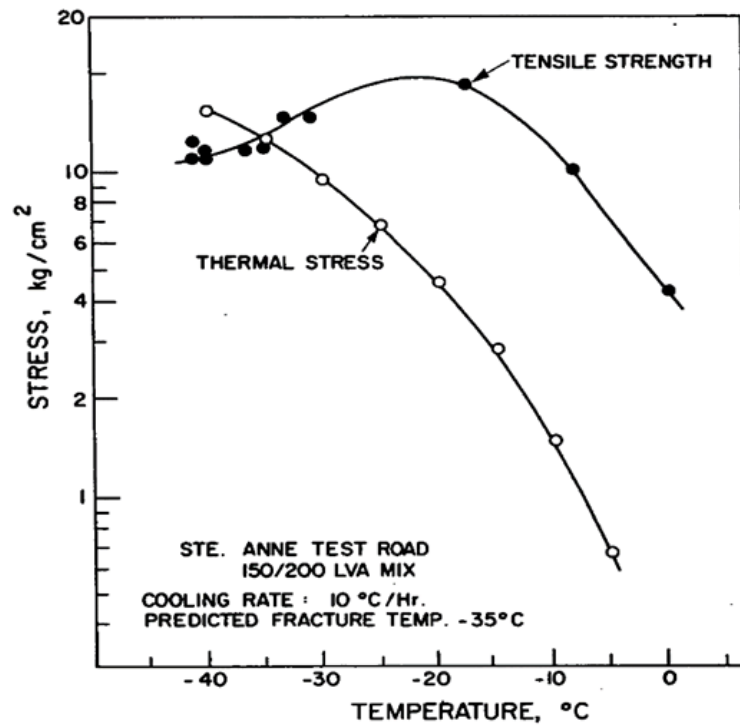


Figure 2.2. Fracture temperature of asphalt concrete

### 2.3 Low temperature cracking

Low temperature cracks in asphalt concrete pavements are commonly seen in areas where air temperature falls below  $-20\text{ }^{\circ}\text{C}$ , or so low that the developed thermal stress exceeds the thermal strength of asphalt concrete and cause cracks. Low temperature cracking reduces the roadway's driving comfort by the increased surface roughness due to fractures, leading to the seepage of melting snow and rainfall water into the subgrade through the surface cracks and causes loss of bearing capacity. Combined with the disruption caused by traffic loading, low temperature cracking weakens the structural integrity of the pavement and eventually increases roadway maintenance and rehabilitation costs. According to research conducted by (Witczak et al. 2002), low temperature cracking is one of the main reasons for pavement deterioration, which is ranked as a second factor in roadway maintenance and repair costs in the United

States. Low temperature cracking is developed perpendicular to the travel direction and is usually formed at equal intervals ranging from 1 to 100 m (Figure 2.3).



**Figure 2.3.** Example of low temperature cracking in asphalt concrete pavement (Minnesota department of transportation)

The mechanism responsible for low temperature cracking is described by the severe reduction in field temperature that is low enough to develop low temperature cracking. In other words, when the air temperature drops, the pavement experiences contraction, and the friction between the pavement and the base layer resists against the contraction, causing an increase in the tensile stress. When the tensile stress induced in the pavement exceeds the strength of the asphalt concrete, micro cracks will develop at the edge and surface of the pavement (Figure 2.4). At colder temperatures or repeated temperature cycles, the cracks will propagate through the full depth and the width of the asphalt concrete layer.

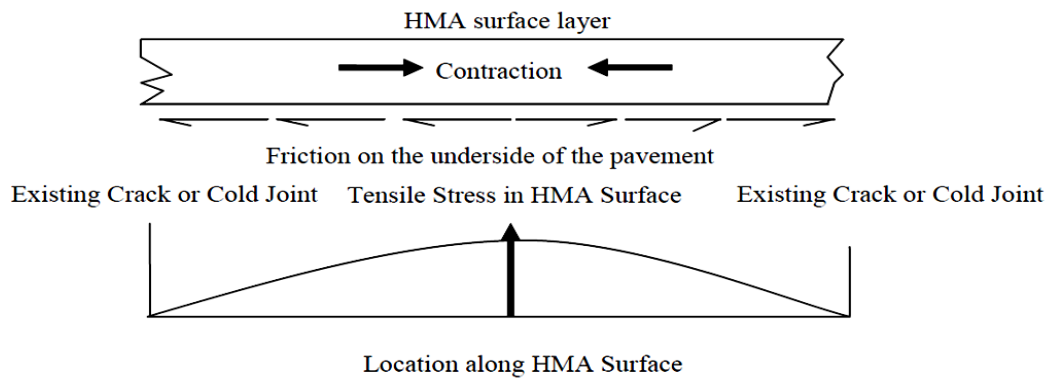


**Figure 2.4.** The mechanism for developing tensile stress by volumetric shrinkage in wearing course

## 2.4 Thermal fatigue cracking

Asphalt concrete pavement is restrained by the base layer, volumetric contraction because of daily temperature variations, cause cyclic tensile stresses. Transverse cracking due to cyclic stresses at low temperatures above the glass transition temperature of asphalt concrete has been referred to as thermal fatigue cracking. In moderate climates, daily temperature variation occurs at higher temperatures than low temperature cracking, so thermal stresses are not large enough to cause a quick fracture. However, over time these thermal stresses can induce fatigue similar to load associated fatigue in the AC pavements. According to a study by (Carpenter ,1983), thermal fatigue occurrence is expected at a temperature range between  $-7^{\circ}\text{C}$  ( $20^{\circ}\text{F}$ ) and  $21^{\circ}\text{C}$  ( $70^{\circ}\text{F}$ ). At higher temperatures, the pavement is in the stress relaxation mode, and at temperatures below the  $-7^{\circ}\text{C}$ , low temperature cracking becomes the prevailing distress mode (Figure 2.5).

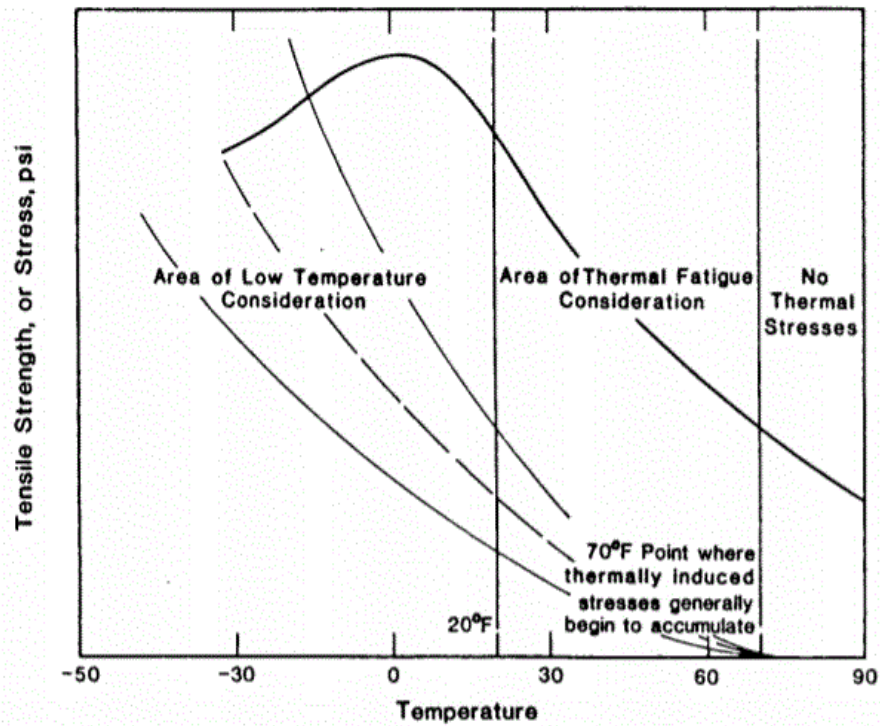


**Figure 2.5.** Thermal stress versus temperature relationship for different test samples (Carpenter 1983)

## 2.5 Factors affecting thermal fatigue cracking

It is known that material, environmental factors, and also asphalt mixture properties are effective in the formation of thermal cracks in asphalt concrete. Previous studies indicate that several factors affect the thermal resistance of asphalt concrete against thermal cracking (Vinson et al. 1989). Among these factors, mixture properties, environmental factors, and asphalt concrete properties are the most significant ones that need further discussion, as given in the below section.

### 2.5.1 Component material properties

The components of asphalt concrete consist of aggregate, asphalt binder, and air voids (Figure 2.6). Asphalt modifier, as an additive to asphalt binder to improve its thermal behavior or other properties, can also be considered one of the contributing factors for thermal fatigue. Aggregates constitute 90 to 95 percent of asphalt concrete by mass of total mixture, and adequate gradation, strength, and toughness are the required properties for mixture stability. The asphalt binder constitutes 4 to 7 percent of asphalt concrete by mass. Selecting the proper grade of asphalt binder according to traffic and climate condition is necessary for AC pavement design. The components of asphalt concrete control its mechanical response under different conditions. The thermal behavior of AC is also profoundly affected by the properties of mixture components. These properties include asphalt binder, asphalt content, asphalt binder modification, aggregate source, gradation, and air voids. A brief discussion of these factors is given in the below sections.

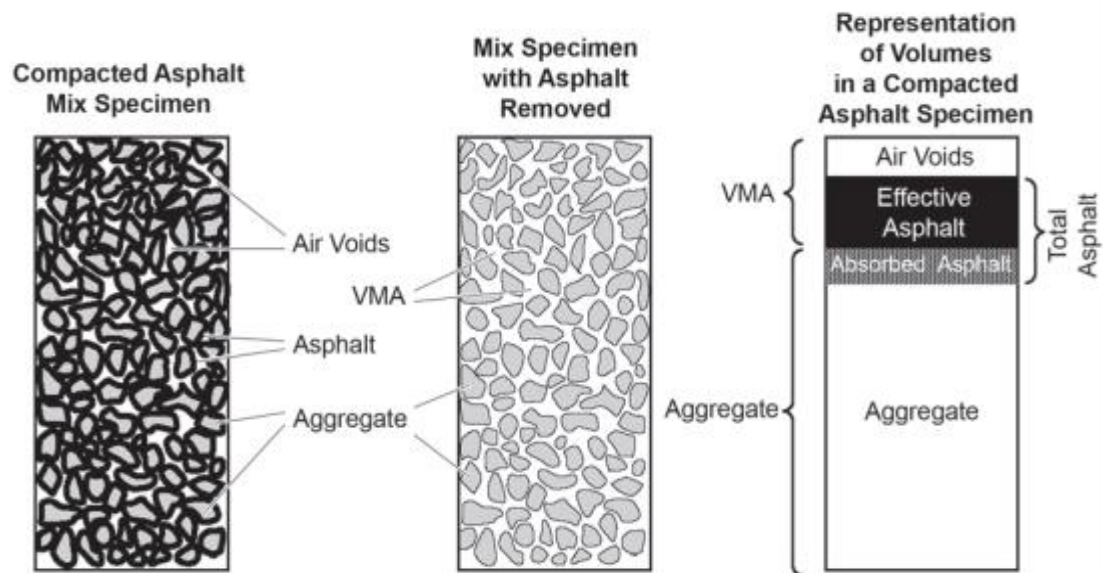


**Figure 2.6.** Diagram for components of asphalt concrete(Asphalt Institute 2014)

### a) Asphalt binder grading

It is understood that the essential material component in terms of thermal fatigue cracking of asphalt concrete is the asphalt binder. Notably, it is demonstrated that the degree of penetration of asphalt binder has a strong relationship with low temperature cracking strength; the mixtures containing low penetration asphalt have a higher cracking temperature or lower cracking resistance. In recent years, it is common practice to improve asphalt concrete's low temperature performance by adding polymer modified additives to asphalt. One common polymer modified additive to avoid thermal cracking in asphalt concrete is Styrene Butadiene Styrene (SBS), this additive by enhancing elastic properties of asphalt binder increases the flexibility of AC pavements at low temperatures.

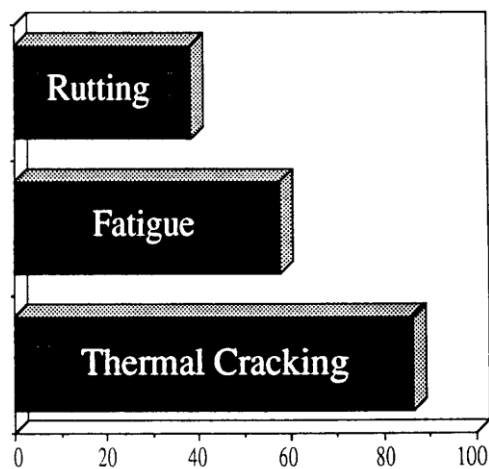


**Figure 2.7.** Pavement distresses affected by asphalt binder (SHRP-A-410, 1994)

## b) Asphalt content

Asphalt content must be sufficient to provide adequate workability and durability, and not so large to cause bleeding, rutting, and instability in asphalt concrete (Harvey et al. 1995). The acceptable range of asphalt content for different types of distresses is shown in Figure 2.8. Since asphalt binder's thermal conductivity is greater than that of aggregate, the higher asphalt content increases the thermal coefficient of asphalt concrete. At the same time, higher asphalt content results in thicker asphalt film that transfer stresses through the mixture; therefore, stress and strain in asphalt binder decrease. It is also known that increased asphalt content reduces the initial stiffness of the mixture (ASTM STP 1265 1995). As an overall effect, the raised asphalt content improves the performance of AC pavements against thermal fatigue significantly.

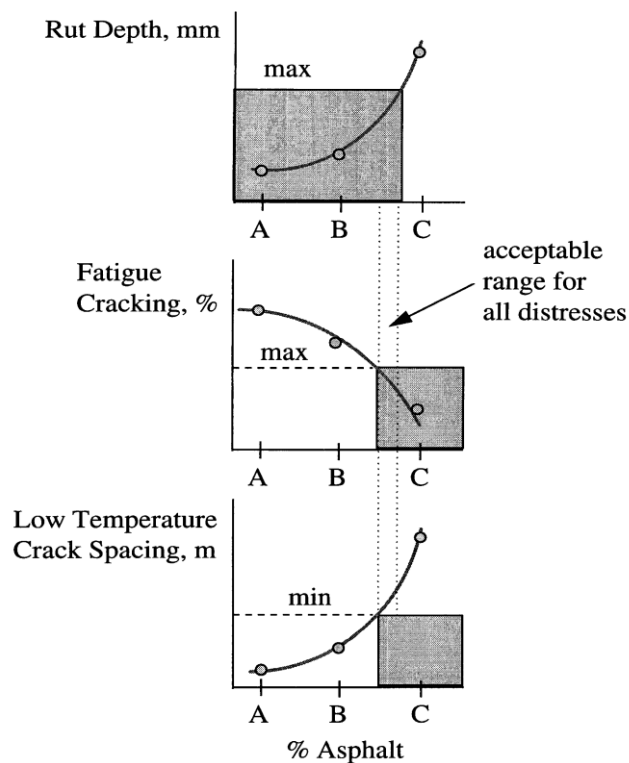


**Figure 2.8.** The acceptable range of asphalt content for different types of distresses(SHRP-A-410 1994)

### c) Asphalt binder modification

Many modifiers are used in paving applications to improve temperature related properties of asphalt binder. Generic types of modifiers can be classified into eight groups: mineral fillers, extenders, polymers, crumb rubbers, oxidants, hydrocarbons, anti-strips, fibers, antioxidants (Bahia, Hussain 1996). The most common additives to modify asphalt binders for highways and airports are the polymers, which can be manufactured in two types, plastomers, and elastomers. Plastomers make binders stiffer and reduce the binder's temperature susceptibility, so AC pavements containing plastomer modifiers would be less useful to resist low temperature and thermal fatigue cracking. On the other hand, elastomer modifiers improve the elastic recovery of asphalt binders by using Styrene Butadiene (SB), Styrene Butadiene Rubber (SBR), and Styrene Butadiene Styrene (SBS), which is also used in this study, are the conventional elastomers in pavement applications. Epps (1999) found that using a crumb rubber modifier as an additive also enhances the thermal fatigue performance of asphalt concrete. Table 2.1 summarize the effect of known additives against different distresses in AC pavements.

**Table 2.1.** Selection of proper asphalt modifier for thermal fatigue experiment (Shell Bitumen Handbook- 2003)

Type of Modifier	Permanent deformation	Thermal cracking	Fatigue cracking	Moisture damage	Aging
Elastomers	✓	✓	✓		✓
Plastomers	✓				
Tire rubber		✓	✓		
Carbon black	✓				✓
Lime				✓	✓
Sulphur	✓				
Chemical	✓				
Antioxidants					✓
Adhesion				✓	✓
Hydrated Lime				✓	✓



#### **d) Aggregate source and gradation**

Many studies have been conducted on the effect of aggregate type and mixture gradation on low temperature cracking, but only a few studies are available in the literature on the effect of aggregate type and gradation on the thermal fatigue performance of asphalt concrete. A review of previous studies indicates that there is no consensus about the significance of gradation and aggregate type for low temperature cracking resistance; however, it was reported by many researchers that aggregate with high resistance to freeze-thaw cycles and low absorption is more resistant against thermal cracking. It is believed that absorptive aggregates reduce the strength of asphalt concrete at low temperatures because more asphalts would be absorbed to aggregate, and therefore the film thickness necessary for bonding will be less as compared to a mixture with non-absorptive aggregate. In a study by (Epps, 1999), the difference between the effect of dense gradation and gap gradation on the thermal fatigue performance of test samples was evaluated, and the results showed that the difference was statistically significant. (Arabzadeh 2015) also researched to investigate how mixture design variables affect the thermal fatigue behavior of asphalt concrete. Their findings indicated that aggregate type and gradation were highly influential parameters for asphalt concrete thermal fatigue resistance.

#### **e) Air void content**

Air void content plays a significant role in the performance of asphalt concrete. AC pavements with lower air void content (<3%) are prone to rutting and bleeding. On the other hand, pavements with very high air void content are susceptible to stripping and aging because of excessive oxidation. Reduced air void content improves the performance of asphalt concrete against fatigue (thermal and load associated) for the following reasons. Lower air void in asphalt concrete results in a more homogenous mixture. Therefore, stress concentration reduces, especially in contact location of aggregates. Because of the reduction in size and number of voids, micro-cracks

development would decrease, and cracks formation would be delayed. Another explanation for this behavior is related to oxidation. Mixtures with decreased porosity allow less aging by oxidation(Harvey et al. 1995).

## 2.5.2 Environmental factors

### a) Temperature

The pavement temperature depends on the ambient temperature (Figure 2.9), so the air temperature can be considered as the most influential parameter for low temperature cracking and thermal fatigue cracking. Sudden thermal cracks can be formed when the pavement surface temperature drops down to the fracture temperature of asphalt concrete, which is not necessarily higher than its glass transition temperature. Daily temperature variations cause thermal stresses, and when the repeated stresses exceed the AC surface layer's fatigue resistance, thermal cracks will develop. Field experiments (Al-Qadi et al. 2005) showed that temperature variation could cause a high strain variation of 350  $\mu\text{m}/\text{m}$  in AC pavements. Since applying thermal cycles in the laboratory is time consuming, using loading cycles at low frequency to simulate daily temperature fluctuation seems reasonable.

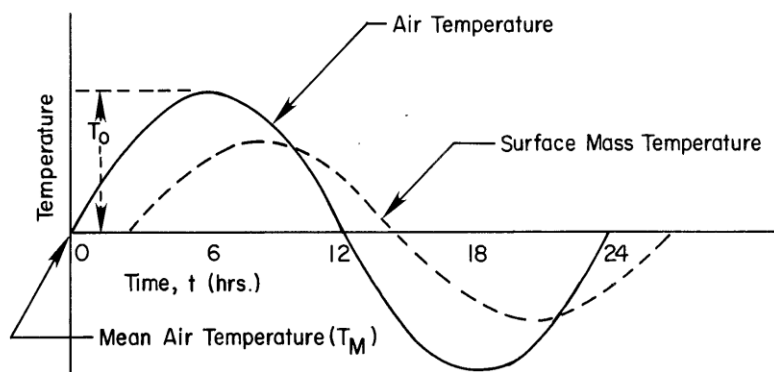


**Figure 2.9.** Air temperature and surface temperature as functions of time(Barber 1957)

## **b) Pavement aging**

Asphalt concrete aging in the field can be divided into two stages: short term aging and long term aging. Short term aging occurs when the asphalt mixture is exposed to very high temperature during the production in the plant and during the compaction in the field. In this stage, the chemistry of asphalt binder changes because of volatilization and oxidation. Volatilization occurs due to the evaporation of lighter components at very high temperatures, and oxidation takes place due to the chemical reaction of asphalt bitumen with oxygen. The second stage of asphalt concrete aging, which is also termed as long term aging, continues during the service life of asphalt concrete, in which case the oxidative aging becomes a dominant factor as the aging rate gets slower in comparison with the short term aging process.

Figure 2.10 shows how aging changes the asphalt binder rheology in different stress modes. Aging causes AC layers to be stiffer and more brittle, increasing the potential for thermal cracks and load associated cracks under traffic loading. It was reported by Jung & Vinson (1994) that the fracture and the glass transition temperature of AC layers were significantly affected by aging, and the aged specimen failed at a higher temperature, and the fracture strength of the aged specimen was lower than unaged ones. Jackson & Vinson (1992) conduct a study to evaluate thermal fatigue in asphalt concrete, and they found that in the absence of environmental aging, thermal fatigue would not be dominant distress in the early years of asphalt concrete pavement. As shown in Figure 2.11, A.h.Gerritsen & et.al (1989) simulated thermal fatigue by performing a fatigue test at very low frequency and at two temperatures of 0° C and 10°C. One of the objectives of this study was to evaluate the fatigue life of asphalt concrete subjected to severe aging. A dramatic drop was discovered in the fatigue resistance of the test samples at 0° C due to aging when loading was performed at high strain levels which resulted in a brittle fracture rather than cracking propagation by the thermal fatigue process. However, at low strain levels aged samples outperformed unaged ones.

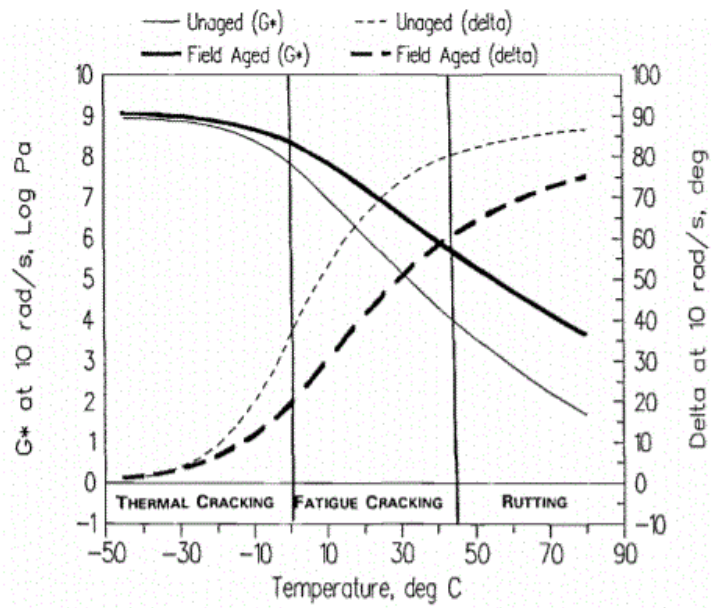


**Figure 2.10.** Pavement main distress modes in relation to rheological behavior of asphalt binders before and after aging (ASTM STP 1241, 1995)

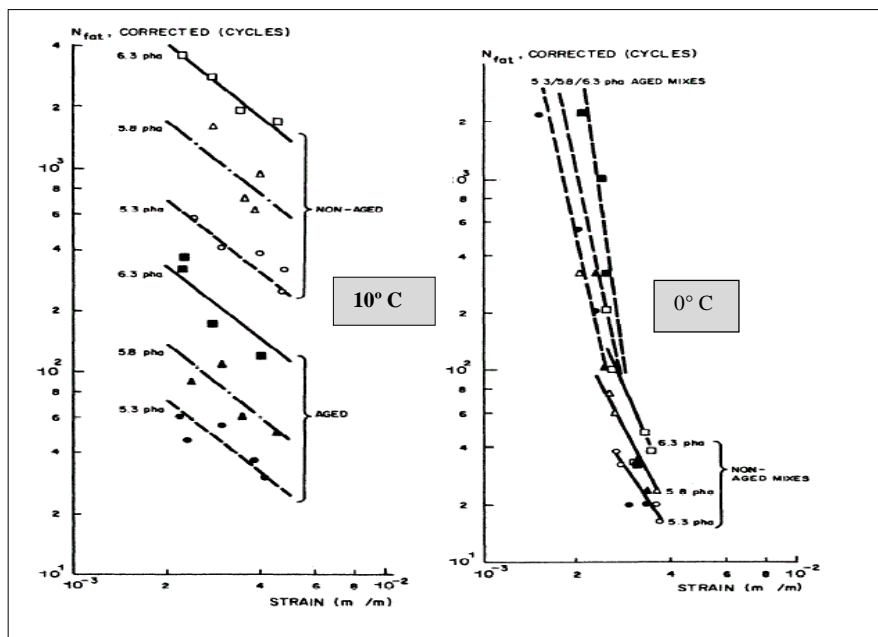


**Figure 2.11.** Comparison between fatigue life of aged and unaged asphalt mixtures tested at 0.0004 Hz and different temperatures (Gerritsen and Jongeneel, 1999)

### **2.5.3 Asphalt mixture properties**

Since the mechanistic based approach was conducted in this study to investigate the performance of asphalt concrete, the combined effect of asphalt concrete constituents also becomes very significant for thermal fatigue cracking. The previous studies indicate that the evolution of thermal stress in asphalt concrete is mainly governed by the mixture stiffness and its thermovolumetric properties such as thermal expansion/contraction coefficient, and glass transition temperature. The effect of these factors is further discussed in the following sections.

#### **a) Stiffness of asphalt mixture**

Asphalt mixture stiffness is one of the significant factors for the performance of AC pavements. A general rule of thumb used by the asphalt pavement practitioners to accept or reject the mixture is that if the measured stiffness ( $|G^*|$ ) at 40°C and 10 Hz loading frequency is higher than 250 MPa, then the asphalt mixture is acceptable for execution in the field. Asphalt mixture performance under thermal and load associated fatigue can be evaluated with its stiffness modulus. During the performance tests like constant shear, uniaxial, and flexural fatigue tests, the stiffness modulus reduction occurs because of crack initiation under the cyclic loading, which gradually propagates through the thickness. In the past, the flexural fatigue test was utilized by many researchers to simulate field conditions, in which a beam specimen was subjected to cyclic bending until failure. Since the test was conducted in the strain control mode, a complete fracture in the sample could not be a criterion for failure. So, it was proposed to apply different levels of reduction in stiffness (25%, 50%, 75%) as failure criteria. Epps (1999) applied 50% reduction in the initial stiffness as a termination criterion when she employed four points bending test on the beam specimens in the strain control mode and sinusoidal loading cycles to simulate thermal fatigue on the field. During the bending fatigue test, the relationship between stiffness

and the number of the loading cycle can be displayed in two phases: Initial or adaptation phase and secondary or stationary phase. After starting the test, there is a dramatic drop in the test sample's stiffness during the first few cycles of the initial phase. Some researchers relate this drop in stiffness to creep, as a viscous response of asphalt concrete (Mamlouk et al. 2012b), while heating of asphalt concrete due to the effect of dissipated energy and the binder thixotropy is considered by other researchers (Di Benedetto et al. 2004). Despite the different opinions regarding this phenomenon, there is consensus that mixture behavior in the initial phase is not due to fatigue. In the second phase of the test, fatigue plays a dominant role in the stiffness reduction of asphalt concrete, and it continues until the complete failure of the test sample.

#### **b) Thermal properties of asphalt concrete**

As the air temperature decreases, the pavement temperature drops, resulting in stress accumulation due to the surface layer's volumetric contraction. The constant  $\alpha$  denotes the thermal coefficient of AC, and it is the primary thermo-volumetric property controlling the development of thermal stress in thermal fatigue and low temperature distresses. Using the thermal coefficient of contraction, the relationship between the thermally induced strain and temperature change can be computed using Eq. (2.1):

$$\alpha = \frac{d\varepsilon^T(T)}{dT} \quad (2-1)$$

A list of measured coefficients of thermal expansion/contraction, tested specimen geometries, measuring sensors, and temperature ranges in previous studies are given in Table 2.2.

**Table 2.2.** Measured coefficients of thermal expansion/contraction for AC in previous studies

References	Test samples geometry	Measurement method	Temperature range	CTC
				$10^{-5}/^{\circ}\text{C}$
(Domaschuk and et.al. 1964)	Beams of 63mm × 100mm × 250mm	Strain gage	-9.4 to -31	
(Littlefield n.d,1967)	Beam sample	Extensometer	0 to 54	1.6
(JONES et al, 1968)	Beam sample	Dial deflection gauge & Glass dilatometer	-23 to 60	3.69
(Osterkamp, 1986)	Beam sample	Lvdt	-55 to 10	1.7 - 2.2
(Janoo et al, 1993)	Beams of 76mm × 76mm × 305mm	Lvdt	-40 to 0	2.4
(Stoffels and Kwanda, 1996)	Cylindrical samples of 150mm diameter and 50mm height	Strain gages	-25 to 0	1.33 - 2.97
(Mehta et al, 1998)	Cores of 150mm diameter 50mm height	Lvdt	-25 to 0	1.58 - 2.33
(Zeng and Shields, 1999)	Beams of 51mm × 51mm × 340mm	Lvdt	-40 to 40	1.35
(Mamlouk et al, 2005)	Beams of 50mm × 50mm × 390mm	Lvdt	0 to 60	2.0 - 6.3
(Qadir Adnan, 2010)	Beams of 50mm by 65mm by 300mm in the TSRST machine	Lvdt	-80 to 20	3.20 - 4.3
(Xu and Solaimanian, 2008)	Cores of 100 mm diameter 150mm height	Extensometer	-5 to 40	1.85 - 2.65

## **2.6 Approaches to measuring the performance of asphalt concrete under thermal fatigue**

Thermal fatigue is a phenomenon for which there is no consensus about modeling this distress mode yet. Two methods have been proposed to evaluate the performance of asphalt concrete under thermal fatigue: phenomenological and mechanistic methods, which are described as follows (Vinson et al. 1989).

### **2.6.1 Phenomenological approach**

In the phenomenological method, different tests are conducted at different levels of stress or strain to investigate the number of cycles to failure. Some researchers (Sugawara, T. 1984) conducted tests at temperatures close to the mixture fracture temperature. They concluded that the fatigue life of hot mix asphalt is shorter in the thermal mode compared to load associated mode. Miner's hypothesis is the common equation used for fatigue analysis. The hypothesis proposes that the damage due to fatigue is accumulated, and the failure happens when the summation of fatigue life rates is equal or larger than one.

$$\sum \frac{n_i}{N_i} = 1 \quad (2-2)$$

$n_i$  = the number of cycles accumulated at stress or strain level  $i$

$N_i$  = the number of cycles to failure

### **2.6.2 Mechanistic approach**

Mechanistic methods correlate between pavement distress and main material properties such as temperature, loading time, stress, strain. Fracture mechanics parameters comprise a major part of mechanistic approach models developed for thermal fatigue cracking of asphalt concrete. Stress intensity factor ( $K$ ), J integral, and



Energy release rate integral (C\*-line integral) are several fracture mechanics parameters used for this purpose.

## **2.7 Summary of previous researches on thermal fatigue cracking**

Thermal cracking has been studied since 1960, in the beginning, there was an idea that thermal fatigue because of its very low frequency cannot initiate and propagate transverse cracking in flexible pavements until mid-1970's which pavement engineers in west Texas observed severe transverse cracking. This was unusual because pavements do not experience extreme low temperature in that area, so the idea about the second type of thermal cracking was initiated.

A limited number of studies about thermal fatigue are available. The most important causes for this distress can be summarized as the effect of thermal fatigue cracking on the pavement performance is difficult to be understood, and the thermal fatigue test includes long-term and complicated experiments.

It is evident from some studies in recent years, that the thermal stress is not individually the reason for the deterioration of the roadways, because thermal stresses are small and unable to generate immediate fracture. However, it is probable that cyclic thermal fluctuations above the fracture temperature cause cyclic fatigue in the pavement and make it more prone to cracking under consecutive thermal and traffic induced stresses.

An essential part of the work done on the thermal behavior of AC pavement has focused on sudden thermal cracks formed at low temperatures. The next section covers the essential elements of thermal fatigue cracking experiments. A summary of laboratory based studies on thermal fatigue performance of asphalt concrete is given in Table 2.3.

**Table 2.3.** Recent laboratory studies on thermal fatigue cracking

References	Applied method	Test type	Test samples Geometry	Failure criteria
(Sugawara,T. 1984)	Phenomenological	Three point bending fatigue test	Beam of $\times 25\text{mm}$ $25\text{mm}\times 250\text{mm}$	Fracture
(A.h.Gerritsen and et.al 1989)	Mechanistic	Two point bending fatigue	Trapezoidal beam of $30\text{mm}\times (25-55)\text{mm}\times 160\text{mm}$	Reduction in stiffness
(Jackson and Vinson 1992)	Phenomenological	Tension/ Compression	Cylindrical samples of $254\text{mm}(\text{Length})\times 57.2\text{mm}$ (diameter)	Fracture
(Epps 1999)	Mechanistic	Four point bending fatigue test	Beam of $\times 51\text{mm}$ $64\text{mm}\times 381\text{mm}$	50% Reduction in stiffness
(Pérez-Jiménez et al. 2011)	Mechanistic	Tension/ Compression	Beam of $50\text{mm}\times 50\text{mm}\times 60\text{mm}$	Fracture
(Arabzadeh 2015)	Mechanistic	Tension/ Compression	Beam of $50\text{mm}\times 65\text{mm}\times 250\text{mm}$	35% & 50% Reduction in stiffness

## 2.8 General evaluation of previous thermal fatigue tests in the literature

The studies summarized above are briefly evaluated by taking into consideration the proposed research subject and scope. After compiling the information obtained from the literature, the thesis's subject and method have been determined. The assessments about different determining parameters in thermal fatigue test are as follows.

### 2.8.1 Sample selection

Gerritsen & et.al (1989) used trapezoid specimens with 160mm length and 20-55 mm width under two points bending fatigue test to evaluate influential factors on asphalt concrete's thermal fatigue performance. To model thermal fatigue behavior, Jackson & Vinson (1992) employed kneading compactor to produce beam specimens of 57mm

× 57mm × 254mm for the DTT test. Epps (1999) subjected 64mm×54mm×381 mm rectangular beams to flexural fatigue test using a four-point bending device to measure thermal fatigue resistance of asphalt concrete. Perez & et.al (2011) used Prismatic specimens with 50 mm width and thickness and 60mm height under cyclic loading to simulate the combined effect of thermal fatigue and load associated fatigue.

As seen from the studies summarized above, specimens used in fatigue tests were not selected according to a specific method or standard, and test specimens used in almost every study had different dimensions. It is known that the sample sizes used in fatigue tests had a significant influence on the test results.

The beam samples used in many studies required separate compaction equipment because they could not be produced from cylindrical samples used in the mixture design. According to the conducted studies in the literature, the reason for the variation of results in different studies is unknown. It could be a test sample size effect on the presented results or because the test specimens with different sizes were used. It should also be mentioned that the air void distribution in the beam specimen is more variable than cylindrical one, so the extension of air void variability in the reported test results is unclear.

### **2.8.2 Loading frequency**

The loading frequency used in fatigue tests was different in each study, fast loading represents fatigue under the traffic load while slow loading is more representative of thermal behavior, so thermal fatigue modeling requires low frequency loading. A.h.Gerritsen et.al (1989) conducted fatigue tests at different frequencies (0.004Hz and 0.0004Hz). The results indicated that the loading speed would significantly impact the fatigue performance. (Figure 2.12). The reason for this behavior is that the different regeneration rates of the mixtures would show different healing behavior. In thermal fatigue tests, since the thermal temperature cycle is replaced by mechanical loading, the selected loading frequency must reflect the actual thermal stress behavior. Epps

(1999) also employed a beam fatigue test at a slow frequency (0.05 Hz) to compare the thermal fatigue resistance of different mixtures.

(Jimenez et al., 2011) applied the loading frequency of 10 Hz for both load associate and thermal fatigue. However, it was not possible that the obtained response at this loading rate would represent thermal fatigue. There are significant differences between the loading frequencies used in previous experiments. It is seen that the selected loading frequency is from 0.0004 Hz (A.h.Gerritsen et.al, 1989) to 10 Hz (Jimenez et al., 2011).

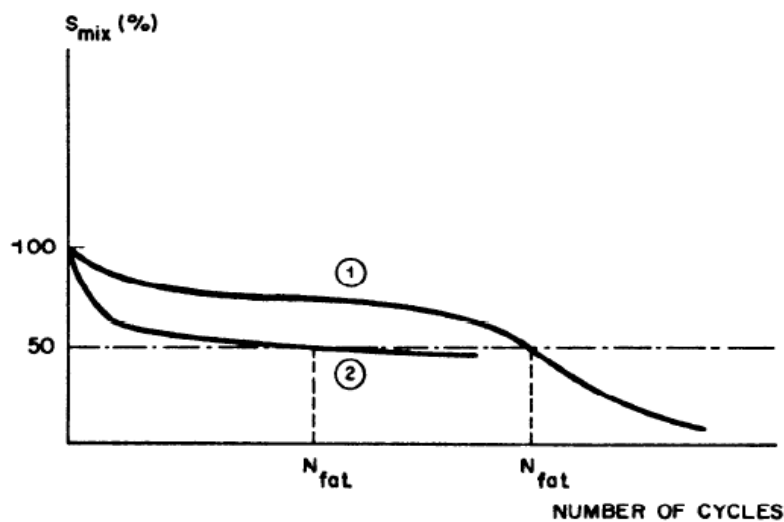


**Figure 2.12.** Comparison between high frequency (40 Hz, 1) and low frequency (0.0004Hz, 2) fatigue test (A.h.Gerritsen and et.al 1989)

### 2.8.3 Type and shape of the loading

In previous studies, to simulate thermal fatigue, both strain and stress controlled loading was applied, and the preference was more in the direction of the strain-controlled loading. According to Al-Qadi et al. (2005), the level of stress-strain was recognized as a critical factor in thermal fatigue cracking. Based on the results

obtained from the actual field measurements, it was suggested that thermal fatigue tests should be applied in the controlled strain mode. In previous studies, the amplitude of stress or strain values were chosen differently for unknown reasons, and the loading magnitude corresponding to temperature changes in the field conditions was not examined (Figure 2.13).

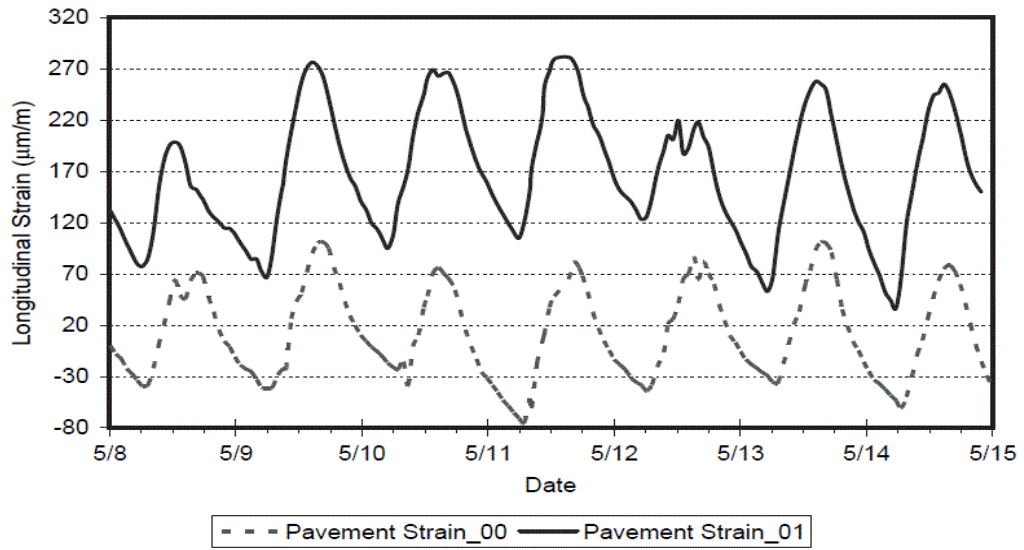


**Figure 2.13.** Variation of Measured strain under the wearing surface (Al-Qadi et al., 2005)

It is generally accepted that haversine and sinusoidal loading simulates daily temperature fluctuation the best (Figure 2.14). Most of the researchers used sinusoidal waveform of loading for the thermal fatigue test, some applied sinusoidal loading through flexural bending test (Epps 1999) and (A.h.Gerritsen and et.al 1989), while others implied this wave shape of loading by direct tension test (Jackson and Vinson 1992), and (Arabzadeh 2015).

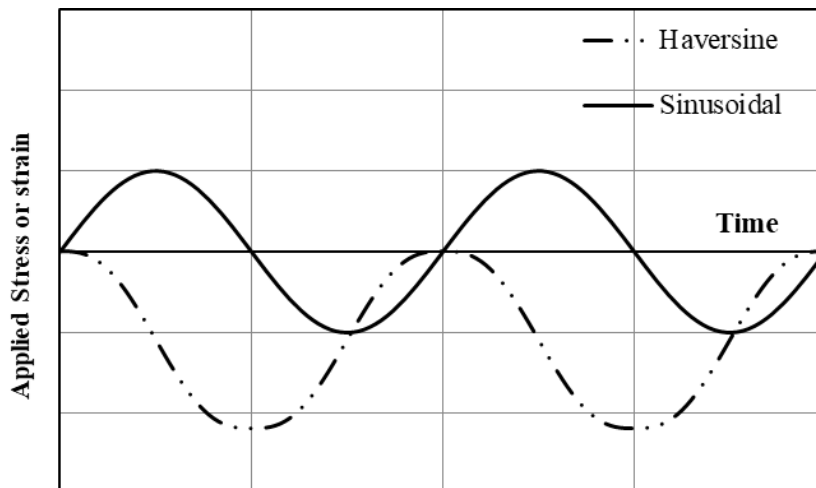


**Figure 2.14.** Illustration of sinusoidal and haversine loading waveform

#### 2.8.4 Rest time

Many works have been performed on the effect of rest time on load associated fatigue life of asphalt concrete. As shown in Figure 2.15, studies show that adding a rest period to any sinusoidal or haversine loading would increase the fatigue life of asphalt concrete up to 5 times (Raithby and Sterling 1970). It was also found that there was an upper limit, which after that, adding more rest time would not affect fatigue life. (Van Dijk et al. 1972). Rest periods can be applied either by discontinuous loading or by intermittent loading. In discontinuous loading, loading is continuous for a specific period and then rest time is exerted, in case of intermittent loading, each cycle of loading is followed by the rest time. It is established by many studies, that rest periods between consecutive loadings increase the fatigue life in both controlled strain and controlled stress modes in laboratory tests (Bonnaure et al. n.d.). All of the mentioned studies were employed to assess load associated fatigue, but no study has been conducted that includes impact of rest time in thermal distresses. The effect of the rest period, as a test variable, on thermal fatigue cracking is evaluated in this study.

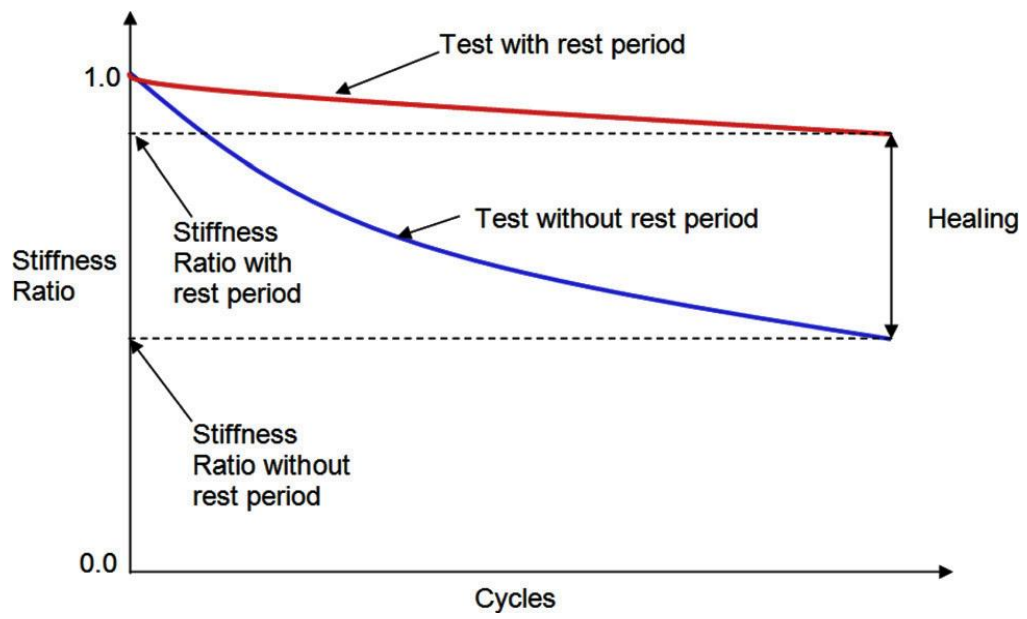


**Figure 2.15.** Number of cycles versus stiffness ratio with and without rest periods in load associated fatigue (Mamlouk et al. 2012a)





## **CHAPTER 3**

### **METHODOLOGY AND MATERIALS**

#### **3.1 Introduction**

This chapter describes the methodology applied in this research. Significant portion of this chapter is devoted to the design, fabrication, programming of a thermal chamber for measuring thermal coefficient, and design of a new procedure for thermal fatigue test by applying a bending test on a semi-circular specimen. The experimental design for laboratory tests include the number of specimens needed to be produced, detailed procedure of the Superpave mix design method, determining mixing and compaction temperature, mixture conditioning procedure, and calculation of the volumetric properties of compacted samples. The discussion also includes details about the preparation of test setup and the formation of a module program in the control software environment. Figure 3.1 gives a summary of the methodology followed in this research.

#### **3.2 Thermal coefficient test setup**

##### **3.2.1 Design and fabrication of thermal chamber**

Although many researchers have conducted the thermal coefficient test for asphalt concrete, there is no consensus on the test procedure yet. Because of the individual requirement for measuring the thermal coefficient in this study, a thermal chamber was designed and fabricated. The manufactured thermal chamber was insulated in such a way to measure thermal properties at both low and high temperature range from -70 °C to +85 °C as shown in Figure 3.2 and 3.3.

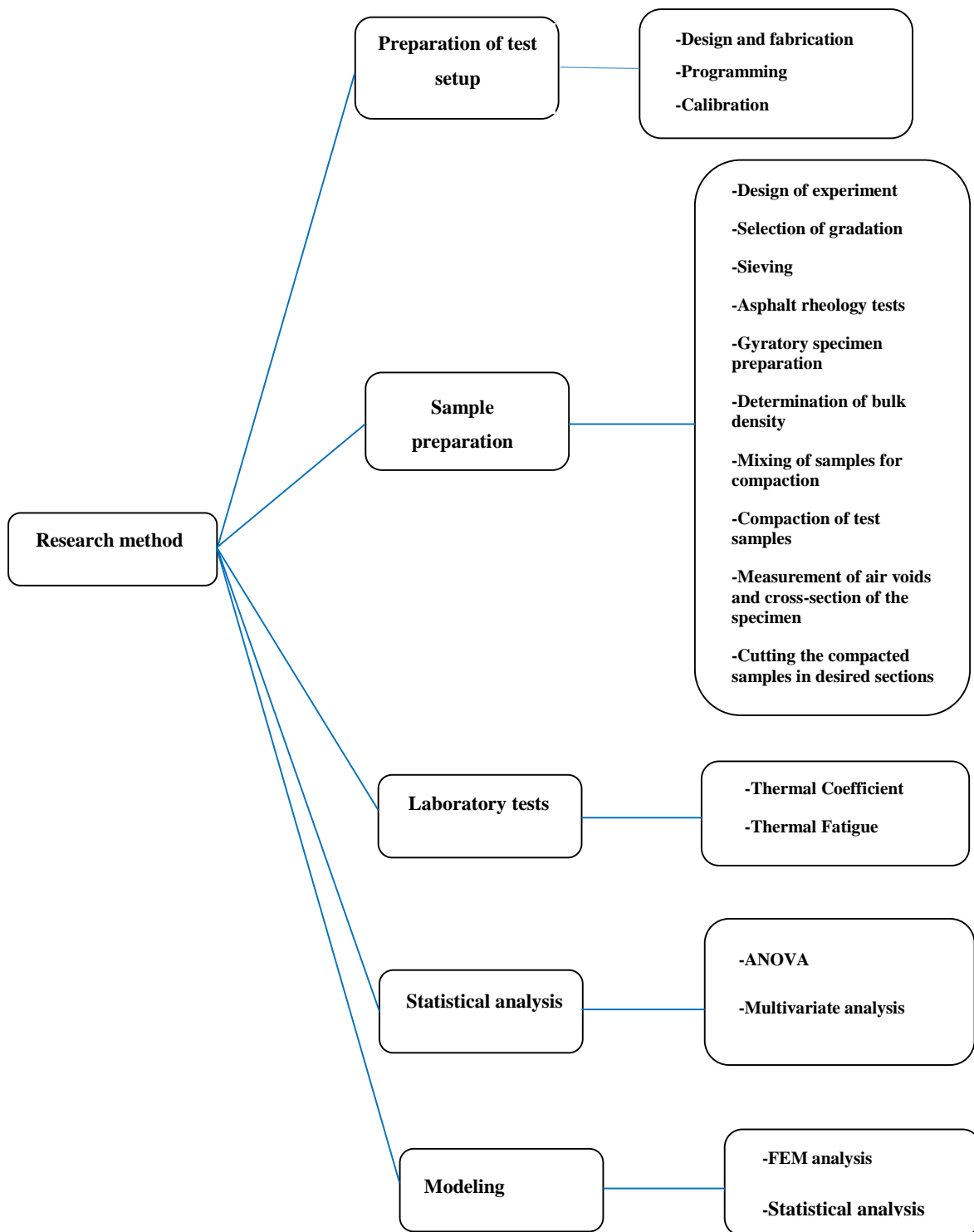


**Figure 3.1.** Diagram for research methodology

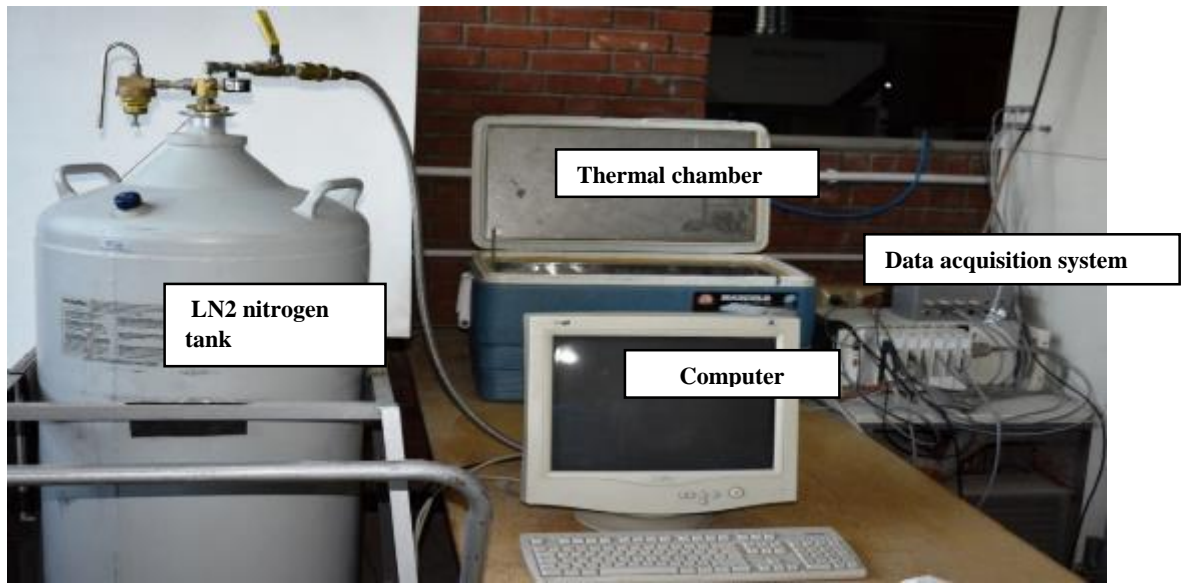


**Figure 3.2.** Test set up for measuring the thermal coefficient of asphalt concrete

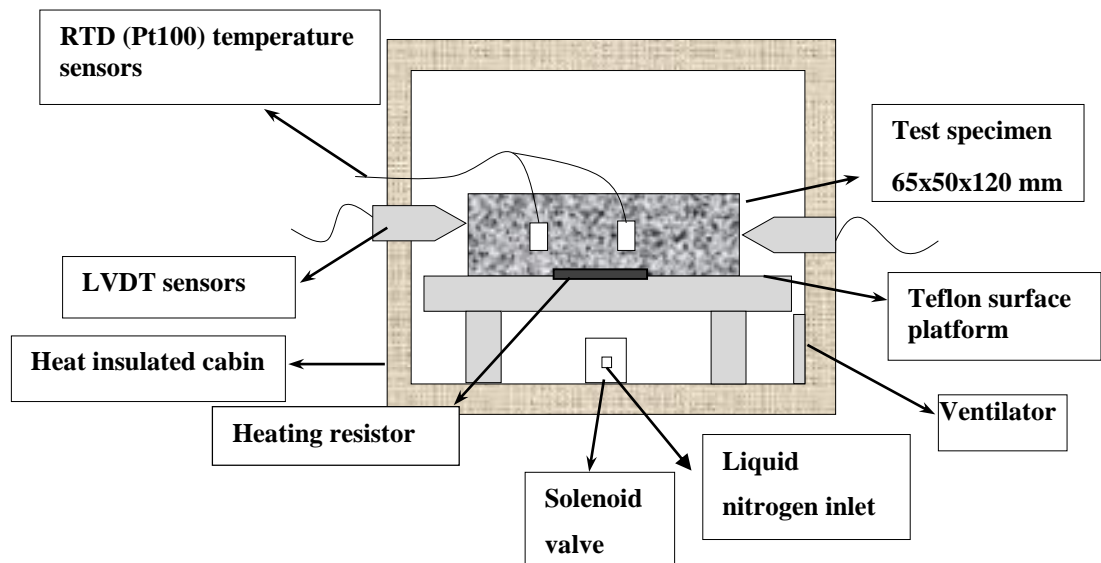


**Figure 3.3.** General schematic of the thermal chamber for measuring thermal coefficient

The thermal chamber was manufactured using 66 liters cooler with exterior dimensions of 750×420×405mm and the interior dimensions of 625×325×325mm. The cooler was enhanced with fiberglass sheets covered with stainless steel sheets to prevent deformation due to temperature variation. A flat platform to stand the test specimen was also constructed using double aluminum plates separated by a fiberglass sheet, which can prevent uncontrolled heat transfer from the heating resistant to the specimen. To prevent friction between the specimen and the platform during contraction while the specimen is cooled down, a 5mm thick Teflon sheet was placed onto the platform before starting the test (Figure 3.4).

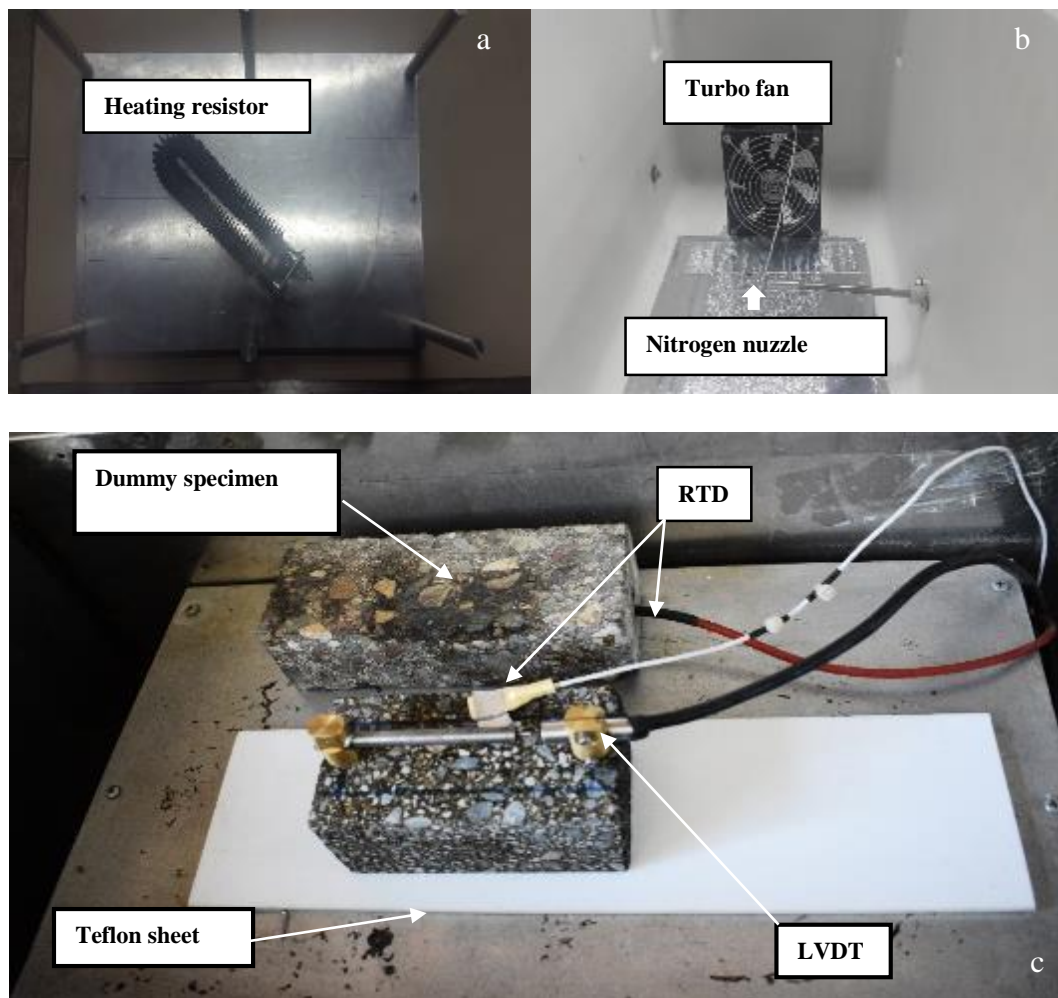


**Figure 3.4.** Thermal chamber components: a) Heating resistor, b) Turbo fan & nitrogen nuzzle, c) Test set up

A heating resistor was installed below the stand to adjust the chamber temperature that was required for the conditioning stage. The inside temperature was uniformly distributed by a fan installed at the bottom of the thermal chamber. In the cooling stage, the chamber's temperature was dropped at 60 °C/h by the inflow of LN2 through a computer controlled solenoid valve. The setup for measuring the thermal coefficients also included a temperature controller, a LN2 tank (150 liters), compressor, and resistance temperature detectors (RTD'S). Temperatures at the surface and the core of the specimen were monitored by RTD's which were connected to the data acquisition system. Data obtained from the RTDs controlled the amount of liquid nitrogen required to adjust the set cooling rate up to the minimum temperature, for which the measurement was taken. For transferring the liquid nitrogen into the chamber, a special nozzle system was fabricated from aluminum and installed at the bottom side of the chamber, so that the LN2 would be sprayed uniformly inside the thermal chamber (Figure 3.4).

### **3.2.2 Programming**

The data acquisition system consisted of sensors, a DAQ measurement hardware, and a PC with programmable software. The RTDs and LVDT (also-called transducers) converted the temperature and the amount of dimensional change (contraction or expansion) data to measurable electrical signals through the data acquisition system and stored in PC for further analysis. A user interface program developed in LabVIEW (also referred to as G) was used to control the measurements and store data into the computer.

### **3.2.3 Measurement of thermal coefficient**

The first step in measuring the thermal coefficient of asphalt concrete was to apply temperature conditioning to achieve a uniform temperature distribution within the test specimens. The specimens were first heated up to a selected conditioning temperature for 3 hours, and after temperature stabilization, the cooling step was then started at the selected cooling rate. During the specimen's contraction, the displacement data corresponding to the current temperature was recorded at a predefined frequency. The program interface has two parts: the control section and the indicators section. System control mode, test control mode, and testing time constitute the control section. In the indicator section, two graphs are displayed: displacement versus temperature and time versus temperature. The thermal coefficient of contraction is calculated in real time and plotted in the displacement versus temperature plot (Figure3.5).

#### **3.2.3.1 The system control**

The system control includes buttons to switch on and off the fan, solenoid, and heat resistor. During conditioning, the button for the heater resistor is switched on. During the cooling step, the button for the solenoid valve must also be on for transferring the vaporized nitrogen into the chamber. The fan switch must be on in both cases to apply air circulation inside the chamber.

#### **3.2.3.2 The test control**

In the test control, the temperature control phase is defined by selecting the thermal conditioning or temperature profile. In the user interface program, after conditioning at the target temperature for a predefined duration of 3hours, the control button starts blinking, which indicates that the conditioning period is completed. It is worth

mentioning that switching from the thermal conditioning to the temperature profile stage was applied manually. Other controls in the user interface are allocated to defining the log file path and the logging period for the recorded data. The logging frequency is defined by a time lag between 2 data points, which was chosen 30 seconds in this study.

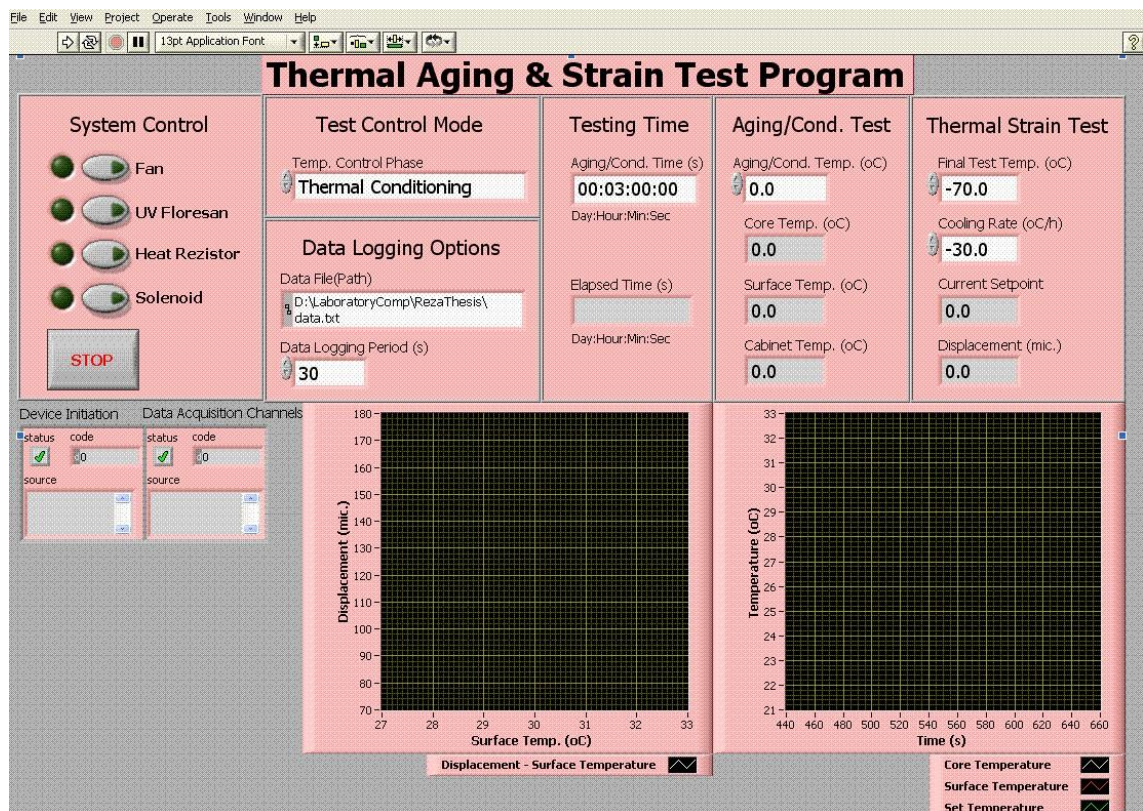


**Figure 3.5.** A view of the user interface program in the LabView program for measuring the thermal coefficient

### 3.2.3.3 Temperature control

In this study, conditioning temperature, final test temperature, and cooling rate as components of the temperature control section were taken as 30°C, -30 °C, and 60 °/h, respectively. Readings from different RTDs were also displayed in this section for the core temperature, the surface temperature, and the temperature inside the chamber.

### 3.2.4 Calibration of linear variable differential transformers (LVDT)

As shown in Figure 3.6, the displacement measurement system consisted of LVDT, an extension bar, and fixtures. Because these materials also contract during the cooling phase and affect the thermal coefficient measurement, the deformation sensors need to be calibrated together with the invar bars and the mounting fixtures. For this purpose, a modified setup was prepared to obtain the calibration data and then used to correct the measurements for the thermal coefficient of asphalt concrete samples.

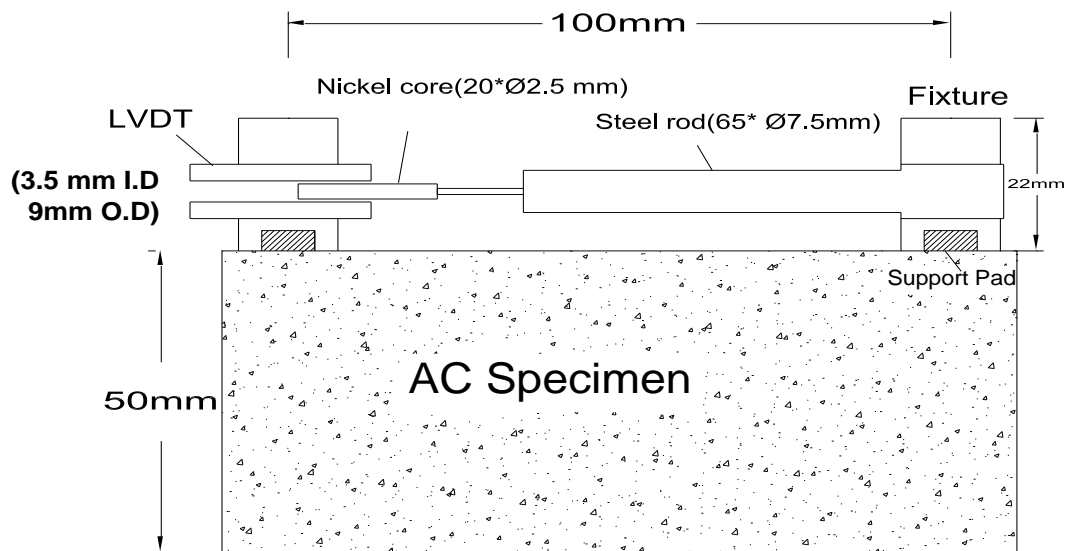


**Figure 3.6.** LVDT installation for displacement measurement



The LVDT used to measure the deformations is manufactured as SM series by Solartron Metrology Comp. The sensors are of type inductive LVDT with a nominal linear range of  $\pm 3$  mm and temperature operating range of  $-40^{\circ}\text{C}$  to  $+85^{\circ}\text{C}$ , the sensitivity of is  $118 \text{ mV/V/mm @ 1kHz}$ . Before starting the measurements, the entire measurement setup was calibrated by using auxiliary fixtures of known thermal coefficients, i.e., a ceramic beam and steel beam, with a length of 100 mm. To be able to calculate the thermal coefficient of the LVDT sensor, a dummy sample and an invar bar meeting the LVDT sensor were manufactured from the same steel of known thermal coefficient. The test was also repeated by using the ceramic sample and the steel invar bar, so that the unknown thermal coefficient of the LVDT can be calculated from the equations generated from the two testing's. The thermal coefficients of the ceramic and the steel material were reported as  $0.81 \times 10^{-5}/^{\circ}\text{C}$  and  $1.16 \times 10^{-5}/^{\circ}\text{C}$  by the manufacturer, respectively (Figure 3.7).



**Figure 3.7.** Test setup for calibration of LVDT and steel rod using ceramic and steel beam

After 3h conditioning at 30°C, calibration tests were conducted at a cooling rate of 60 °C /h. The following adjustment was made to displacement measurements: In the test with a ceramic beam, the total deformation ( $\delta_{total}$ ) measured is the deformation of the ceramic beam minus the deformation of the steel rod and the LVDT in Eq.(3.1) (Figure 3.8).

$$\delta_{total} = \delta_{ceramic} - \delta_{steel\ rod} - \delta_{LvdT} \quad (3.1)$$

The total deformation was also calculated by using the steel dummy sample in the same way by Eq. (3.2):

$$\delta_{total} = \delta_{Steel\ beam} - \delta_{Steel\ rod} - \delta_{LvdT} \quad (3.2)$$

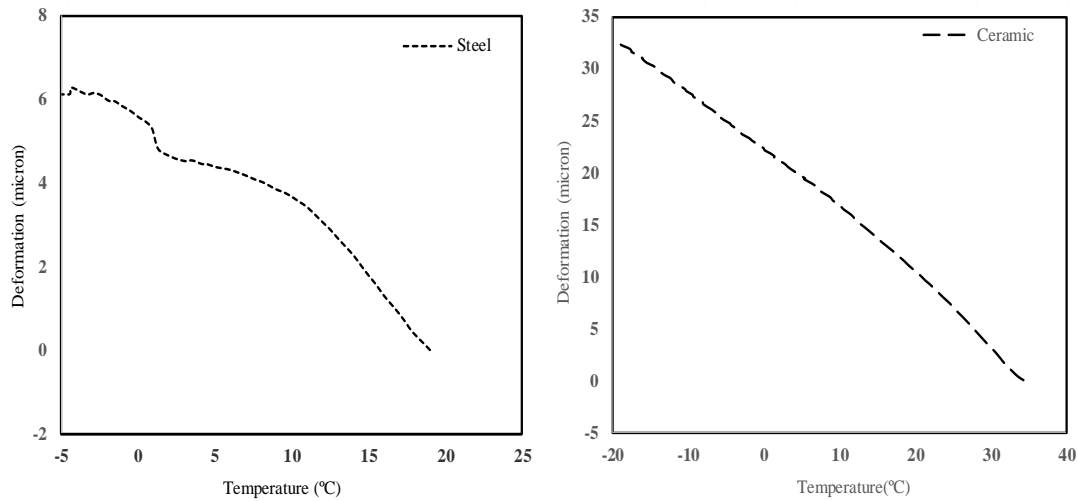


**Figure 3.8.** Deformation of steel and ceramic versus temperature variation

The coefficients of thermal contraction for the steel rod and LVDT were obtained by solving Eq. (3.1) and (3.2) as listed in Table 3.1.

**Table 3.1.** Thermal coefficients of LVDT and steel rod sample

Material	Coefficient of thermal contraction(/°C)
LVDT	$2.55 \times 10^{-5}$
Steel rod	$1.16 \times 10^{-5}$

### 3.2.5 Preparation of beam specimens for thermal coefficient test

In this study, the beam specimens needed to measure the thermal coefficients were obtained from the gyratory compactor samples using a diamond saw cutter. From each compacted sample, two test specimens could be acquired with a specimen length equal to the height of the samples produced by the gyratory compactor, which varied between 120 mm to 125 mm. The obtained specimens had a cross section dimension of 65 mm × 50 mm. One of the beams produced was aged to test for the effect of aging on the thermal coefficient. The specimen was placed in an oven for 120 hours at 85°C to be aged according to the AASHTO R30 standard before testing (Figure 3.9& 3.10).

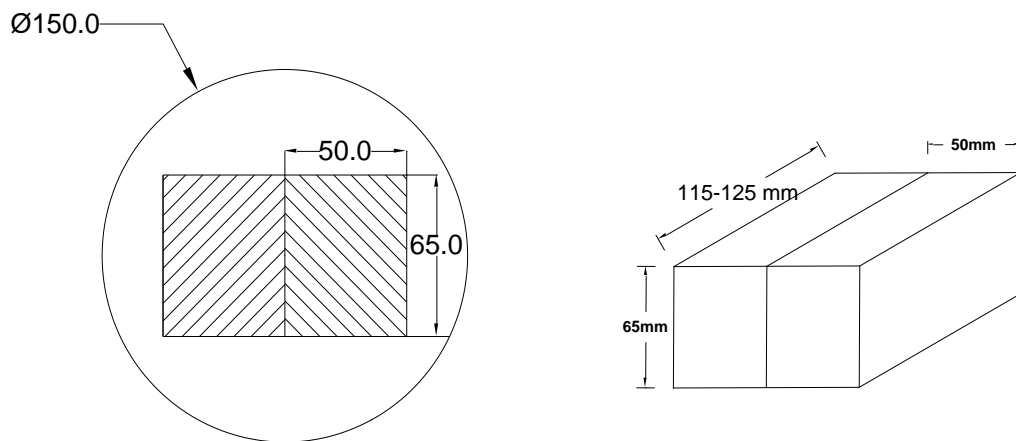


**Figure 3.9.** Gyratory specimen section for cutting to obtain beam sample



**Figure 3.10.** a) Prepared beam specimens for thermal coefficient measurement, b) Beam specimens before and after aging according to (AASHTO R30 2006)

### **3.2.6 Sample preparation for thermal coefficient measurement tests**

#### **3.2.6.1 Mounting support pads for LVDT (Linear variable differential transformer)**

Supports for holding LVDT were fixed on the specimen by installing the steel pads onto a reference steel plate at a distance of 100 mm. The epoxy compound was then prepared, consisting of two parts: epoxy resin and epoxy hardener. The epoxy compound was applied to the wider surface of the specimen (65 mm) in previously marked points. Then, the steel plate with attached steel pads was put on the beam precisely, so the steel pads could thoroughly go inside the epoxy resin and have complete contact with the specimen. After 1-hour waiting, the epoxy compound

hardened, and the plate was separated from the support pads by unscrewing the steel pads (Figure 3.11).

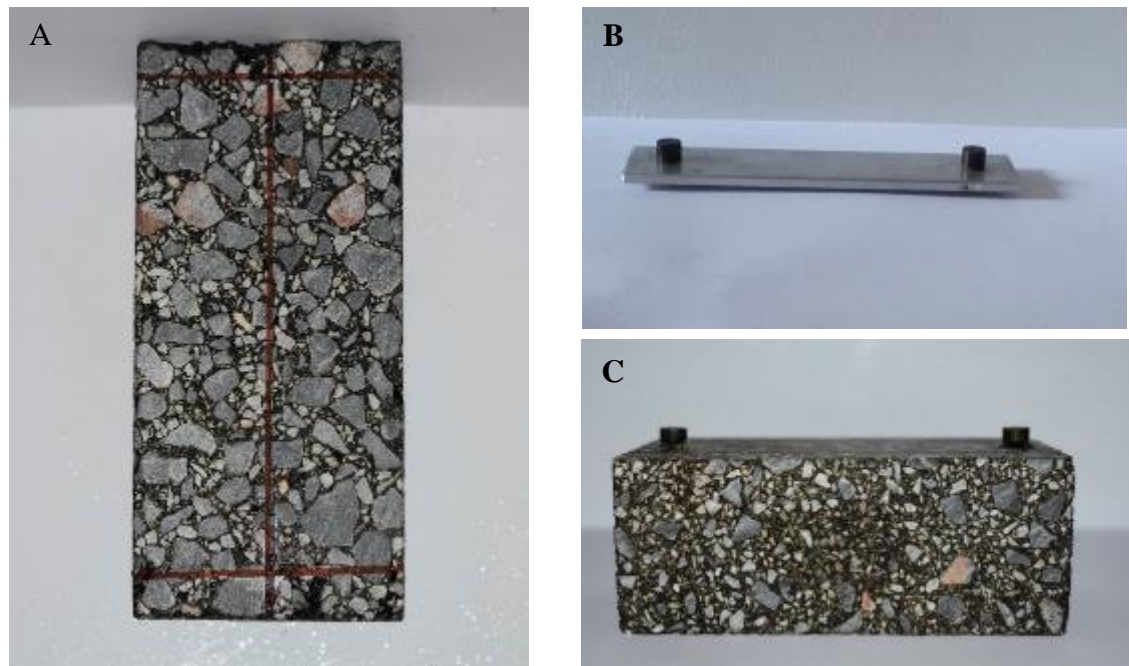


**Figure 3.11.** Mounting support pads on beam samples for thermal coefficient measurement

### 3.2.6.2 Installation of LVDT sensor on test specimens

The LVDT used in this study to measure strain at the bottom surface of the specimen is an inductive type designed for high resolution position measurement. As shown in Figures 3.6 and 3.12, an inductive LVDT comprises a core and coil assembly, the core is made of a very thin iron-nickel cylinder shape and attached to the steel rod coil assembly consisting of wound coils with three wires. During measurement, two holders were attached to the steel pads to keep the steel rod and the LVDT sensor parallel to the specimen's surface. The displacement of the core inside the LVDT due

to specimen's shrinkage generates the required displacement for the calculating of the thermal coefficient of the test specimens.

### 3.2.6.3 Installation of LVDT sensor on test specimens

RTDs (resistance temperature detector) were used in the test setup to measure the surface and the core temperature of the test specimens as shown in Figures 3.12. For each thermal coefficient measurement, a dummy sample was put horizontally inside the thermal chamber, and a probe RTD was inserted inside the specimen to measure the core temperature.

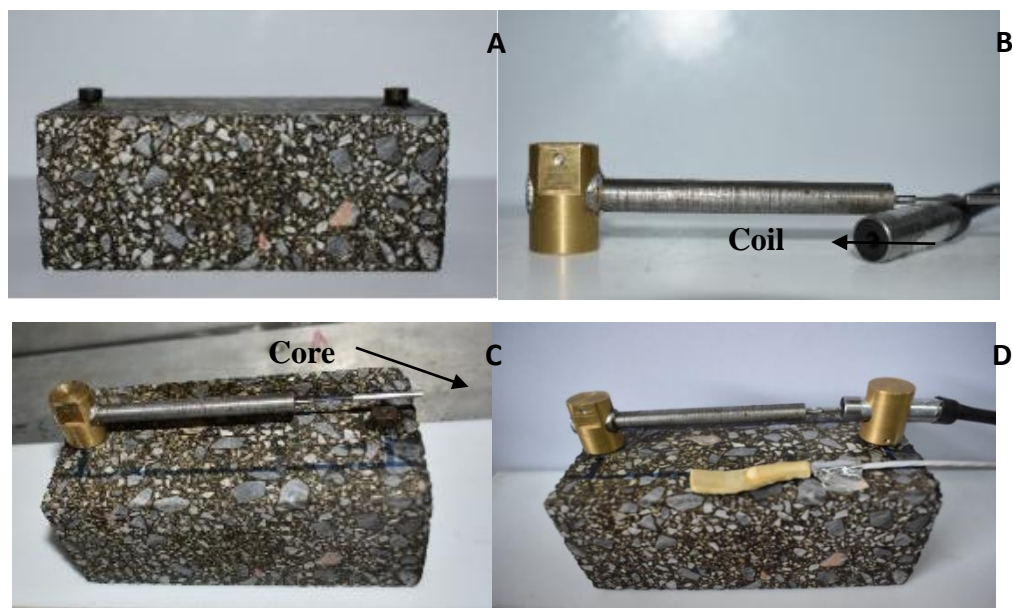


**Figure 3.12.** Mounting LVDT on beam specimen for measuring thermal coefficient

### 3.3 Thermal fatigue test setup

#### 3.3.1 Test equipment

Thermal fatigue tests were conducted using a 16 kN capacity dynamic testing system (DTS 16) equipment, as shown in Figure 3.13. This equipment includes a data acquisition system (CDAS), and a pneumatic pressure system, which can produce a maximum of 20 kN static loading and 16 kN dynamic loading. The actuator applies load to the specimen through a loading frame, depending on the test protocol used. Further information for DTS 16 system is given in Table 3.2. (Universal Testing Machine General-PAVETEST 2014). The environmental chamber that was used for this test is an LMS cooled incubator with internal dimensions of 550×700× 1170 mm and an operational temperature range between -10°C to +60° C. To gather temperature data during the thermal fatigue test, a dummy specimen was placed inside the chamber.

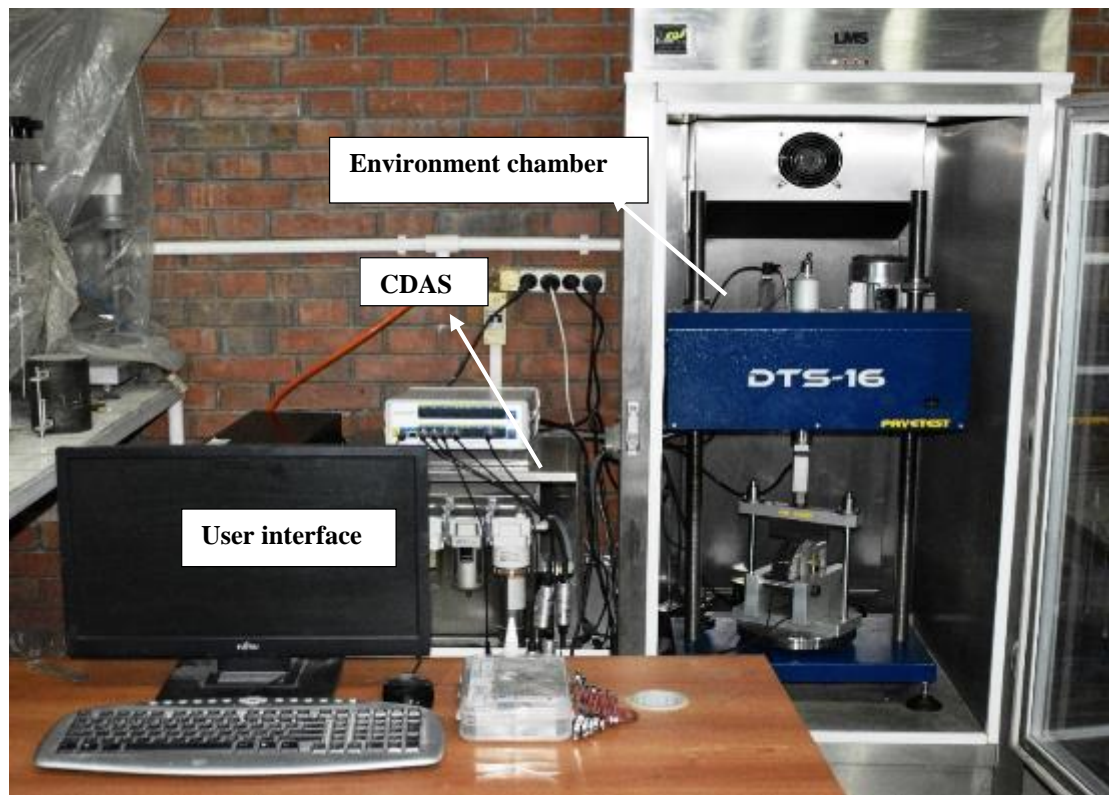


**Figure 3.13.** Thermal fatigue test setup

**Table 3.2.** DTS16 test machine specifications

<b>Item</b>	<b>Description</b>
Machine dimensions	450 (d) x 500 (w) x 1020 (h) mm
Static load capacity	+/-16kN
Effective vertical space	650mm
Space between columns	345mm
Load cell	+/- 20kN

### **3.3.2 Programming for test protocol**

#### **3.3.2.1 Data acquisition system**

The data acquisition and the control system (CDAS) used in this test gathered signals from various transducers through 16 channels with the capability of 200,000 samplings per second. Technical specifications for CDAS are given in Table 3.3 (Universal Testing Machine General-PAVETEST 2014).

**Table 3.3.** Specifications for data acquisition system

<b>Item</b>	<b>Description</b>
Acquisition	16CH normalized input, resolution:20 bit
Sampling rate	All channels, maximum 200KHz
Smoothing	Maximum 64 times through sampling
Calibration	Automatically
No of control axis	4
Communication	Ethernet or usb
Dimensions	31(d)× 25(w) ×10(h) cm
Power	50/60Hz - 90-264v



### 3.3.2.2 Closed loop servo control

After starting the test, the transducers transfer the signal to the data acquisition system, and after the data processing, the difference between the requested input and the response from the transducer is considered an error, so the servo valve regulates the air pressure to correct this error. To minimize the error during the test, PID (Proportional, Integral, Derivative) as a control loop procedure was applied. During the tests, all PID parameters are adjusted to obtain optimum performance during the thermal fatigue test (Figure 3.14).

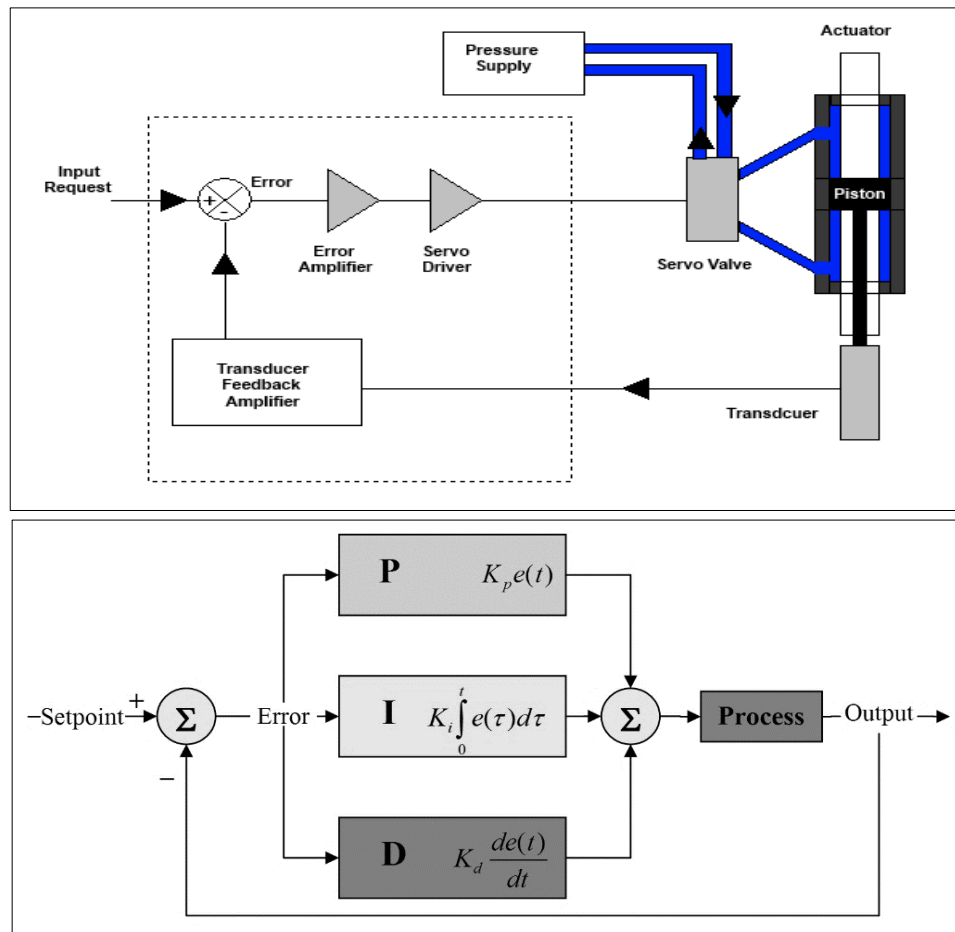


**Figure 3.14.** Schematic diagram of a) closed-loop diagram, b) PID controller

### **3.3.2.3 Programming software**

Testlab is a material testing software devised by Pavetest Ltd to interface the CDAS control and the data acquisition system as well as the servo pneumatic loading device. There are standard test methods in Testlab program in which scripts are saved to a customized method file for a particular testing protocol. The method file consists of transducers, control parameters, calibration allocations, test termination criteria. The method file used for this study does not exist, so a new method file was written using the test designer program to carry out the test protocols.

#### **a) Test navigation menu**

The test navigation menu consists of several repeated parts allocated for the different aspects of the test protocol. The main parts of the navigation menu are summarized in the below sections.

##### **1. General**

This section consists of two parts: The first part gives some information about the project name and operator name. In the second part, the method file name and description and the directory path are indicated. The method file name used for this study was called generic fatigue test.

##### **2. Pretest mode**

In this section, firstly, specimen dimensions are entered, which are 150 mm for specimen diameter and 35 mm for its thickness. The test parameters are also presented in two columns. Target test temperature, support Span, CMOD gauge length, and LLD gauge length are entered in the first column. The second column consists of assumed loading cycles for initial stiffness, termination stiffness reduction criterion, maximum

termination cycle, and maximum displacement of the actuator. Table 3.4 lists necessary test data for the thermal fatigue test protocol.

**Table 3.4.**Input test parameters in Pre Test section

<b>Parameters 1</b>		<b>Parameters 2</b>	
Target test temperature	4°C	Initial stiffness@ cycle	1
Support span (mm)	120 mm	Termination stiffness reduction (%)	75
Gauge length CMOD (mm)	25	Termination max cycles	2000
Gauge length LLD (mm)	30	Max.actuator displacement (mm)	1

### **3. Loading**

The loading section comprises two parts; the first part is about loading sequence settings. The thermal fatigue test in this study included two sequences, a conditioning sequence, and the main loading sequence. Since the conditioning sequence was considered a zero sequence by software, the number of sequences was assumed 1 in the related box, but the actual number was two. In this study, the number of loading cycles for the conditioning sequence was defined 10 cycles, and the number of cycles to display in the software interface was selected 5. The second part of this section included more details of loading as initial load for conditioning, Initial main loading force, peak strain, contact force, load cycle width, load cycle repeat time, frequency, and adaptation rate.

The Initial loading force for conditioning and main loading sequences were selected based on FEM analysis. The Initial load was modified through trial and error tests on a dummy specimen for each mix design.

The applied load for conditioning was chosen to limit output strain in a linear range (<100 micro-strain), and the initial load for the main loading stage was selected proportional to an assigned peak thermal strain for each specimen. The peak thermal

strain was calculated individually for each mix design based on the test results for thermal coefficients. The contact force was assumed 0.05 kN for all mixtures. Load cycle width and Load cycle repeat time were determined considering the frequency and rest times. If the specimen is subjected to under 0.01 loading frequency with 10 s rest time, then the load cycle width and the load cycle repeat time would be 100000 ms and 110000 ms, respectively. Test specimens were tested at two loading frequencies: 0.1Hz and 0.01Hz; the adaptation ratio was selected as 0.75 (Figure 3.15).

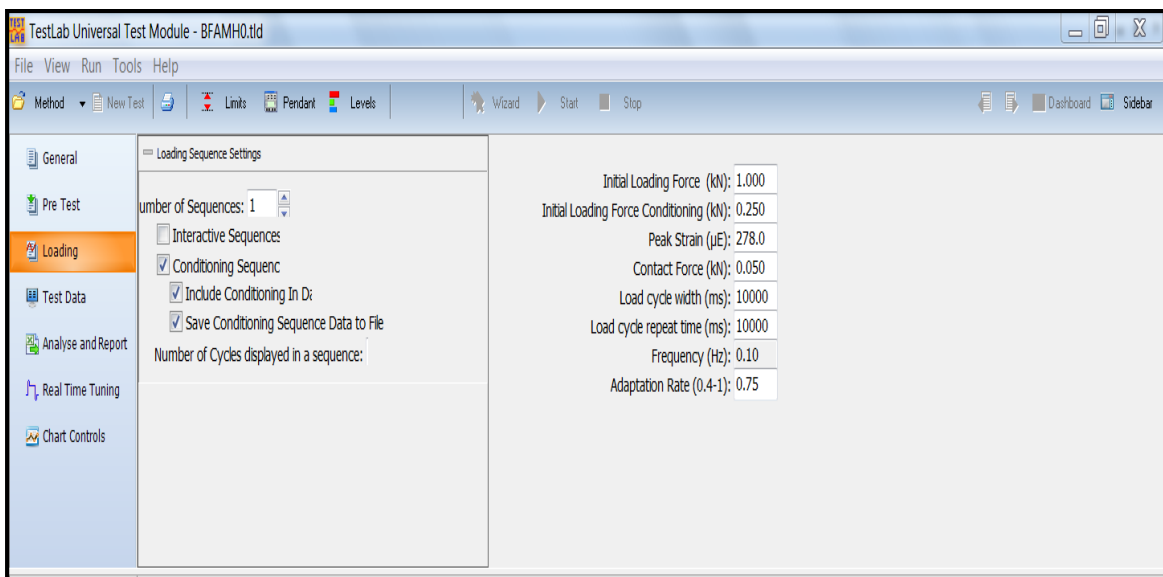


**Figure 3.15.** The loading section in the test navigation menu

#### 4. Test data

The test parameters obtained by different transducers are displayed in this section, so that the entire progress can be observable throughout the testing. As previously stated, each sequence up to 10 last cycles could be shown by the software; however, only the last five cycles are displayed for clarity (Figure 3.16).

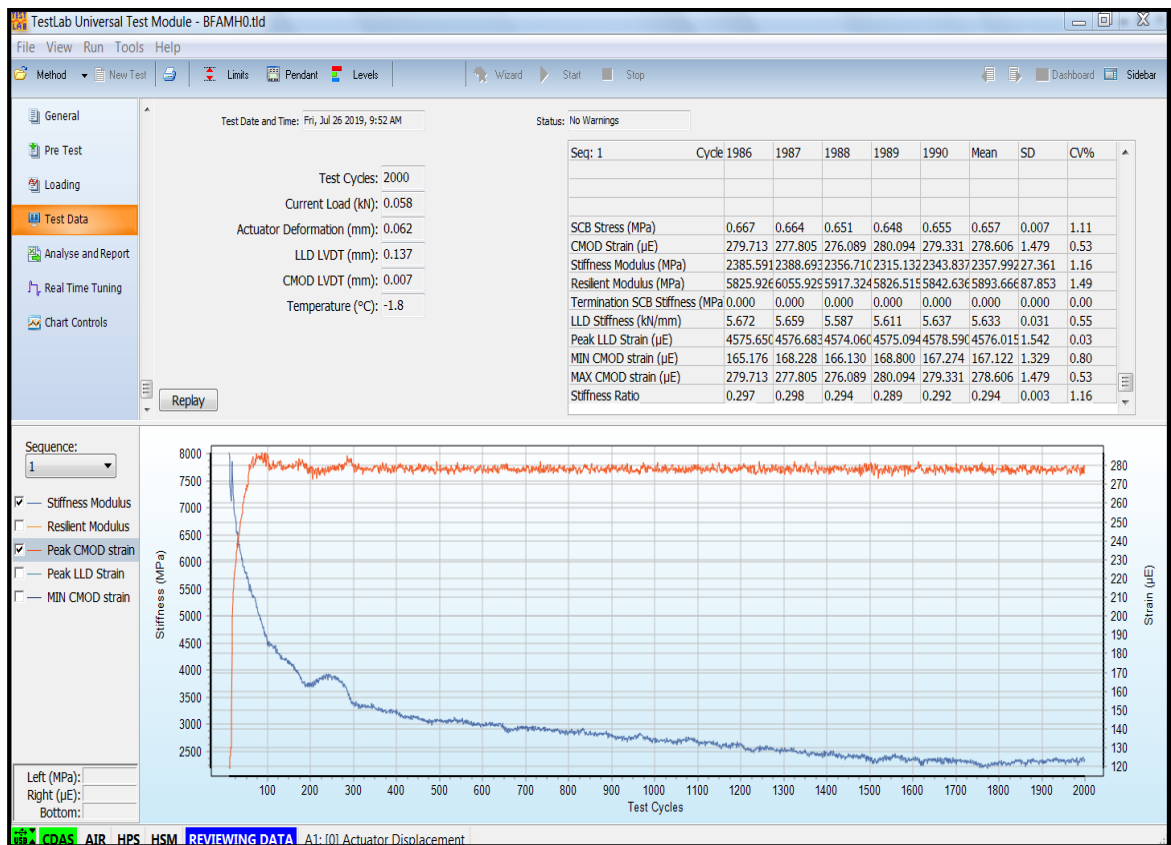


Figure 3.16. A view of the Testlab program showing test data in the test navigation menu

## 5. Analysis and report

This feature exports data from CDAS to Excel sheet for post-processing, and after the analysis, the data summary can be displayed in the Test lab again.

## 6. Real time tuning

This section comprised two parts; the part in the left displays waveform of the loading signal along with parameters of y and x-axis of the chart. After each test, the wave button appeared above the chart. By clicking on it, the chart switched between the first cycle of the first sequence and the last cycle of the last sequence. In the second part, real time loading block tuning is shown, which includes PID tuning section and adaptive control options. In this study, the test procedure was designed as a multi-sequence, so PID values for different sequences could be edited separately (Figure 3.17).

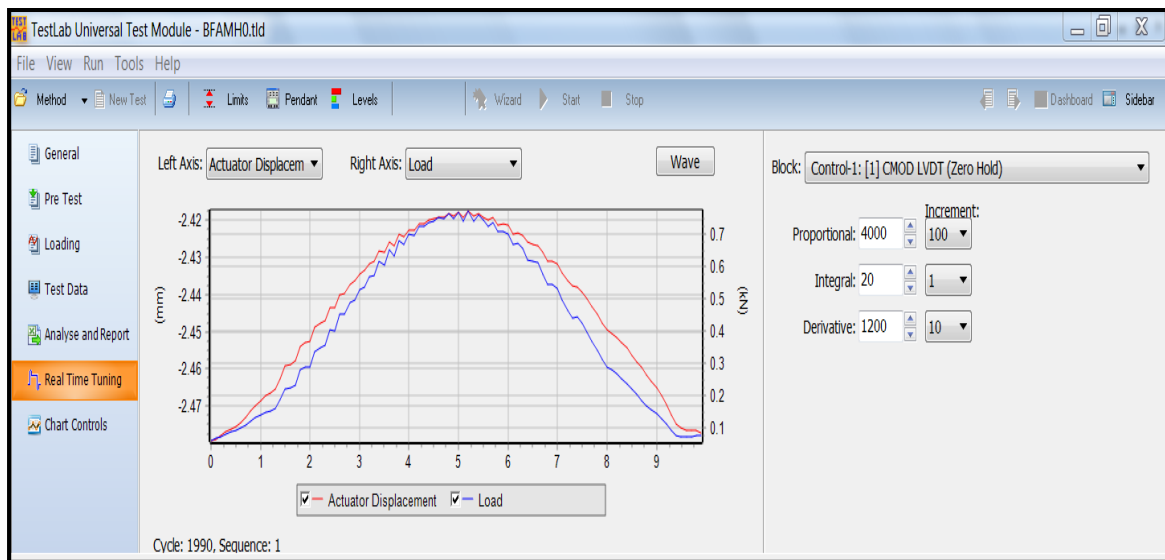


**Figure 3.17.** A real-time tuning in the test navigation menu

## 7. Chart controls

In the charting section, variables are presented along three axes of a chart. After the test started, charting option could be selected from the real-time screen. Normally, the horizontal axis is used to display time fractions when the right and left axes show other variables. In the current testing program, the right and left axes were used to display

stiffness modulus and CMOD strain, respectively, and the horizontal axis displayed the number of loading cycles.

## **b) Test designer**

As previously stated, no pre-defined method file was prepared by the manufacturer of the TestLab software for a semicircular specimen in the strain control mode, so by using the test designer application, a new test procedure was developed for the thermal fatigue test in strain control mode. The generated test module consists of the following sections:

### **1. Test system**

The test layout is the first part of this section. The test layout can be a multi-sequence or single sequence. It was found that multi-sequence and multi-chart layout more suit with the test procedure in this study. In the other part of this section, various channels were assigned to different functions, such as control or data acquisition. Specimen option is the last part of this section; the shape of the specimen and its volume and density were defined in this part.

### **2. Loading parameters**

The first part of this section can be shown in two display modes. If the test is defined as a single sequence, then it has two columns of static parameters. In the case of a multi-sequence test, one column is allocated to dynamic parameters when the other is for static parameters. Static parameters refer to material or test parameters that remain constant during loading, and this constant parameter is whether load or displacement. In this study, static parameters were initial loading force, peak strain, contact force, load cycle width, load cycle repeat time, frequency, and adaptation rate, which are identified by ID numbers of L20 to L27. The loading parameters setting is another part

of this section. Precision display, units, default value, and value range were specified in this part (Figure 3.18).

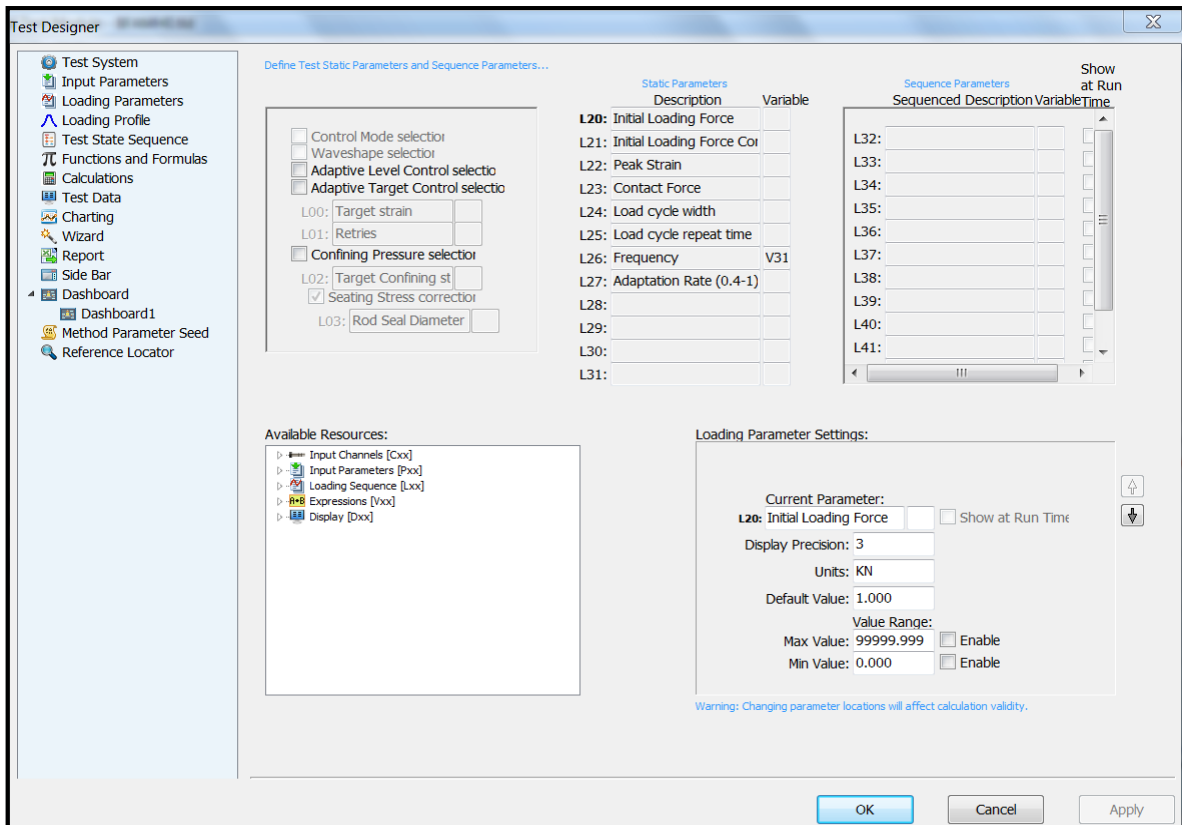


**Figure 3.18.** A view of the Testlab program showing loading parameter in the test designer

### 3. Loading profile

The beginning part of this section is the loading control block, and the loading shape to apply by the actuator during the test was determined by this part. By adding new blocks to this part, the sequence of loading can be specified. For this testing program, the control block comprises three blocks, the test started with zero hold block, and the second block is the main loading, the test is finalized with an unloading block (Figure 3.19). The next part of this section is the control mode. According to the type of test to be conducted, actuator displacement, and load could be chosen as a control mode.



For this study, the first block or zero hold block is in strain control mode, and the unloading block is applied in the load control mode. Another part of this section is about the loading function. For each control mode, a loading function must be selected, such as hold, rate, ramp, and loading waveform. If the waveform is chosen as a loading function, more detailed options become available under the loading function part. For the first block in the strain control mode, the ramp was preferred as a loading function. In the main loading block, the waveform was selected as a loading function, and haversine is the type of the waveform chosen for the main loading function of the thermal fatigue test. In the third block, similar to the first block, the ramp was assigned to the unloading block. In the last part of this section, different conditions for the block transfer are specified; those conditions are loading cycles, actuator displacement and load. If the conditions are met for the block transfer, another box appears to address the next block of the loading procedure (Figure 3.19).



acquisition channel becomes active in this step. In the next part of this section, the number of sequences and waiting time between two sequences were determined. There were two sequences for the thermal fatigue test in this study: conditioning sequence and main sequence, the waiting time between the two sequences was 600s. Two conditions were defined to end the main loading state: max loading cycles achieved or reduced stiffness of the specimen meeting the failure criteria. In the case of this study, the maximum number of loading cycles for the conditioning sequence was 10 cycles, and for the main sequence was 2000 cycles. Whenever the test termination criteria are met, the test could go to the next state, which is unloading (Figure 3.20).

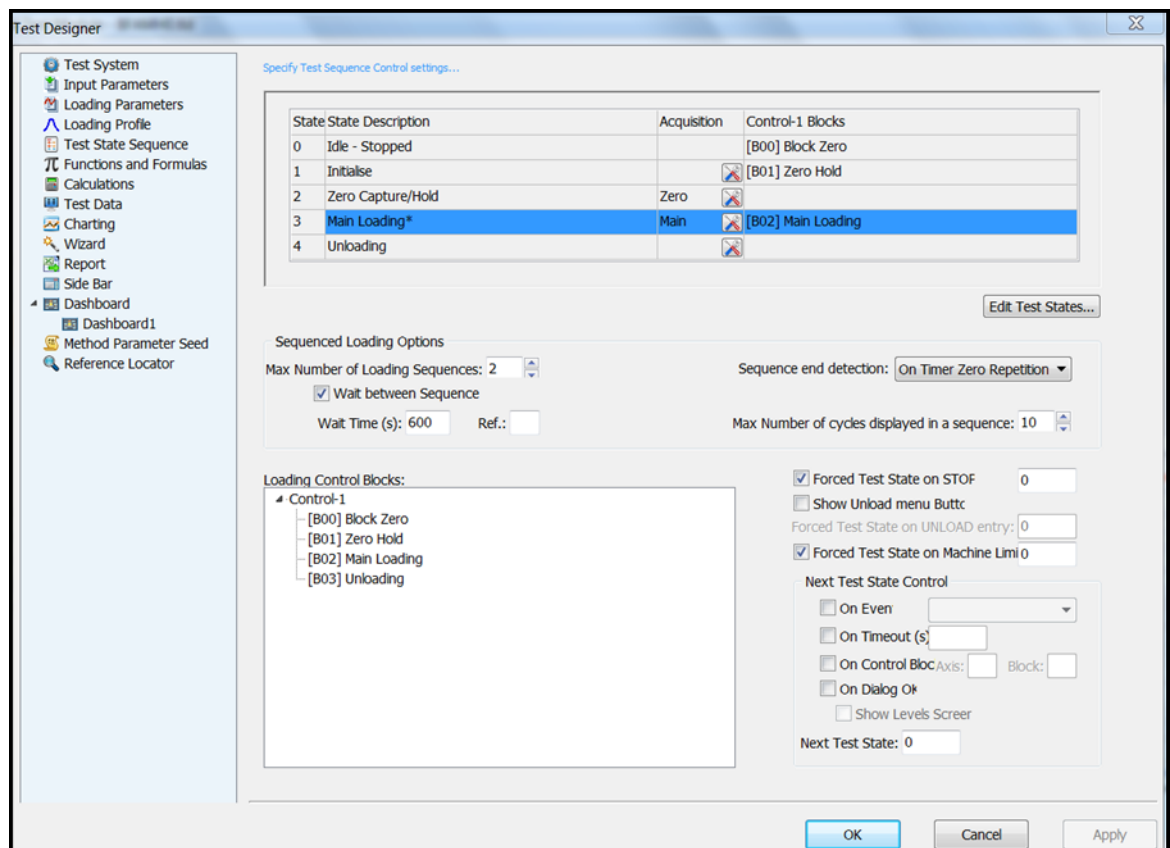


**Figure 3.20.** A view of the Test lab program showing test state sequence in the test designer

## **5. Functions and formulas**

Required functions and formulas to design a test procedure were defined in this section. Functions are classified into the following types: input channel functions, input parameter functions, math functions, special functions, and logical operations. Formulas are given in two types: user pre-defined and user defined formulas, which according to the new test procedure for this study, were introduced in this section.

## **6. Calculations**

The first part of this section is about available resources. By using parameters placed in this part, new expressions and variables can be generated. Available sources consist of input channels, input parameters, loading sequences, expressions, and displays. In the expression builder part, the required expressions are built by dragging formulas and functions from available resources and placing them inside the if condition box or the expression box. The details for calculations are attached to Appendix A.

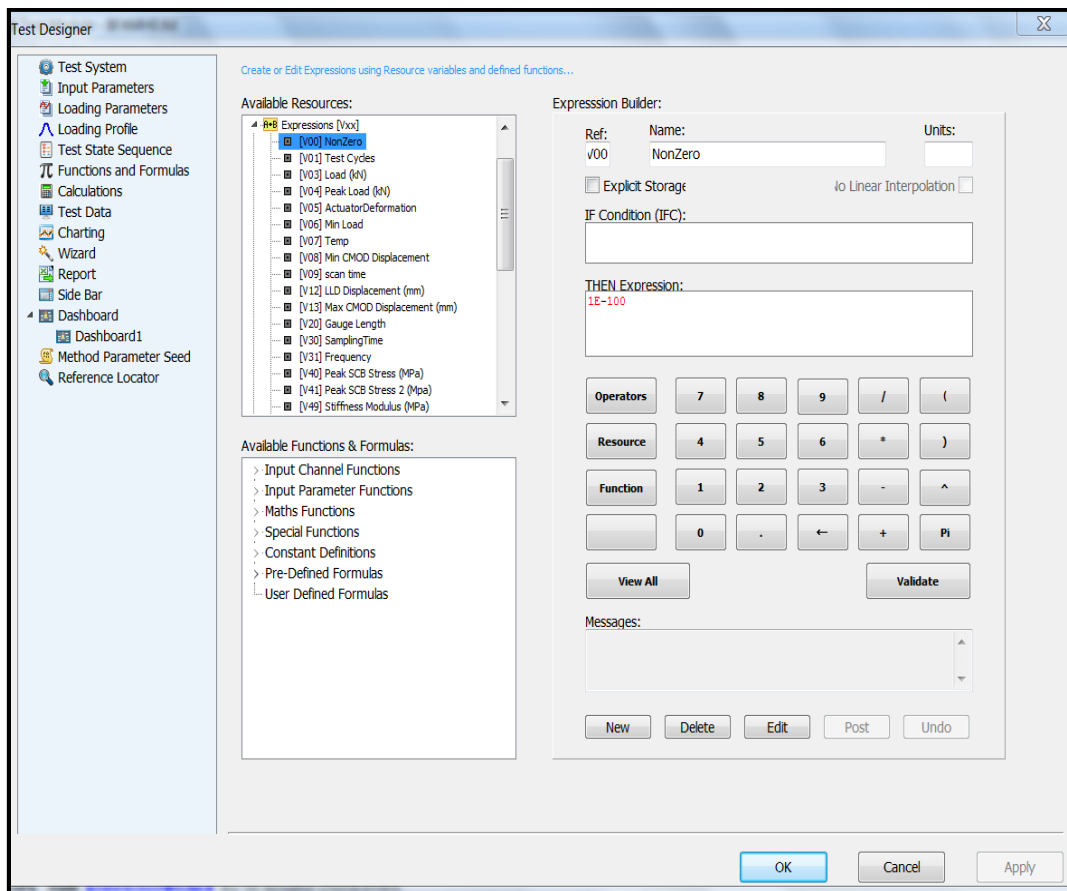


**Figure 3.21.** A view of the Testlab program showing calculations in the test designer

## 7. Charting

In the charting section, variables are presented along with three axes of the chart. After the test started charting option could be selected from the real time screen. Normally, the horizontal axis was used to display the time element, while the right and left axes are used to show other variables. In the test module developed for this study, the right axis and left axis were used to observe stiffness modulus and strain, while the horizontal axis displayed the number of loading cycles.

## **8. Wizard**

Not applied in this study

## **9. Report**

In this section, two methods are proposed for exporting data to Excel file for further analysis: manual mapping and automatic mapping. For this test, automatic mapping was selected, so input parameters, the data file info, specimen info, method file info, loading parameters, test data, and time series data for different sequences were exported to predetermined positions in the separate Excel worksheets.

## **10. Sidebar**

Not involved in this study

## **11. Dashboard**

Not applied in this study

## **12. Method parameter seed**

Not used in this study

## **13. Reference locator**

Not used in this study

\*Detailed information about the above options can be found in Pavetest test designer manual (Testlab Software Reference - Test Designer-PAVETEST V1.03 2014).

### **3.4 The temperature difference for measuring thermal strain of asphalt concrete**

To determine thermal strain in asphalt concrete, the temperature difference between the maximum and minimum temperature was required. In this research, Ankara province was considered to evaluate the resistance of asphalt concrete against thermal fatigue cracking. For this purpose, weather data for 19 years from 2000 to 2019 were obtained from weather organization, so based on data analysis, 10 °C was found to be the most frequent temperature difference. The thermal strain calculation to measure thermal fatigue was then established on the mentioned temperature difference.

### **3.5 Determination of thermal strains for applying cyclic haversine loading**

Applied thermal strain for each mixture is a function of its measured thermal coefficient. By using equation 3.3, thermal strain due to temperature change was calculated for different specimens. The cyclic haversine loads were applied on different specimens at the constant strain amplitude to investigate the resistance of various asphalt mixtures against thermal fatigue.

$$\varepsilon = \alpha \Delta t \quad (3.3)$$

where:

$\varepsilon$  = thermal strain at a specified temperature difference

$\alpha$  = thermal coefficient

$\Delta t$  = maximum frequency of temperature differentials

### 3.6 Applying constant strain mode for semicircular bending geometry

The thermal fatigue behavior of asphalt concrete under constant strain loading was already investigated by Arabzadeh and Guler (2015). They conducted thermal fatigue tests in the strain control mode through the direct tension test. Applying a constant strain in three-point bending test is a more complicated procedure than a direct tension test because the strain cannot be directly controlled in the bending test. In the first step, the initial load is applied (initial load is estimated by trial and error on dummy specimen) to the top of the semicircular specimen. In the next cycles, considering the measured strain in the bottom midpoint of the specimen, the load is modified by the software to reach the target strain. After reaching the target strain, this procedure continues to keep the induced strain at the desired level during the test until failure of the specimen or until the maximum number of cycles has been reached (Figure 3.22 &23).

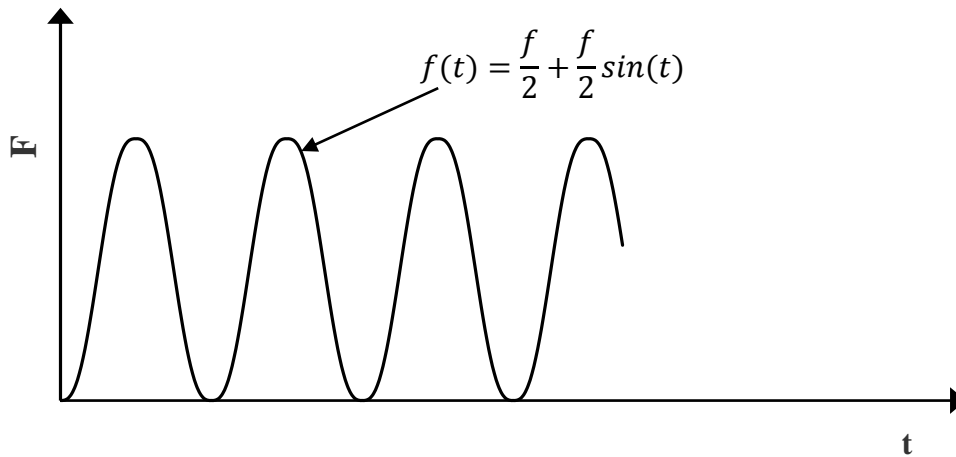


**Figure 3.22.** The waveform for applied force on the specimen



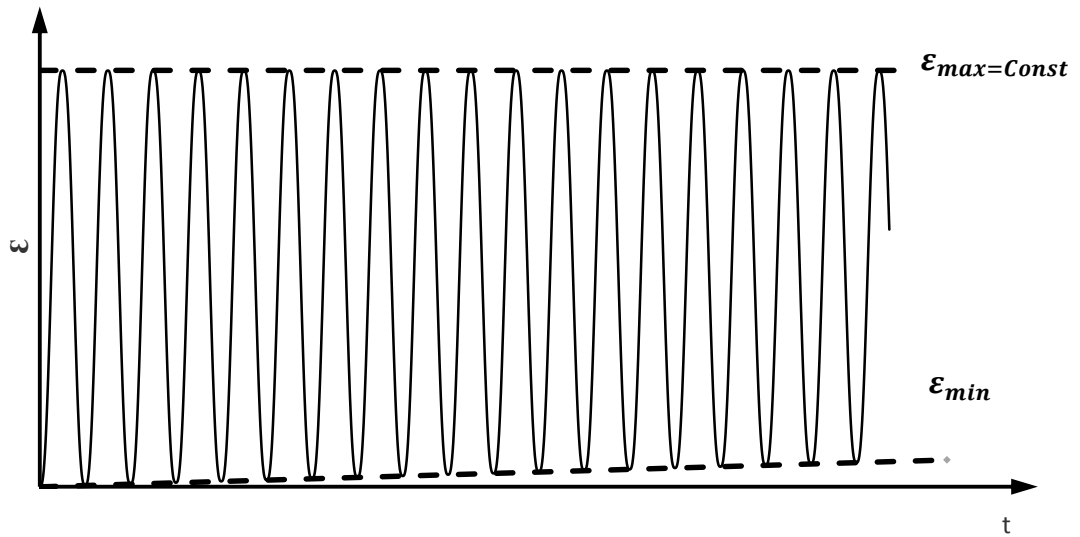


**Figure 3.23.** The waveform for strain at the bottom center of the specimen

### 3.7 Preparation of semicircular specimen for thermal fatigue test

In this step of the study, semicircular specimens were produced from SGC samples of different mixtures. A diamond saw cutter was used to produce two SGC slices with 35 mm thickness from the center of each cylindrical sample. Each slice was then cut into two identical halves, and the remaining parts of the cylindrical samples were thrown away. Four semicircular specimens were produced from each SGC cylinder sample, and each semicircular specimen was used for an individual fatigue test (Figure 3.24).



**Figure 3.24.** a) Sliced SGC specimen 35mm from center, b) cutting cylinder sample to obtain semicircular specimen, c) cut semicircular samples

### 3.8 Preparation of semicircular specimen for thermal fatigue test

To evaluate the resistance of different mixtures against thermal fatigue, the applied deformations were measured by the CMOD gauge and the LLD gauge during a three-point bending test. The gauge length for CMOD was selected 25mm, based on the stress distribution of a semicircular specimen in the bending mode according to the results of FEM analysis. The main purpose of conducting the FEM analysis is given in chapter 4. To attach CMOD gauge to the surface of the specimen, two steel knives were glued to the bottom surface of the SCB specimen in the following steps: The

midpoint of the bottom surface of the specimen was determined by a caliper and then the gauge length was marked. In the next step, the steel beam template with 10mm width was placed over the marked line, so the centerline of the beam was completely matched to the drawn line. At the final step, two knives were placed in two sides of the steel beam with an equal distance from the specimen's side edges. By using 502 Cyanoacrylate Adhesive, steel knives were glued to the specimen surface (Figure 3.25a). To measure LLD, a steel gauge point was mounted on the specimen, and the gauge length for measuring linear line displacement was adjusted to 30mm. To properly install the LLD gauge point, a rectangular metal template with 150×75 mm dimensions and a 10mm diameter hole for gauge point was prepared in the laboratory (Figure 3.25b). The template was placed over the SCB specimen, so its longer side coincided with the bottom edge of the specimen, then a steel pad with 8mm diameter and 6mm height was placed inside the embedded hole and glued to the specimen (Figure 3.26).

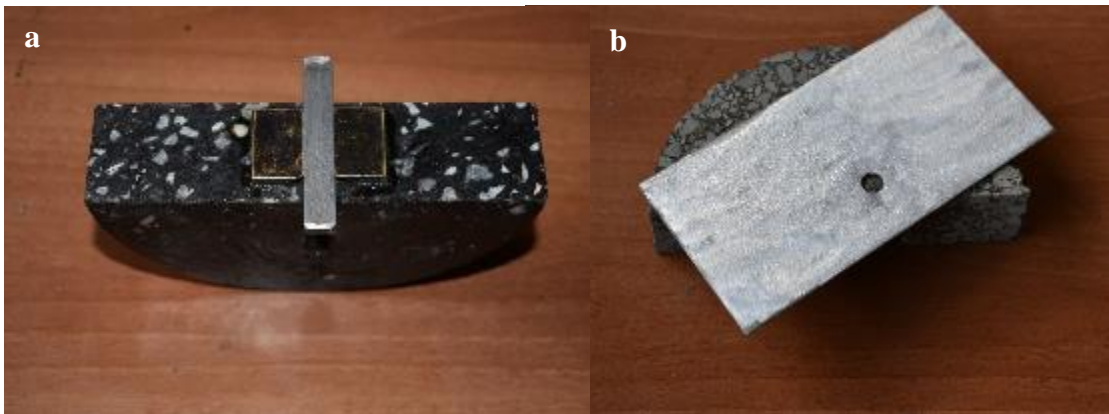


**Figure 3.25.a)** Mounting steel knives to CMOD measurement using steel beam, **b)** Mounting point gauge for LLD using a template

To measure CMOD and LLD Amatek Solartron metrology MD/5 and AX/5 series were used, respectively, and the LVDT for CMOD is the inductive miniature sensor, and the LVDT for LLD measurement is a spring push type LVDT. Both LVDTs have a nominal linear range of  $\pm 5$  mm and temperature operating range of  $-10^{\circ}\text{C}$  to  $+85^{\circ}\text{C}$ ; the sensitivity of LVDTs are  $105\text{mV/V/mm}$ .



**Figure 3.26.** Attachment of gauges and LVDT to measure strains from CMOD and LLD

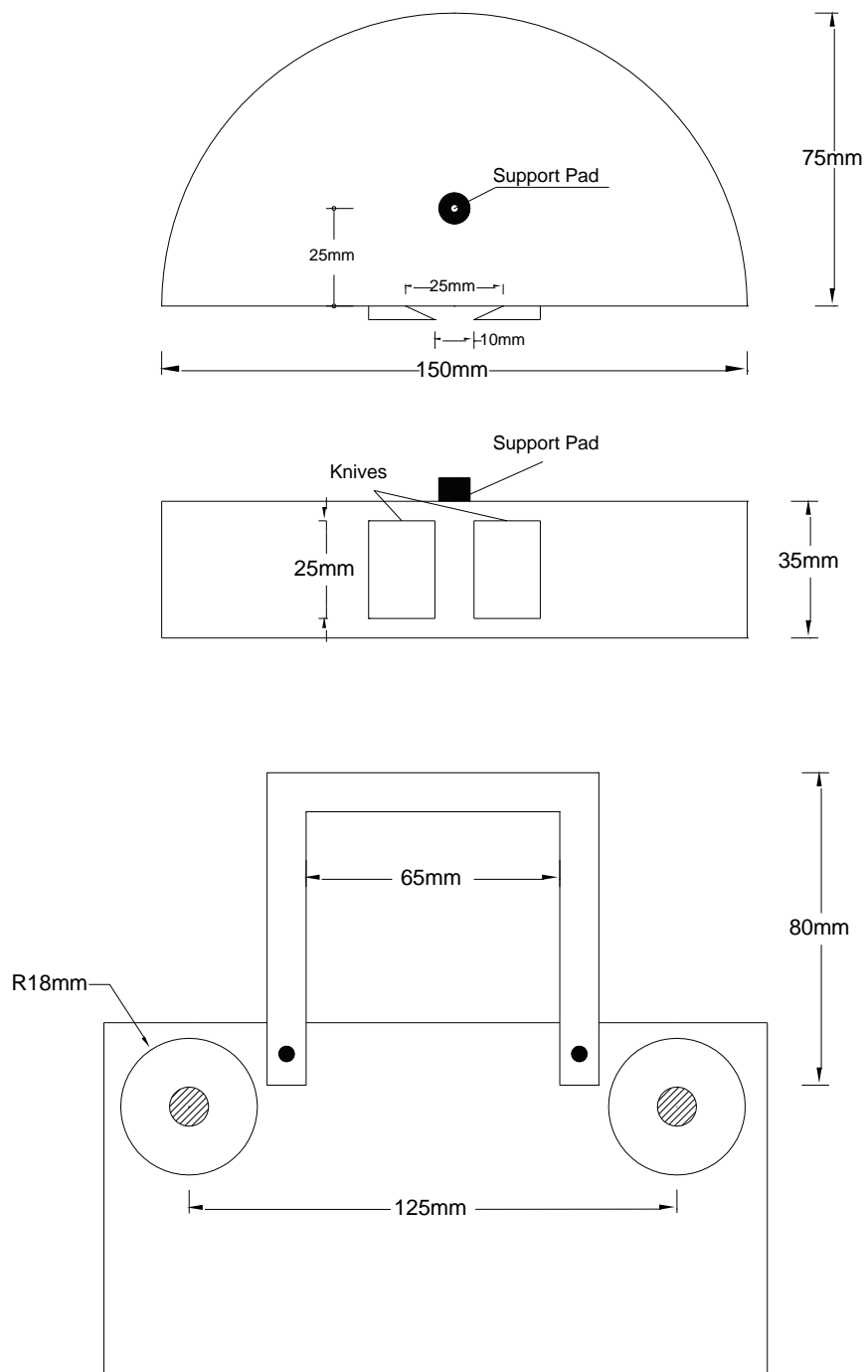


**Figure 3.27.** Schematic SCB test setup to measure thermal fatigue resistance

### 3.9 Design of experiment

In this study, the effect of mix design parameters including gradation, aggregate type, asphalt type, aging, and test parameters involving loading frequency and rest time on the performance of asphalt concrete under thermal fatigue was evaluated. To assess the various variables properly, and by considering available sources, an experimental program was required. Diagram for implied experimental design is shown in Figure 3.28. There are two levels of aggregates, limestone and basalt. For each type of aggregate, two types of gradation were defined as coarse and fine. Mixtures were produced by mixing the aggregate with two levels of asphalt modification, unmodified 50-70 asphalt, and modified 50-70 asphalt with 4.5% SBS. Specimens were aged at two levels: aged and unaged. Specimens were also tested at two levels of loading frequency, 0.1Hz, and 0.01Hz, in each frequency tests were conducted at three different rest times.

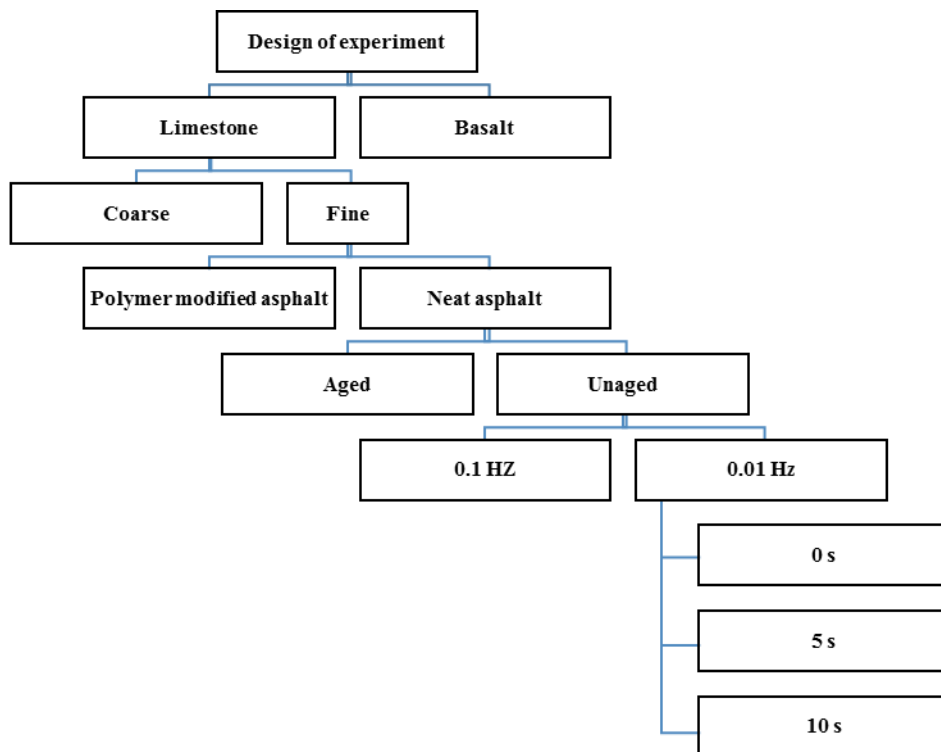


Figure 3.28. Diagram of the experimental design

Since full factorial design consumes a significant amount of time and resources, fractional factorial design of  $2^{5-1} \times 3$  was selected for this study. Fractional factorial experiments use variables of design to reduce the size of an experiment selectively. Design variables in this research comprised two types of gradations, two types of aggregates, two levels of asphalt modification, two aging rates, two frequencies, and three rest times (Table 3.5).

**Table 3.5.** Details of variables used in the design

S.no	Name of variable	Alphabet	Level	Symbol	Coded
1	Aggregate type	X1	2	L, B	+1,-1
2	Gradation	X2	2	C, F	+1,-1
3	Polymer modification	X3	2	N, M	+1,-1
4	Aging	X4	2	A, U	+1,-1
5	Frequency	X5	2	S, H	+1,-1
6	Rest time	X6	3	0, 5, 10	+1,0,-1

To reduce the number of required specimens, aggregate type and gradation were selected as confounding variables. Hence the number of configurations was calculated 48, and considering three replicate for each configuration, the total number of required specimens for testing was obtained 144. Table 3.6 shows a typical design matrix needed for the fractional factorial design, with five variables having two levels and one confounding variable. Table 3.7 indicates the matrix of a design factor having three levels, which in this study is the rest time. By summing Tables 3.6 and 3.7, the given data in Table 3.8 were generated, which determined the required specimens for the thermal fatigue test. It is worth mentioning that at the final step of the experimental design, specimens were randomized in Microsoft Excel to avoid any bias in the test results. The summary of specimens prepared for thermal coefficient measurement and thermal fatigue test is given in Table 3.9.

**Table 3.6.** Standard matrix available for the fractional factorial design of  $2^{5-1}$  (NIST-Engineering Statistics Handbook)

<b>Design Matrix for a Fractional Factorial</b>											
<b>Seq</b>	<b>X1</b>	<b>X2</b>	<b>X3</b>	<b>X4</b>	<b>X5=X1X2</b>	<b>Seq</b>	<b>X1</b>	<b>X2</b>	<b>X3</b>	<b>X4</b>	<b>X5=X1X2</b>
<b>1</b>	-1	-1	-1	-1	+1	<b>9</b>	-1	-1	-1	+1	+1
<b>2</b>	+1	-1	-1	-1	-1	<b>10</b>	+1	-1	-1	+1	-1
<b>3</b>	-1	+1	-1	-1	-1	<b>11</b>	-1	+1	-1	+1	-1
<b>4</b>	+1	+1	-1	-1	+1	<b>12</b>	+1	+1	-1	+1	+1
<b>5</b>	-1	-1	+1	-1	+1	<b>13</b>	-1	-1	+1	+1	+1
<b>6</b>	+1	-1	+1	-1	-1	<b>14</b>	+1	-1	+1	+1	-1
<b>7</b>	-1	+1	+1	-1	-1	<b>15</b>	-1	+1	+1	+1	-1
<b>8</b>	+1	+1	+1	-1	+1	<b>16</b>	+1	+1	+1	+1	+1

**Table 3.7.** Design matrix for 1 Level 3 factor design

<b>Seq</b>	<b>X6</b>
<b>1</b>	-1
<b>2</b>	0
<b>3</b>	1



**Table 3.8.** Design matrix as a result of fractional factorial design  $2^{5-1} \times 3$ (3 replication)

Seq.	X1	X2	X3	X4	X5	X6	Seq.	X1	X2	X3	X4	X5	X6
1	-1	-1	-1	-1	1	-1	31	-1	1	1	1	-1	0
2	1	-1	-1	-1	-1	-1	32	1	1	1	1	1	0
3	-1	1	-1	-1	-1	-1	33	-1	-1	-1	-1	1	1
4	1	1	-1	-1	1	-1	34	1	-1	-1	-1	-1	1
5	-1	-1	1	-1	1	-1	35	-1	1	-1	-1	-1	1
6	1	-1	1	-1	-1	-1	36	1	1	-1	-1	1	1
7	-1	1	1	-1	-1	-1	37	-1	-1	1	-1	1	1
8	1	1	1	-1	1	-1	38	1	-1	1	-1	-1	1
9	-1	-1	-1	1	1	-1	39	-1	1	1	-1	-1	1
10	1	-1	-1	1	-1	-1	40	1	1	1	-1	1	1
11	-1	1	-1	1	-1	-1	41	-1	-1	-1	1	1	1
12	1	1	-1	1	1	-1	42	1	-1	-1	1	-1	1
13	-1	-1	1	1	1	-1	43	-1	1	-1	1	-1	1
14	1	-1	1	1	-1	-1	44	1	1	-1	1	1	1
15	-1	1	1	1	-1	-1	45	-1	-1	1	1	1	1
16	1	1	1	1	1	-1	46	1	-1	1	1	-1	1
17	-1	-1	-1	-1	1	0	47	-1	1	1	1	-1	1
18	1	-1	-1	-1	-1	0	48	1	1	1	1	1	1
19	-1	1	-1	-1	-1	0	49	-1	-1	-1	-1	1	-1
20	1	1	-1	-1	1	0	50	1	-1	-1	-1	-1	-1
21	-1	-1	1	-1	1	0	51	-1	1	-1	-1	-1	-1
22	1	-1	1	-1	-1	0	52	1	1	-1	-1	1	-1
23	-1	1	1	-1	-1	0	53	-1	-1	1	-1	1	-1
24	1	1	1	-1	1	0	54	1	-1	1	-1	-1	-1
25	-1	-1	-1	1	1	0	55	-1	1	1	-1	-1	-1
26	1	-1	-1	1	-1	0	56	1	1	1	-1	1	-1
27	-1	1	-1	1	-1	0	57	-1	-1	-1	1	1	-1
28	1	1	-1	1	1	0	58	1	-1	-1	1	-1	-1
29	-1	-1	1	1	1	0	59	-1	1	-1	1	-1	-1
30	1	-1	1	1	-1	0	60	1	1	-1	1	1	-1

**Table 3.8. Continued**

<b>Seq.</b>	<b>X1</b>	<b>X2</b>	<b>X3</b>	<b>X4</b>	<b>X5</b>	<b>X6</b>	<b>Seq.</b>	<b>X1</b>	<b>X2</b>	<b>X3</b>	<b>X4</b>	<b>X5</b>	<b>X6</b>
<b>61</b>	-1	-1	1	1	1	-1	<b>91</b>	-1	1	-1	1	-1	1
<b>62</b>	1	-1	1	1	-1	-1	<b>92</b>	1	1	-1	1	1	1
<b>63</b>	-1	1	1	1	-1	-1	<b>93</b>	-1	-1	1	1	1	1
<b>64</b>	1	1	1	1	1	-1	<b>94</b>	1	-1	1	1	-1	1
<b>65</b>	-1	-1	-1	-1	1	0	<b>95</b>	-1	1	1	1	-1	1
<b>66</b>	1	-1	-1	-1	-1	0	<b>96</b>	1	1	1	1	1	1
<b>67</b>	-1	1	-1	-1	-1	0	<b>97</b>	-1	-1	-1	-1	1	-1
<b>68</b>	1	1	-1	-1	1	0	<b>98</b>	1	-1	-1	-1	-1	-1
<b>69</b>	-1	-1	1	-1	1	0	<b>99</b>	-1	1	-1	-1	-1	-1
<b>70</b>	1	-1	1	-1	-1	0	<b>100</b>	1	1	-1	-1	1	-1
<b>71</b>	-1	1	1	-1	-1	0	<b>101</b>	-1	-1	1	-1	1	-1
<b>72</b>	1	1	1	-1	1	0	<b>102</b>	1	-1	1	-1	-1	-1
<b>73</b>	-1	-1	-1	1	1	0	<b>103</b>	-1	1	1	-1	-1	-1
<b>74</b>	1	-1	-1	1	-1	0	<b>104</b>	1	1	1	-1	1	-1
<b>75</b>	-1	1	-1	1	-1	0	<b>105</b>	-1	-1	-1	1	1	-1
<b>76</b>	1	1	-1	1	1	0	<b>106</b>	1	-1	-1	1	-1	-1
<b>77</b>	-1	-1	1	1	1	0	<b>107</b>	-1	1	-1	1	-1	-1
<b>78</b>	1	-1	1	1	-1	0	<b>108</b>	1	1	-1	1	1	-1
<b>79</b>	-1	1	1	1	-1	0	<b>109</b>	-1	-1	1	1	1	-1
<b>80</b>	1	1	1	1	1	0	<b>110</b>	1	-1	1	1	-1	-1
<b>81</b>	-1	-1	-1	-1	1	1	<b>111</b>	-1	1	1	1	-1	-1
<b>82</b>	1	-1	-1	-1	-1	1	<b>112</b>	1	1	1	1	1	-1
<b>83</b>	-1	1	-1	-1	-1	1	<b>113</b>	-1	-1	-1	-1	1	0
<b>84</b>	1	1	-1	-1	1	1	<b>114</b>	1	-1	-1	-1	-1	0
<b>85</b>	-1	-1	1	-1	1	1	<b>115</b>	-1	1	-1	-1	-1	0
<b>86</b>	1	-1	1	-1	-1	1	<b>116</b>	1	1	-1	-1	1	0
<b>87</b>	-1	1	1	-1	-1	1	<b>117</b>	-1	-1	1	-1	1	0
<b>88</b>	1	1	1	-1	1	1	<b>118</b>	1	-1	1	-1	-1	0
<b>89</b>	-1	-1	-1	1	1	1	<b>119</b>	-1	1	1	-1	-1	0
<b>90</b>	1	-1	-1	1	-1	1	<b>120</b>	1	1	1	-1	1	0

**Table 3.8.** Continued

Seq.	X1	X2	X3	X4	X5	X6	Seq.	X1	X2	X3	X4	X5	X6
121	-1	-1	-1	1	1	0	133	-1	-1	1	-1	1	1
122	1	-1	-1	1	-1	0	134	1	-1	1	-1	-1	1
123	-1	1	-1	1	-1	0	135	-1	1	1	-1	-1	1
124	1	1	-1	1	1	0	136	1	1	1	-1	1	1
125	-1	-1	1	1	1	0	137	-1	-1	-1	1	1	1
126	1	-1	1	1	-1	0	138	1	-1	-1	1	-1	1
127	-1	1	1	1	-1	0	139	-1	1	-1	1	-1	1
128	1	1	1	1	1	0	140	1	1	-1	1	1	1
129	-1	-1	-1	-1	1	1	141	-1	-1	1	1	1	1
130	1	-1	-1	-1	-1	1	142	1	-1	1	1	-1	1
131	-1	1	-1	-1	-1	1	143	-1	1	1	1	-1	1
132	1	1	-1	-1	1	1	144	1	1	1	1	1	1

**Table 3.9.** Summary of specimen prepared for thermal coefficient measurement and thermal fatigue test

S.no	Variables	Explanation	
1	Aggregate type	Limestone (L), Basalt (B)	
2	Asphalt type	Neat (N), Modified (M)	
3	Gradation	Coarse (C), Fine (F)	
4	Shape of specimen	Prismatic	Semicircular
5	Specimen size	120×65×50mm	150×75×35mm
6	No of specimen prepared	16	144
7	SGC specimen prepared	48	

### **3.9.1 Multivariate analysis of design variables**

Multivariate data analysis is an expanded bivariate analysis in which some variables are assumed to be dependent, and the others are independent variables. Dependent variables are the parameters that are influenced by the independent variables. The objective of multivariate analysis is to show whether independent variables are significant or not; hence, by applying multiple regression, the effect of each independent variable on dependent variables would be clarified. In this study, the multivariate analysis of variance (MANOVA) was used to measure the effect of 6 non-metric independent variables on some dependent metric variables. Independent variables included: aggregate type, gradation, asphalt type, aging, frequency, rest time. Metric dependent variables consisted of different levels of reduction in stiffness modulus of test specimens.

### 3.10 Aggregate

#### 3.10.1 Gradation and maximum density curve

The gradations for this study were selected by following the Turkish General Directory of Highways (TGDH) specification book (Karayolları Genel Müdürlüğü 2013). According to the TGDH limits for wearing coarse, two types of gradations were selected: type 1 and type 2. While type 1 represents coarse gradation, type 2 is defined for fine gradation. The reason that two types of gradation were selected for this research was to cover a wide range of gradations used in Turkish highway networks. Figures 3.29 and 3.30 represent the selected gradations plotted on a gradation chart with sieve sizes scaled to power 0.45. As shown in Table 3.10 and 3.11, TGDH control points were chosen as criteria for the upper and lower limits of the gradations.

**Table 3.10.** Gradation type 1

Sieve size	KGM control points	Percent passed	
		Basalt	Limestone
19	100-100	100	100
12.5	88-100	95	96
9.5	72-90	85	87
4.75	42-52	48	52
2	25-35	29	26
0.425	10-20	15	11
0.18	7-14	10	7
0.075	3-8	5.5	3

**Table 3.11.** Gradation type 2

Sieve size	KGM control points	Percent passed	
		Basalt	Limestone
12.5	100-100	100	100
9.5	80-100	98	96
4.75	55-72	60	70
2	36-53	38	46
0.425	16-28	18	16
0.18	8-16	11	9
0.075	4-8	6	3

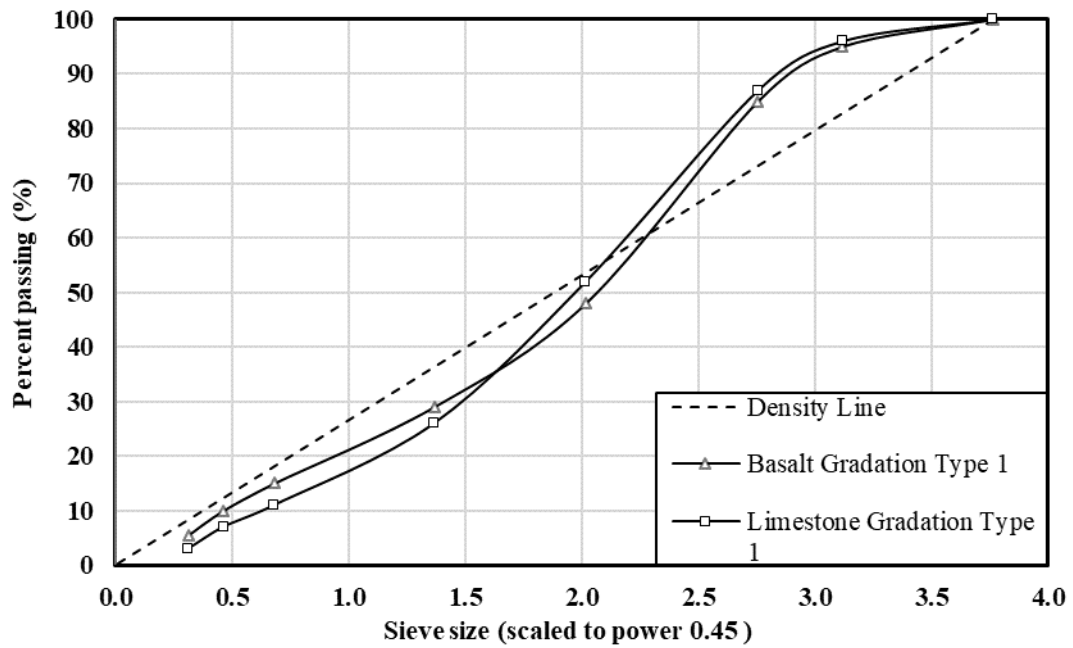


**Figure 3.29.** Selected aggregate gradation type 1 (Coarse)

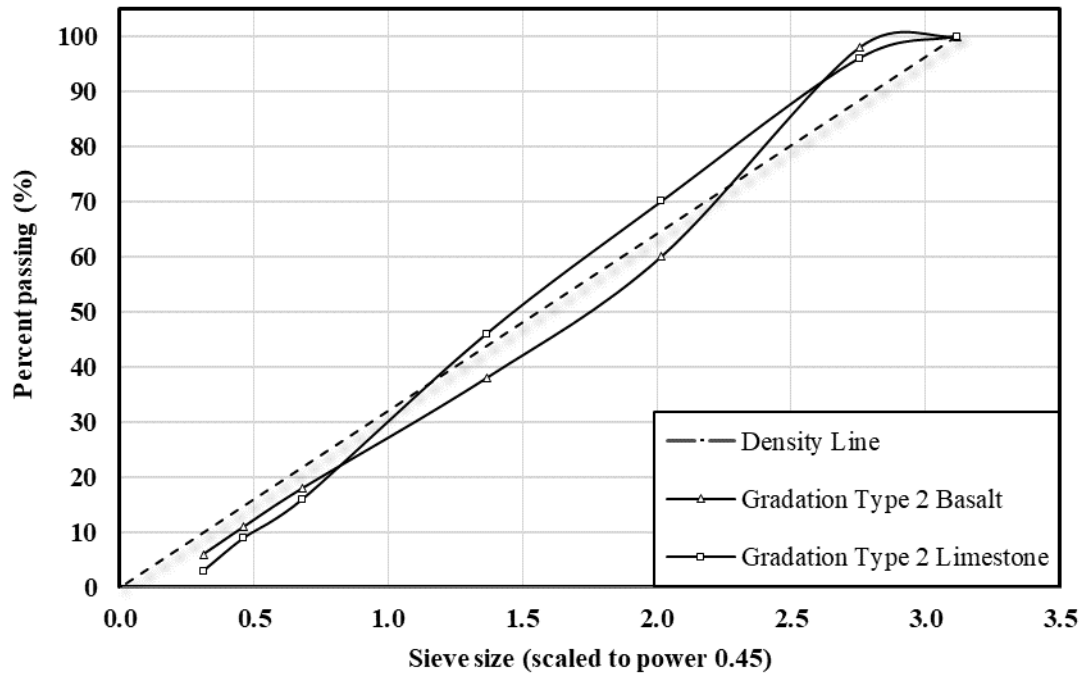


**Figure 3.30.** Selected aggregate gradation type 2 (Fine)

### 3.10.2 Aggregate properties

Two types of aggregate source were used in this study: Basalt and Limestone. The specific gravity, water absorption, and Los Angeles tests were performed on coarse and fine gradations of both basalt and limestone aggregates. The measured properties of aggregates are given in Table 3.12 and 3.13.

**Table 3.12.** Measured properties of coarse aggregates (larger than 4.75 mm)

Properties	Aggregates		Standard name/No
	Limestone	Basalt	
Specific gravity (OD)	2.693	2.545	(ASTM C127 2015)
Average H <sub>2</sub> O absorption	0.44	2.58	(ASTM C127 2015)
LA abrasion value (%)	30.0	17.3	(ASTM C131 2012)

**Table 3.13.** Measured properties of fine aggregates (finer than 4.75 mm)

Properties	Aggregates		Standard name/No
	Limestone	Basalt	
Specific gravity (OD)	2.725	2.596	(ASTM C128 2015)
Average H <sub>2</sub> O absorption (%)	0.52	1.64	(ASTM C128 2015)
Specific Gravity*	2.750	2.664	(ASTM D854 2000)

\* (Finer than 0.075 mm)

### 3.11 Asphalt binder

In this research, 50-70 asphalt binder with two levels of modification was used; modified and unmodified. The modified asphalt binder was produced by adding 4.5% SBS to asphalt 50-70. Measured properties of asphalt binders can be found in Table 3.14 and 3.15. To discriminate between the rheological behavior of two asphalt binders, the viscosity test was implied by Brookfield Rotational Viscometer for both modified and unmodified asphalt binders. The results for these tests are given in Figure 3.31.

**Table 3.14.** Measured properties of asphalt 50-70

Properties	Measured value	Standard name/No
Penetration	51	(ASTM D5 2008)
Specific gravity (kg/m <sup>3</sup> )	1.025	(ASTM D36 2014)
Softening point (ring and ball method)	47.5	(ASTM D 70 2014)
Flash point (°C)	+300	(ASTM D92 2005)
Ductility (5 cm/min, 25 °C)	+100	(ASTM D113 2007)
Kinematic viscosity @135° (C.P)	372	(ASTM D445 2008)



**Table 3.15.** Measured properties of 50-70 polymer modified asphalt binder

Properties	Measured value	Standard name/No
Type and percentage of modifier	SBS,4.5%	-
Penetration	31	(ASTM D5 2008)
Specific gravity (kg/m <sup>3</sup> )	1.024	(ASTM D36 2014)
Softening point (ring and ball method)	68	(ASTM D 70 2014)
Flash point (°C)	+328	(ASTM D92 2005)
Ductility (5 cm/min, 25 °C)	+150	(ASTM D113 2007)
Kinematic viscosity @135° (C.P)	2342	(ASTM D445 2008)

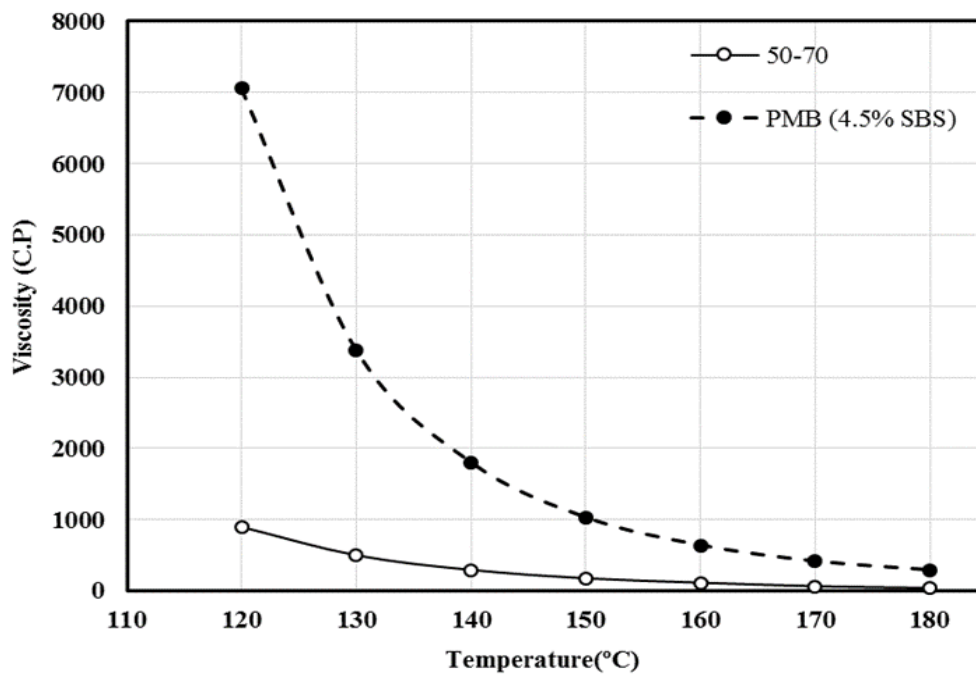


**Figure 3.31.** Comparison between measured viscosity of neat asphalt and polymer modified asphalt

### **3.12 Superpave method for mix design**

Superpave method is a thorough approach to design mixtures based on distinctive performance criteria constrained by the environmental condition, traffic level, and structural section for a specific pavement. This method simplifies the procedure for selecting asphalt mixture components, including asphalt, aggregate, and any substantial modifier, to reach the necessary degree of pavement performance. One of the significant aims of design by the Superpave method is to identify a blend of asphalt binder and aggregate that produces paving mix with sufficient voids and asphalt binder which can satisfy performance characteristics of the pavement over its service life.

### **3.13 Mixing and compacting temperature**

#### **3.13.1 Unmodified asphalt binder (50-70)**

To determine mixing and compaction temperature of unmodified binders according to ASTM D2493 (Referred to as equiviscous), the viscosity was measured with Brookfield Rotational Viscometer, DVII+PRO. In order to conduct a test, a script file in DVII+PRO software was prepared according to ASTM D2493; this code is attached to Appendix B. The rotational viscosity was determined at constant speed of 20 rpm. The start and finish temperature of the test were selected as 120°C and 180°C, respectively, and the viscosity of asphalt binder was determined in 10 degree increments. The viscometer was programmed to reach the next target temperature in 30 minutes and stay at that temperature for 15 minutes to get stabilized. After the temperature was settled, the viscosity of the asphalt binder was measured at every 30 seconds interval for 3 minutes. In each temperature, 6 data points were gathered, and the average value of the data points was set as the viscosity in that temperature. The viscosities were plotted versus temperature in a logarithmic scale. The temperature ranges corresponding to  $170 \pm 20$  C.P was chosen for mixing, and the temperature range corresponding to  $280 \pm 30$  C.P was chosen for compaction. Using the equiviscous

method, mixing and compaction temperatures were calculated as 141°C and 151°C, respectively. (Figure 3.32).

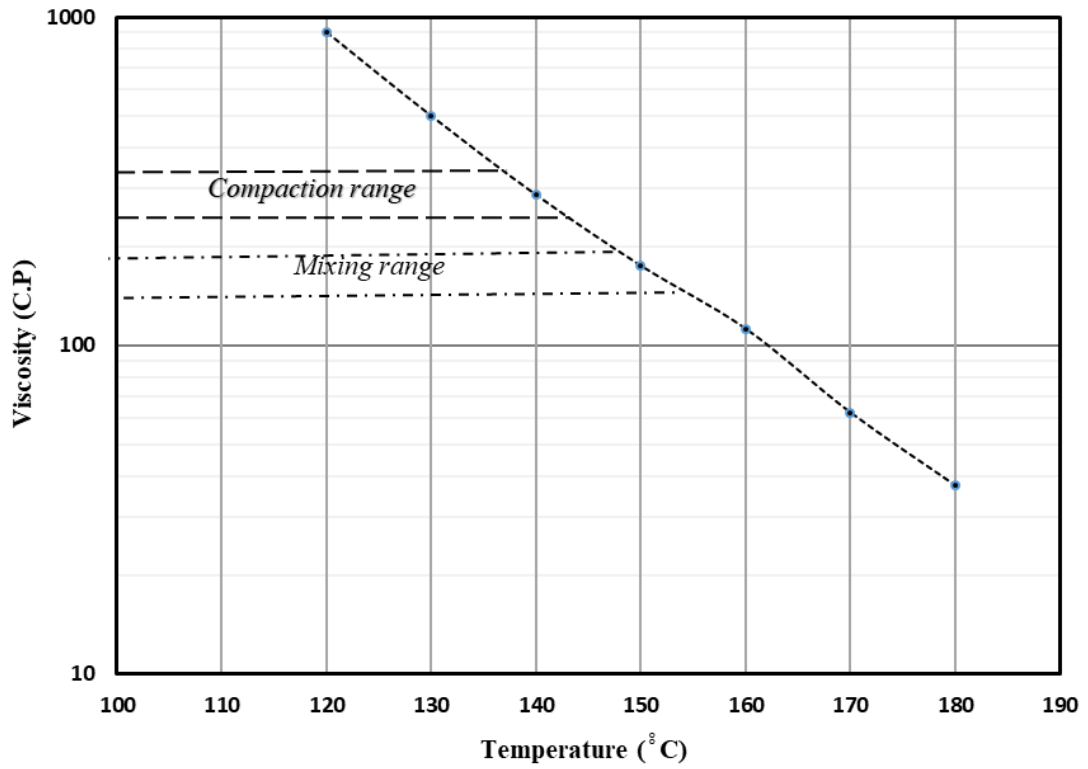


**Figure 3.32.** Mixing and compaction temperature for 50-70 asphalt binder(ASTM D2493 2000)

### 3.13.2 Polymer modified asphalt binder

Most of the mixtures that are prepared by modified binders should be mixed and compacted at higher temperatures both in the laboratory as well in the field, so that around the same degree of workability of mixtures with unmodified binders can be reached. Applying the equiviscous method to calculate the mixing and compaction temperatures for the modified binder results in excessive temperatures, which would dramatically change the rheological properties of modified binders. Most agencies rely on asphalt binder manufacturers to define mixing and compaction temperature because there is no certain procedure to follow. In this study, by employing the Dynamic Shear Rheometer (DSR), the phase angle method was implied to calculate compaction and mixing temperature of modified binder (NCHRP 648, 2010). In this approach, the frequency sweep test was applied on asphalt binder at four temperatures (90° C, 100° C, 110° C, 120° C). Test frequency varied from 0.1 to 100 rad/s with 10 points decade. To see the transition from elastic to viscous behavior over a reasonable range of frequency, the reference temperature was assumed to be 100 °C. Based on the reference temperature, a master curve at reduced frequencies was built for the modified asphalt binder. According to the phase angle method, the part of the master curve that is placed between  $\delta = 85^\circ$  and  $90^\circ$  shows the transition from visco-elastic to absolute viscous behavior. The frequency corresponding to  $\delta = 86^\circ$  was selected as the reference point for the required calculations by this technique. (Figure 3.33 &3.34).

Mixing and compaction temperatures were achieved according to the following equations:

$$\text{Mixing temperature ( }^\circ\text{F): } 310 \omega^{-0.01} \quad (3.4)$$

$$\text{Compaction temperature ( }^\circ\text{F): } 300 \omega^{-0.012} \quad (3.5)$$

Using equation (3.4) and (3.5), 172° C and 158° C were selected as mixing and compaction temperatures for the modified asphalt binder used in this study.

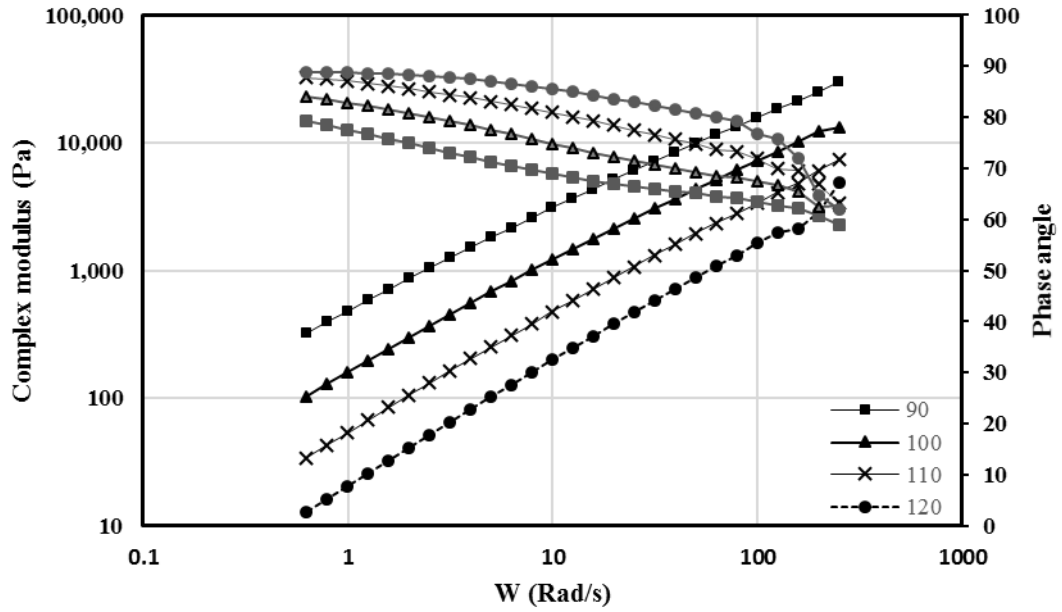


Figure 3.33. Frequency sweep test results at high temperatures

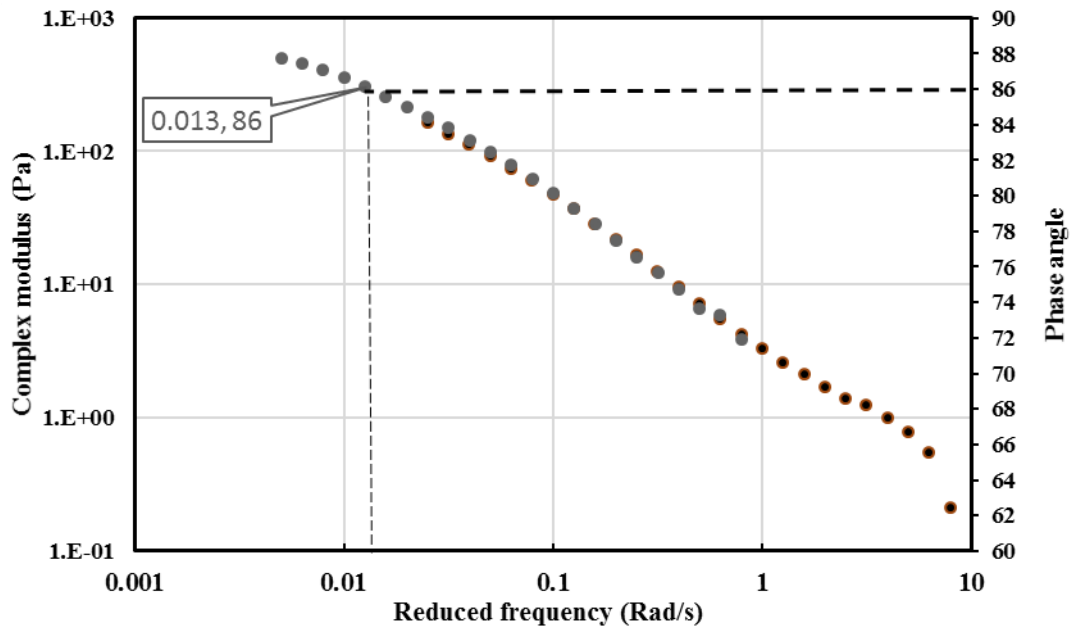


Figure 3.34. Binder master curve @ reduced frequency

### 3.14 Asphalt mixture conditioning

Short term aging occurs during the production of asphalt concrete in the mixing plant and then proceeds during storage and transportation stages. To simulate short term aging, mixtures were conditioned for 2 hours  $\pm$ 5 minutes at the compaction temperature (AASHTO R30 2006). The compaction temperature for mixtures with the unmodified binder was determined as 141 ° C. This temperature is the average temperature that corresponds to the kinematic viscosity of 280  $\mp$  30 C. P, estimated in compliance with AASHTO T 316. In the case of mixture with the modified binder, the conditioning temperature was calculated to be 158 ° C by the phase angle method (Figure 3.35).



**Figure 3.35.** Loose HMA conditioned samples in the oven at compaction temperature

### 3.15 Asphalt mixture compaction

After the short term aging, the test mixtures were transferred to 300 mm high and 150 mm diameter molds for compaction. The mixtures were compacted using ICT 250 gyratory compactor at temperatures that were previously established. The ICT 250 device compacts test mixtures by applying kneading action generated thru rotational shear movements. This method of compaction permits particles to move close to each other to achieve a more densely packed aggregate structure (Figure 3.36).



**Figure 3.36.** Sample compaction by gyratory compactor for Superpave design method (AASHTO T 312 2019)

According to AASHTO T312, the applied pressure must be 600 kPa, the gyratory internal angle  $1.16^\circ$ , and the speed of gyration 30 rounds per minute. After finishing the compaction, a specially designed apparatus was employed to extract the sample from the mold (Figure 3.36). In the last step, the bulk specific gravity of the samples was measured after reaching the environment temperature (Figure 3.37).



**Figure 3.37.** Compacted mix design samples according to the Superpave method

### **3.15.1 Gyrotory compaction parameters**

The density of specimens was assessed at three levels through the densification curve (Figure 3.38 and 3.39). The aggregate gradation and asphalt content of the mixture were selected such that the densification curve meets 96 percent of the theoretical maximum specific gravity of the mixture at the design number of gyrations ( $N_{\text{design}}$ ). The design number of gyrations is normally selected based on the estimated traffic level in the project site ( $N_{\text{design}} = 100$ , for this study), which is shown in Table 3.16.



**Table 3.16.** Design number of gyrations based on traffic levels according to Superpave method

Design ESALs (Million)	Compaction parameters			Typical roadway implementations
	N <sub>initial</sub>	N <sub>max</sub>	N <sub>design</sub>	
<0.3	6	75	50	Implementations cover roadways with very low levels of traffic.
0.3 to 3	7	115	75	Implementations cover many access streets and collector roads.
3 to 30	8	160	100	Implementations cover many multilane highways, dual carriageways, and disciplined access roadways.
>30	9	205	125	Implementations cover the vast majority of freeway systems.

The specific gravity of the mixture should not exceed 98 percent of the theoretical maximum specific gravity; in other words, the air void content of the compacted mixture must be less than two percent. The value of  $N_{max}$  is selected from Table 3.16 based on the ESAL level of the project site and can also be obtained from the following equation:

$$\log N_{max} = 1.1 \log N_{design} \quad (3-6)$$

The specific gravity of the mixture should not exceed 89 percent of the theoretical maximum specific gravity at the initial number of gyrations ( $N_{init}$ ). The value of  $N_{init}$  can also be either selected from Table 3.16 or calculated from the following equation:

$$\log N_{init} = 0.45 \log N_{design} \quad (3-7)$$

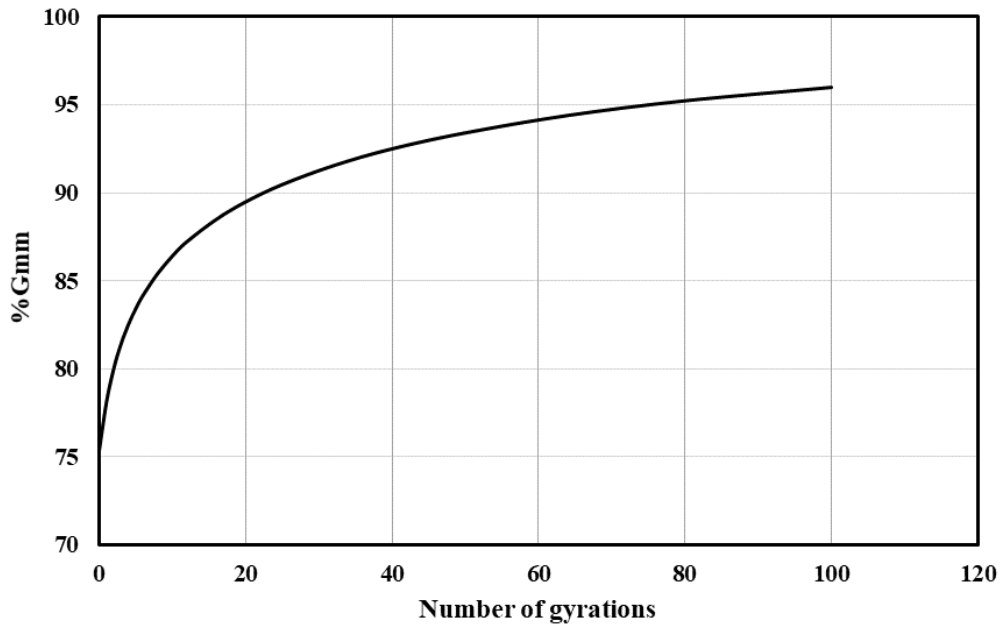


**Figure 3.38.** Compaction curve of a design sample (Mixture ID: BCM)

### 3.16 Design aggregate structure

In this step of volumetric design, the effect of the aggregate skeleton on mixture volumetric properties was evaluated. The SGC specimens were produced at  $N_{max}$  of 160 cycles according to Table 3.16 limits. Superpave requirements for the aggregate structure according to the AASHTO standard were applied to all mix designs as follows:

- VMA at 4 percent air voids according to the design number of gyrations
- Bulk density at  $N_{init}$  gyrations
- Bulk density  $N_{max}$  gyrations

Densification curve for one of the mix designs is shown in Figure 3.39.

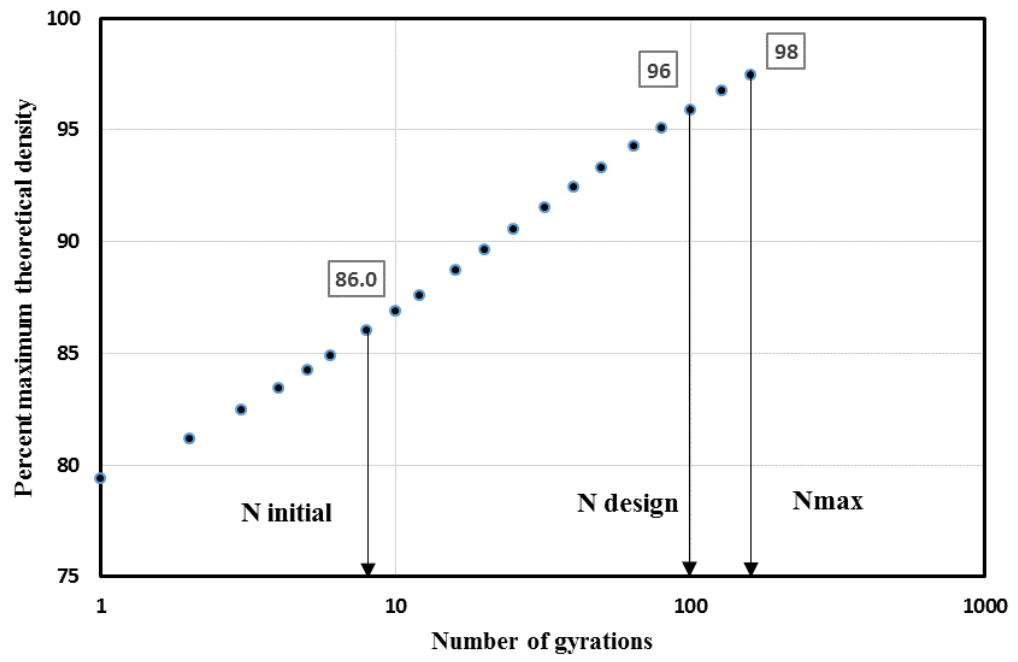


**Figure 3.39.** Densification curve obtained from a compacted sample (Mixture ID: BCM)

### 3.17 Optimum asphalt content for the design gradation

The optimum asphalt content is defined as the asphalt content corresponding to 4 percent air voids at  $N_{\text{design}}$  gyrations. After controlling the aggregate structure design, mixtures were prepared at four asphalt contents and 4 replications for each asphalt content, then were compacted to  $N_{\text{Design}}$  gyrations. The asphalt content that produced 4 percent air void was selected as the optimum asphalt content (Figure 3.40).

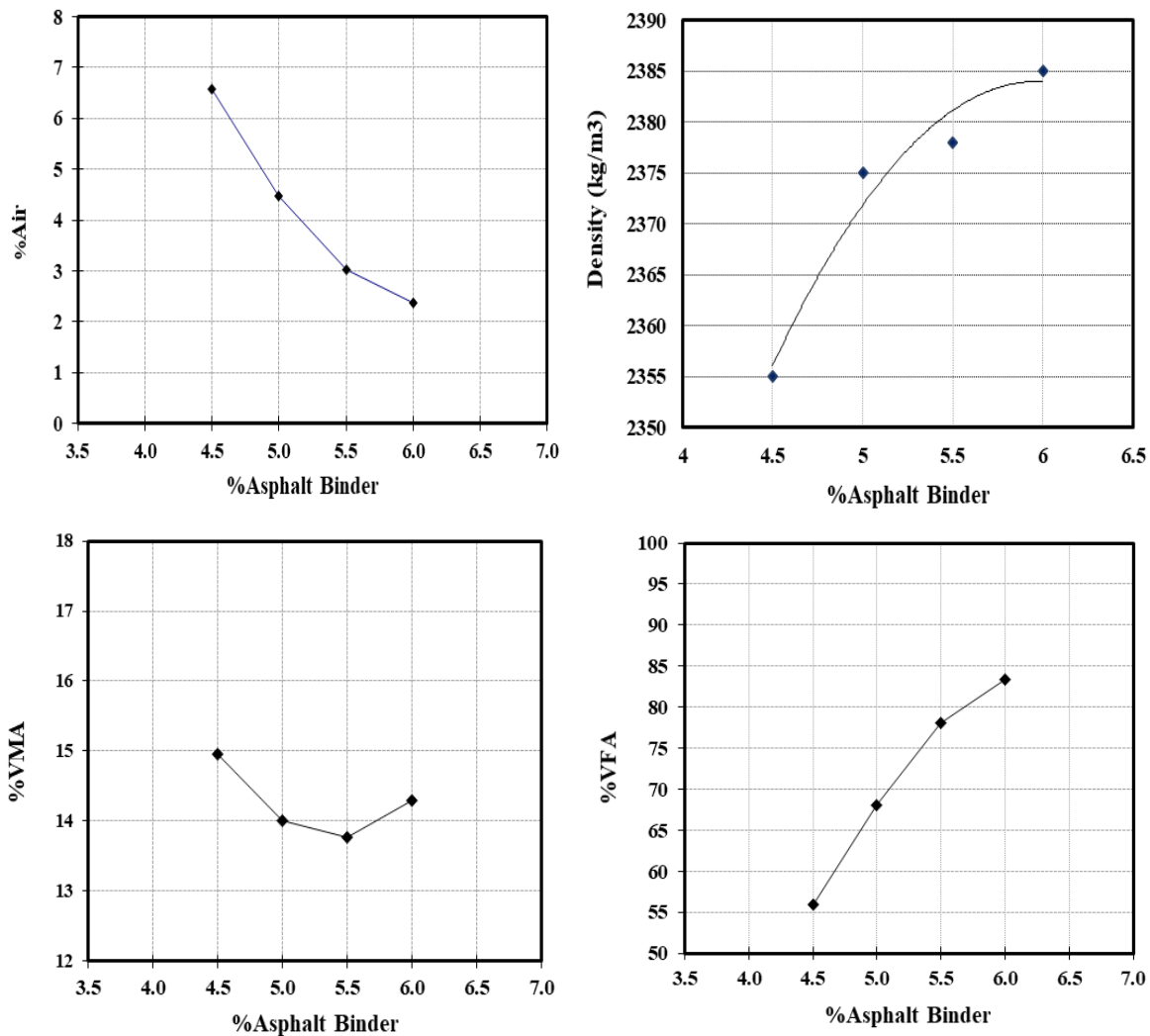


**Figure 3.40.** Plots of percent VMA, Percent air voids, Percent VFA, and density versus percent asphalt content (Mixture ID: BCM)

It was necessary to measure bulk density and theoretical maximum density to calculate the optimum asphalt content and other volumetric properties. Standard methods (AASHTO T166 2010) and (AASHTO T209 2016) were applied to determine the bulk specific gravity and the theoretical maximum density of the compacted samples. Volumetric design data, bulk specific gravity, and theoretical maximum densities at different asphalt contents for one of the mix designs are given in Table 3.17.

**Table 3.17.** Design data at different asphalt contents (Mixture ID: BCM)

<b>P<sub>b</sub>(%)</b>	<b>V<sub>a</sub></b>	<b>VMA (%)</b>	<b>VFA(%)</b>	<b>Density (kg/m<sup>3</sup>)</b>	<b>Max density (Kg/m<sup>3</sup>)</b>
4.5	6.58	14.96	56.01	2352	2474
5	4.48	14.10	68.03	2375	2461
5.5	3.02	13.77	78.05	2378	2444
6	2.38	14.29	83.34	2381	2426

It is worth mentioning that a tolerance limit of  $\pm 0.05$  percent was assumed for air void content. This strict tolerance considerably increased the number of produced SGC samples to identify the optimum asphalt content. On the other hand, providing design samples at optimum asphalt content prevented the interaction of air voids as a new variable with pre-defined experimental design variables. Totally, 8 mix designs were prepared at optimum asphalt content and then the volumetric properties including voids in mineral aggregate (VMA), voids filled with asphalt (VFA) and filler to binder ratio were calculated as listed in Table 3.18. TGDH and (AASHTO R35 2015) standards were applied to verify the sample's volumetric design properties.

**Table 3.18.** Volumetric properties for different mixture

<b>Mixture ID</b>	<b>AC (%)</b>	<b>VMA (%)</b>	<b>VFA (%)</b>	<b>Filler/Binder</b>
<b>BCN</b>	5.3	14.75	72.6	1.04
<b>BCM</b>	5.15	14.0	71.25	1.07
<b>LCN</b>	5	15.5	73	0.60
<b>LCM</b>	4.95	14.6	73.5	0.61
<b>BFN</b>	6	15.6	74.3	1.00
<b>BFM</b>	5.4	14.2	72	1.11
<b>LFN</b>	5.3	15.1	73.5	0.57
<b>LFM</b>	5	14.0	71.2	0.60

Symbols used: Aggregate type: L-limestone, B-Basalt; Gradation: C- Coarse, F-Fine; Size; Modification: N-No modification, M-SBS modification; VMA-Voids in the mineral aggregate; VFA-Voids filled with asphalt.

## **CHAPTER 4**

### **ANALYSIS OF TEST RESULTS AND DISCUSSION**

#### **4.1 Introduction**

This chapter describes the measurement of thermal coefficient and thermal fatigue in asphalt concrete mixtures. It also presents statistical analyses of several variables for 144 thermal fatigue and 16 thermal coefficient tests. Different variables are involved in the mixture design, which affects the thermal coefficient and thermal fatigue life of the design mixtures. In this chapter, the thermal fatigue performance of asphalt concrete is also discussed in relation to mixture design variables used as input parameters in the statistical analyses.

#### **4.2 Results of measurement for thermal coefficient**

The procedure for measuring the thermal coefficient has been described in chapter 3. The test starts at 30 ° C followed by cooling at a rate of 60 ° C/hour until it reaches -30°C. The temperature is measured on the surface and inside the center of a dummy specimen. Deformations of specimens were measured by LVDT, and the thermal coefficients for different specimens were calculated from deformation-temperature curve. The results for thermal coefficients are given in Table 4.1.

**Table 4.1.** Thermal coefficients of test specimens

<b>Specimen ID</b>	<b>Thermal coefficient(/°C)</b>	<b>Specimen ID</b>	<b>Thermal coefficient(/°C)</b>
BCNU	3.35E-05	BCNA	3.00E-05
BFNU	3.09E-05	BFNA	3.08E-05
BCMU	3.43E-05	BCMA	2.98E-05
BFMU	2.95E-05	BFMA	2.78E-05
LCNU	2.91E-05	LCNA	2.36E-05
LFNU	2.59E-05	LFNA	2.67E-05
LCMU	2.97E-05	LCMA	2.35E-05
LFMU	2.31E-05	LFMA	2.68E-05

### **4.3 Result of analysis for measured thermal coefficients**

The thermal coefficients were measured for 16 specimens, and then to find a significant mixture variable affecting the thermal coefficient, results were statistically analyzed. Table 4.2 presents the statistic parameters and probability values calculated through ANOVA. As is apparent from the ANOVA results, the aggregate type is the most significant design variable because its p-values for a confidence interval of 95% was found approximately zero. According to P values, it seems the effect of other variables on the thermal coefficient of asphalt concrete was negligible.



**Table 4.2.** Statistic parameters and ANOVA results for thermal coefficient

<b>Design Variable</b>	<b>Mixture ID</b>	<b>Mean</b>	<b>Std. deviation</b>	<b>F-value</b>	<b>P-value</b>
<b>Aggregate</b>	Basalt	3.08E-05	2.14E-06	16.8	0.001
	Limestone	2.60E-05	2.53E-06		
<b>Aging</b>	Aged	2.74E-05	2.81E-06	1.6	0.220
	Unaged	2.95E-05	3.70E-06		
<b>Gradation</b>	Coarse	2.92E-05	3.96E-06	0.8	0.388
	Fine	2.77E-05	2.67E-06		
<b>Asphalt type</b>	Modified	2.81E-05	6.22E-05	0.0	0.665
	Neat	2.88E-05	6.38E-05		

In Figure 4.1, specimens are grouped according to the aggregate type. As shown, the thermal coefficient for specimens with Limestone aggregate is generally less than the thermal coefficient for specimens with basalt aggregate. Figure 4.2 shows the test results for thermal strain ( $\epsilon^T$ ) versus specimen temperature (T) measured during the cooling phase. It can be seen from Figure 4.2 that slopes are steeper at the beginning of the test and more horizontal at lower temperatures.

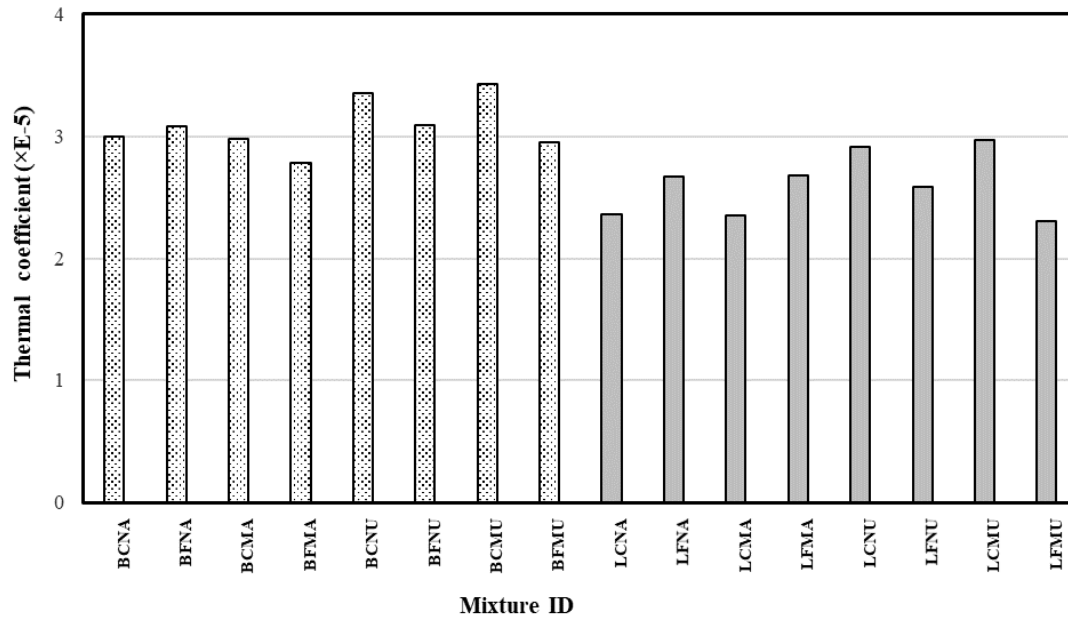


**Figure 4.1.** Thermal coefficient for different mixtures based on the aggregate type

These two regions are separated by the glass transition temperature; for this study, the thermal coefficient above glass transition and between 0° C and 10°C was employed to calculate thermal strains. This is the temperature range that thermal fatigue occurs in the field. To simulate thermal fatigue in the laboratory environment, the test temperature of 4° C was selected, which is inside the chosen range to calculate thermal strain.

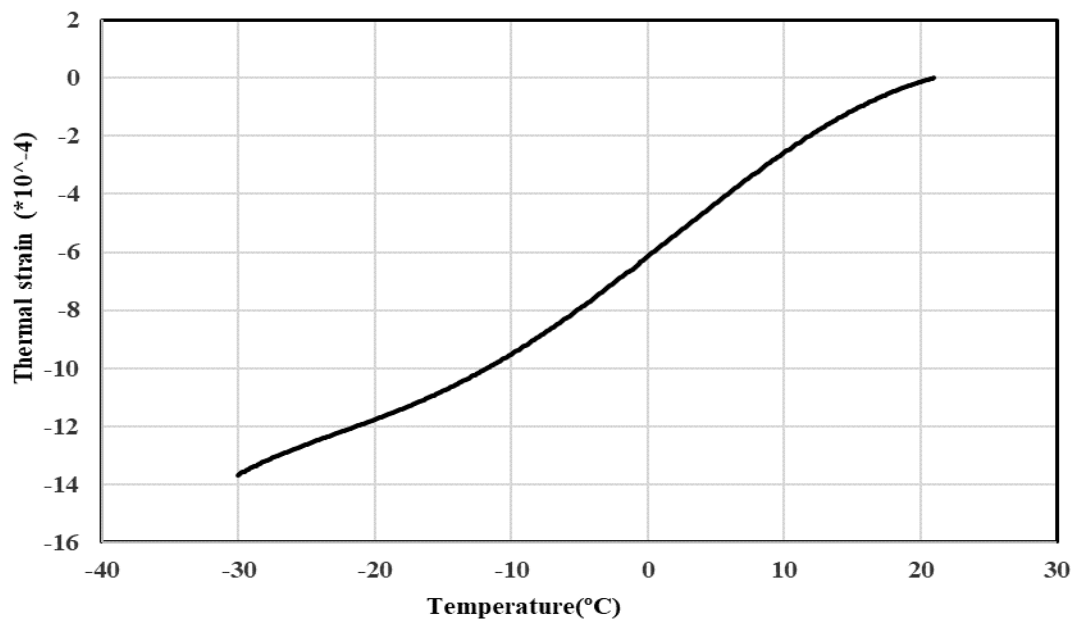


**Figure 4.2.** Thermal strain versus temperature

The next phase of the study was performing a thermal fatigue test on semicircular specimens to assess the resistance of different mixtures against this distress mode. To conduct a thermal fatigue test, the calculation of thermal strain to be applied to each specimen was necessary. As previously discussed in Chapter 3, the thermal strains were calculated using Equation 4.1 by assuming that the daily temperature change with the highest frequency of repetition is 10° C.

$$\varepsilon = \alpha \Delta t \quad (4.1)$$

$\varepsilon$  = thermal strain at the determined temperature difference

$\alpha$  = thermal coefficient of asphalt concrete;

$\Delta t$  = daily temperature changes with the highest frequency of repetition

#### 4.4 Stress analysis in semicircular bending test

To simulate thermal fatigue loading, three-point flexural test was implemented by the application of a concentrated load in the midpoint of the semicircular beam while lying on two steel roller supports. The loading configuration of the semicircular bending test is shown in Figure 4.3. Longitudinal tensile strain at the center point of the specimen's bottom surface is the main controlling parameter of the thermal fatigue test. In order to select the proper gauge length for measuring strain, analysis of stress, and strain at the bottom surface of the specimen was necessary. Stress analysis also gives a reasonable hint for the magnitude of the initial point load applied on top of the specimen generating the target strain underneath the specimen's bottom surface. To determine the load to be applied, the finite element method was employed for stress-strain analysis of the test specimen.

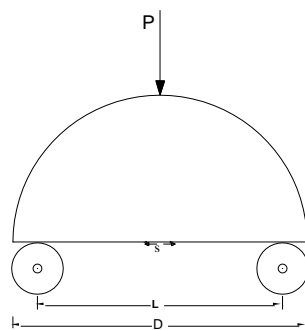


**Figure 4.3.** Setup for semicircular bending test

##### 4.4.1 Finite element analysis

The finite element method through commercial software ABAQUS was utilized to explore the behavior of semicircular specimens under the bending test. In the FEM analysis, it was assumed that the asphalt concrete is isotropic and the solution was

done for both viscoelastic and linear elastic material behavior. The support bars and loading head are assumed to be rigid during the solution.

In this analysis, the modulus of elasticity of asphalt concrete was estimated 10,250 MPa at test temperature of 4 °C, according to the AASHTO design guide (AASHTO 1993). The analysis was conducted by applying a constant load of  $P=1,750$  N, which was selected by trial and error for the viscoelastic material model, frequency of 0.01Hz, specimen thickness of  $t=35$  mm, Poisson's ratio of  $\nu =0.30$  and friction coefficient of  $\mu = 0.1$  between the specimen and the rigid rollers. The diameter of the specimen and the distance between the supports were selected as  $D= 150$  mm and  $L=120$ mm, respectively. To utilize the viscoelastic material model in the FEM analysis, a separate procedure was followed, as described in the below sections.

#### **4.4.2 Developing a viscoelastic material model**

##### **4.4.2.1 Developing dynamic modulus master curve**

To develop a viscoelastic model for asphalt concrete, it was necessary to build a dynamic modulus master curve at a test temperature, which was selected as 4°C in this study. According to AASHTO TP62 (2007) guidelines, dynamic modulus test was conducted at five temperatures (-10, 4.4, 21, 37, 54) and six loading frequencies (25,10, 5, 1, 0.5, 0.1 Hz). The mix design used for this analysis included basalt aggregate with fine gradation and unmodified asphalt. It should be mentioned that the dynamic modulus test was conducted by the Turkish highway administration laboratory. In the first step of building a dynamic modulus master curve, experiment data were fitted to a sigmoidal function given by the mechanistic-empirical pavement design guide (MEPDG). The reduced frequency was calculated using shift factors by considering 4° C as a reference temperature. At the final step, by applying numerical optimization through the Excel Solver function, the master curve for the test specimen was obtained (Figure 4.4).

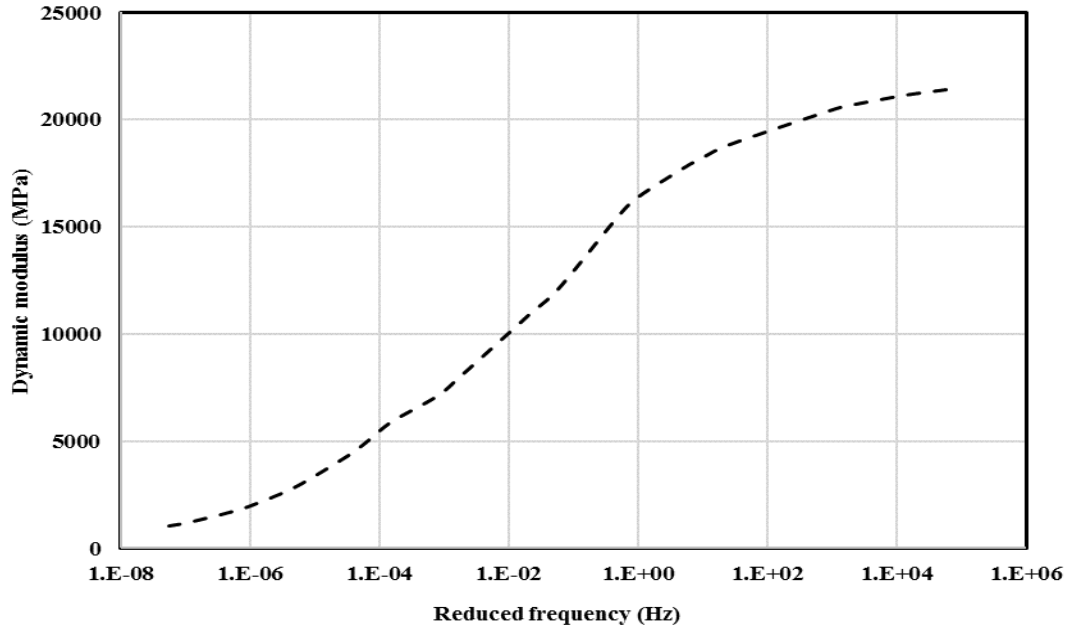


**Figure 4.4.** Dynamic modulus versus reduced frequency at 4° C

#### 4.4.2.2 Determination of prony series coefficients

To assign viscoelastic properties to the asphalt concrete in ABAQUS software, Prony series coefficients must first be obtained. This was achieved by fitting the experimental data (dynamic modulus versus reduced frequency) to the generalized Maxwell model through the following equations:

$$G'(\omega_r) = G_0 \left(1 - \sum_{i=1}^N g_i\right) + G_0 \sum_{i=1}^N \frac{g_i}{1 + \tau_i^2 \omega_r^2} \tau_i^2 \omega_r^2 \quad (4.1)$$

$$G''(W_r) = G_0 \sum_{i=1}^N \frac{g_i}{1 + \tau_i^2 W_r^2} \tau_i W_r \quad (4.2)$$

Where :  $G'(\omega_r)$  = storage shear modulus,  $G''(W_r)$  = Loss shear modulus,

$G_0$  = instantaneous shear modulus       $\tau_i, g_i$  =Prony series coefficients

A total of 10 term Prony series coefficients were calculated for the generalized Maxwell model, as shown in Table 4.3.

**Table 4.3.** Prony series coefficients for asphalt mixture

Reference temperature = 4°C		$G_0 = 8.5 \text{ Gpa}$	
$g_1$	0.035	$\tau_1$	1E-05
$g_2$	0.043	$\tau_2$	1E-04
$g_3$	0.060	$\tau_3$	1E-03
$g_4$	0.078	$\tau_4$	1E-02
$g_5$	0.079	$\tau_5$	1E-01
$g_6$	0.177	$\tau_6$	1E+00
$g_7$	0.141	$\tau_7$	1E+01
$g_8$	0.092	$\tau_8$	1E+02
$g_9$	0.084	$\tau_9$	1E+03
$g_{10}$	0.134	$\tau_{10}$	1E+04

After meshing and determining the boundary conditions, elastic and viscoelastic properties were assigned to the FEM model. The haversine loading was employed in the model at different frequencies to simulate the thermal fatigue test. In this study, tests were conducted at two frequencies: Low (0.01Hz) and high (0.1Hz) to investigate the initial loading magnitude, which was one of the objects for FEM modeling. The magnitude of the applied load was determined by trial and error according to the target strain in the middle of the bottom surface of the semicircular specimen for one cycle. As is apparent from Figure 4.5 for the same tensile strain, a smaller load was applied at low frequency compared to a loading with high frequency. According to the FEM analysis, to achieve a target strain of  $309 \mu\epsilon$ , 2.25 kN load must be applied at the high frequency mode, while 1.75 kN load can generate the same amount of tensile strain when the loading was performed at low frequency.

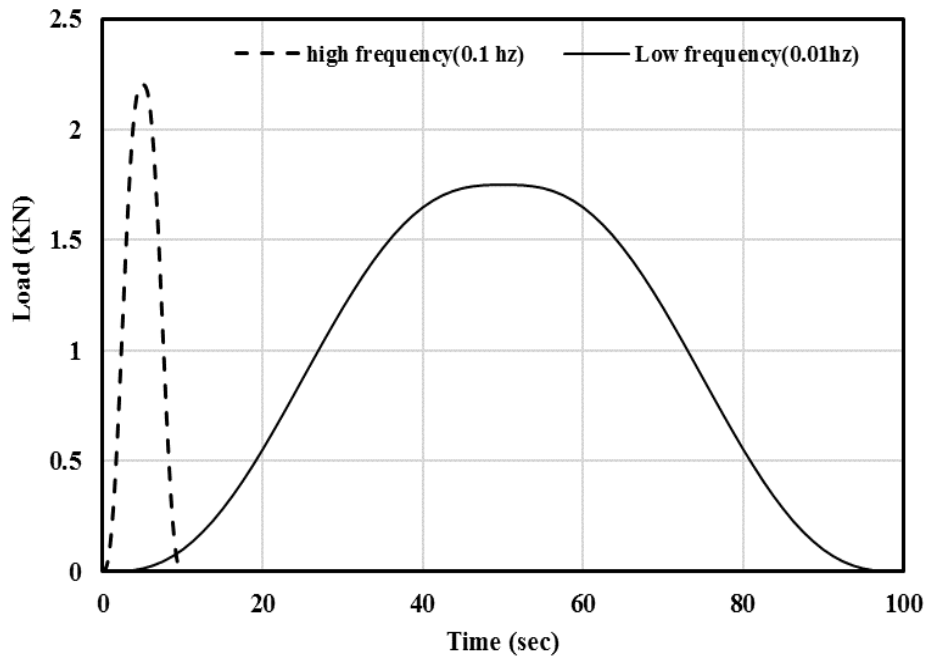


**Figure 4.5.** Haversine loading according to target strain in the middle of the bottom surface of specimen at different frequencies (from FEM analysis)

Stress versus strain at the bottom surface and the center point of the specimen for different loading frequencies are illustrated in Figure 4.6. As can be seen, the maximum strain remains the same; however, the stress becomes different for two loading frequencies; it is 1.79 MPa for high frequency and 1.32 MPa for low frequency. The tensile strain developed at the bottom surface of the semicircular specimen is a combination of elastic and inelastic (viscoelastic) strains. Figure 4.7 and Figure 4.8 show these components at different loading frequencies. As figures indicate, when the model was executed at high frequency, the elastic strain was a dominant portion of the total strain, while at low frequency the inelastic strain played a major role in the total strain.



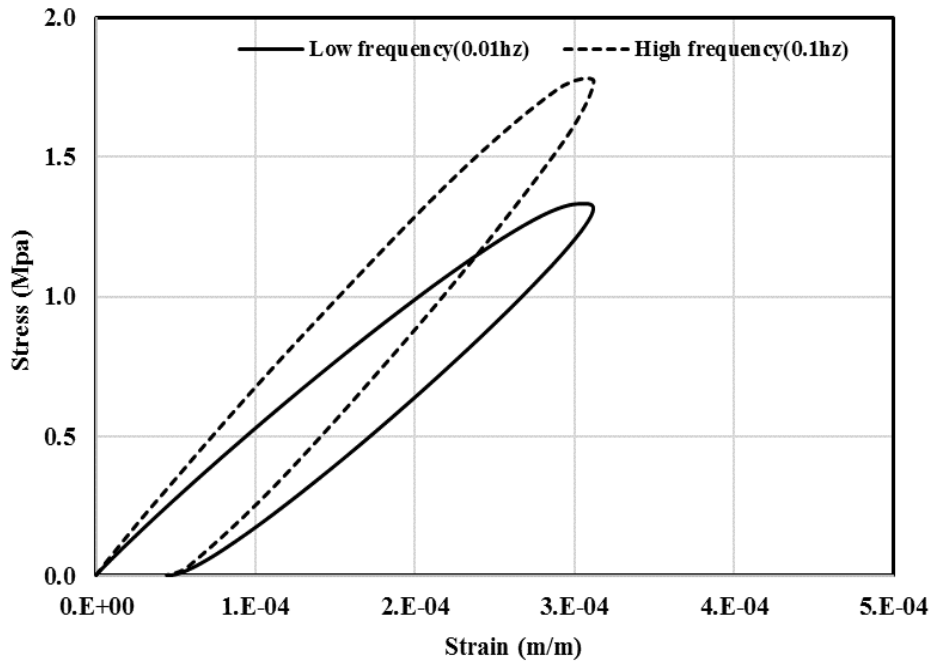


**Figure 4.6.** Stress versus strain in the middle of bottom surface of specimen at different frequencies (from FEM analysis)

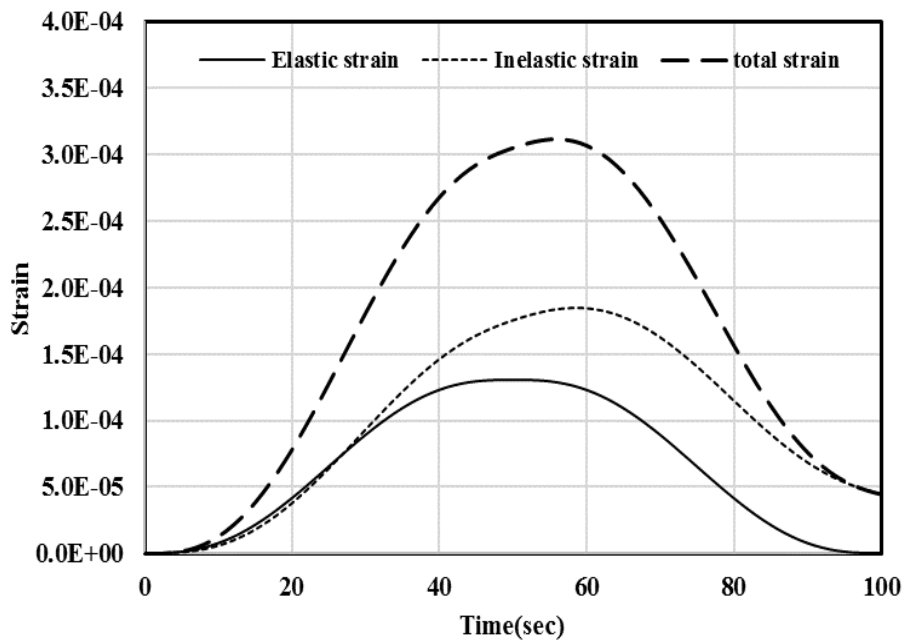


**Figure 4.7.** Tensile strain components from FEM analysis in the middle of bottom surface of semicircular specimen at low frequency loading (0.01 Hz)

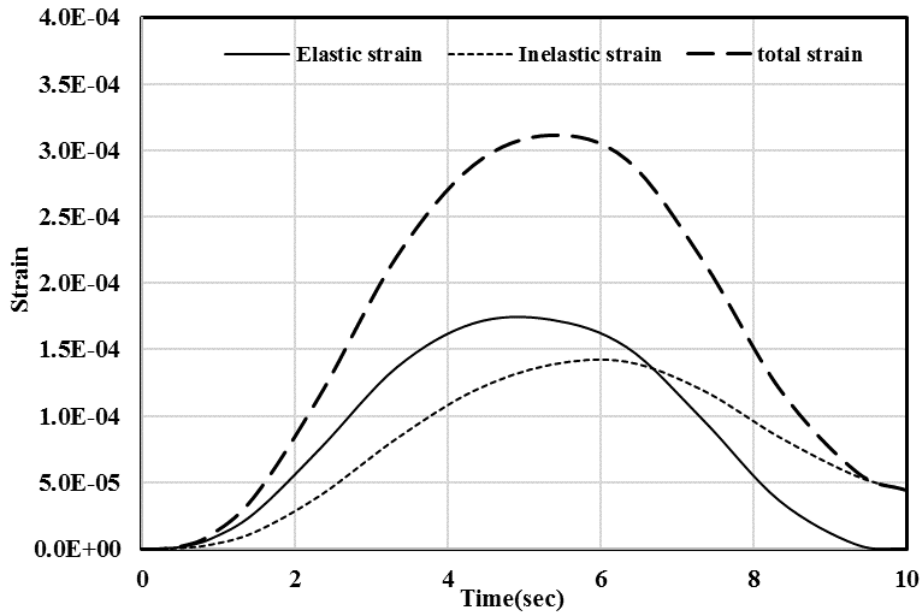


**Figure 4.8.** Tensile strain components from FEM analysis in the middle of bottom surface of semicircular specimen at high frequency loading (0.1Hz)

#### 4.4.3 FEM analysis for stress distribution in semicircular bending test

In Figures 4.9 and 4.10, the obtained horizontal stress and strain contours obtained after the FEM solution are shown, respectively. In the FEM model, the loading wave shape is haversine, the upper surface of the specimen is under compression, and the stress sign is negative in that region. It can be seen in Figure 4.9 that toward the bottom of the specimen, the tensile stress increases, and the maximum tensile stress due to bending is generated in the middle part of the semicircular specimen, as marked by red color in the meshed model. Strain distribution also follows the same trend as the stress distribution, and the maximum strain was found in the middle of the bottom surface, around 12.5 mm from the centerline in each direction (Figure 4.10). It was concluded that the measurement of strain should be performed inside this range. The results of FEM analysis for the horizontal stress and strain distributions at the bottom surface of the specimen along the X-axis is shown in Figure 4.11. The tensile stress

and strain reached their maximum value in the center of the specimen; however, they start to decrease toward the specimen edges.

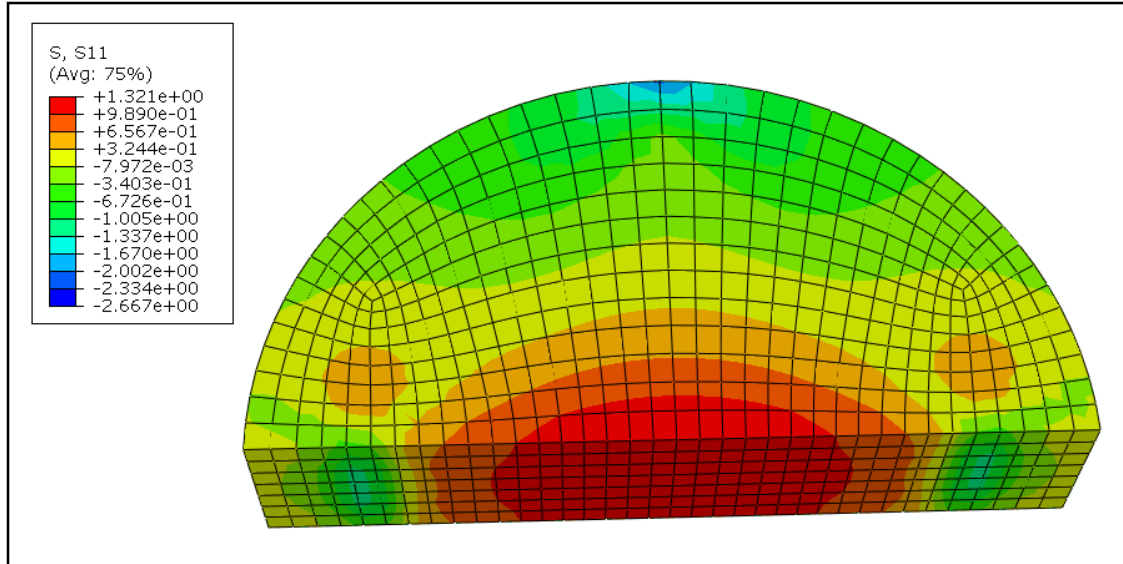


**Figure 4.9.** Finite element meshed model and horizontal stress contour

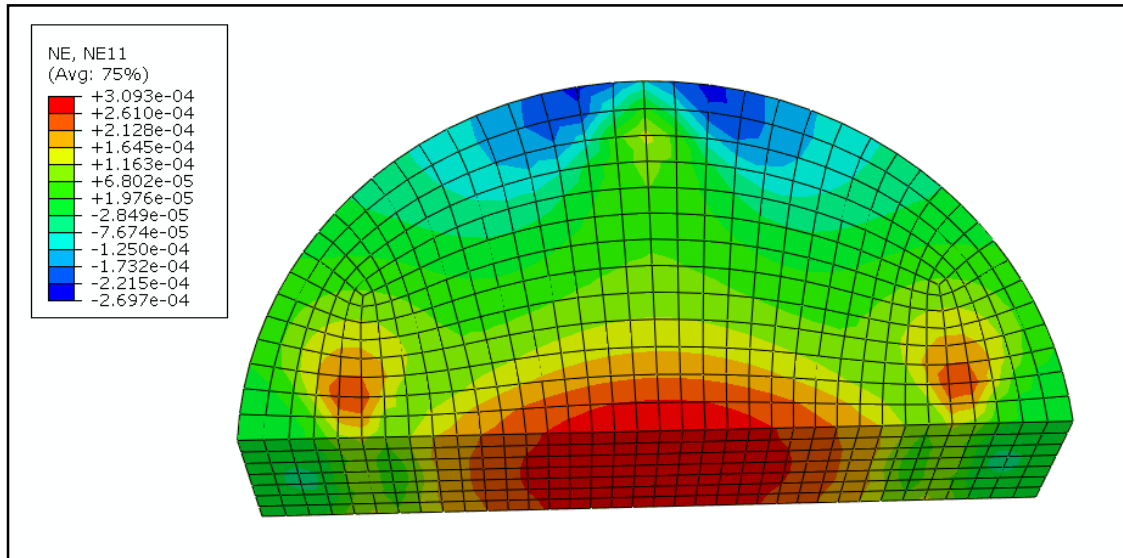


**Figure 4.10.** Finite element meshed model and horizontal strain contour

For the stress and strain distribution along the Y-axis, it can be observed in Figure 4.12 that toward the loading point the tensile stress decreases, and the maximum compression stress develops in the upper part of the specimen under the loading head. Using the FEM analysis, stresses and strains at different points of the semicircular specimen were determined. Based on the results of FEM analyses, a gauge length of 25 mm (12.5 mm distance from the center of the specimen in each direction of the X-axis) was chosen for the measurement of the tensile strain from the bottom surface of the semicircular specimen when conducting the fatigue tests in the laboratory.

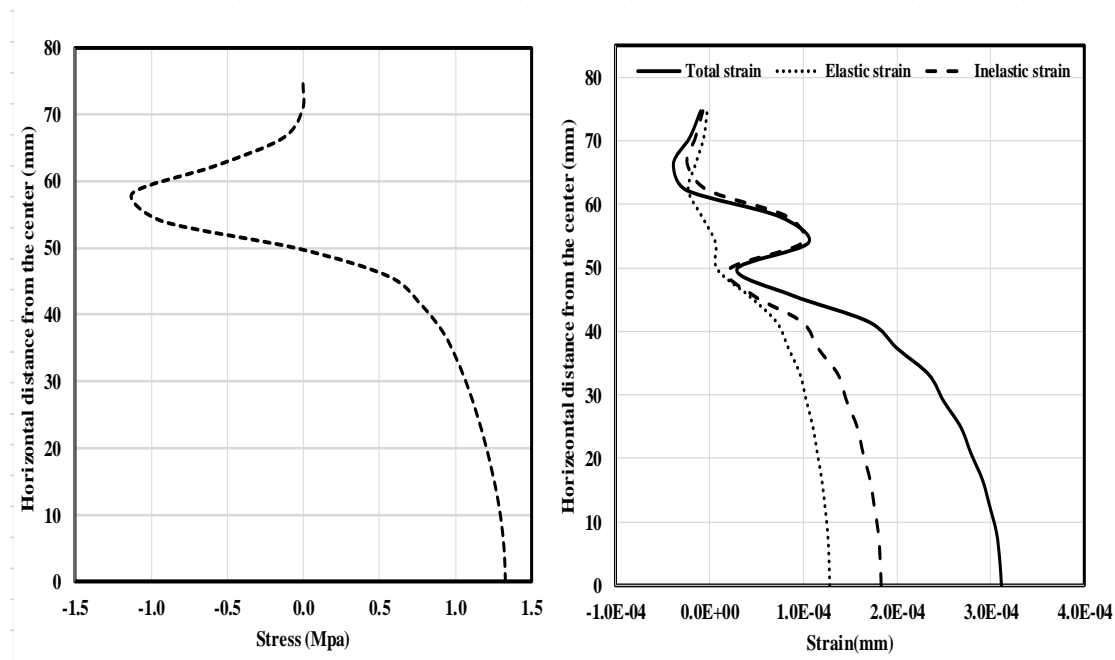


**Figure 4.11.** Horizontal stress and strain distribution at the bottom surface and along the X axis

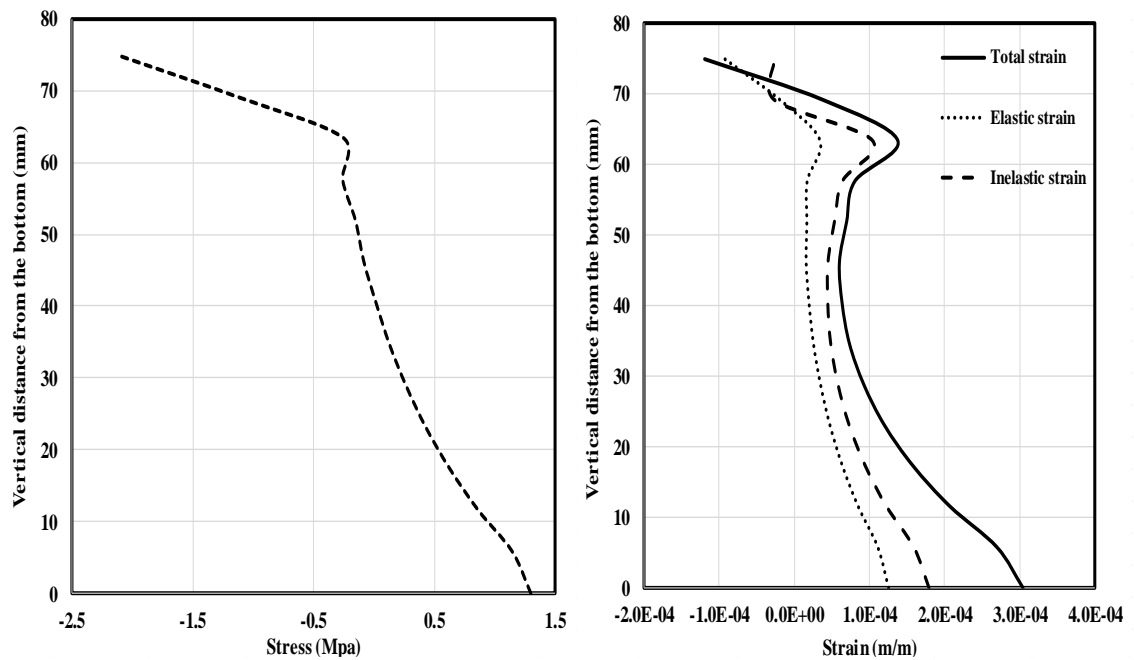


**Figure 4.12.** Horizontal stress and strain distribution along the Y axis of the specimen

#### 4.5 Test results for the performance of asphalt concrete under thermal fatigue

After calculating the thermal coefficients of the beam specimens, thermal strains to be applied to each semicircular specimen were determined. In the thermal fatigue test, the longitudinal strain underneath the semicircular specimen was chosen as the target strain to achieve during testing. This strain level was also considered as a controlling parameter for the closed-loop servo-controlled testing system. As shown in Figure 4.13, after the first cycle of loading, the applied load was justified to achieve the target strain. As the test proceeds, the loading continues with the target strain until the maximum number of 2000 cycles is reached or the stiffness of the mixture is reduced to 25% of its initial stiffness.

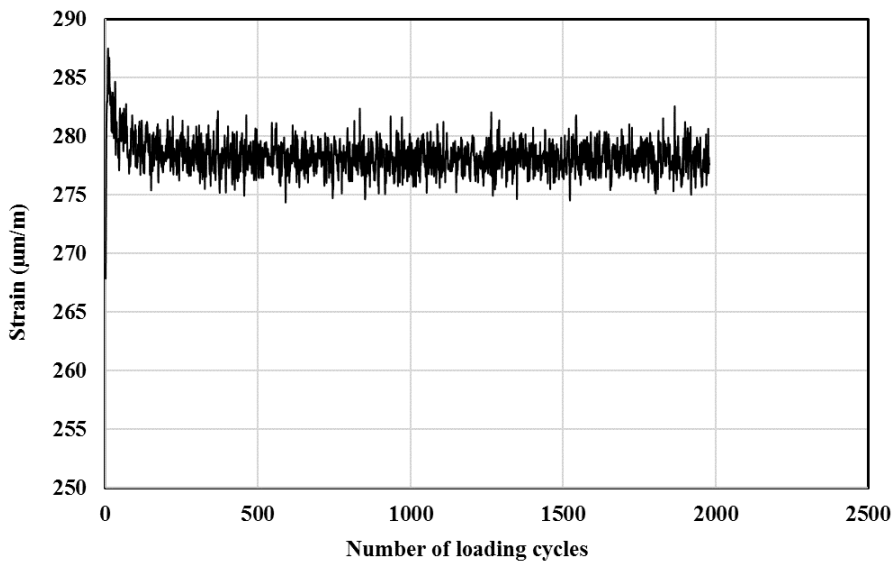


**Figure 4.13.** Applied thermal strain at the bottom of semicircular specimen (Specimen ID: BFMAH10)

The stiffness of the specimen is calculated by dividing the maximum stress to maximum strain in each cycle. Figure 4.14 gives an example of stiffness reduction for a semicircular specimen under the target strain loading.

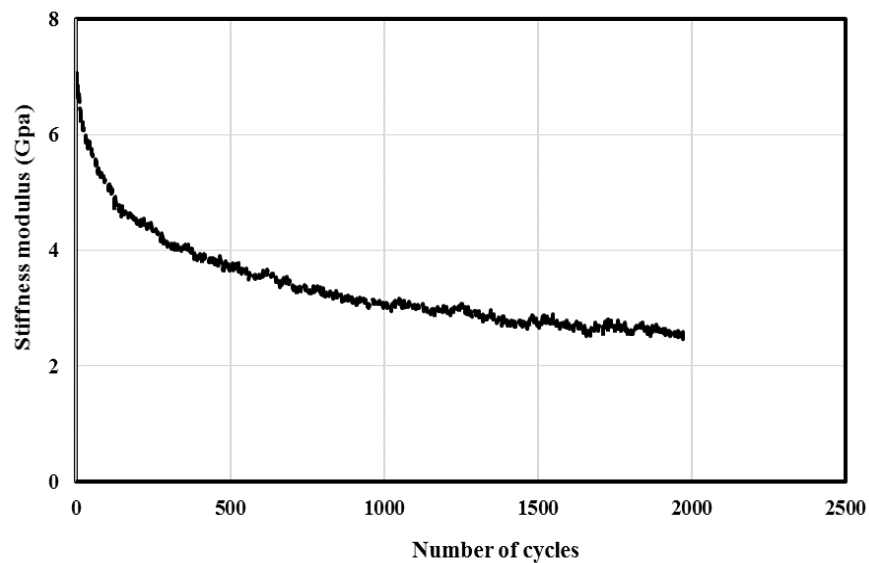


**Figure 4.14.** Stiffness versus number of loading cycles for test specimen (Specimen ID: BFMAH0)

#### **4.6 Determination of the slope of the line fitted to log-log scale data**

In addition to the number of cycles at different stiffness levels and also initial stiffness, the slope of the line fitted to stiffness versus cycle number in the logarithmic scale can be used as an alternative method to compare the performance of different mixtures. The slope of the fitted line to a log-log scale data highly correlates with micro crack development in each specimen. A smaller slope value shows slower propagation of micro cracks and, therefore, longer fatigue life for the specimen (Figure 4.15).

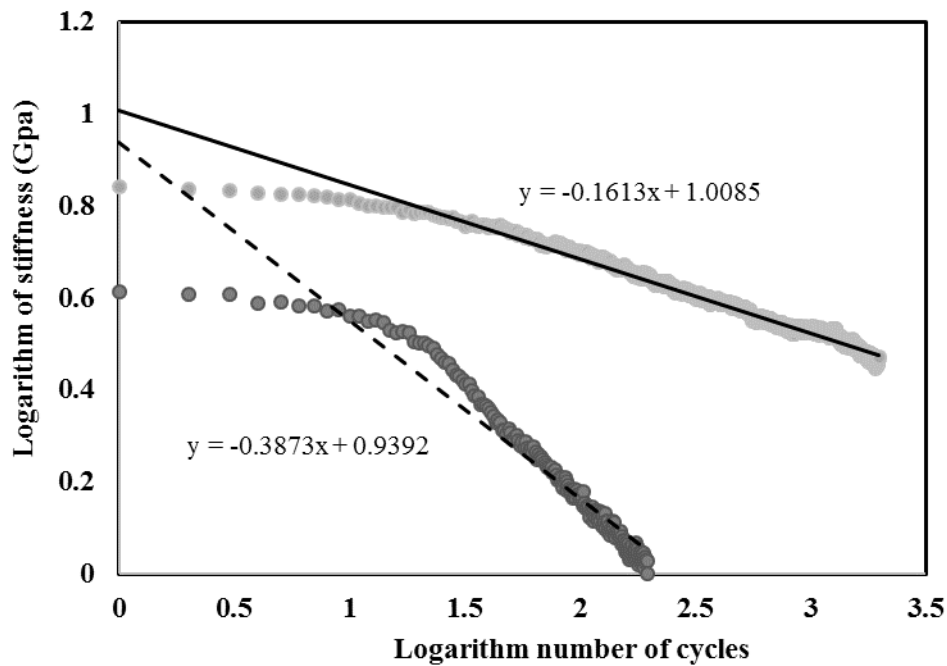


**Figure 4.15.** Slopes of fitted lines in a logarithmic scale for two different specimens

From Figure 4.15, the difference between the slopes of two lines fitted to the logarithmic scale data can be easily distinguished. The specimen with the continuous line has a better fatigue performance because of its smaller absolute slope value.

#### **4.7 Fatigue life extrapolation for reduced stiffness using the power model**

Thermal fatigue tests were conducted up to 2000 cycles, and some specimens were more resistant and did not reach 75% reduced stiffness at the end of the test. Hence, extrapolation was needed to predict the number of loading cycles at 75% reduced stiffness. Different functions like exponential, power, and logarithmic have been used by researchers to extrapolate the fatigue failure cycles. In this study, power model, which is a preferred method for fitting data in load-associated fatigue, was selected for extrapolation as follows:



$$S = \alpha n^\beta$$

S: Stiffness,

$\alpha$  and  $\beta$ : fatigue constants

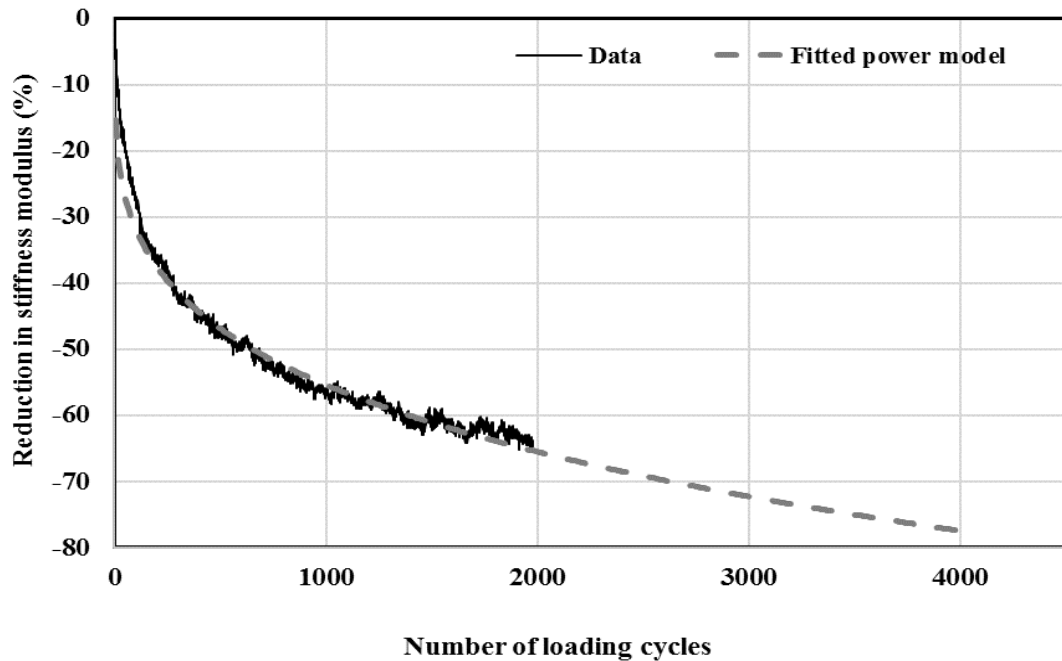


**Figure 4.16.** Power model fitted for stiffness versus number of loading cycles (Specimen ID:BFMAH0)

Figure 4.16 shows fitted power model to data obtained from one of the specimens which did not reach 75% reduction in stiffness at the end of 2000. In Figure 4.17 the number of loading cycles in the log scale versus stiffness has been plotted. The discrete points at the beginning of the path is an indicator of nonlinear portion in stiffness versus cycle number. This part was eliminated in the extrapolation because it will cause overestimation for the number of loading cycles by the power model.

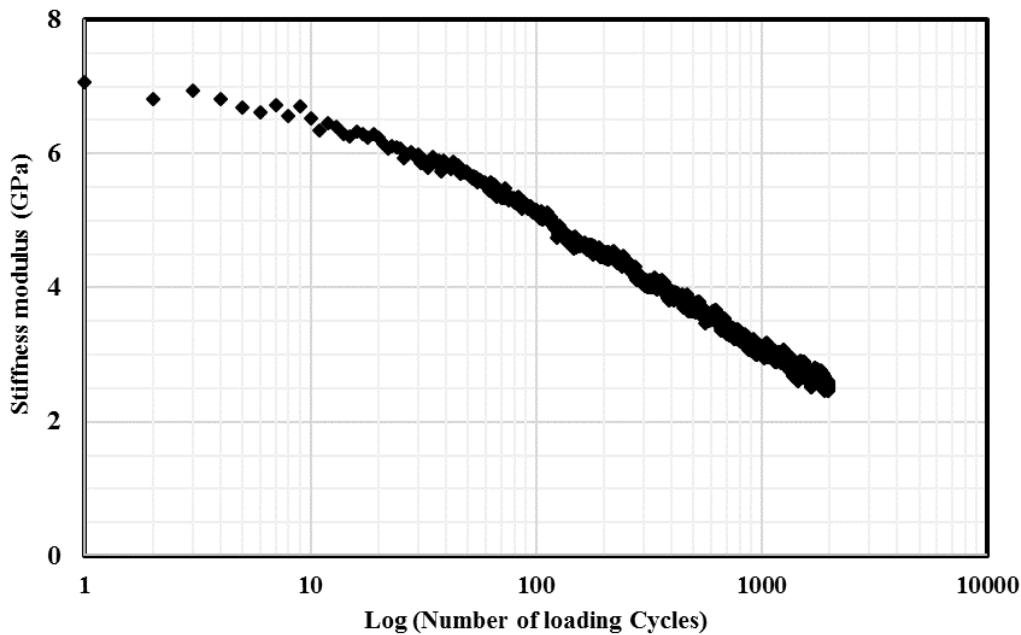


**Figure 4.17.** Number of loading cycles versus stiffness (log scale)

#### **4.8 Multivariate analysis for the number of loading cycles at different levels of reduced stiffness**

Multivariate analysis at three different levels of reduction in stiffness (25%,50%,75%) versus the number of loading cycles and also at 50% reduced stiffness modulus was applied to investigate the significant variables affecting the thermal fatigue life of asphalt concrete. For each stiffness level, statistical parameters and significant variables are determined and then the average number of cycles for each specimen is given in another table. Bar charts and boxplots for the significant variables are given for the number of cycles at 50% reduction in stiffness, and also for 50% reduced stiffness, as shown in the following sections. The trend of bar charts and box plots for the number of cycles at 25% and 75% reduction in stiffness is very similar to the trend at 50% reduction in stiffness. The charts for these reduction levels are given in Appendix E and F.

#### **4.8.1 Multivariate analysis for the number of loading cycles at 50% reduced stiffness**

The number of loading cycles for 50% reduced stiffness for different mixtures are given in Table 4.5. Since 50% reduced stiffness modulus have been conventionally used as a failure criterion in load associated fatigue tests. The effect of a design variable in this level of reduced stiffness was also evaluated by using multivariate analysis. P-values given in Table 4.4 shows that all the design variables are significant for thermal fatigue behavior of asphalt concrete. According to f-values, the sequence of significant variables was: asphalt type, frequency, aggregate type, gradation, rest time, aging. In addition to the main effects, the significance of the interaction between the test variables was also investigated. The interaction between asphalt type and aggregate type and interaction between asphalt type and frequency are the most significant interactions. Besides, asphalt type, and frequency are individually the most significant variables. Considering the fact that the viscosity of the asphalt decreases with increase in loading frequency and because of the large difference in the viscosity of the neat asphalt and the modified binder, the interaction of these two variables also become important. The next significant interaction was between aggregate and asphalt type; the adhesive bond is a determinant factor for the interaction of these two variables, which is mostly affected by aggregate type. Hence, the significance of this interaction is likely due to variations in the mineralogical structure of aggregates and adhesive properties of asphalt binders. The interaction of asphalt type and gradation and the interaction of rest time with asphalt type, aggregate type, frequency, and gradation constitute other significant interactions, respectively. In the next section, the effects of these design variables on thermal fatigue performance of 144 asphalt concrete specimens for the number of loading cycles at 50% reduced stiffness would be evaluated. These comparisons are made between two specimens with similar ID but different for a particular variable, i.e. asphalt type, aggregate type, etc. Then, the overall performance of all the specimens against thermal fatigue according to a particular significant variable for 50% drop in the initial stiffness are compared

statistically. To evaluate the results in a more detailed manner, bar charts and boxplots are utilized. Using boxplots helps to compare maximum, median, minimum, first and third quartile between paired design variables.

**Table 4.4.** Multivariate analysis for number of loading cycles at 50 % reduced stiffness

Design Variable		Levels	Symbol	Mean	Std. Deviation	F-Value	P-Value
Main effects	Asphalt Type	Modified	M	195.3	202.4	155.1	0.000
		Neat	N	35.5	31.8		
	Frequency	High	H	177.8	209.4	94.6	0.000
		Low	S	53.0	56.4		
	Aggregate type	Basalt	B	164.5	213.6	58.5	0.000
		Limestone	L	66.3	66.7		
	Gradation	Coarse	C	74.0	62.7	41.5	0.000
		Fine	F	156.8	218.1		
	Rest time	0 second	0	90.1	109.7	9.8	0.000
		5 second	5	100.9	127.2		
10 second		10	155.2	228.7			
Aging	Aged	A	130.2	166.1	5.3	0.023	
	Unaged	U	100.6	164.0			
Variables interaction	Frequency*Asphalt type	Modified	M	195.3	202.4	49.7	0.000
		Neat	N	35.5	31.8		
	Asphalt type*Aggregate type	Basalt	B	164.5	213.6	39.9	0.000
		Limestone	L	66.3	66.7		
	Asphalt type * Gradation	Coarse	C	74.0	62.7	24.4	0.000
		Fine	F	156.8	218.1		
	Asphalt type * Rest time	0 second	0	90.1	109.7	8.3	0.000
		5 second	5	100.9	127.2		
		10 second	10	155.2	228.7		
	Rest time*Aggregate type	Basalt	B	164.5	213.6	7.9	0.001
		Limestone	L	66.3	66.7		
	Rest time *Frequency	High	H	177.8	209.4	6.2	0.003
		Low	S	53.0	56.4		
	Rest time *Gradation	Coarse	C	74.0	62.7	5.0	0.008
		Fine	F	156.8	218.1		
	Aging*Asphalt type	Modified	M	195.3	202.4	2.1	0.151
		Neat	N	35.5	31.8		
	Rest time*Aging	Aged	A	130.2	166.1	0.83	0.437
		Unaged	U	100.6	164.0		
	Aging*Gradation	Coarse	C	74.0	62.7	0.5	0.476
Fine		F	156.8	218.1			
Aging*Frequency	High	H	177.8	209.4	0.001	0.974	
	Low	S	53.0	56.4			

**Table 4.5.** The average number of loading cycles at 50% reduced stiffness

Specimen ID	Cycle	Specimen ID	Cycle	Specimen ID	Cycle	Specimen ID	Cycle
BFMAH0	369	BCMAS0	83	LCMAH0	205	LFMAS0	116
BFMAH5	415	BCMAS5	144	LCMAH5	129	LFMAS5	93
BFMAH10	670	BCMAS10	148	LCMAH10	153	LFMAS10	125
BFMUH0	218	BCMUS0	78	LCMUH0	80	LFMUS0	35
BFMUH5	364	BCMUS5	62	LCMUH5	113	LFMUS5	31
BFMUH10	758	BCMUS10	111	LCMUH10	167	LFMUS10	43
BFNAH0	48	BCNAS0	15	LCNAH0	28	LFNAS0	31
BFNAH5	129	BCNAS5	19	LCNAH5	27	LFNAS5	22
BFNAH10	95	BCNAS10	18	LCNAH10	42	LFNAS10	43
BFNUH0	39	BCNUS0	12	LCNUH0	55	LFNUS0	17
BFNUH5	53	BCNUS5	18	LCNUH5	23	LFNUS5	12
BFNUH10	62	BCNUS10	21	LCNUH10	35	LFNUS10	16

#### 4.8.1.1 Asphalt type

Figure 4.18 shows the trend for stiffness reduction for two specimens fabricated with different asphalt binders: neat and modified asphalt (4.5% SBS). It can be noted that a considerable deviation exists in the thermal fatigue performance for the specimens of different binder types; the specimen with neat asphalt reached the failure point at 390 cycles while the specimen with modified asphalt did not even fail until the 2000 loading cycles. The number of cycles at 50% reduced stiffness as shown in Figures 4.19 and 4.20 indicates that all the specimens have a similar trend. This difference in behavior results from the fact that the SBS modifier drastically increases the asphalt mixture's elastic properties, leading to a longer thermal fatigue life for the specimens. According to Table 4.4, adding SBS modifier increases the fatigue life five times at 50% reduced stiffness level. This result also agrees with the conclusions of (Epps, 1999) and (Khattak and Baladi, 2001) that use of elastomers (CRM, SBS) increases the fatigue life of asphalt concrete.

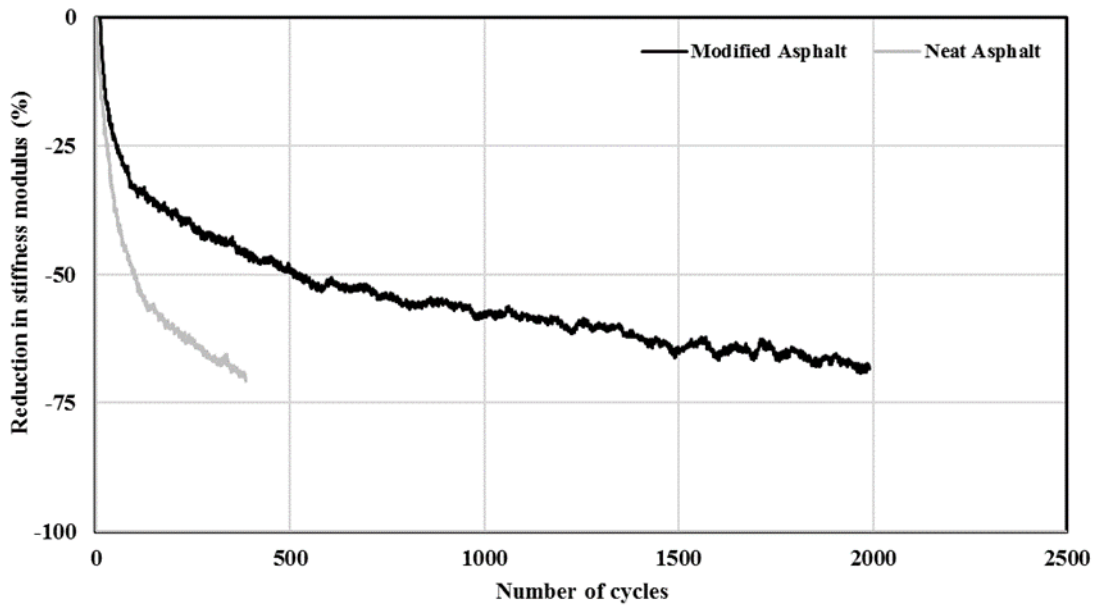


**Figure 4.18.** Stiffness reduction versus number of loading cycles for two mixtures with similar ID and different asphalt types

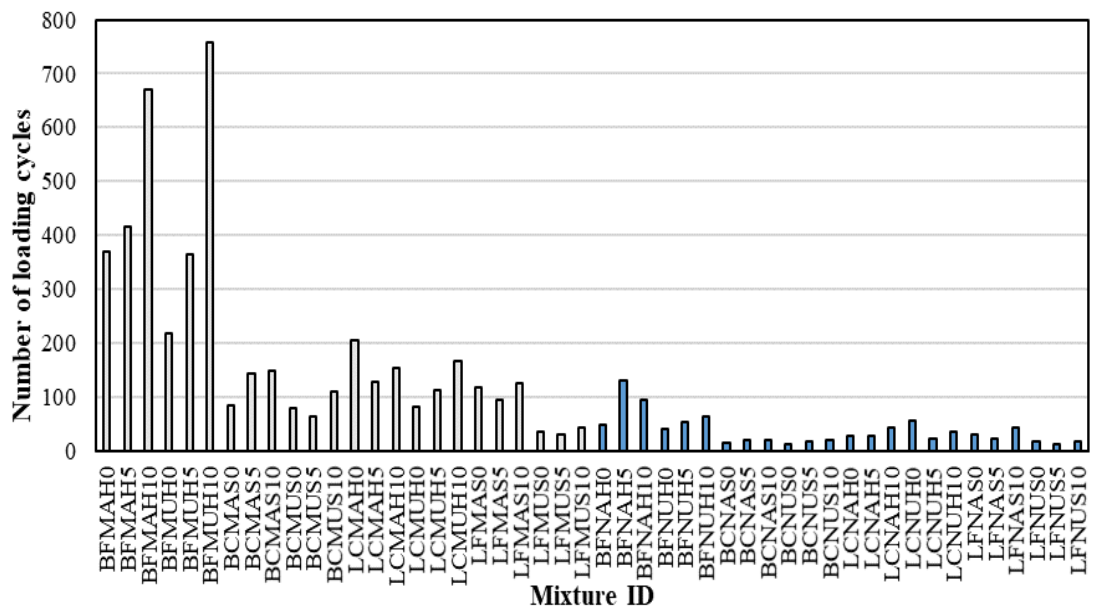


**Figure 4.19.** The average number of loading cycles for different mixtures at 50% reduced stiffness, grouped based on the asphalt type

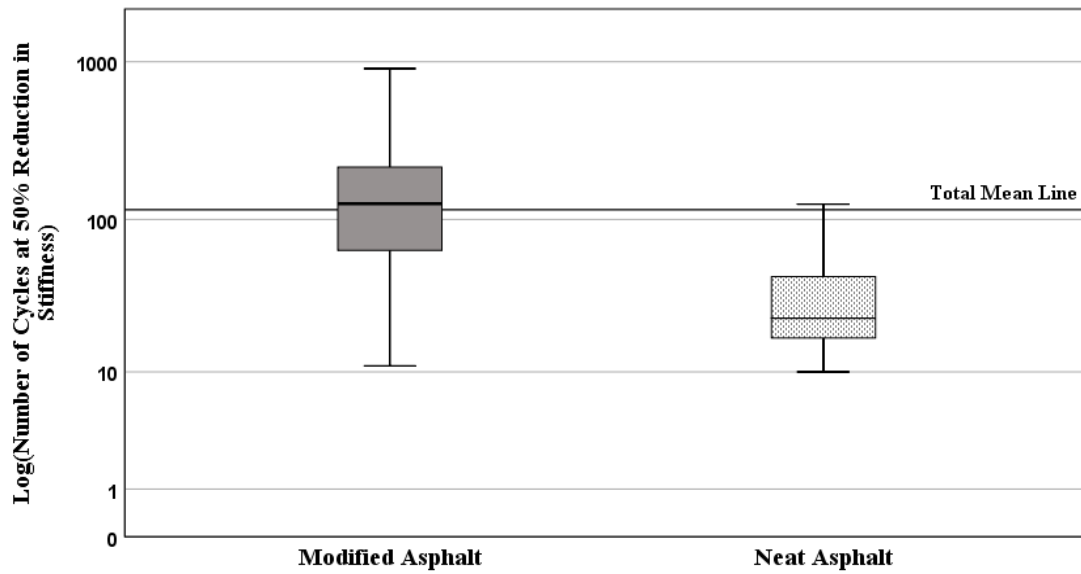


**Figure 4.20.** Box plot for number of loading cycles at 50% reduced stiffness, grouped based on the asphalt type

#### 4.8.1.2 Frequency of loading

Loading frequency is the next test variable, whose effect on different mixtures' thermal fatigue resistance was investigated. Haversine loading was applied at two frequency levels: High (0.1 Hz) and Low (0.01 Hz). Figure 4.21 compares the effect of loading frequency on two identical specimens; the specimen, which was test with high loading frequency, failed at 1227 cycles while the other specimen, tested with low frequency, failed at 630 cycles. It seems that the specimens under high frequency of loading perform better, as given results in Table 4.5 verify this conclusion.



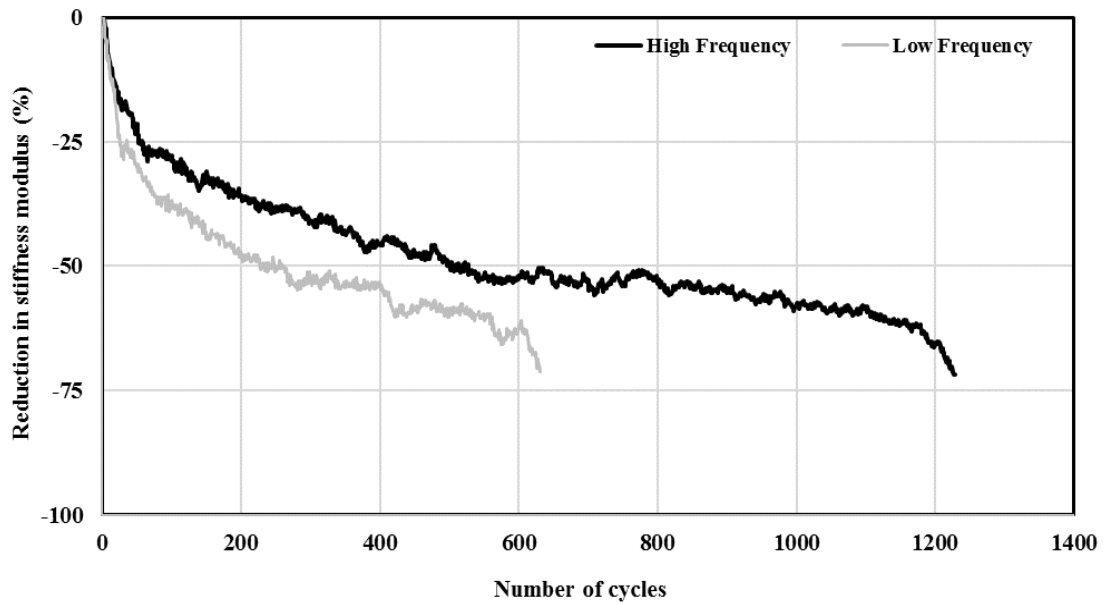


**Figure 4.21.** Stiffness reduction versus number of loading cycles for two mixtures with similar ID and different loading frequency

A similar trend can be seen in Figures 4.22 and 4.23, in which specimens are divided into two groups based on the loading frequency, and comparison is made based on the number of cycles at 50% reduction in stiffness. It is obvious from figures that the specimens under higher loading frequency show more resistance to thermal fatigue. This conclusion is also compatible with the previous findings of (A.h.Gerritsen and et.al 1989). This finding can be expected because the specimens tested at low frequencies are subjected to loading time longer, which causes development of micro cracks, on the other hand, healing becomes more prevalent due to extended time period.

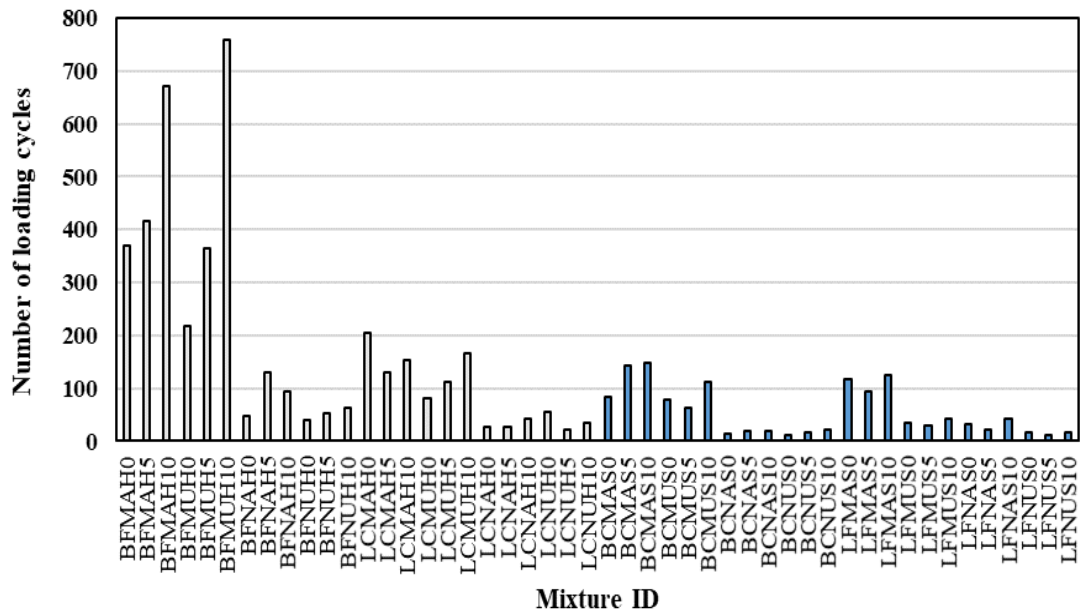


**Figure 4.22.** The average number of loading cycles for different mixtures at 50% reduced stiffness, grouped based on the loading frequency

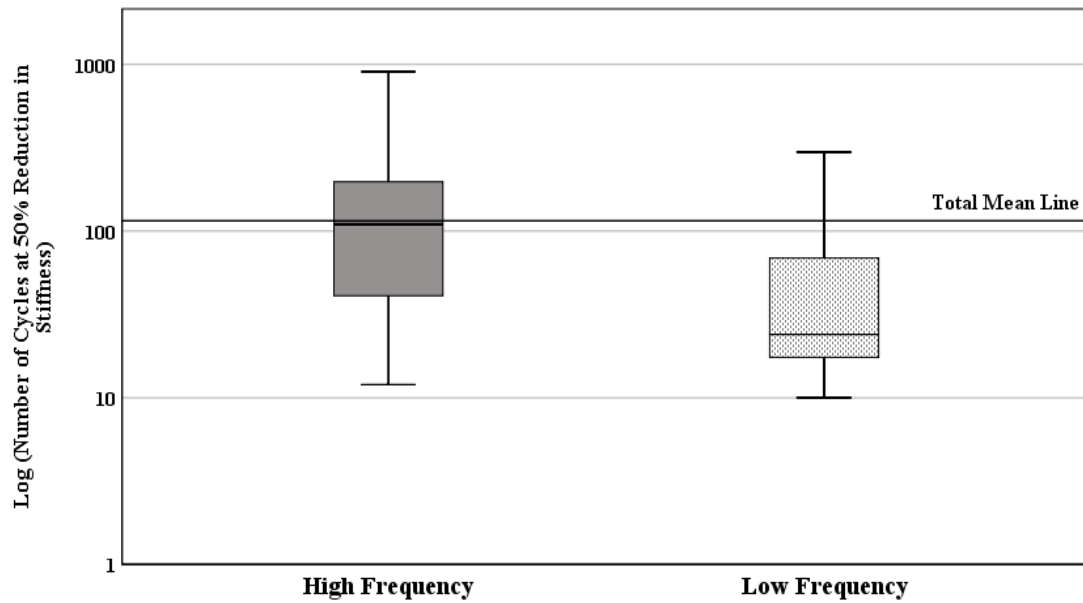


**Figure 4.23.** Box plot for number of loading cycles at 50% reduced stiffness, grouped based on the loading frequency

### 4.8.1.3 Aggregate type

Figure 4.24 shows the influence of aggregate type on thermal fatigue performance of the test specimens. It can be observed that the specimen fabricated with basalt aggregate does not fail up to 2000 cycles, and the specimen with limestone reached to failure condition at 1222 cycles. This example and the number of loading cycles for 50% reduction in stiffness given in Table 4.5 show that basalt aggregate outperforms limestone aggregate against thermal fatigue.

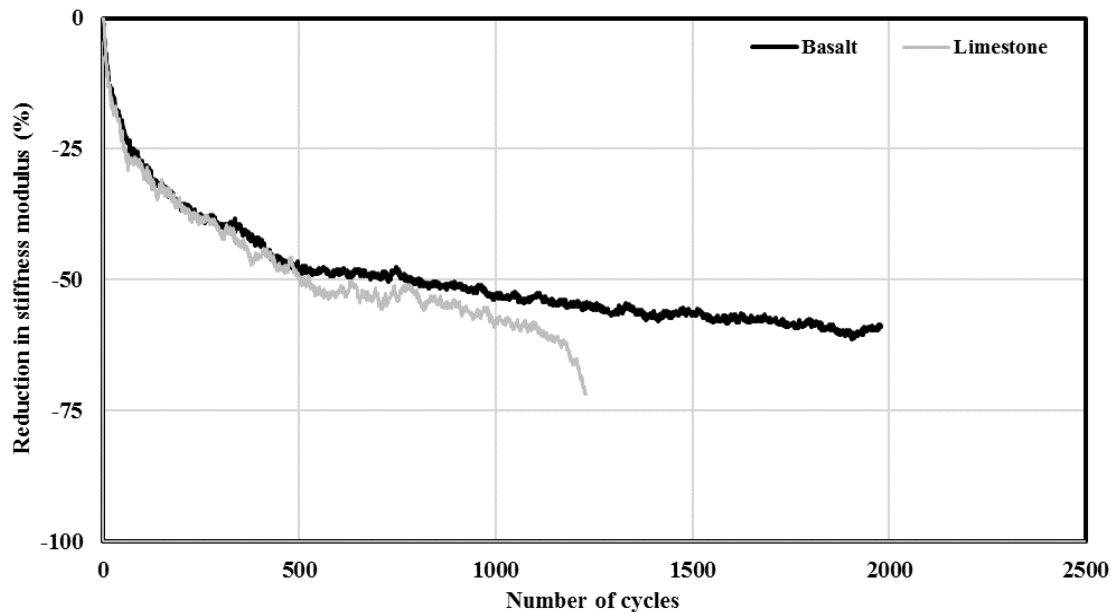


**Figure 4.24.** Stiffness reduction versus number of loading cycles for two mixtures with similar ID and different aggregate type

In Figures 4.25 and 4.26, specimens are divided into two groups based on the type of aggregate that have been used for their fabrication. It can be seen that specimens with limestone aggregate reach to 50% stiffness earlier than those with basalt aggregate. According to Figure 4.26 and given data in Table 4.4, for 50% reduced stiffness level, the mean number of cycles for specimens with basalt is 207 while it is only 67 for those with limestone aggregate. This outcome is compatible with the finding of (Kim

et al. 1992) that aggregates that are very hard and tough can demonstrate higher fatigue-resistance.

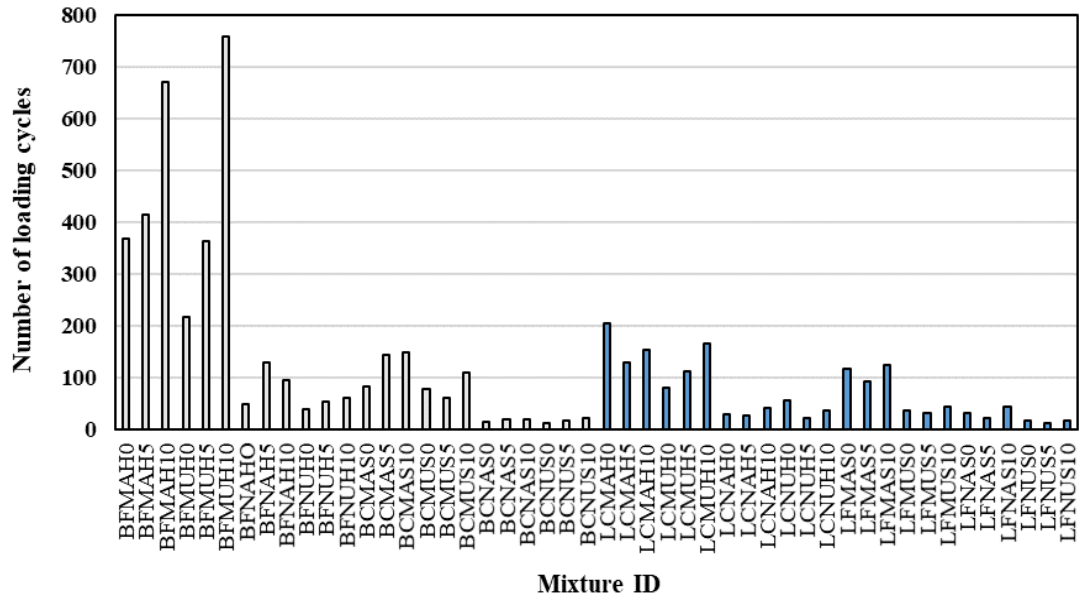


**Figure 4.25.** The average number of loading cycles for different mixtures at 50% reduced stiffness, grouped based on the aggregate type

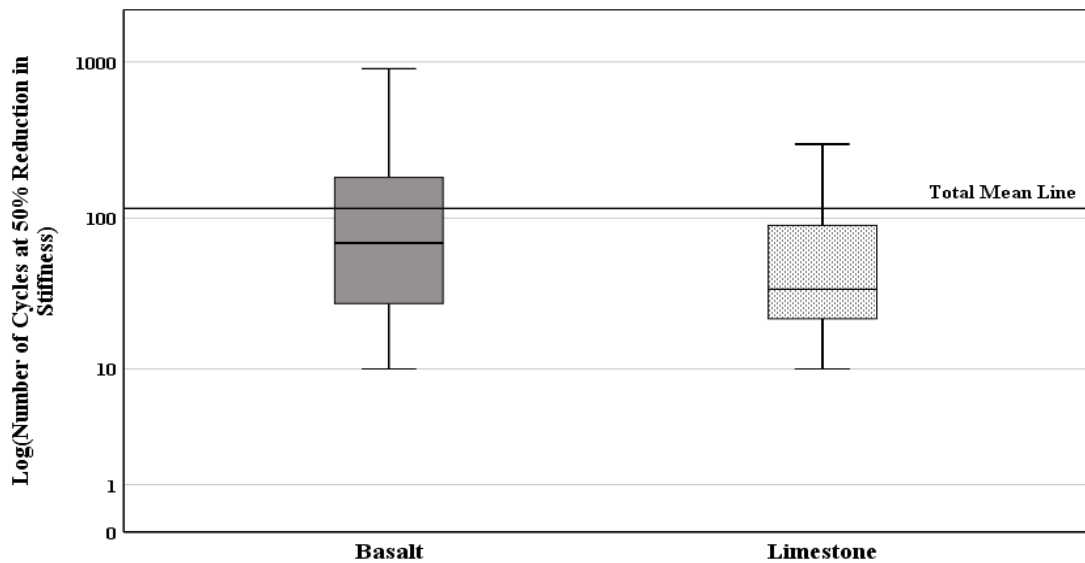


**Figure 4.26.** Box plot for number of loading cycles at 50% reduced stiffness, grouped based on the aggregate type

#### 4.8.1.4 Gradation

An example of the effect of gradation on thermal fatigue resistance of asphalt concrete is given in Figure 4.27. It seems the specimen with finer gradation has a lower rate of stiffness reduction than that of a coarse graded specimen. This example and given data in Table 4.5 show that fine graded specimens outperform coarse ones. In Figures 4.28 and 4.29, specimen's performance at 50% reduction in stiffness modulus is compared between coarse graded and fine graded specimens. According to Table 4.4, the mean cycle number at 50% reduction stiffness level for fine and coarse graded specimen are 157 and 74, respectively. The reason for better performance of fine graded specimens against fatigue is that fine aggregates have a larger surface area and provide better bonding with asphalt binder. Besides, fine graded specimens have a better aggregate interlock within the mixture structure, thereby increasing the overall fatigue performance. This finding also agrees with the results of (Kim et al. 2002; Nejad et al. 2010) study.

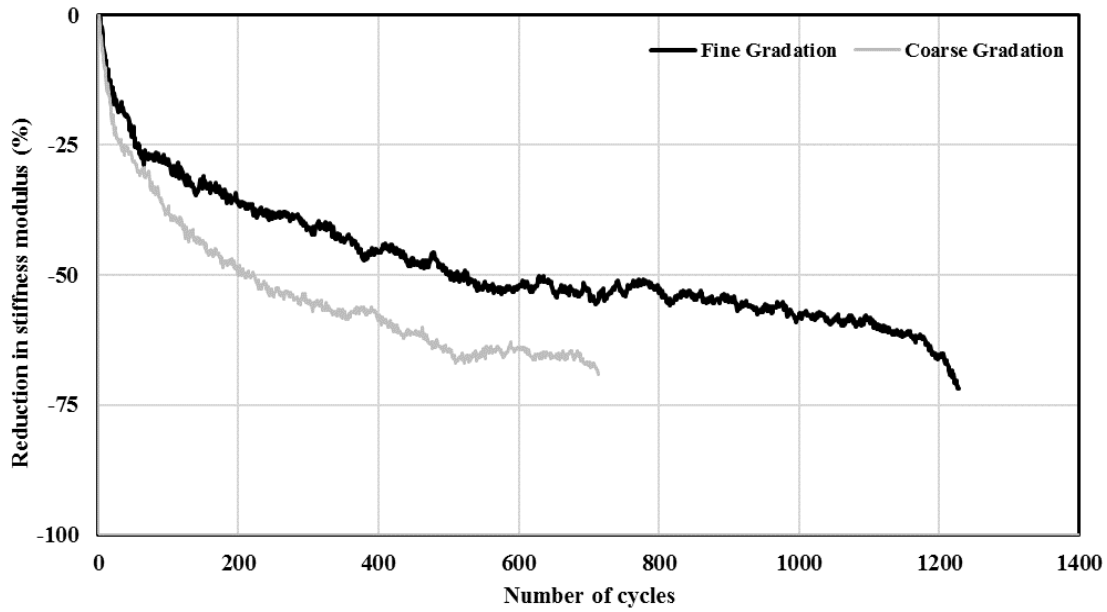


**Figure 4.27.** Stiffness reduction versus number of loading cycles for mixtures with similar ID and different gradations

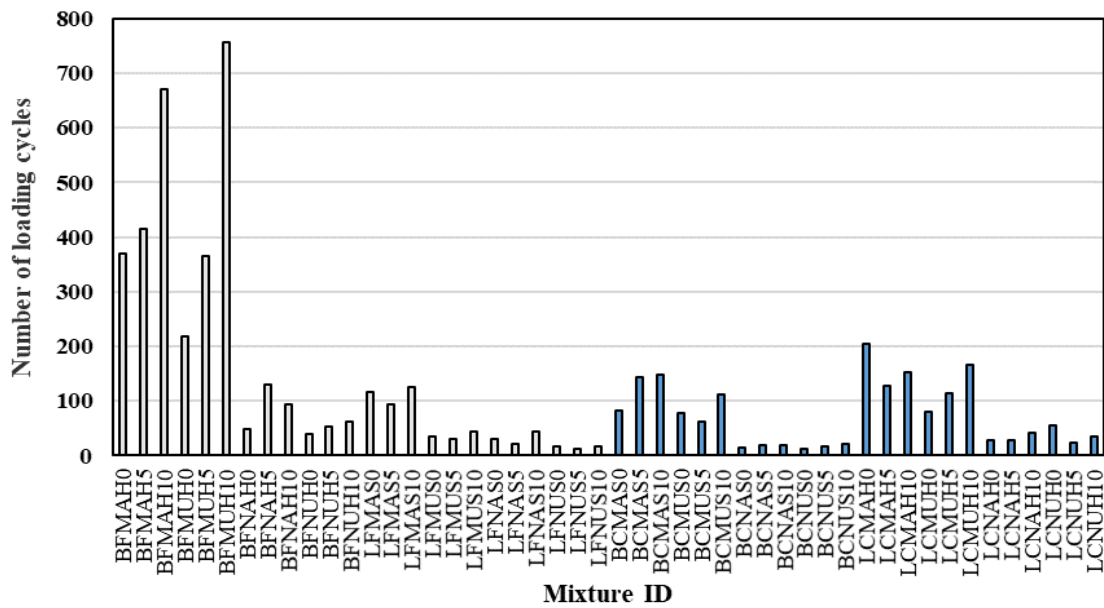


**Figure 4.28.** The average number of loading cycles for different mixtures at 50% reduced stiffness, grouped based on the gradation

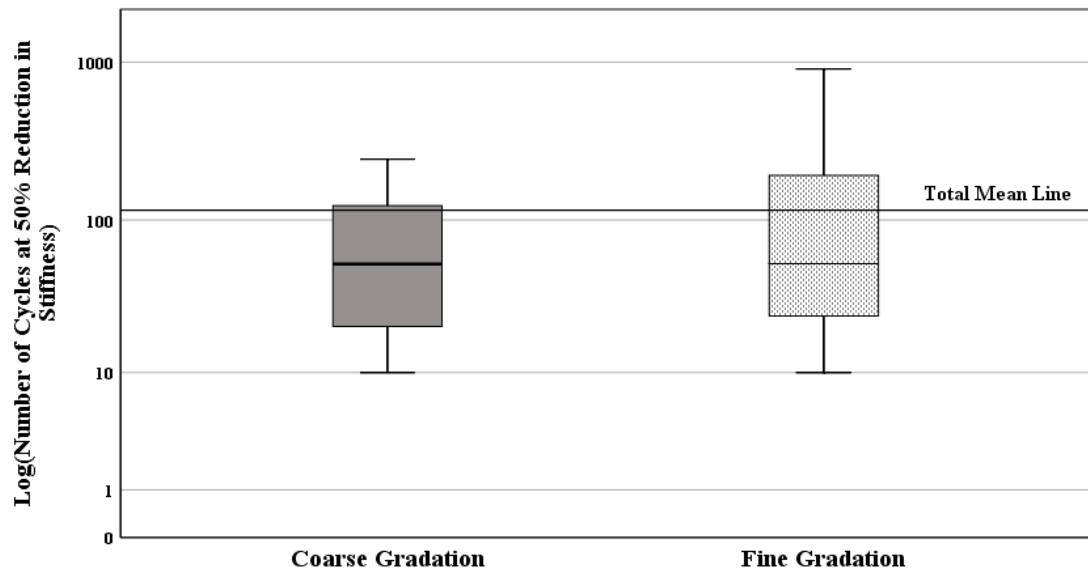


**Figure 4.29.** Box plot for number of loading cycles at 50% reduced stiffness, grouped based on the gradation

#### 4.8.1.5 Rest time

Figure 4.30 shows an example for the effect of rest time on the asphalt concrete's performance under thermal fatigue. Three specimens of the same design mixture were tested with different rest times. Rest time was applied at three levels: 0 s, 5 s, and 10 s. As shown in Figure 4.30, the specimen with 10 s rest time outperformed ones with 5 s and no rest time, as well. Figure 4.31 and 4.32 compare the effect of rest period on the performance of all specimens at 50% reduction in the stiffness modulus. It can be seen that specimens tested with higher rest periods generally show better fatigue performance. This can be related to asphalt concrete's relaxation behavior during the rest time, which causes micro crack healing and improves the stiffness modulus and hence fatigue life of asphalt concrete. Detailed information regarding the effect of rest time can be found in (Zeida et al. 2014) study.

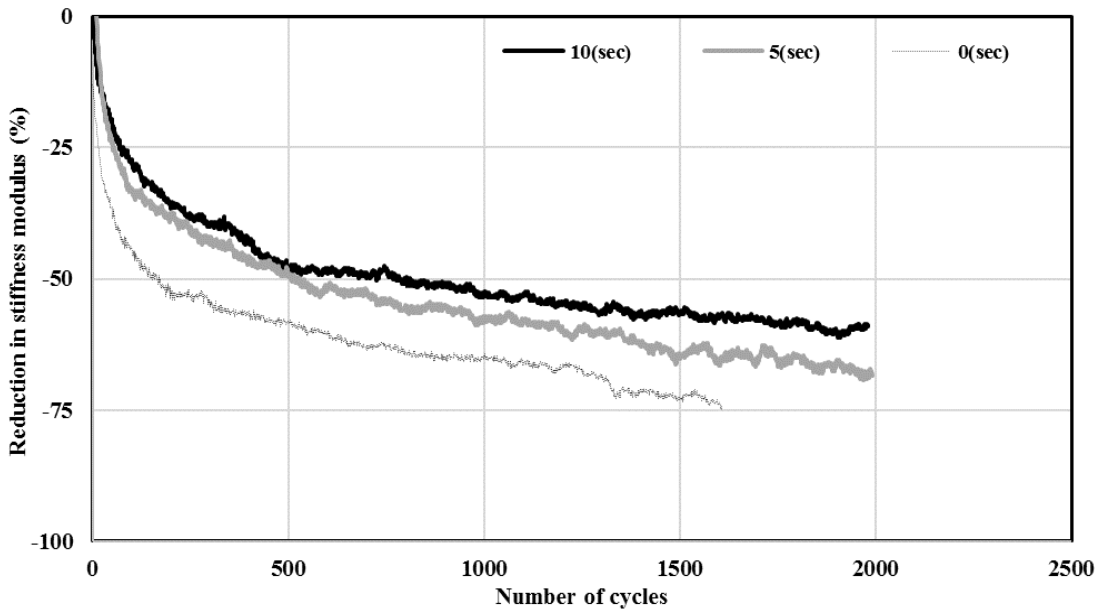


**Figure 4.30.** Stiffness reduction versus number of loading cycles for mixtures with similar ID and different rest times

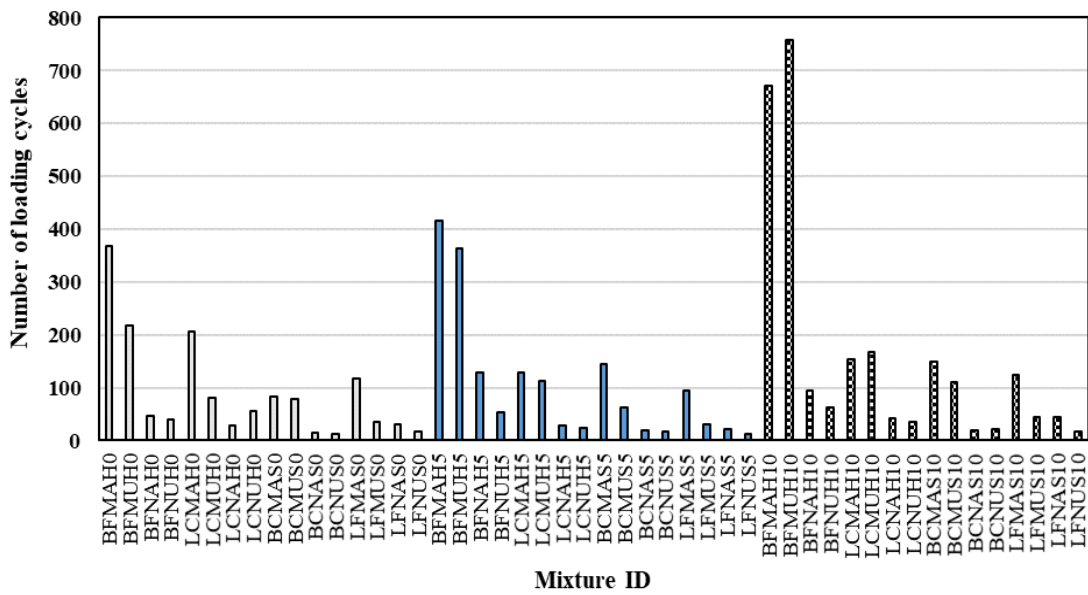


**Figure 4.31.** The average number of loading cycles for different mixtures at 50% reduced stiffness, grouped based on the rest time



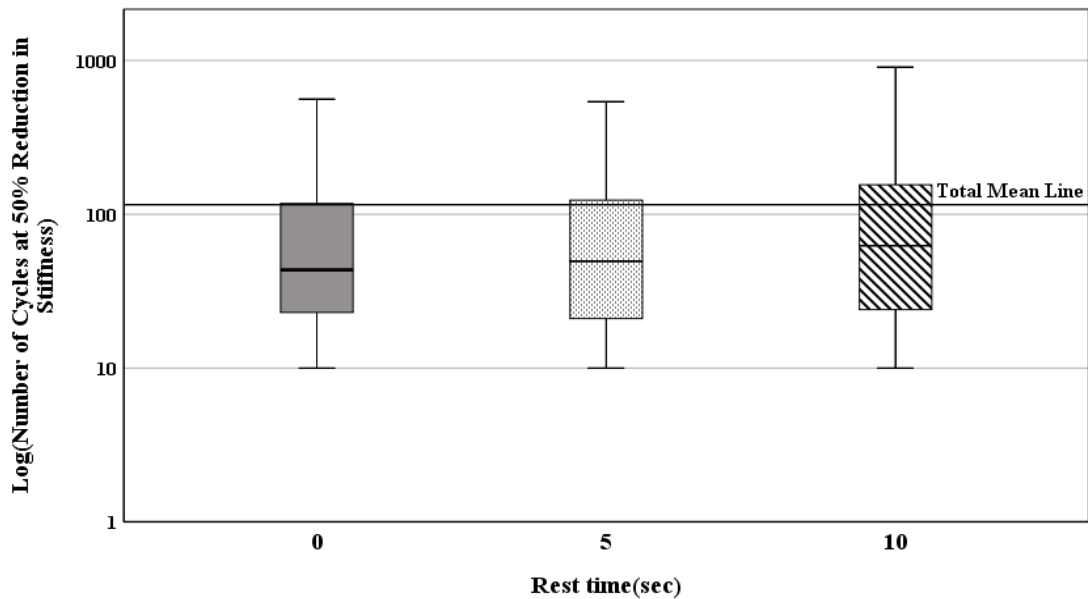
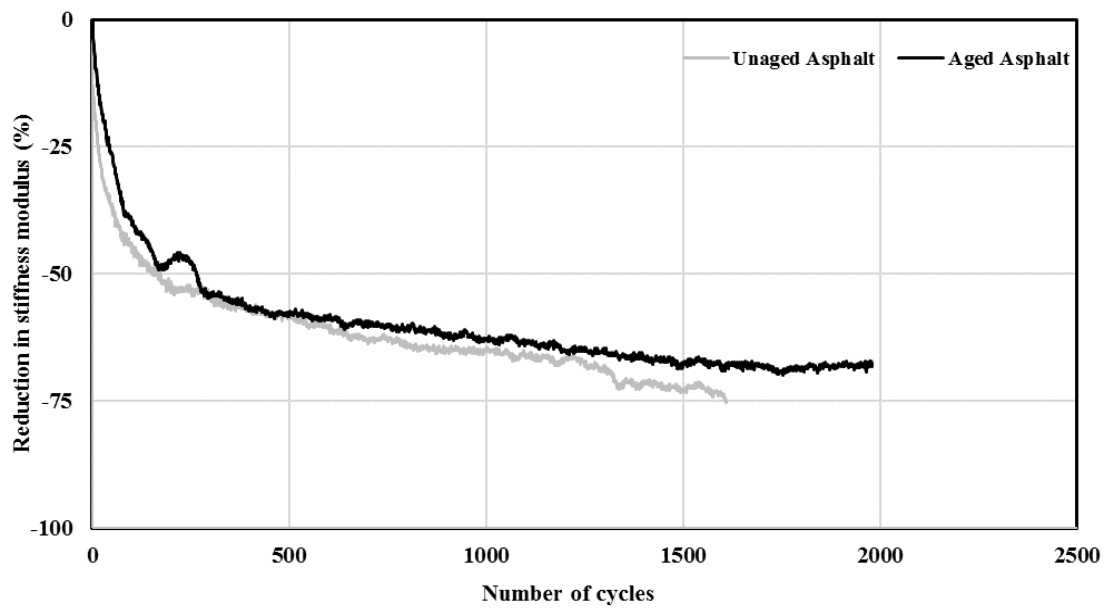


**Figure 4.32.** Box plot for number of loading cycles at 50% reduced stiffness, grouped based on the rest time

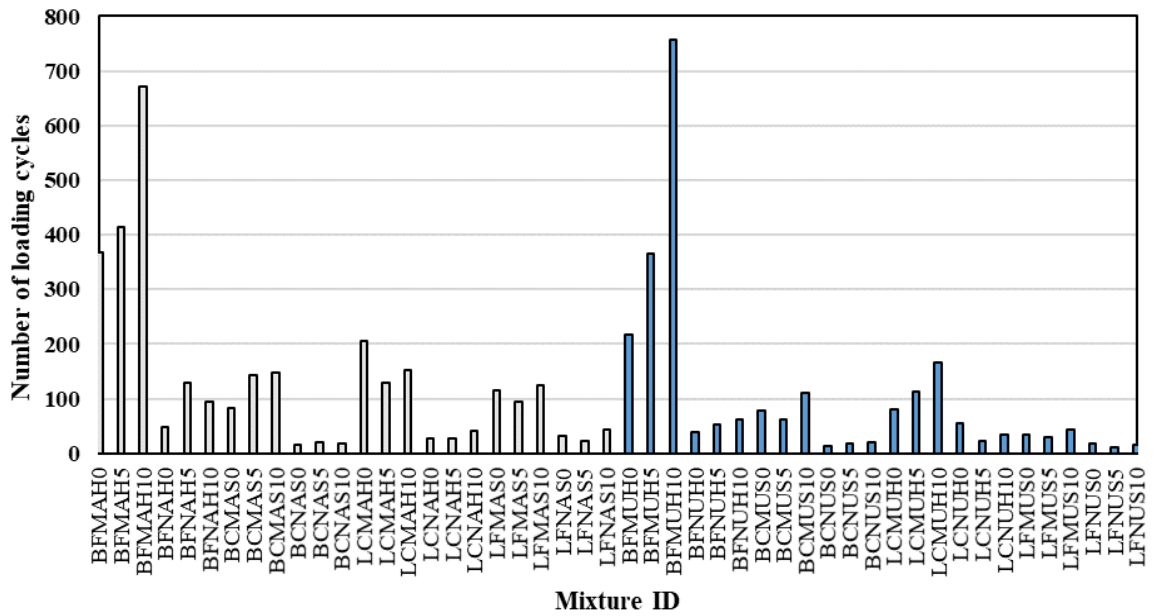
#### 4.8.1.6 Aging

Figure 4.33 shows the effect of aging on stiffness of two identical specimens prepared with different aging conditions. It can be noticed that the aged specimen performed slightly better than those of unaged ones. However, it is also apparent that aging is not as significant variable as asphalt type or frequency. Figure 4.34 and 4.35, in which specimens are divided into two groups according to aging condition, show the response of each specimen to variations in aging condition. The responses are the number of loading cycles at 50% reduction in stiffness. The mean cycle numbers are given in Table 4.4 showing that aged specimens with 130 cycles outperform unaged specimens with 100 cycles. This outcome is, however, controversial to findings of (Raad et al. 2001) in that aging makes asphalt binder more brittle and reduces the fatigue life of beam samples at low temperatures. However, based on the study of

(Harvey et al. 1995), long-term oven aged samples have a slightly better performance than aged ones because of increased stiffness. These findings are compatible with those of (A.h. Gerritsen and et.al 1989) that fatigue life of aged samples tested at low strain level near 0° C is generally higher than for unaged samples.



**Figure 4.33.** Stiffness versus number of loading cycles for mixtures with different aging condition



**Figure 4.34.** The average number of loading cycles for different mixtures at 50% reduced stiffness, grouped based on the rest time

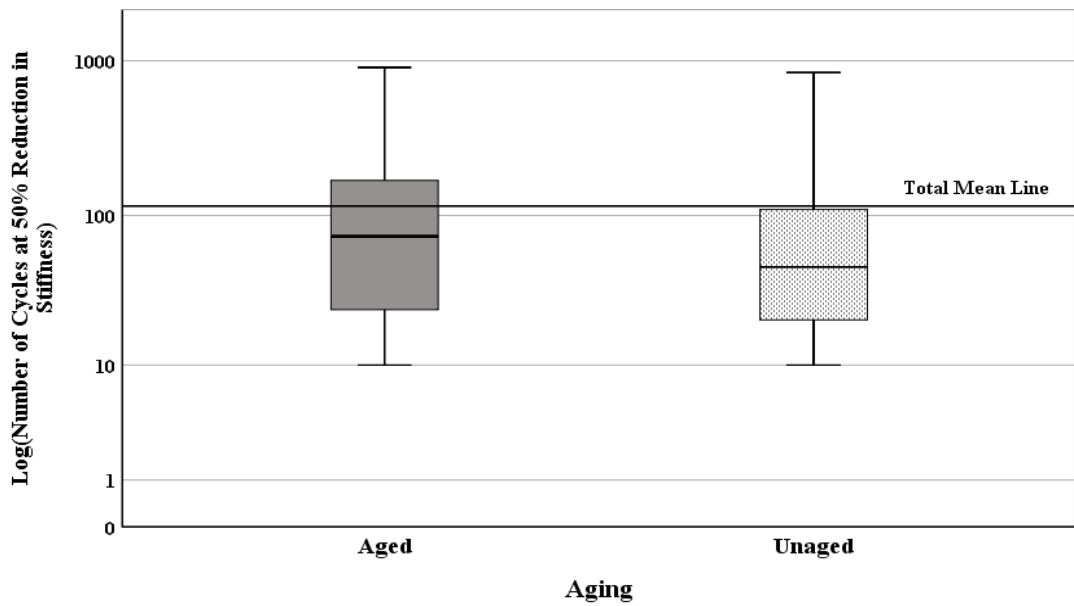


**Figure 4.35.** Box plot for number of loading cycles at 50% reduced stiffness, grouped based on the aging

#### **4.8.2 Multivariate analysis for the number of loading cycles at 25% reduced stiffness**

In order to find significant variables affecting the thermal fatigue performance of asphalt concrete, a total of 144 specimens were tested and the number of loading cycles at 25% reduction in stiffness are calculated. Statistic parameters and multivariate analysis results for 25% reduced stiffness are given in Table 4.6. Besides, the effect of design variables and the interaction between these variables were also evaluated using multivariate analysis. As apparent from the p-values in Table 4.6, all the test variables were found to be significant. Since the probability value for all the factors was less than 0.05, F (Fisher) value as a determinant criterion was used to sort out the design variables based on their significance levels. Generally, the greater the f value, the more significant the test variable. Results of the multivariate analysis indicated that loading frequency, asphalt type, aggregate type, gradation and aging are all significant variables for thermal fatigue performance. However, the calculated F values indicate that the rest time is the least significant variable in terms of number of loading cycles. On the other hand, there are interaction of variables appearing relatively less significant at 50% reduced stiffness. The interaction between gradation and aging was not considered significant in the previous analysis for 50% reduced stiffness, but it was placed among the significant interactions in this analysis. The interaction of rest time with asphalt type, frequency, and gradation has been also removed from the significant variables for the same reason. The interaction between aging and gradation is added to significant variables as gradation plays a dominant role for thermal fatigue behavior of asphalt concrete. More detailed explanations about the interaction of the design variables are given in the previous sections for 50% reduction in stiffness level. The average number of loading cycles at 25% reduced stiffness is given in Table 4.7. Statistical comparisons of different levels of design variables for the number of loading cycles at 25% reduced stiffness using bar charts, and box plots are given in Appendix E.

**Table 4.6.** Multivariate analysis for number of loading cycles at 25% reduced stiffness

Design Variable		Levels	Symbol	Mean	Std. Deviation	F-Value	P-Value
Main Effects	Frequency	High	H	30.6	24.6	78.8	0.000
		Low	S	12.6	6.7		
	Asphalt type	Modified	M	28.8	25.2	50.4	0.000
		Neat	N	14.4	8.5		
	Aggregate type	Basalt	B	26.6	25.9	24.3	0.000
		Limestone	L	16.6	9.8		
	Gradation	Coarse	C	16.9	10.5	21.8	0.000
		Fine	F	26.3	25.7		
	Aging	Aged	A	24.5	23.2	8.3	0.005
		Unaged	U	18.7	16.1		
Rest time	0 second	0	19.9	15.5	2.1	0.124	
	5 second	5	20.3	20.2			
	10 second	10	24.5	23.8			
Variables interaction	Aggregate type * Asphalt type	Modified	M	28.8	25.2	18.3	0.000
		Neat	N	14.4	8.5		
	Asphalt type * Frequency	High	H	30.6	24.6	18.2	0.000
		Low	S	12.6	6.7		
	Gradation * Aging	Aged	A	24.5	23.2	10.4	0.002
		Unaged	U	18.7	16.1		
	Gradation * Asphalt type	Modified	M	28.8	25.2	7.8	0.006
		Neat	N	14.4	8.5		
	Rest time * Aggregate type	Basalt	B	26.6	25.9	4.1	0.020
		Limestone	L	16.6	9.8		
	Aggregate type * Aging	Aged	A	24.5	23.2	3.5	0.065
		Unaged	U	18.7	16.1		
	Aging*Asphalt type	Modified	M	28.8	25.2	2.5	0.117
		Neat	N	14.4	8.5		
	Asphalt type * Rest time	0 second	0	19.9	15.5	2.2	0.117
		5 second	5	20.3	20.2		
		10 second	10	24.5	23.8		
	Rest time*Gradation	Coarse	C	17.75	11.6	1.9	0.157
		Fine	F	31.33	30.4		
	Aging * Frequency	High	H	30.6	24.6	1.7	0.196
Low		S	12.6	6.7			
Rest time*Aging	Aged	A	24.5	23.2	0.9	0.427	
	Unaged	U	18.7	16.1			
Rest time * Frequency	High	H	30.61	24.6	0.4	0.641	
	Low	S	12.57	6.7			

**Table 4.7.** The average number of loading cycles at 25% reduced stiffness

Specimen ID	Cycle	Specimen ID	Cycle	Specimen ID	Cycle	Specimen ID	Cycle
BFMAH0	62	BCMAS0	16	LCMAH0	28	LFMAS0	12
BFMAH5	77	BCMAS5	20	LCMAH5	22	LFMAS5	20
BFMAH10	85	BCMAS10	18	LCMAH10	22	LFMAS10	22
BFMUH0	29	BCMUS0	12	LCMUH0	27	LFMUS0	12
BFMUH5	35	BCMUS5	13	LCMUH5	27	LFMUS5	9
BFMUH10	67	BCMUS10	25	LCMUH10	27	LFMUS10	11
BFNAH0	20	BCNAS0	8	LCNAH0	15	LFNAS0	18
BFNAH5	28	BCNAS5	9	LCNAH5	14	LFNAS5	13
BFNAH10	26	BCNAS10	8	LCNAH10	19	LFNAS10	11
BFNUH0	14	BCNUS0	7	LCNUH0	27	LFNUS0	10
BFNUH5	20	BCNUS5	8	LCNUH5	13	LFNUS5	6
BFNUH10	21	BCNUS10	10	LCNUH10	13	LFNUS10	9

#### **4.8.3 Multivariate analysis for the number of loading cycles at 75% reduced stiffness**

After fitting a power model to stiffness modulus, the number of loading cycles for specimens whose stiffness did not reduce 75% after 2000 cycle was calculated and listed in Table 4.9. As shown in Table 4.8, the results of multivariate analyses show that all the test variables are significant. The sequence for the significance of variables according to F values is similar to those calculated at 50% reduced stiffness except for aging and rest time, in which the order of two variables is interchanged. All of the two-level interactions between asphalt type and the other variables are significant, as for the interaction between gradation and aging. More details about the interaction of variables can be found in the previous section for the multivariate analyses of loading cycles at 50% reduced stiffness. Statistical comparisons of different levels of design variables for the loading cycles at 75% reduced stiffness using bar charts and box plots are given in Appendix F.

**Table 4.8.**Multivariate analysis for number of loading cycles at 75 % reduced stiffness

	<b>Design Variable</b>	<b>Levels</b>	<b>Symbol</b>	<b>Mean</b>	<b>Std. Deviation</b>	<b>F Value</b>	<b>P- Value</b>
<b>Main effects</b>	Asphalt type	Modified	M	1328.7	1549	151	0.000
		Neat	N	107.5	117		
	Frequency	High	H	1167.4	1615	81.8	0.000
		Low	S	268.8	387		
	Aggregate type	Basalt	B	1095.9	1623	57.8	0.000
		Limestone	L	340.3	494		
	Gradation	Coarse	C	381.6	442	45.9	0.000
		Fine	F	1054.7	1656		
	Aging	Aged	A	855.0	1456	7.6	0.007
		Unaged	U	581.2	1005		
Rest time	0 second	0	672.4	1287	3.9	0.023	
	5 second	5	576.0	943			
	10 second	10	905.9	1477			
<b>Variables interaction</b>	Asphalt type * Frequency	High	H	1167.4	1615	58.7	0.000
		Low	S	268.8	387		
	Asphalt type* Aggregate type	Basalt	B	1095.9	1623	42.9	0.000
		Limestone	L	340.3	494		
	Asphalt type*Gradation	Coarse	C	381.6	442	34.4	0.000
		Fine	F	1054.7	1656		
	Asphalt type * Aging	Aged	A	855.0	1456	5.8	0.018
		Unaged	U	581.2	1005		
	Aging * Gradation	Coarse	C	381.6	442	4.2	0.042
		Fine	F	1054.7	1656		
	Rest time *Asphalt type	Modified	M	1328.7	1549	3.3	0.042
		Neat	N	107.5	117		
	Rest time * Frequency	High	H	1167.4	1615	2.0	0.134
		Low	S	268.8	387		
	Rest time *Aging	Aged	A	855.0	1456	1.9	0.159
		Unaged	U	581.2	1005		
	Aging*Aggregate type	Basalt	B	1095.9	1623	1.6	0.207
		Limestone	L	340.3	494		
	Rest time* Aggregate type	0 second	0	672.42	1287	1.2	0.316
		5 second	5	576.04	943		
10 second		10	905.87	1477			
Aging*Frequency	High	H	1167.42	1615	1.1	0.301	
	Low	S	268.81	387			
Rest time* Gradation	Coarse	C	381.6	442	0.3	0.750	
	Fine	F	1054.7	1656			

**Table 4.9.** The average number of loading cycles at 75% reduced stiffness

Specimen ID	Cycle	Specimen ID	Cycle	Specimen ID	Cycle	Specimen ID	Cycle
BFMAH0	4686	BCMAS0	439	LCMAH0	1094	LFMAS0	932
BFMAH5	2902	BCMAS5	751	LCMAH5	527	LFMAS5	498
BFMAH10	4883	BCMAS10	807	LCMAH10	942	LFMAS10	619
BFMUH0	1802	BCMUS0	401	LCMUH0	561	LFMUS0	199
BFMUH5	2843	BCMUS5	275	LCMUH5	532	LFMUS5	129
BFMUH10	3823	BCMUS10	773	LCMUH10	1388	LFMUS10	221
BFNAH0	222	BCNAS0	32	LCNAH0	80	LFNAS0	60
BFNAH5	340	BCNAS5	69	LCNAH5	94	LFNAS5	36
BFNAH10	373	BCNAS10	46	LCNAH10	118	LFNAS10	221
BFNUH0	161	BCNUS0	19	LCNUH0	81	LFNUS0	24
BFNUH5	215	BCNUS5	64	LCNUH5	36	LFNUS5	17
BFNUH10	331	BCNUS10	46	LCNUH10	71	LFNUS10	25

#### **4.8.4 Multivariate analysis for stiffness modulus at 50% reduction**

In addition to the number of loading cycles, stiffness modulus itself can also be used as a response variable for comparison of fatigue performance. For this purpose, multivariate analysis for the number of loading cycles were performed at three levels of stiffness reduction of 25%, 50%, and 75%. Since the stiffness of specimens in each reduction level is a coefficient of specimen's initial stiffness, multivariate analysis for the stiffness modulus was performed only at 50% reduced stiffness level. Measured stiffness modulus for the test specimens are given in Table 4.10. According to P and F value's asphalt type, aggregate type, frequency, aging, and gradation are significant variables. Since p-value for the rest time is slightly greater than 0.05, this variable is the least significant one among the other main effects. The number of significant interactions for stiffness modulus is limited to interaction between asphalt type and gradation by small variations in p-value, and also the interaction between aggregate type and rest time (Table 4.11). From Figure 4.36 to 4.45, all the test variables were statistically compared through bar charts and box plots at 50% reduced stiffness



modulus. The significant variables and difference between their levels would be investigated thru bar charts and boxplots in the following sections.

**Table 4.10.** Multivariate analysis for stiffness (50% reduction)

Design Variable		Levels	Symbol	Mean	Std. Deviation	F-Value	P-Value
Main effects	Asphalt type	Modified	M	3413.5	1271.7	201.2	0.000
		Neat	N	1923.7	998.7		
	Aggregate type	Basalt	B	3303.5	1389.8	146.2	0.000
		Limestone	L	2033.7	995.5		
	Frequency	High	H	3248.3	1385.8	121.8	0.000
		Low	S	2088.9	1066.9		
	Aging	Aged	A	2945.1	1389.3	27.7	0.000
		Unaged	U	2392.1	1286.4		
	Gradation	Coarse	C	2450.0	931.0	17.3	0.000
		Fine	F	2887.2	1666.2		
Rest time	0 second	0	2499.8	1304.5	2.6	0.079	
	5 second	5	2743.8	1508.6			
	10 second	10	2762.2	1276.2			
Variables interaction	Gradation * Asphalt type	Coarse	C	2450.0	931.0	14.4	0.000
		Fine	F	2887.2	1666.2		
	Aggregate type * Rest time	0second	0	2499.8	1304.5	3.1	0.051
		5 second	5	2743.8	1508.6		
		10 second	10	2762.2	1276.2		
	Gradation * Aging	Aged	A	2945.1	1389.3	2.5	0.117
		Unaged	U	2392.1	1286.4		
	Aggregate type * Aging	Basalt	B	3303.5	1389.8	2.3	0.136
		Limestone	L	2033.7	995.5		
	Asphalt type * Frequency	High	H	3248.3	1385.8	1.6	0.203
		Low	S	2088.9	1066.9		
	Asphalt type * Rest time	Modified	M	3413.5	1271.7	1.0	0.372
		Neat	N	1923.7	998.7		
	Aggregate type * Asphalt type	Basalt	B	3303.5	1389.8	0.8	0.376
		Limestone	L	2033.7	995.5		
	Asphalt type * Aging	Aged	A	2945.1	1389.3	0.3	0.610
		Unaged	U	2392.1	1286.4		
	Gradation * Rest time	Coarse	C	2450.0	931.0	0.1	0.901
		Fine	F	2887.2	1666.2		
	Aging * Rest time	Aged	A	2945.1	1389.3	0.0	0.960
Unaged		U	2392.1	1286.4			
Aging * Frequency	High	H	3248.3	1385.8	0.0	0.905	
	Low	S	2088.9	1066.9			
Frequency * Rest time	0second	0	2499.8	1304.5	0.0	0.996	
	5 second	5	2743.8	1508.6			
	10 second	10	2762.2	1276.2			

**Table 4.11.** Stiffness modulus of specimens at 50% reduction

<b>Specimen ID</b>	<b>Stiffness</b>	<b>Specimen ID</b>	<b>Stiffness</b>	<b>Specimen ID</b>	<b>Stiffness</b>	<b>Specimen ID</b>	<b>Stiffness</b>
BFMAH0	3626	BCMAS0	2562	LCMAH0	2295	LFMAS0	1228
BFMAH5	3794	BCMAS5	2250	LCMAH5	2147	LFMAS5	1917
BFMAH10	3298	BCMAS10	2400	LCMAH10	2104	LFMAS10	2119
BFMUH0	3162	BCMUS0	1613	LCMUH0	1684	LFMUS0	1639
BFMUH5	3694	BCMUS5	1766	LCMUH5	1744	LFMUS5	1440
BFMUH10	3301	BCMUS10	1531	LCMUH10	1720	LFMUS10	1672
BFNAH0	2051	BCNAS0	1081	LCNAH0	1321	LFNAS0	683
BFNAH5	2385	BCNAS5	1993	LCNAH5	1168	LFNAS5	531
BFNAH10	2318	BCNAS10	1513	LCNAH10	1641	LFNAS10	1672
BFNUH0	1703	BCNUS0	899	LCNUH0	832	LFNUS0	503
BFNUH5	1823	BCNUS5	1262	LCNUH5	942	LFNUS5	390
BFNUH10	1894	BCNUS10	1173	LCNUH10	1516	LFNUS10	561

In Figures 4.36 and 4.37, the test specimens are divided into two groups based on asphalt type used. A comparison of 50% reduced stiffness for two groups shows that specimens with modified asphalt have higher stiffness values. According to Table 4.10, specimens with modified binder and mean stiffness value of 3413 MPa outperform the unmodified ones with a mean value of 1923 MPa. The stiffness of asphalt mixture is highly correlated to the stiffness of the asphalt binder used in its fabrication. Since the stiffness modulus of polymer modified asphalt binder is much higher than the neat asphalt binder, the outcomes in Figures 4.36 and 4.37 are highly expected.

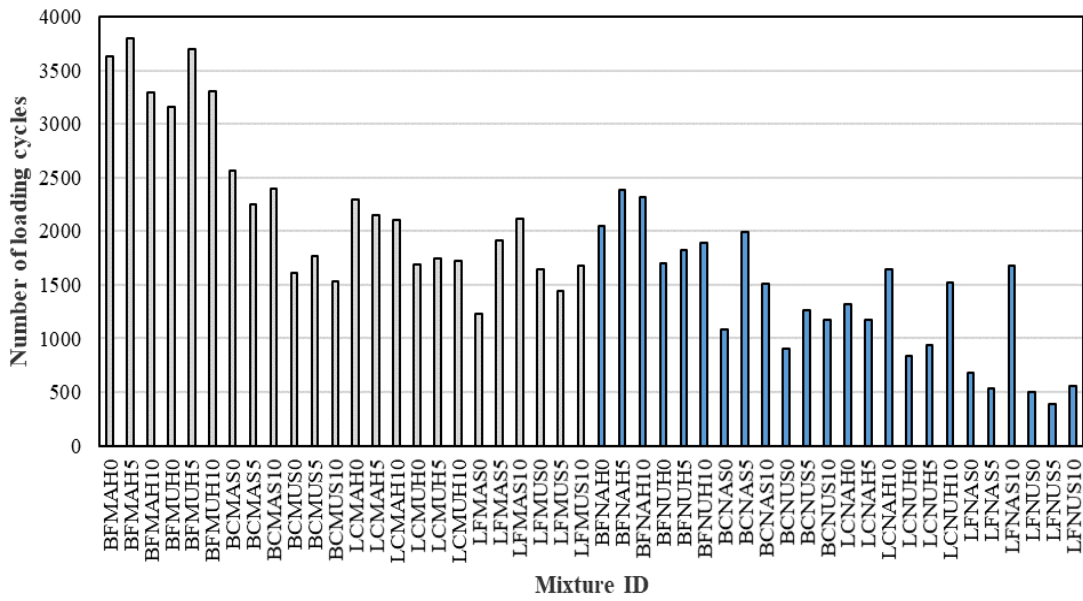


Figure 4.36. The average stiffness modulus at 50 % reduction grouped based on asphalt type

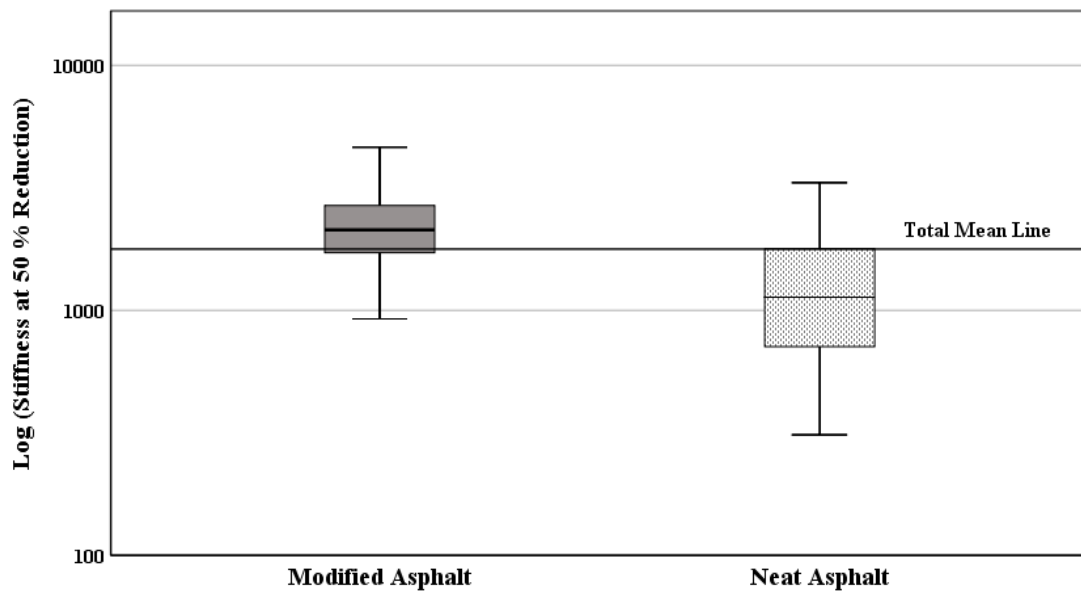
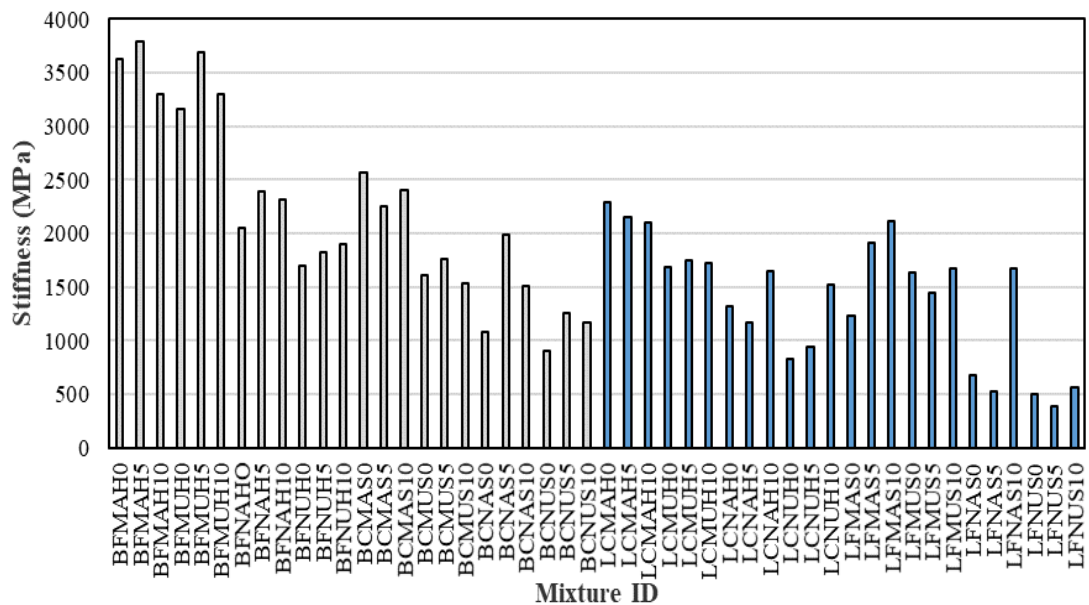
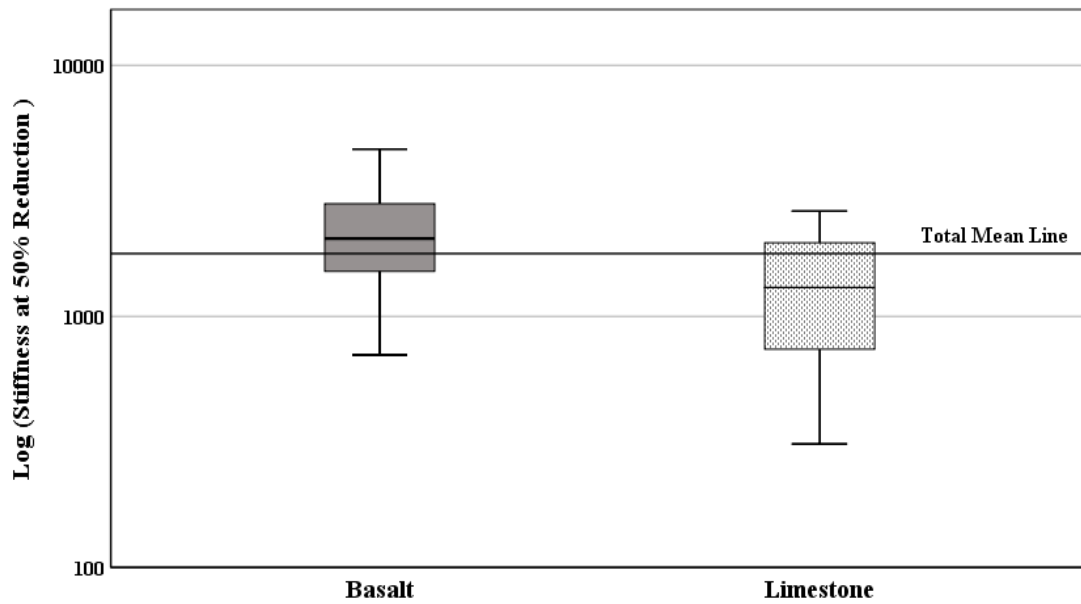


Figure 4.37. Box plot of average stiffness at 50% reduction grouped based on asphalt type

In Figures 4.38 and 4.39, the specimens are divided into two groups based on aggregate type used. The 50% reduced stiffness is the criteria for comparison of basalt and limestone aggregate. As can be observed from Figures 4.38 and 4.39, the specimens with basalt aggregate have higher stiffness and longer fatigue life. It seems that basalt aggregate due to its angular shape, rough surface texture, and high toughness leads to have higher stiffness modulus. The mean stiffness for these specimens with basalt aggregate is produced 3,303 MPa stiffness as can be seen in Table 4.10, while it is only 2,033 MPa for ones prepared with limestone aggregate.



**Figure 4.38.** The average stiffness modulus at 50 % reduction grouped based on aggregate type



**Figure 4.39.** Box plot of average stiffness at 50% reduction grouped based on aggregate type

In Figures 4.40 and 4.41, the effect of loading frequency on specimen's fatigue life is investigated. It is apparent that the mean stiffness of the specimens is larger at high frequency (0.1Hz) than at low frequency (0.01 Hz). These measured stiffness values are 3,248 MPa for high frequency loading and 2,088 MPa for low frequency, respectively. The reason for this behavior is that the loading at very low frequencies gives sufficient time to the development of micro cracks and when combined with relatively low environment temperature (4° C), the recovery by healing becomes difficult.

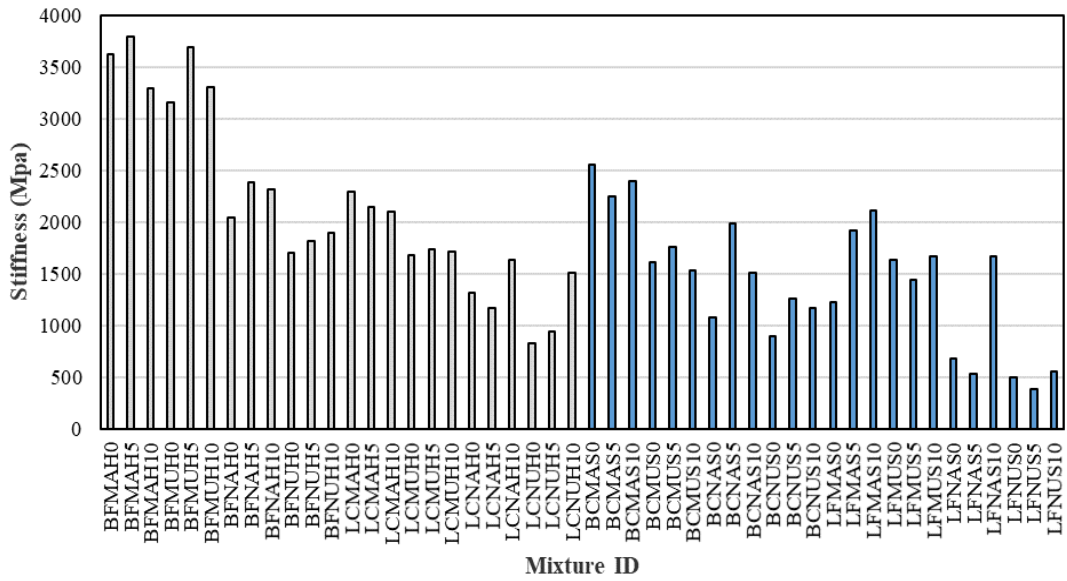


**Figure 4.40.** The average stiffness modulus at 50 % reduction grouped based on loading frequency

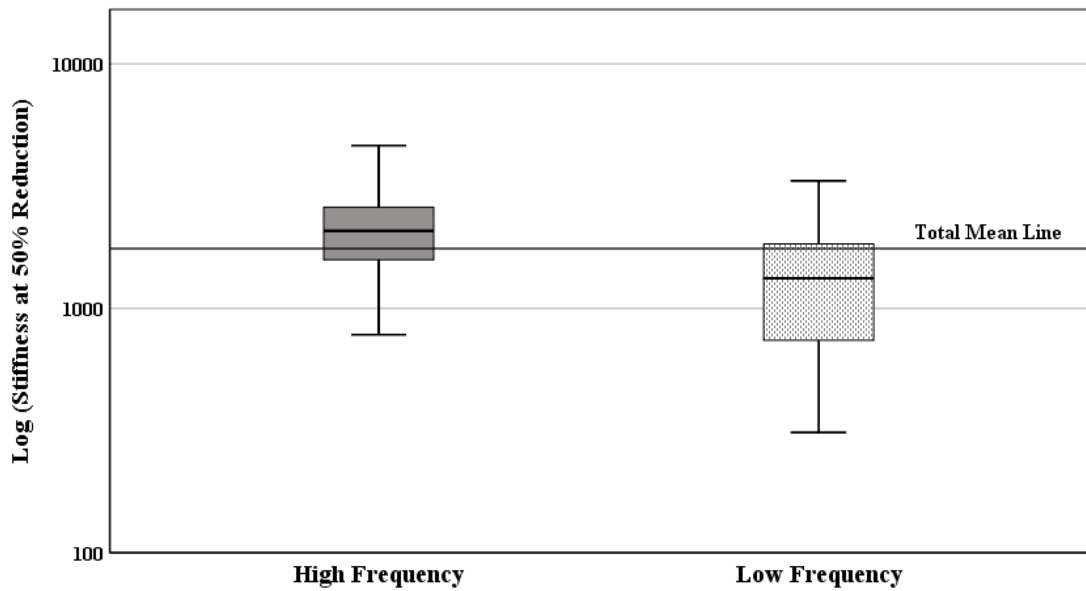


**Figure 4.41.** Box plot of average stiffness at 50% reduction grouped based on loading frequency

Figures 4.42 and 4.43, showing the specimen group based on aging level, reveal the response of specimens to different aging conditions. For loading up to 50% reduced stiffness, aging contributes to increase in specimen's stiffness, as confirmed by the data presented in Figure 4.42 and 4.43. However, the mean stiffness values for the aged and unaged samples (2,945.1MPa and 2,392.1MPa) don't show a noticeable difference (Table 4.10).

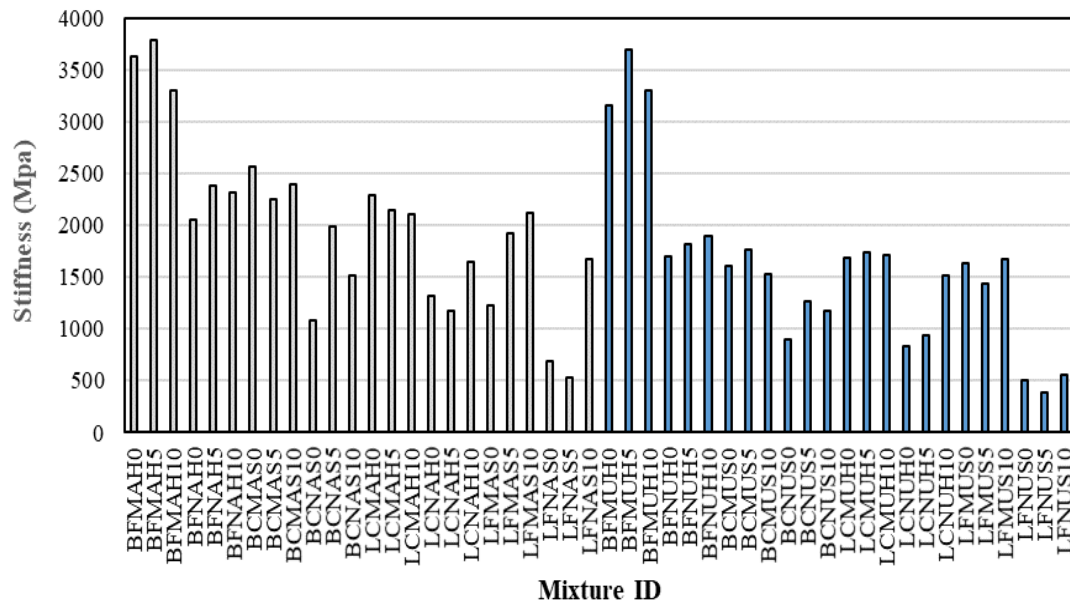


**Figure 4.42.** The average stiffness modulus at 50% reduction grouped based on aging



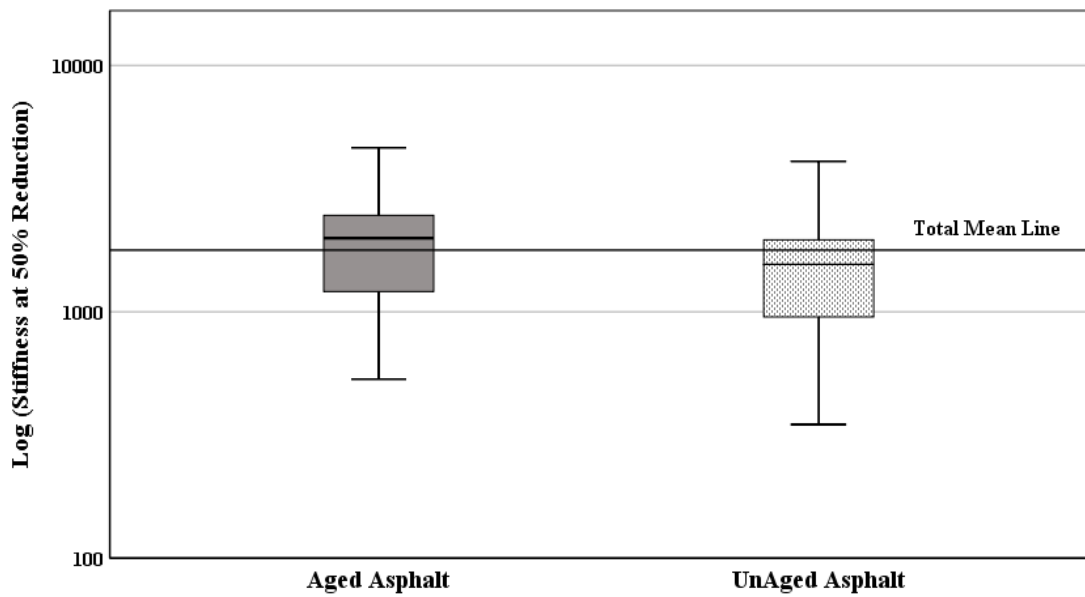


**Figure 4.43.** Box plot of average stiffness at 50% reduction grouped based on aging

In Figure 4.44 and 4.45, specimens' performance is compared based on the gradation type used. The results indicate that the terminal stiffness at 50% reduction is higher for finer gradation. The reason is that higher binder content exists in fine graded mixtures, and they have a larger surface area, leading to a better interlock in the aggregate structure and, therefore, produce denser mixtures. As a result, the mean stiffness of the fine graded specimens showed improvement (2,887 MPa) as compared to coarse one (2450 MPa).

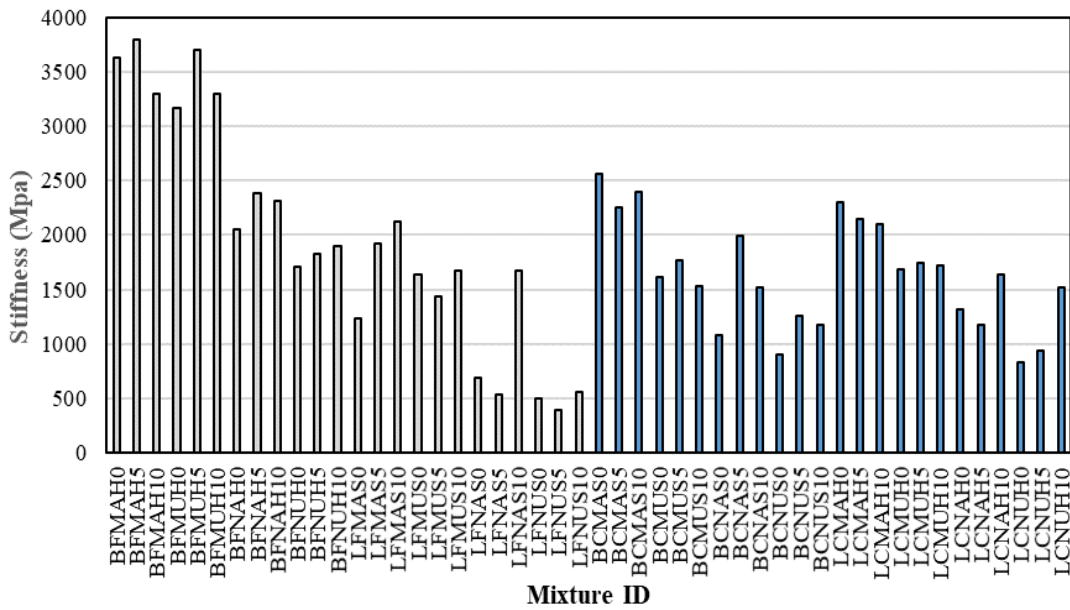


Figure 4.44. The average stiffness modulus at 50 % reduction grouped based on gradation

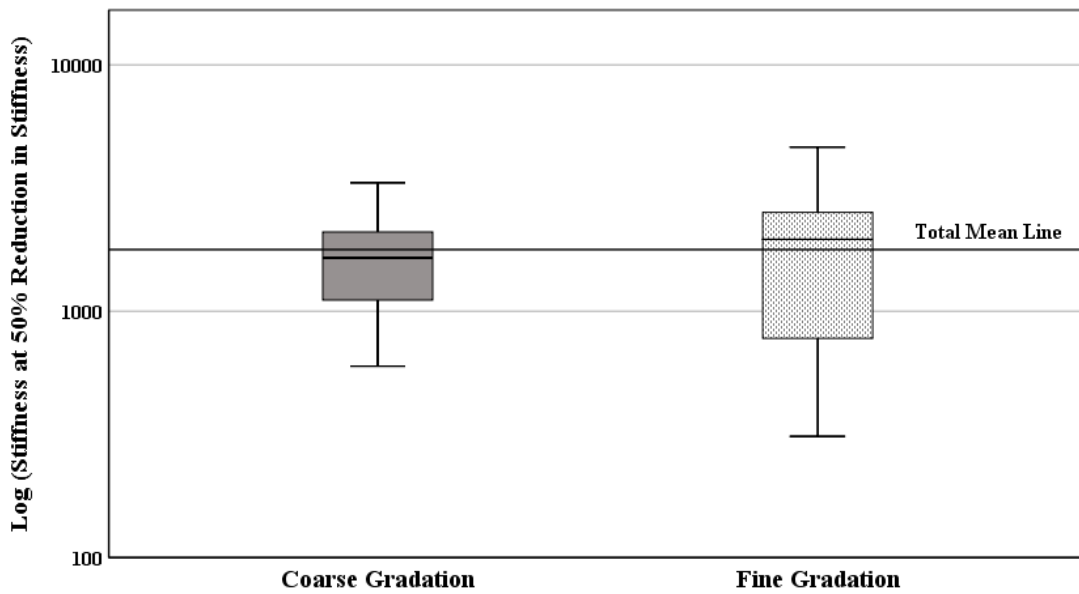


Figure 4.45. Box plot of average stiffness at 50% reduction grouped based on gradation

#### 4.8.5 Multivariate analysis according to total dependent variables (number of loading cycles at 25%+50%+75%+reduced stiffness at 50%)

In previous sections, the analysis of variance for the number of loading cycles at each level of reduced stiffness (25%, 50%,75%) and the effect of design variables on stiffness modulus at 50% reduction was performed separately. In this section, multivariate analysis was performed to investigate the effect of design variables on all the dependent variables together. According to the p-values computed (Table 4.12), all the design variables seem to be significant for the main dependent variables and based on the F values, asphalt type seems to be the most significant effect among the other test variables. It can be seen that two-level interactions of asphalt type with the other design variables are also significant. Two level interactions for aging-gradation, rest time-aggregate type, and aging-aggregate type were also found to be significant.

**Table 4.12.** Multivariate test results for test variables (number of loading cycles at 25%+50%+75% reduced stiffness +reduced stiffness modulus at 50%)

	Design Variable	F-Value	P-Value
Main effects	Asphalt type	105.3	0.000
	Frequency	72.53	0.000
	Aggregate type	56.48	0.000
	Gradation	23.62	0.000
	Aging	10.85	0.000
	Rest time	3.49	0.001
Variables interaction*	Frequency*Asphalt type	24.6	0.000
	Asphalt type* Aggregate type	19.4	0.000
	Asphalt type * Gradation	15.3	0.000
	Aging*Gradation	6.03	0.000
	Rest time* Aggregate type	3.1	0.003
	Aging* Aggregate type	2.94	0.022
	Asphalt type * Rest time	2.98	0.006
	Aging*Asphalt type	2.4	0.055
	Rest time *Frequency	1.89	0.062

#### 4.9 ANOVA results for rate of reduction in stiffness

144 specimens were evaluated on the basis of slope of the line in the log-log scale for stiffness versus the number of cycles. They were then statistically analyzed for finding the significant design variables for the rate of stiffness reduction. Since only one dependent variable was involved in this analysis, ANOVA method is selected to determine the significance test variables. Table 4.13 presents the probability values calculated through ANOVA. As it is obvious from the ANOVA results that asphalt type, aggregate type, and frequency are the most significant design variables as their p-values are less than 0.05. The gradation with a p value of 0.077 can also be considered as important test variable, although its p-value is slightly higher than 0.05. Table 4.14 lists the average slopes related to each type of mixture. Interaction between asphalt type and aging and interaction between asphalt type and aggregate type seem to be the most significant ones affecting the rate of reduction in stiffness. The interaction between aggregate type and aging also can be assumed as a significant interaction, as well.

**Table 4.13.** ANOVA results for slope of the fitted line

Design Variable		F-Value	P-Value
Main effects	Asphalt type	460	0.000
	Aggregate type	67.8	0.000
	Frequency	9.93	0.002
	Gradation	3.2	0.077
	Aging	1.4	0.235
	Rest time	0.86	0.423
Variables interaction*	Asphalt type * Aging	7.27	0.008
	Asphalt type* Aggregate type	4.28	0.041
	Aggregate type * Aging	3.27	0.073

\* just significant variables interaction is mentioned in the table

**Table 4.14.** The averaged measured slope for different specimens

<b>Specimen ID</b>	<b>Slope</b>	<b>Specimen ID</b>	<b>Slope</b>	<b>Specimen ID</b>	<b>Slope</b>	<b>Specimen ID</b>	<b>Slope</b>
BFMAH0	0.20	BCMAS0	0.25	LCMAH0	0.22	LFMAS0	0.23
BFMAH5	0.22	BCMAS5	0.23	LCMAH5	0.23	LFMAS5	0.23
BFMAH10	0.19	BCMAS10	0.21	LCMAH10	0.21	LFMAS10	0.25
BFMUH0	0.22	BCMUS0	0.24	LCMUH0	0.29	LFMUS0	0.27
BFMUH5	0.23	BCMUS5	0.26	LCMUH5	0.28	LFMUS5	0.28
BFMUH10	0.18	BCMUS10	0.18	LCMUH10	0.27	LFMUS10	0.27
BFNAH0	0.31	BCNAS0	0.37	LCNAH0	0.37	LFNAS0	0.43
BFNAH5	0.30	BCNAS5	0.34	LCNAH5	0.36	LFNAS5	0.41
BFNAH10	0.32	BCNAS10	0.34	LCNAH10	0.41	LFNAS10	0.39
BFNUH0	0.32	BCNUS0	0.36	LCNUH0	0.40	LFNUS0	0.38
BFNUH5	0.33	BCNUS5	0.30	LCNUH5	0.38	LFNUS5	0.37
BFNUH10	0.31	BCNUS10	0.34	LCNUH10	0.35	LFNUS10	0.39

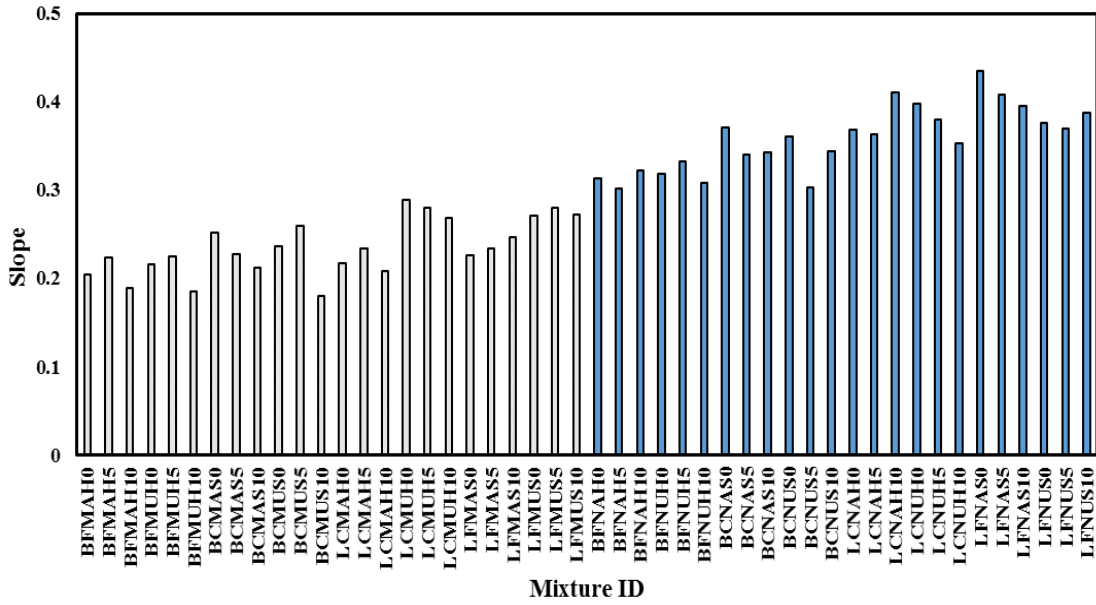


Figure 4.46. The average slope for specimens grouped based on asphalt type

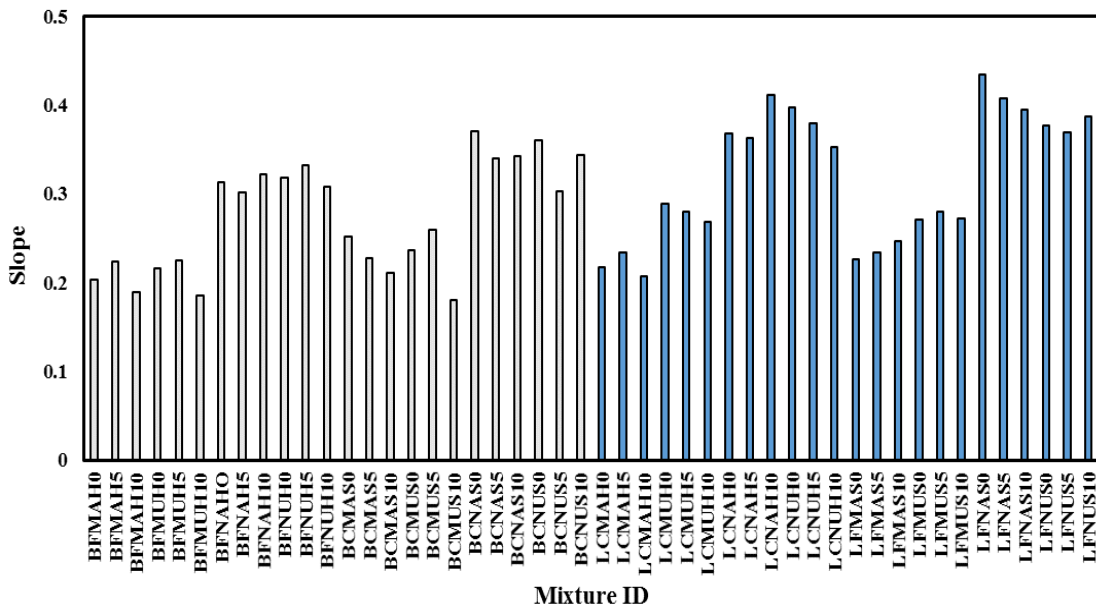


Figure 4.47. The average slope for specimens grouped based on aggregate type

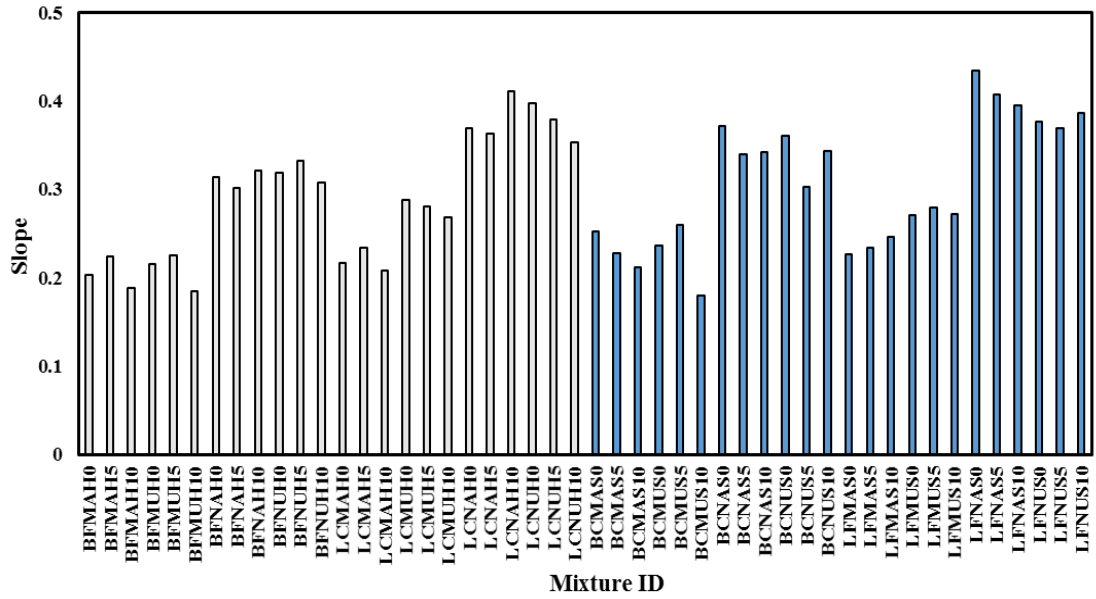


Figure 4.48. The average slope for specimens grouped based on loading frequency

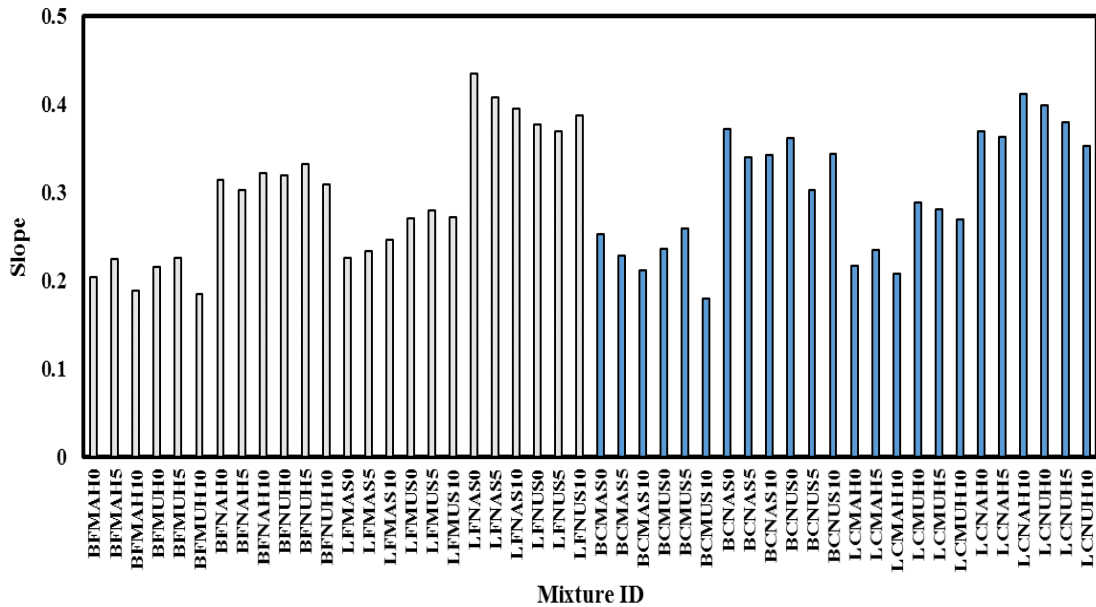


Figure 4.49. The average slope for specimens grouped based on gradation

In Figure 4.46, specimens are divided into two groups based on asphalt type, and the calculated slopes (rate of stiffness reduction) are plotted as a response variable. The magnitude of slopes indicates how fast the micro cracks develop within different asphalt concrete specimens. It can be seen that a modified asphalt binder increases the elastic properties of asphalt concrete and improves its thermal fatigue life. As shown in Figure 4.47, changes in aggregate type affects the slope of the fitted lines. The result related to the aggregate type are highly correlated with the findings for analysis at different levels of reduction in stiffness obtained from the fatigue tests on semicircular specimens. Changes in the loading frequency is also influential on the slope of the fitted lines (see Figure 4.48). The results show that the specimens which are loaded under high frequency have a smaller slope and hence a longer fatigue life regardless of asphalt type, aggregate source, and gradation. Figure 4.49 shows grouped specimens for aggregate gradation. It can be noticed that the specimens with fine gradation outperform coarse graded ones by having smaller slopes, i.e., rate of stiffness reduction.

It is believed that fine graded mixtures behave relatively more ductile as compared to coarse graded mixtures under repeated fatigue loading by dissipating applied energy from the cyclic loading. The calculated slopes in the log-log scale for 144 specimens are given in Appendix G.

#### **4.10 Analysis of force – load line displacement (LLD) data**

##### **4.10.1 Determination of stiffness from load line displacement**

Analyses of the relationship between the number of loading cycles and stiffness were already presented in the previous sections. Since the induced strain underneath the test specimen in the bending mode is the main controlling factor for fatigue failure, priority was given to the analysis of fatigue based on this loading mode. In this section, an alternative method has been proposed to analyze the thermal fatigue performance of



the test specimens. In this approach, so called load line displacement (LLD), stiffness is calculated from the load-line displacement picked during the testing using a separate displacement sensor. In normal three-point bending tests with semicircular specimens, load line displacements were also recorded using a separate LVDT mounted on the specimen's side face. The stiffness of the semicircular specimens based on the load line displacement-force relationship is calculated from the slope of the curve in the linear portion as shown in Figure 4.50.

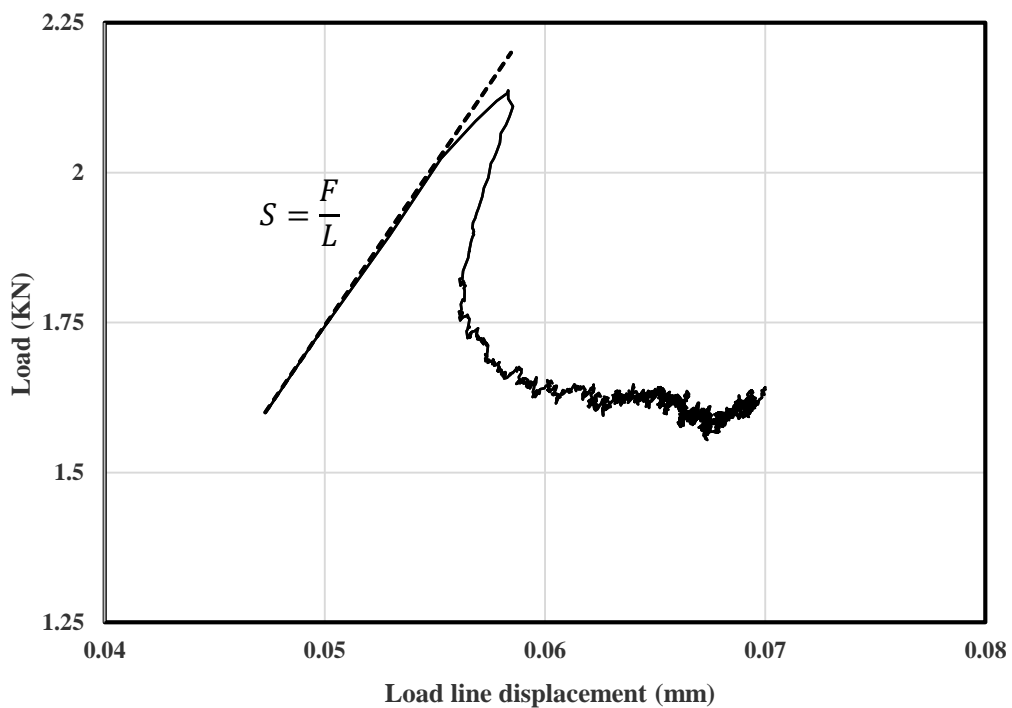


**Figure 4.50.** Load versus load-line displacement relationship for a test specimen

Since the target strain calculated from the thermal coefficient of the specimen is unique for each mixture sample, the applied load and the load line displacement can also be expected different from one specimen to another as shown in Figure 4.51.

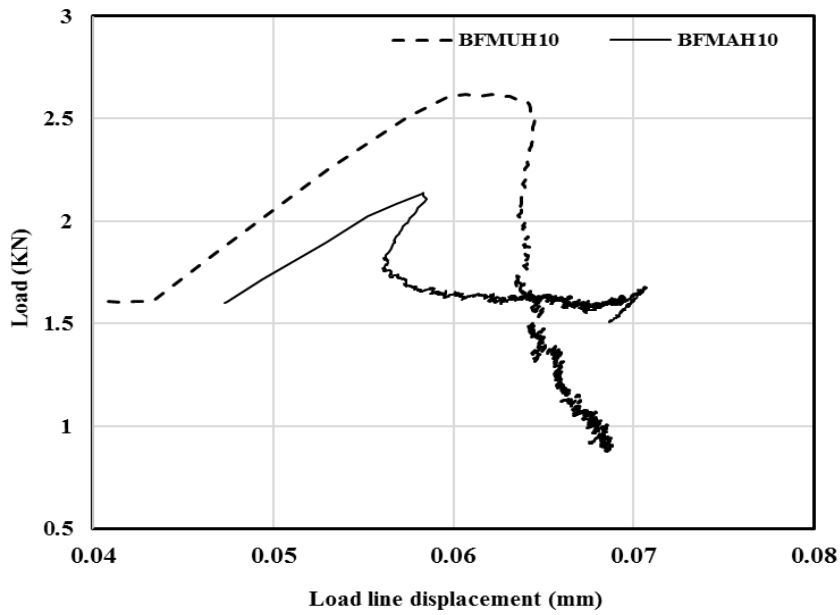


**Figure 4.51.** Load versus LLD for two specimens with similar ID and different aging conditions

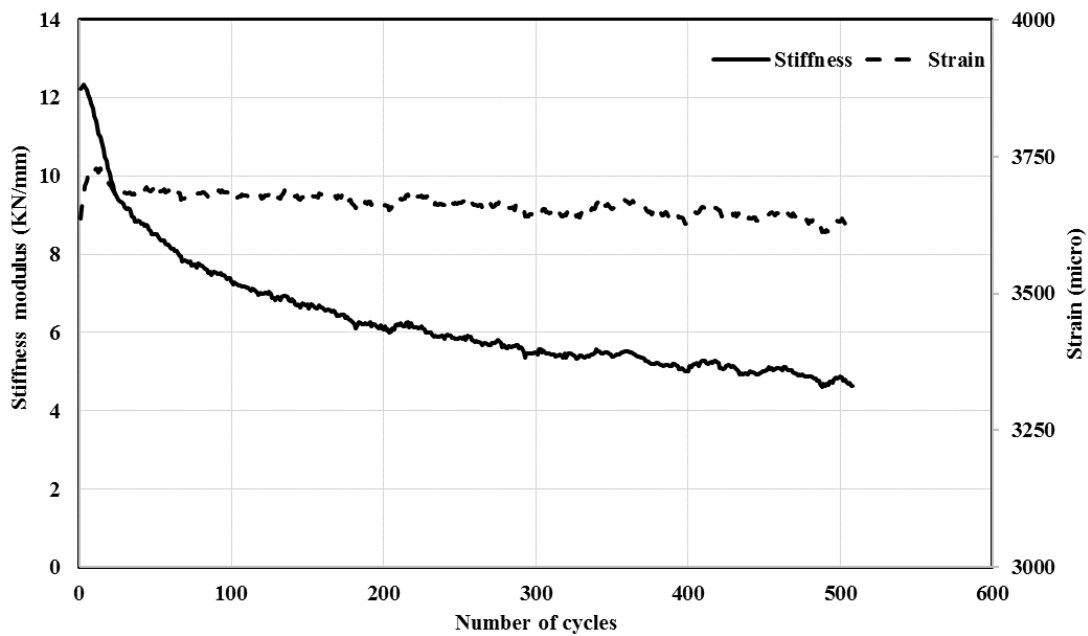


**Figure 4.52.** Stiffness and strain versus number of loading cycles calculated from LLD (specimen ID: LCMAH0)

Figure 4.52 shows the stiffness modulus and strain versus the number of cycles calculated from LLD. It can be noticed that the trend for stiffness degradation is very similar to one calculated from the strain measured in the three-point bending test except that the measured strains are considerably higher in this case. The results for stiffness path versus the number of cycles obtained from LLD method for all specimens are attached to Appendix H and I.

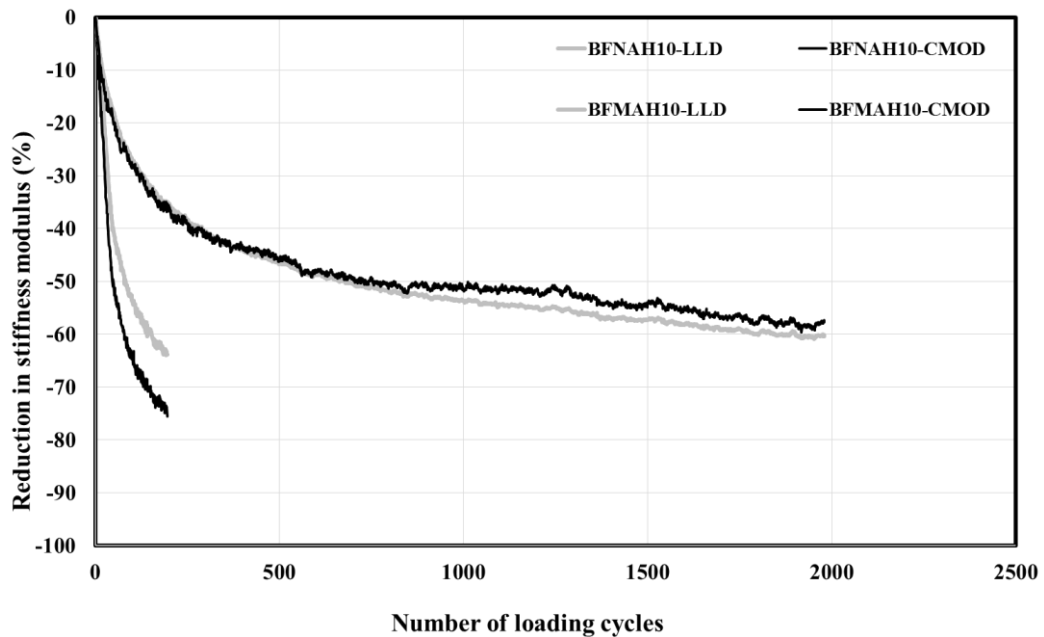


**Figure 4.53.** Stiffness versus number of loading cycles calculated from LLD and CMOD for specimens with similar ID and different asphalt type

An example to compare the results from these two methods is given in Figure 4.53. Black colored curves are indicators of stiffness path measured from the bottom surface of specimen with similar ID and different asphalt type. Gray colored curves denote the stiffness path for the same specimens but measured from force-load line displacement curve. As can be seen from Figure 4.53, the stiffness reduction path for the two methods are quite similar. The correlation between the outcome of the two methods will be investigated in next sections.

#### **4.10.2 Multivariate analysis for the number of loading cycles at different levels of reduced stiffness from load-line displacement curve**

In order to find the significant variables for LLD, multivariate analysis was performed on 144 specimens for different levels of stiffness reductions (25%,50%,75%) calculated from LLD. Results of the analysis show that according to the p-values for test variable, all the design variables except the rest time are significant for thermal fatigue resistance. Asphalt type and frequency are the most significant variables for all levels of analysis (Table 4.15). Most of the results are very similar to those obtained from the stiffness reductions versus number of loading cycles calculated from the semicircular specimens (CMOD), details of which are presented in the previous sections. In the next section, statistical parameters for the two procedures are compared in detail, and the correlation between them is investigated.

**Table 4.15.** Multivariate analysis for number of loading cycles at different level of reduced stiffness calculated from LLD curve

Reduced stiffness	Design variable	Mean	Std.deviation	F-Value	P-Value
25%	Frequency	31.2	39	20.397	0.000
	Asphalt type			17.154	0.000
	Aging			9.615	0.002
	Gradation			6.559	0.012
	Aggregate type			5.980	0.016
	Rest time			2.430	0.092
50%	Asphalt type	160.5	254	51.782	0.000
	Frequency			23.839	0.000
	Aggregate type			13.111	0.000
	Aging			8.491	0.004
	Gradation			7.282	0.008
	Rest time			0.686	0.506
75%	Asphalt type	758.8	1248	73.559	0.000
	Frequency			41.533	0.000
	Aggregate type			24.636	0.000
	Gradation			16.447	0.000
	Aging			4.533	0.035
	Rest time			0.370	0.691

### 4.10.3 Statistical comparison of the results between two approaches

The number of loading cycles corresponding to the stiffness reductions at 25%, 50%, and 75% was calculated from both three-point bending tests and LLD measurements. Comparisons for the two methods are presented in Figure 4.54 to 4.56. Except for a few specimens, the number of loading cycles from the two methods seems quite similar. The statistical parameters calculated from the both approaches are also listed in Table 4.16. It can be noticed that the mean and the median values are quite close to each other. This is also verified by the calculated Pearson correlation values of 0.666, 0.664, 0.815 at 25%, 50%, and 75% reduction levels, respectively, indicating that the results of the two procedures at different levels of stiffness reduction are strongly correlated.

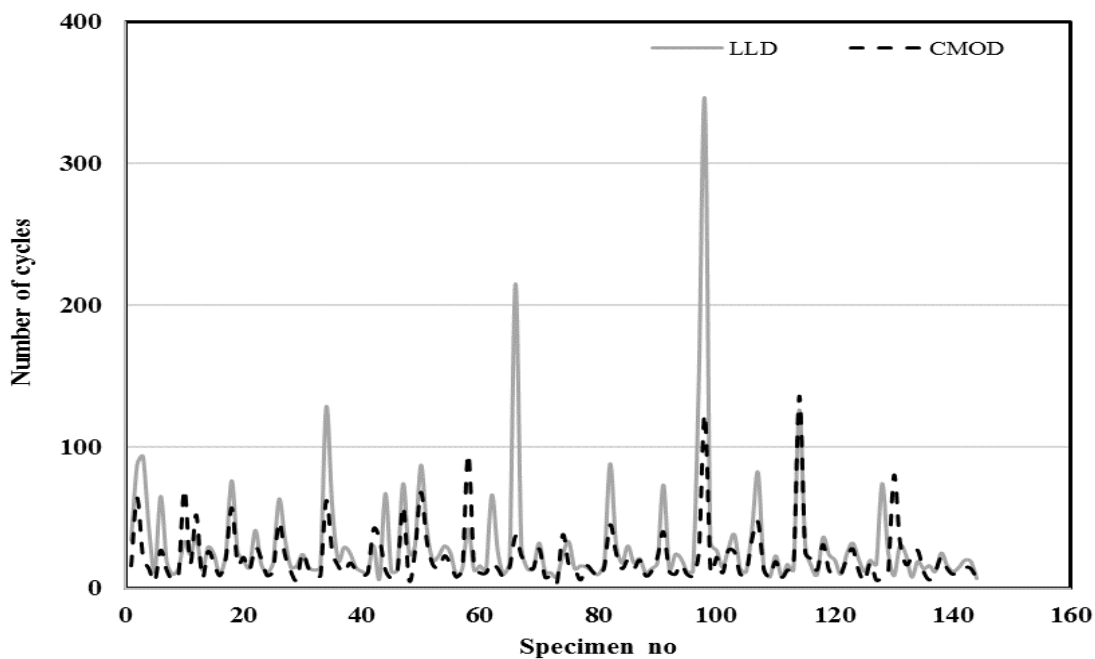


**Figure 4.54.** Comparison of number of loading cycles at 25% reduced stiffness obtained from CMOD and LLD for all specimens

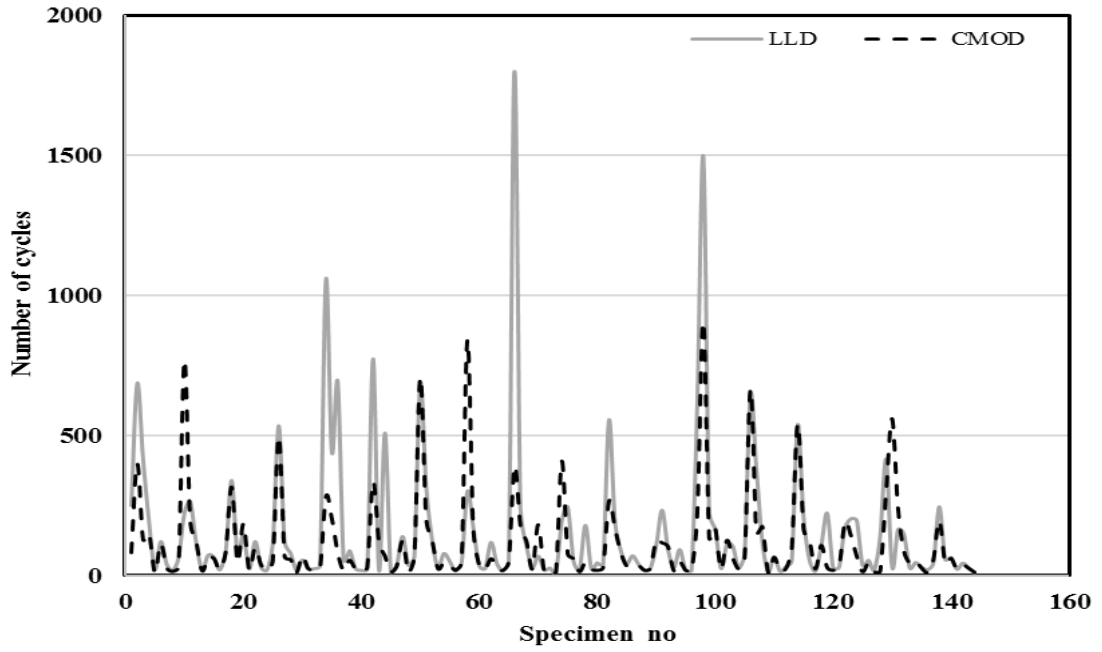


**Figure 4.55.** Comparison of number of loading cycles at 50% reduced stiffness obtained from CMOD and LLD for all specimens

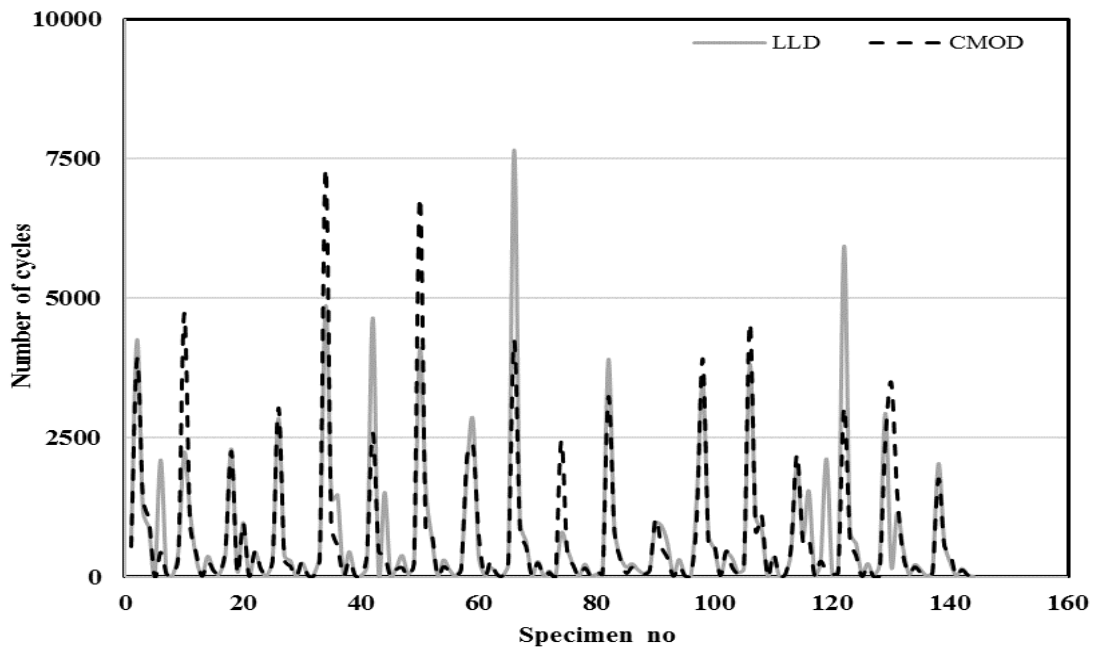


**Figure 4.56.** Comparison of number of loading cycles at 75% reduced stiffness obtained from CMOD and LLD for all specimens

**Table 4.16.** Comparison of statistical parameters for number of loading cycles at different levels of stiffness reductions for CMOD and LLD

<b>Stiffness measurement procedure</b>	<b>Stiffness reduction level</b>	<b>Minimum</b>	<b>Maximum</b>	<b>Standard deviation</b>	<b>Mean</b>	<b>Median</b>	<b>Pearson correlation</b>
<b>CMOD</b>	25%	4	136	20	21.6	14.5	0.666
<b>LLD</b>		7	345	39	31.8	20	
<b>CMOD</b>	50%	10	906	165.1	115.4	52.5	0.664
<b>LLD</b>		12	1800	254	160.5	66.5	
<b>CMOD</b>	75%	13	7236	1254	718.1	236	0.814
<b>LLD</b>		17	7650	1248	758.5	249	



## CHAPTER 5

### CONCLUSIONS AND RECOMMENDATIONS

#### 5.1 Conclusions

This chapter sums up the findings of this research and makes some recommendations for future works. Although the testing procedure was employed in this study to measure the thermal coefficient and the thermal fatigue resistance of asphalt concrete was innovative, the results of this study largely depended on experimental design, used material for the fabrication of test specimens, and procedure of the tests.

According to the previous studies in the literature, most of the researchers used beam specimens of varying sizes causing size dependent variations in the measured properties. The other factor affecting the test results is the high variations in air void content produced during the specimen fabrication process. To eliminate the variability associated with thermal fatigue tests, all the test samples were produced by the Superpave design method using a standard gyratory compactor with very restricted criteria for air void content,  $4 \pm 0.05$  %, and volumetric requirements. These samples were utilized in the testing program to produce specimens for both thermal coefficient and thermal fatigue tests.

In the first phase, 16 beam specimens with dimensions of 65mm×50mm×120mm were produced from the compacted samples to measure their thermal coefficients to calculate thermal strains. The temperature range for thermal coefficient measurements was selected between -30 to 30 with a cooling rate of 60° C/h.

In the second phase, a total of 144 semicircular specimens with 35mm thickness were produced from the gyratory compacted samples to conduct thermal fatigue tests. Haversine waveform was used for loading in a three-point bending mode to apply constant thermal strain calculated from the specimen's thermal coefficient.

In several studies, different levels of stress and strain were employed to simulate thermal fatigue in asphalt concrete pavements; however, no specific procedure for selecting the appropriate strain or stress level was proposed. In this study, loading mode and magnitude were selected based on the developed thermal strain for each mixture based on the thermal coefficient and the most frequent temperature difference in the research location.

While direct tension-compression test in the strain control mode has been applied in some studies to evaluate the thermal fatigue performance of asphalt concrete, a three-point bending with strain control loading was first time used for a semicircular test specimen. The applied strain at the bottom of the specimen in the bending mode cannot be controlled instantly; it needs few cycles to regulate the response strain by modifying the applied load using a closed-loop PID control of the test frame. In conventional tension-compression tests, the applied strain is zero at the start and finish of each cycle, but in the flexural fatigue test, after the test started, the applied strain never declines to zero, and the residual strain gradually increases during the test because of the viscoelastic response of asphalt concrete. This behavior is more compatible with the performance of asphalt concrete in the field under thermal cycles due to daily temperature fluctuations.

Experimental variables selected in this study can be divided into two groups: Independent variables and Dependent variables. The independent variables include asphalt type, gradation, aggregate type and aging as design variables, and the rest time and frequency as the test variables. Stiffness and number of loading cycles at different stiffness reduction levels were selected as

dependent variables. ANOVA and Multivariate analysis were both employed to investigate the significance of the independent variables for thermal coefficient and thermal fatigue resistance of the asphalt concrete samples. In addition, a separate multivariate analysis was also conducted for 50% stiffness reduction for the evaluation of the thermal fatigue test results. . Based on the results of these statistical analyses, the findings of this study can be summarized as follows:

- 1- ANOVA results showed that aggregate type is a determinant factor for the thermal coefficient of asphalt concrete. Because aggregates constitute a major portion of the mixtures, it should be expected that aggregates with different thermal properties would lead to different thermal behaviors and hence distinctive thermal coefficients for each mixture sample. However, the effect of other test variables on thermal coefficient was found to be negligible.
- 2- FEM analysis using the viscoelastic material model for asphalt concrete was employed to investigate the stress-strain distribution in a semicircular specimen. This analysis facilitates the selection of appropriate strain gauge length and location to measure the induced strain underneath a semicircular specimen and also help to estimate initial loading to be applied at different loading frequencies.
- 3- The multivariate analysis result showed that the asphalt type plays an important role in the performance of asphalt concrete under thermal fatigue, and the samples with polymer modified asphalt outperformed ones with neat asphalt by a considerable effect on their measured fatigue life. The explanation for this behavior can be related to the improvement in asphalt concrete's elastic properties because of using a modified asphalt binder.

- 4- The effect of loading frequency in thermal fatigue resistance was shown to be highly significant. Reducing loading frequency caused a drastic drop in the number of loading cycles. The mechanism responsible for this response can be related to the viscoelastic properties of asphalt concrete.
- 5- The aggregate type was found to be a significant factor for the thermal fatigue life of asphalt concrete, and specimens with basalt aggregate outperformed ones fabricated with limestone. The reason for this response can be related to the adhesion strength between aggregate and asphalt, which highly depends on aggregate source and its related mineralogical structure.
- 6- Gradation was recognized to be significant variable in the thermal fatigue performance of asphalt concrete. Specimens with finer gradation had longer fatigue life, which can be attributed to a better interlocking and increased packing of mixture aggregates.
- 7- In this study, asphalt binder aging was also found to be important; the aged samples outperformed unaged samples and had a longer fatigue life, which was contrary to the previous studies that unaged samples were less susceptible to thermal fatigue. It is believed that the laboratory accelerated aging procedure employed in this study (AASHTO R30) does not exactly simulate the field aging process, which takes place over a long period of time.
- 8- The effect of rest time between the sequential loading cycles was another test variable whose function in the thermal fatigue performance of asphalt concrete was investigated. It is known that applying rest time between loading cycles facilitates healing of developed microcracks. In the testing program, each type of specimen was tested without rest time and with two different rest times. The finding indicate rest time is also a significant variable for the thermal fatigue performance of asphalt concrete.

9- In addition to the main effects, interactions between the design and test variables (independent variables) were also investigated. The interaction between asphalt type and frequency and between asphalt type and aggregate type were found as the most significant 2nd level interactions. Asphalt type and frequency gave rise to individually the most significant variables. Since the viscosity of asphalt decreases with an increase in the loading frequency, and because of the major difference in the asphalt binder's properties used, the interaction of these two variables become also important. The next significant interaction was between aggregate and asphalt, as the adhesive bond between aggregate and asphalt is a defining factor that is mostly influenced by aggregate type. This outcome could be expected due to combining different of aggregate sources with rheologically different asphalt binders.

10- ANOVA results for the rate of stiffness reduction (slope of the fitted line) show that the asphalt type, aggregate type, and frequency are the most significant variables. The gradation is also important, although its p-values is slightly more than 0.05. The magnitude of slopes indicates how fast the micro cracks develop within different asphalt concrete specimens. It was found that modified asphalt binder, basalt aggregate, fine gradation, and high loading frequency are test variables decreasing the rate of stiffness reduction and extend the thermal fatigue life of asphalt concrete.

11- Another approach used for measuring the stiffness reduction was based on load line displacement. Multivariate analysis results for the measurements were quite similar to those obtained from the three-point bending test results except that the rest time was not included among the significant variables by this method.

## 5.2 Recommendation for future works

The following recommendation for future studies can be made based on the findings of this study:

1. Specimens used in this study were aged according to the long term oven aging (LTOA) procedure. The results of the study show that aged samples have a longer fatigue life than unaged ones. This finding is in contrast to the previous load associated fatigue studies in the field and laboratory. The first reason that can explain this outcome is that the LTOA does not simulate field aging conditions thoroughly. The second reason may be related to conditions of the thermal fatigue test, which is different from load associated fatigue tests. The low strain level and relatively low temperature are the components of thermal fatigue test, which can be the reason for this controversy. Future studies should be conducted to investigate the aging process in the field combined with strain control loading at low frequencies.
2. In the case of haversine loading applied in this study, in which the permanent deformation is not removed from the specimen, as opposed to conventional four-point beam fatigue or push-pull direct tension tests, the difference in creep behavior of specimens affects the test results. The dramatic difference between the performance of modified and unmodified asphalt concrete can be partially related to this phenomenon. Remained tensile strain in the semicircular specimens makes the laboratory simulation of thermal fatigue more realistic. But to simulate field condition exactly, even if it seems complicated and difficult to execute, the remained tensile strain should be controlled and limited like maximum target strain.

## REFERENCES

- A.h.Gerritsen, and et.al. (1989). "FATIGUE PROPERTIES OF ASPHALT MIXES UNDER CONDITIONS OF VERY LOW LOADING FREQUENCIES." Association of Asphalt Paving Technologists Technical Sessions, Volume: 57, 94–115.
- AASHTO. (1993). "AASHTO guide for design pavement structures."
- AASHTO R30. (2006). "Standard practice for mixture conditioning of hot mix asphalt (HMA)." American Association of State Highway and Transportation Officials, 02, 1–6.
- AASHTO R35. (2015). "Standard Practice for Superpave Volumetric Design for Asphalt Mixtures." American Association of State Highway and Transportation Officials, 1–28.
- AASHTO T 312. (2019). "Standard method of test for preparing and determining the density of asphalt mixture specimens by means of the superpave Gyratory compactor." Association of State Highway and Transportation Officials, 3.
- AASHTO T166. (2010). "Standard method of test for bulk specific gravity (Gmb) of compacted hot mix asphalt (HMA) using saturated surface-dry specimens." American Association of State Highway and Transportation Officials, 3–8.
- AASHTO T209. (2016). "Standard Method of Test for Theoretical Maximum Specific Gravity and Density of Hot-Mix Asphalt Paving Mixtures Paving Mixtures." American Association of State Highway and Transportation Officials, 12(2016), 1–16.
- AASHTO TP62. (2007). "Standard Method of Test for Determining Dynamic Modulus of Hot Mix Asphalt (HMA)." American Association of State Highway and Transportation Officials.

Al-Qadi, I., Hassan, M., and Elseifi, M. (2005). "Field and theoretical evaluation of thermal fatigue cracking in flexible pavements." *Transportation Research Record: Journal of the Transportation Research Board*, 1919(1), 87–95.

Arabzadeh. (2015). "THE INFLUENCE OF DIFFERENT MIXTURE DESIGN VARIABLES ON THERMAL FATIGUE CRACKING OF ASPHALT CONCRETE PAVEMENTS A." *Journal of applied microbiology*, 119(3), 859–867.

Asphalt Institute. (2014). *Mix Design Methods for Asphalt*, 7th edition.

ASTM C127. (2015). "Standard Test Method for Density, Relative Density (Specific Gravity), and Absorption of Coarse Aggregate." *American Society for Testing and Materials*, 04(Reapproved), 1–3.

ASTM C128. (2015). "ASTM C128 Standard Test Method for Density , Relative Density (Specific Gravity ) , and Absorption." *American Society for Testing and Materials*, 1–6.

ASTM C131. (2012). "Standard Test Method for Resistance to Degradation of Large -Size Coarse Aggregate by Abrasion and Impact in the Los Angeles Machine." *American Society for Testing and Materials*, i, 1–5.

ASTM D 70. (2014). "Standard Test Method for Density of Semi-Solid Bituminous Materials (Pycnometer)." *American Society for Testing and Materials*, 04, 1–4.

ASTM D113. (2007). "Ductility of Bituminous Materials." *American Society for Testing and Materials*, i, 42–45.

ASTM D2493. (2000). "Standard Practice for Viscosity-Temperature Chart for Asphalts." *American Society for Testing materialsl ASTM Standards*, 44(0), 0–5.



- ASTM D36. (2014). “Standard Test Method for Softening Point of Bitumen (Ring-and-Ball Apparatus).” American Society for Testing and Materials, 1(d), 1–5.
- ASTM D445. (2008). “Standard Test Method for Kinematic Viscosity of Transparent and Opaque Liquids (the Calculation of Dynamic Viscosity).” American Society for Testing and Materials, 126-126–8.
- ASTM D5. (2008). “Standard Test Method for Penetration of Bituminous Materials.” American Society for Testing and Materials, i, 47-47–3.
- ASTM D854. (2000). “D854 - Standard Test Methods for Specific Gravity of Soil Solids by Water Pycnometer.” American Society for Testing and Materials, 2458000(C), 1–7.
- ASTM D92. (2005). “ASTM D2500-05: Standard Test Method for Cloud Point of Petroleum Products.” American Society for Testing and Materials, (March), 1–11.
- ASTM STP 1241. (1995). Physical Properties of Asphalt Cement Binders. Physical Properties of Asphalt Cement Binders.
- Bahia Hussain, D. P. (1996). “CURRENT PRACTICES FOR MODIFICATION OF PAVING MATERIALS.” Materials Science.
- Barber, E. S. (1957). “Calculation of maximum pavement temperatures from weather reports.” Highway Research Board, 168(3), 1–8.
- Di Benedetto, H., De La Roche, C., Baaj, H., Pronk, A., and Lundström, R. (2004). “Fatigue of bituminous mixtures.” Materials and Structures/Materiaux et Constructions, 37(267), 202–216.
- Bonnaure, F. P., Huibers, A., and Boonders, A. (n.d.). “A LABORATORY INVESTIGATION OF THE INFLUENCE OF REST PERIODS ON THE FATIGUE CHARACTERISTICS OF BITUMINOUS MIXES.” Association of Asphalt Paving Technologists Technical Sessions.

- Carpenter, S. H. (Samuel H. (1983). Thermal cracking in asphalt pavements : an examination of models and input parameters.
- D.H.Jung T.S.Vinson. (1994). SHRP-A- 400- Low-Temperature Cracking: Test Selection. Technology.
- Van Dijk, W., Moreaud, H., Quedeuille, A., and Uge, P. (1972). "THE FATIGUE OF BITUMEN AND BITUMINOUS MIXES." Transportation Research Board.
- Domaschuk, and et.al. (1964). "Cracking of Asphalt Pavements Due to Thermal Contraction." Montreal, Quebec, pp 395-402.
- Epps, A. L. (1999). "An approach to examine thermal fatigue in asphalt concrete." Journal of the Association of Asphalt Paving Technologists, 68, 319–348.
- Harvey, J. T., Deacon, J. A., Tsai, B., and Monismith, C. L. (1995). Fatigue Performance of Asphalt Concrete Mixes and its Relationship to Asphalt Concrete Pavement Performance in California.
- Jackson, N., and Vinson, T. (1992). "Analysis of Thermal Fatigue Distress of Asphalt Concrete Pavements." Transportation Research Record: Journal of the Transportation Research Board.
- Janoo, V., Bayer, J., and Walsh, M. (1993). Thermal Stress Measurements in Asphalt concrete. US Army corps of engineering.
- JONES, G. M., Darter, M. I., and Littlefield, G. (1968). "Thermal Expansion-Contraction of Asphalt Concrete." Asphalt Pavement Technology, 36, 673–702.
- karayolları Genel Müdürlüğü. (2013). "Karayolu teknik şartnamesi 2013." Karayolu teknik şartnamesi 2013, 2013.

- Khattak, M. J., and Baladi, G. Y. (2001). "Fatigue and permanent deformation models for polymer-modified asphalt mixtures." *Transportation Research Record*, (1767), 135–145.
- Kim, Y. R., Kim, N., and Khosla, N. P. (1992). "Effects of aggregate type and gradation on fatigue and permanent deformation of asphalt concrete." *ASTM Special Technical Publication*, (1147), 310–328.
- Kim, Y. R., Ph, D., Daniel, J. S., and Ph, D. (2002). "Fatigue Performance E Valuation of W Es T Rack a Sp halt M Ixtures U Sing V Isoelastic." (April).
- Littlefield, G. (n.d.). "Thermal Expansion and Contraction Characteristics of Utah Asphalt Concretes." *Proceedings of the Association of Asphalt Paving Technologists*.
- Mamlouk, M. S., Souliman, M. I., Zeiada, W. A., and Kaloush, K. E. (2012a). "Refining Conditions of Fatigue Testing of Hot Mix Asphalt." *Advances in Civil Engineering Materials*, 1(1), 20120018.
- Mamlouk, M., Souliman, M., and Zeiada, W. (2012b). "Optimum Testing Conditions to Measure HMA Fatigue and Healing Using Flexural Bending Test." *TRB 2012 Annual Meeting*, (January).
- Mamlouk, M., Witzak, M., Kaloush, K., and Hasan, N. (2005). "Determination of Thermal Properties of Asphalt Mixtures." *Journal of Testing and Evaluation*, 33(2), 12592.
- Marasteanu, M. O., Li, X., Clyne, T. R., Voller, V. R., Timm, D. H., and Newcomb, D. E. (2004). *Low Temperature Cracking of Asphalt Concrete Pavements*.
- Mehta, Y. A., Chrislensen, D. W., and Stoffels, S. M. (1998). "Determination of Coefficient of Thermal Contraction of Asphalt Concrete Using Indirect Tensile Test Hardware *Journal of Assoc / Q / IO n of Asphalt Paving Technologists*." *Electron. J. Assoc. Asph. Pav- ing Technology*, (814).

- NCHRP648. (2010). Mixing and Compaction Temperatures of Asphalt Binders in Hot-Mix Asphalt.
- Nejad, F. M., Aflaki, E., and Mohammadi, M. A. (2010). "Fatigue behavior of SMA and HMA mixtures." *Construction and Building Materials*, Elsevier Ltd, 24(7), 1158–1165.
- Osterkamp, T. E., et al. (1986). *Low-Temperature Cracks in Asphalt Pavements in Interior Alaska*. Alaska.
- Pérez-Jiménez, F., Valdés, G., Miró, R., Botella, R., and Campana, J. (2011). "Effect of Thermal Stresses on Fatigue Behavior in Bituminous Mixes." *Transportation Research Record: Journal of the Transportation Research Board*, 2210(Figure 1), 90–96.
- Qadir Adnan. (2010). "INVESTIGATION OF LOW TEMPERATURE CRACKING IN ASPHALT CONCRETE PAVEMENT A THESIS SUBMITTED TO THE GRADUATE SCHOOL OF NATURAL AND APPLIED SCIENCES OF THE MIDDLE EAST TECHNICAL UNIVERSITY BY ADNAN QADIR IN PARTIAL FULFILLMENT OF THE REQUIREMENTS FOR THE DEGR."
- Raad, L., Saboundjian, S., and Minassian, G. (2001). "Field aging effects on fatigue of asphalt concrete and asphalt-rubber concrete." *Transportation Research Record*, (1767), 126–134.
- Raithby, K. D., and Sterling, A. B. (1970). "THE EFFECT OF REST PERIODS ON THE FATIGUE PERFORMANCE OF A HOT-ROLLED ASPHALT UNDER REVERSED AXIAL LOADING." *Association of Asphalt Paving Technologists Technical Sessions*.
- Shell Bitumen Handbook 2003. (n.d.). *Shell\_Bitumen\_Handbook\_\_2003.pdf*.
- SHRP-A-410. (1994). *Superior Performing Asphalt Pavements (Superpave): The Product of the SHRP Asphalt Research Program*.

- Stoffels, S. M., and Kwanda, F. D. (1996). "Determination of the coefficient of thermal contraction of asphalt concrete using the resistance strain gage technique." *Asphalt Paving Technology: Association of Asphalt Paving Technologists-Proceedings of the Technical Sessions*, 65, 73–98.
- Sugawara, T., and A. M. (1984). "Thermal fracture of bituminous mixtures." *Paving in cold areas*.
- Testlab Software Reference - Test Designer-PAVETEST V1.03. (2014). Testlab Software Reference - Test Designer.
- Universal Testing Machine General-PAVETEST. (2014). "Universal Testing Machine General-PAVETEST."
- Vinson, T., Janoo, V., and Hass, R. (1989). *Low Temperature and Thermal Fatigue Cracking*.
- Witczak, M. W., Kaloush, K., Pellinen, T., El-Basyouny, M., and Quintus, H. Von. (2002). *Simple Performance Test for Superpave Mix Design*. Design.
- Xu, Q., and Solaimanian. (2008). "Measurement and Evaluation of Asphalt Concrete Thermal Expansion and Contraction." *Journal of Testing and Evaluation*, 36(2), 101024.
- Yoder, E., and M. W. Witczak. (1975). *Principles of Pavement Design*, Second Edition.
- Zeiada, W., Souliman, M., Kaloush, K., Mamlouk, M., and Underwood, B. (2014). "Comparison of Fatigue Damage, Healing, and Endurance Limit with Beam and Uniaxial Fatigue Tests." *Transportation Research Record: Journal of the Transportation Research Board*, 2447, 32–41.
- Zeng, M., and Shields, D. H. (1999). "Nonlinear thermal expansion and contraction of asphalt concrete." *Canadian journal of civil engineering*, 26(1), 26–34.



## APPENDICES

### A. Test designer code for thermal fatigue test

Ref	Name	Expression
V00	Non Zero	1.00E-100
V01	Test Cycles	Cycles()
V03	Load	First(C01)
V04	Peak Load	MAX(C01)
V05	Actuator Deformation	MAX(C00)-MIN(C00)
V06	Min Load	MIN(C01)
V07	Temp	AVG(C04)
V08	Min CMOD	MIN(C02)
V09	scan time	L25
V12	LLD Displacement	MAX(C03)
V13	Max CMOD	MAX(C02)
V20	Gauge Length	IF(P03>0,P03,Length)
V30	Sampling Time	L24/100
V31	Frequency	1000/L24
V40	Peak SCB Stress	6*(V04-V06)*1000*P02/(length*diameter^2)
V41	Peak SCB Stress 2	6*V04*1000*P02/(length*diameter^2)
V49	Stiffness Modulus	(V40/V50)*1000000
V50	Peak CMOD strain	1000000*(V13/P03)
V51	SCB Resilient Modulus	V40/((V55-V54)/1000000)
V52	Peak LLD Strain	1000000*V12/P04
V53	LLD Stiffness	V04/V12
V54	MIN CMOD strain	1000000*V08/P03
V55	MAX CMOD strain	1000000*V13/P03
V60	Modify Control	IFC(V01>9,CyclicModify(1,2,L23,V61))
V61	Adjust Loading	IFC(V01>9,L20+L20*L27*ADAPT(0,L22,V50,V65))
V62	Request Load	IF(V01>0,V61,L21)
V64	Average Load	avgrunning('V04',10)
V65	Secondary Load	IF(V01<=15,0.1,1)
V70	Initial Stiffness	IFC(V01=P13,V49)
V71	Termination Stiffness	IFC(V01=P13,V70*(1-(P14/100)))
V72	Stiffness Ratio	IFC(V01>10,V49/V70)
V96	termination on	IFC(numseq(1)&(v01=10),nextseq())
V97	Max Cycles	IFC(V01>=P15,stop("Test Stopped -- Max Cycles detected"))
V98	Max Displacement	IFC(V05>=P15,stop("Test Stopped -- Max Displacement detected"))
V99	Termination On Stiffness	IFC((V01>P13) & (V49<= V71),stop("Test Stopped -- Terminated on Stiffness detected"))

## **B. Programming code for Brookfield rotational viscometer**



**Rheocalc V2.7** **Brookfield Engineering Labs**

Filename: C:\Documents and Settings\user\My Documents\REZA\main code files\T316-06.RCP

Line #	Command	Command Description	Parameter 1
1	STM	Set Temperature	110 .
2	WTI	Wait Time	06:00
3	STM	Set Temperature	112 .
4	WTI	Wait Time	06:00
5	STM	Set Temperature	114 .
6	WTI	Wait Time	06:00
7	STM	Set Temperature	116 .
8	WTI	Wait Time	06:00
9	STM	Set Temperature	118 .
10	WTI	Wait Time	06:00
11	STM	Set Temperature	120 .
12	SSN	Set Speed	20 .
13	WTI	Wait Time	10:00
14	DCI	Data Interval	00:30
15	WDP	Wait for Data Points	6
16	DSD	Stop Data Collection	
17	SSN	Set Speed	0 .
18	STM	Set Temperature	122 .
19	WTI	Wait Time	06:00
20	STM	Set Temperature	124 .
21	WTI	Wait Time	08:00
22	STM	Set Temperature	126 .
23	WTI	Wait Time	08:00
24	STM	Set Temperature	128 .
25	WTI	Wait Time	08:00
26	STM	Set Temperature	130 .
27	SSN	Set Speed	20 .
28	WTI	Wait Time	10:00
29	DCI	Data Interval	00:30
30	WDP	Wait for Data Points	6

Line #	Command	Command Description	Parameter 1
31	DSD	Stop Data Collection	
32	SSN	Set Speed	0 .
33	STM	Set Temperature	132 .
34	WTI	Wait Time	06:00
35	STM	Set Temperature	134 .
36	WTI	Wait Time	08:00
37	STM	Set Temperature	136 .
38	WTI	Wait Time	08:00
39	STM	Set Temperature	138 .
40	WTI	Wait Time	08:00
41	STM	Set Temperature	140 .
42	SSN	Set Speed	20 .
43	WTI	Wait Time	10:00
44	DCI	Data Interval	00:30
45	WDP	Wait for Data Points	6
46	DSD	Stop Data Collection	
47	SSN	Set Speed	0 .
48	STM	Set Temperature	142 .
49	WTI	Wait Time	06:00
50	STM	Set Temperature	144 .
51	WTI	Wait Time	08:00
52	STM	Set Temperature	146 .
53	WTI	Wait Time	08:00
54	STM	Set Temperature	148 .
55	WTI	Wait Time	08:00
56	STM	Set Temperature	150 .
57	SSN	Set Speed	20 .
58	WTI	Wait Time	10:00
59	DCI	Data Interval	00:30
60	WDP	Wait for Data Points	6
61	DSD	Stop Data Collection	
62	SSN	Set Speed	0 .

**Rheocalc V2.7****Brookfield Engineering Labs**

Line #	Command	Command Description	Parameter 1
63	STM	Set Temperature	152 .
64	WTI	Wait Time	06:00
65	STM	Set Temperature	154 .
66	WTI	Wait Time	08:00
67	STM	Set Temperature	156 .
68	WTI	Wait Time	08:00
69	STM	Set Temperature	158 .
70	WTI	Wait Time	08:00
71	STM	Set Temperature	160 .
72	SSN	Set Speed	20 .
73	WTI	Wait Time	10:00
74	DCI	Data Interval	00:30
75	WDP	Wait for Data Points	6
76	DSD	Stop Data Collection	
77	SSN	Set Speed	0 .
78	STM	Set Temperature	162 .
79	WTI	Wait Time	06:00
80	STM	Set Temperature	164 .
81	WTI	Wait Time	08:00
82	STM	Set Temperature	166 .
83	WTI	Wait Time	08:00
84	STM	Set Temperature	168 .
85	WTI	Wait Time	08:00
86	STM	Set Temperature	170 .
87	SSN	Set Speed	20 .
88	WTI	Wait Time	10:00
89	DCI	Data Interval	00:30
90	WDP	Wait for Data Points	6
91	DSD	Stop Data Collection	
92	SSN	Set Speed	0 .
93	STM	Set Temperature	172 .
94	WTI	Wait Time	06:00

**Rheocalc V2.7****Brookfield Engineering Labs**

Line #	Command	Command Description	Parameter 1
95	STM	Set Temperature	174 .
96	WTI	Wait Time	08:00
97	STM	Set Temperature	176 .
98	WTI	Wait Time	08:00
99	STM	Set Temperature	178 .
100	WTI	Wait Time	08:00
101	STM	Set Temperature	180 .
102	SSN	Set Speed	20 .
103	WTI	Wait Time	10:00
104	DCI	Data Interval	00:30
105	WDP	Wait for Data Points	6
106	DSD	Stop Data Collection	

**C. Stiffness calculated from bottom surface of the specimen (CMOD)**

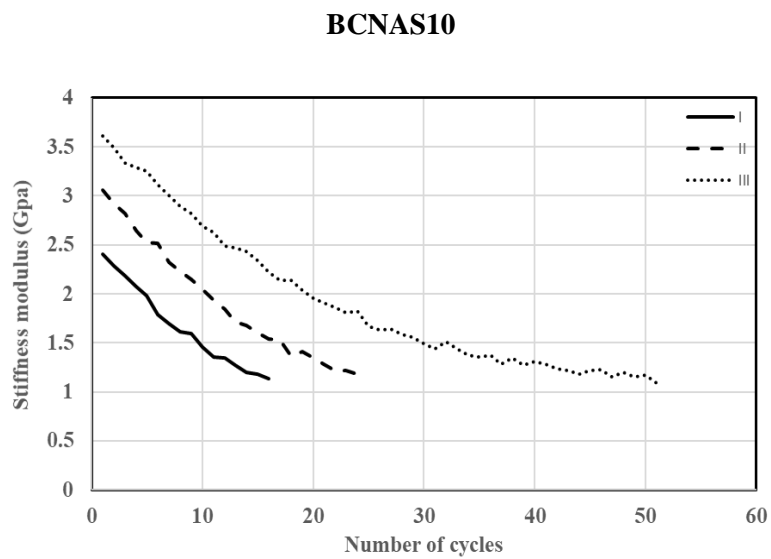
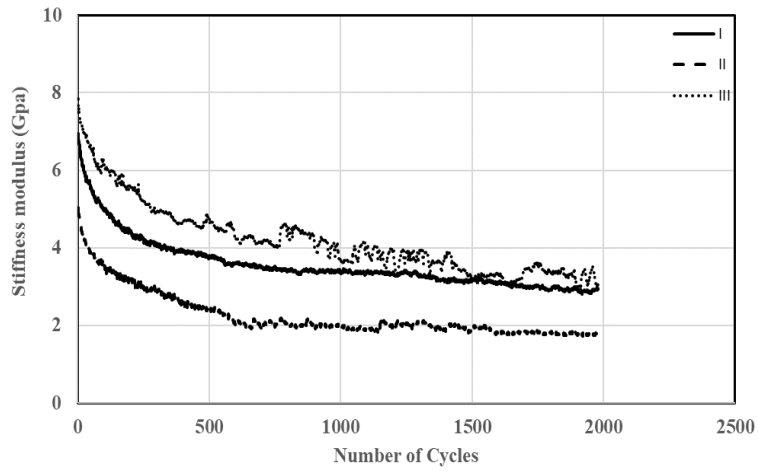


**Figure C. Stiffness for all specimens**

### BFMAH10



### LCMUH10

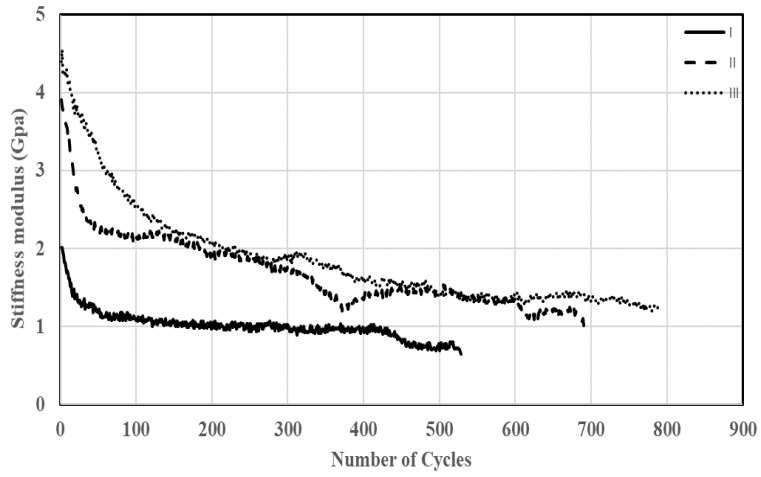
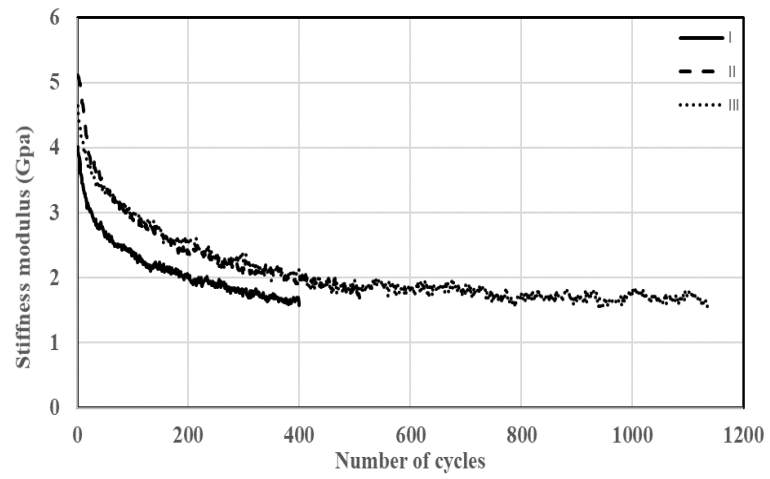


Figure C

### LCMAH0



### LCNUH10

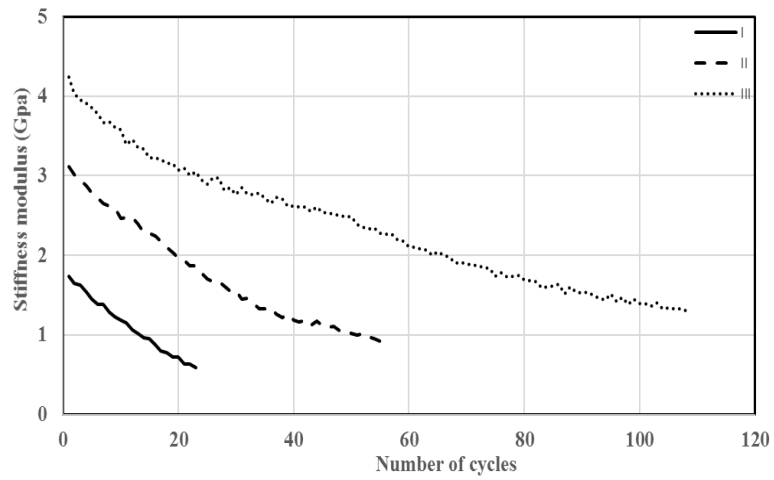
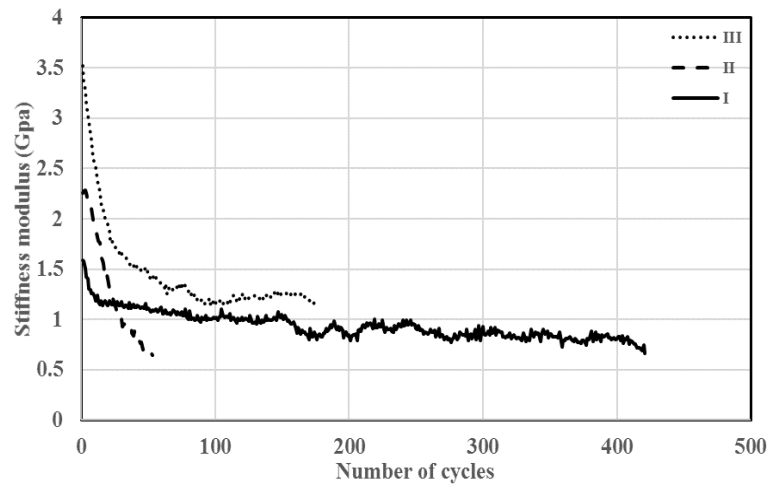


Figure C

### LFMAS0



### LFNUS10

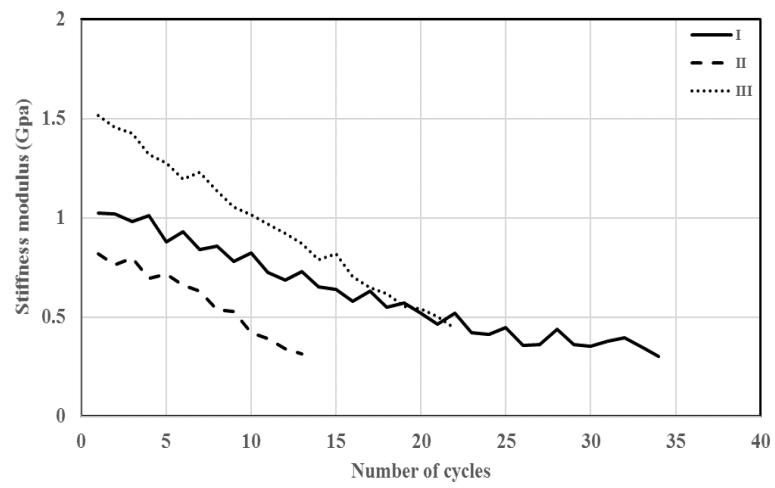
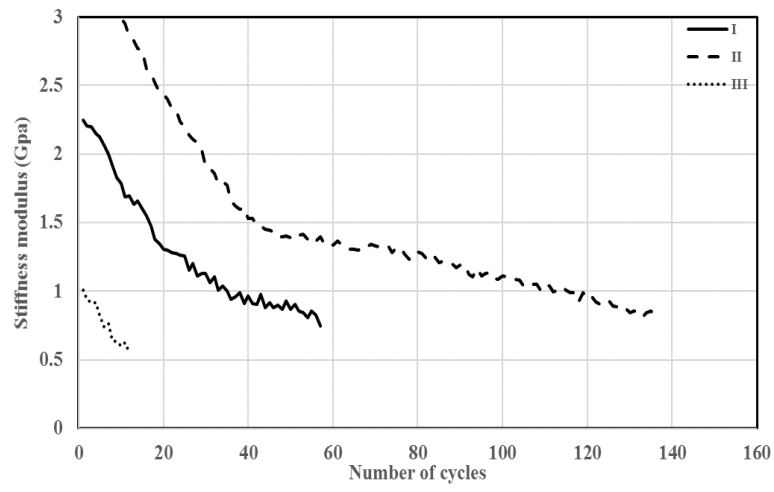


Figure C



### LCNAH5



### LCNAH0

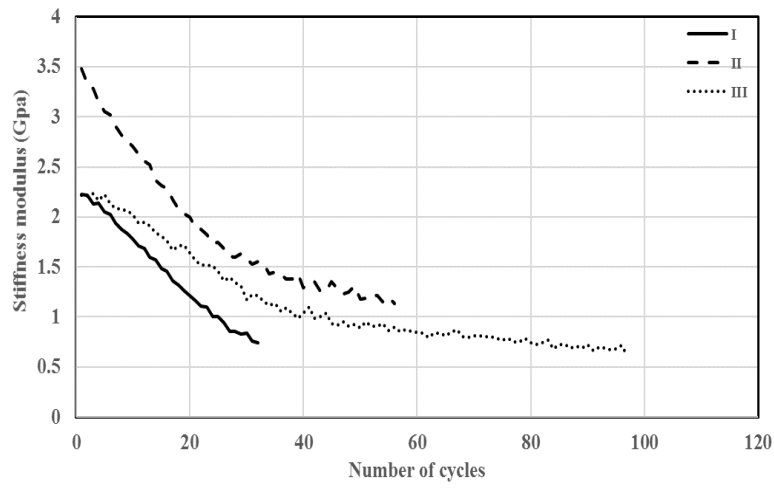
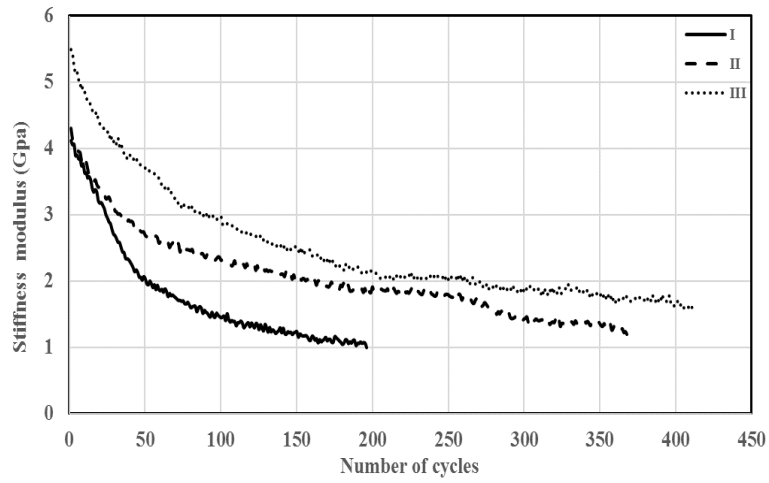


Figure C

### BFNAH10



### LFNUS5

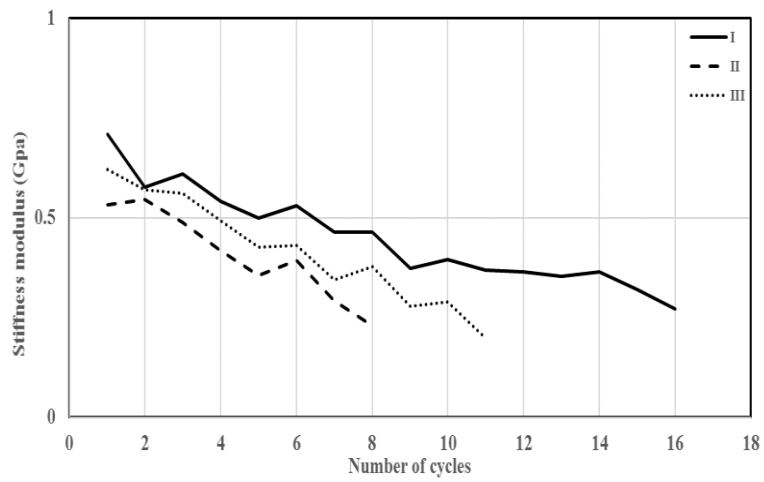
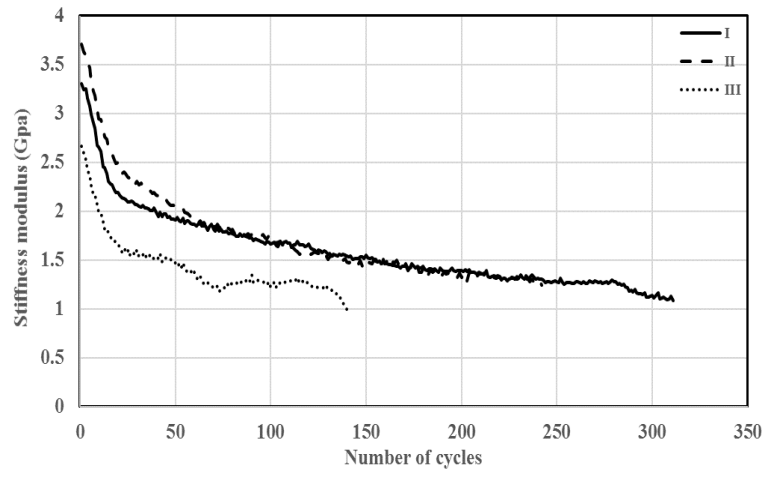


Figure C

### BCMUS0



### BCMAS10

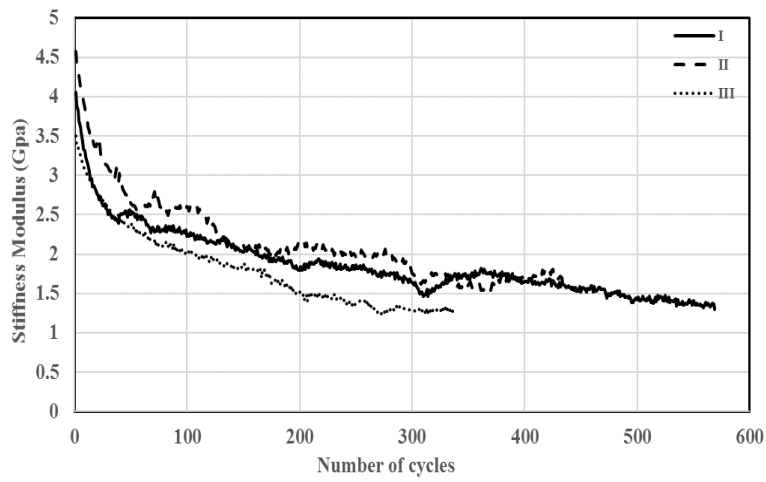
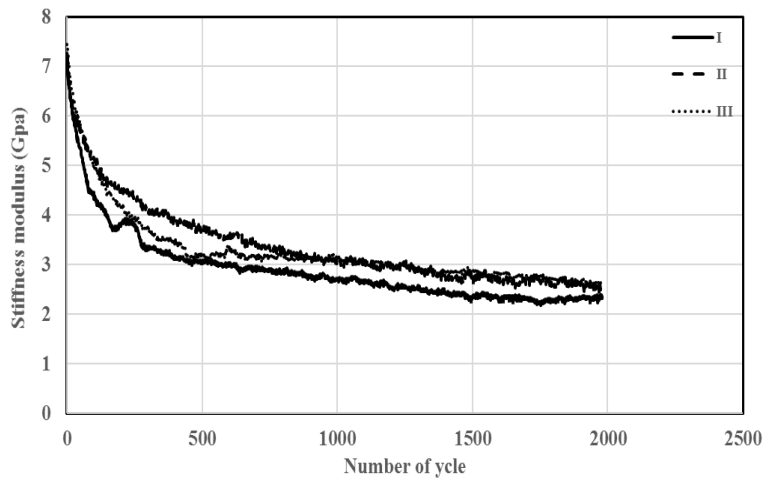


Figure C

### BFMAH0



### BCNAS5

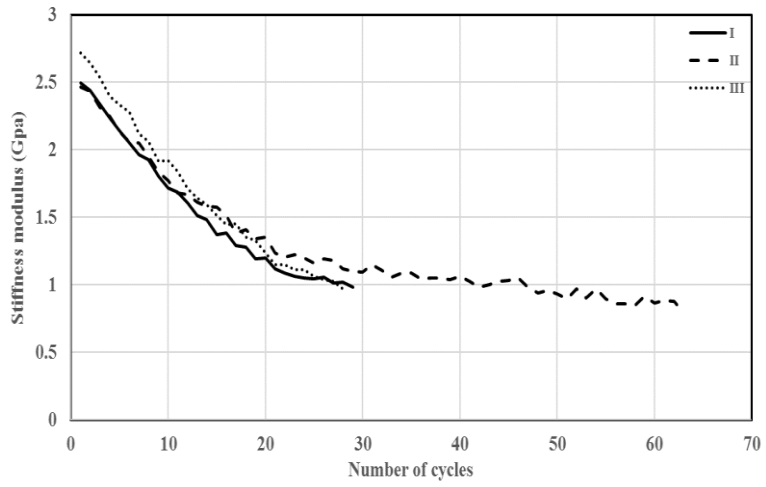
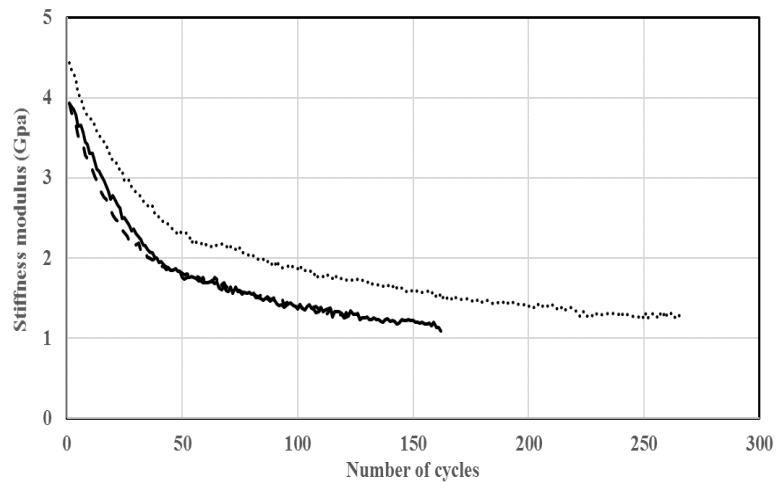


Figure C

### BFNAH0



### BFMUH5

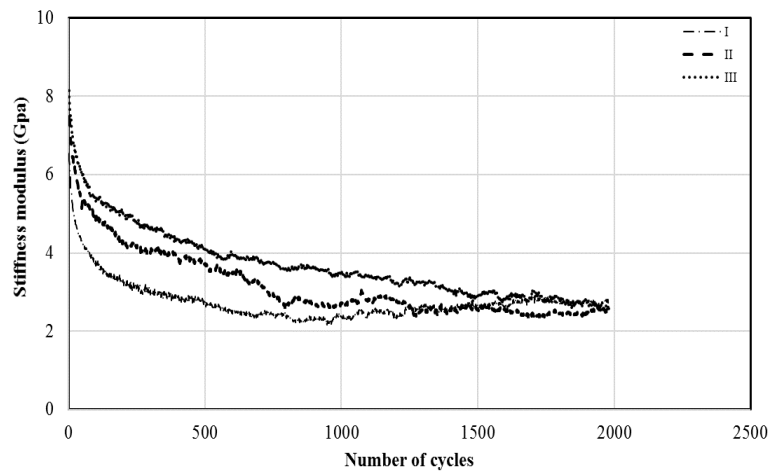
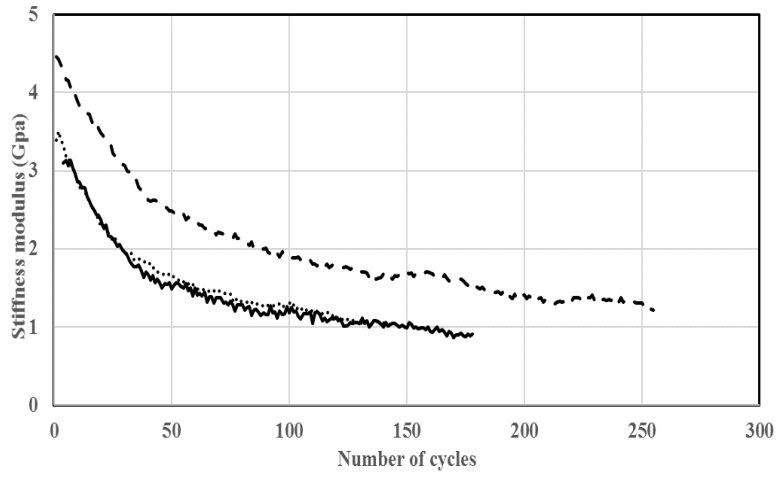


Figure C

### BFNUH5



### BCNUS10

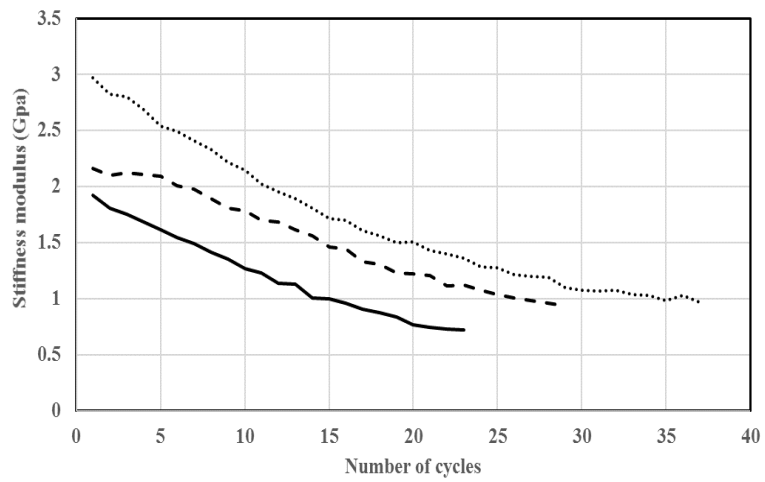
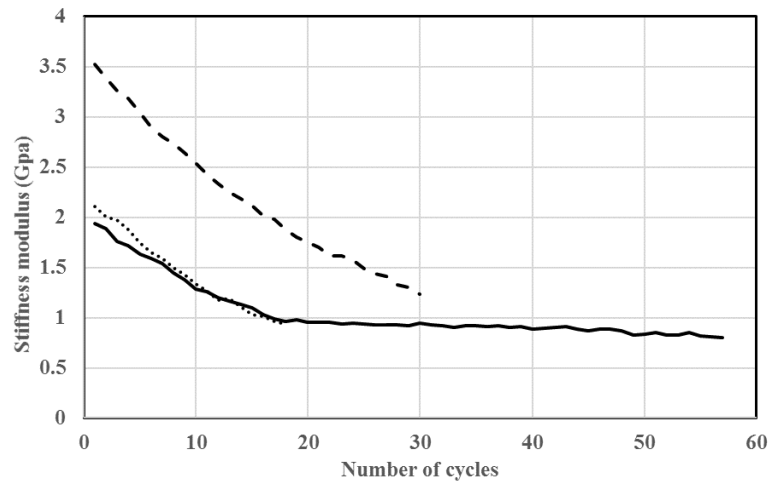


Figure C

### BCNUS5



### LCMAH0

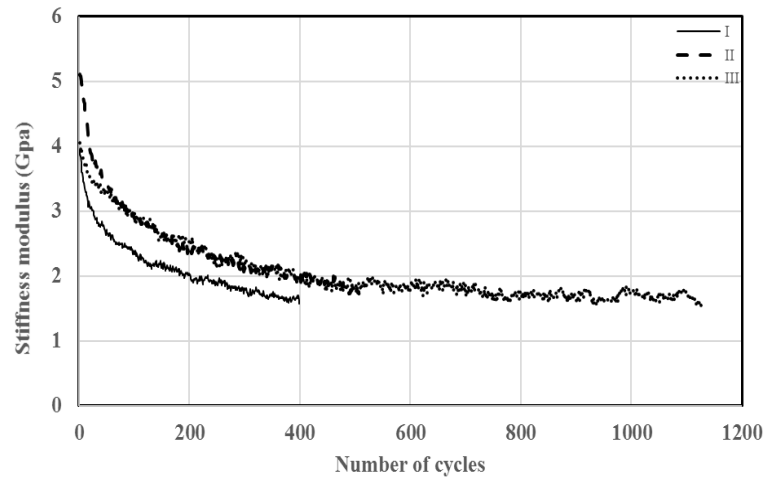
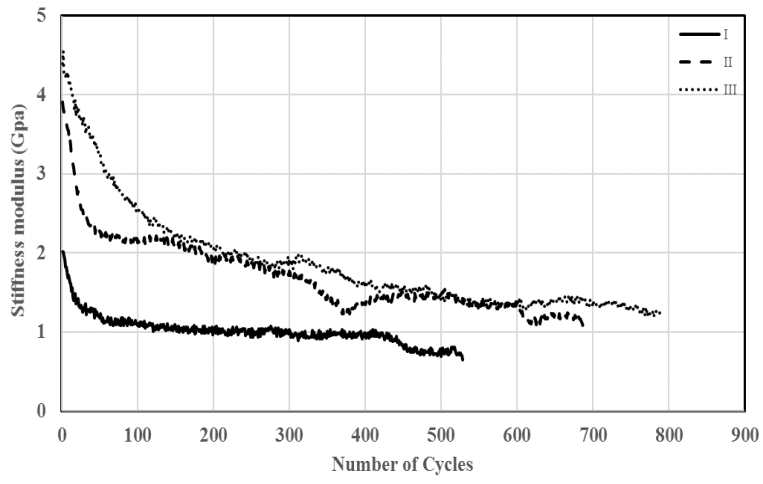


Figure C

### LCMUH10



### BCNUS0

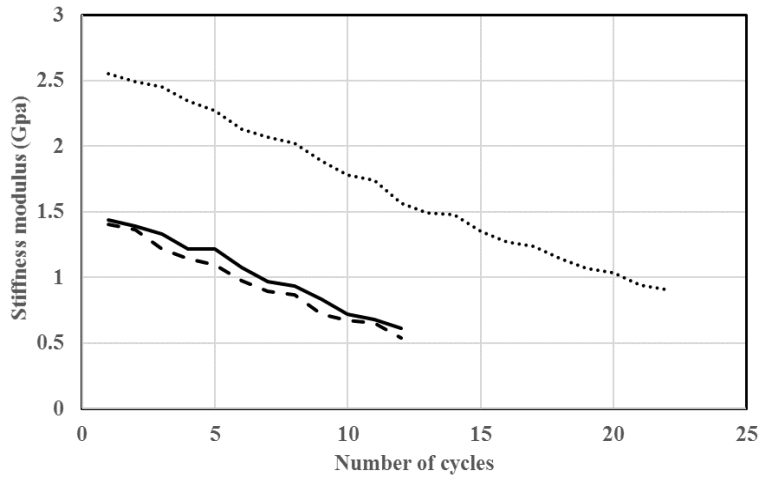
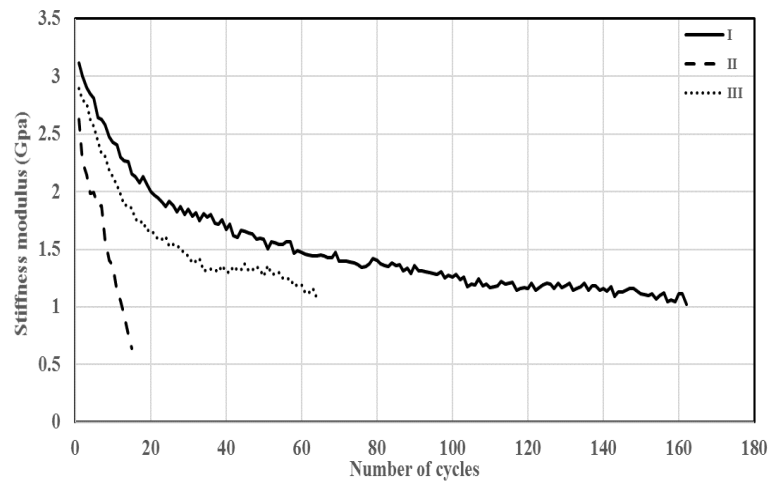


Figure C



### LFMUS5



### LFNAS0

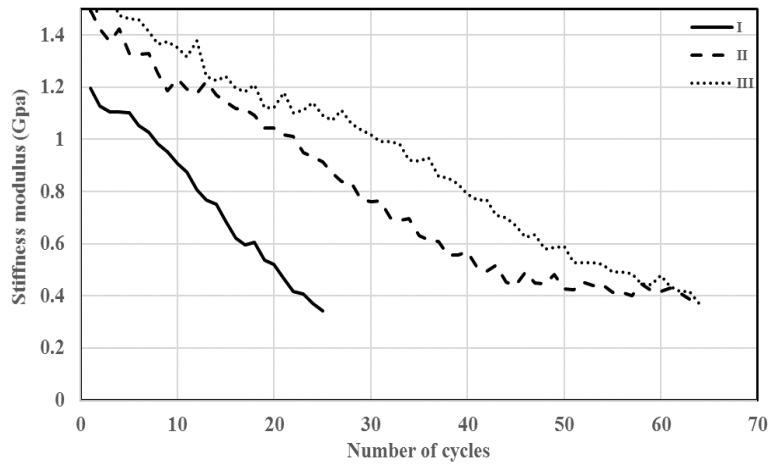
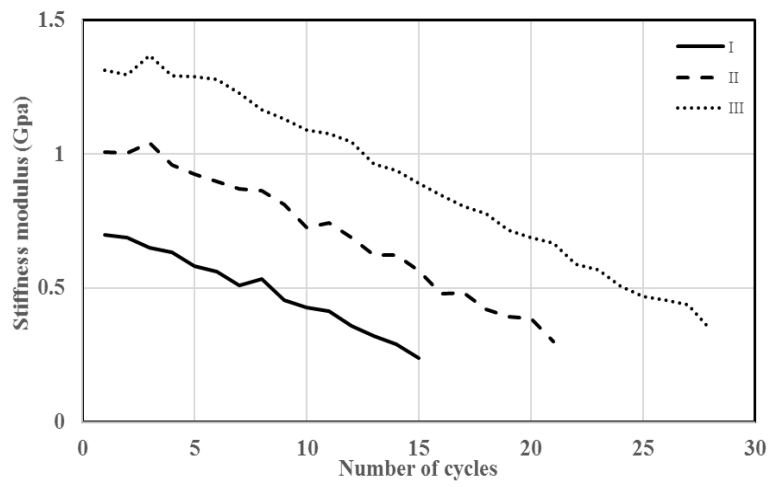


Figure C

### LFNUS0



### BCMUS10

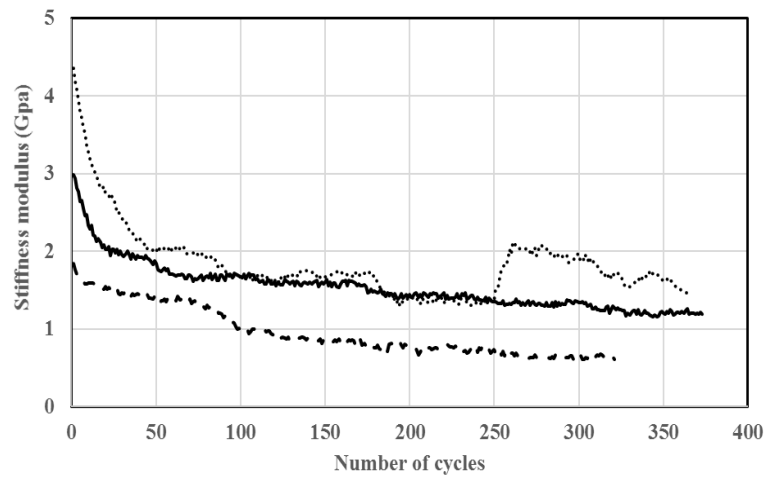
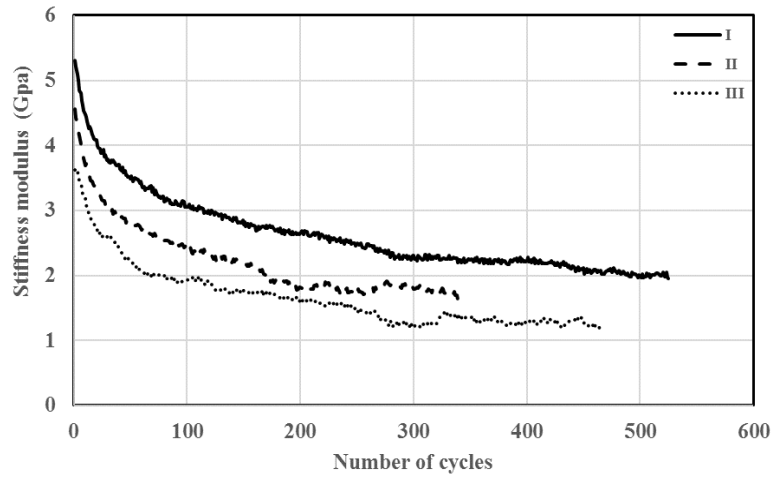


Figure C

### BCMAS5



### LCNUH5

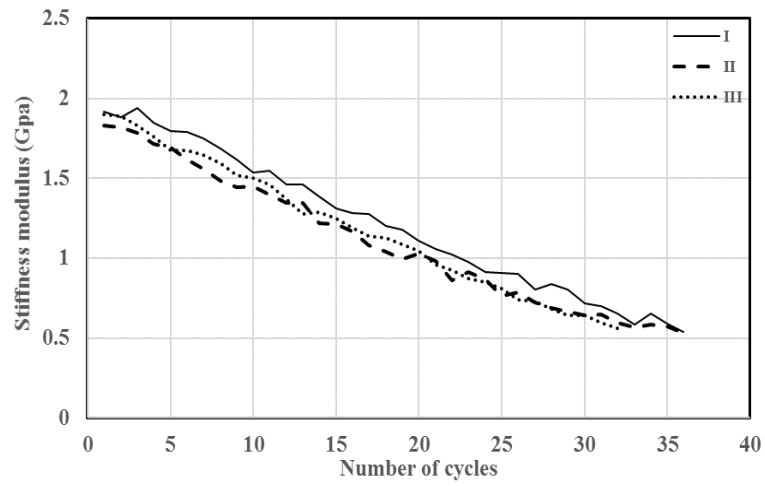
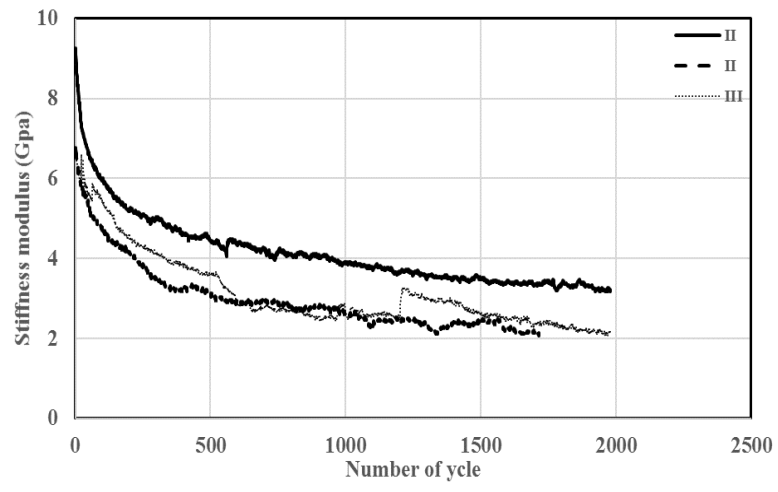


Figure C

### BFMAH5



### LCMAH10

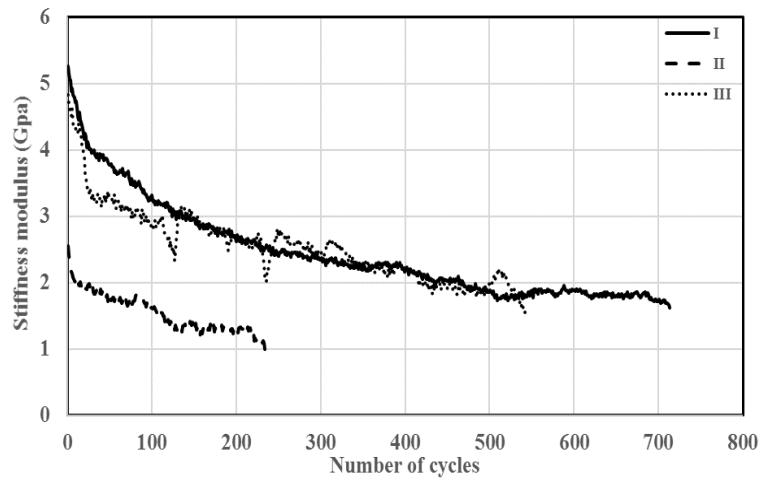
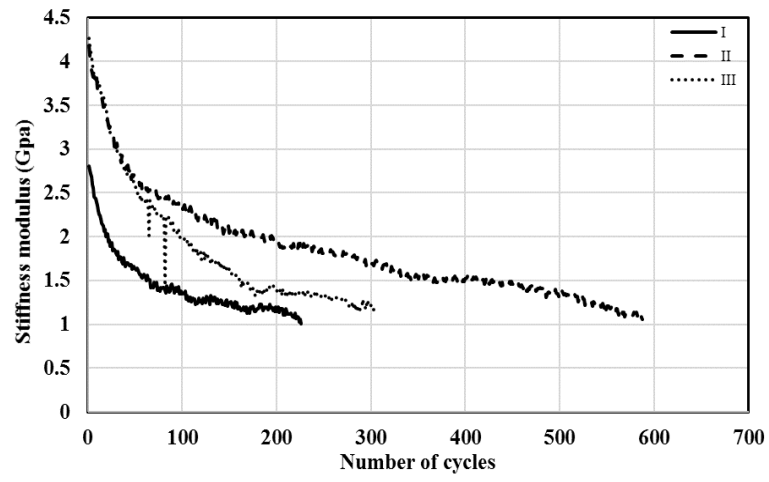


Figure C

### LCMUH5



### BFNUH0

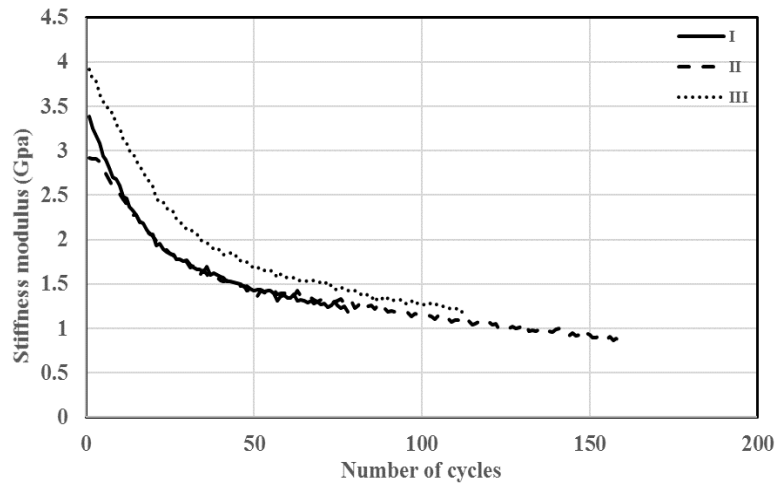
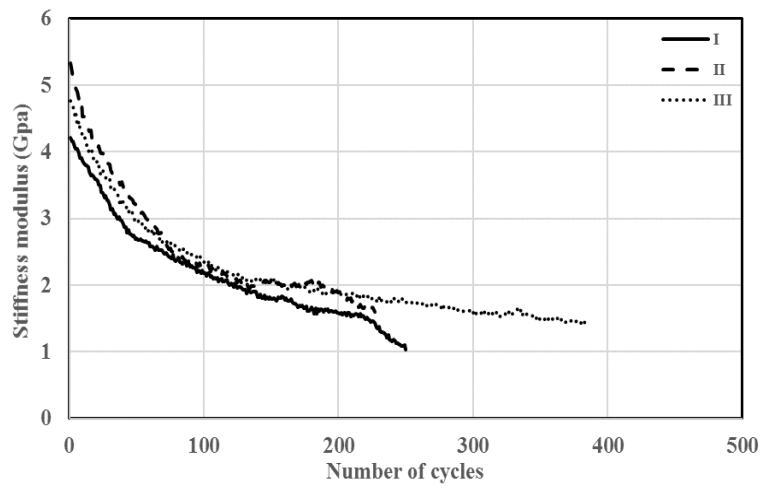


Figure C

### BFNAH5



### LCNAH10

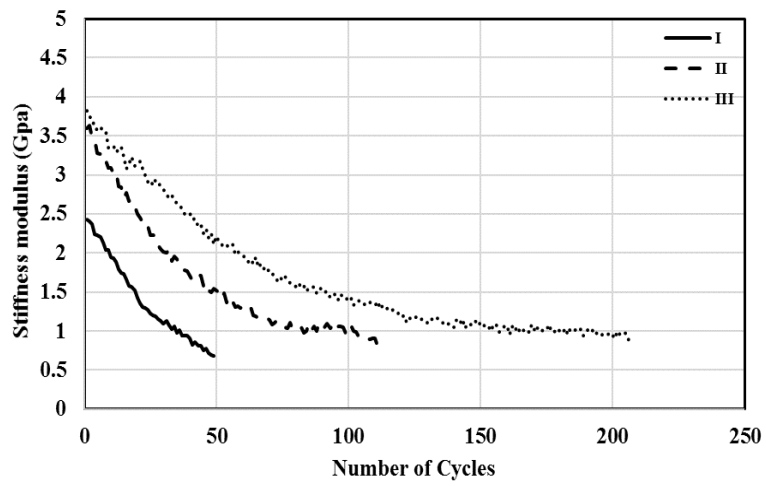
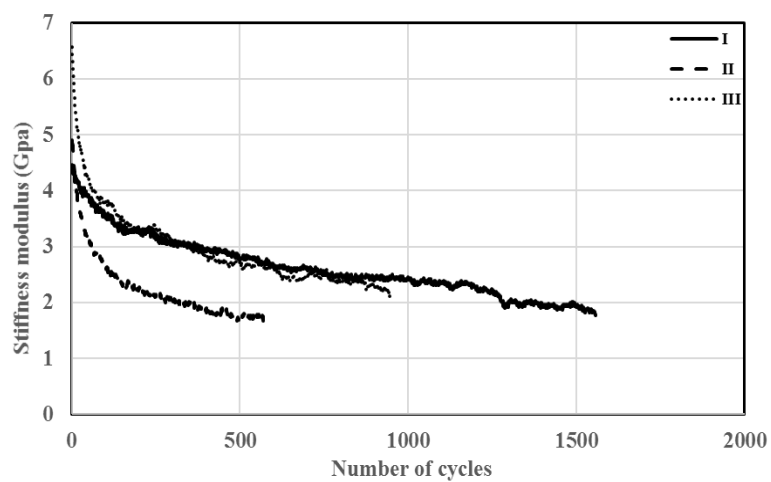


Figure C

### BFMUH0



### BFNUH10

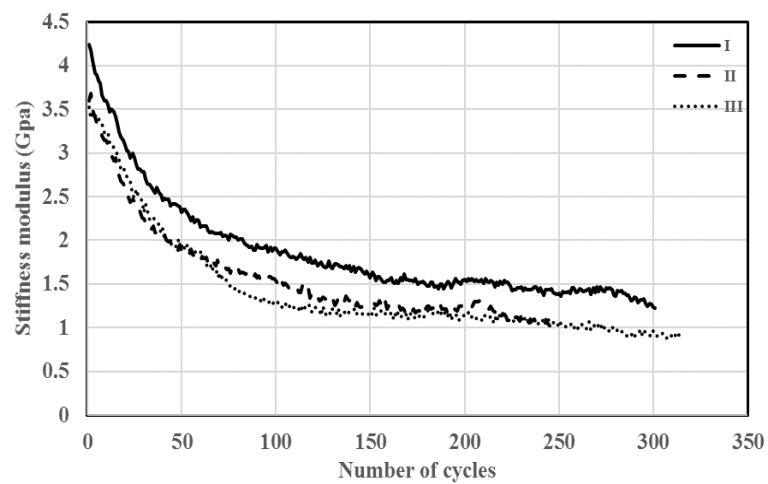
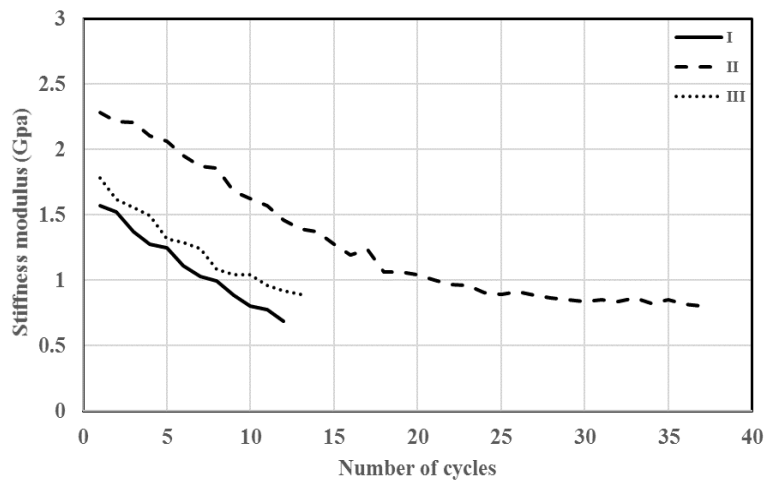


Figure C

### BCNAS0



### LFMUS0

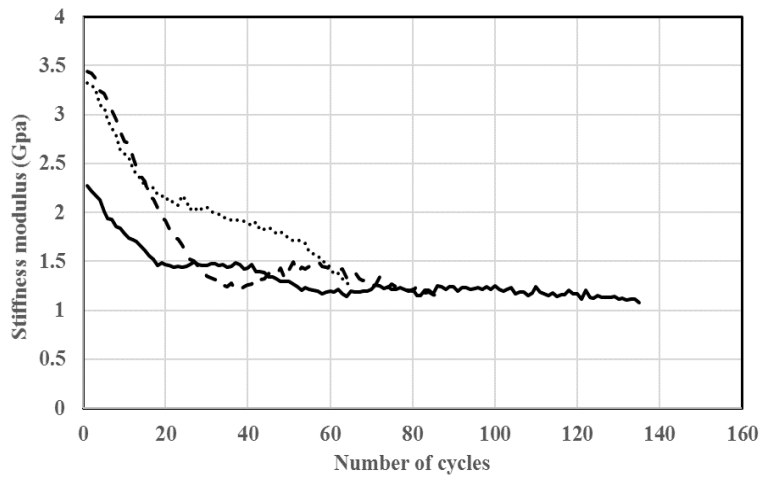
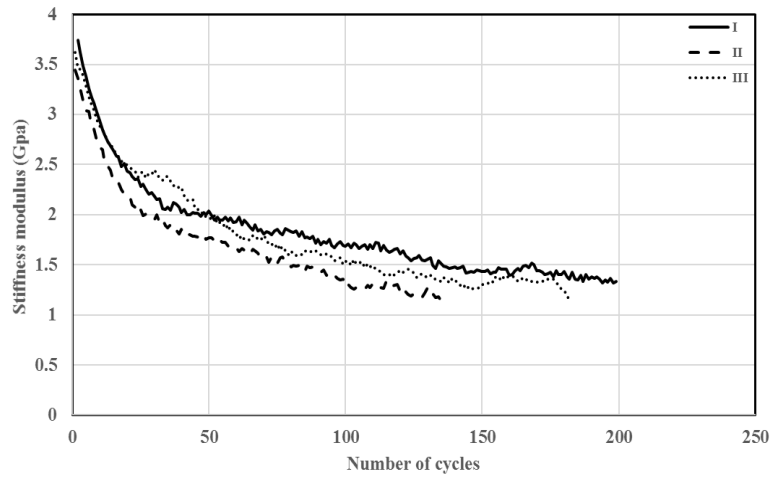


Figure C



### BCMUS5



### LCMUH0

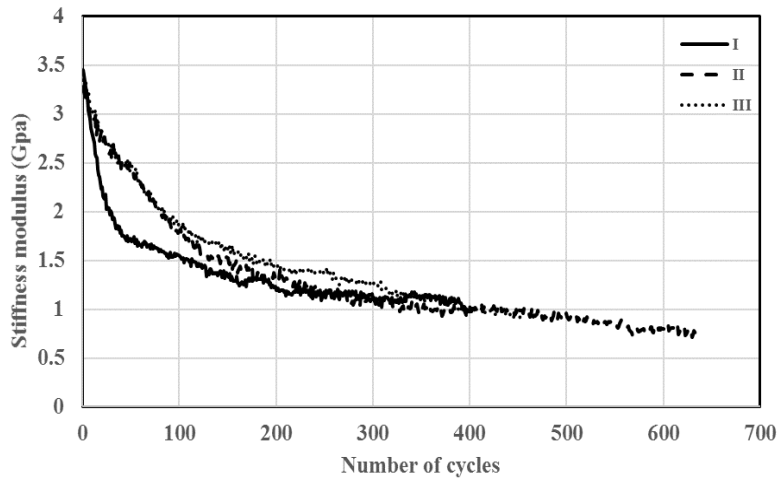
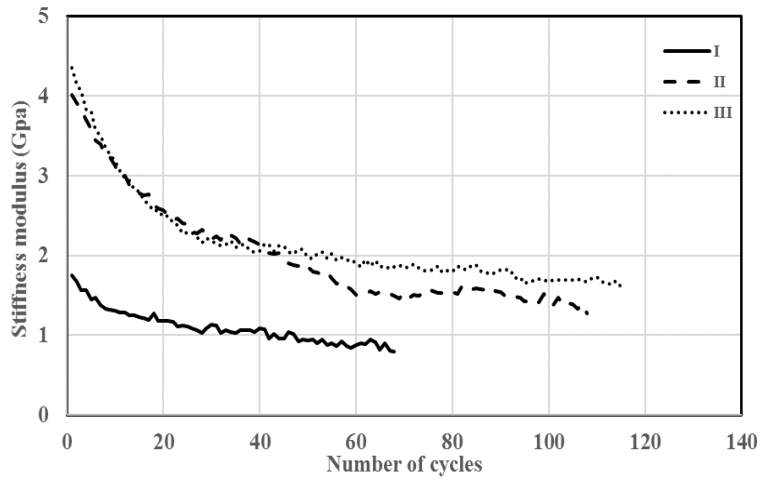


Figure C

### LFMUS10



### LFMAS5

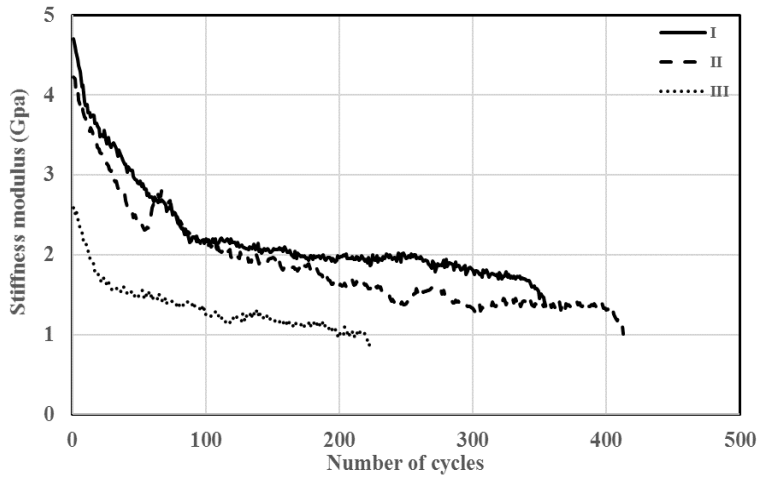
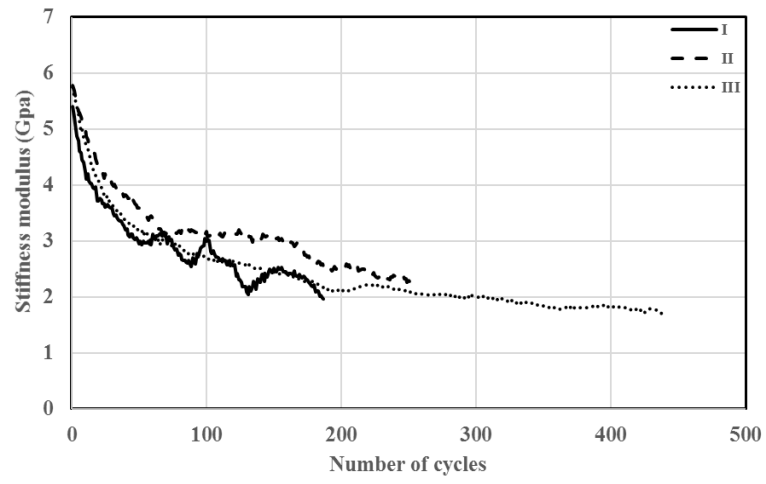


Figure C

### BCMAS10



### LFNAS5

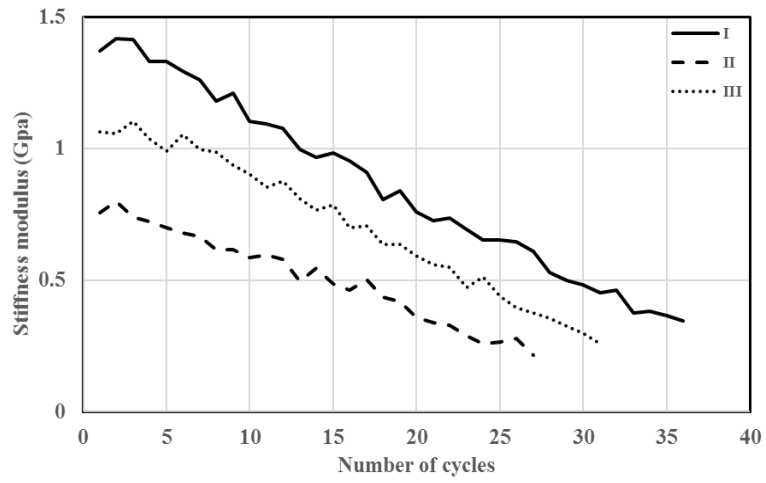
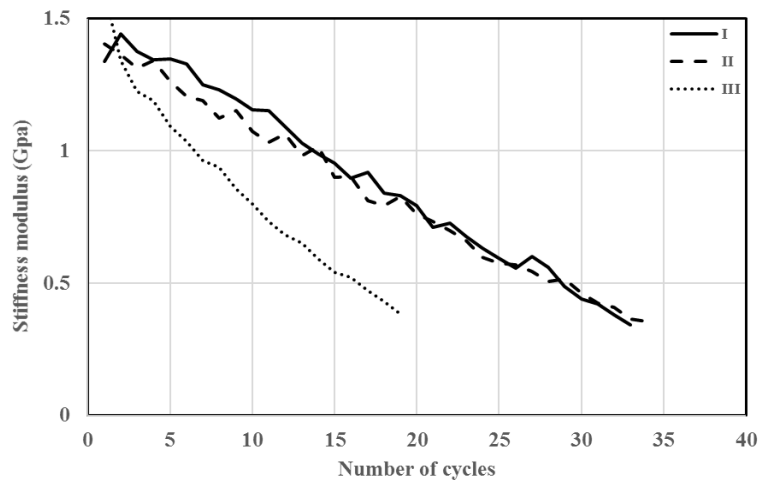


Figure C

### LFNAS10



### LCMAH5

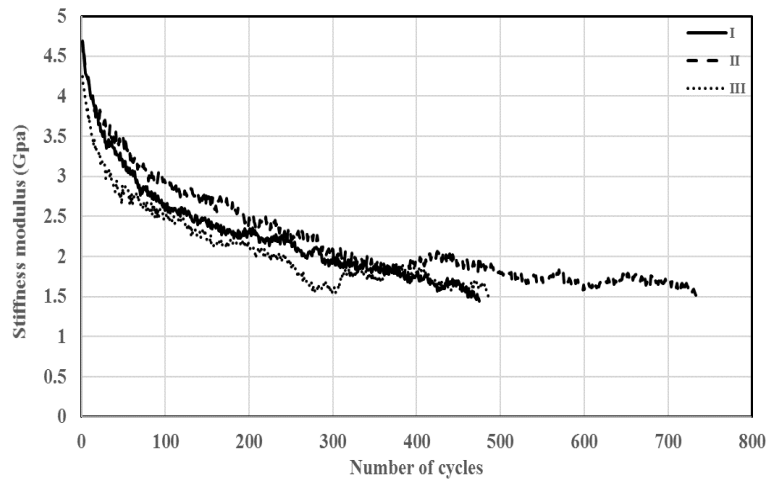


Figure C

# LCNUH0

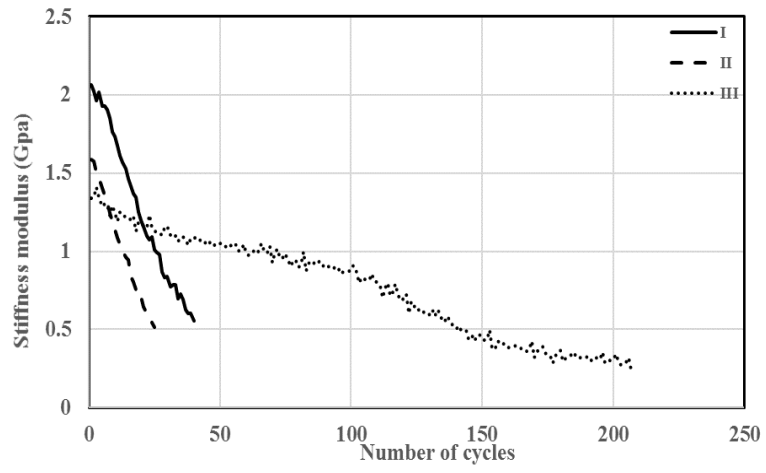
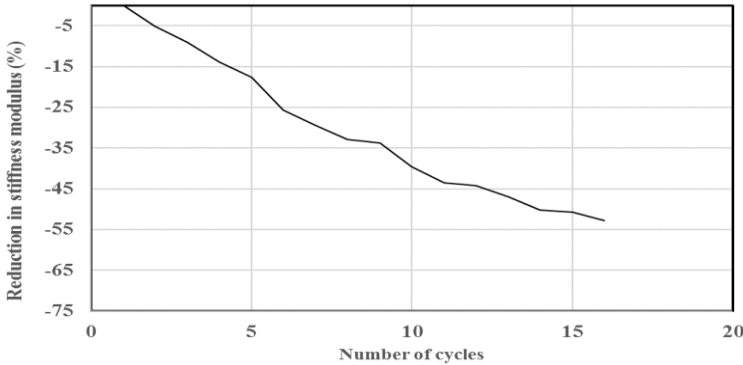


Figure C

**D. Reduction in stiffness calculated from bottom surface of the specimen (CMOD)**

**BCNAS10 (I)**



**BCNAS10 (II)**

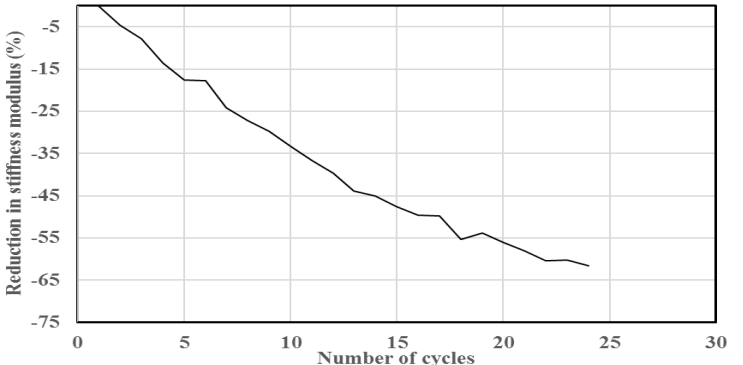
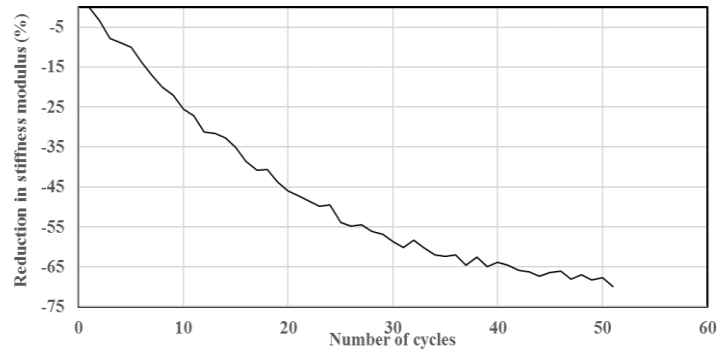
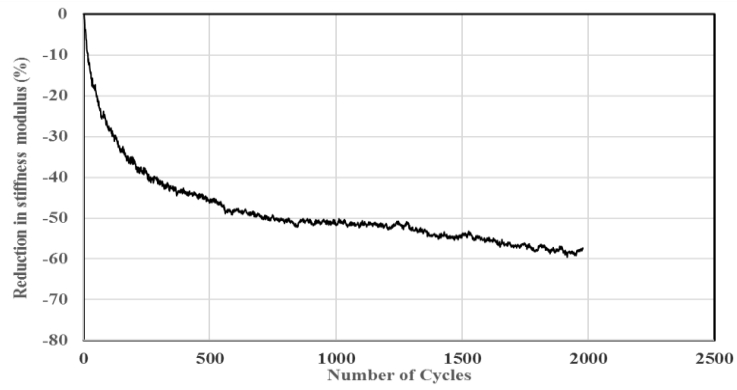


**Figure D. Reduction in stiffness modulus for test specimens**

### BCNAS10 (III)



### BFMAH10 (I)



### BFMAH10 (II)

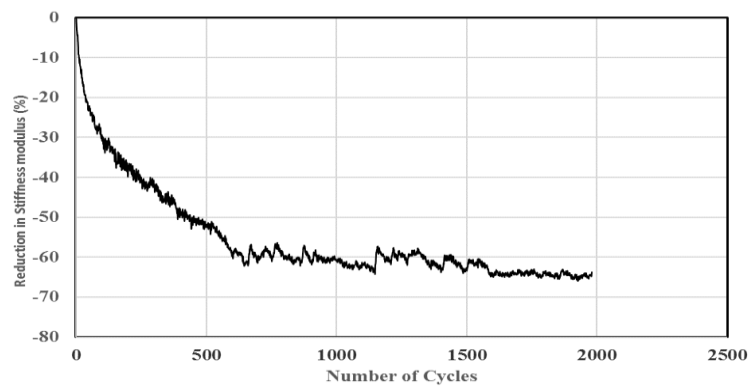
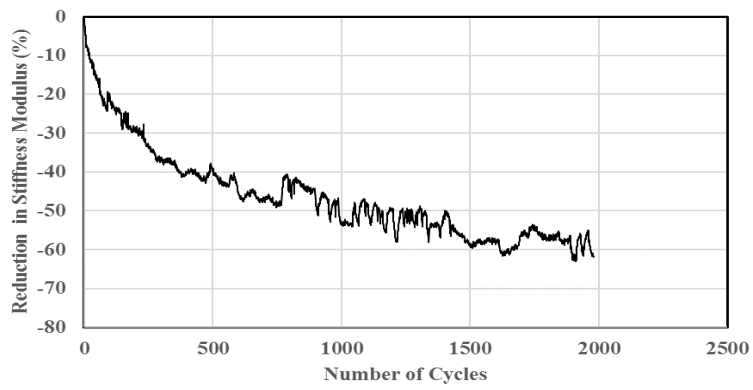
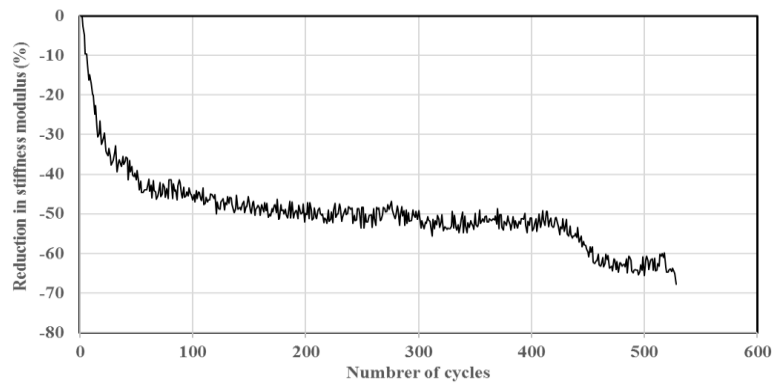


Figure D

### BFMAH10 (III)



### LCMUH10 (I)



### LCMUH10 (II)

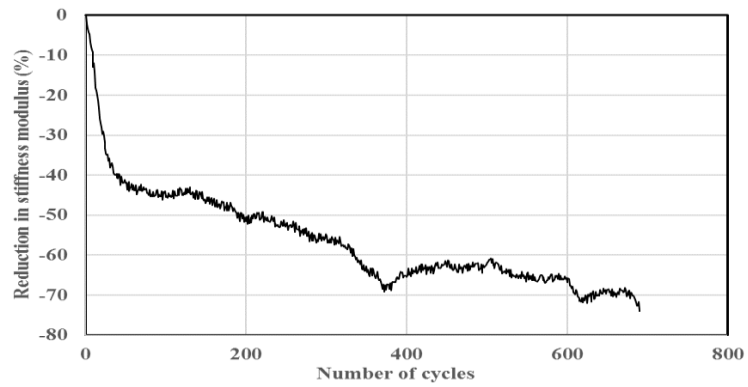
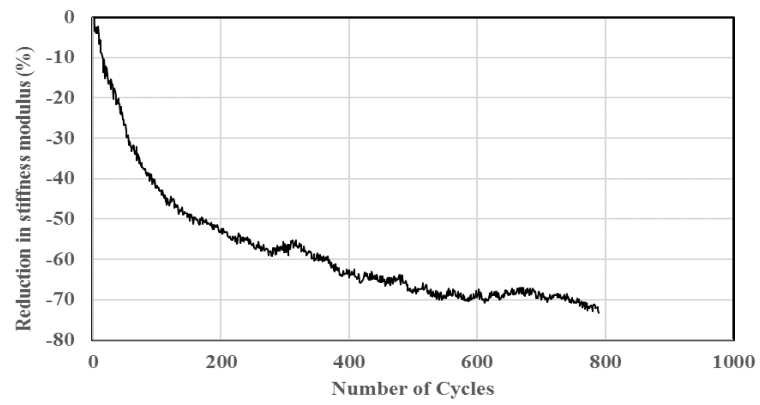


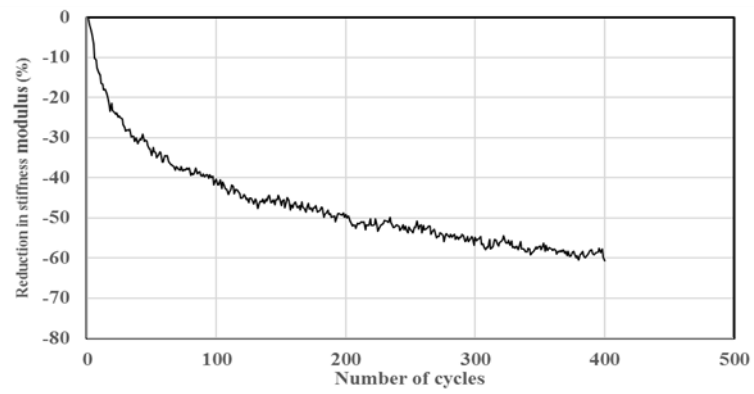
Figure D



### LCMUH10 (III)



### LCMAH0 (I)



### LCMAH0 (II)

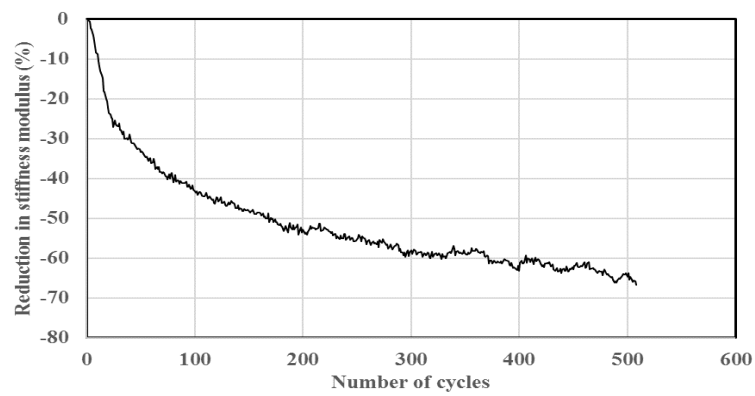
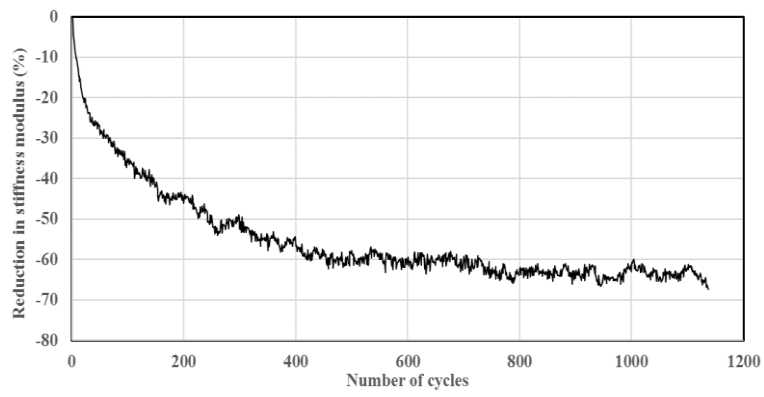
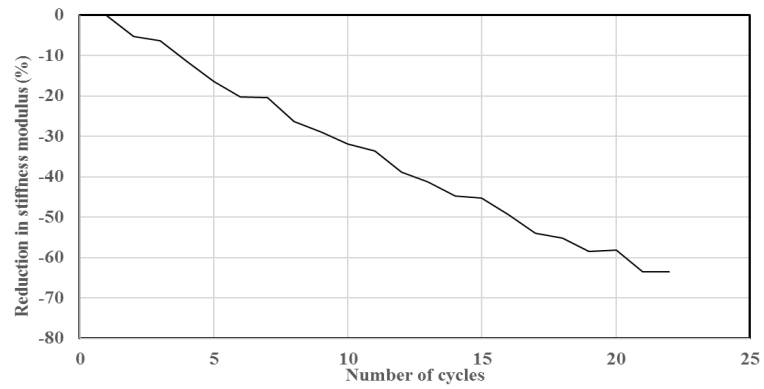


**Figure D**

### LCMAH0 (III)



### LCNUH10 (I)



### LCNUH10 (II)

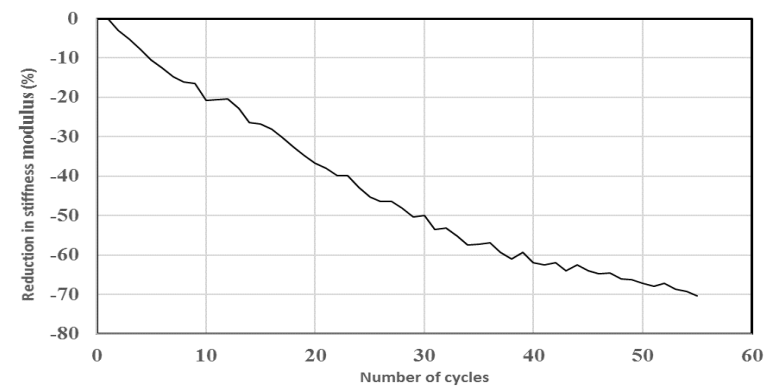
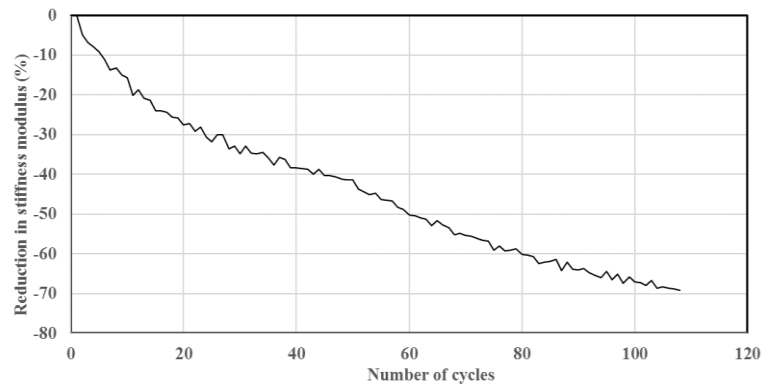
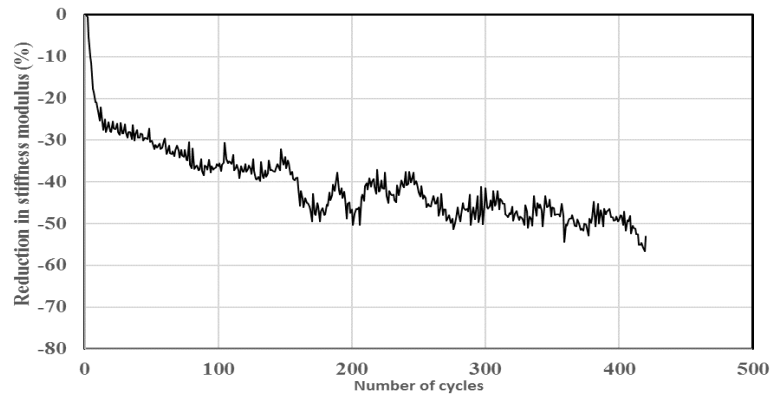


Figure D

### LCNUH10 (III)



### LFMAS0(I)



### LFMAS0(II)

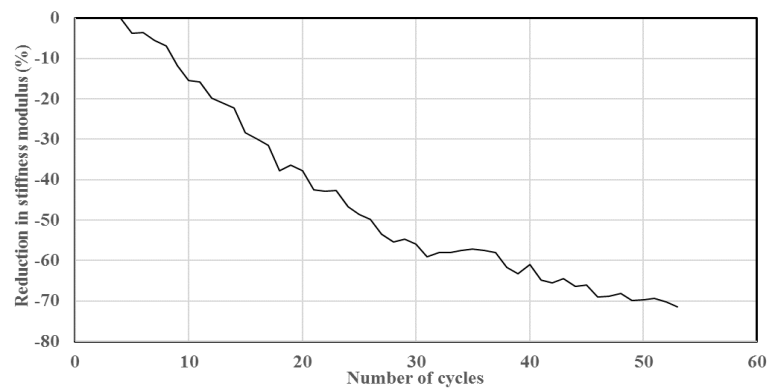
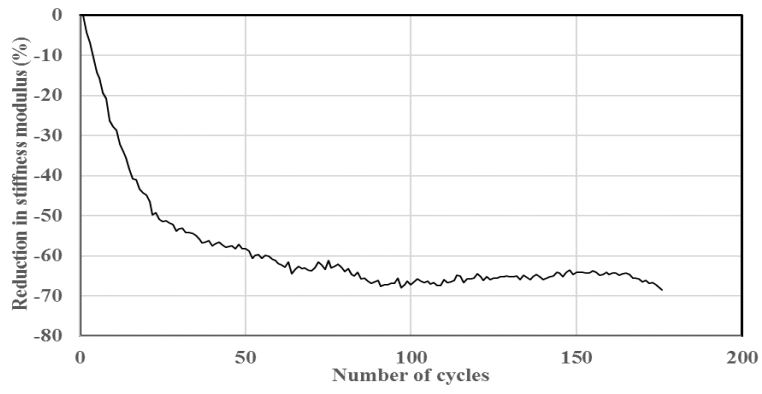
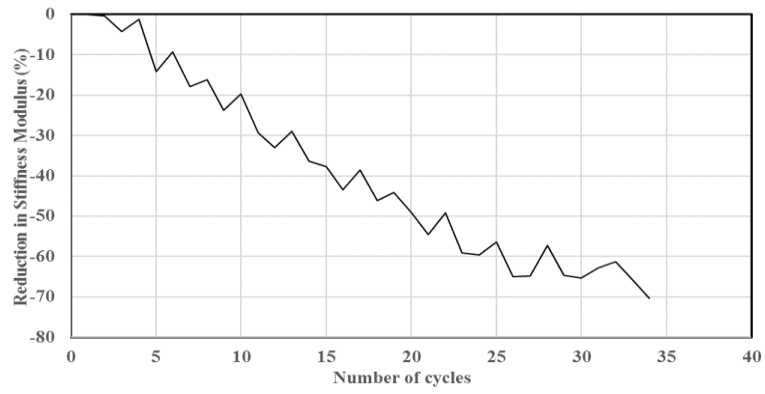


Figure D

**LFMAS0(III)**



**LFNUS10(I)**



**LFNUS10(II)**

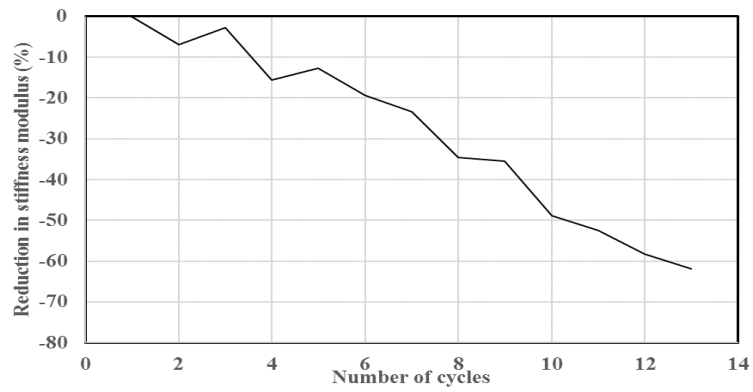
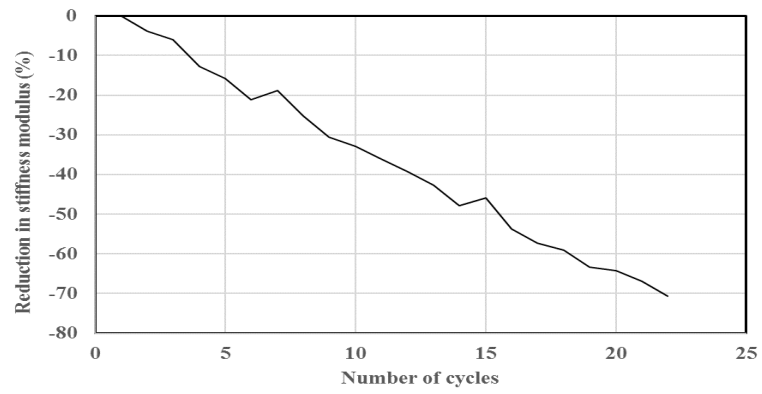
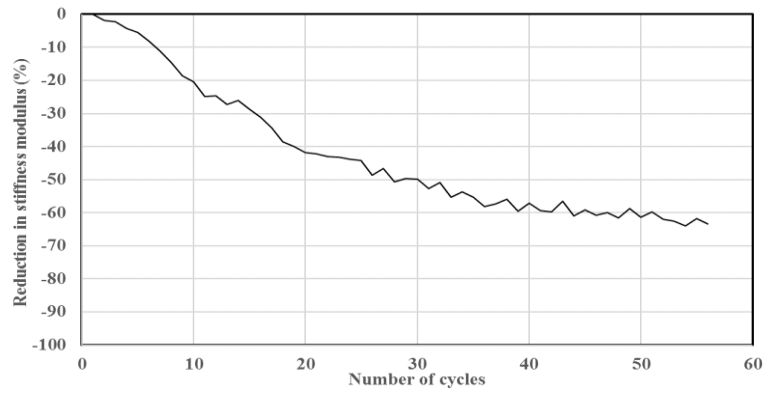


**Figure D**

**LFNUS10(III)**



**LCNAH5(I)**



**LCNAH5(II)**

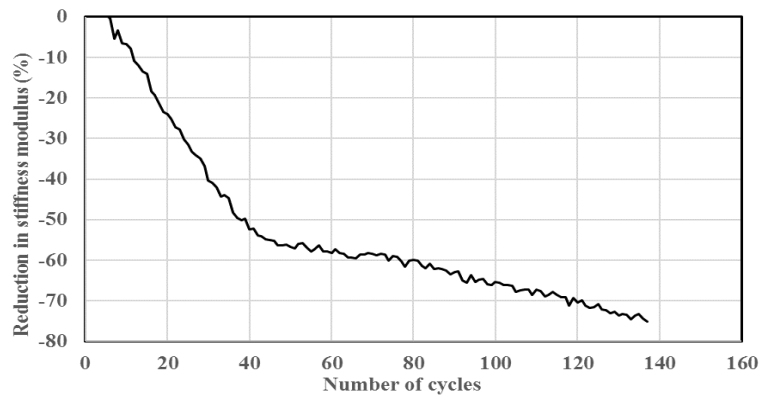
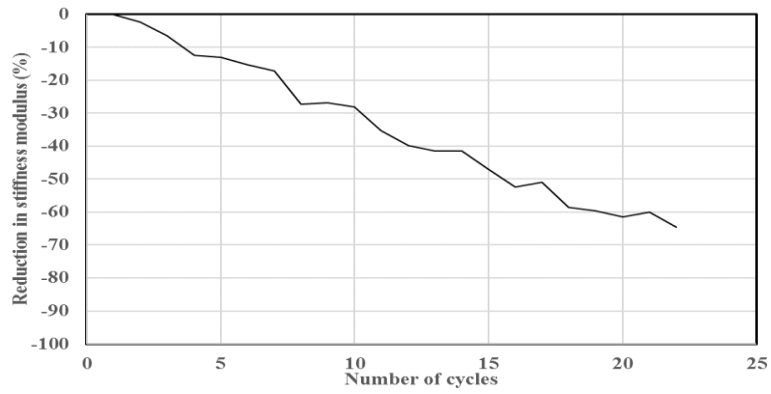
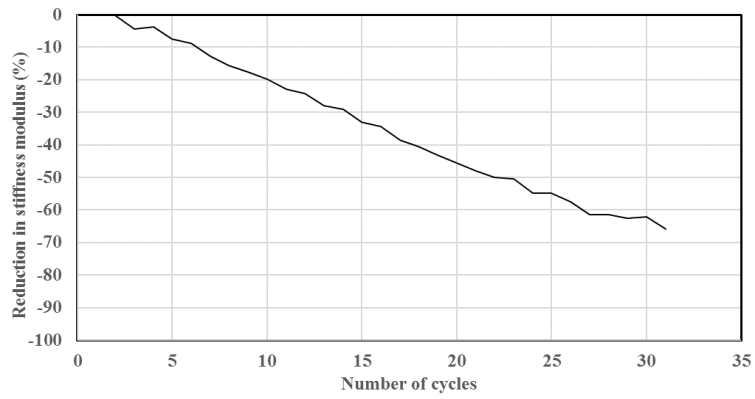


**Figure D**

**LCNAH5(III)**



**LCNAH0(I)**



**LCNAH0(II)**

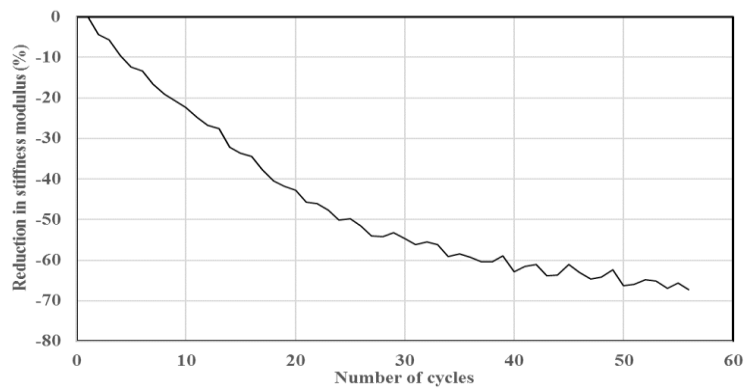
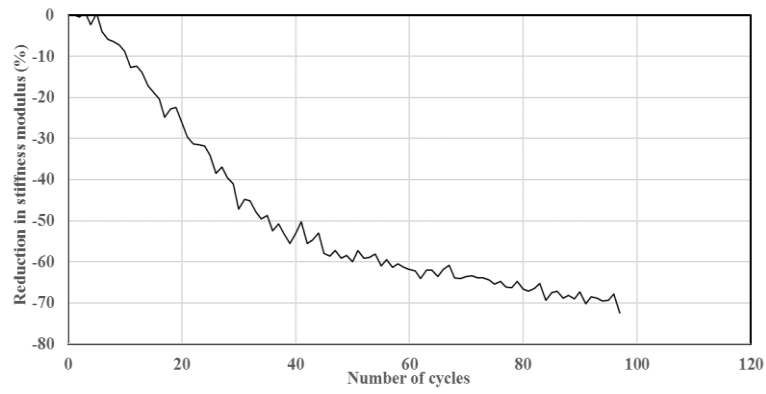
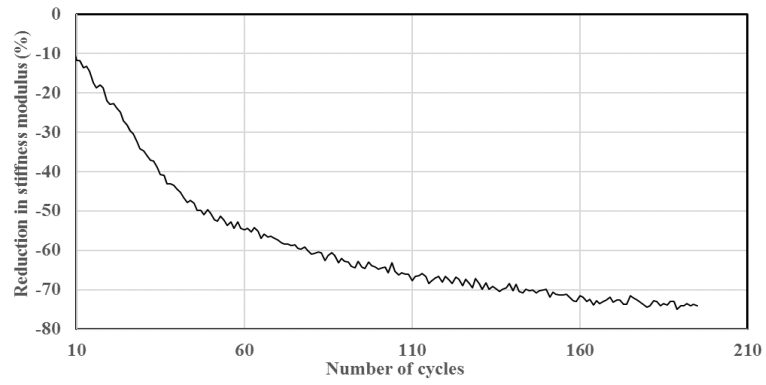


**Figure D**

### LCNAH0(III)



### BFNAH10 (I)



### BFNAH10 (II)

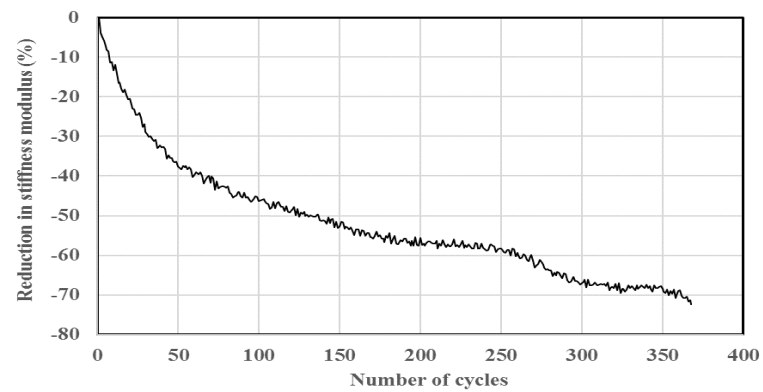
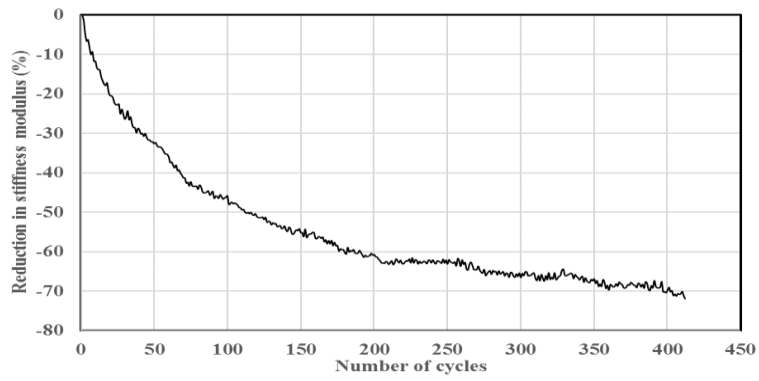
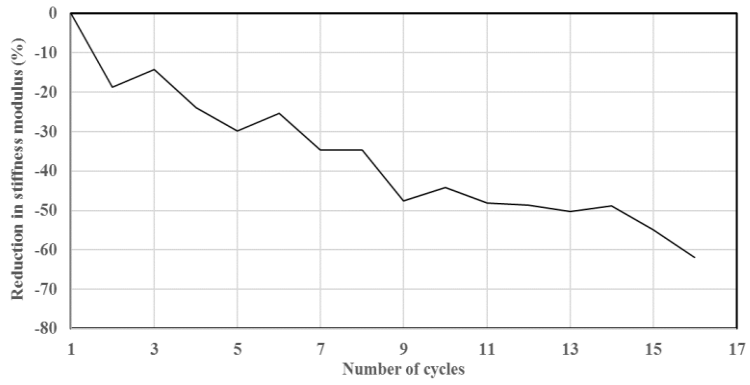


Figure D

### BFNAH10 (III)



### LFNUS5 (I)



### LFNUS5 (II)

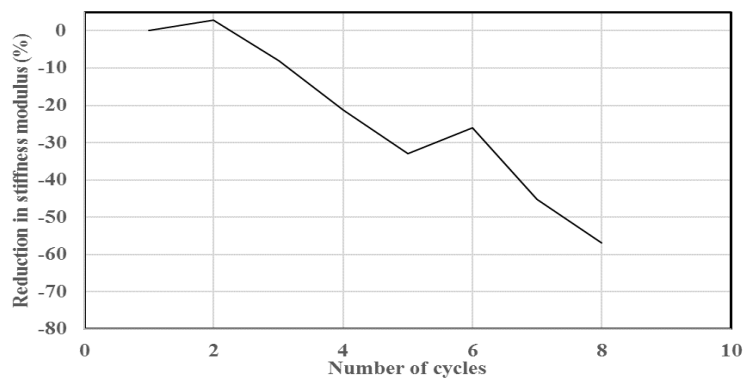
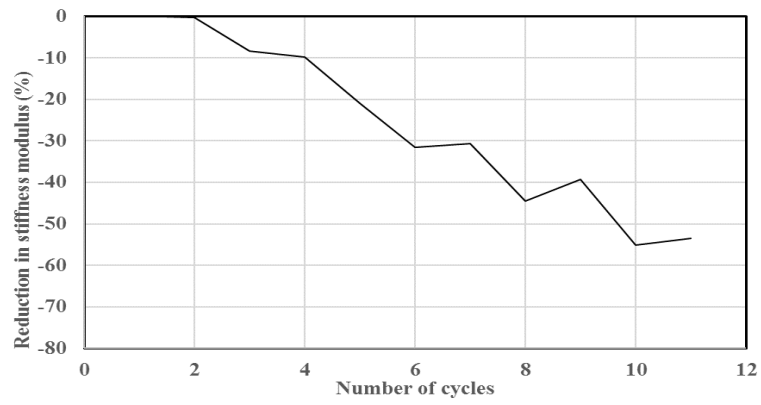


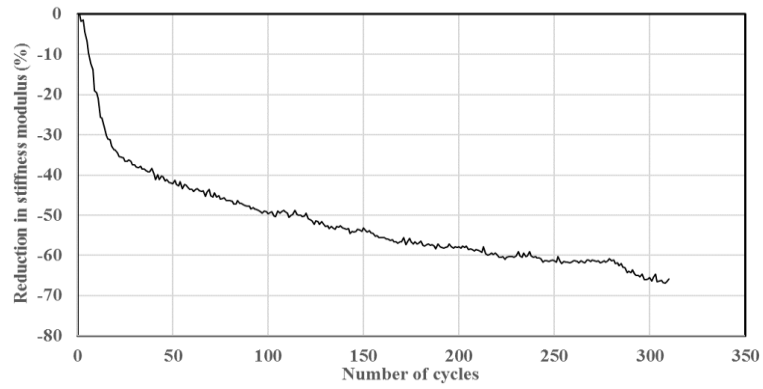
Figure D



### LFNUS5 (III)



### BCMUS0 (I)



### BCMUS0 (II)

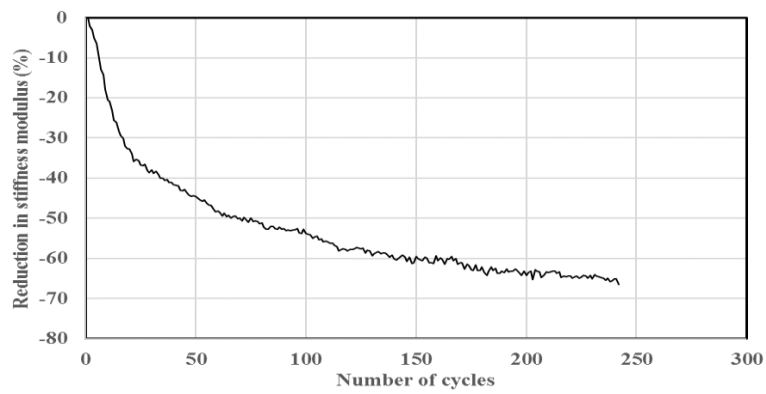
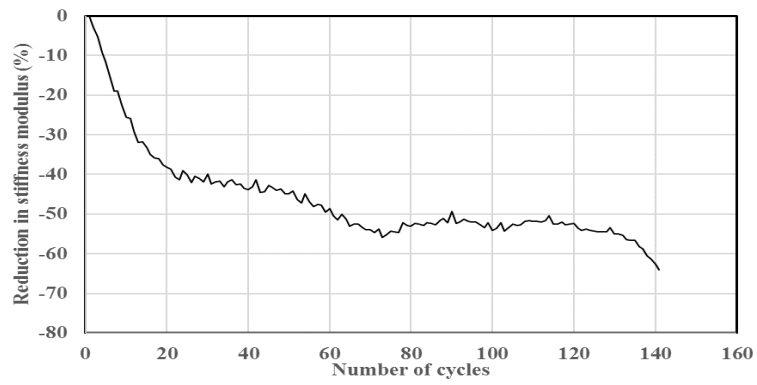
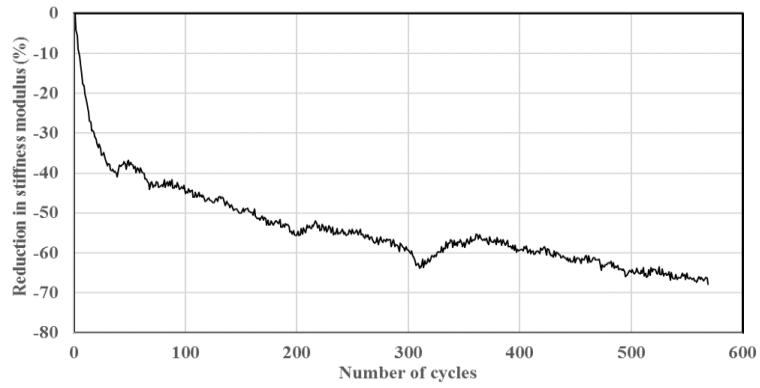


**Figure D**

**BCMUS0 (III)**



**BCMAS10 (I)**



**BCMAS10 (II)**

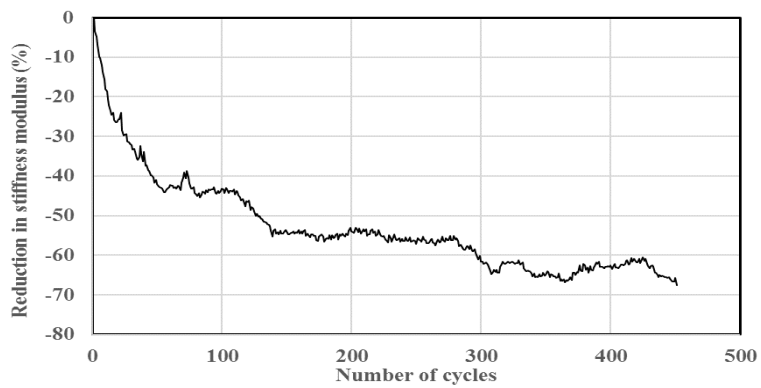
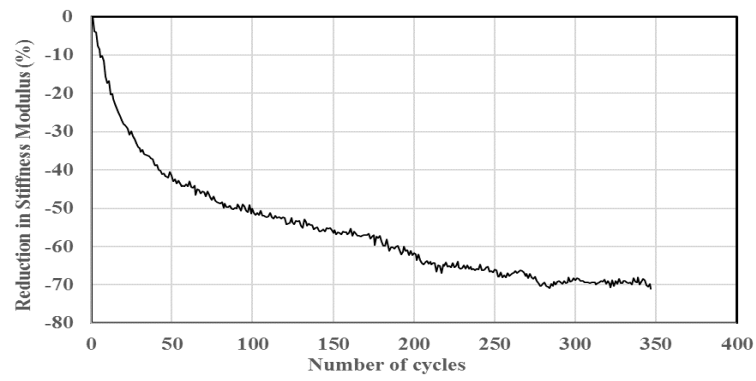
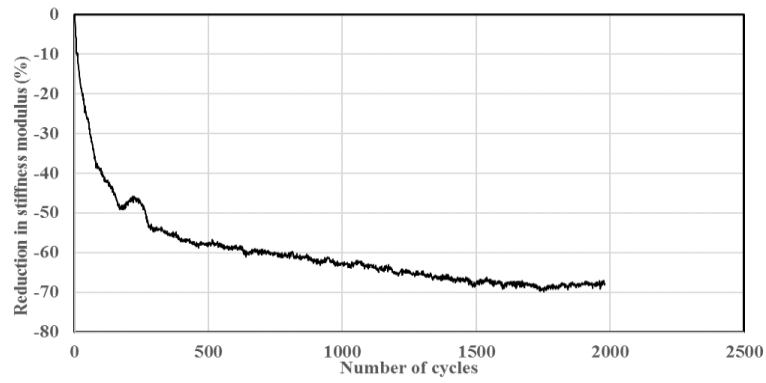


**Figure D**

### BCMAS10 (III)



### BFMAH0 (I)



### BFMAH0 (II)

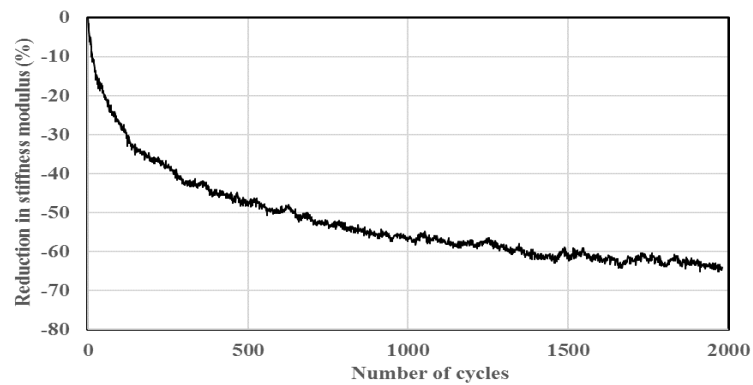
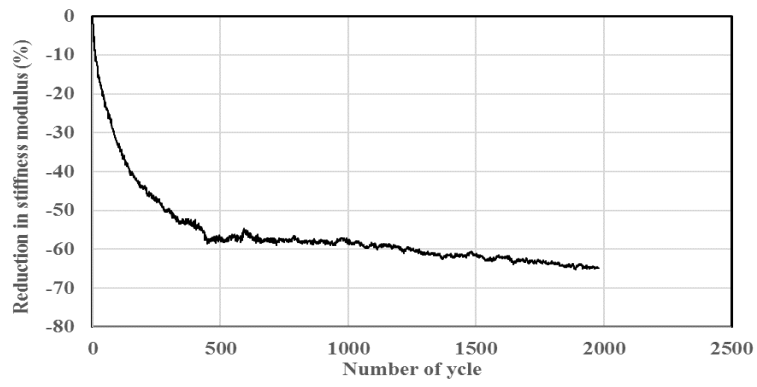
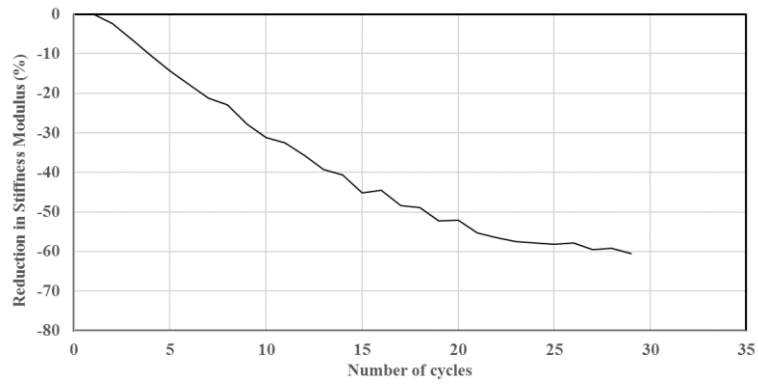


Figure D

### BFMAH0 (III)



### BCNAS5 (I)



### BCNAS5 (II)

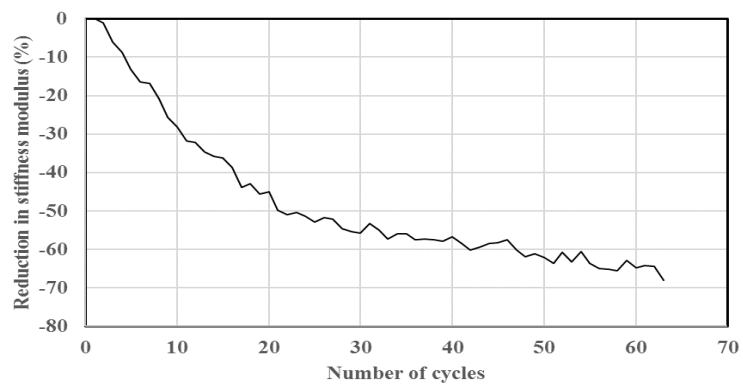
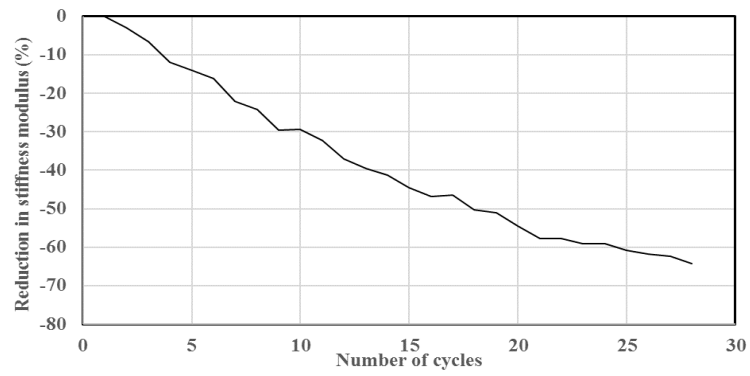
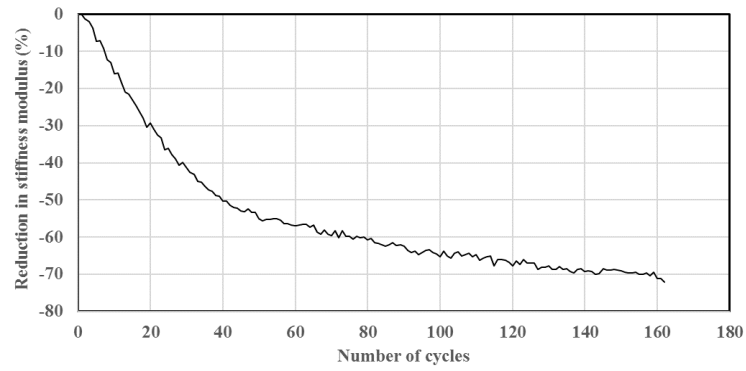


Figure D

### BCNAS5 (III)



### BFNAH0 (I)



### BFNAH0 (II)

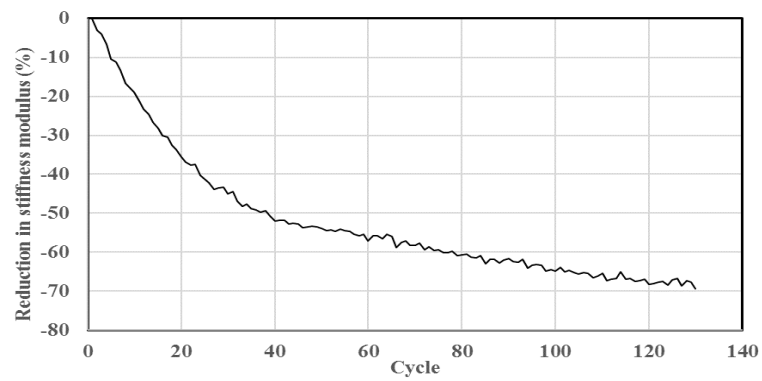
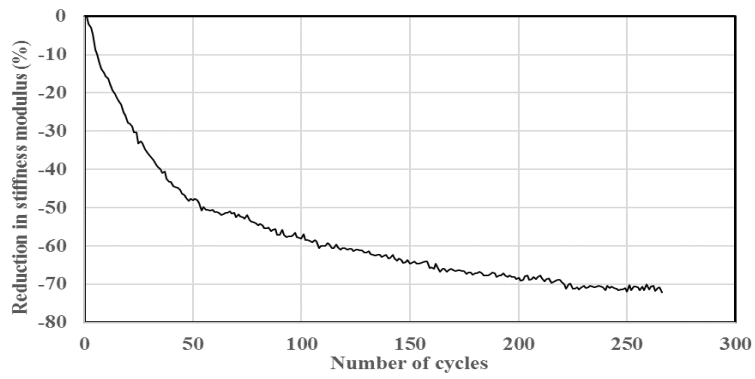
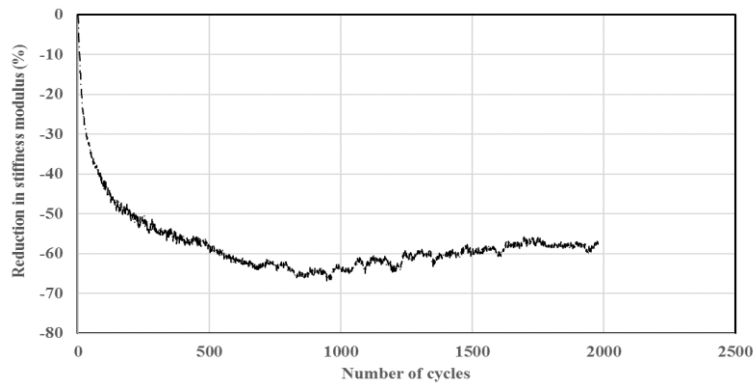


Figure D

### BFNAH0 (III)



### BFMUH5 (I)



### BFMUH5 (II)

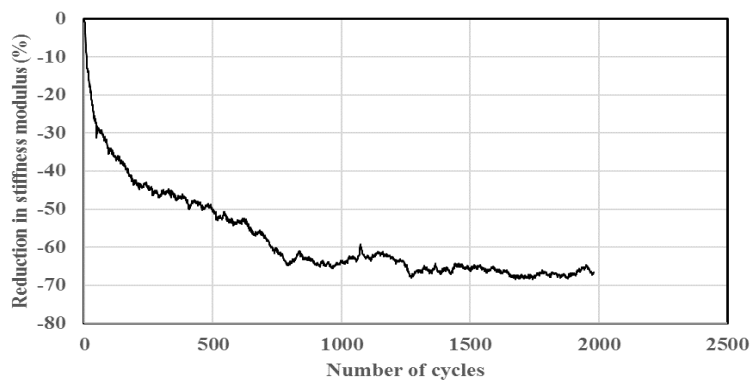
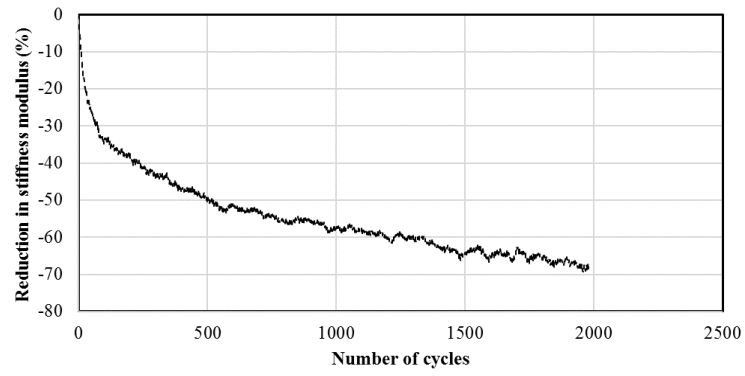
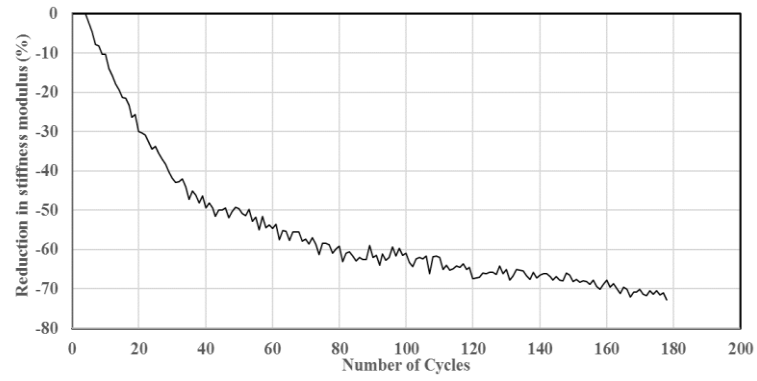


Figure D

### BFMUH5 (III)



### BFNUH5 (I)



### BFNUH5 (II)

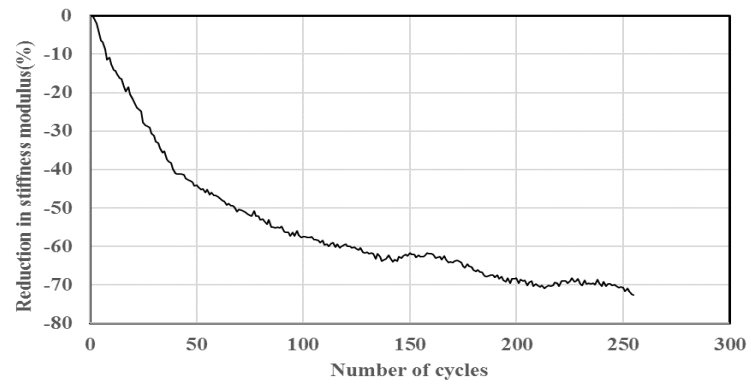
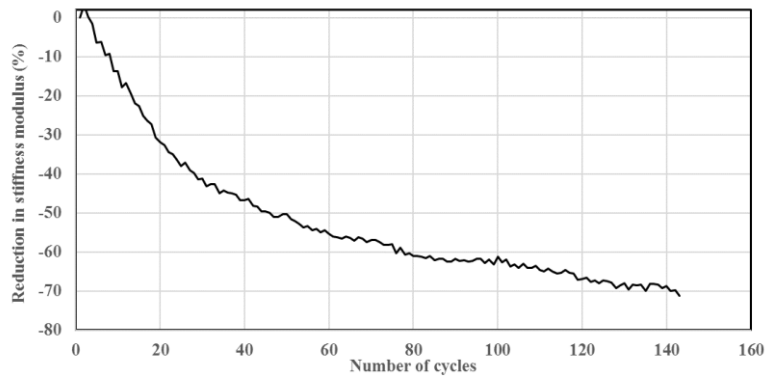
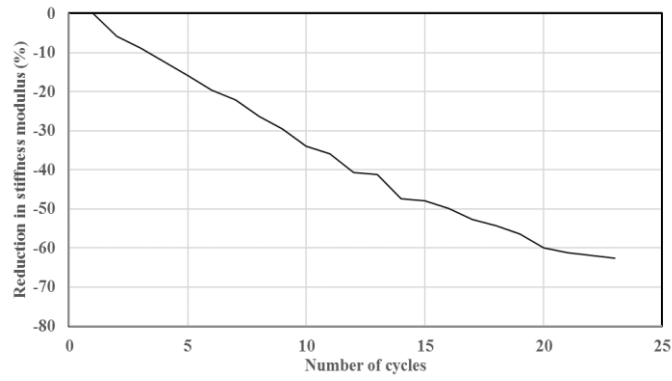


Figure D

### BFNUH5 (III)



### BCNUS10 (I)



### BCNUS10 (II)

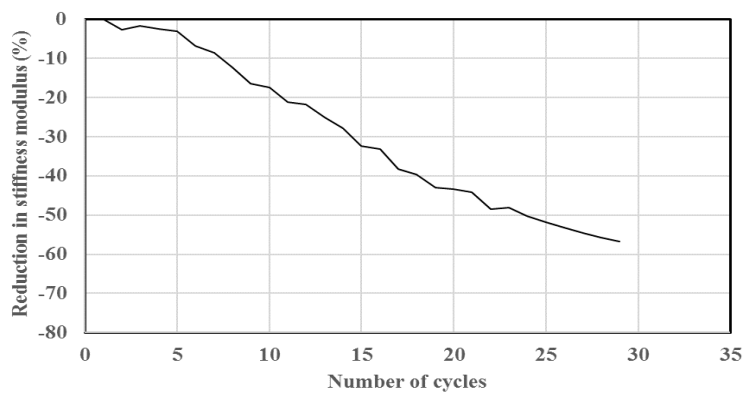
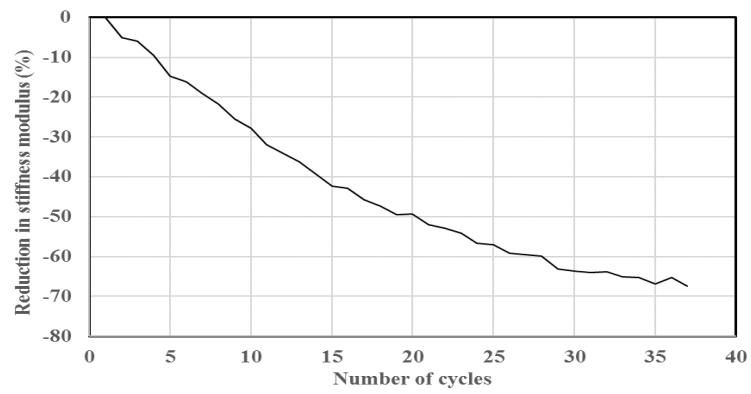


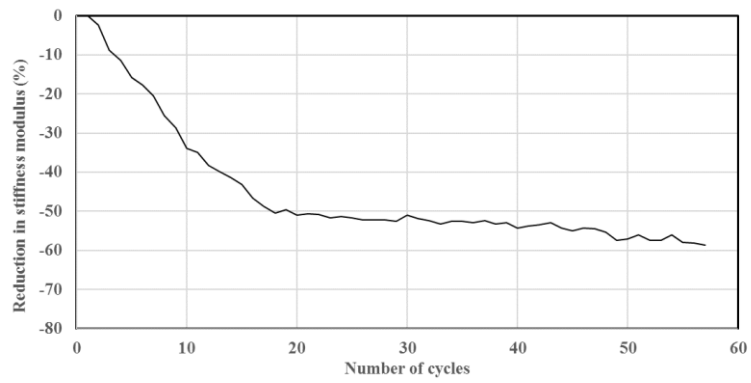
Figure D



### BCNUS10 (III)



### BCNUS5 (I)



### BCNUS5 (II)

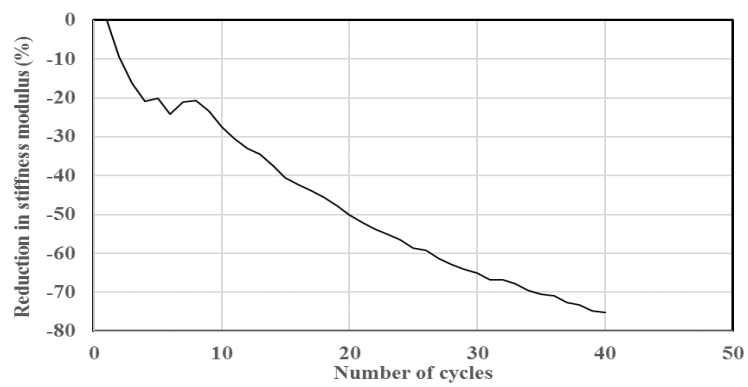
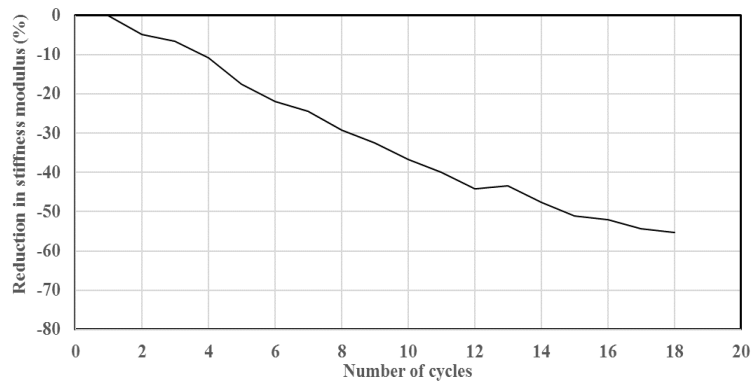
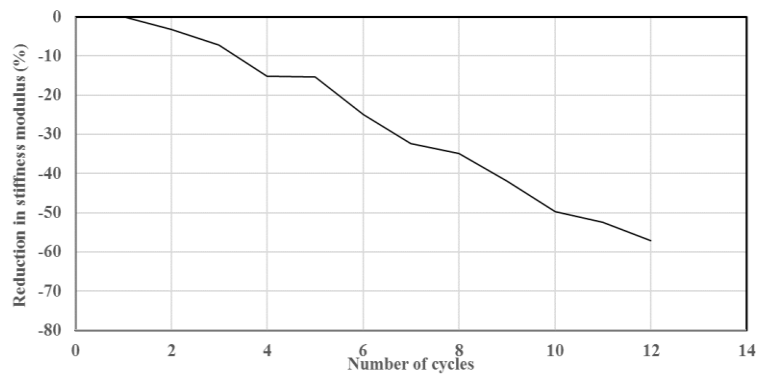


Figure D

### BCNUS5 (III)



### BCNUS0 (I)



### BCNUS0 (II)

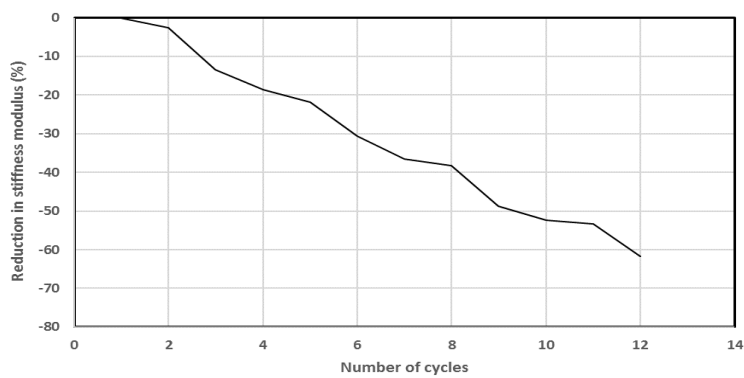
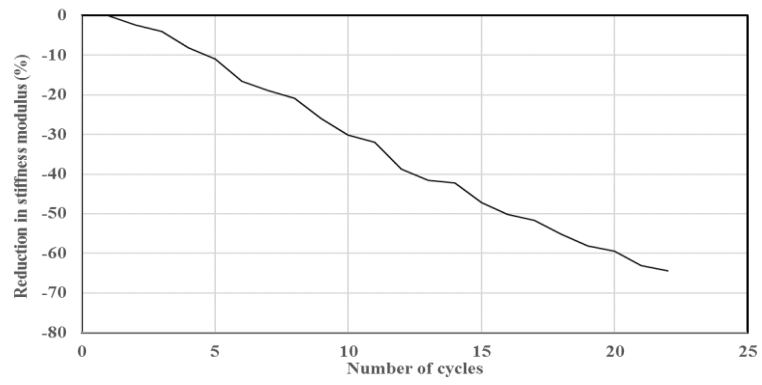
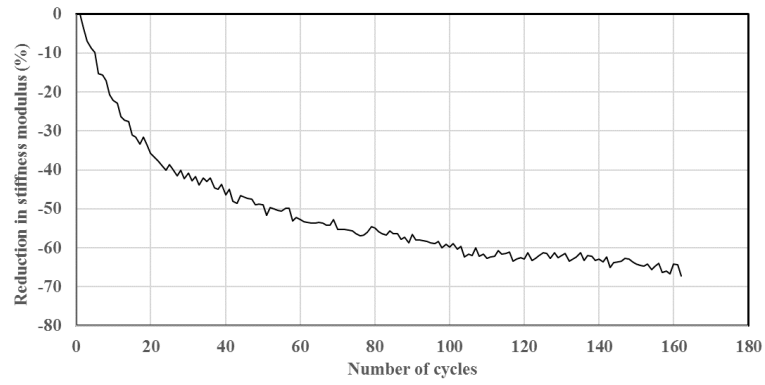


Figure D

### BCNUS0 (III)



### LFMUS5 (I)



### LFMUS5 (II)

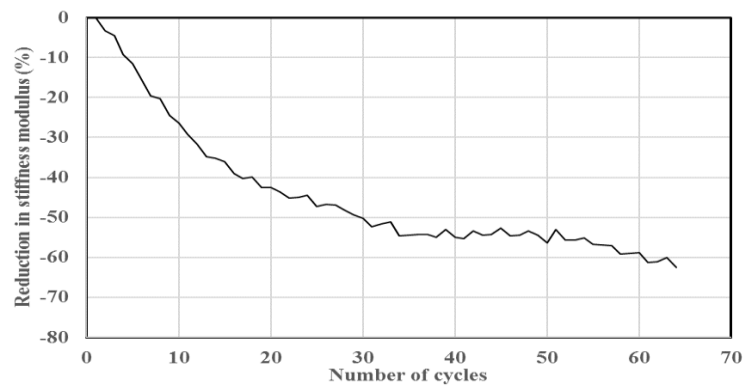
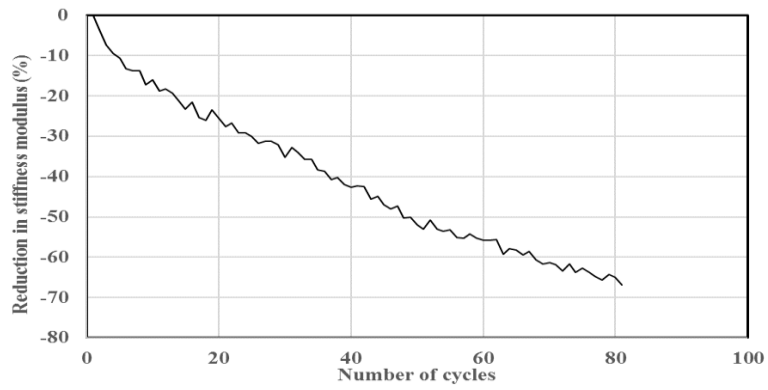
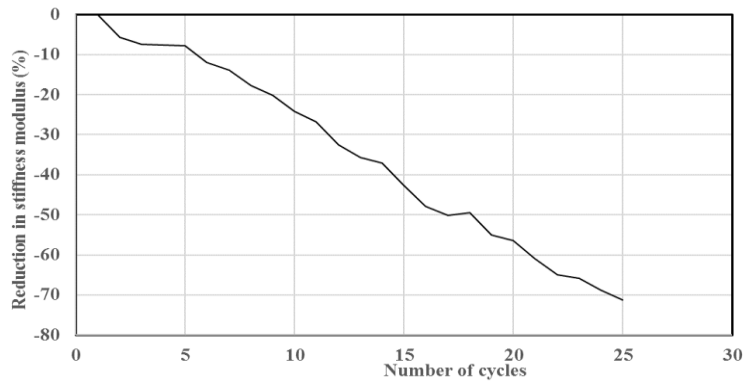


**Figure D**

### LFMUS5 (III)



### LFNAS0 (I)



### LFNAS0 (II)

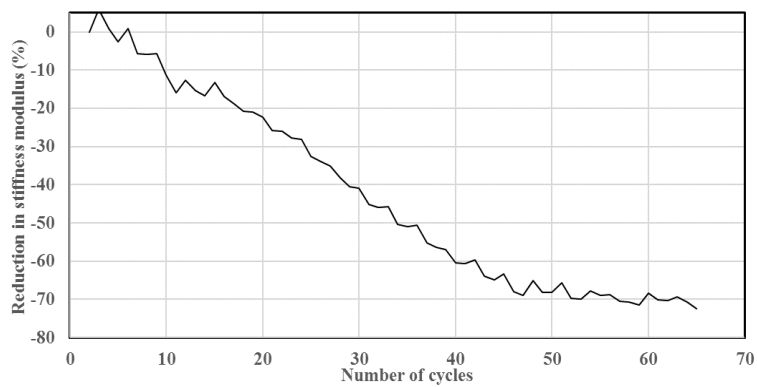
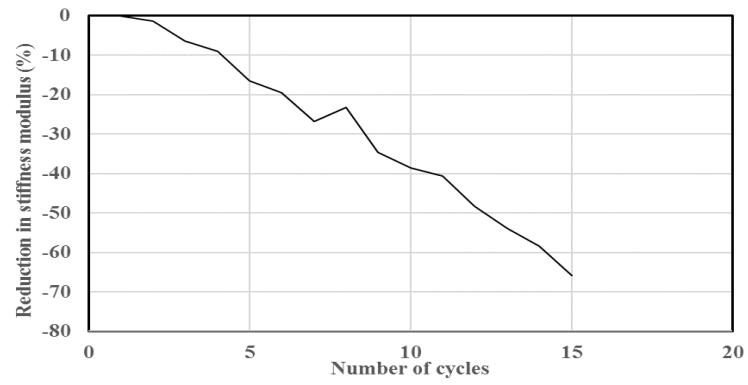


Figure D

### LFNAS0 (III)



### LFNUS0 (I)



### LFNUS0 (II)

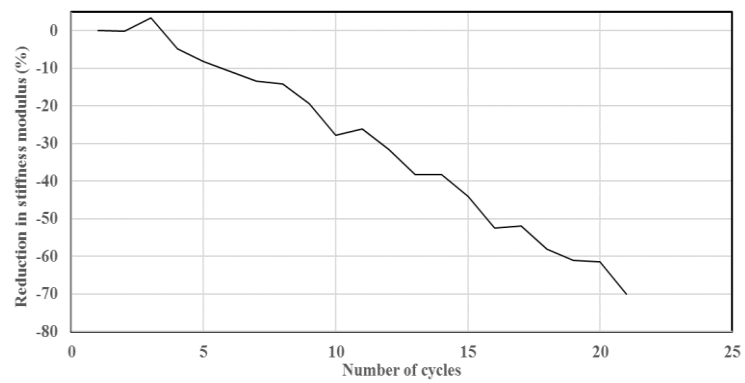
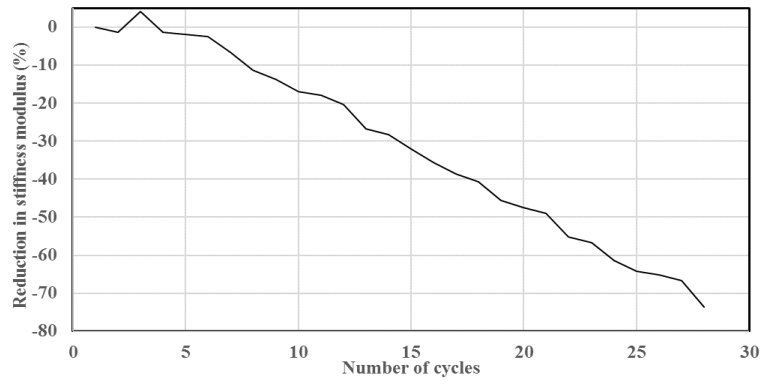
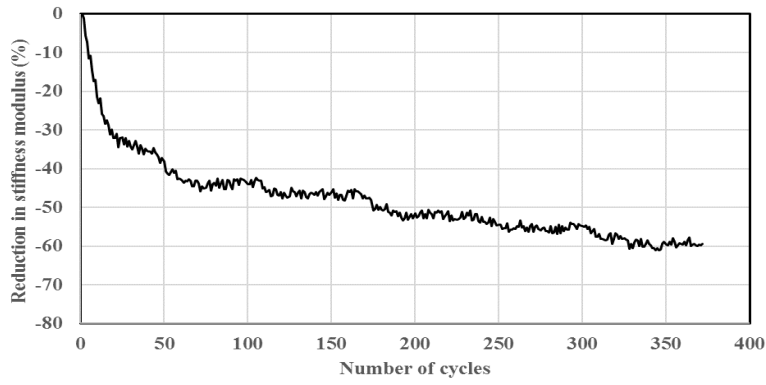


**Figure D**

### LFNUS0 (III)



### BCMUS10 (I)

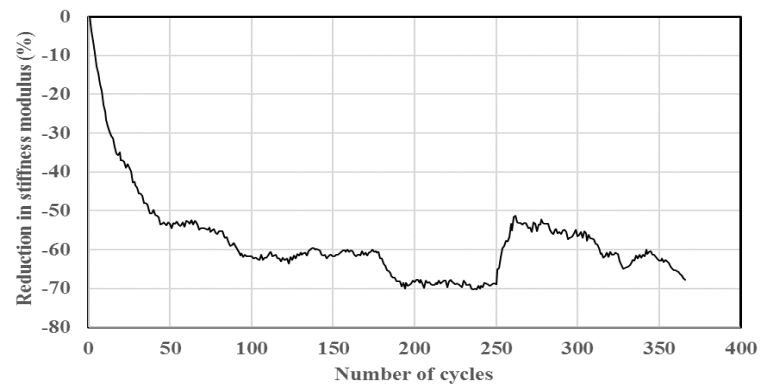


### BCMUS10 (II)

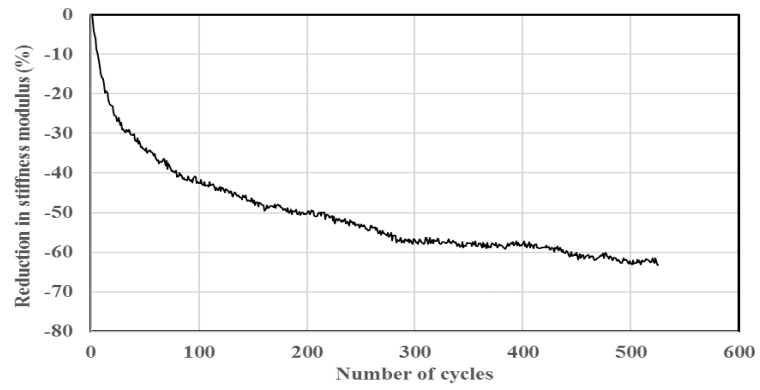


Figure D

**BCMUS10 (III)**



**BCMAS5 (I)**



**BCMAS5 (II)**

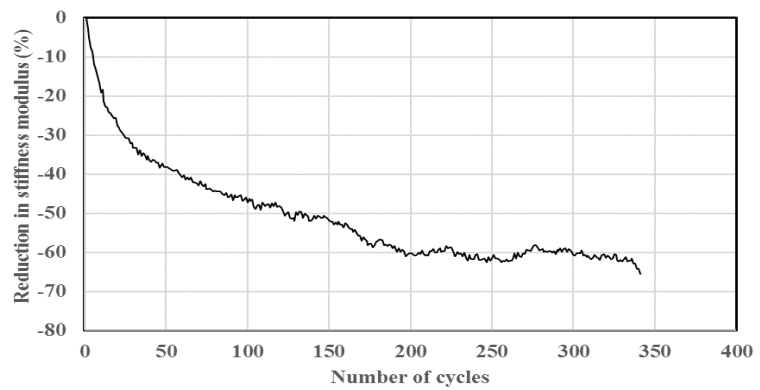
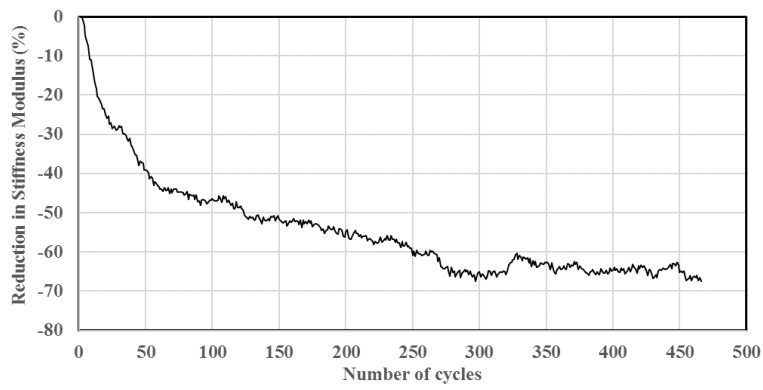
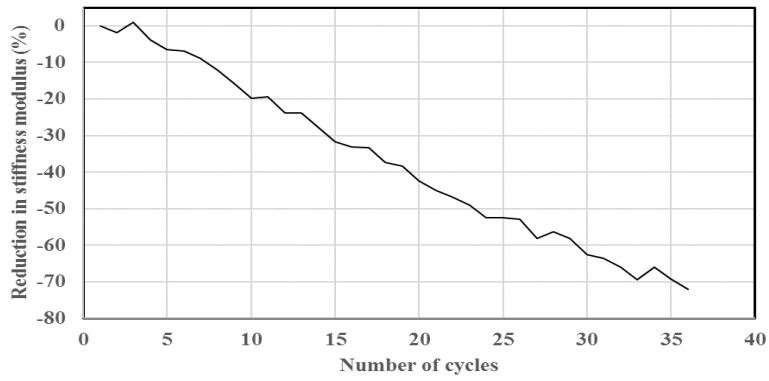


**Figure D**

### BCMAS5 (III)



### LCNUH5 (I)



### LCNUH5 (II)

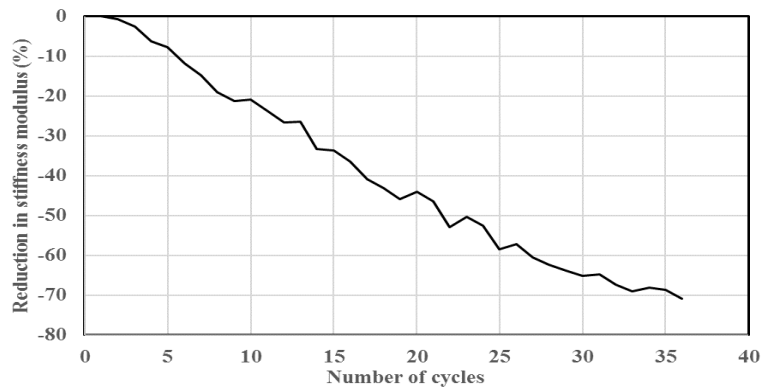
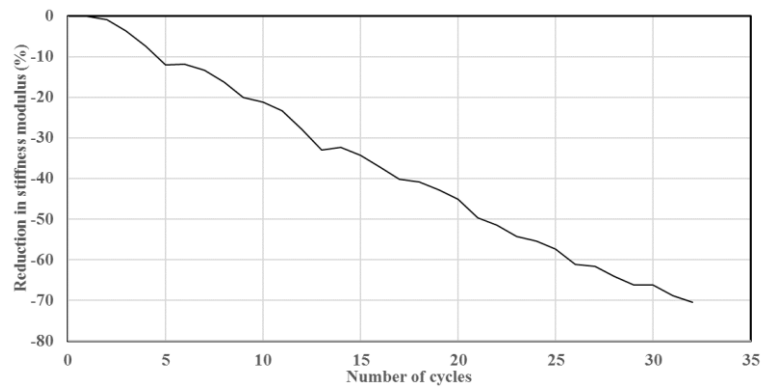


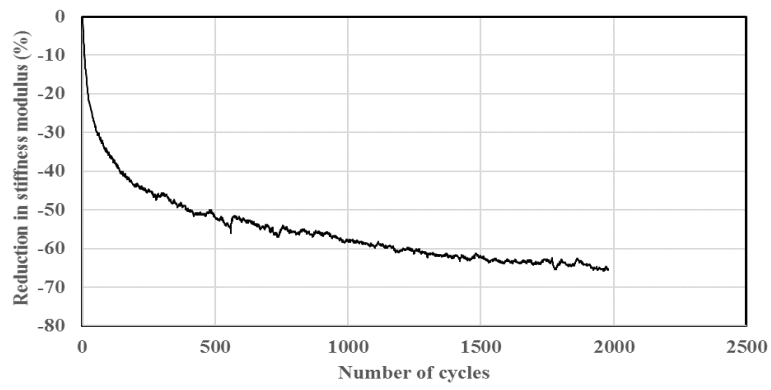
Figure D



### LCNUH5 (III)



### BFMAH5 (I)



### BFMAH5 (II)

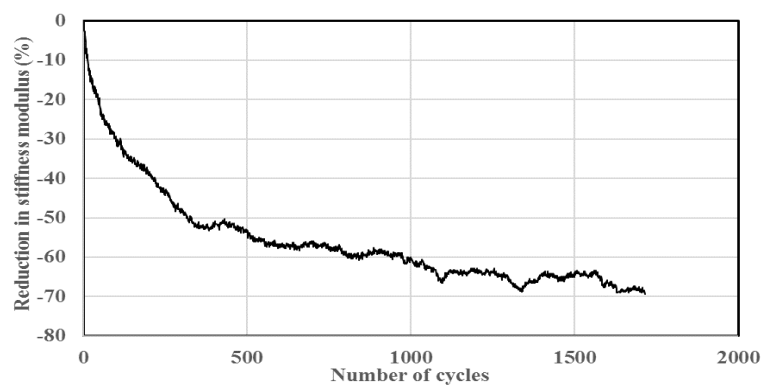
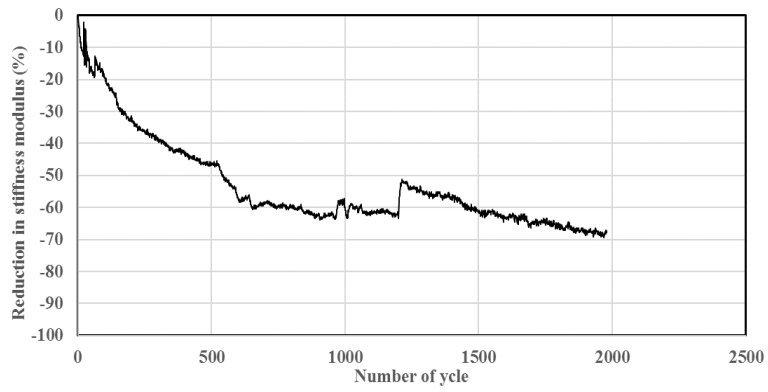
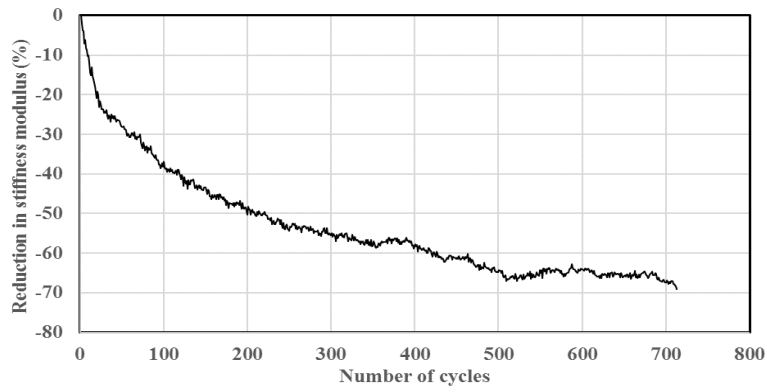


Figure D

### BFMAH5 (III)



### LCMAH10 (I)



### LCMAH10 (II)

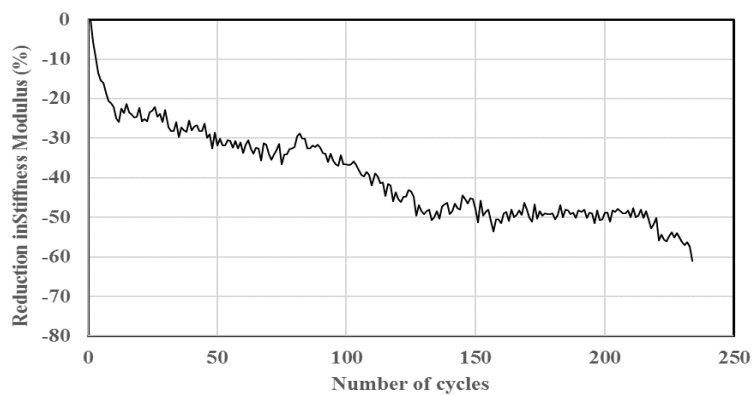
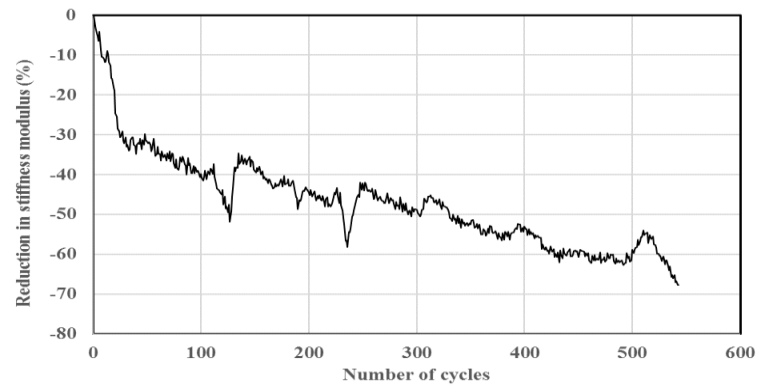
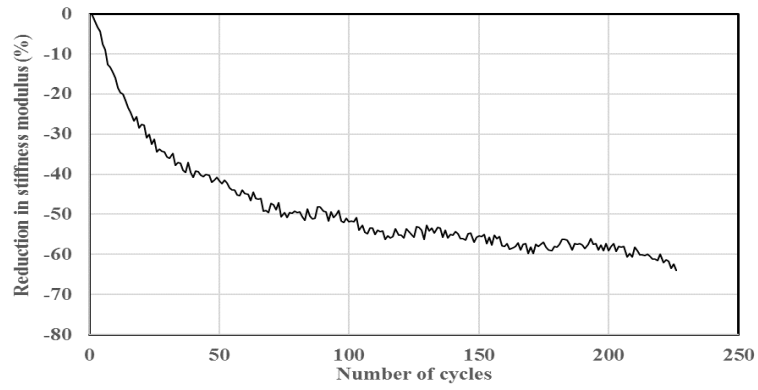


Figure D

### LCMAH10 (III)



### LCMUH5 (I)



### LCMUH5 (II)

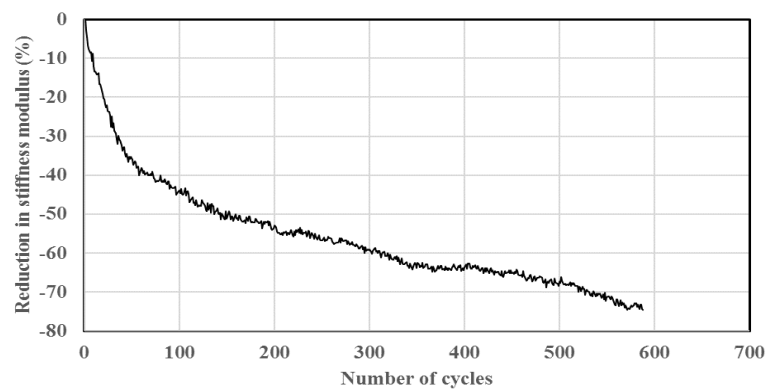
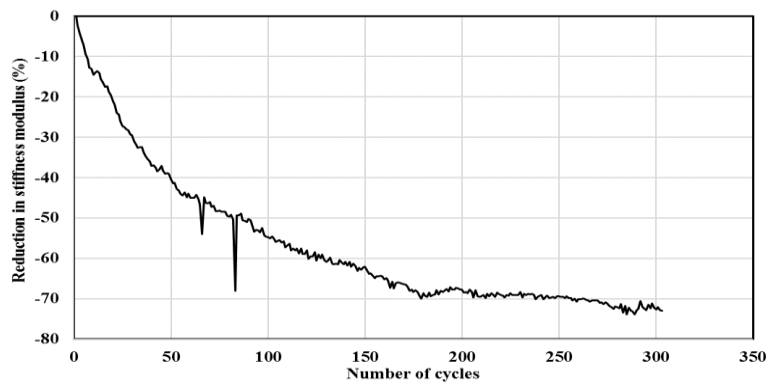
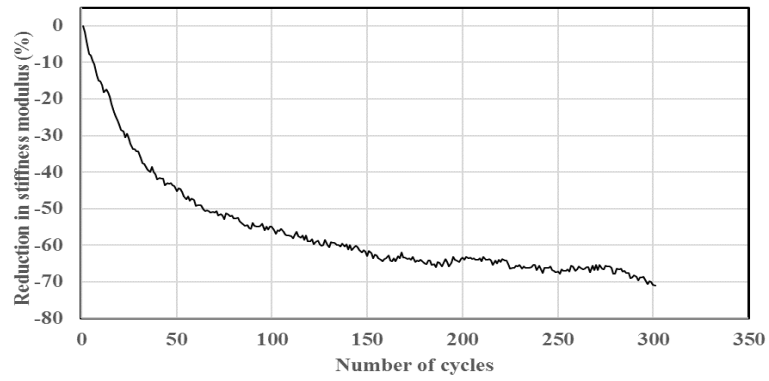


Figure D

### LCMUH5 (III)



### BFNUH10 (I)



### BFNUH10 (II)

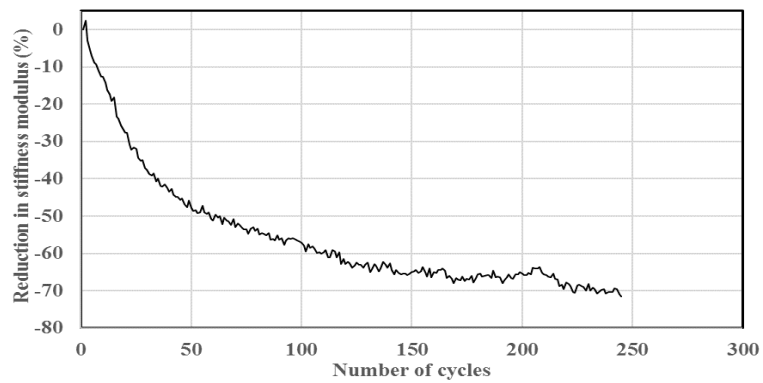
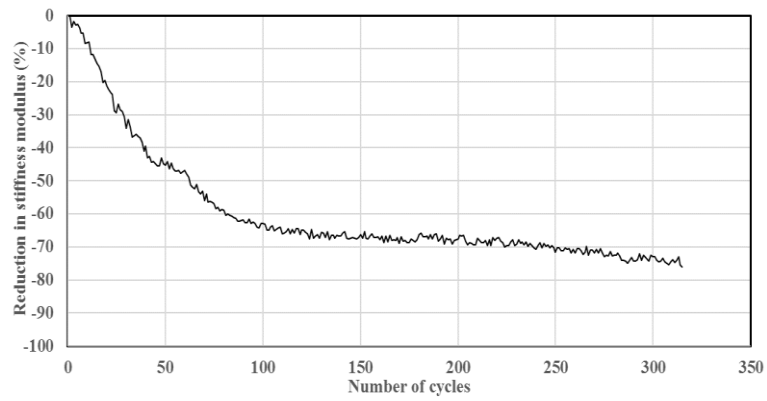
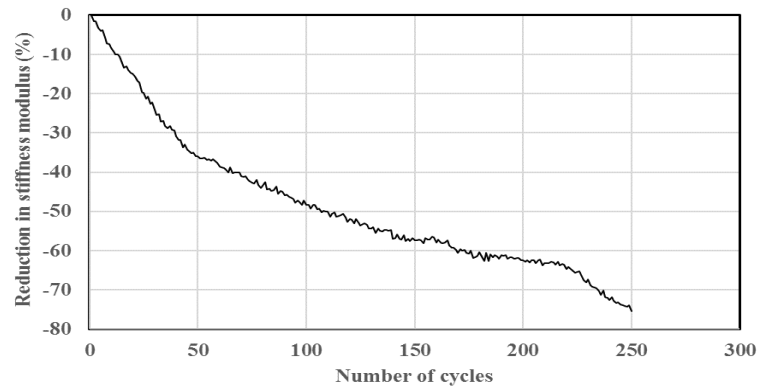


Figure D

### BFNUH10 (III)



### BFNAH5 (I)



### BFNAH5 (II)

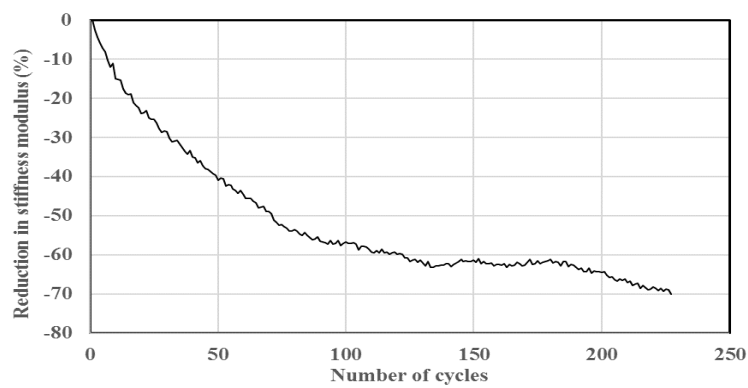
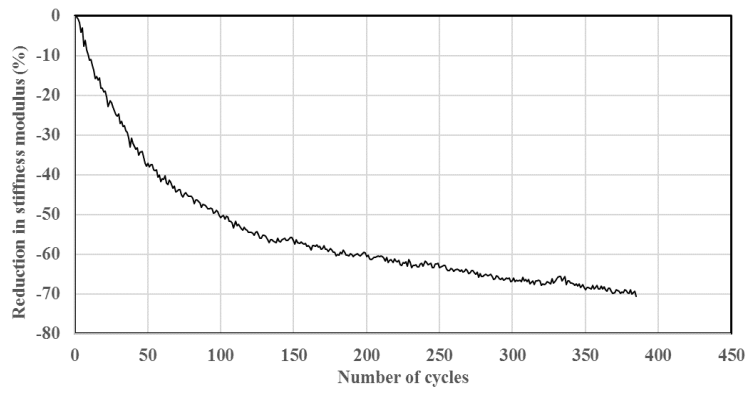
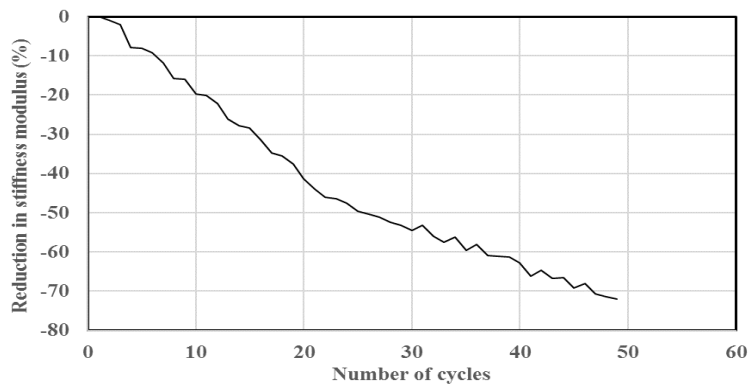


Figure D

### BFNAH5 (III)



### LCNAH10 (I)



### LCNAH10 (II)

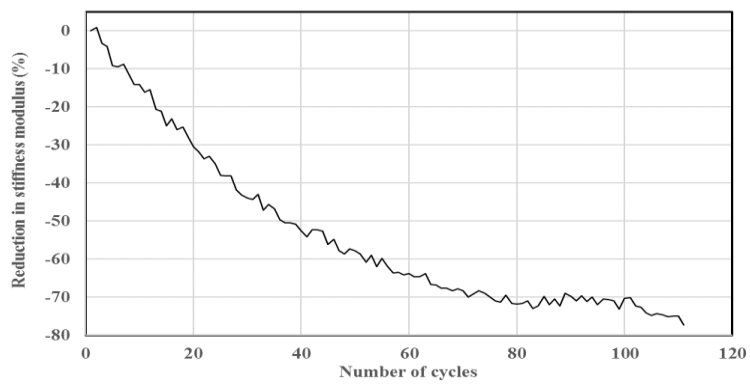
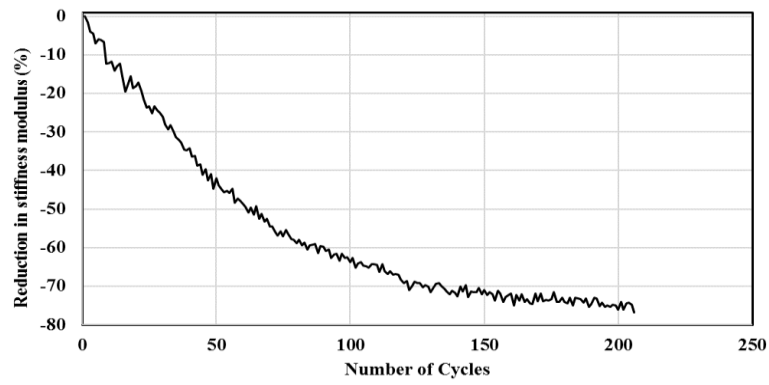
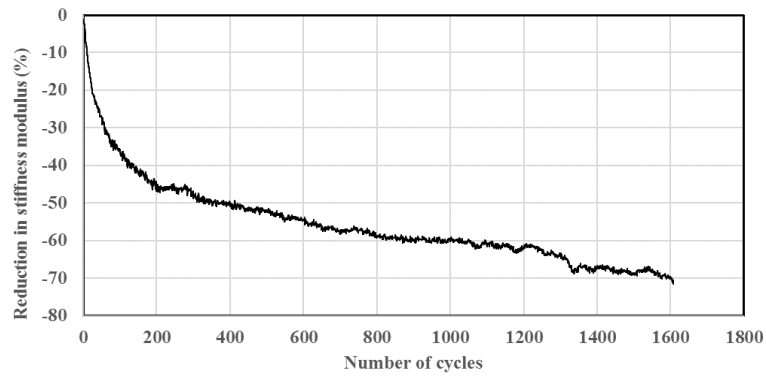


Figure D

### LCNAH10 (III)



### BFMUH0 (I)



### BFMUH0 (II)

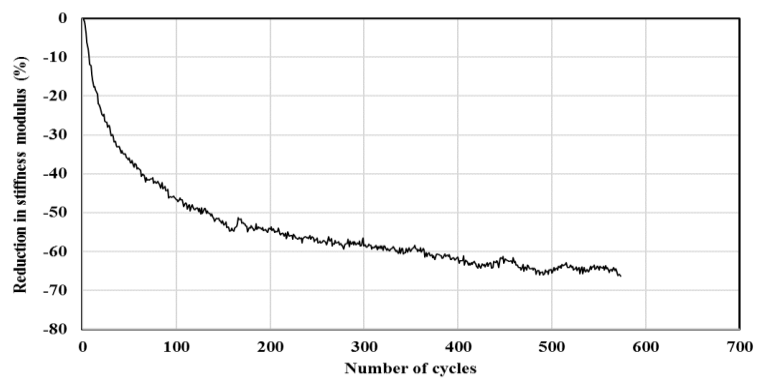
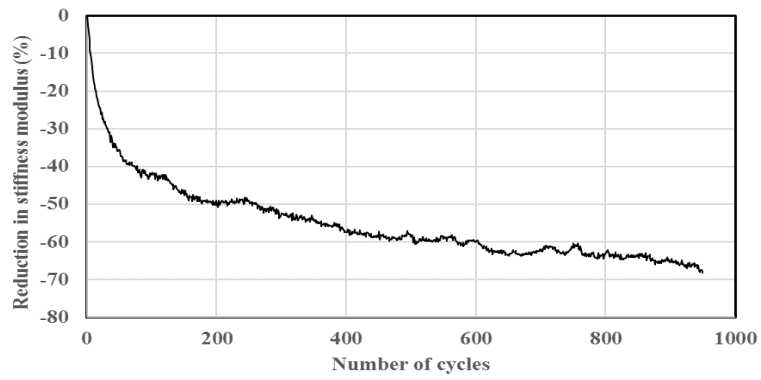
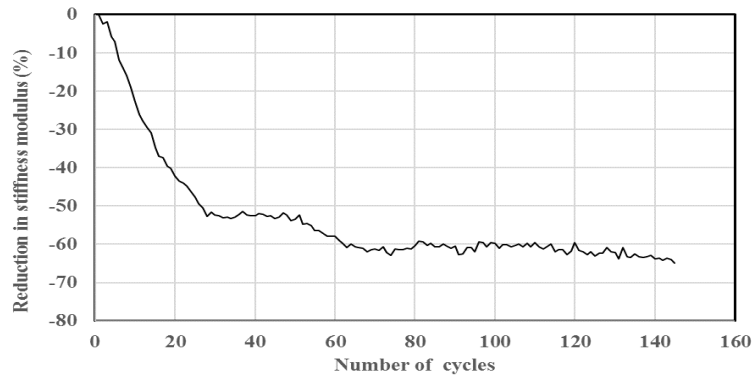


Figure D

### BFMUH0 (III)



### LFMUS0 (I)



### LFMUS0 (II)

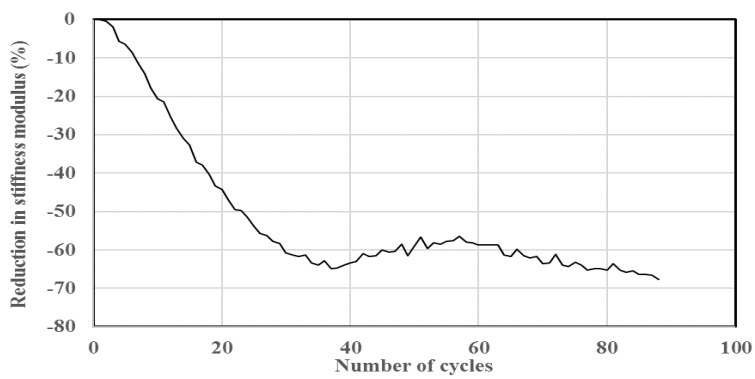
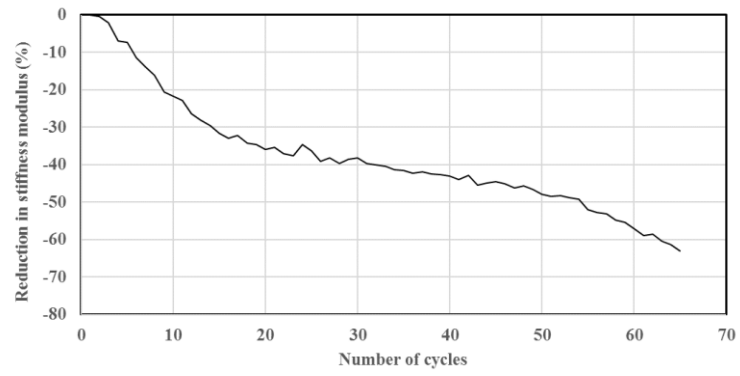


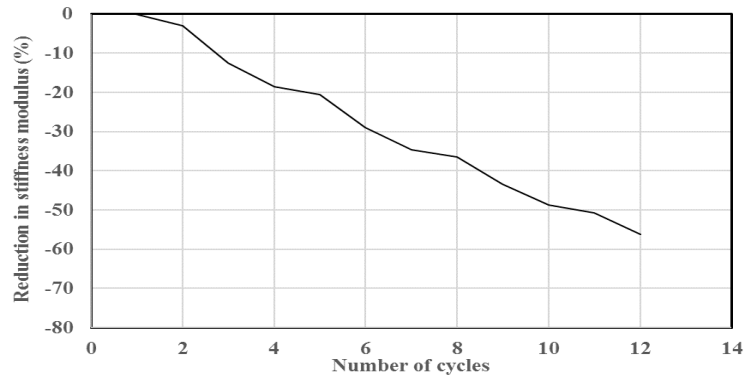
Figure D



### LFMUS0 (III)



### BCNAS0 (I)



### BCNAS0 (II)

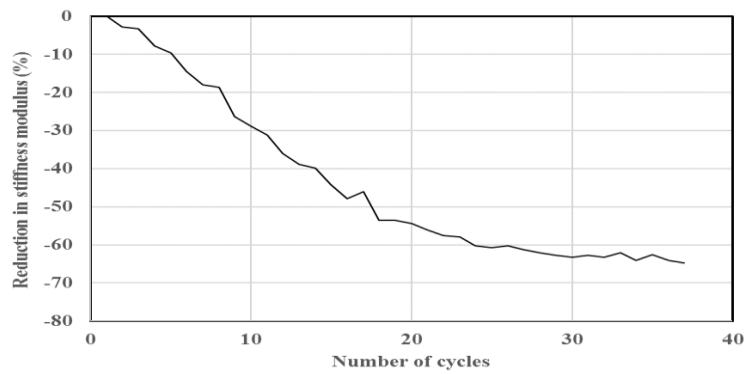
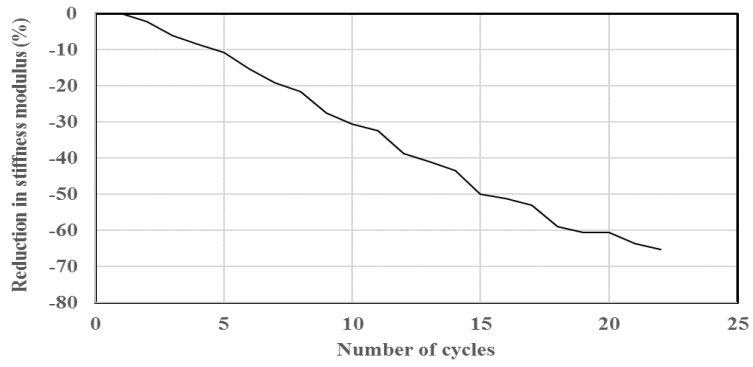
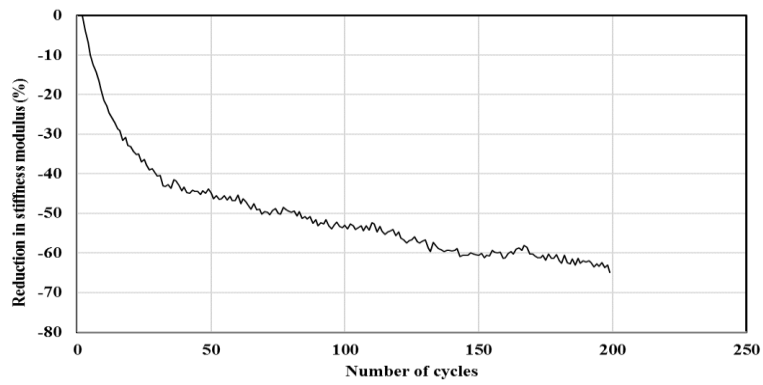


Figure D

### BCNAS0 (III)



### BCMUS5 (I)



### BCMUS5 (II)

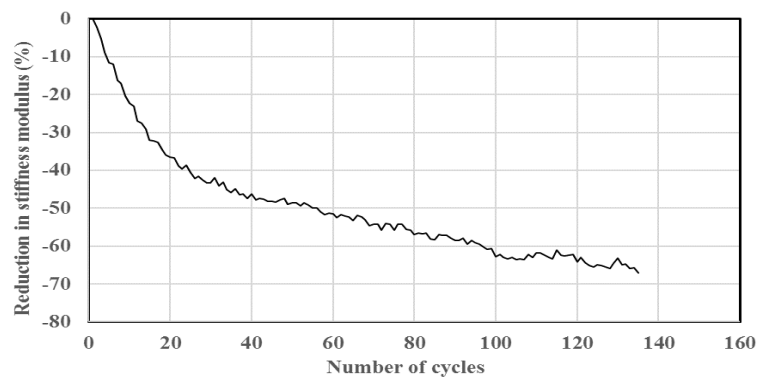
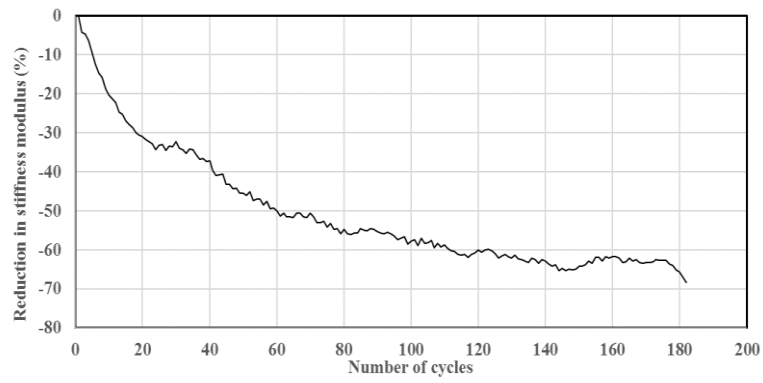
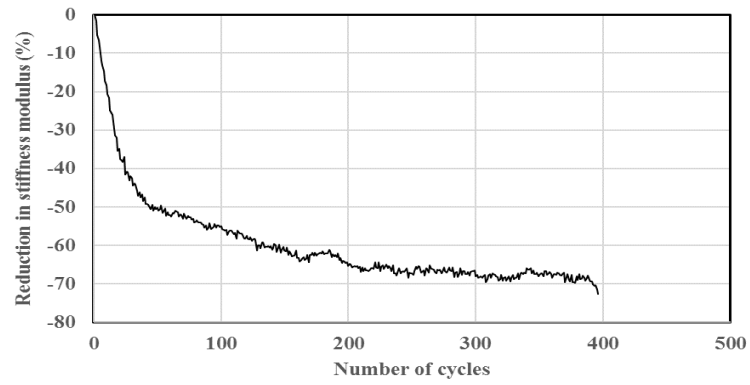


Figure D

### BCMUS5 (III)



### LCMUH0 (I)



### LCMUH0 (II)

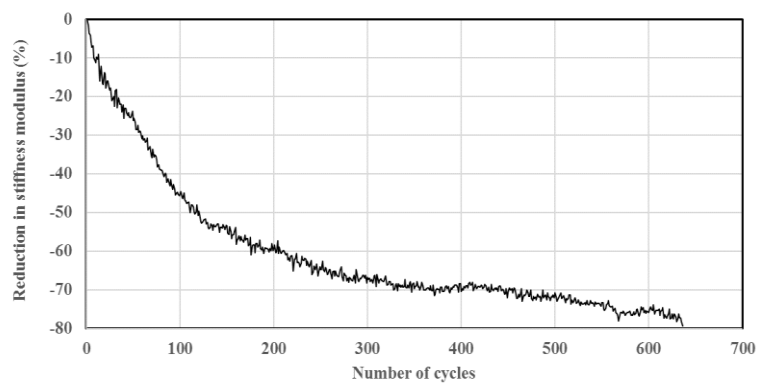
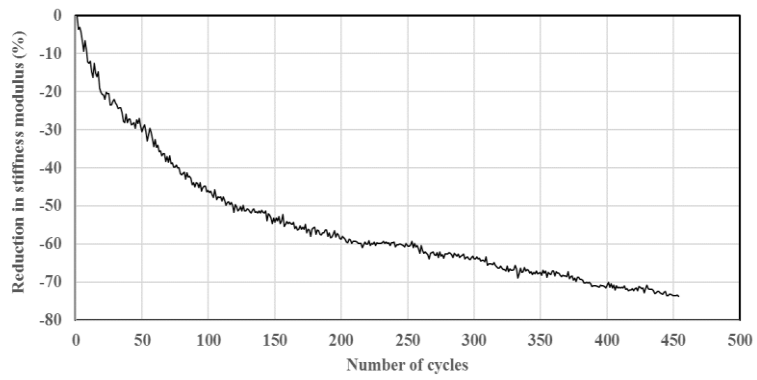
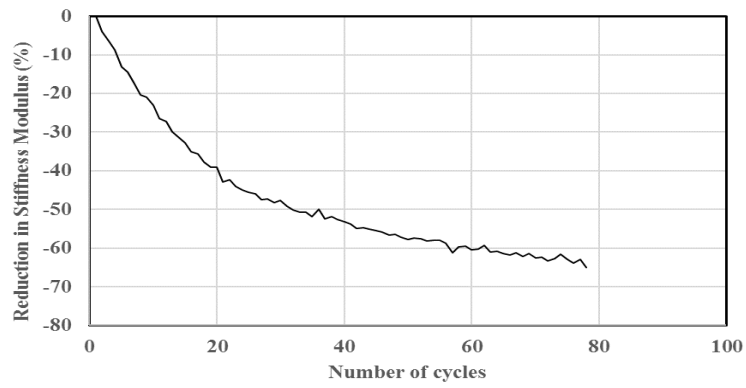


Figure D

### LCMUH0 (III)



### BFNUH0 (I)



### BFNUH0 (II)

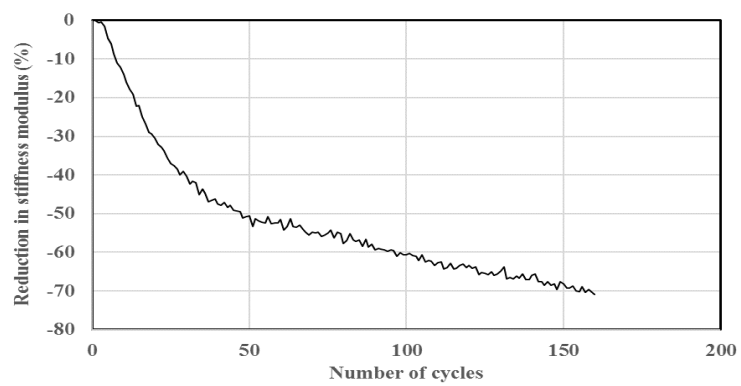
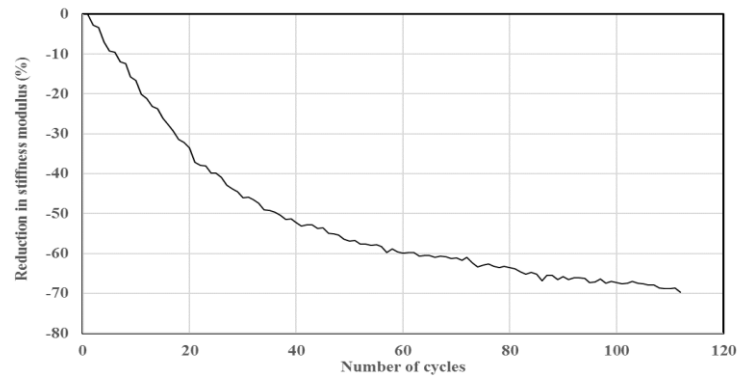
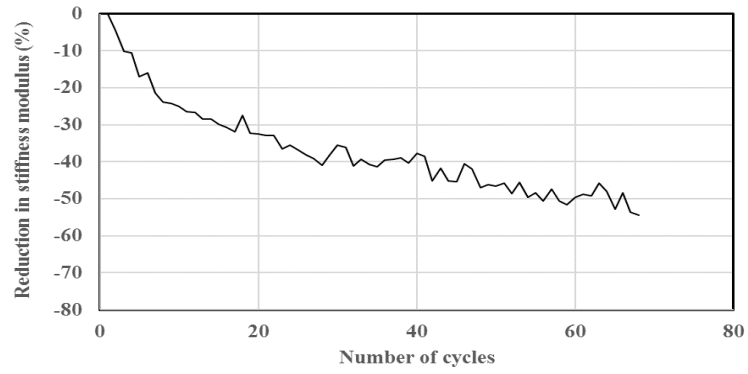


**Figure D**

### BFNUH0 (III)



### LFMUS10 (I)



### LFMUS10 (II)

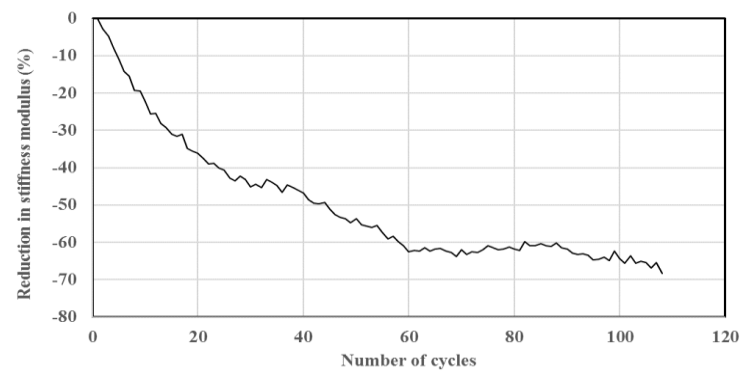
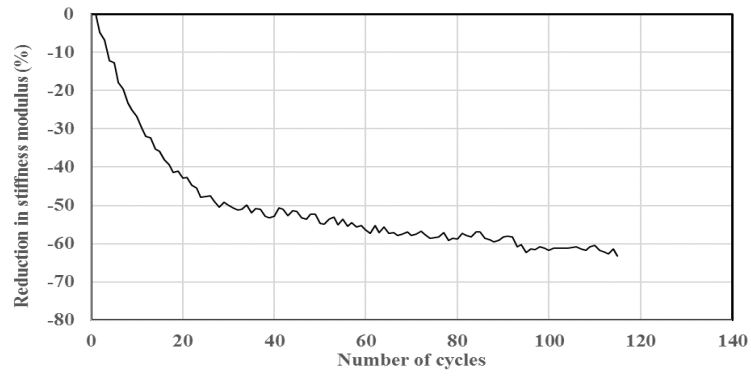
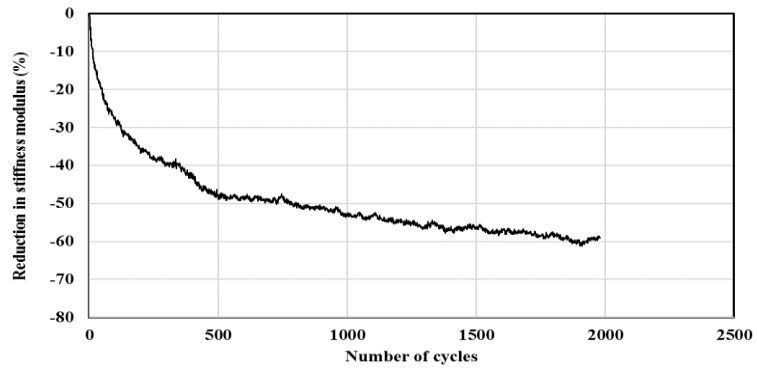


Figure D

### LFMUS10 (III)



### BFMUH10 (I)



### BFMUH10 (II)

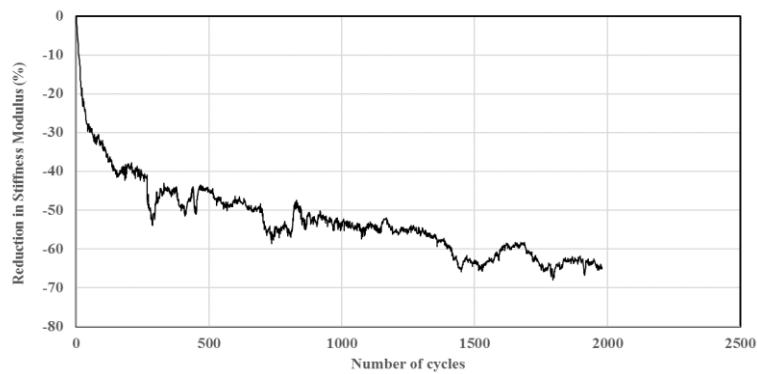
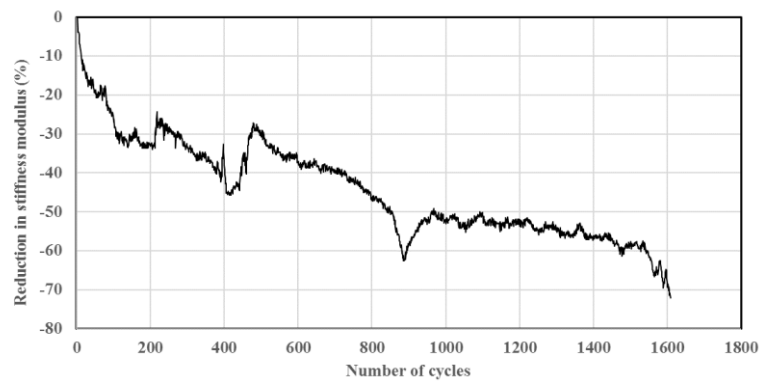
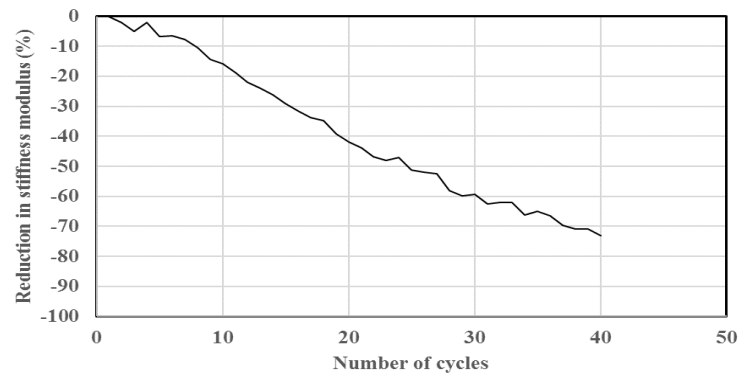


Figure D

### BFMUH10 (III)



### LCNUH0 (I)



### LCNUH0 (II)

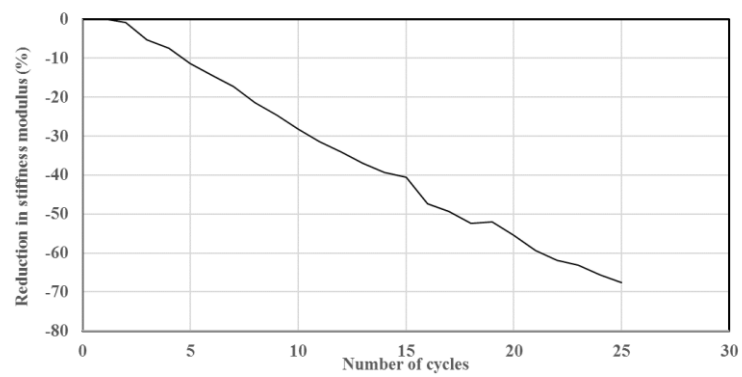
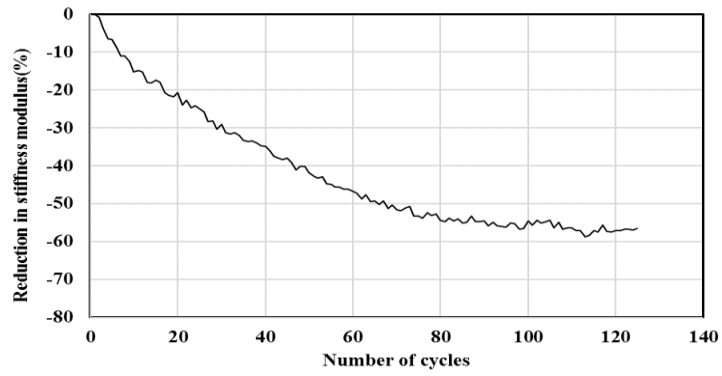


**Figure D**

### LCNUH0 (III)



### LFMAS10 (I)



### LFMAS10 (II)

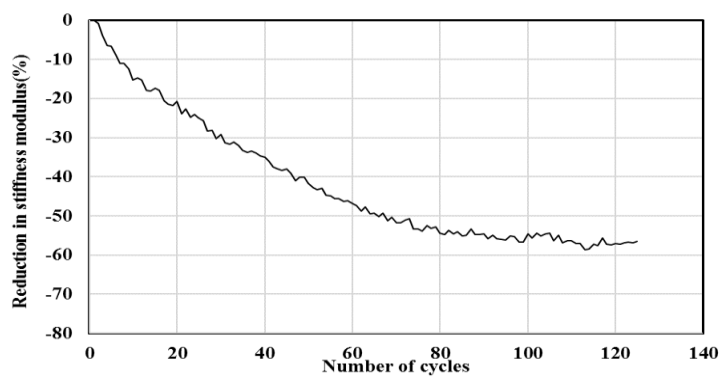
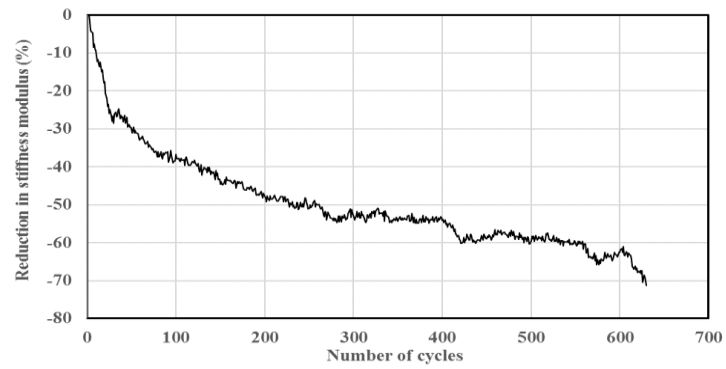


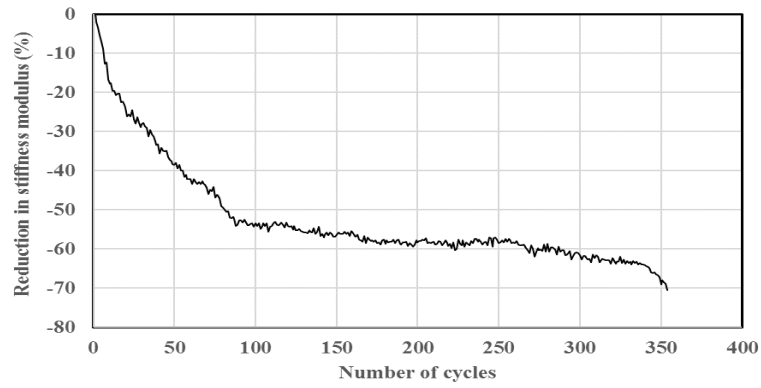
Figure D



### LFMAS10 (III)



### LFMAS5 (I)



### LFMAS5 (II)

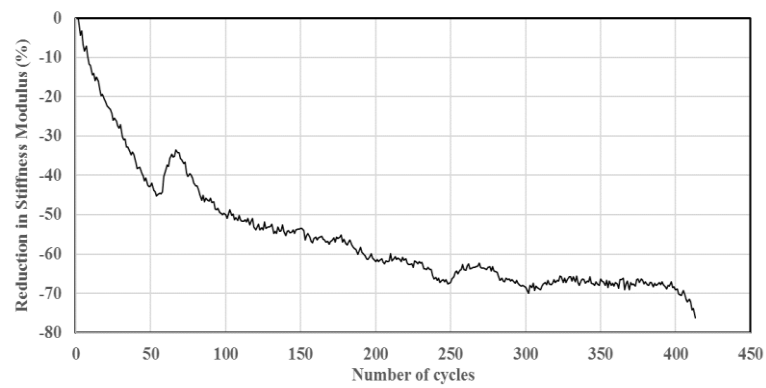
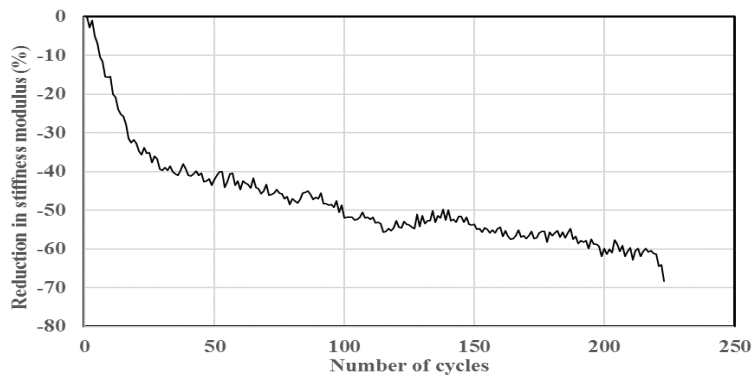
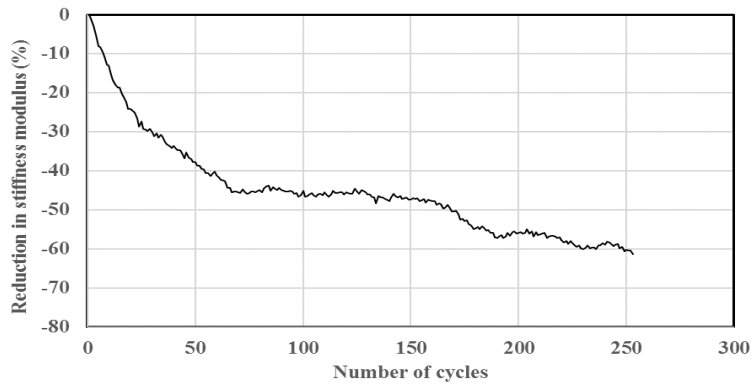


**Figure D**

### LFMAS5 (III)



### BCMAS0 (I)



### BCMAS0 (II)

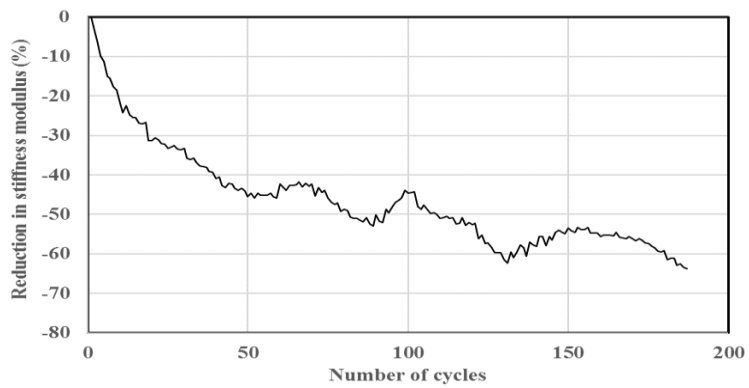
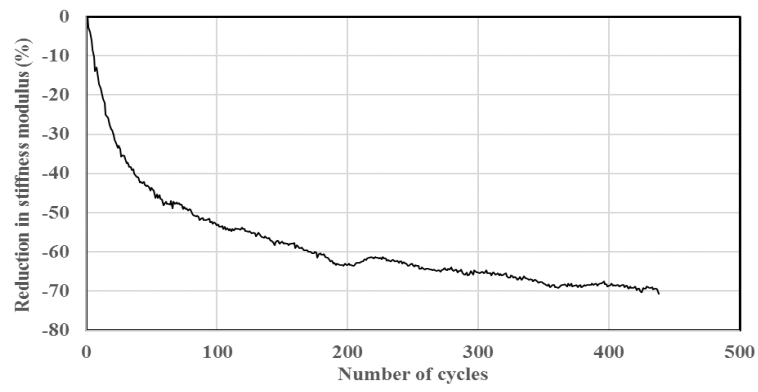
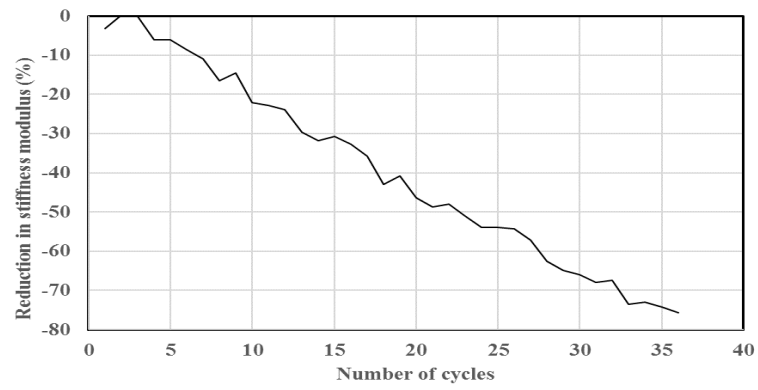


Figure D

### BCMAS0 (III)



### LFNAS5 (I)



### LFNAS5 (II)

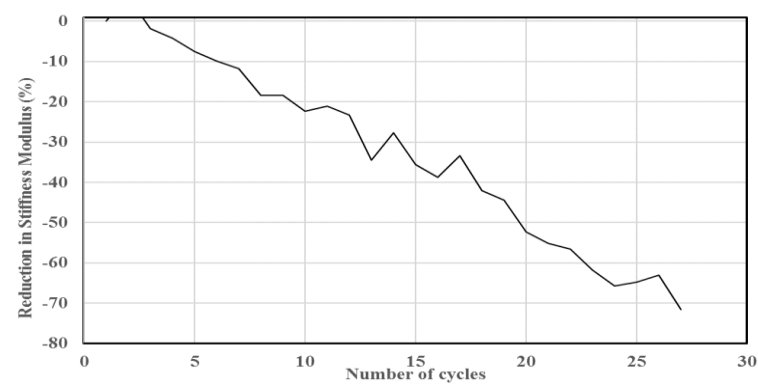
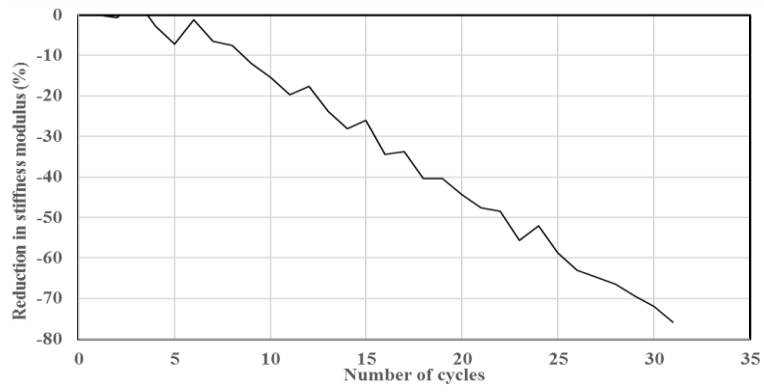
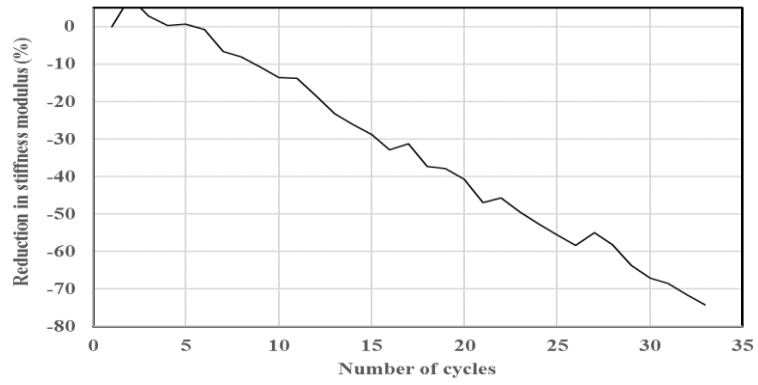


**Figure D**

**LFNAS5 (III)**



**LFNAS10 (I)**



**LFNAS10 (II)**

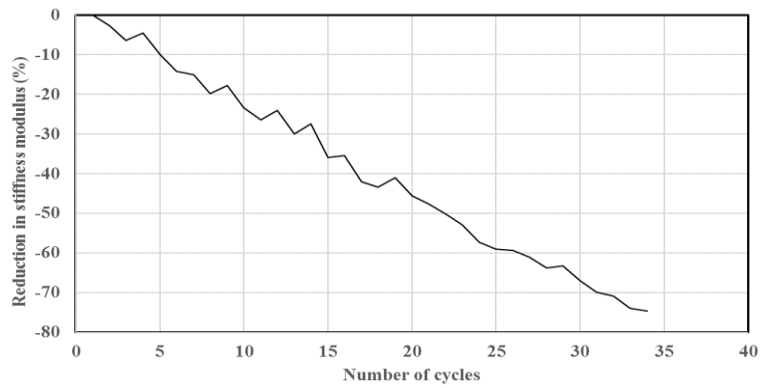
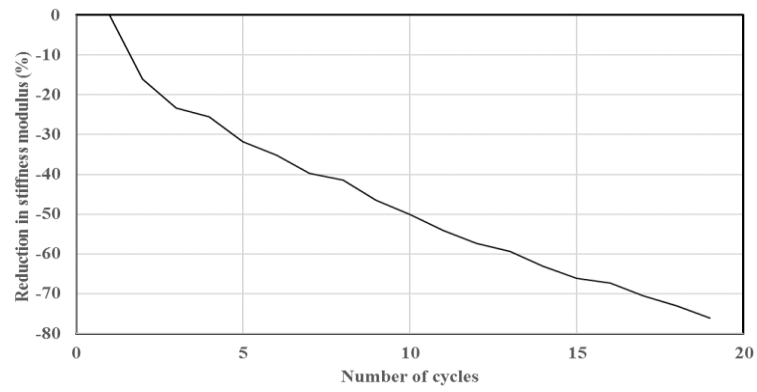
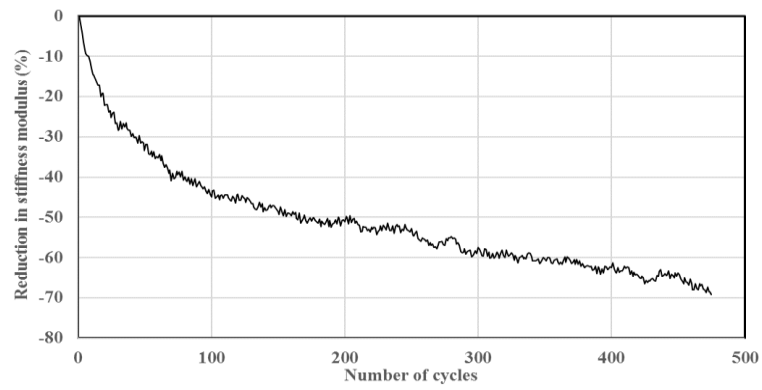


**Figure D**

### LFNAS10 (III)



### LCMAH5 (I)



### LCMAH5 (II)

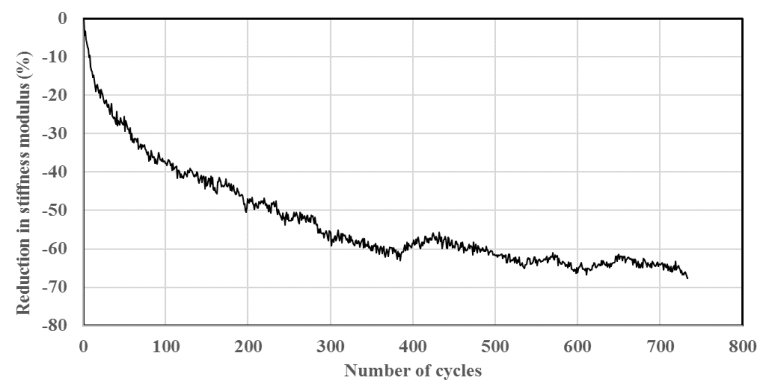


**Figure D**

### LCMAH5 (III)

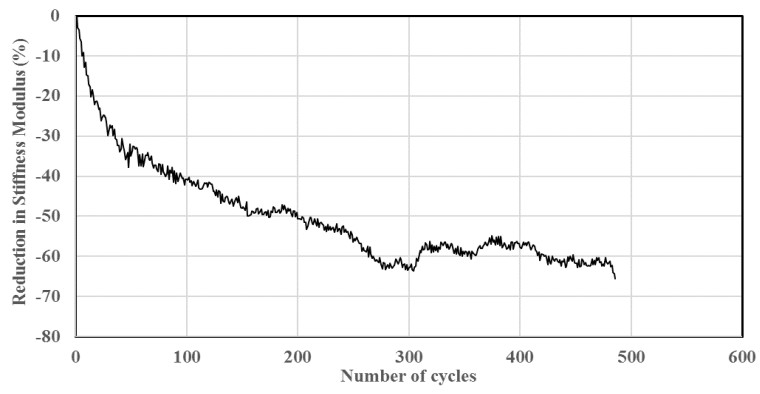
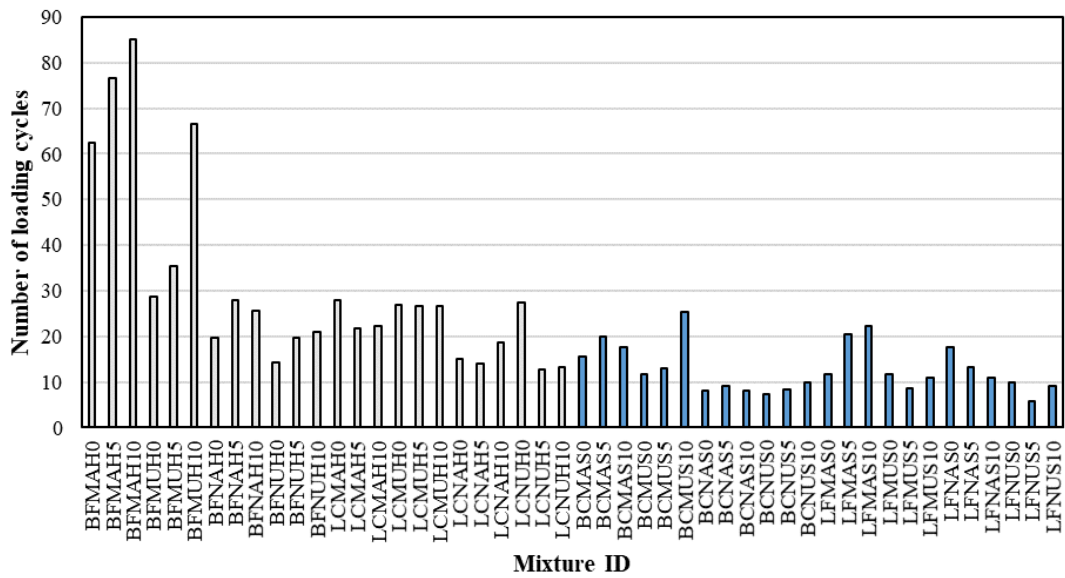
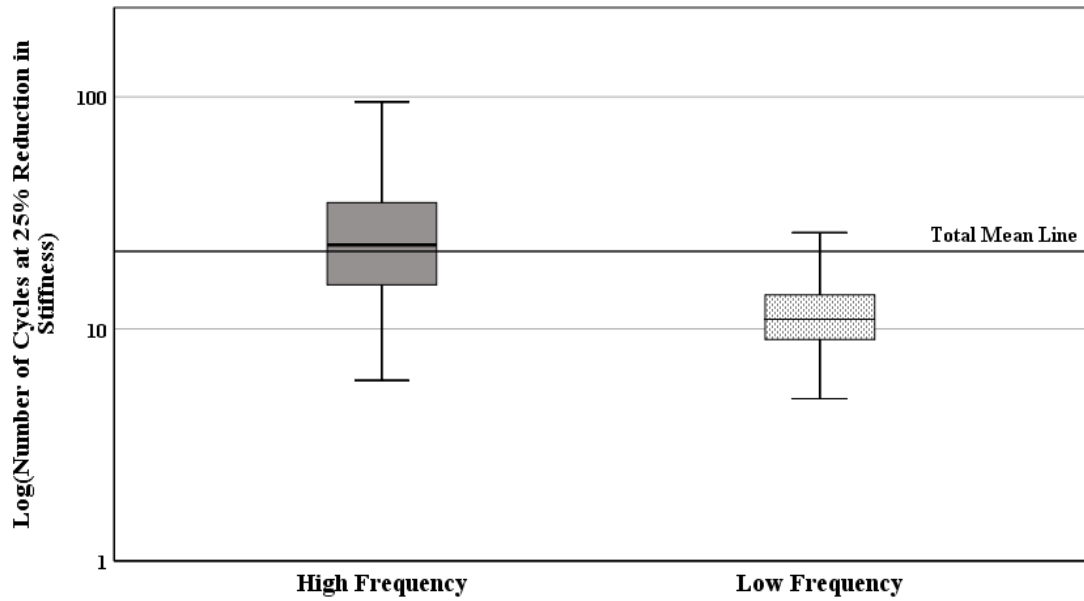


Figure D

**E. Bar charts and boxplots for cycle number at %25 reduced stiffness level (144 specimens)**



**Figure E. 1.** The average number of loading cycles for different mixtures at 25% reduced stiffness grouped based on loading frequency



**Figure E. 2.** Box plot for number of loading cycles at 25% reduced stiffness, grouped based on loading frequency

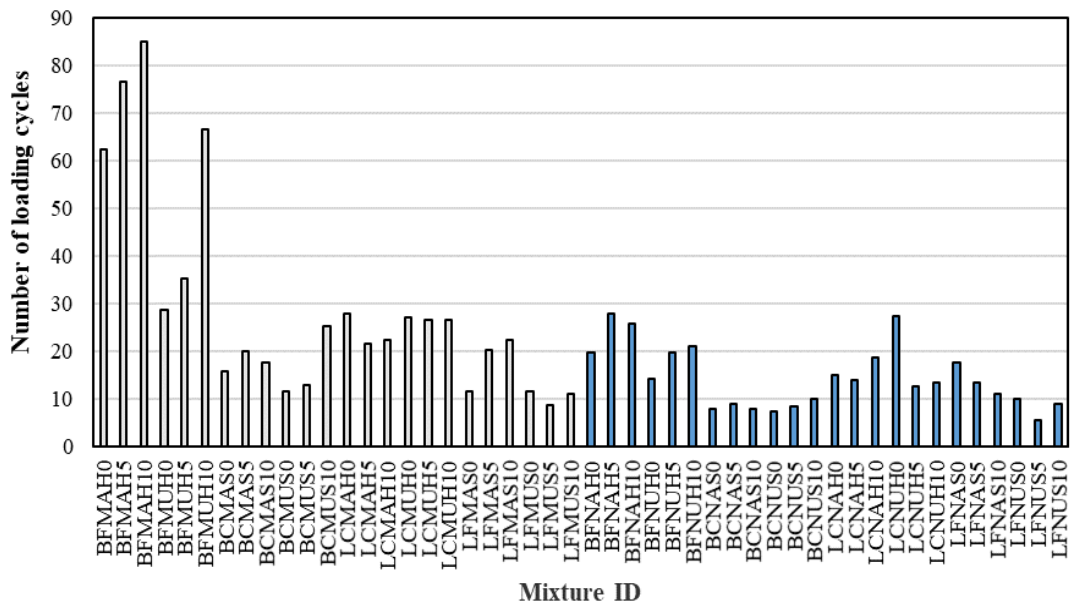


**Figure E. 3.** The average number of loading cycles for different mixtures at 25% reduced stiffness grouped based on asphalt type



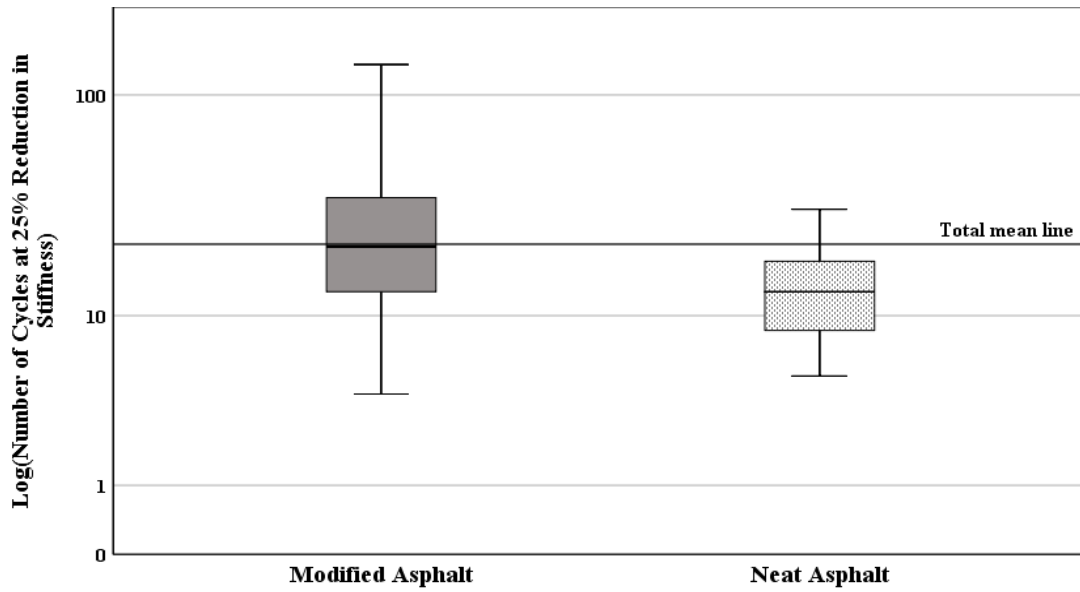


**Figure E. 4.** Box plot for number of loading cycles at 25% reduced stiffness, grouped based on asphalt type

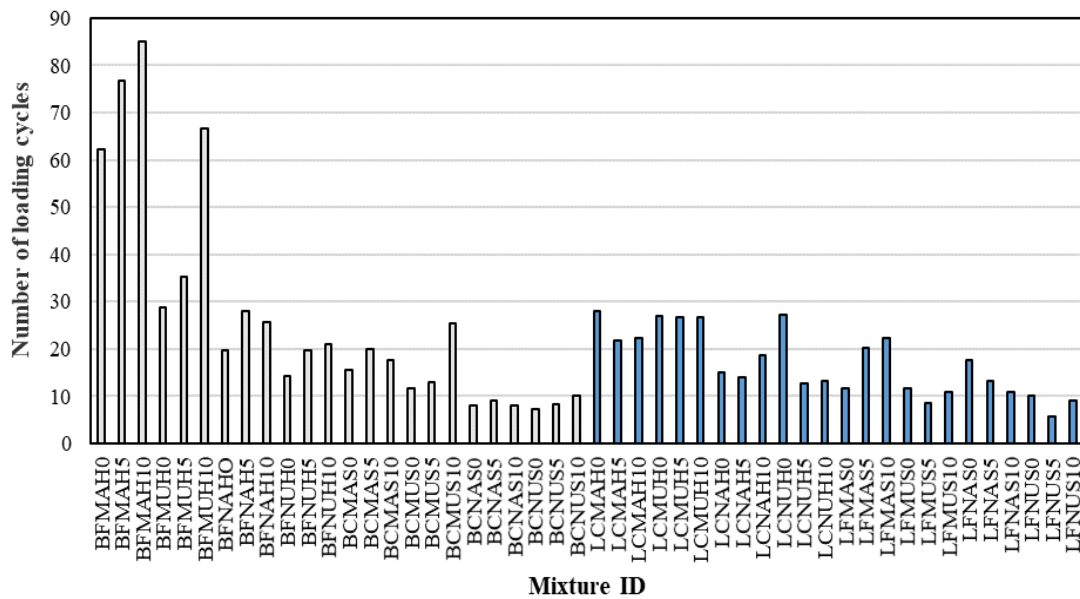


**Figure E. 5.** The average number of loading cycles for different mixtures at 25% reduced stiffness grouped based on aggregate type

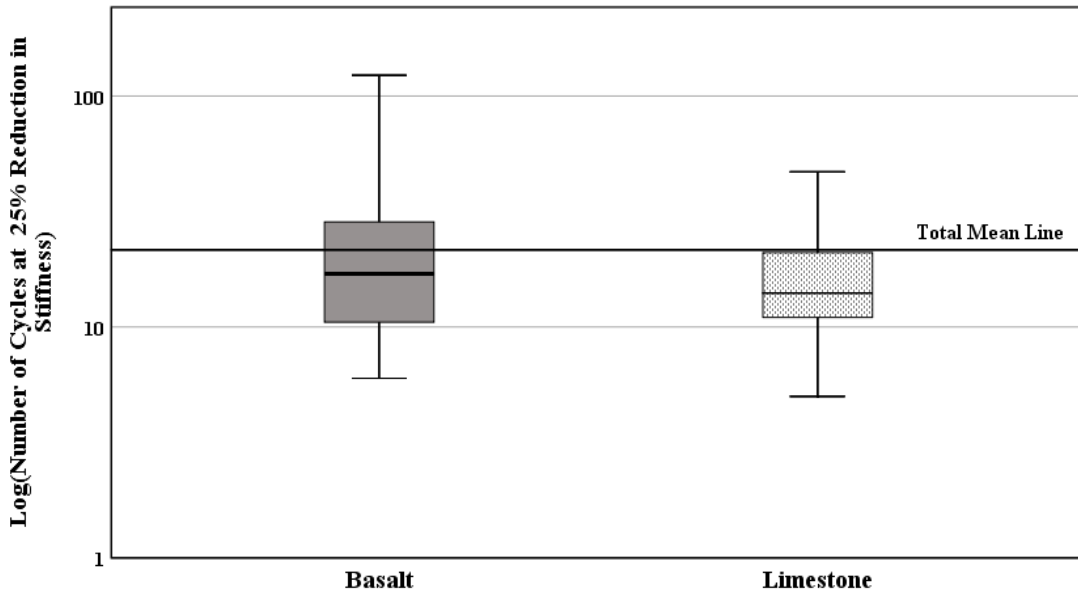


**Figure E. 6.** Box plot for number of loading cycles at 25% reduced stiffness, grouped based on aggregate type

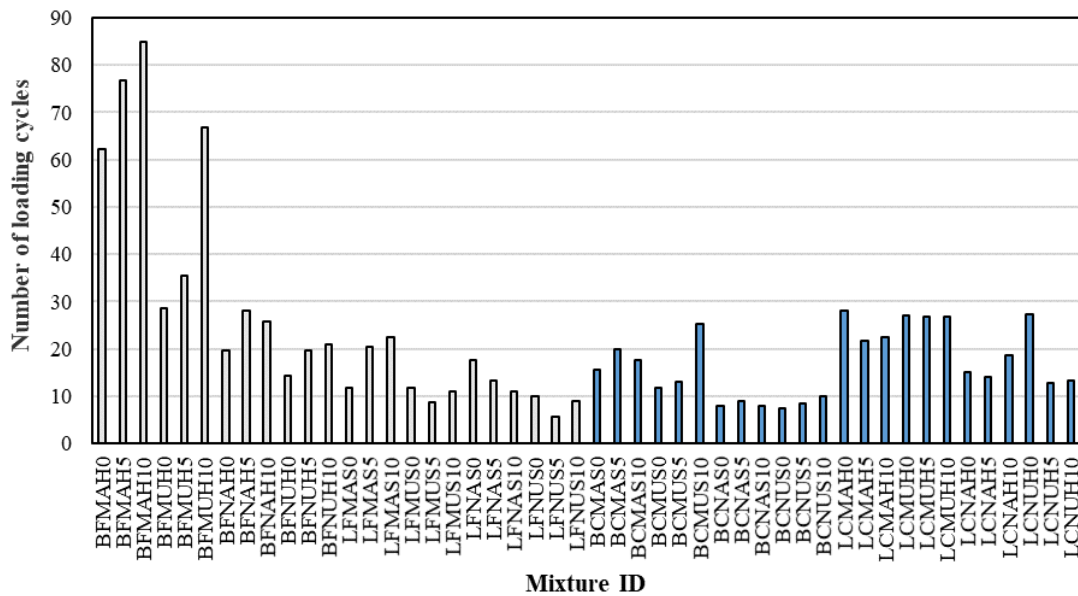


**Figure E. 7.** The average number of loading cycles for different mixtures at 25% reduced stiffness grouped based on gradation

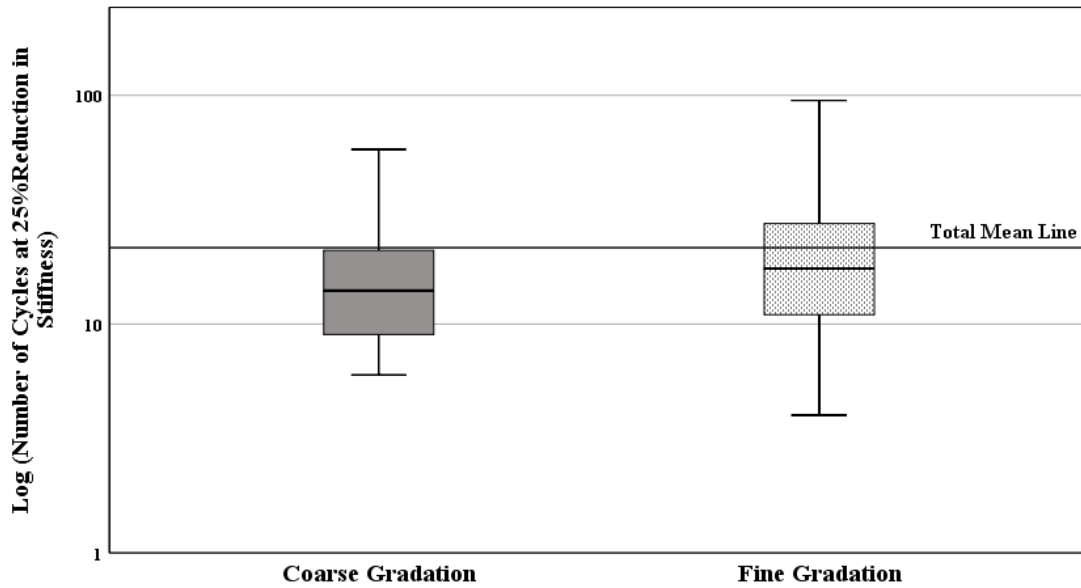


**Figure E. 8.** Box plot for number of loading cycles at 25% reduced stiffness, grouped based on gradation

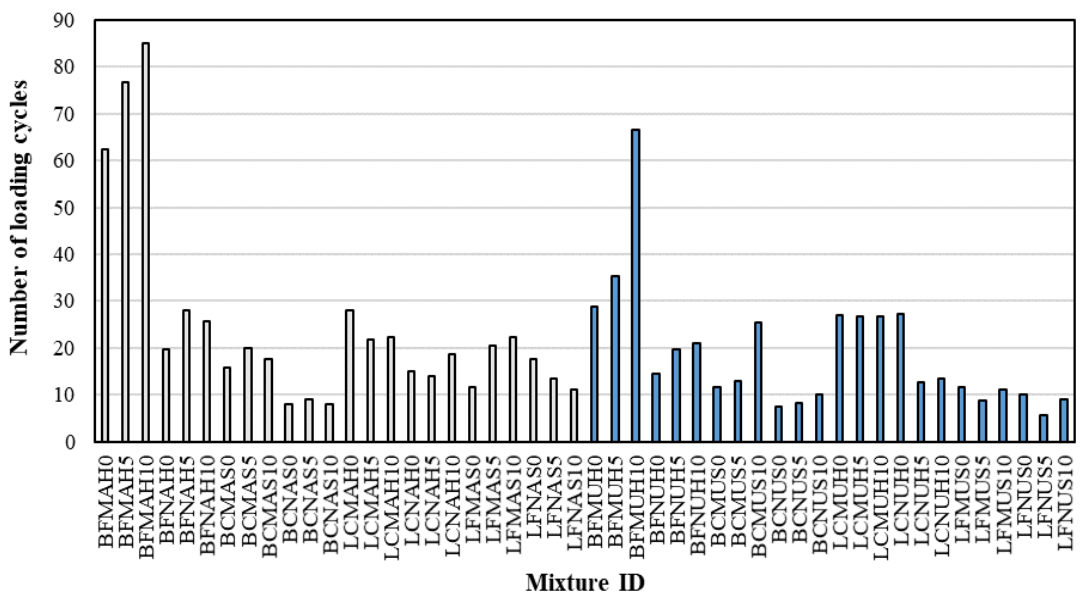


**Figure E. 9.** The average number of loading cycles for different mixtures @25% reduced stiffness, grouped based on asphalt binder aging

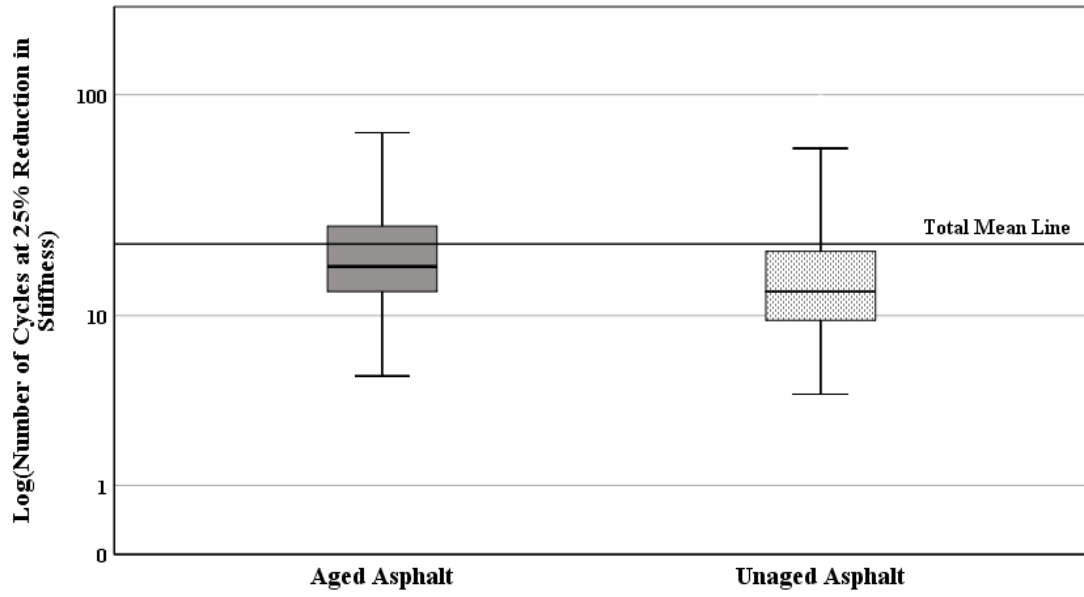


**Figure E. 10.** Box plot for number of loading cycles at 25% reduced stiffness grouped based on asphalt binder aging

**F. Bar charts and boxplots for cycle number at %75 reduced stiffness level (144 specimens)**

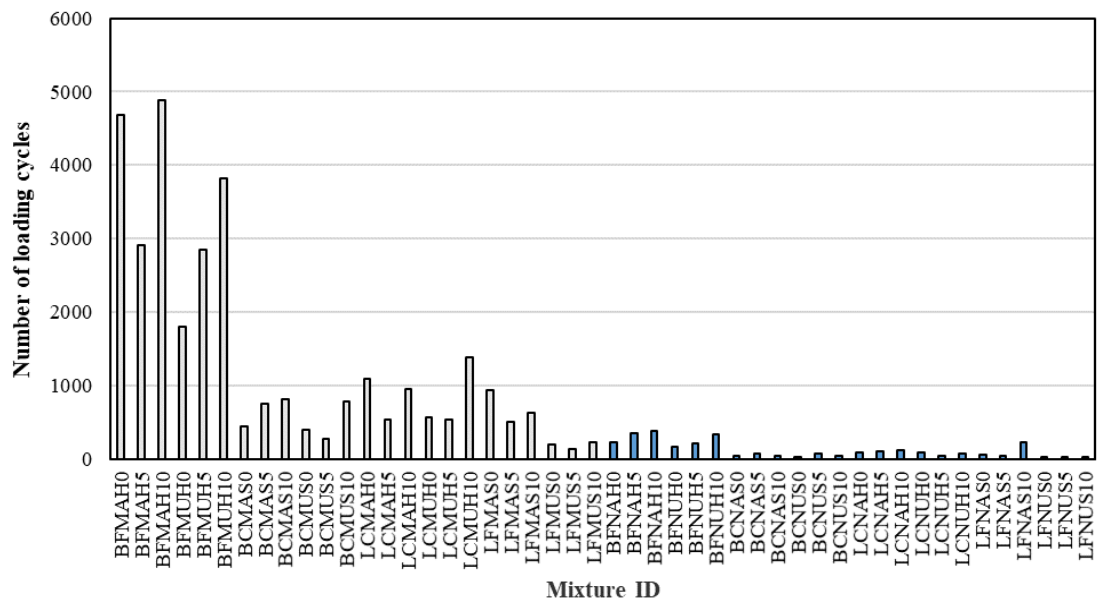


**Figure F. 1.** The average number of loading cycles for different mixtures @75% reduced stiffness, grouped based on the asphalt type

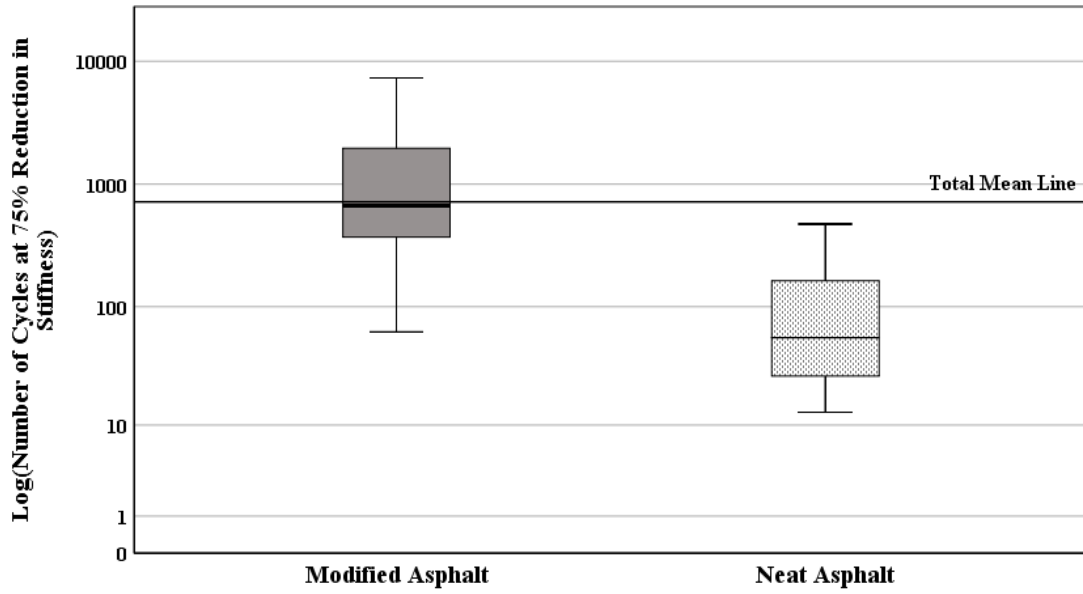


**Figure F. 2.** Box plot for number of loading cycles at 75% reduced stiffness, grouped based on asphalt type

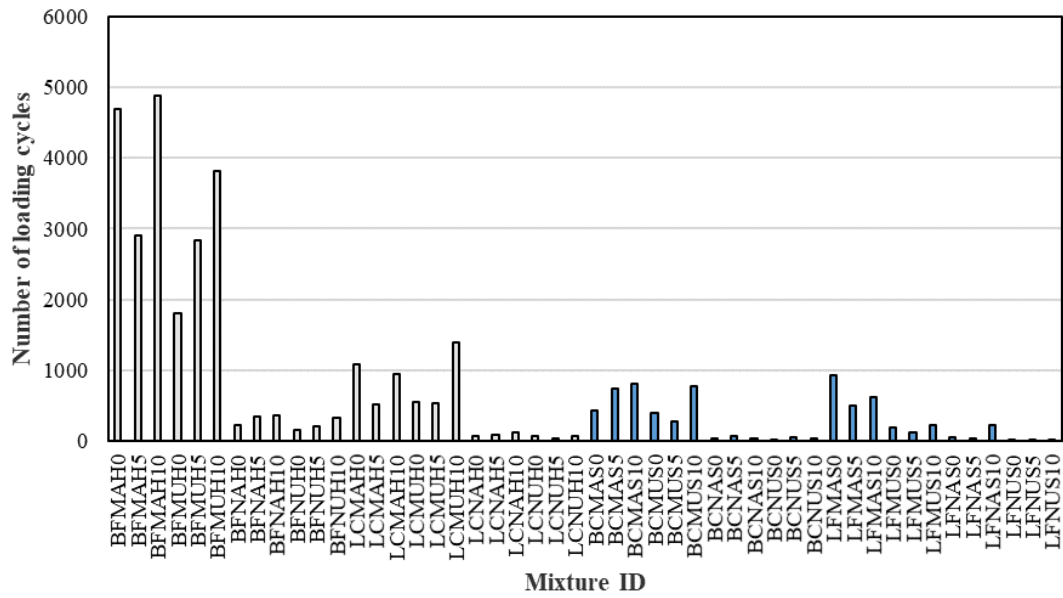


**Figure F. 3.** The average number of loading cycles at 75% reduced stiffness, grouped based on loading frequency

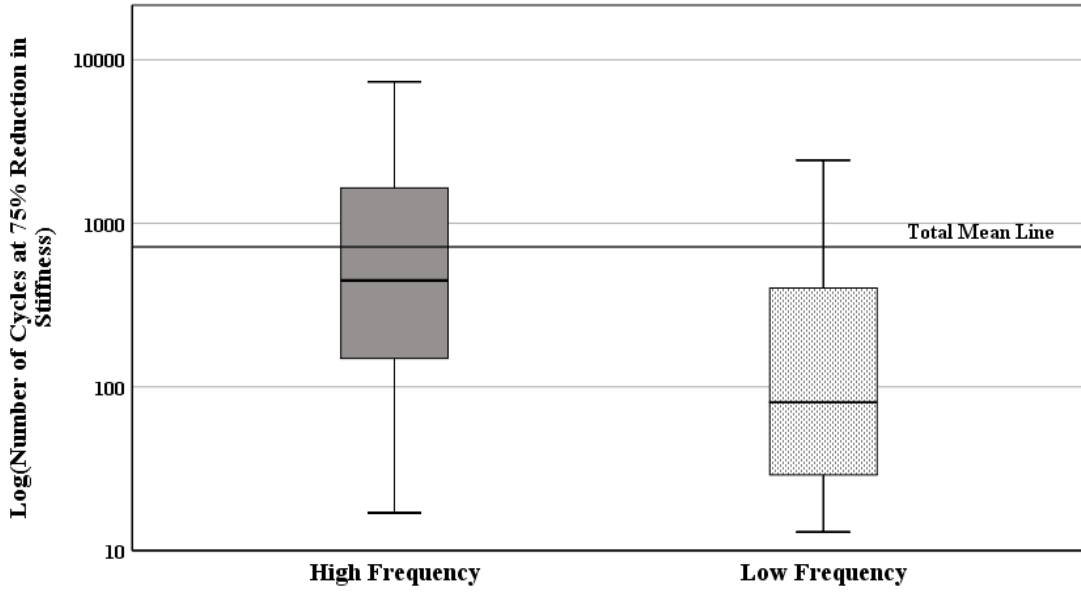


**Figure F. 4.** Box plot for number of loading cycles at 75% reduced stiffness, grouped based on loading frequency

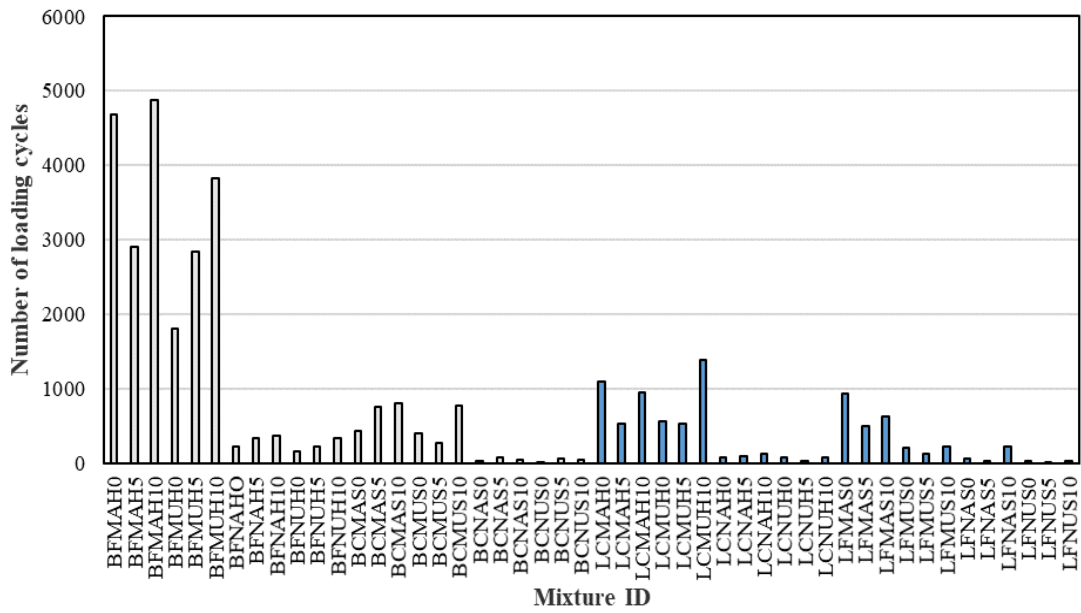


**Figure F. 5.** The average number of loading cycles at 75% reduced stiffness, grouped based on aggregate type

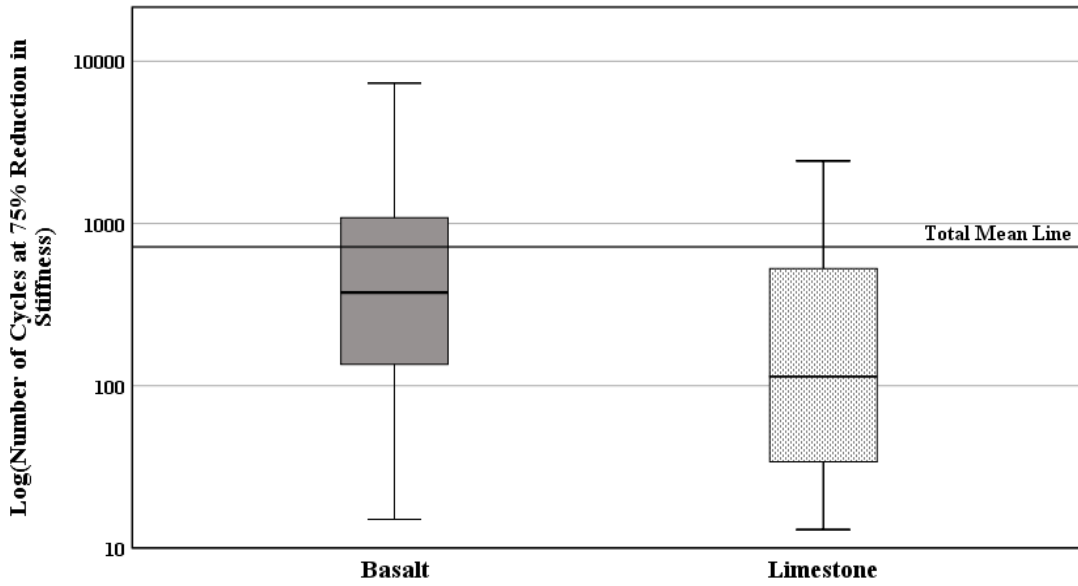


**Figure F. 6.** Box plot for number of loading cycles at 75% reduced stiffness, grouped based on aggregate type

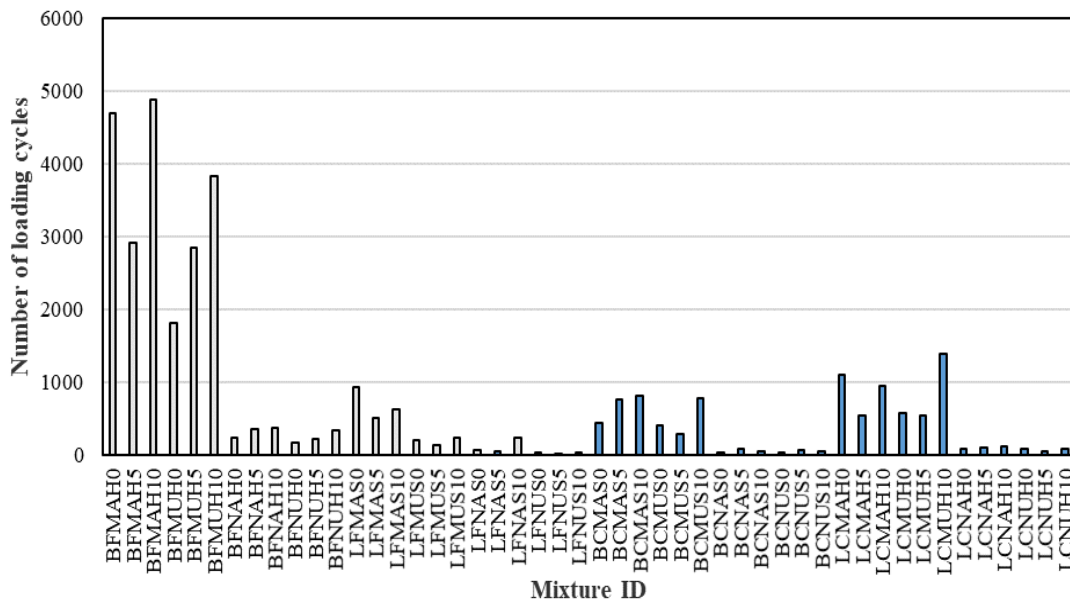


**Figure F. 7.** The average number of loading cycles at 75% reduced stiffness, grouped based on gradation



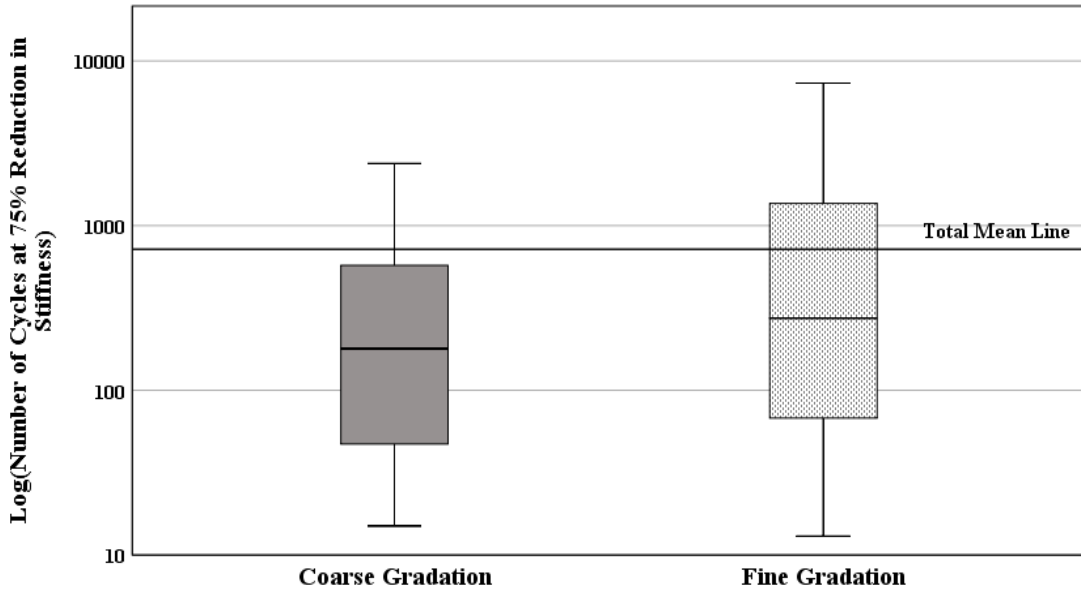


**Figure F. 8.** Box plot for number of loading cycles at 75% reduced stiffness, grouped based on gradation

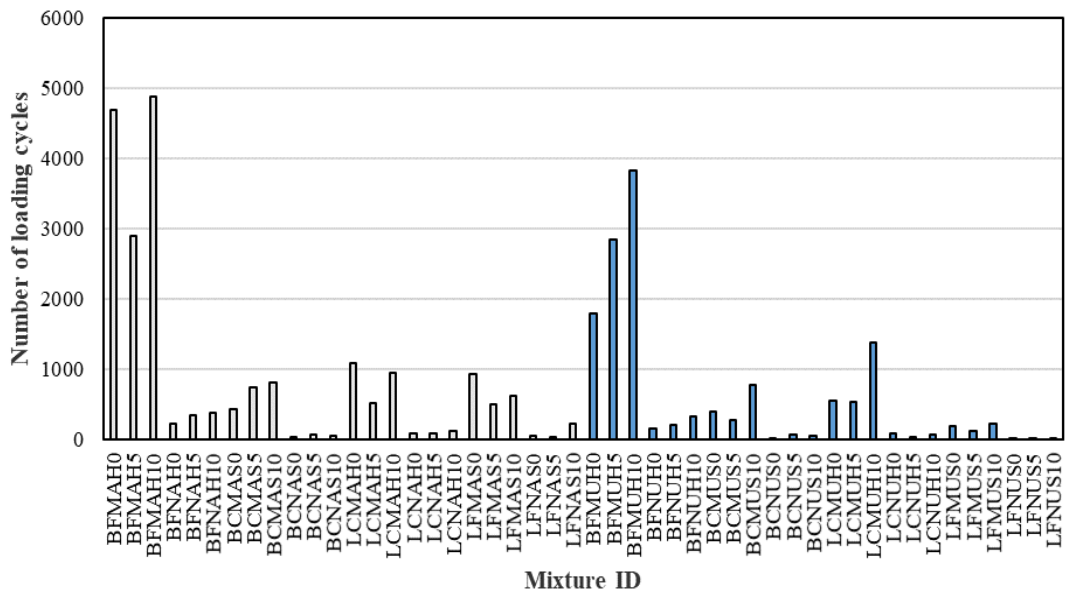


**Figure F. 9.** The average number of loading cycles at 75% reduced stiffness, grouped based on asphalt binder aging

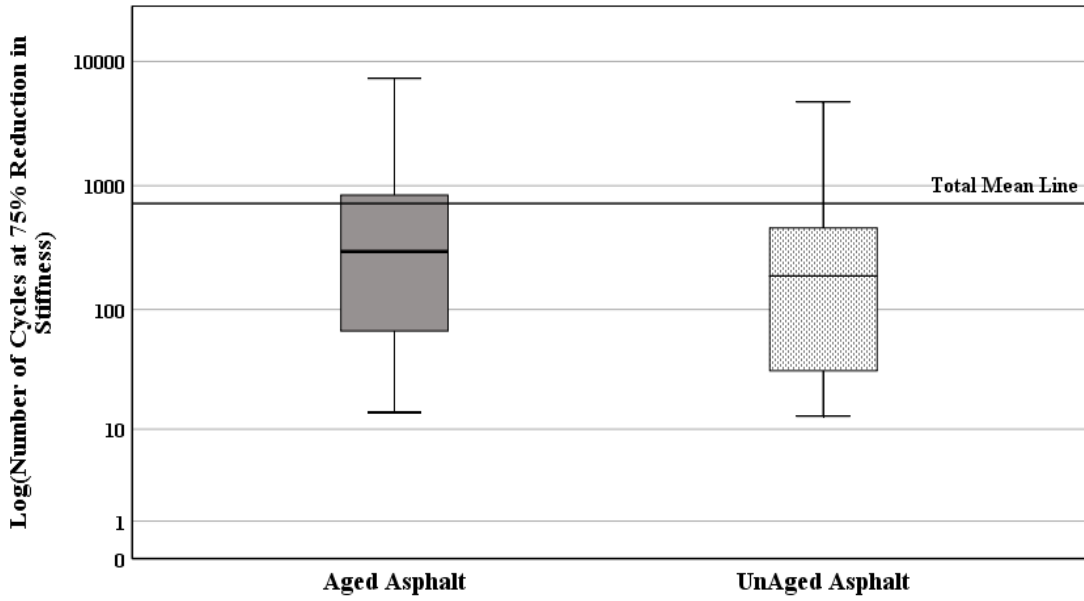


**Figure F. 10.** Box plot for number of loading cycles at 75% reduced stiffness, grouped based on asphalt binder aging

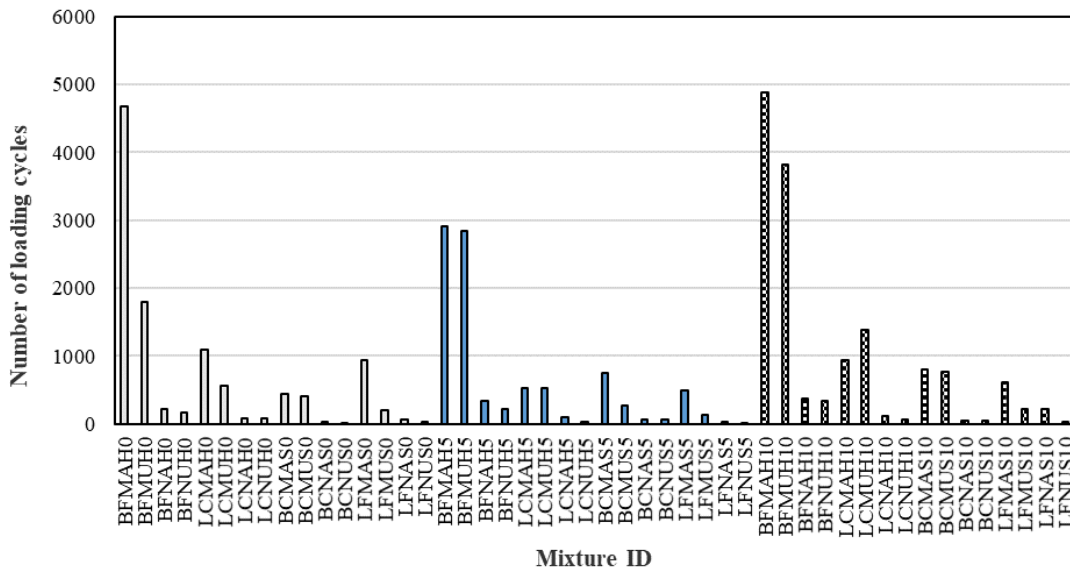


**Figure F. 11.** The average number of loading cycles at 75% reduced stiffness, grouped based on the rest time

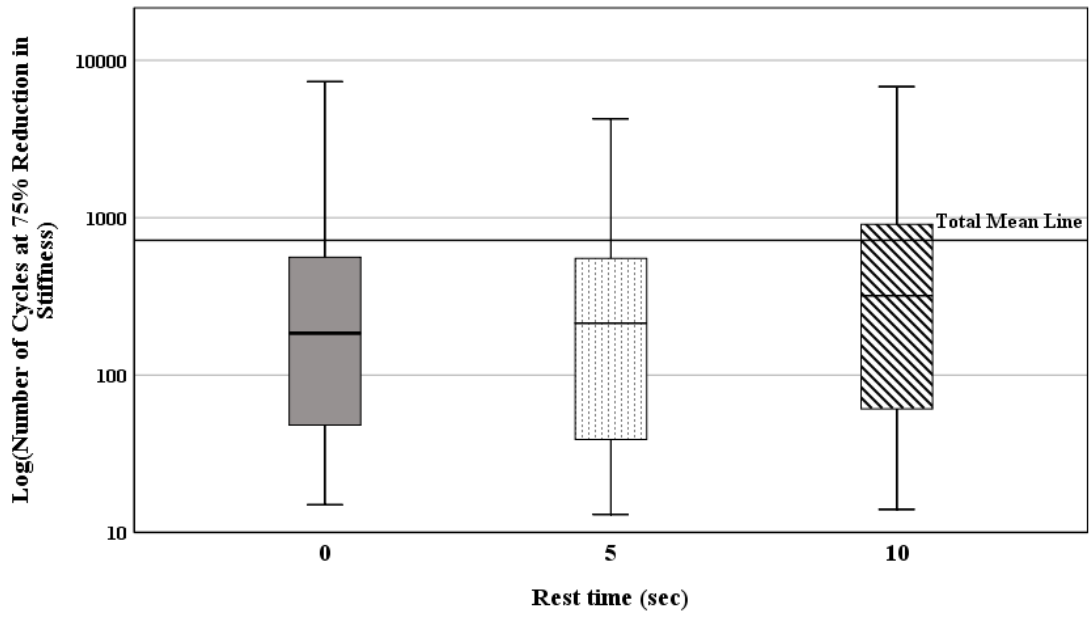
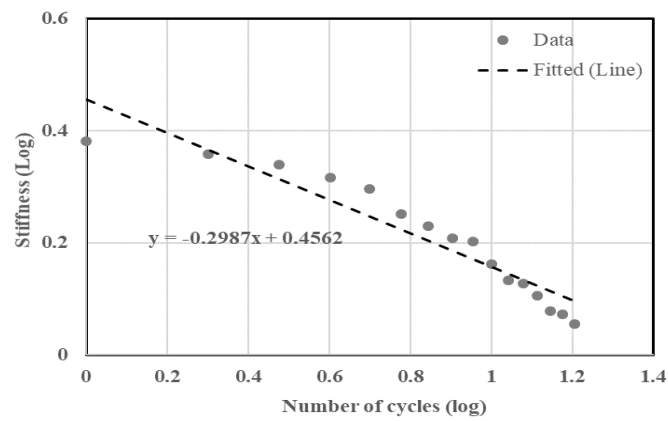


**Figure F. 12.** Box plot for number of loading cycles at 75% reduced stiffness, grouped based on rest time

### G. Stiffness reduction ratio calculated from bottom surface of the specimens

#### BCNAS10 (I)



#### BCNAS10 (II)

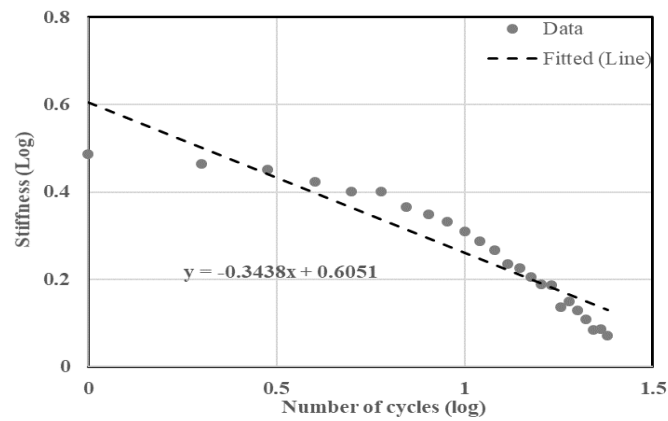
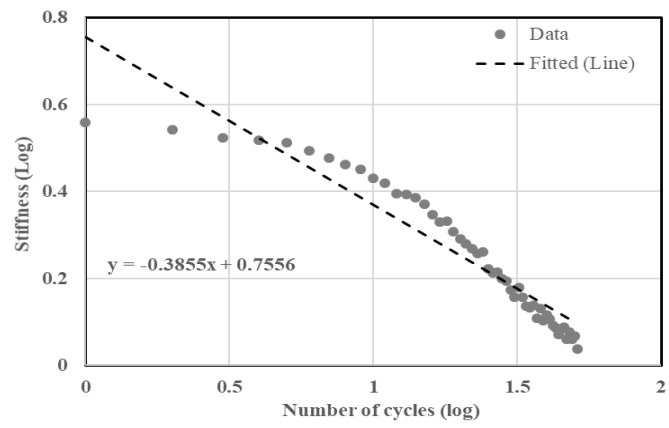
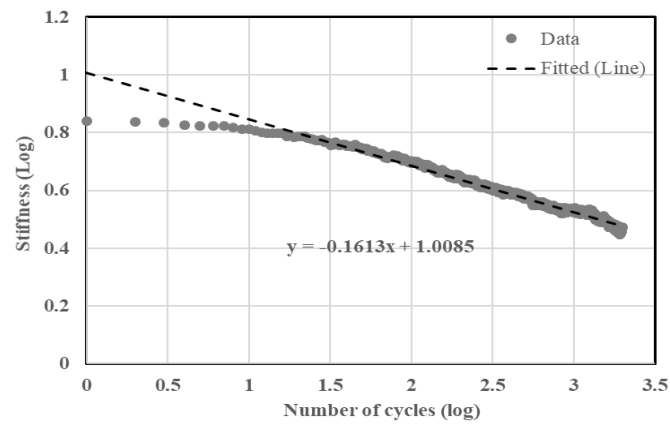


Figure G. Stiffness versus cycle number for specimens in the logarithmic scale

### BCNAS10 (III)



### BFMAH10 (I)



### BFMAH10 (II)

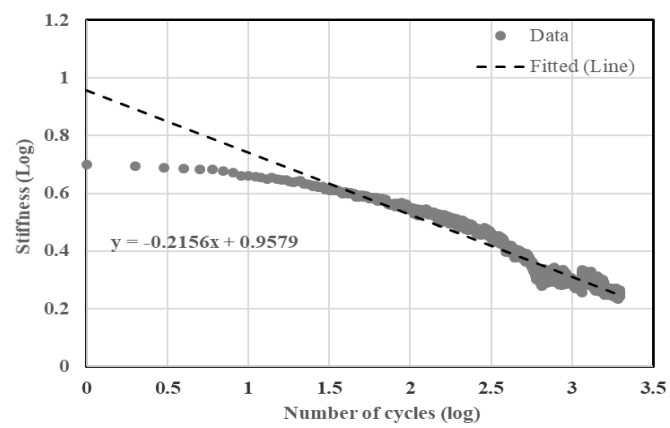
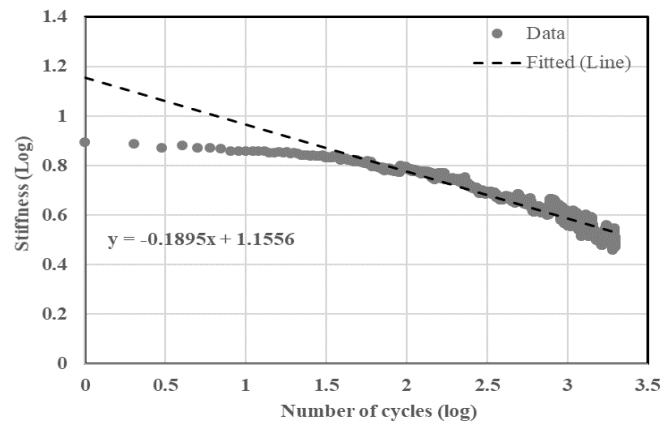
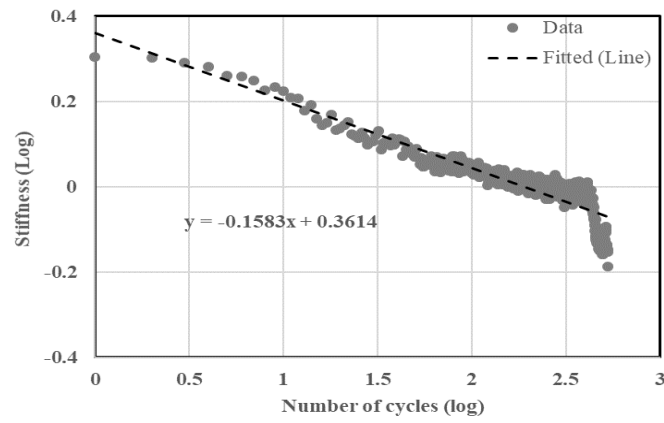


Figure G

### BFMAH10 (III)



### LCMUH10 (I)



### LCMUH10 (II)

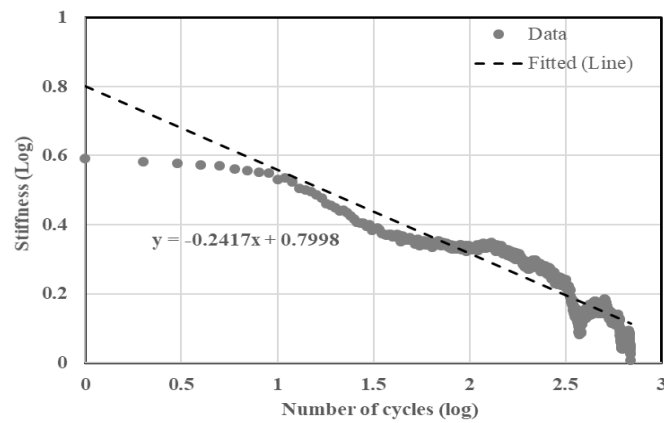
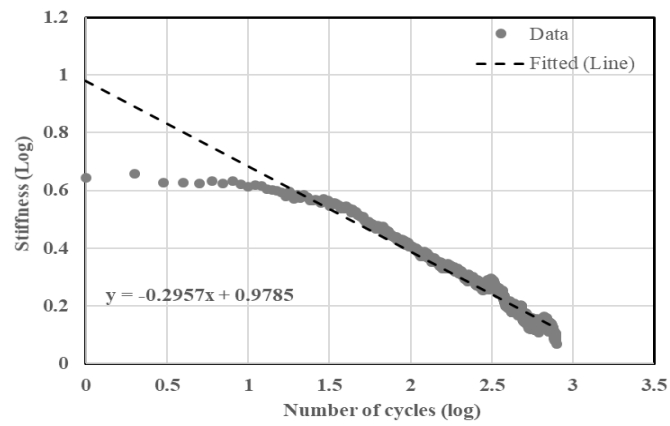
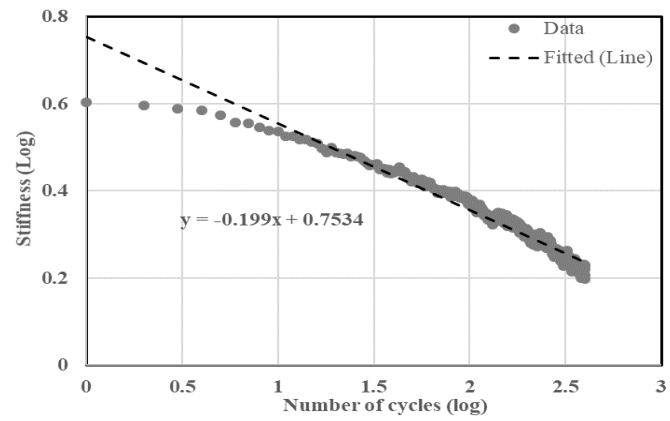


Figure G

### LCMUH10 (III)



### LCMAH0 (I)



### LCMAH0 (II)

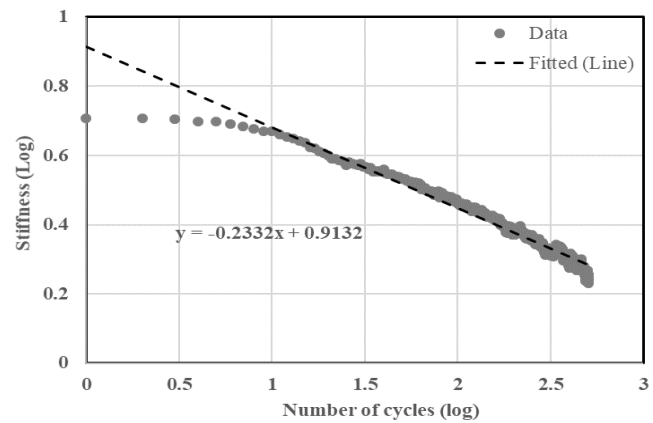
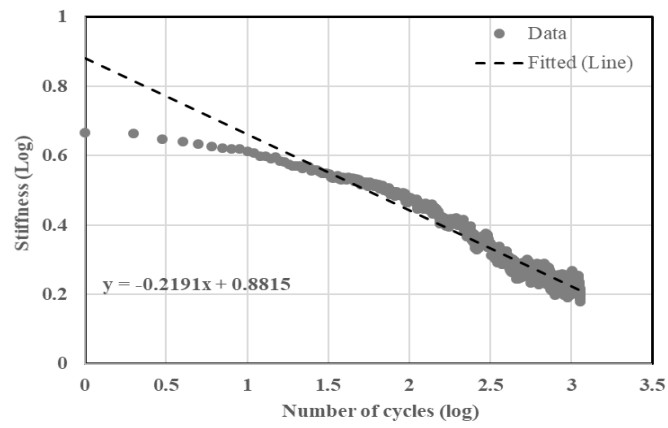
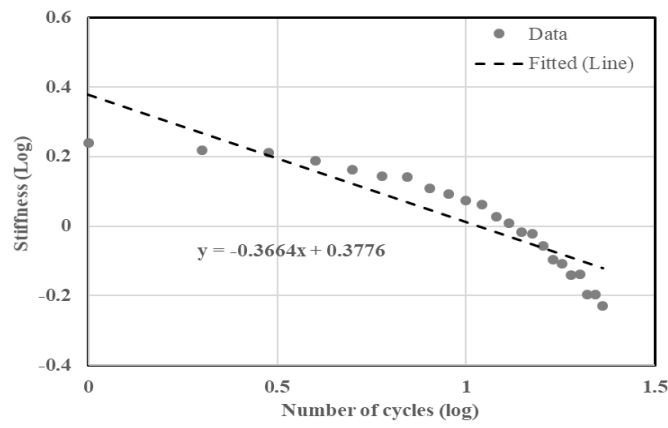


Figure G

### LCMAH0 (III)



### LCNUH10 (I)



### LCNUH10 (II)

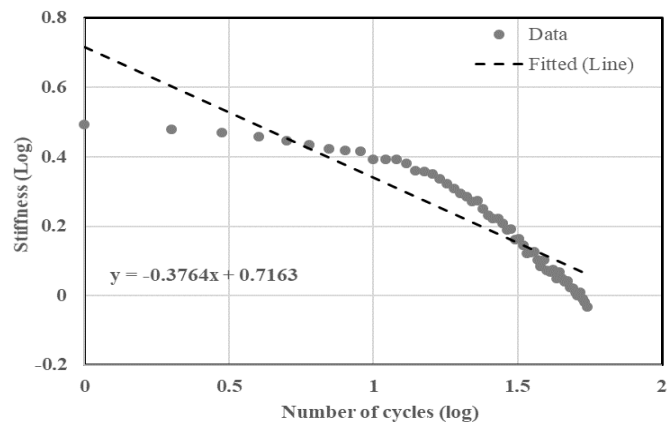
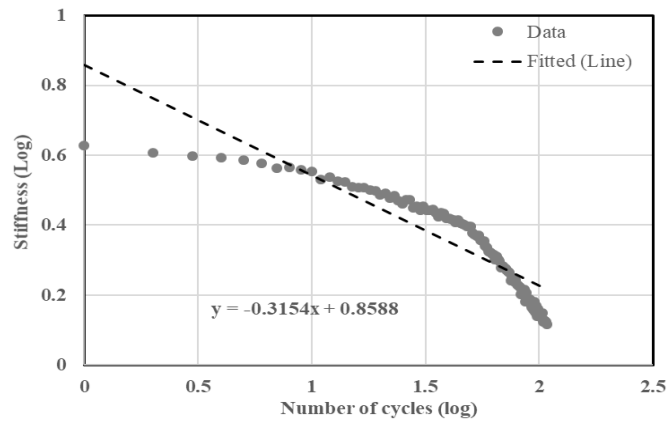


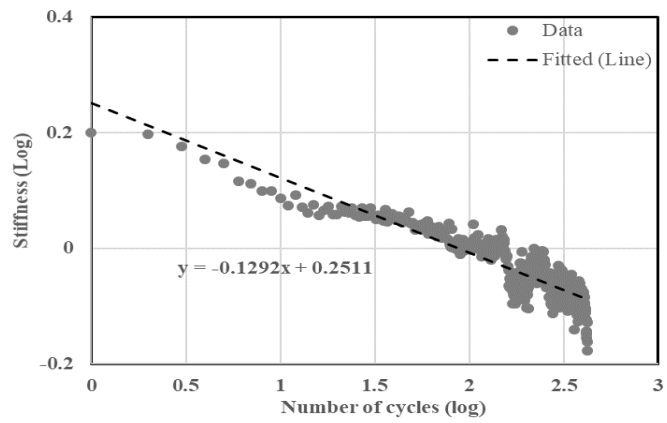
Figure G



### LCNUH10 (III)



### LFMAS0 (I)



### LFMAS0 (II)

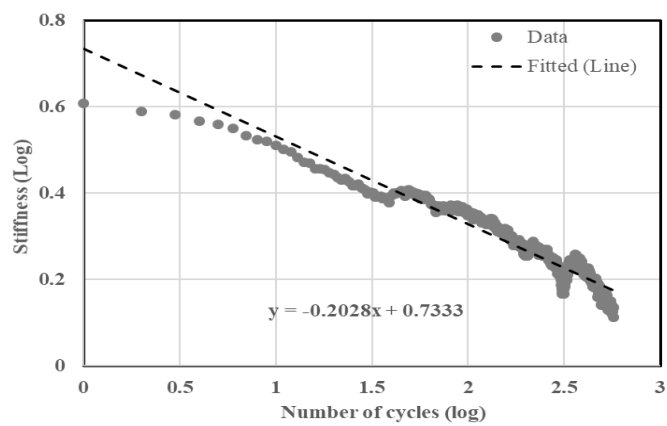
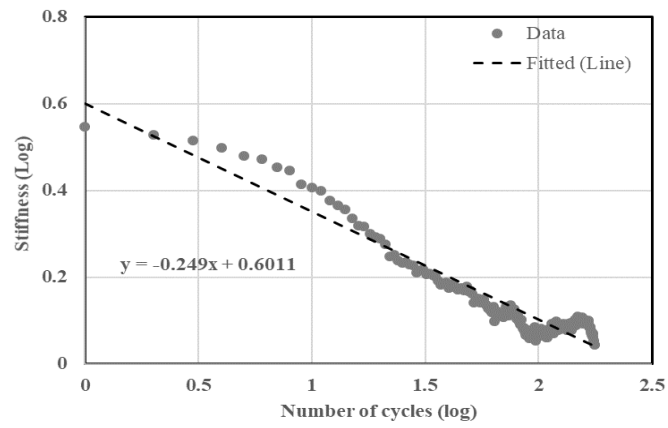
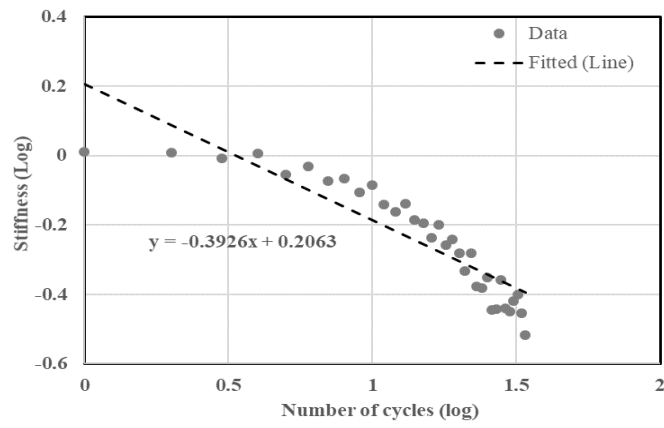


Figure G

### LFMAS0 (III)



### LFNUS10 (I)



### LFNUS10 (II)

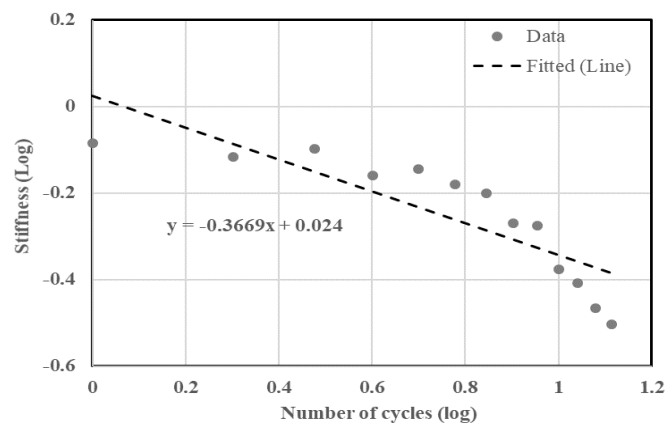
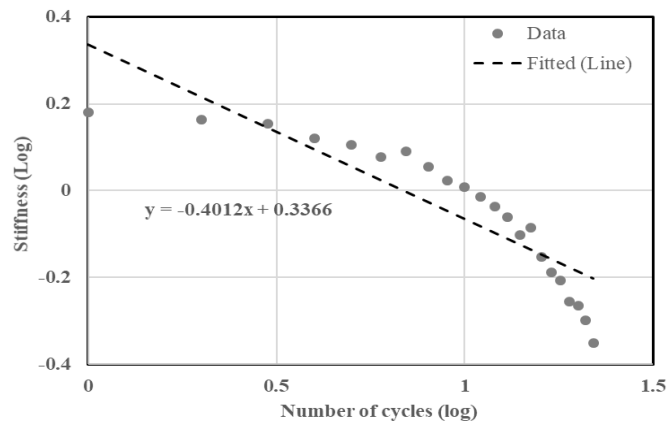
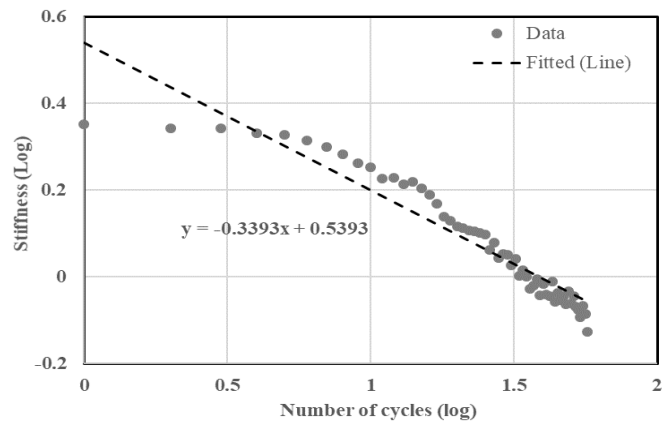


Figure G

### LFNUS10 (III)



### LCNAH5 (I)



### LCNAH5 (II)

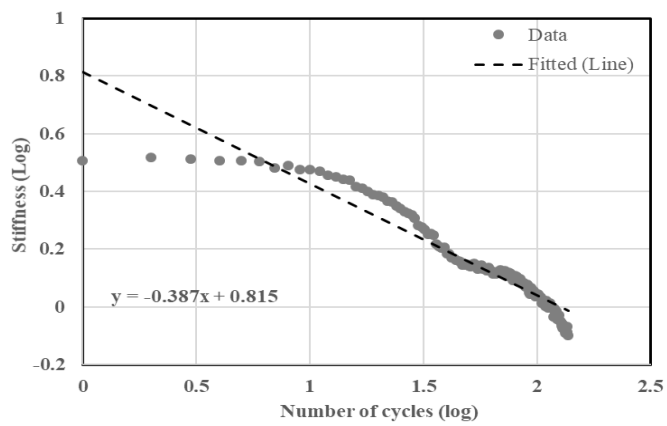
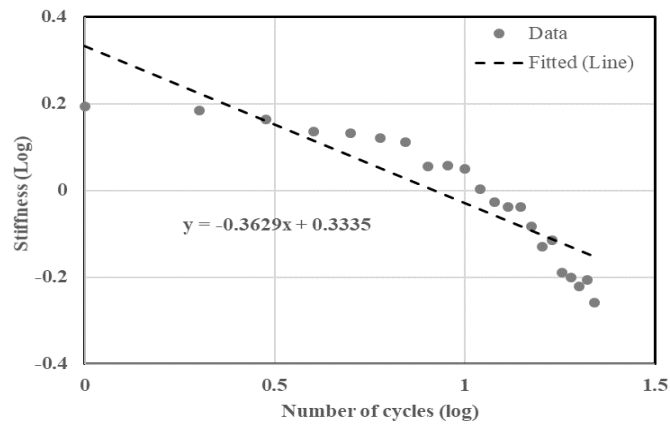
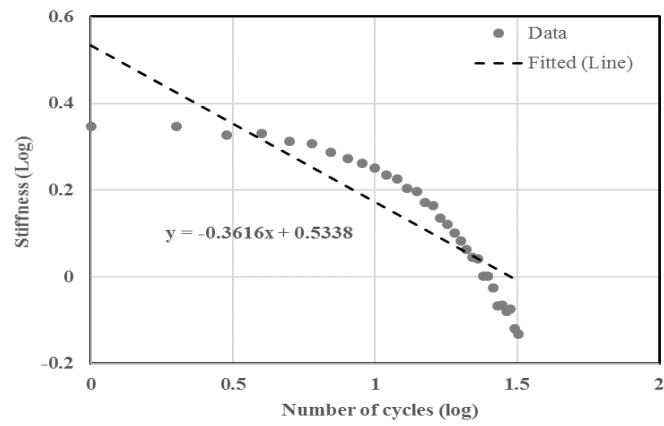


Figure G

### LCNAH5 (III)



### LCNAH0 (I)



### LCNAH0 (II)

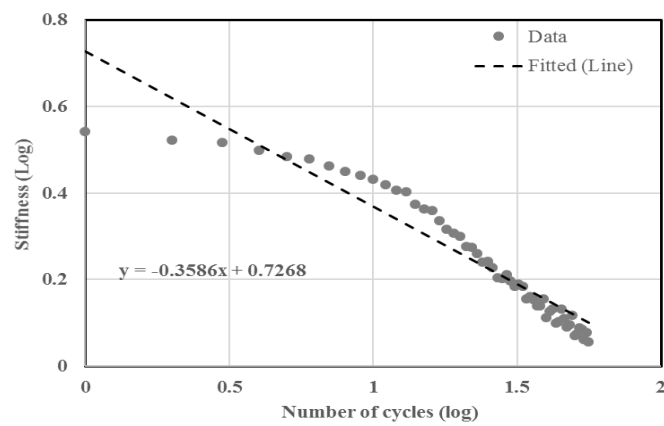
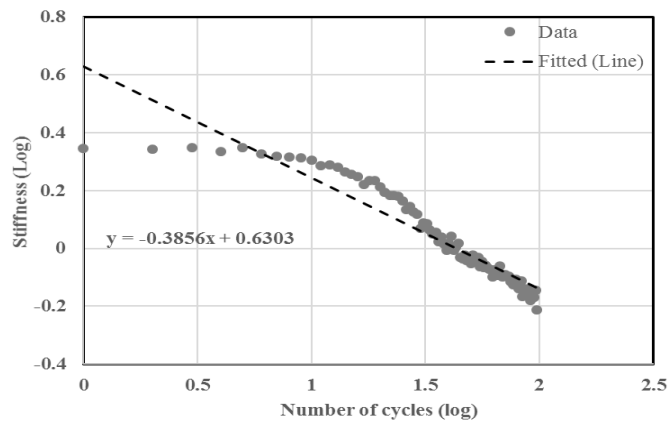
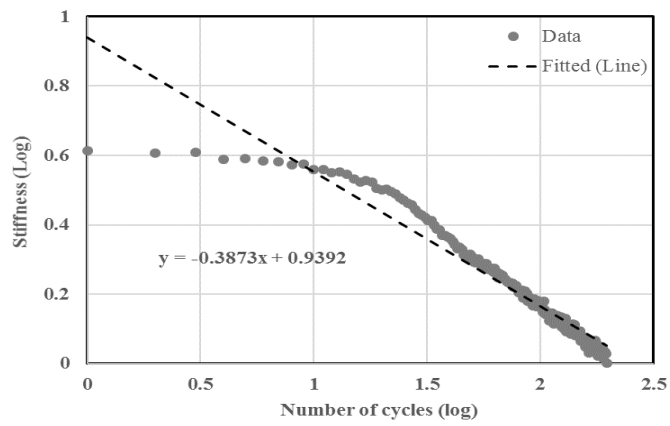


Figure G

### LCNAH0 (III)



### BFNAH10 (I)



### BFNAH10 (II)

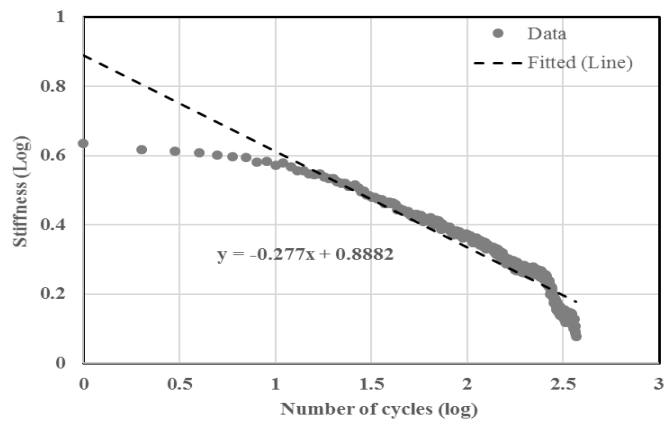
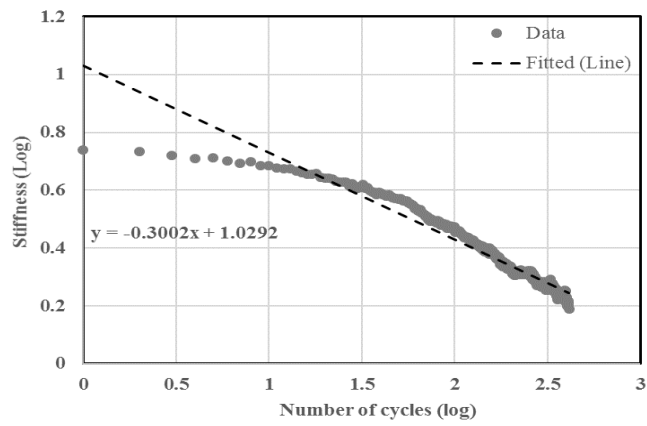
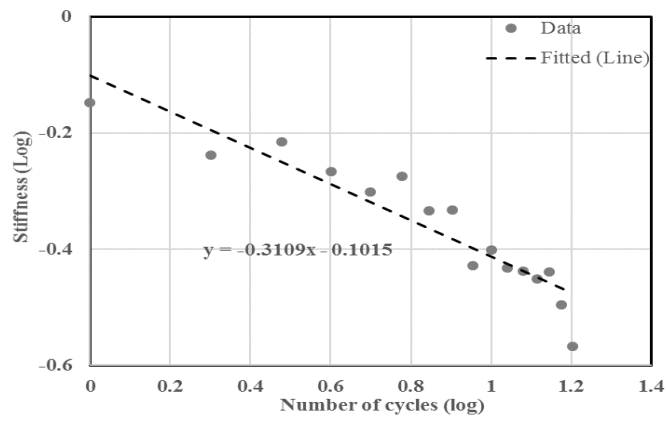


Figure G

### BFNAH10 (III)



### LFNUS5 (I)



### LFNUS5 (II)

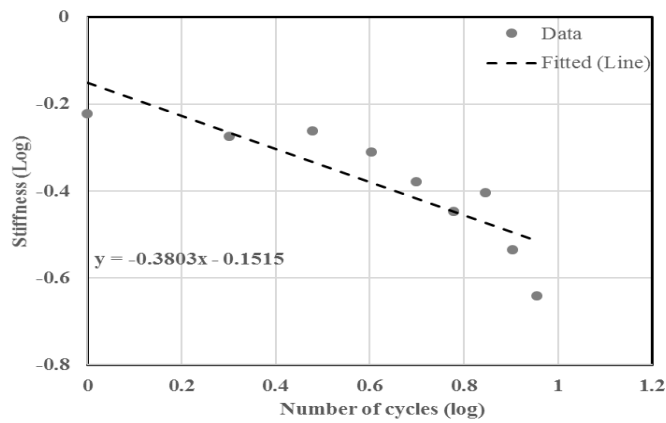
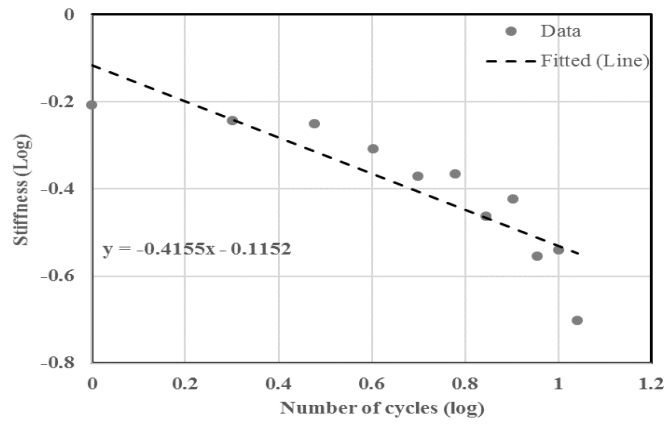
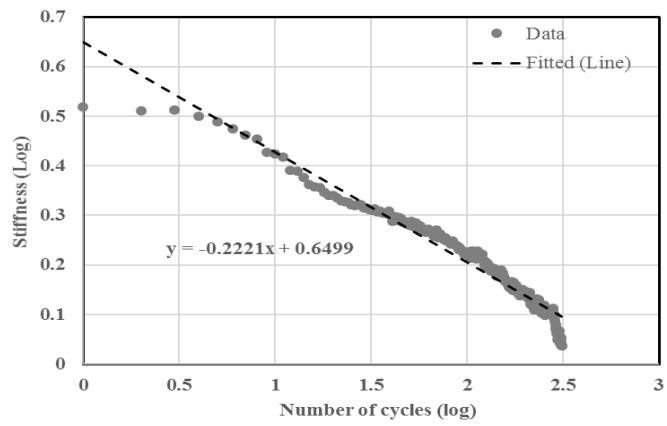


Figure G

### LFNUS5 (III)



### BCMUS0 (I)



### BCMUS0 (II)

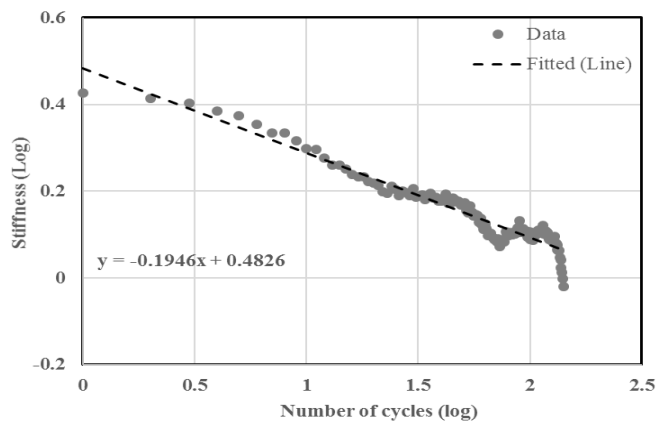
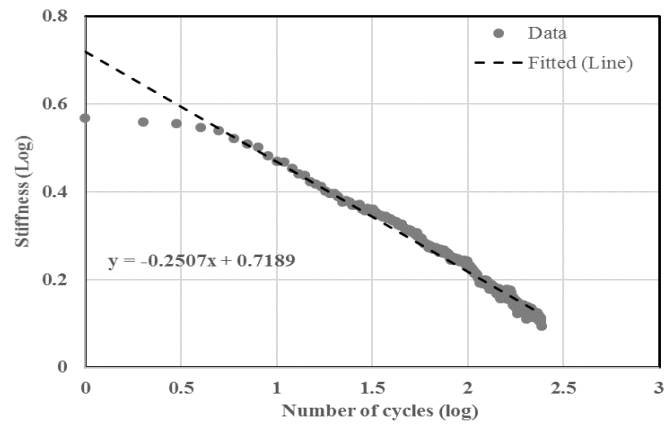
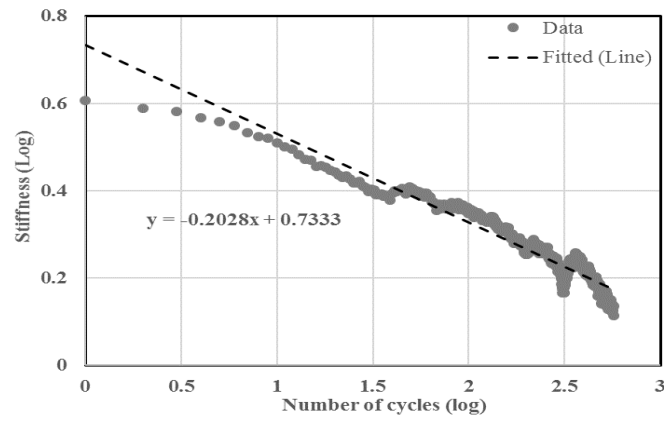


Figure G

### BCMUS0 (III)



### BCMAS10 (I)



### BCMAS10 (II)

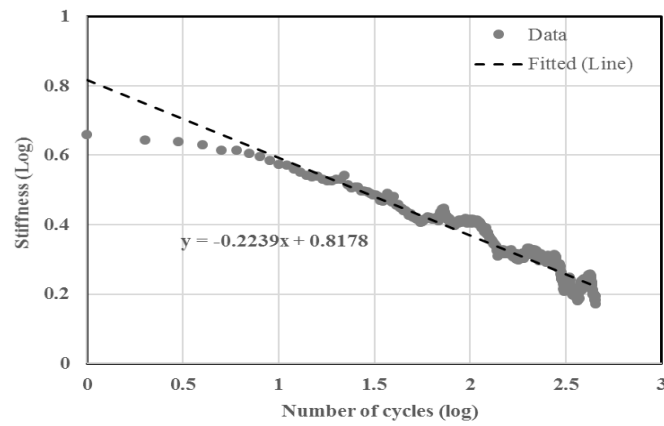
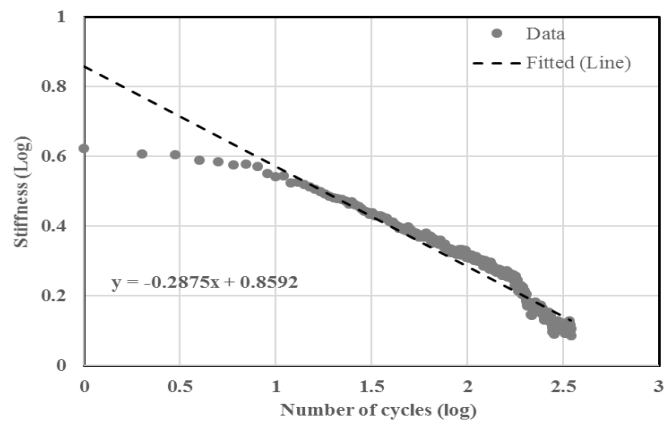


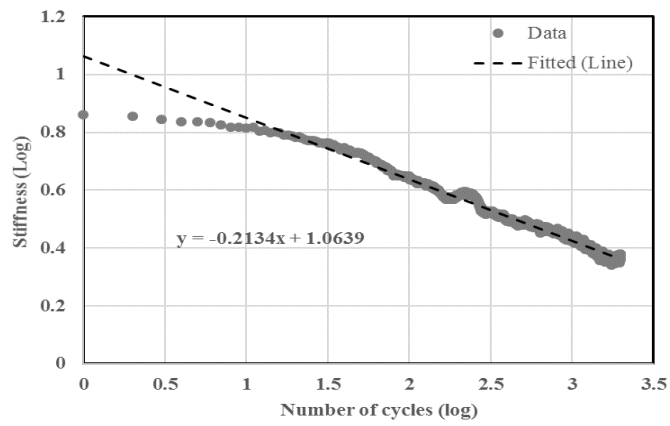
Figure G



### BCMAS10 (III)



### BFMAH0 (I)



### BFMAH0 (II)

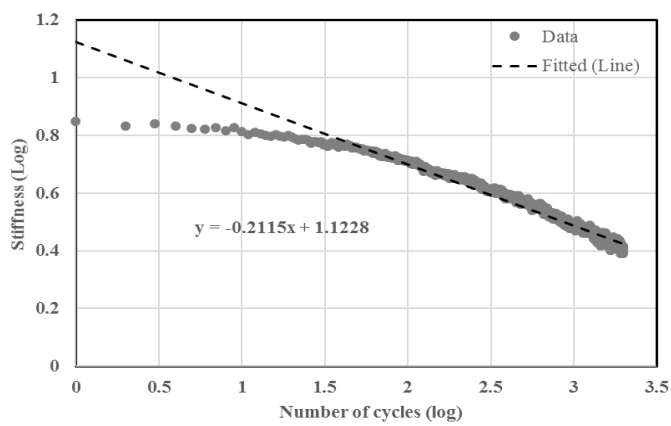
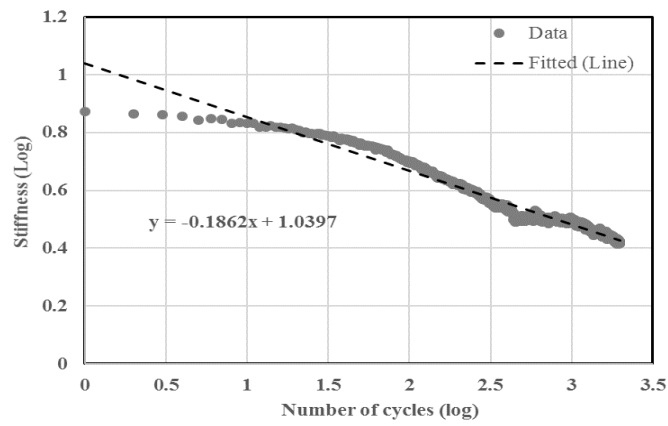
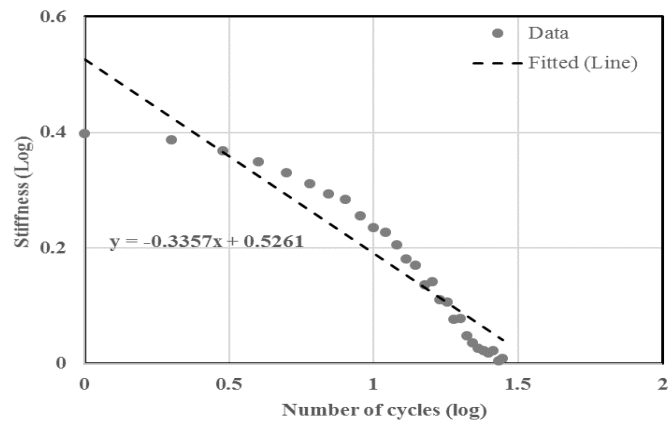


Figure G

### BFMAH0 (III)



### BCNAS5 (I)



### BCNAS5 (II)

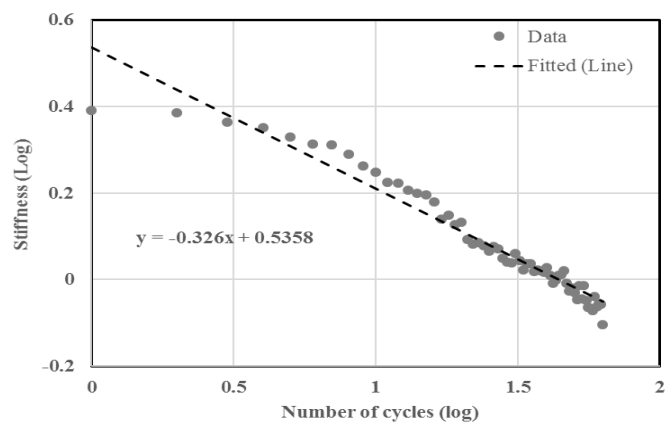
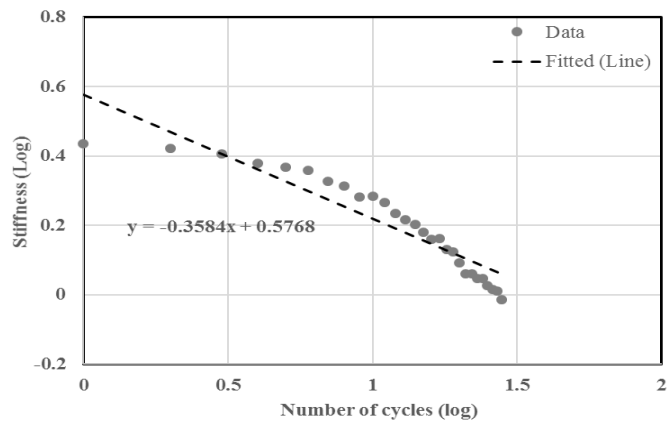
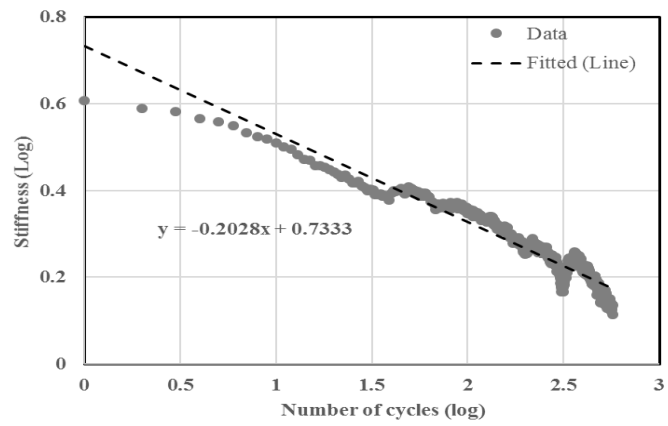


Figure G

### BCNAS5 (III)



### BFNAH0 (I)



### BFNAH0 (II)

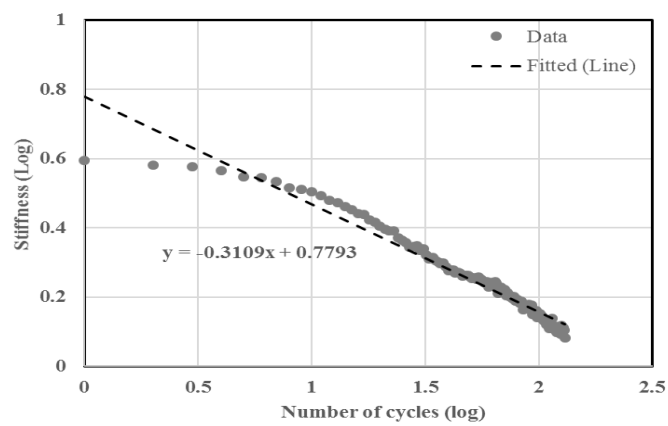
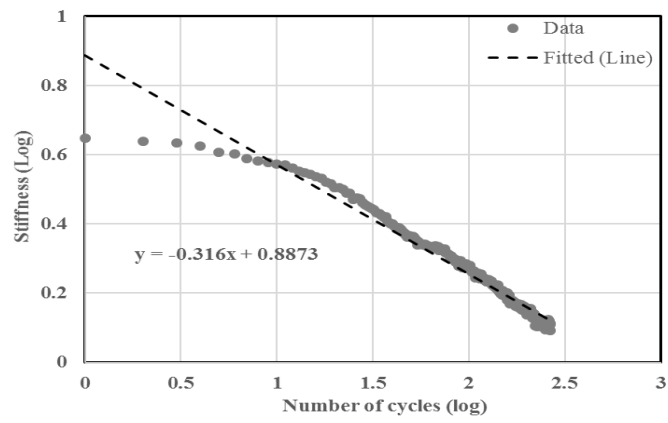
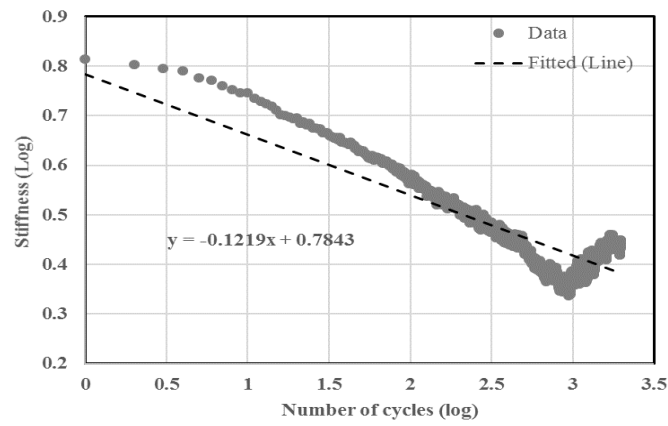


Figure G

### BFNAH0 (III)



### BFMUH5 (I)



### BFMUH5 (II)

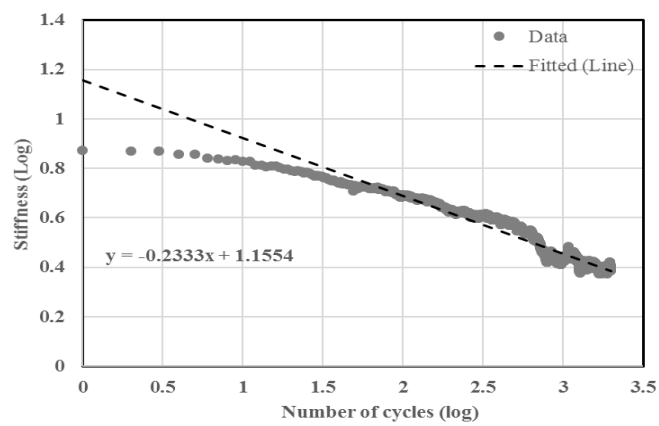
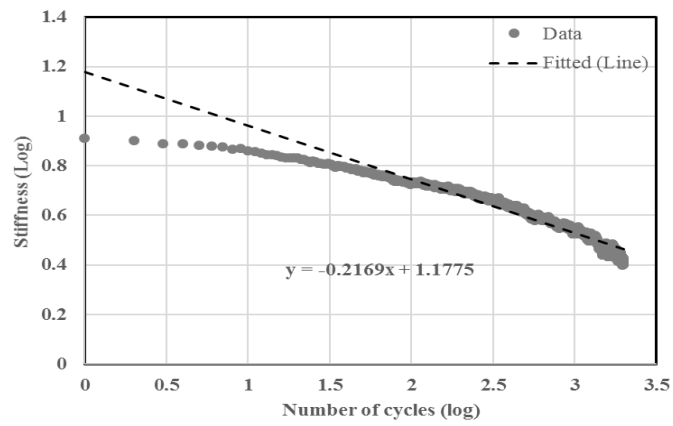
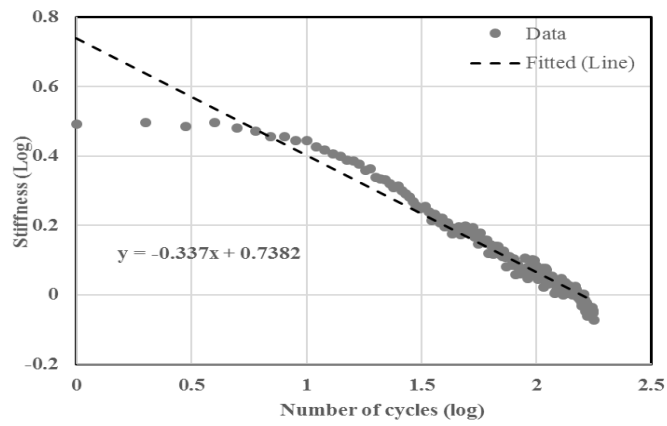


Figure G

### BFMUH5 (III)



### BFNUH5 (I)



### BFNUH5 (II)

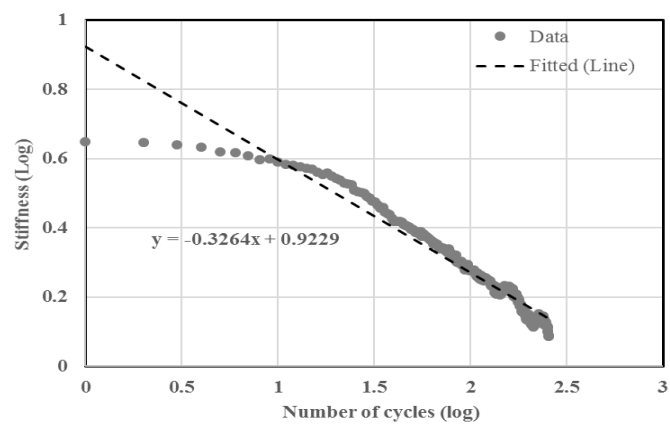
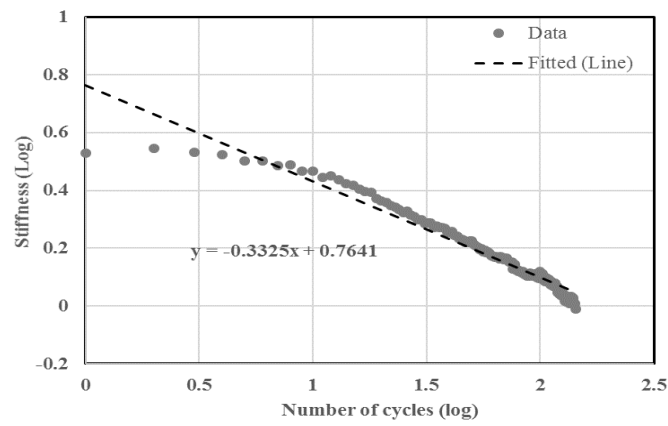
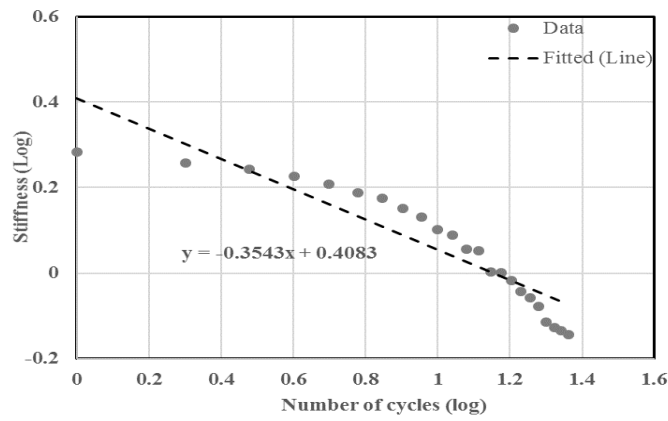


Figure G

### BFNUH5 (III)



### BCNUS10 (I)



### BCNUS10 (II)

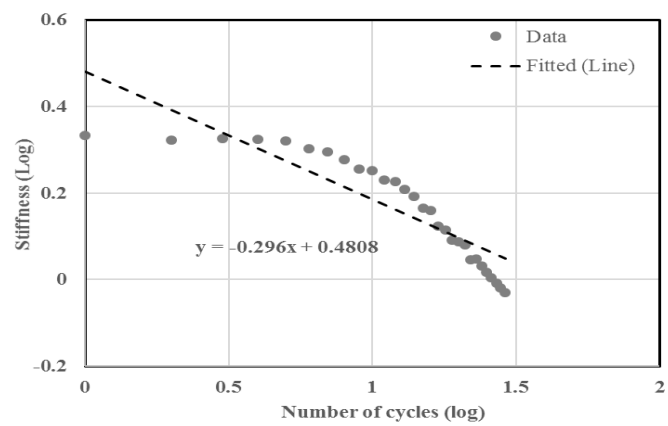
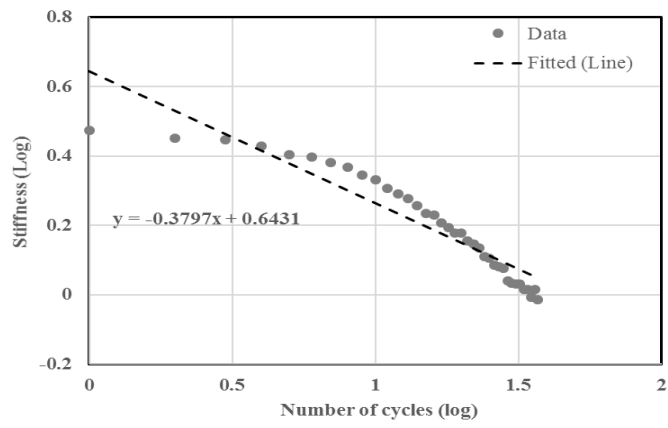
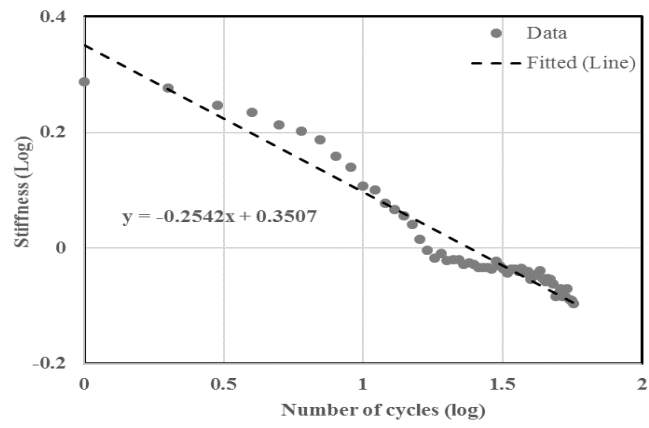


Figure G

### BCNUS10 (III)



### BCNUS5 (I)



### BCNUS5 (II)

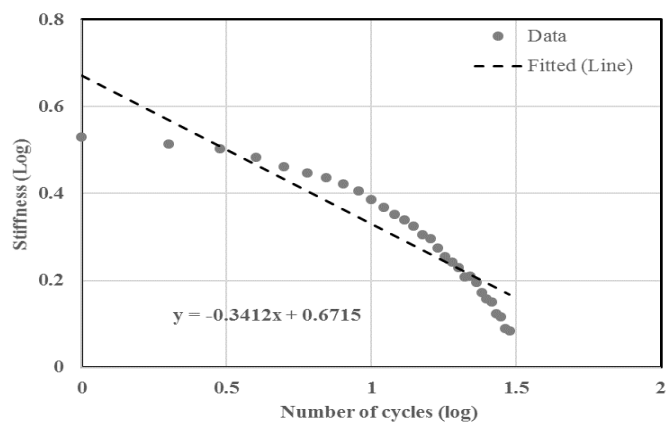
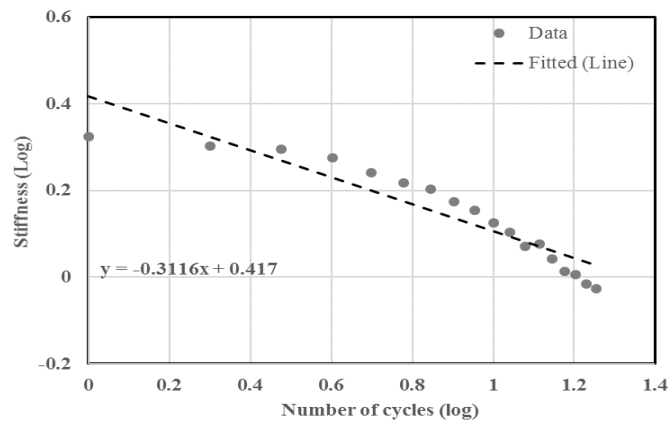
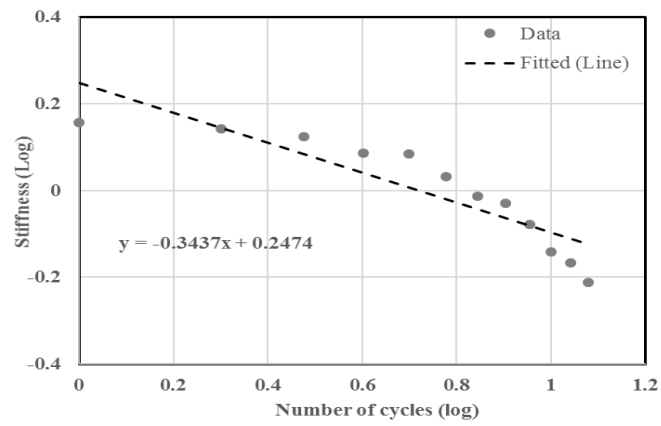


Figure G

### BCNUS5 (III)



### BCNUS0 (I)



### BCNUS0 (II)

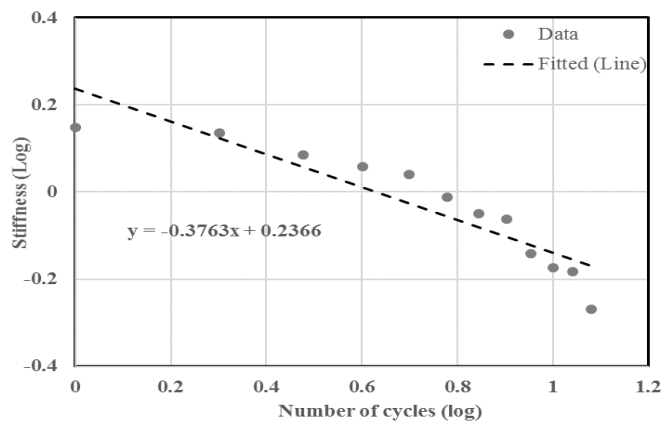
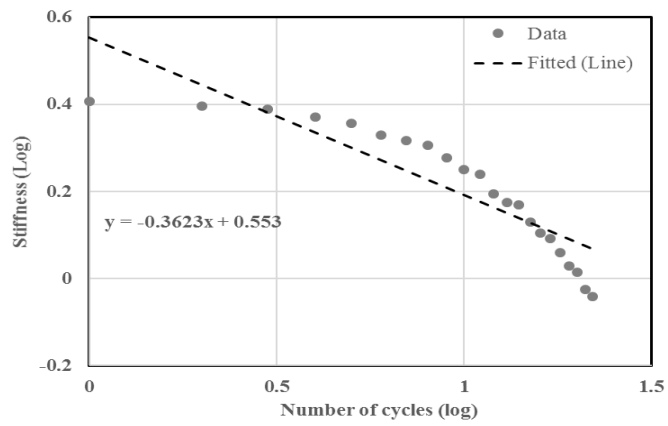


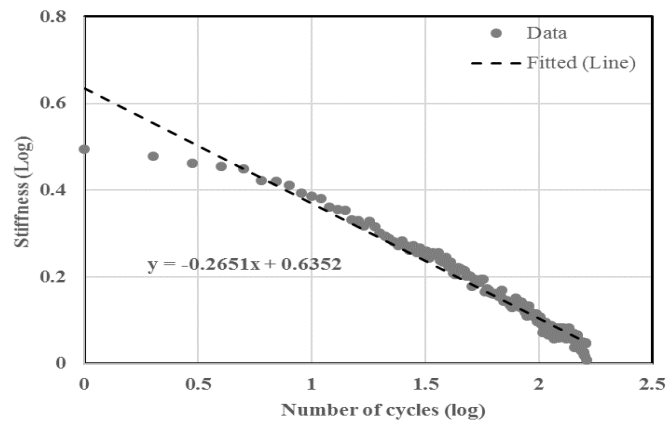
Figure G



### BCNUS0 (III)



### LFMUS5 (I)



### LFMUS5 (II)

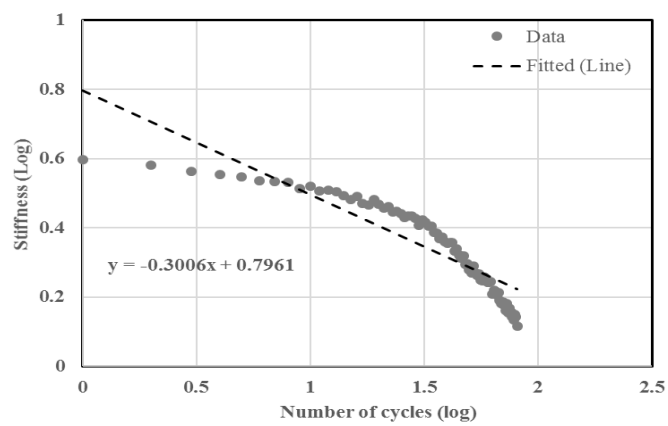
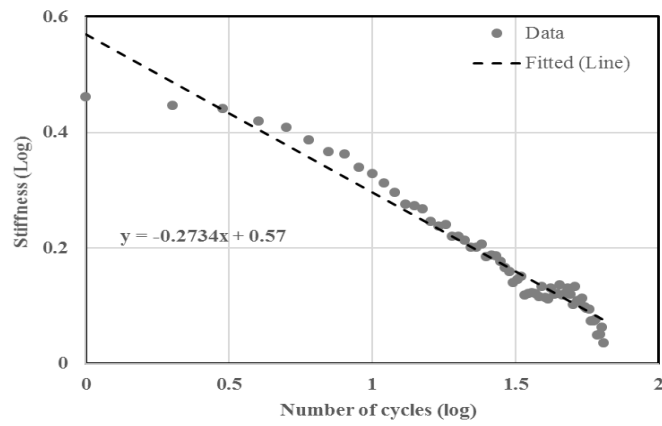
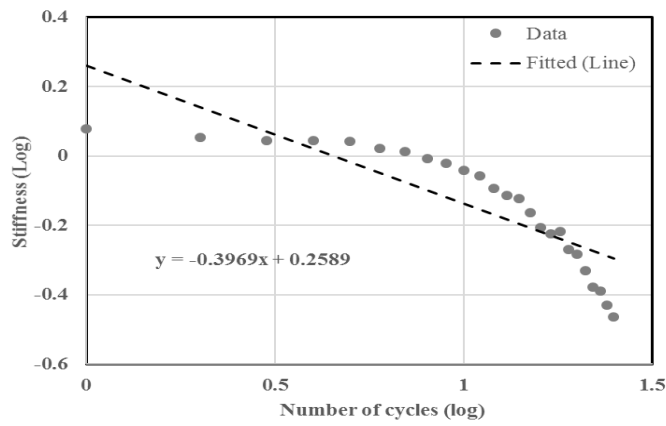


Figure G

### LFMUS5 (III)



### LFNAS0 (I)



### LFNAS0 (II)

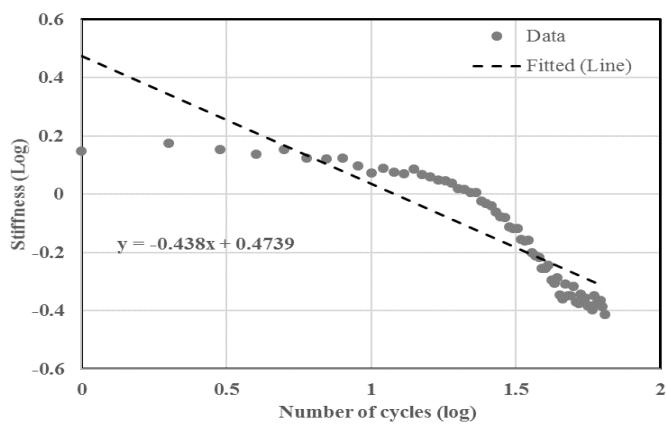
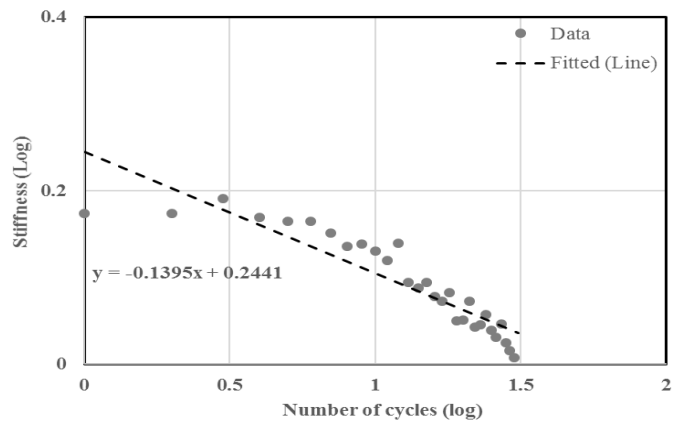
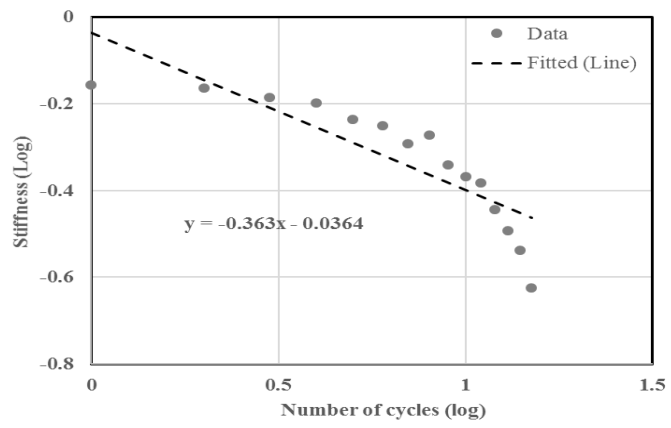


Figure G

### LFNAS0 (III)



### LFNUS0 (I)



### LFNUS0 (II)

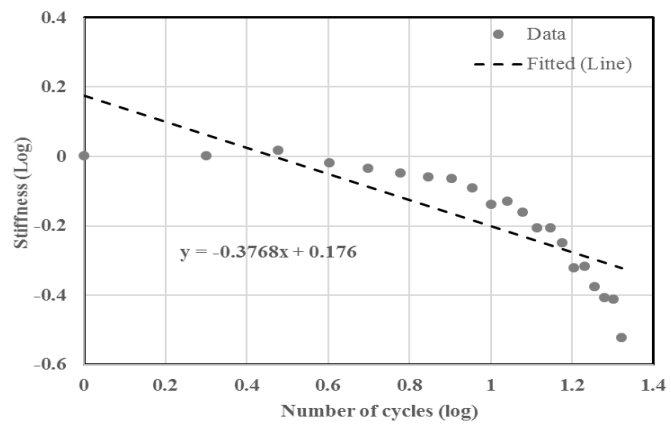
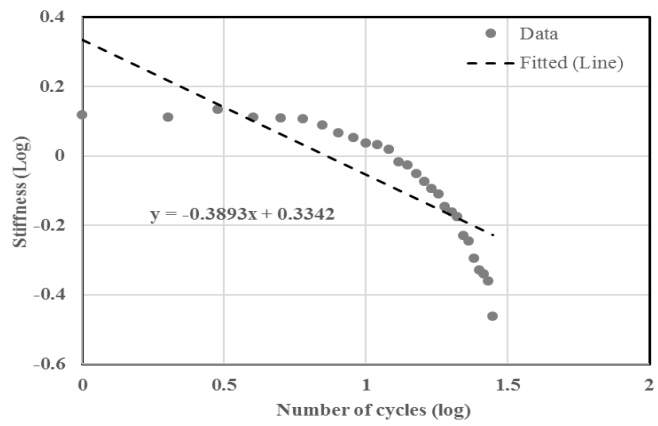
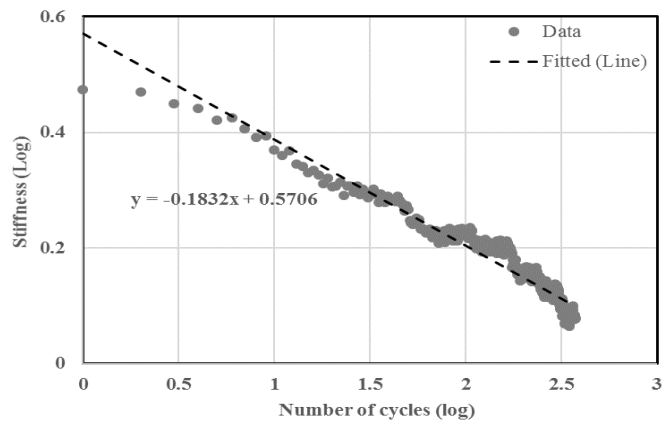


Figure G

### LFNUS0 (III)



### BCMUS10 (I)



### BCMUS10 (II)

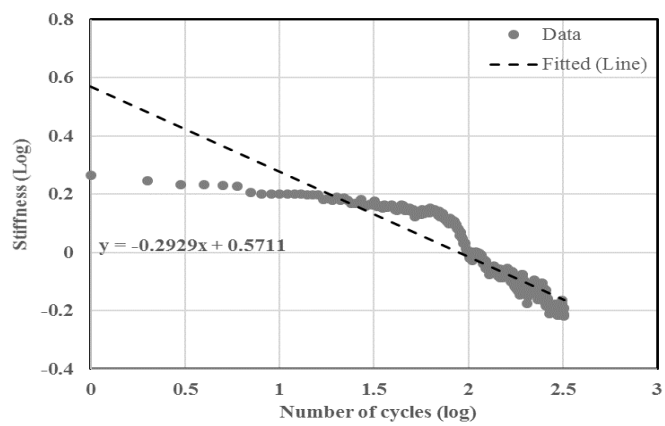
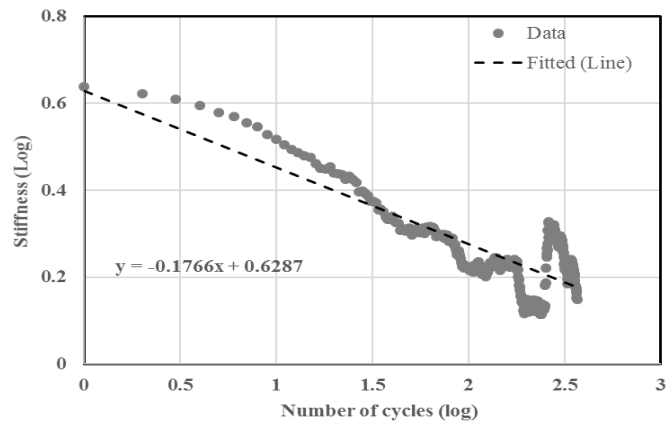
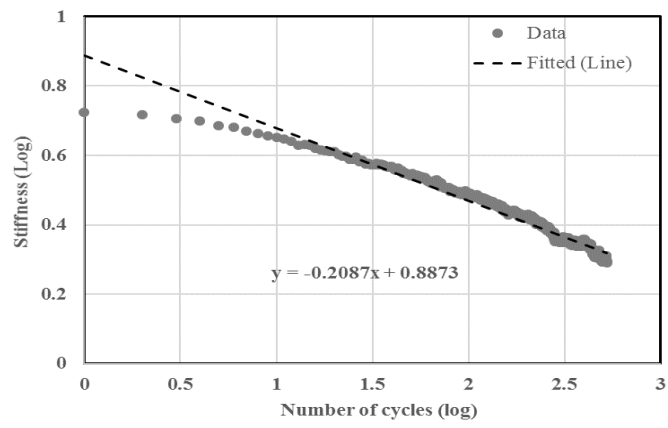


Figure G

### BCMUS10 (III)



### BCMAS5 (I)



### BCMAS5 (II)

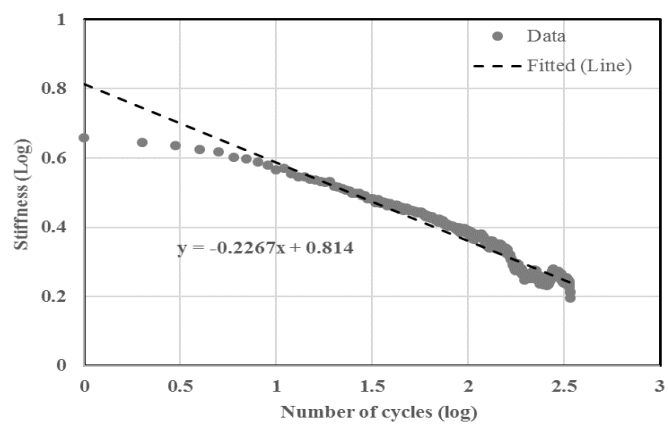
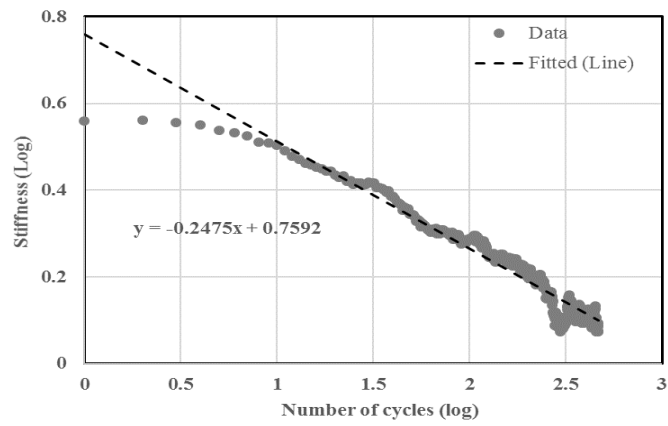
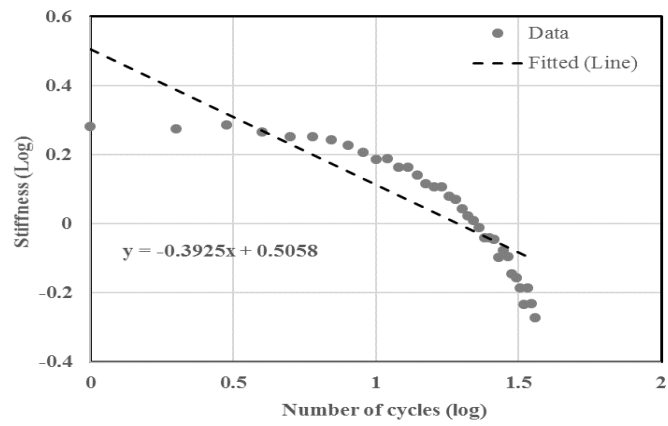


Figure G

### BCMAS5 (II)



### LCNUH5 (I)



### LCNUH5 (II)

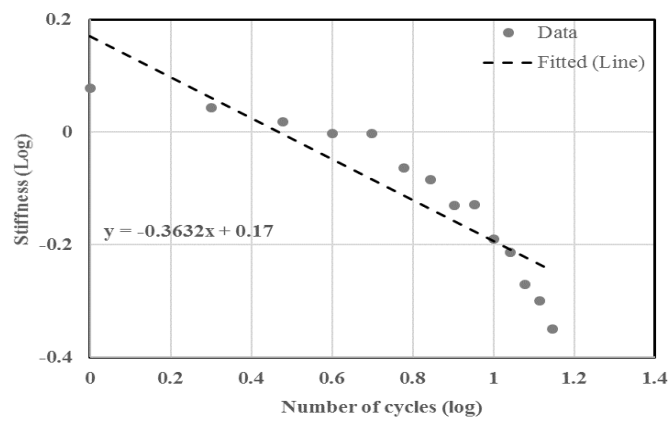
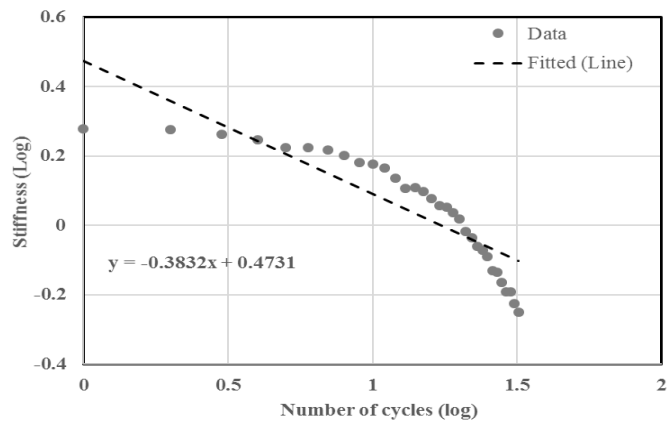
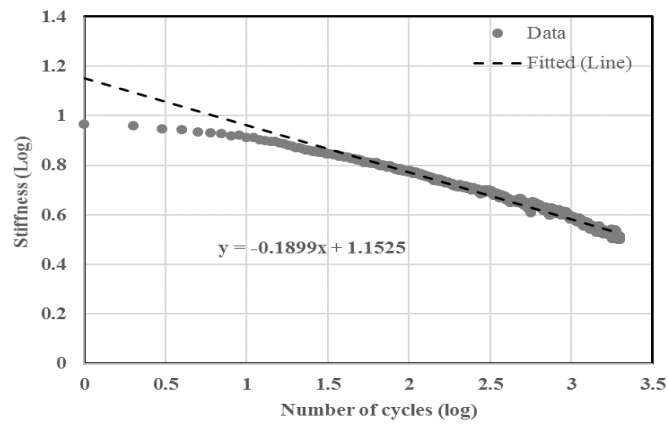


Figure G

### LCNUH5 (III)



### BFMAH5 (I)



### BFMAH5 (II)

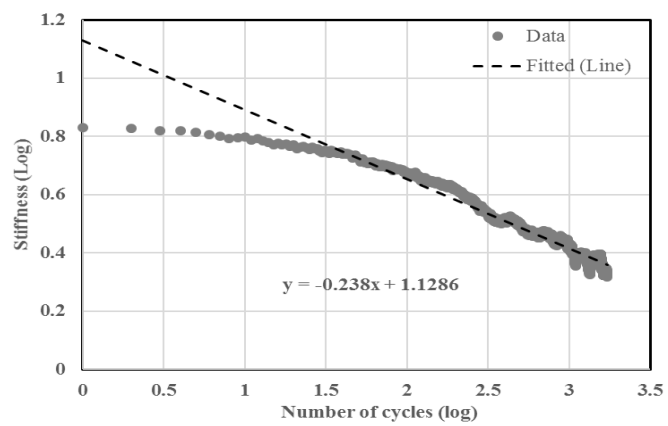
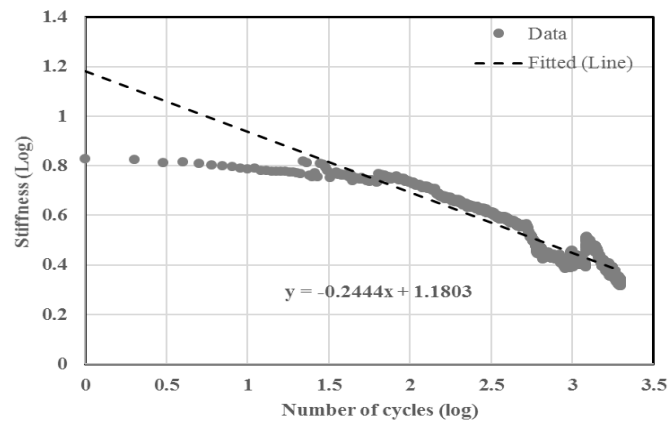
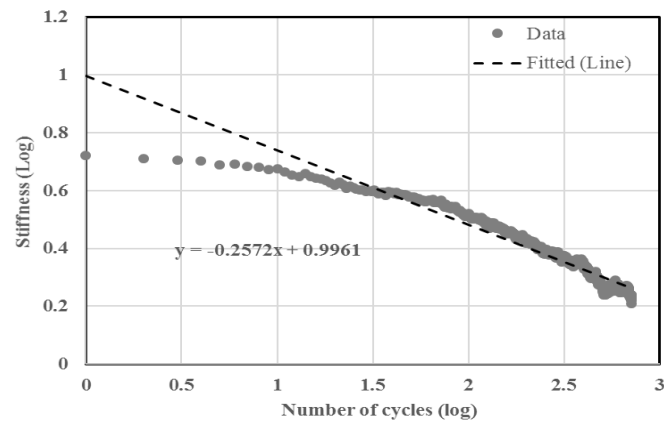


Figure G

### BFMAH5 (III)



### LCMAH10 (I)



### LCMAH10 (II)

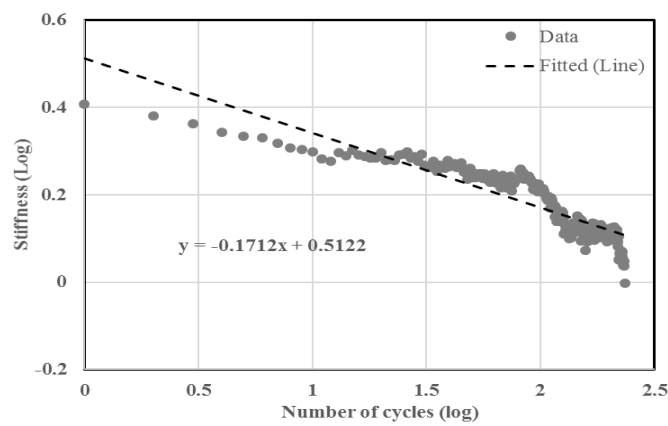
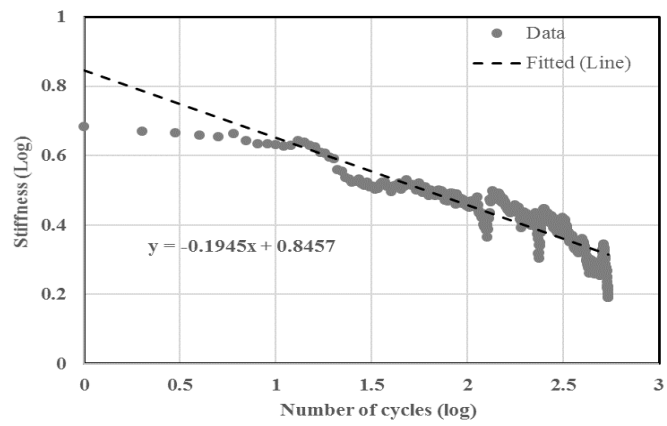


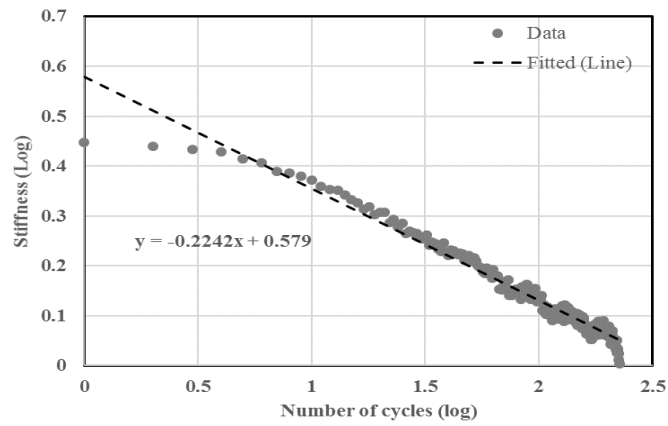
Figure G



### LCMAH10 (III)



### LCMUH5 (I)



### LCMUH5 (II)

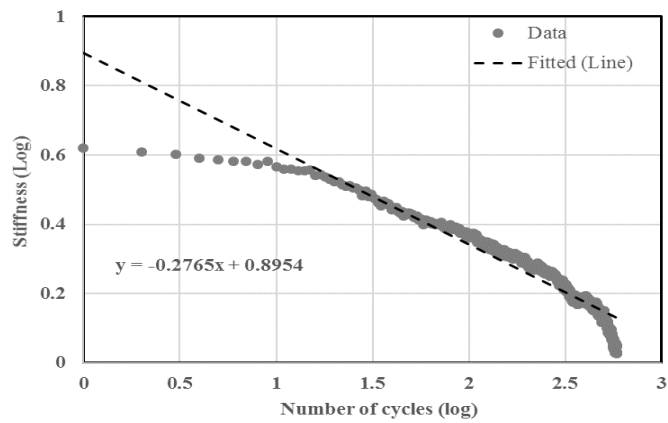
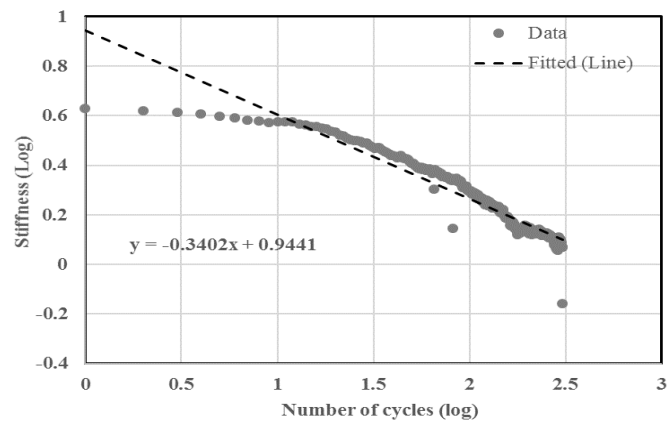
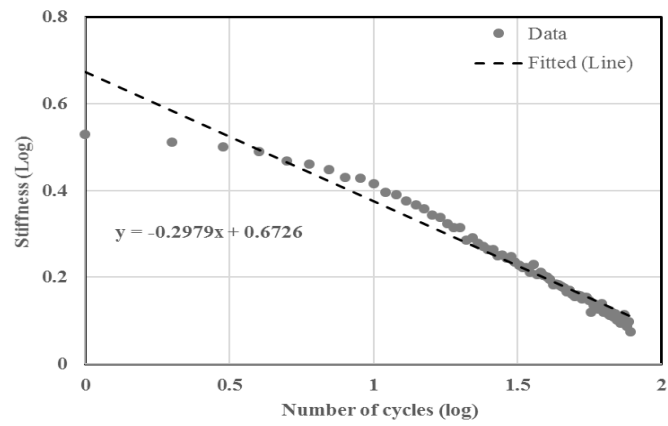


Figure G

### LCMUH5 (III)



### BFNUH0 (I)



### BFNUH0 (II)

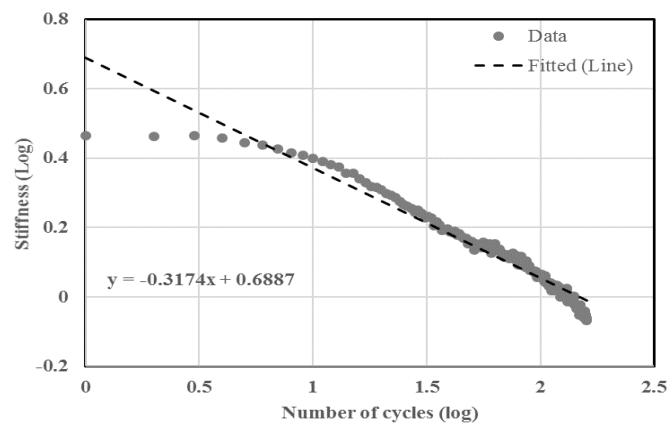
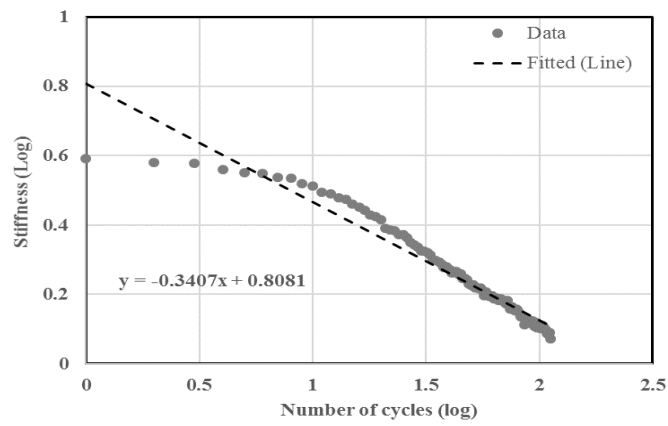
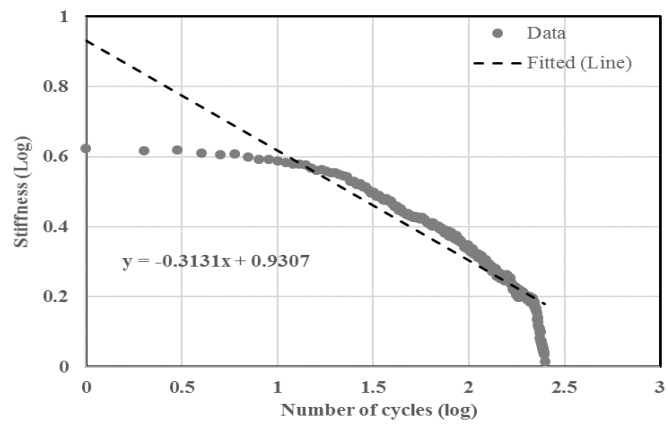


Figure G

### BFNUH0 (III)



### BFNAH5 (I)



### BFNAH5 (II)

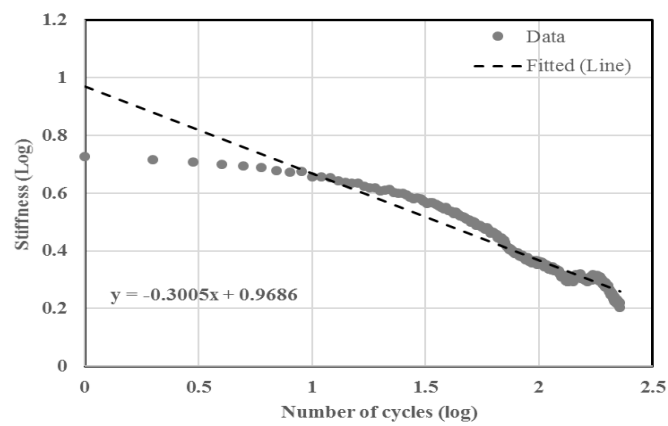
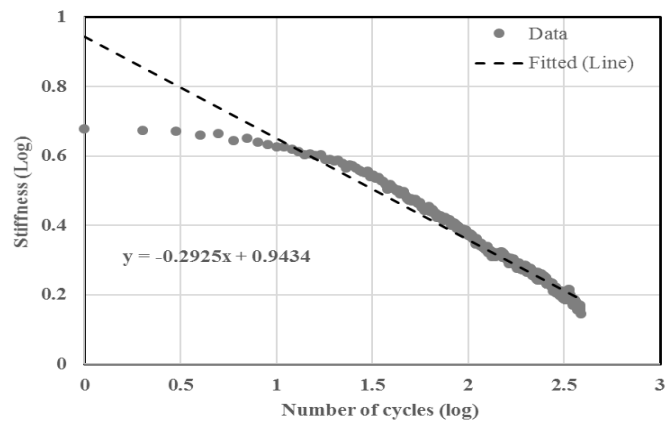
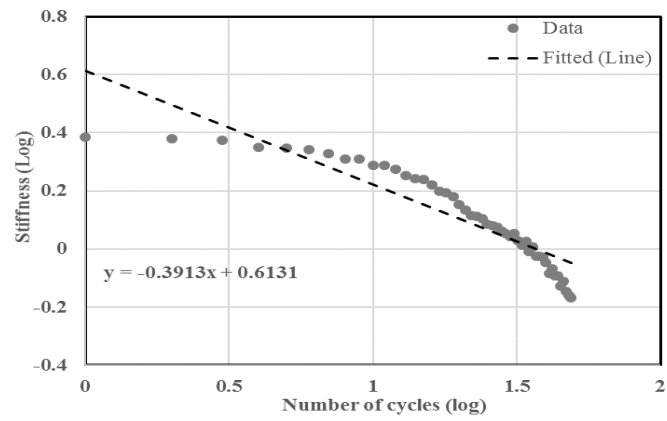


Figure G

### BFNAH5 (III)



### LCNAH10 (I)



### LCNAH10 (II)

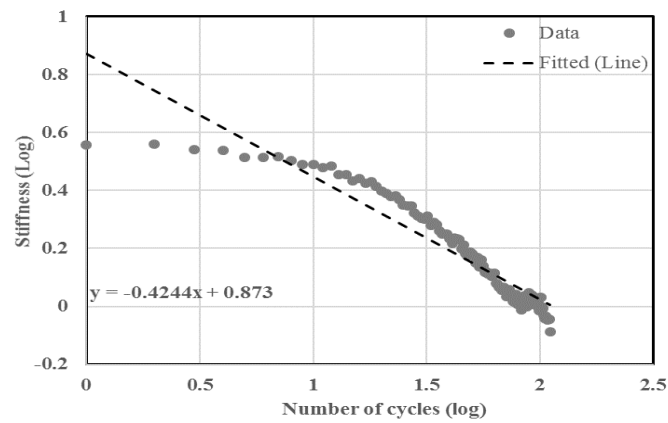
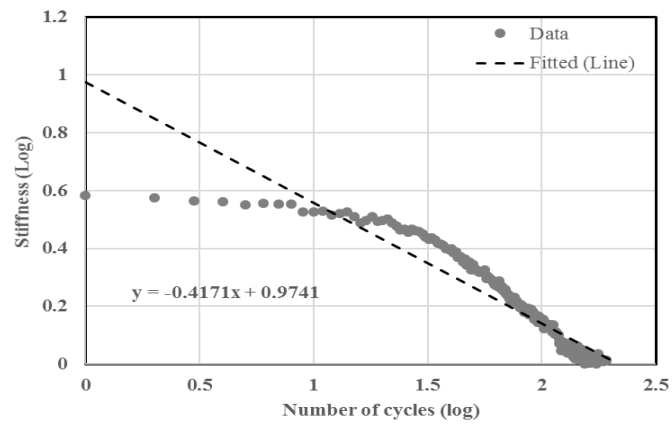
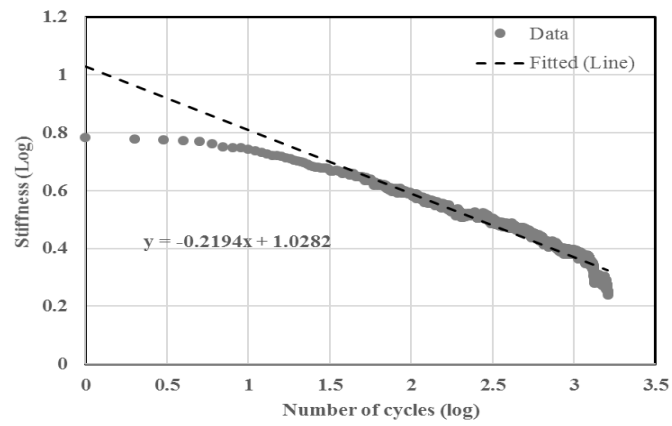


Figure G

### LCNAH10 (III)



### BFMUH0 (I)



### BFMUH0 (II)

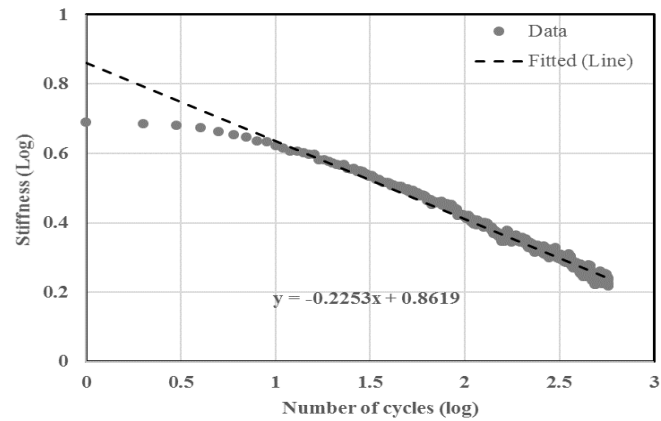
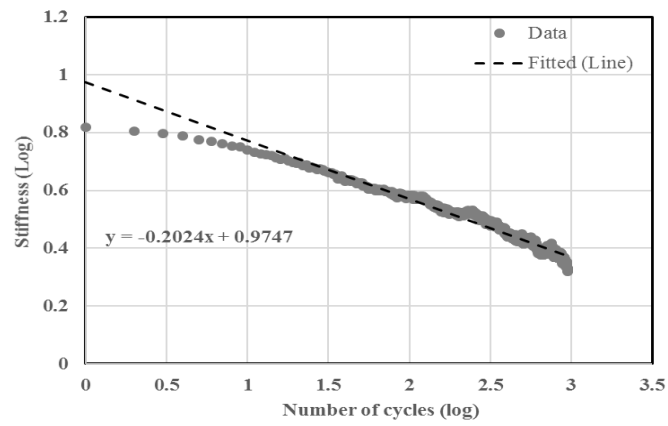
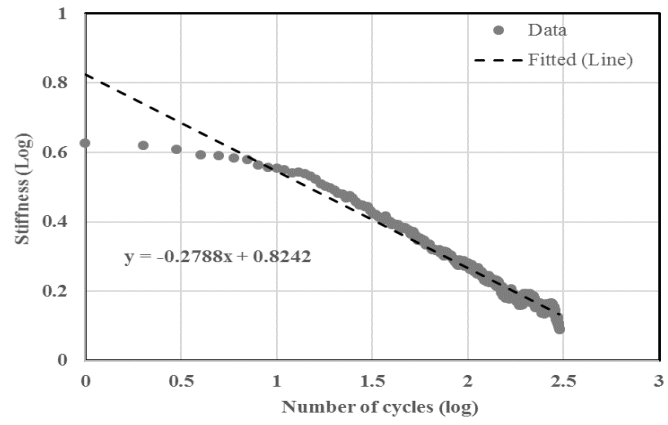


Figure G

### BFMUH0 (III)



### BFNUH10 (I)



### BFNUH10 (II)

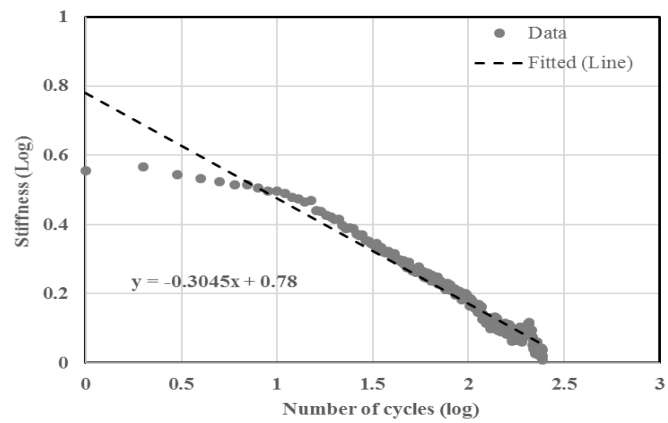
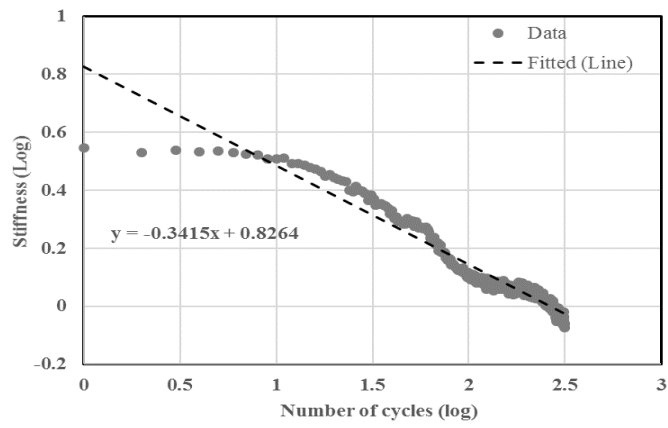
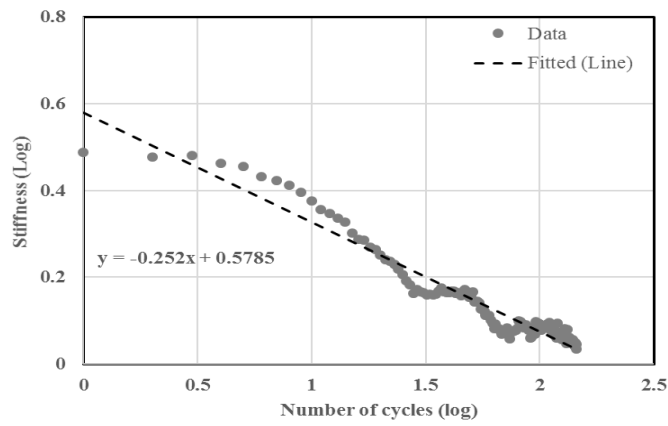


Figure G

### BFNUH10 (III)



### LFMUS0 (I)



### LFMUS0 (II)

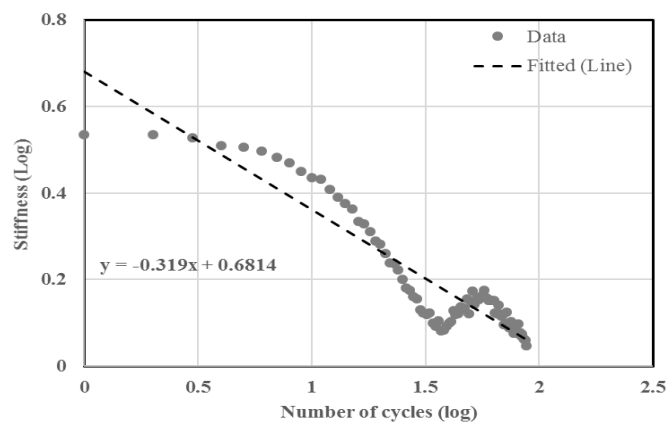
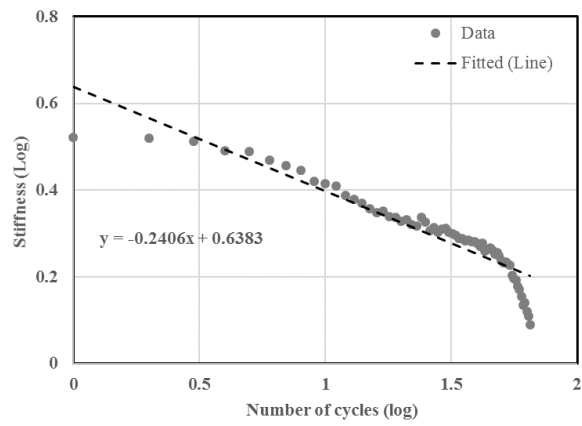
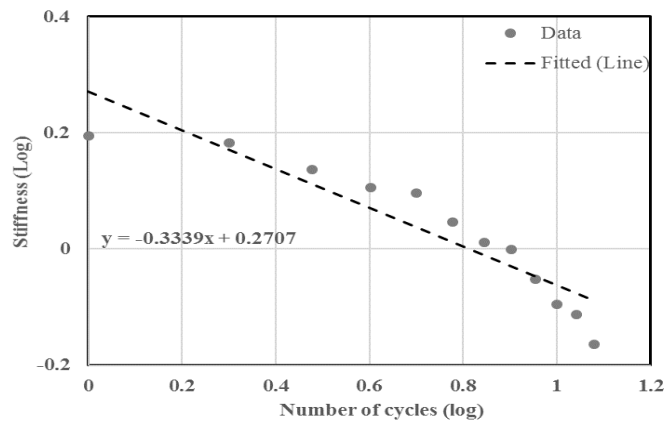


Figure G

### LFMUS0 (III)



### BCNAS0 (I)



### BCNAS0 (II)

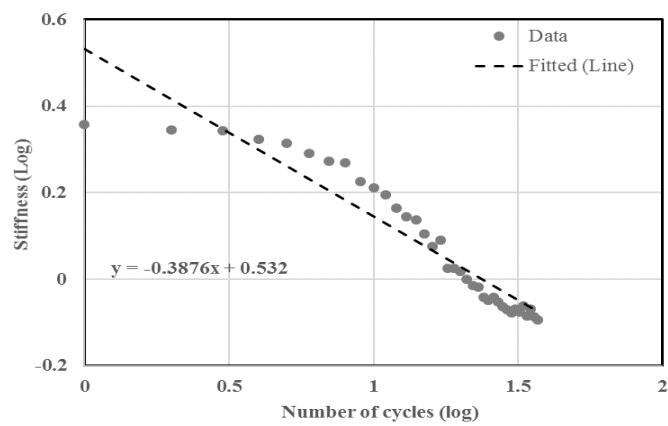
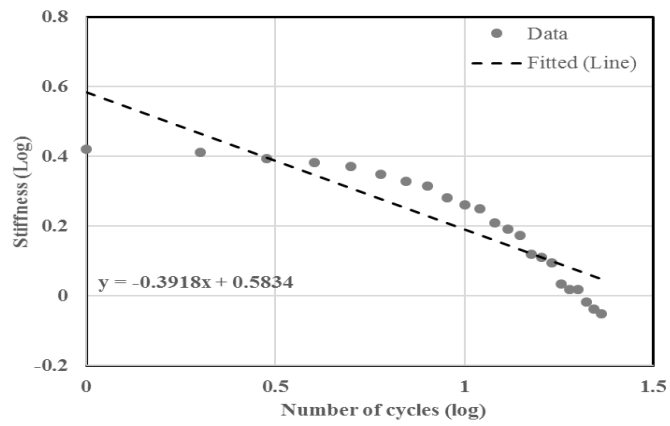


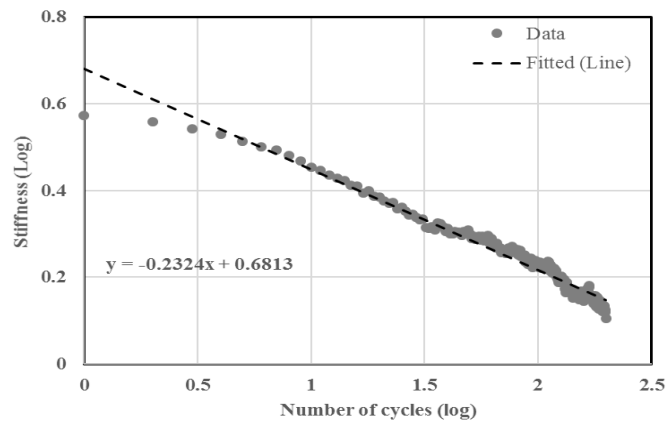
Figure G



### BCNAS0 (III)



### BCMUS5 (I)



### BCMUS5 (II)

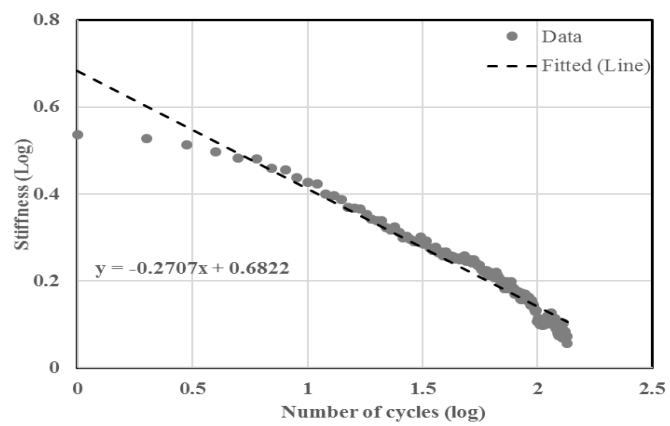
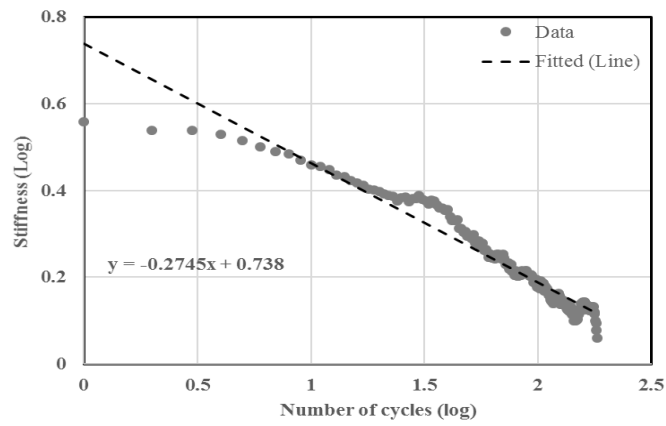
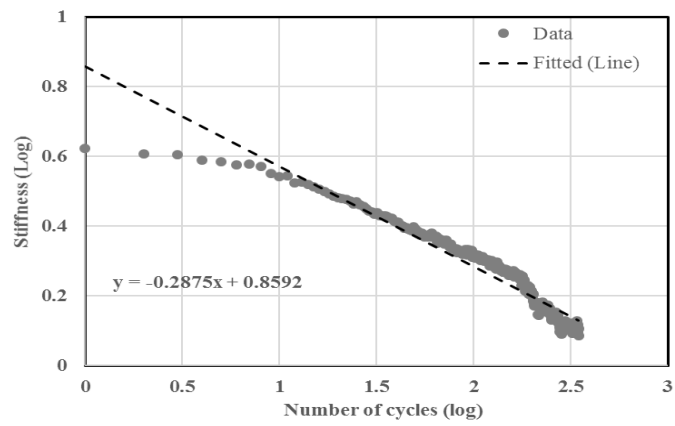


Figure G

### BCMUS5 (III)



### BCMAS0 (I)



### BCMAS0 (II)

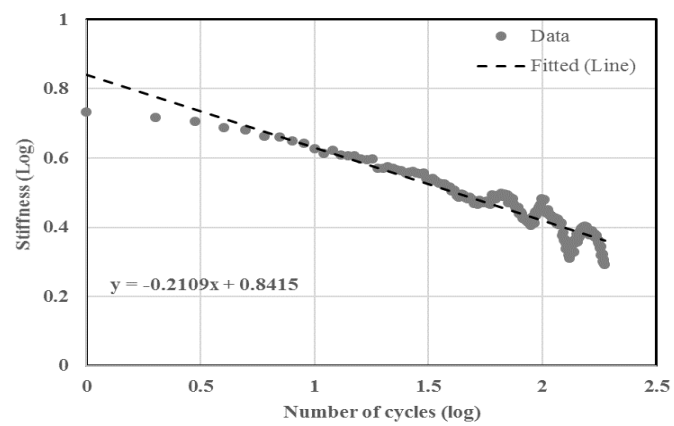
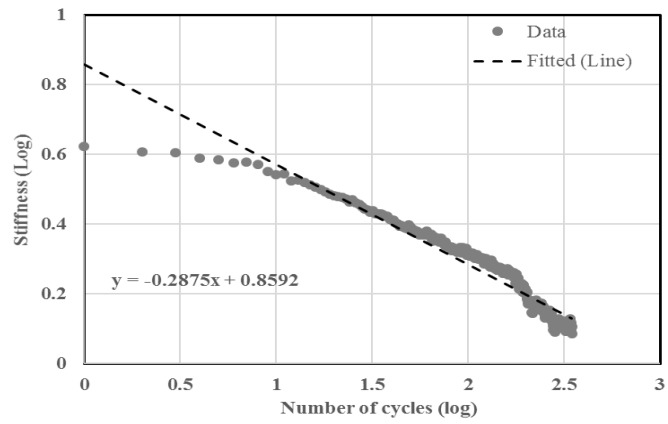
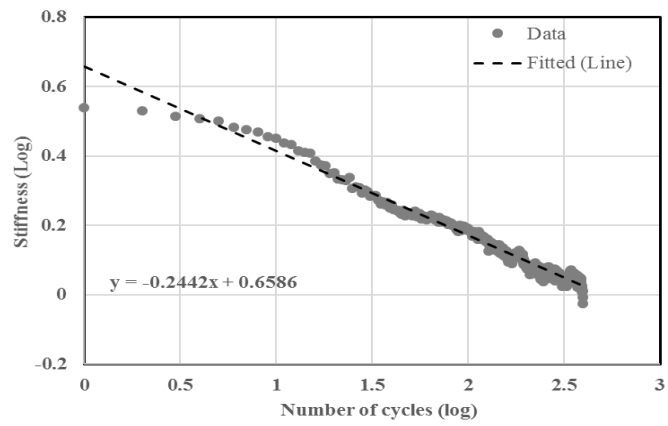


Figure G

### BCMAS0 (III)



### LCMUH0 (I)



### LCMUH0 (II)

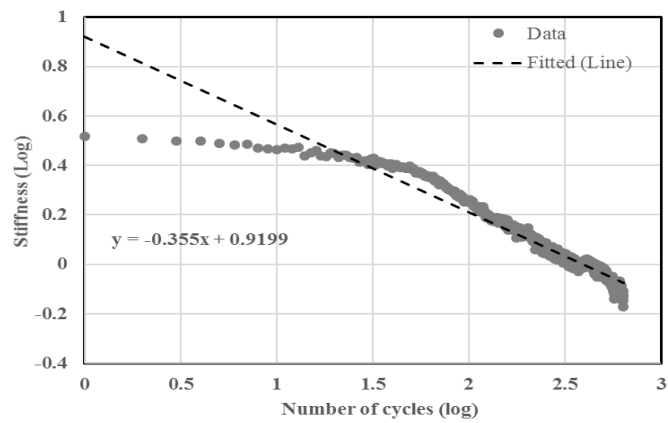
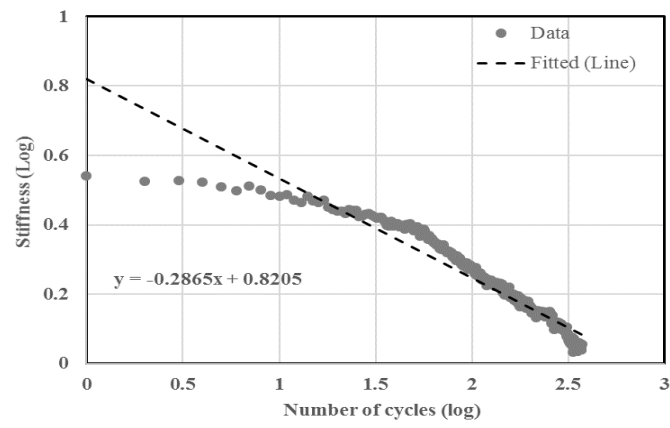
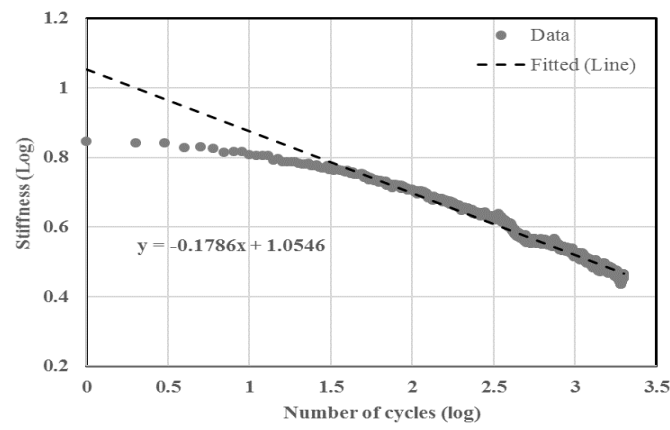


Figure G

### LCMUH0 (III)



### BFMUH10 (I)



### BFMUH10 (II)

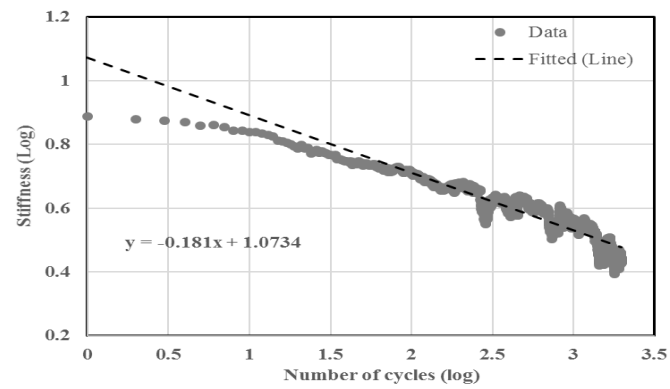
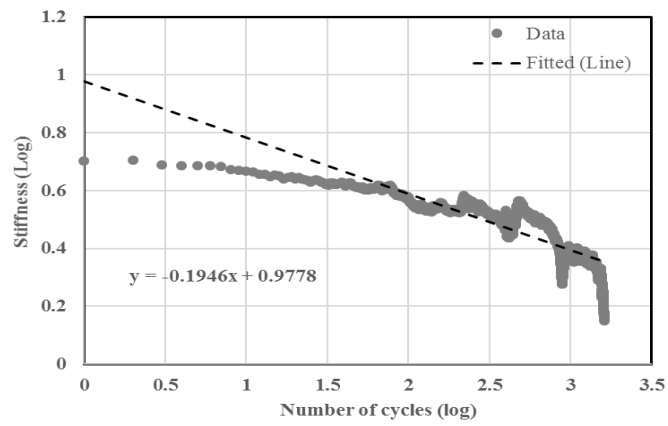
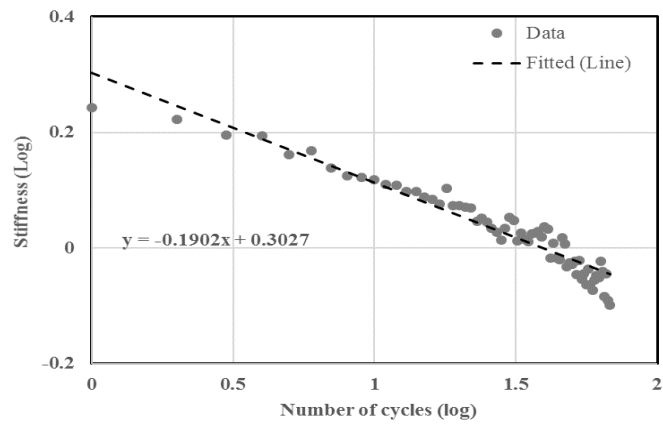


Figure G

### BFMUH10 (III)



### LFMUS10 (I)



### LFMUS10 (II)

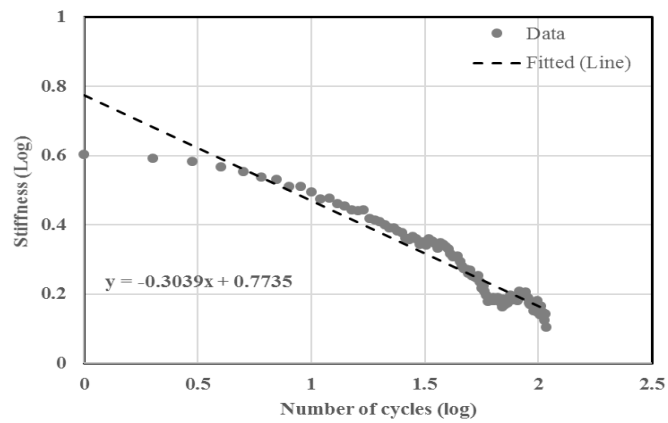
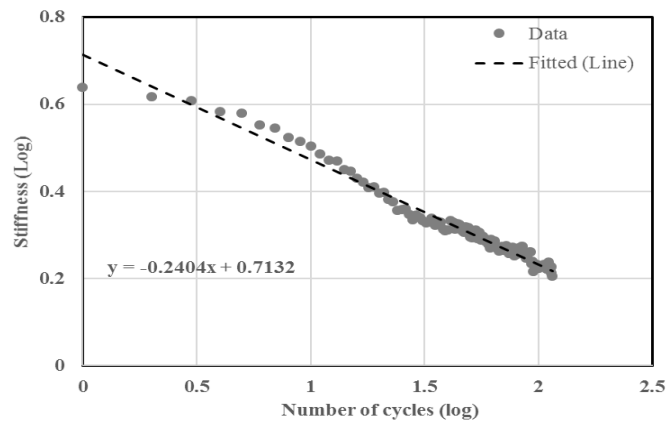
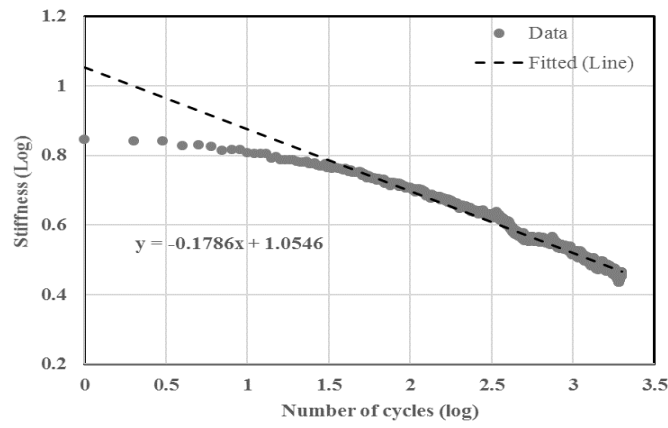


Figure G

### LFMUS10 (III)



### LCNUH0 (I)



### LCNUH0 (II)

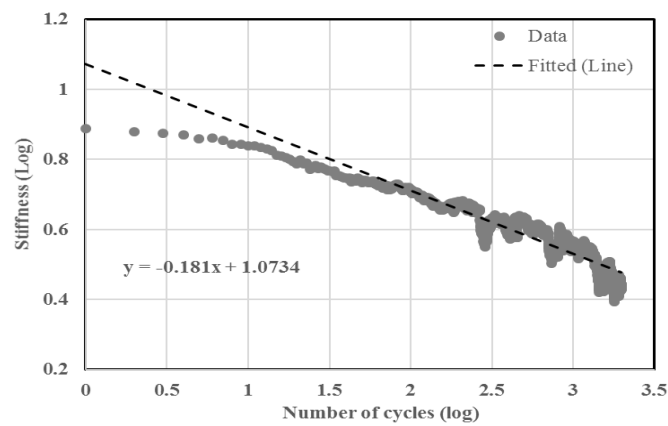
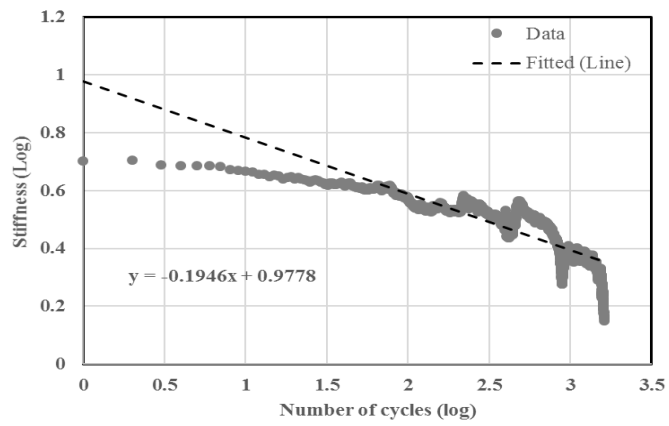
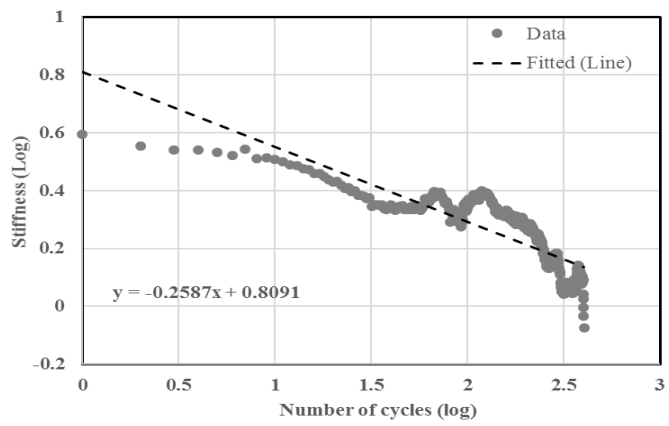


Figure G

### LCNUH0 (III)



### LFMAS10 (I)



### LFMAS10 (II)

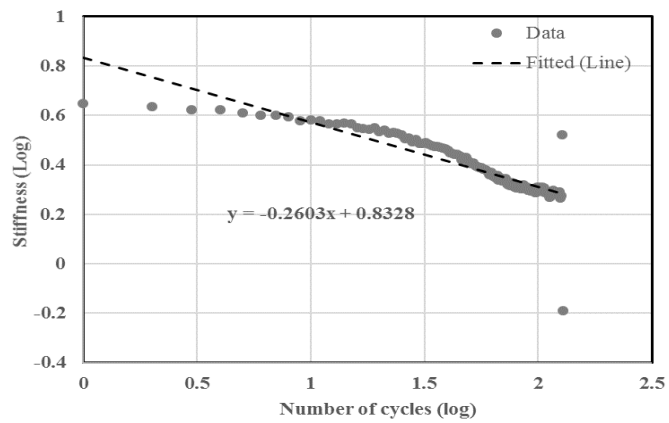
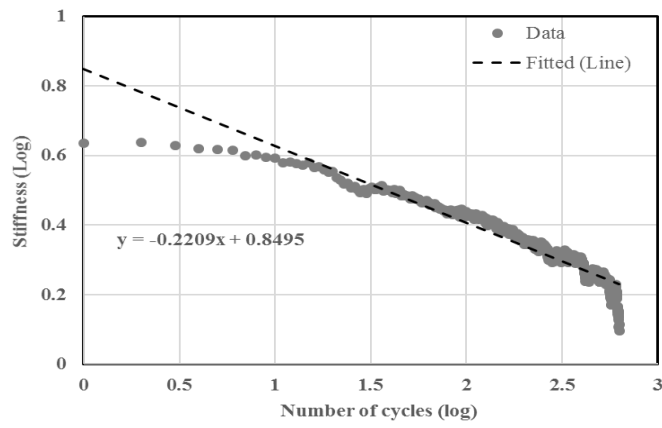
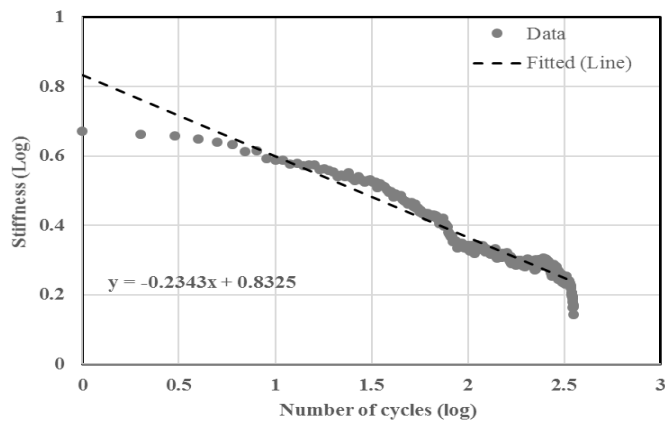


Figure G

### LFMAS10 (III)



### LFMAS5 (I)



### LFMAS5 (II)

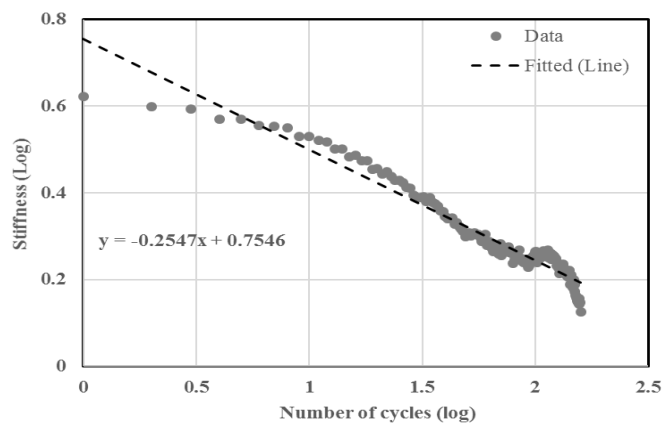
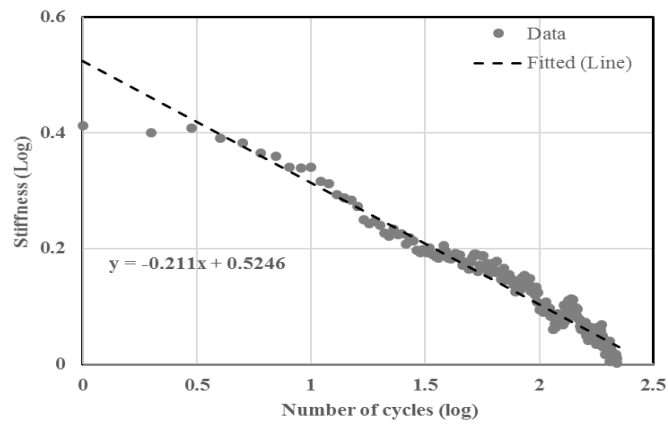


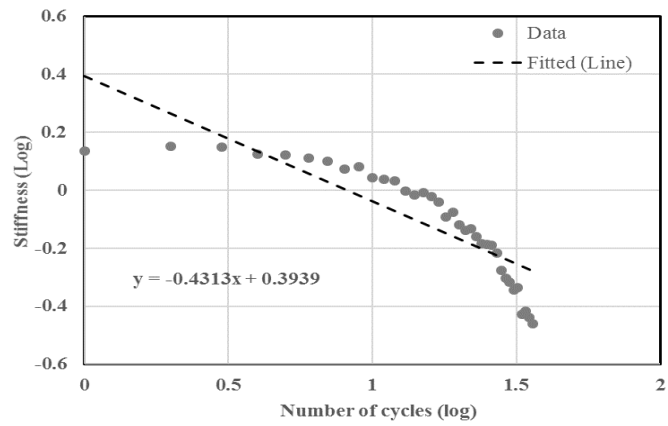
Figure G



### LFMAS5 (III)



### LFNAS5 (I)



### LFNAS5 (II)

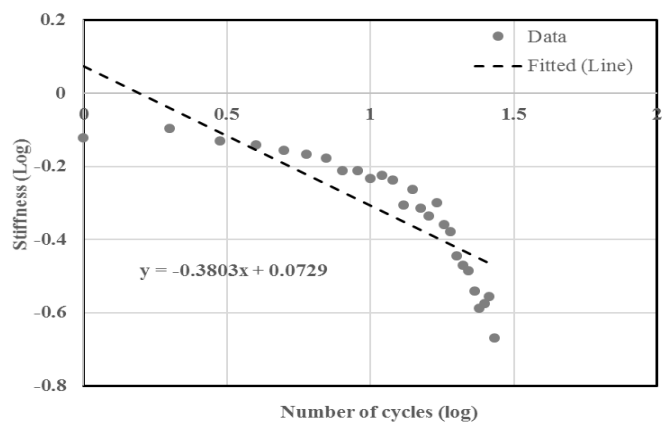
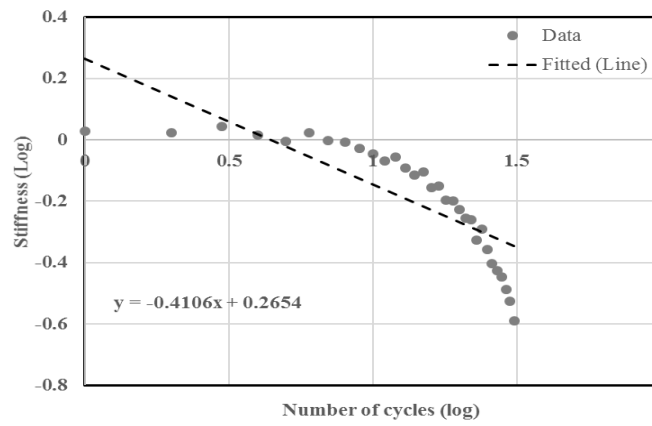
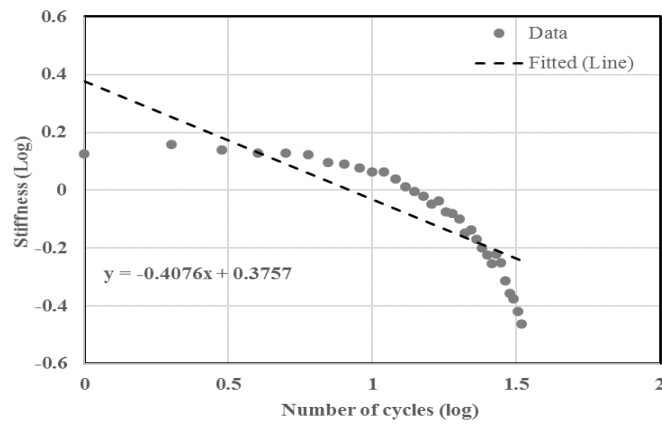


Figure G

### LFNAS5 (III)



### LFNAS10 (I)



### LFNAS10 (II)

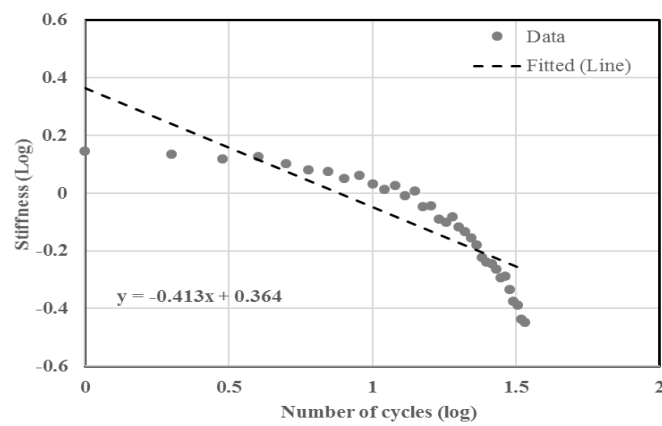
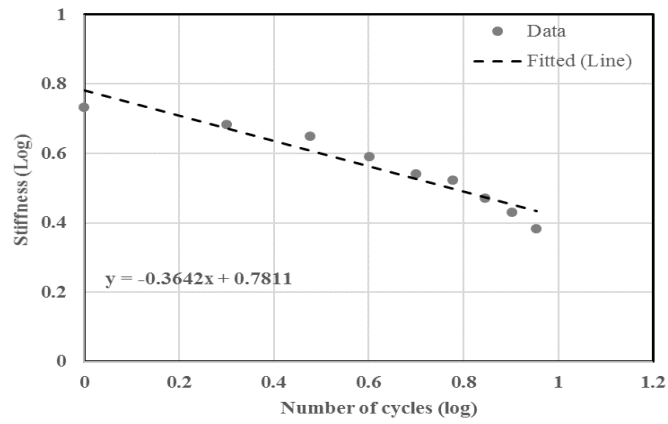
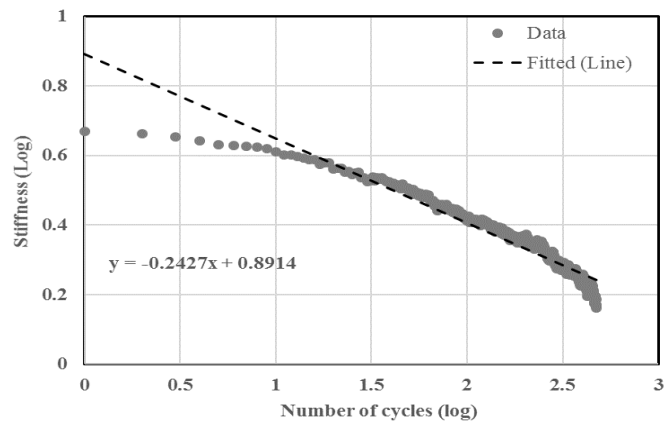


Figure G

### LFNAS10 (III)



### LCMAH5 (I)



### LCMAH5 (II)

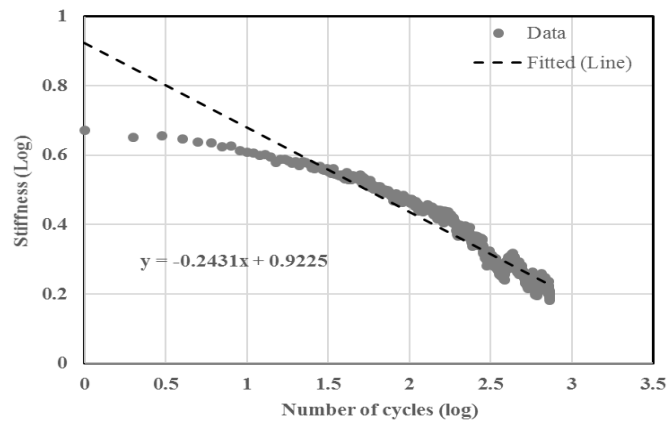


Figure G

### LCMAH5 (III)

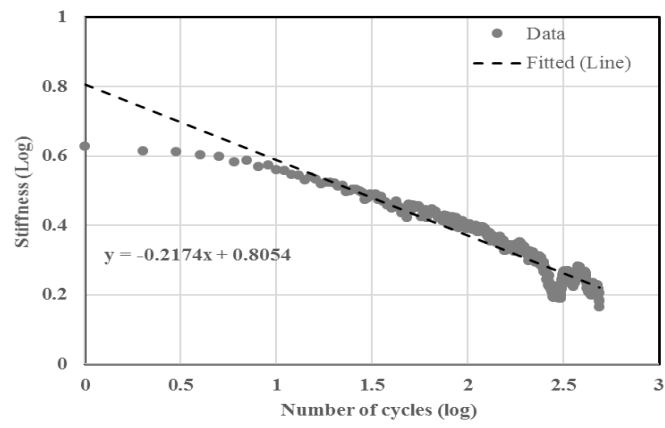
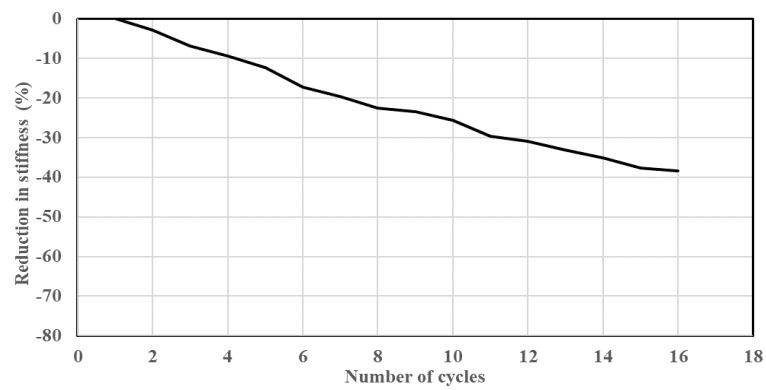


Figure G

## H. Reduction in stiffness, calculated from LLD-force curve

**BCMAS10 (I)**



**BCMAS10 (II)**

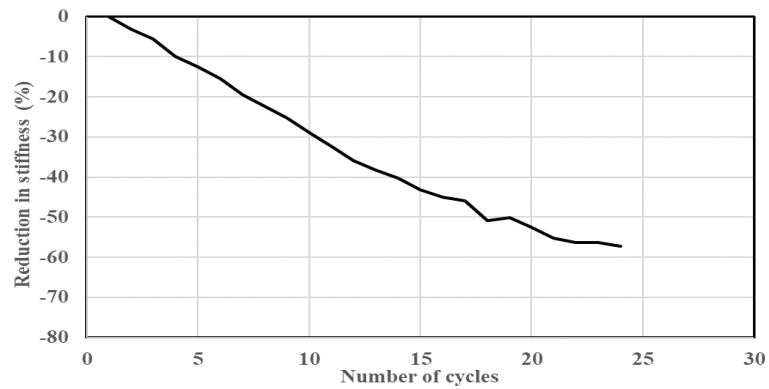
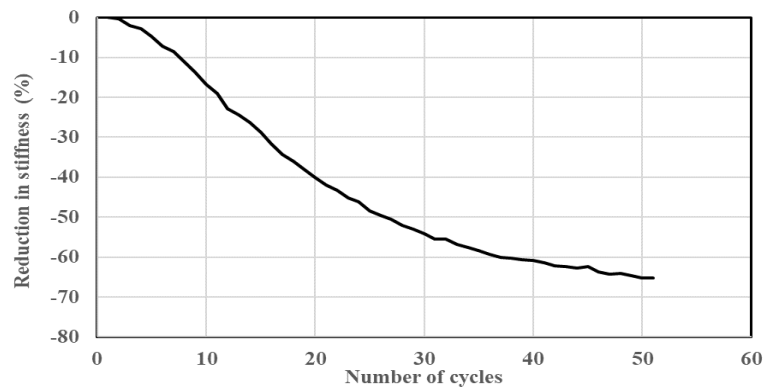
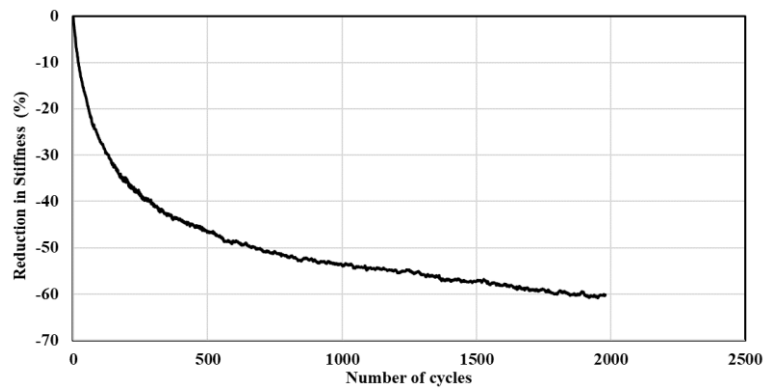


**Figure H.**Reduction in Stiffness versus cycle number, calculated from LLD

**BCMAS10 (III)**



**BFMAH10 (I)**



**BFMAH10 (II)**

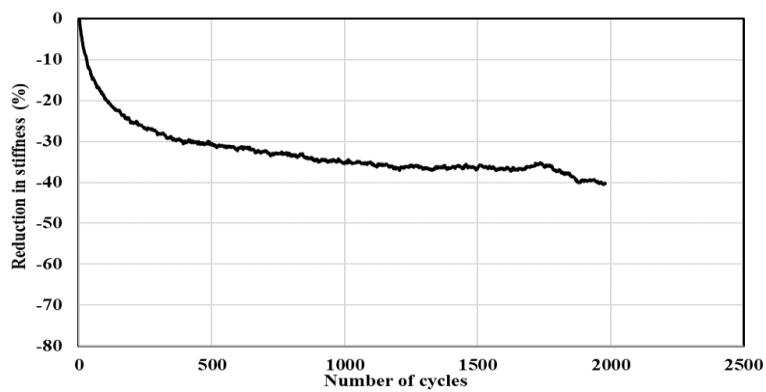
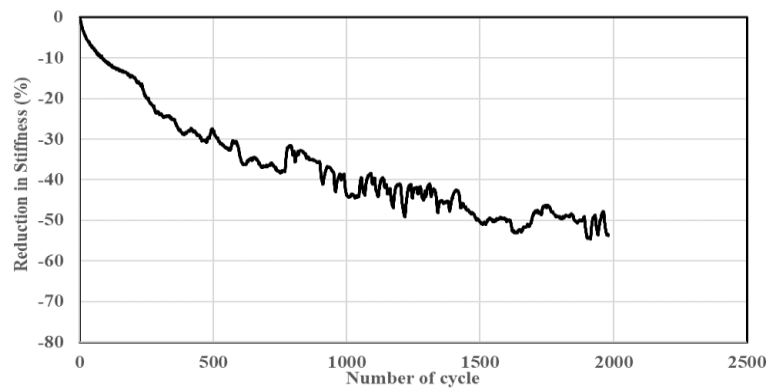
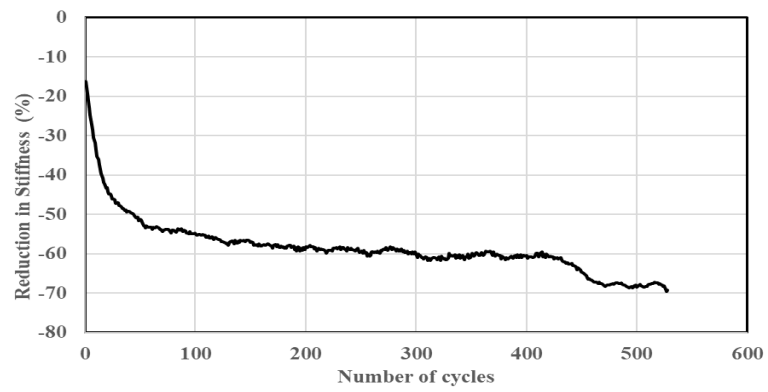


**Figure H**

### BFMAH10 (III)



### LCMUH10 (I)



### LCMUH10 (II)

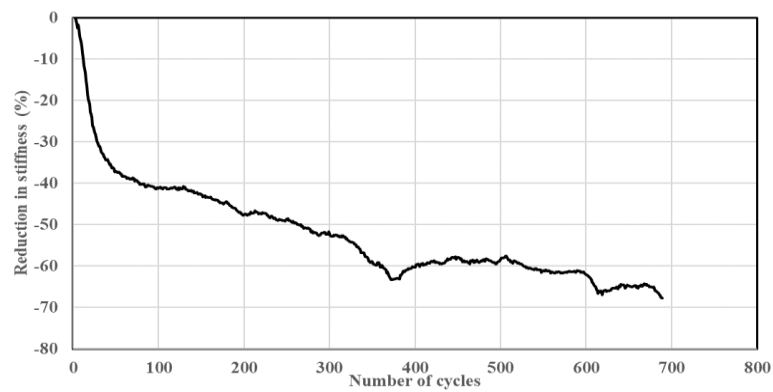
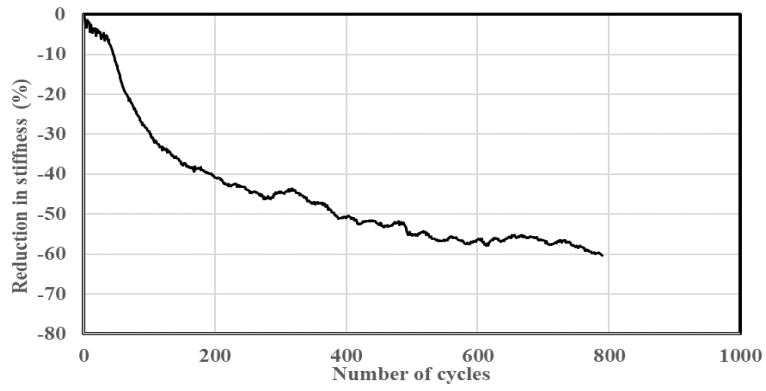
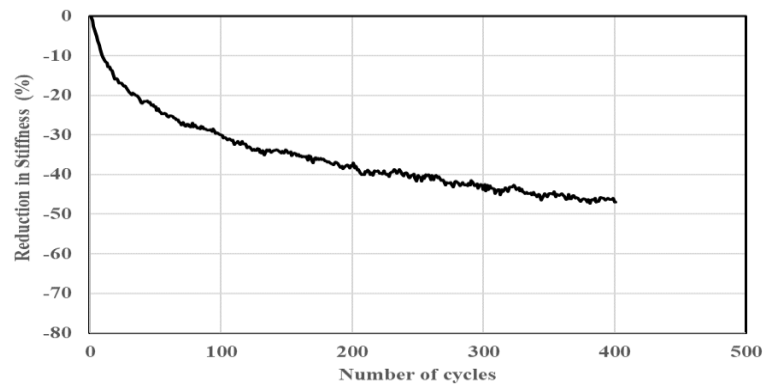


Figure H

**LCMUH10 (III)**



**LCMAH0 (I)**



**LCMAH0 (II)**

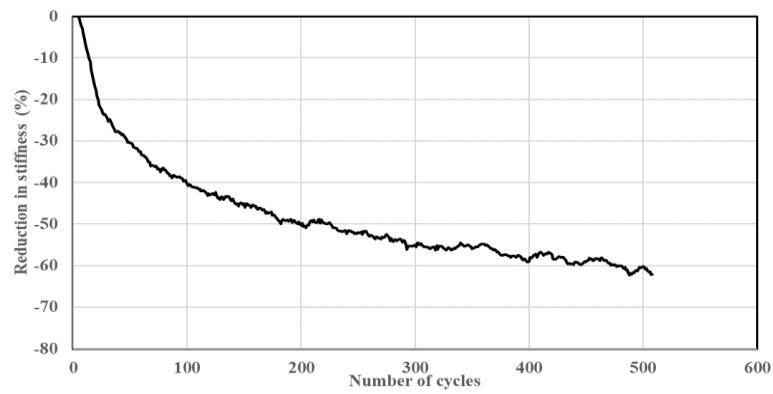
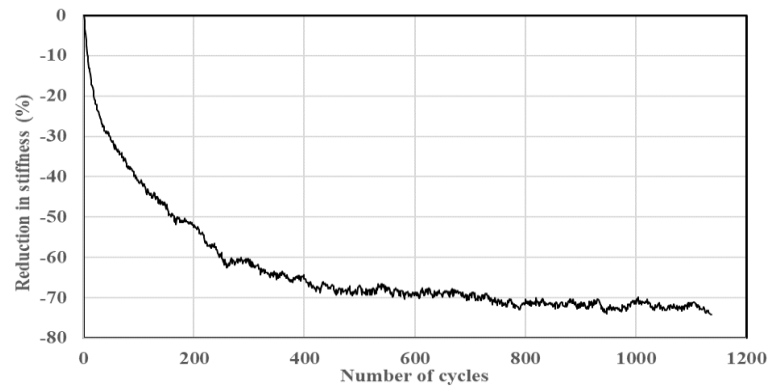


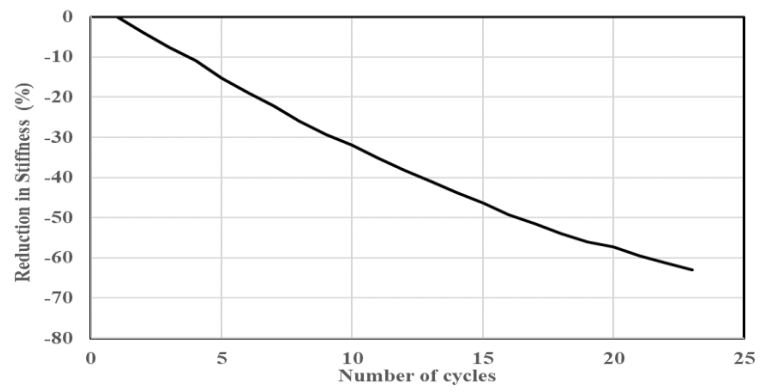
**Figure H**



### LCMAH0 (III)



### LCUHH10 (I)



### LCUHH10 (II)

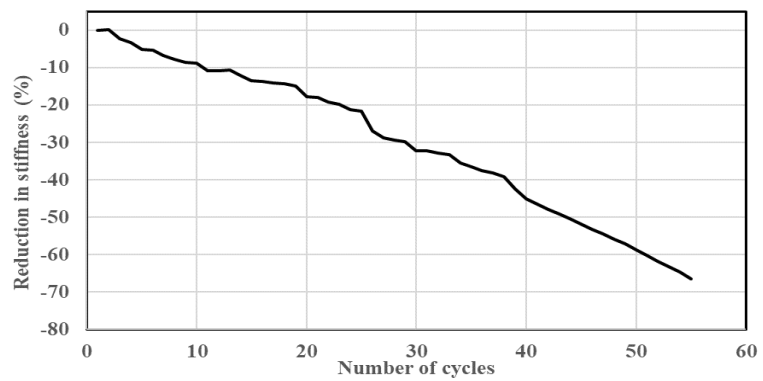
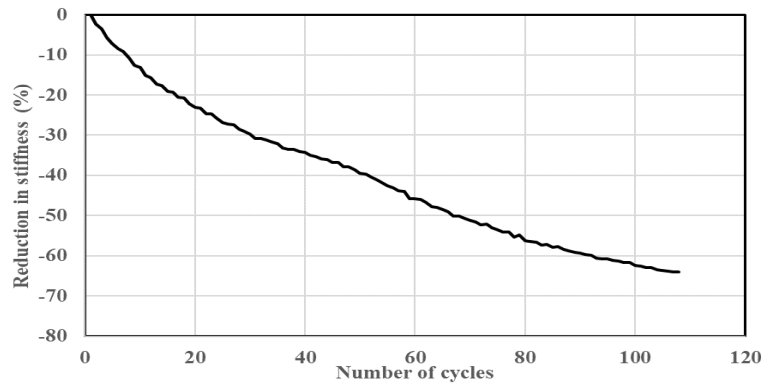
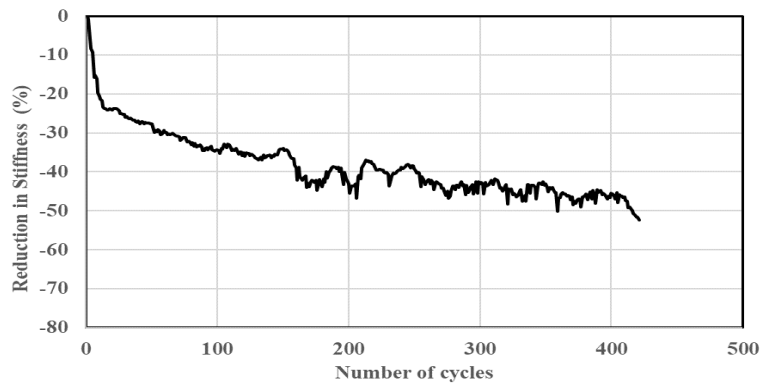


Figure H

### LCUHH10 (III)



### LFMAS0 (I)



### LFMAS0 (II)

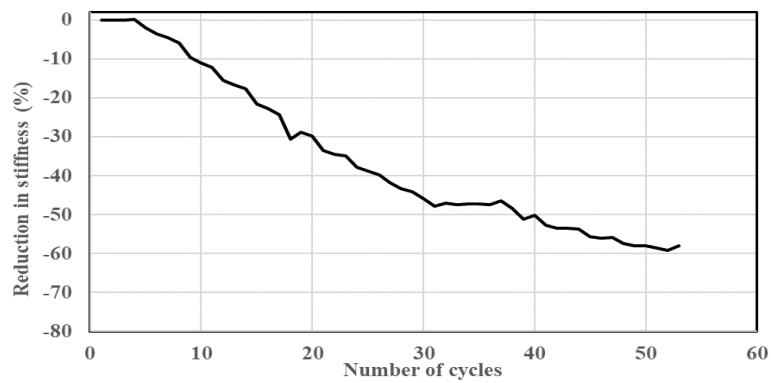
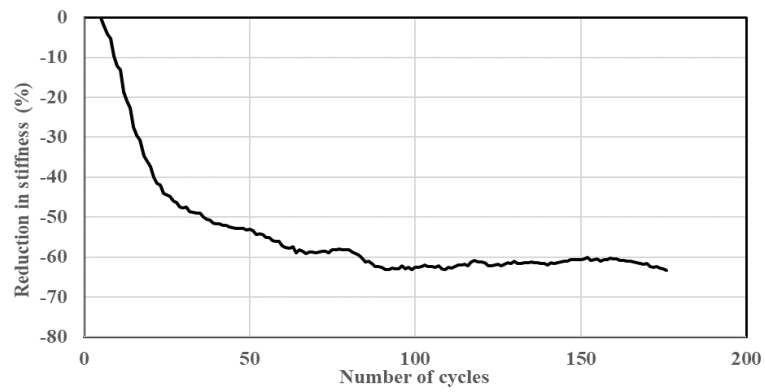
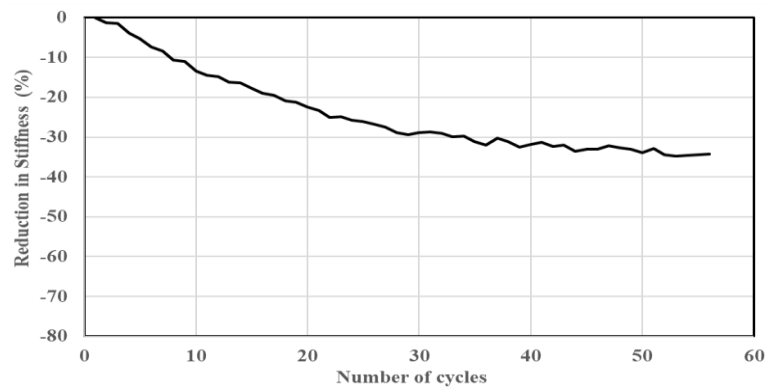


Figure H

### LFMAS0 (III)



### LCNAH5(I)



### LCNAH5(II)

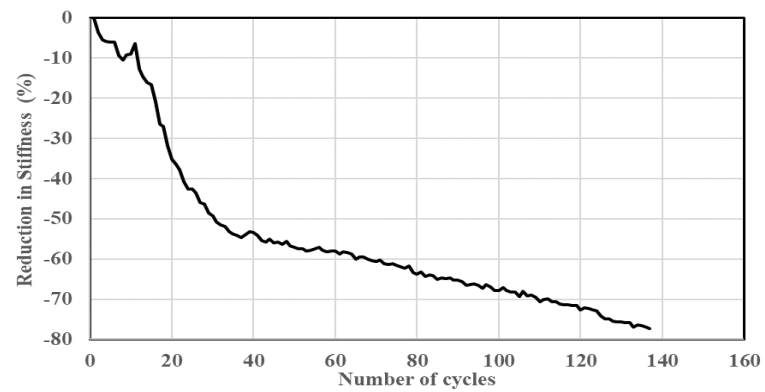
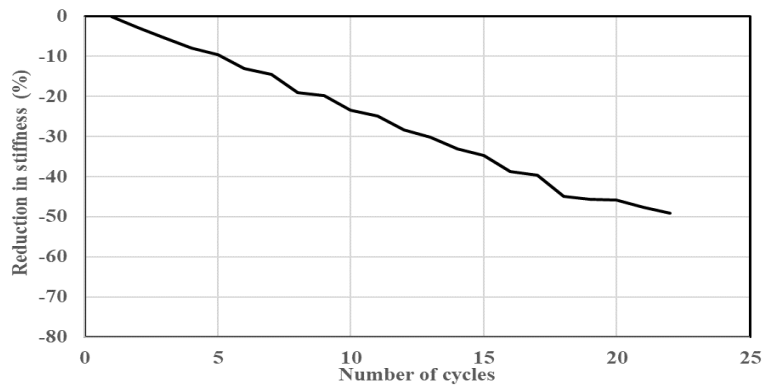
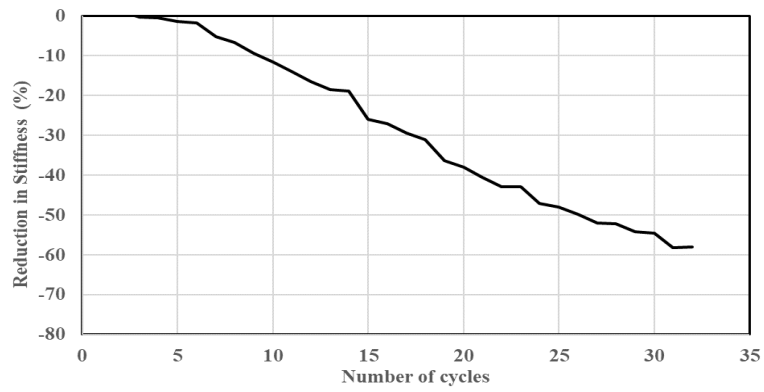


Figure H

**LCNAH5(III)**



**LCNAH0(I)**



**LCNAH0(II)**

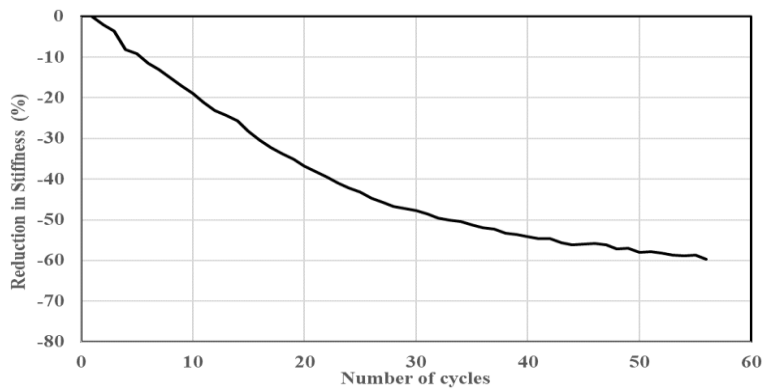
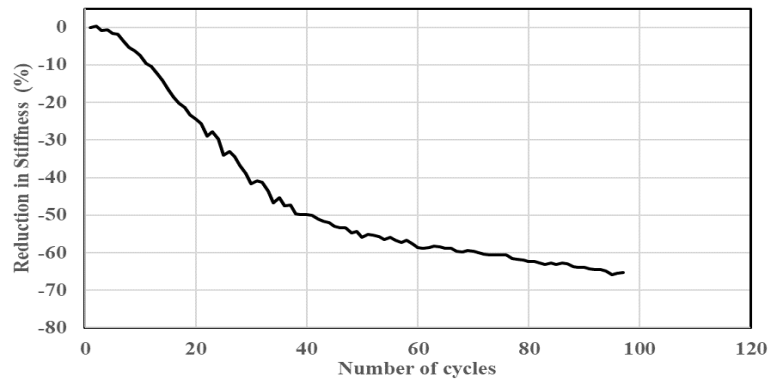
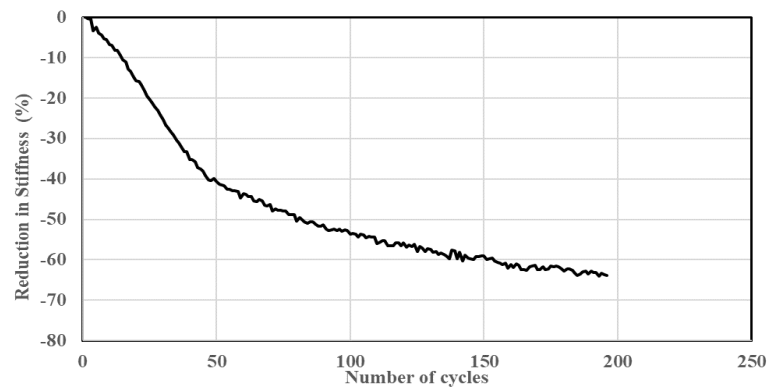


**Figure H**

### LCNAH0(III)



### BFNAH10 (I)



### BFNAH10 (II)

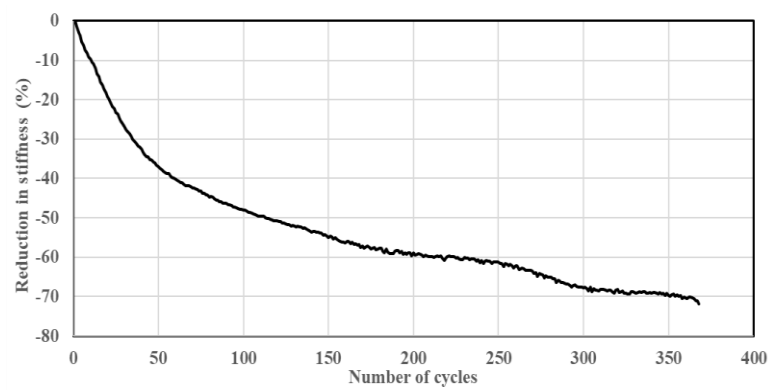
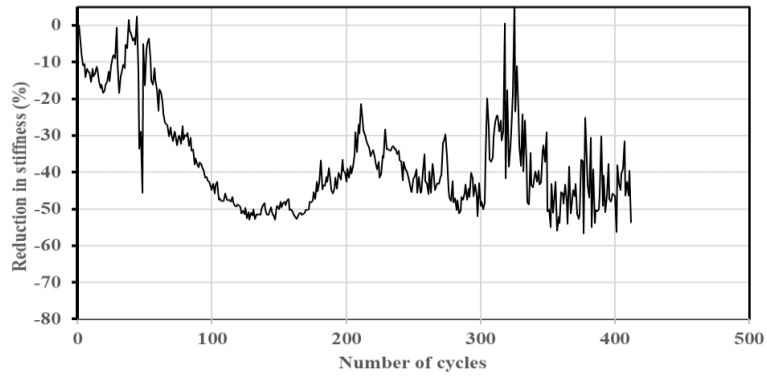
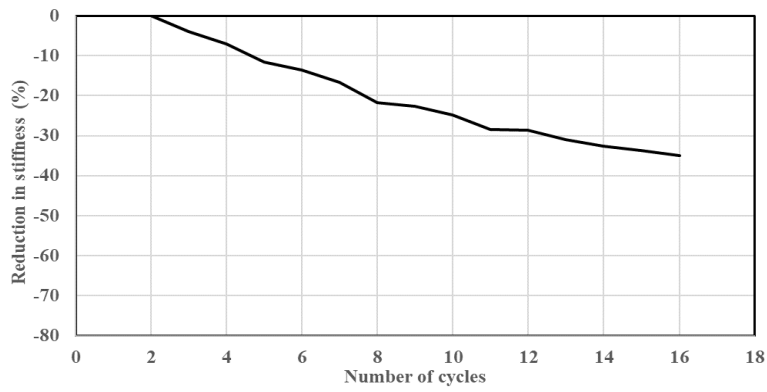


Figure H

### BFNAH10 (III)



### LFNUS5(I)



### LFNUS5(II)

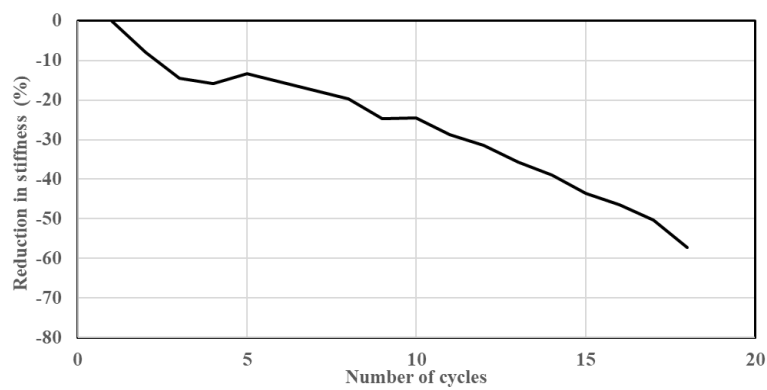
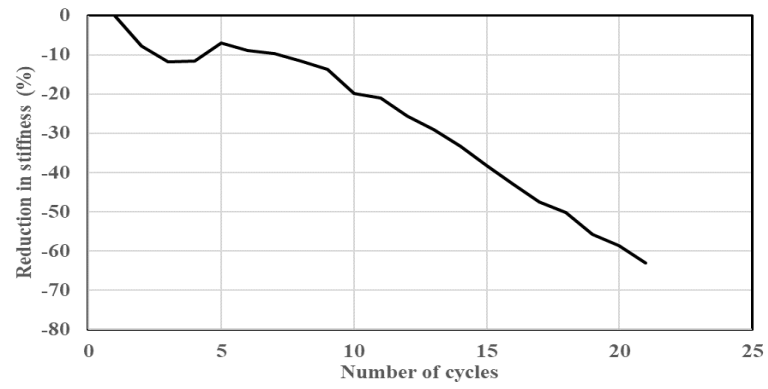
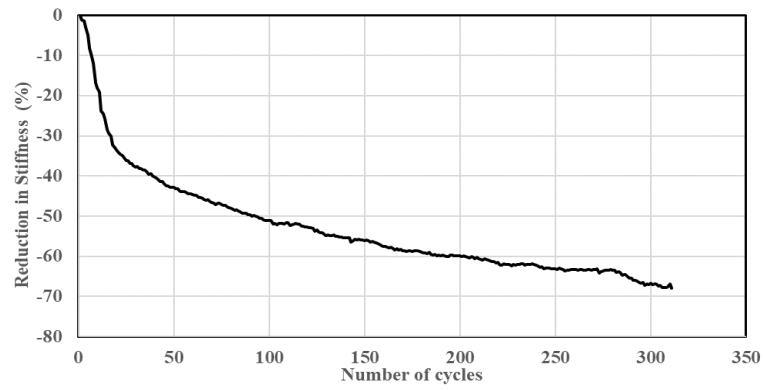


Figure H

**LFNUS5(III)**



**BCMUS0(I)**



**BCMUS0(II)**

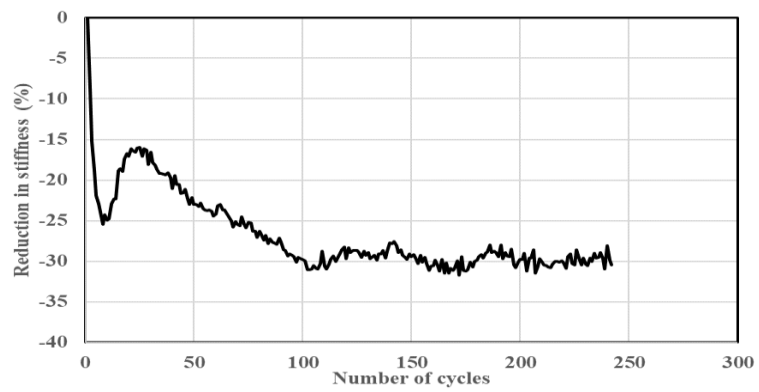
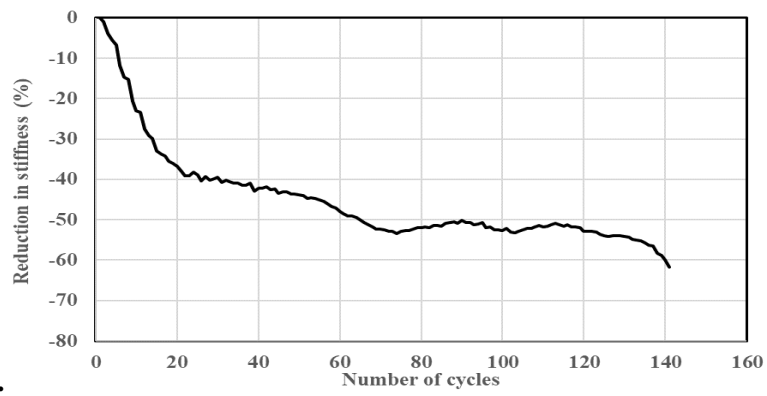
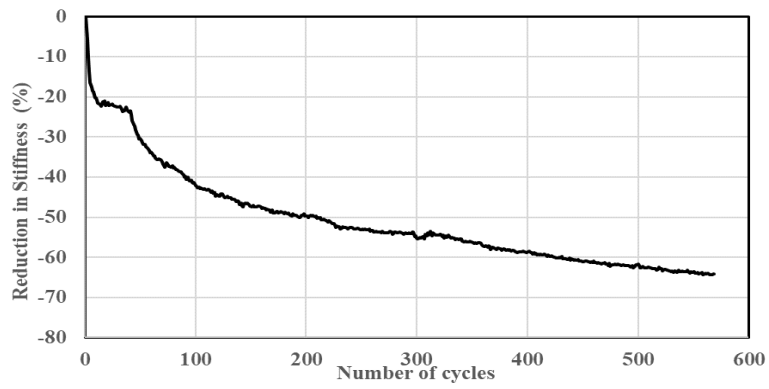


**Figure H**

**BCMUS0(III)**



**BCMAS10 (I)**



**BCMAS10 (II)**

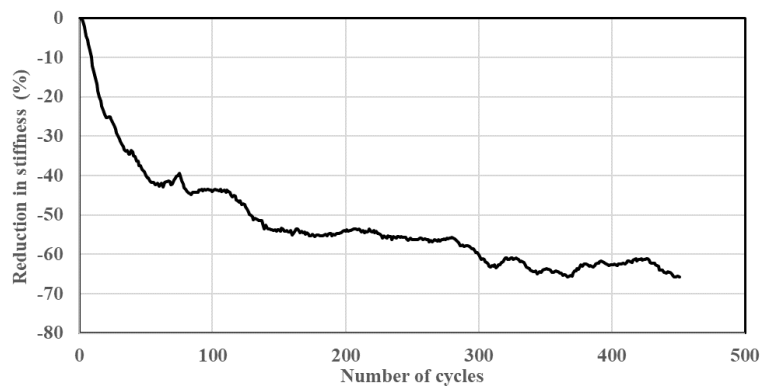
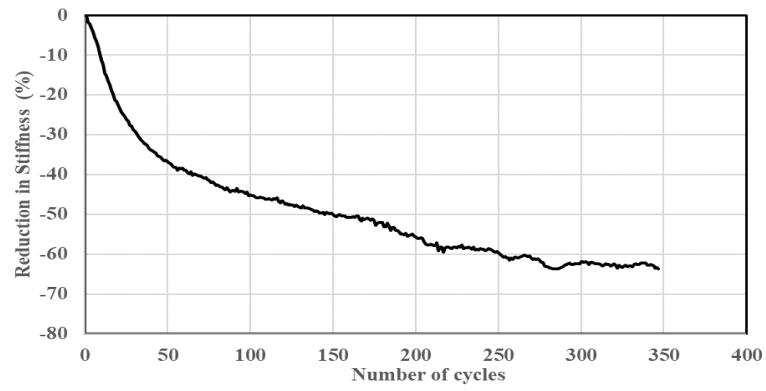


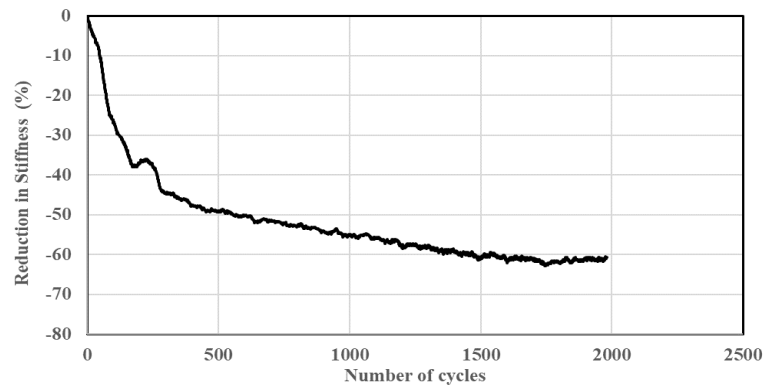
**Figure H**



**BCMAS10 (III)**



**BFMAH0 (I)**



**BFMAH0 (II)**

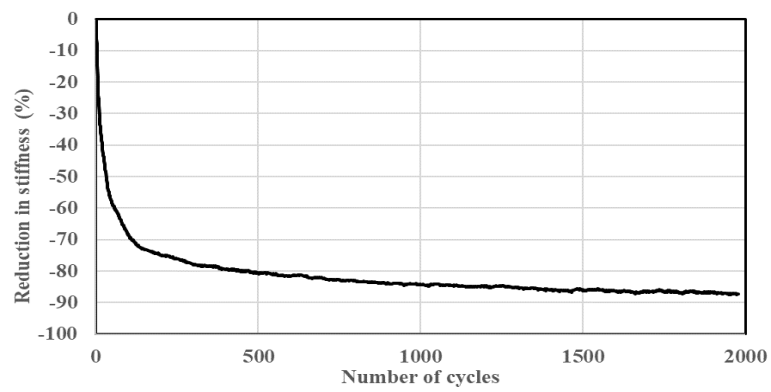
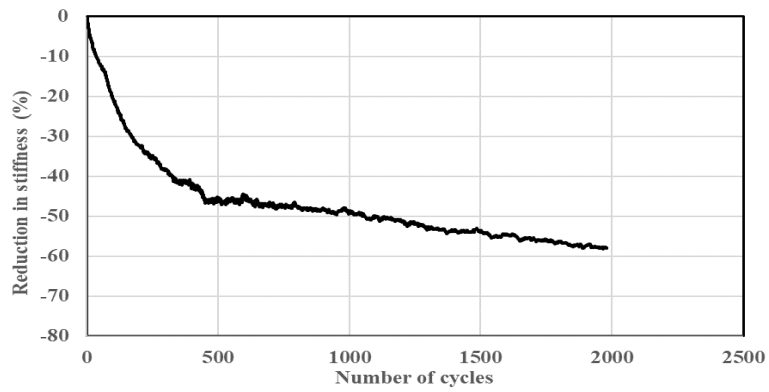
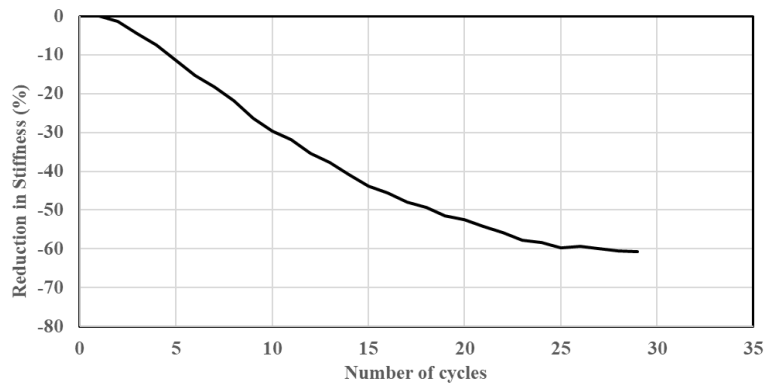


**Figure H**

**BFMAH0 (III)**



**BCNAS5 (I)**



**BCNAS5 (II)**

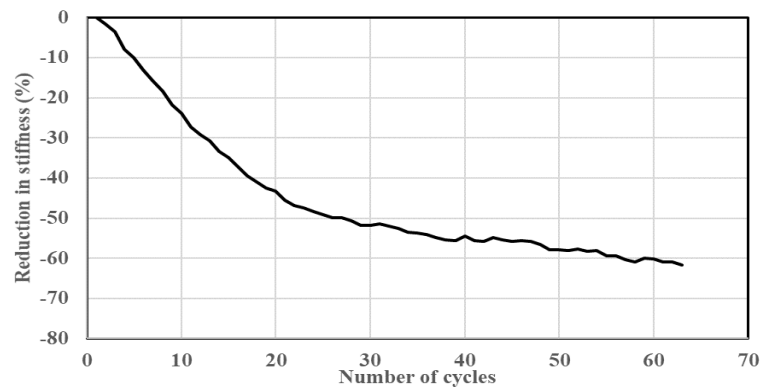
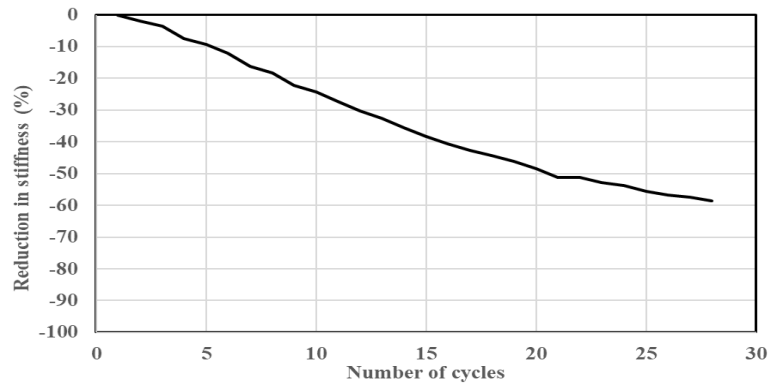
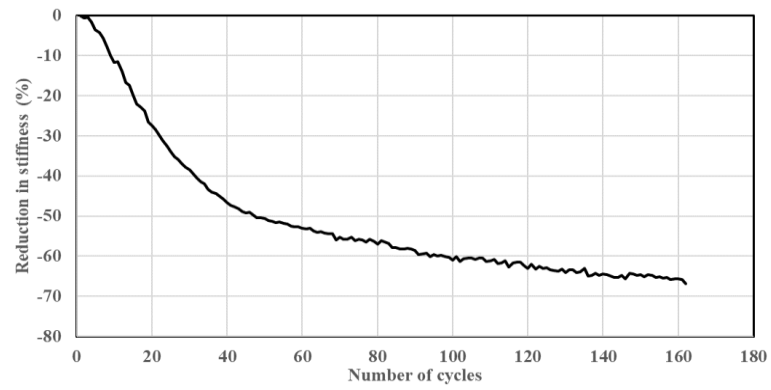


**Figure H**

**BCNAS5 (III)**



**BFNAH0 (I)**



**BFNAH0 (II)**

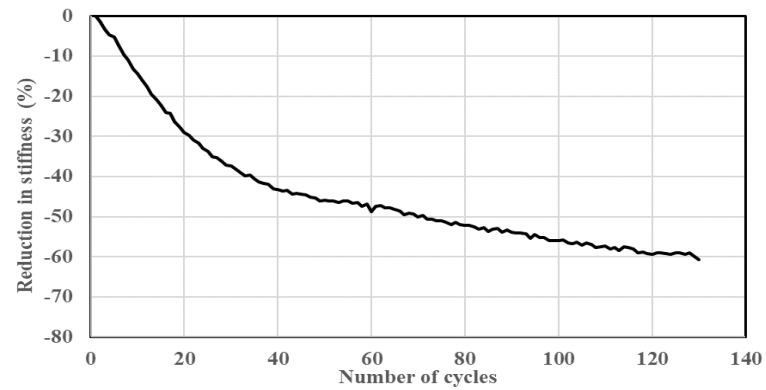
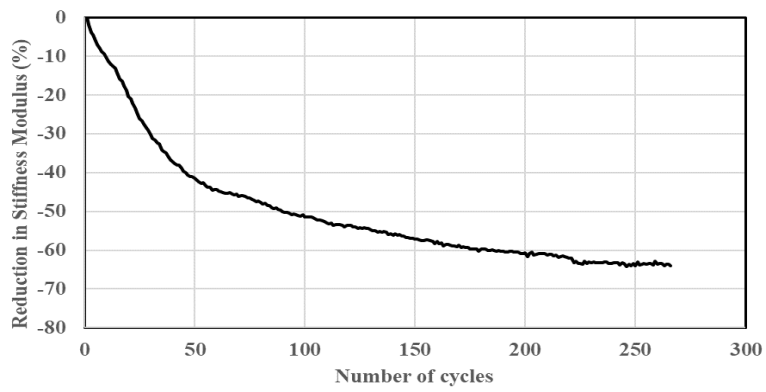
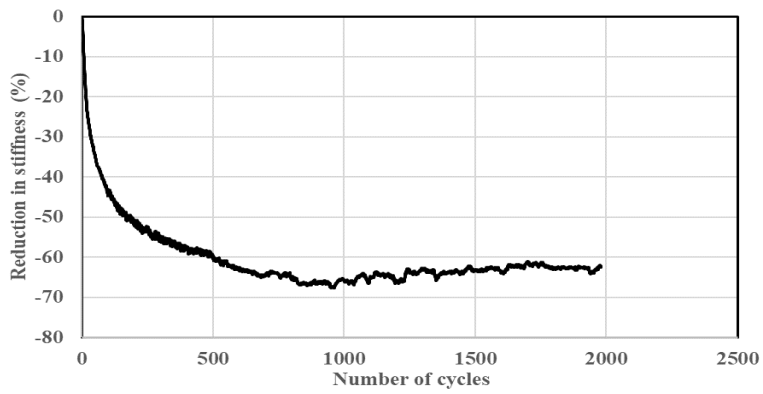


**Figure H**

### BFNAH0 (III)



### BFMUH5 (I)



### BFMUH5 (II)

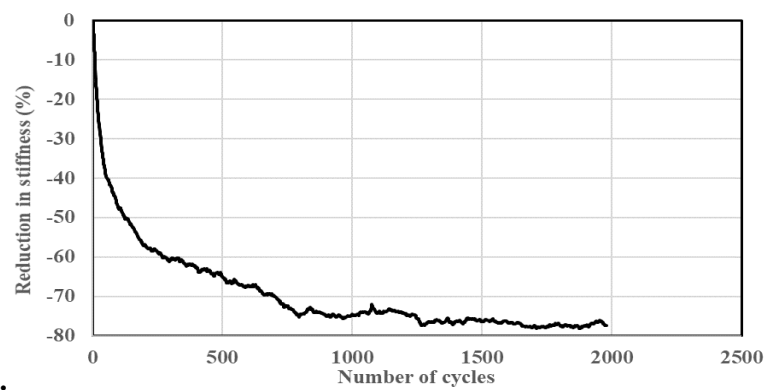
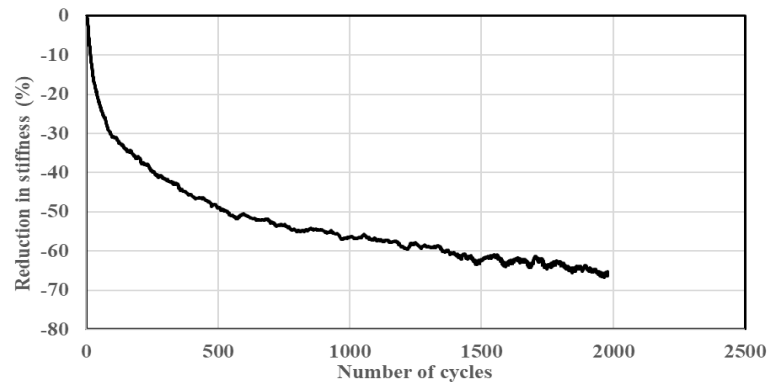
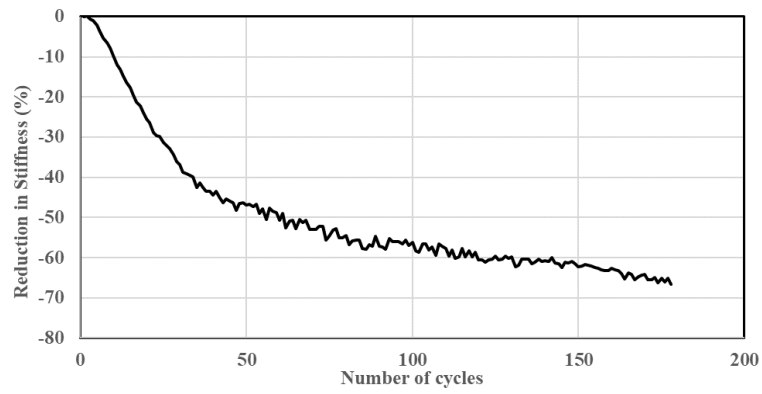


Figure H

### BFMUH5 (III)



### BFNUH5 (I)



### BFNUH5 (II)

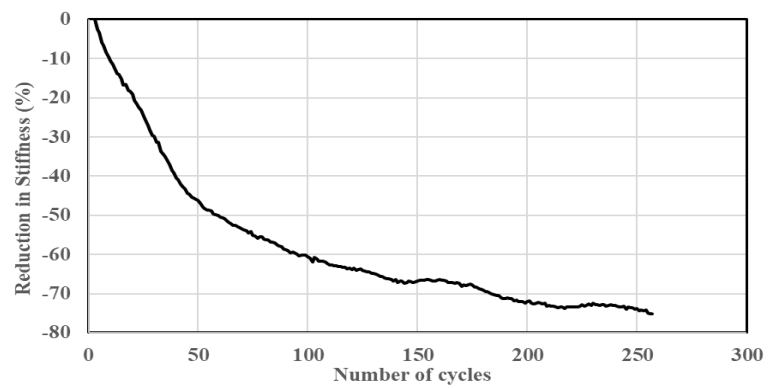
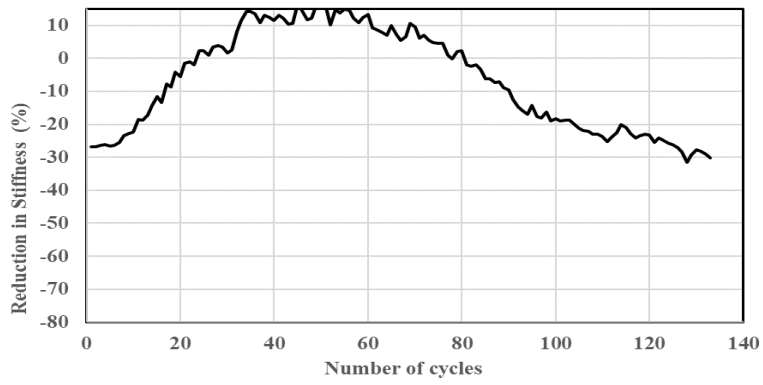
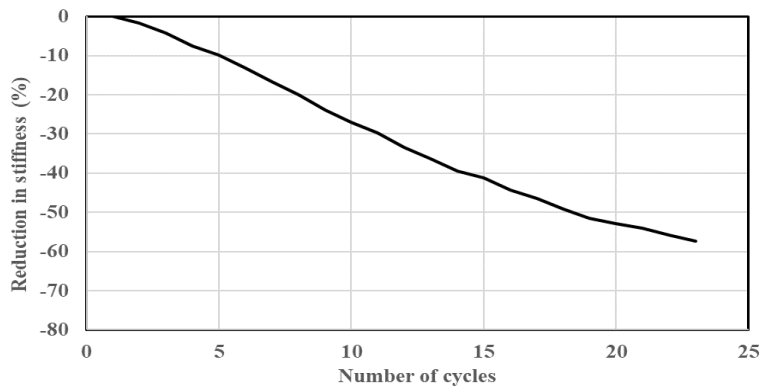


Figure H

### BFNUH5 (III)



### BCNUS10 (I)



### BCNUS10 (II)

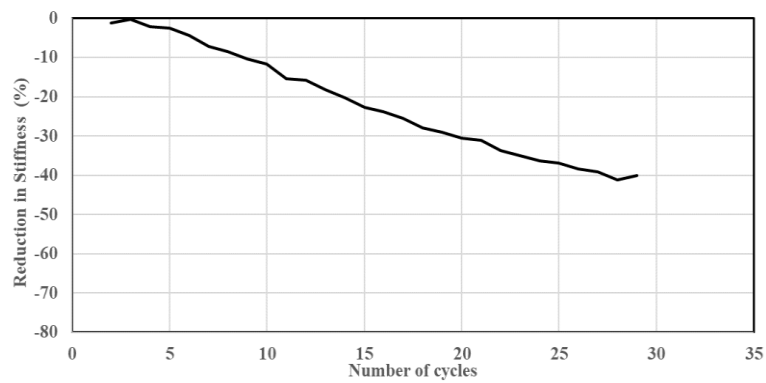
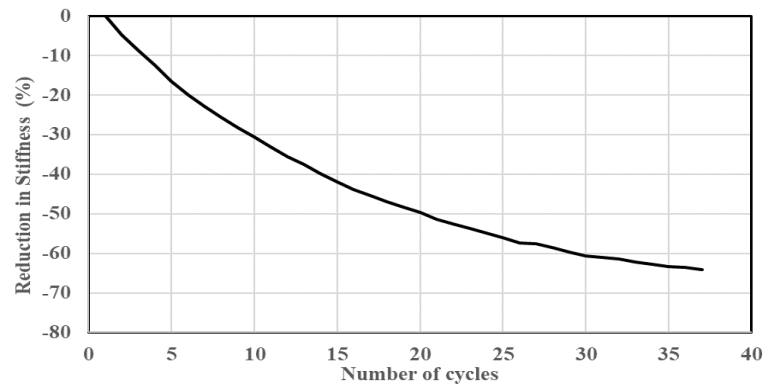
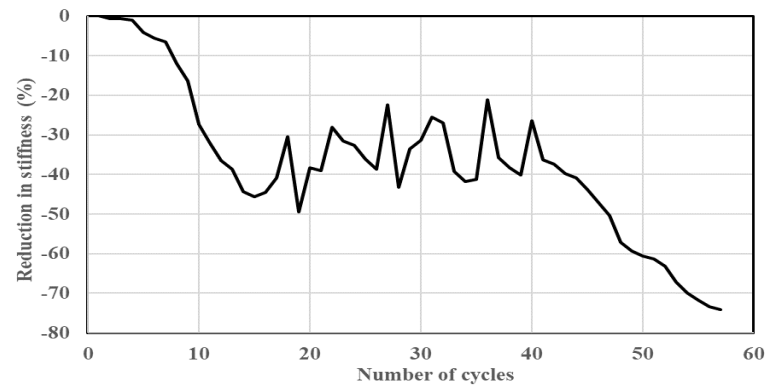


Figure H

**BCNUS10 (III)**



**BCNUS5 (I)**



**BCNUS5 (II)**

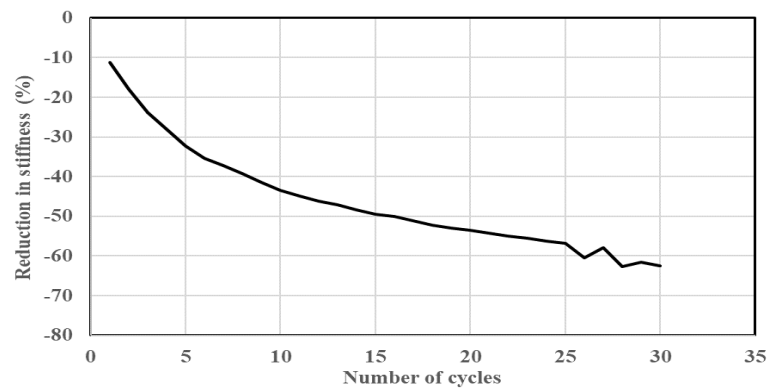
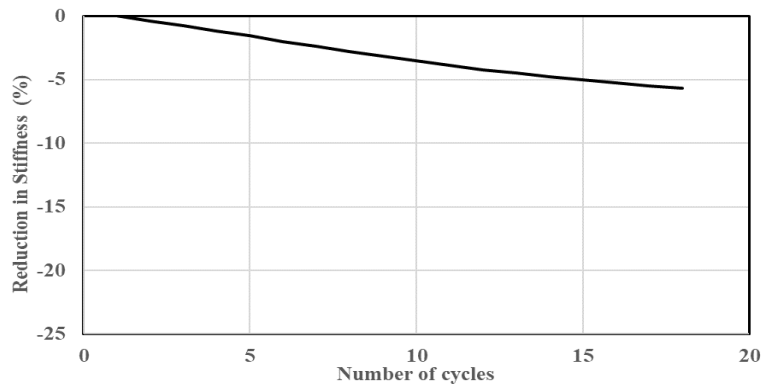
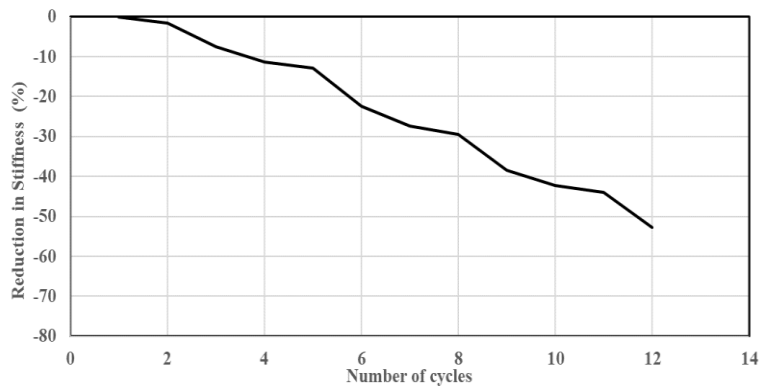


**Figure H**

**BCNUS5 (III)**



**BCNUS0 (I)**



**BCNUS0 (II)**

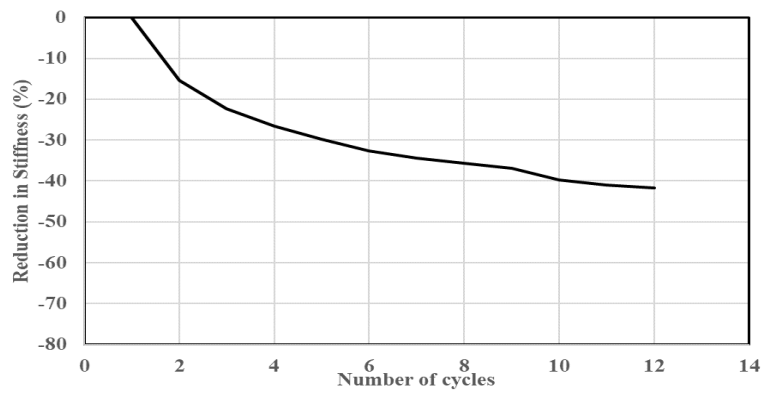
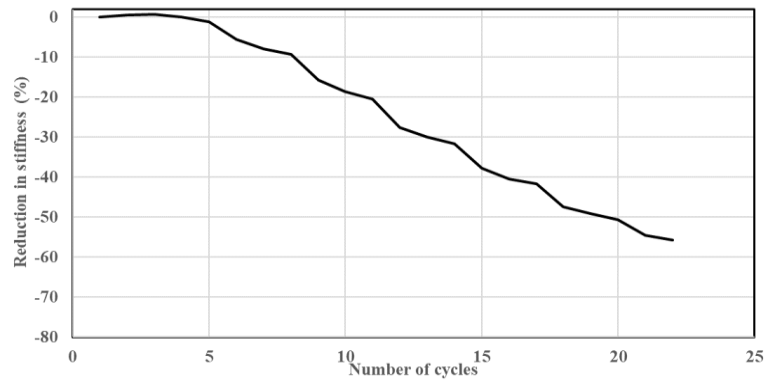


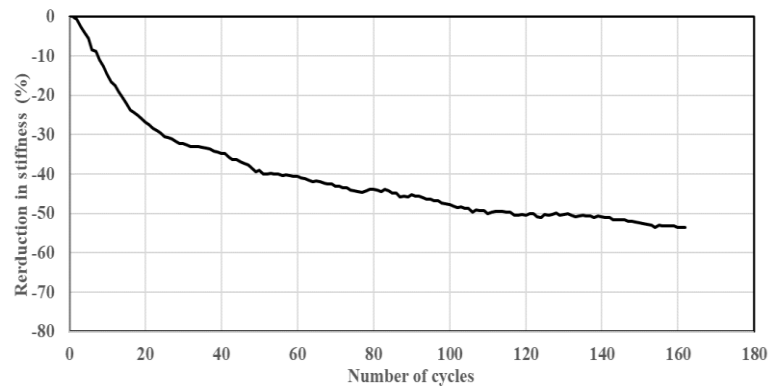
**Figure H**



### BCNUS0 (III)



### LFMUS5 (I)



### LFMUS5 (II)

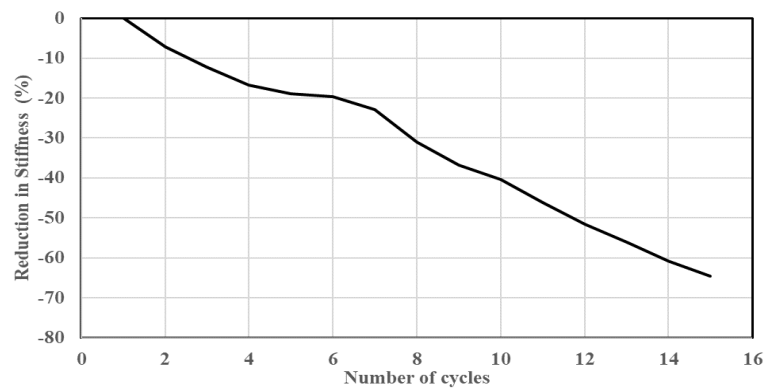
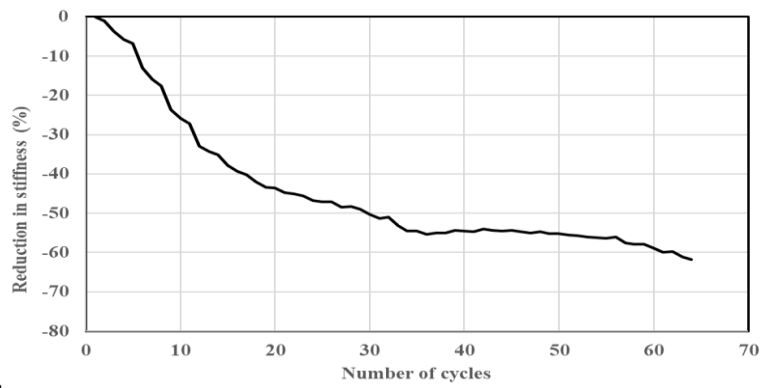
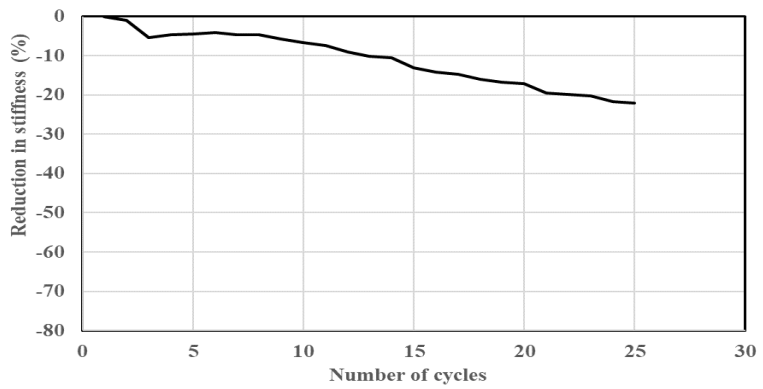


Figure H

### LFMUS5 (III)



### LFNAS0 (I)



### LFNAS0 (II)

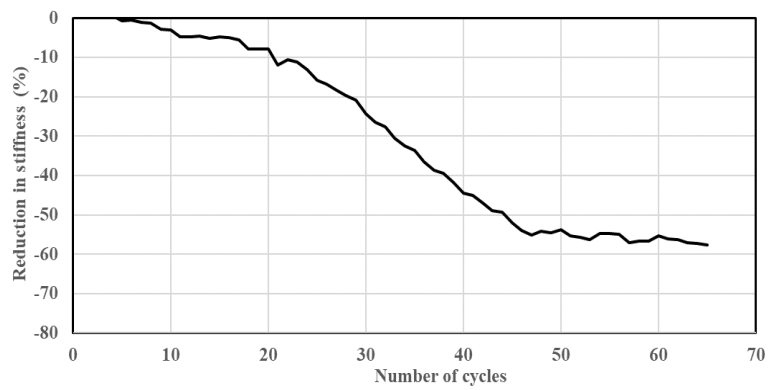
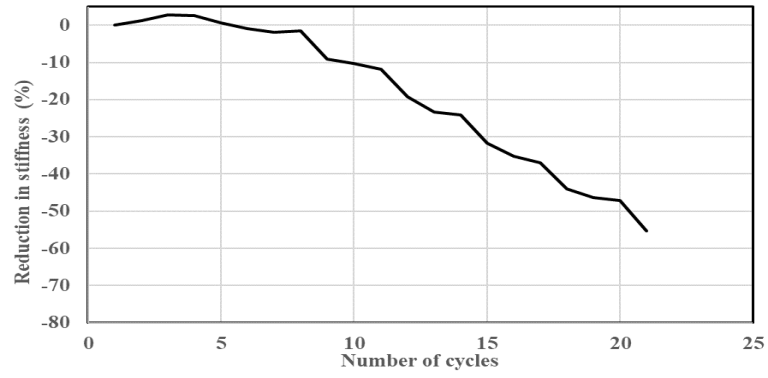


Figure H

**LFNAS0 (III)**



**LFNUS0 (I)**



**LFNUS0 (II)**

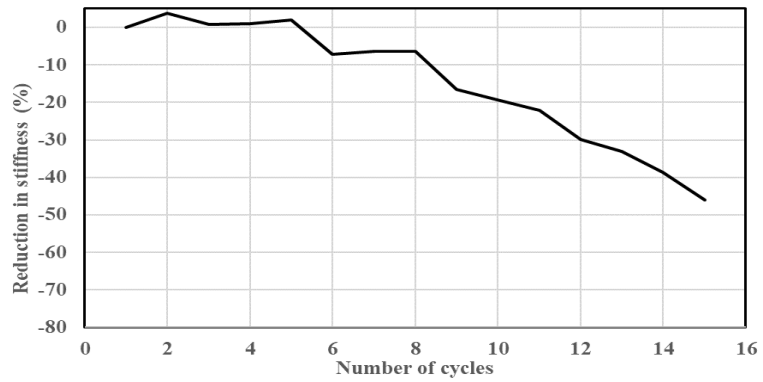
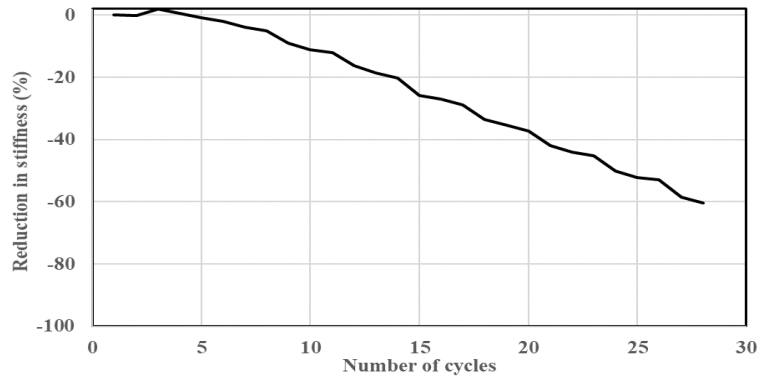
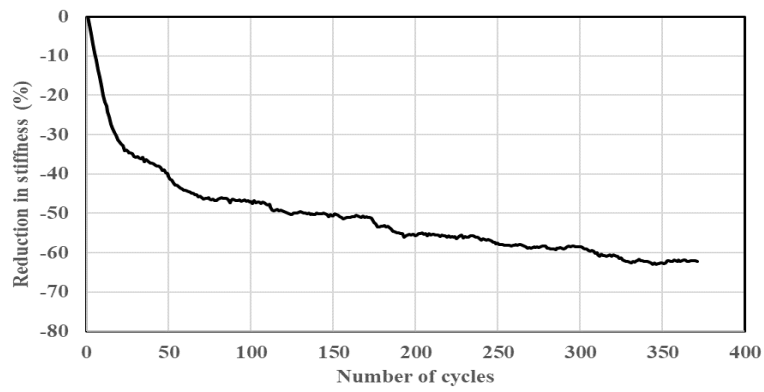


**Figure H**

**LFNUS0 (III)**



**BCMUS10 (I)**



**BCMUS10 (II)**

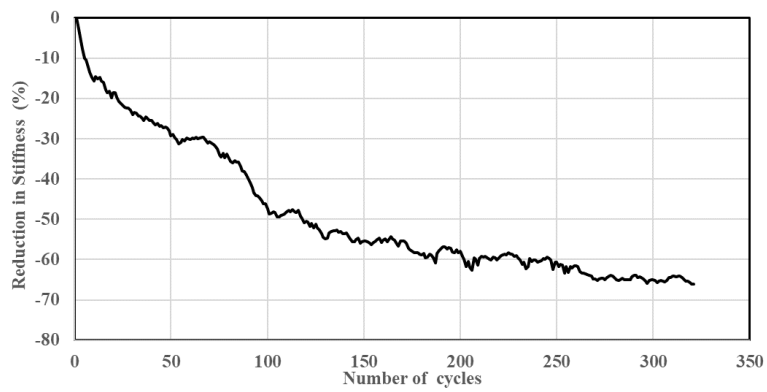
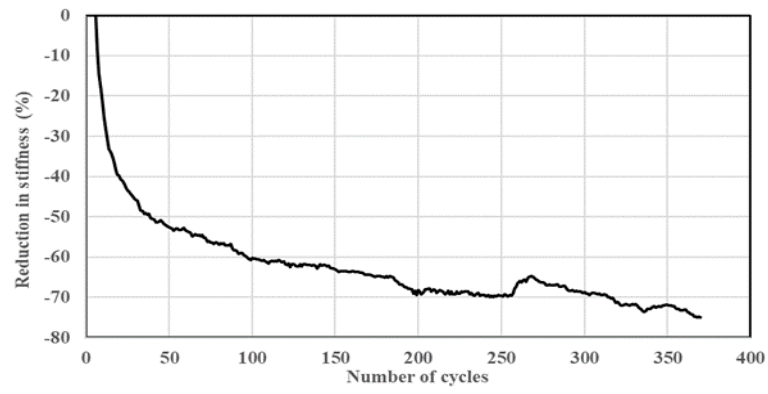
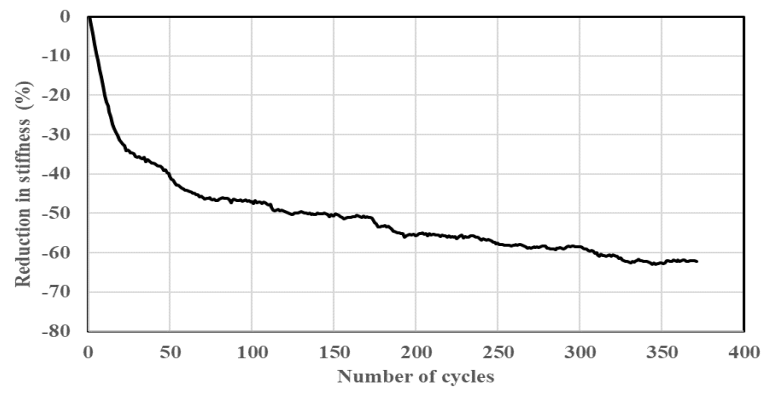


**Figure H**

### BCMUS10 (III)



### BCMUS0 (I)



### BCMUS0 (II)

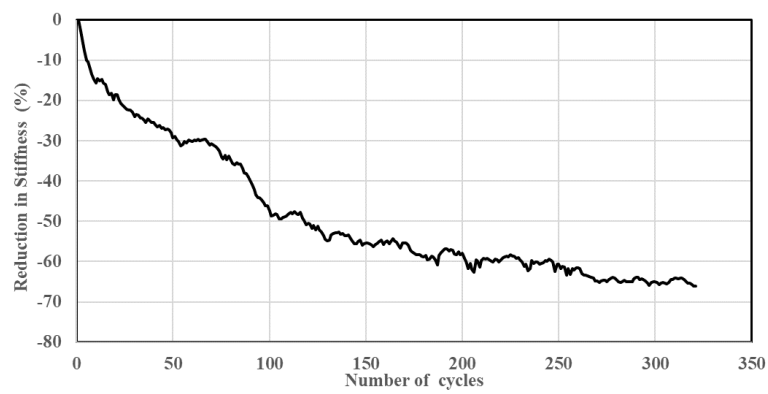
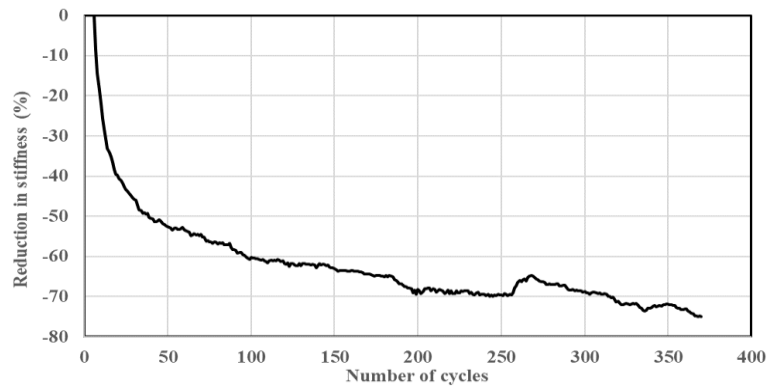
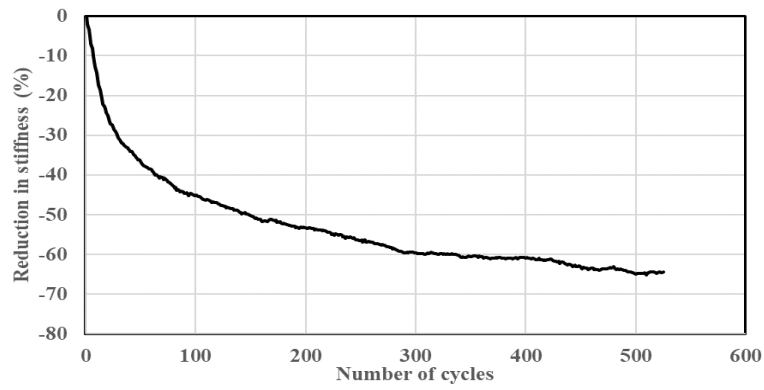


Figure H

**BCMUS0 (III)**



**BCMAS5 (I)**



**BCMAS5 (II)**

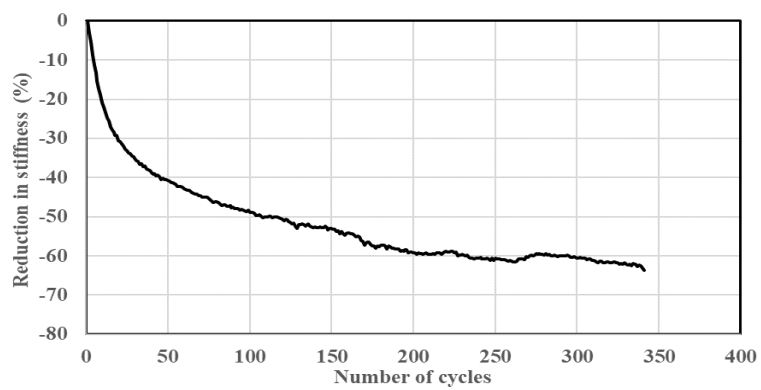
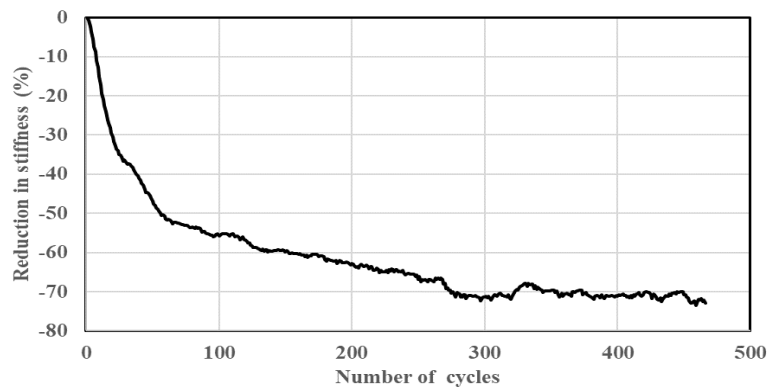
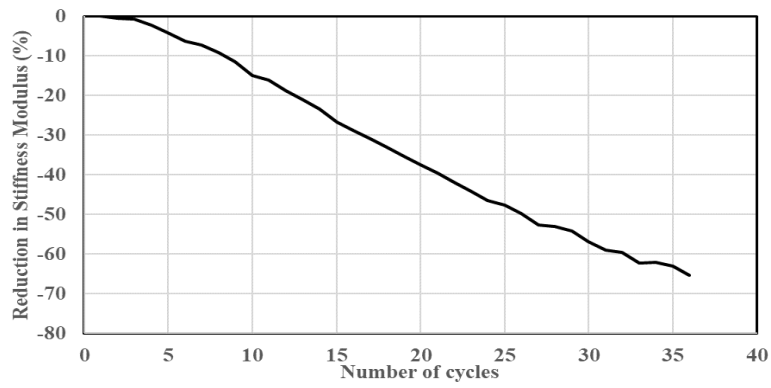


**Figure H**

**BCMAS5 (III)**



**LCNUH5 (I)**



**LCNUH5 (II)**

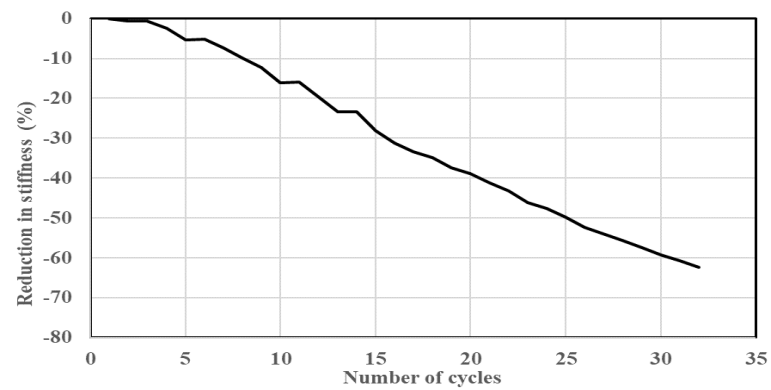
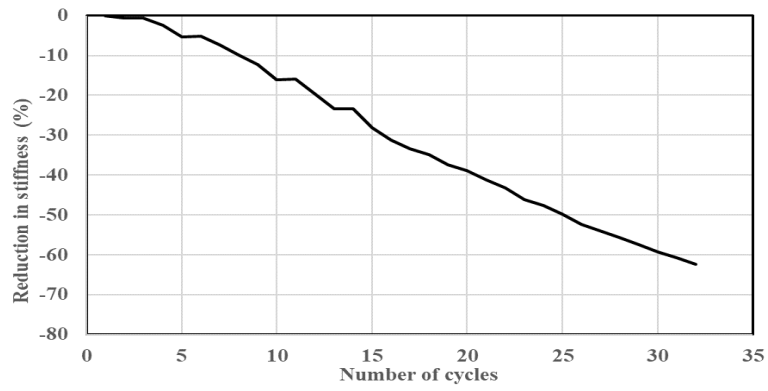
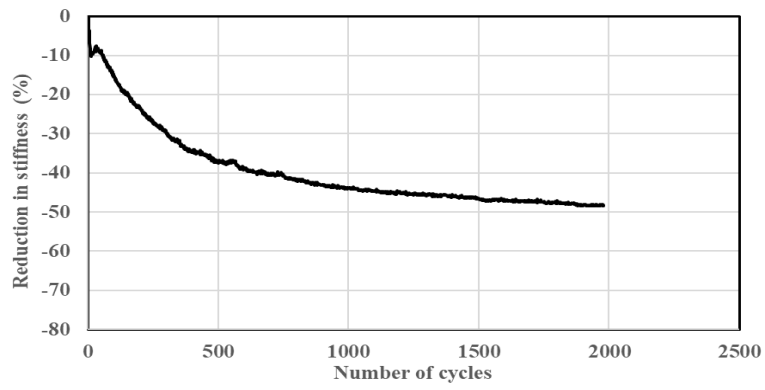


**Figure H**

**LCNUH5 (III)**



**BFMAH5 (I)**



**BFMAH5 (II)**

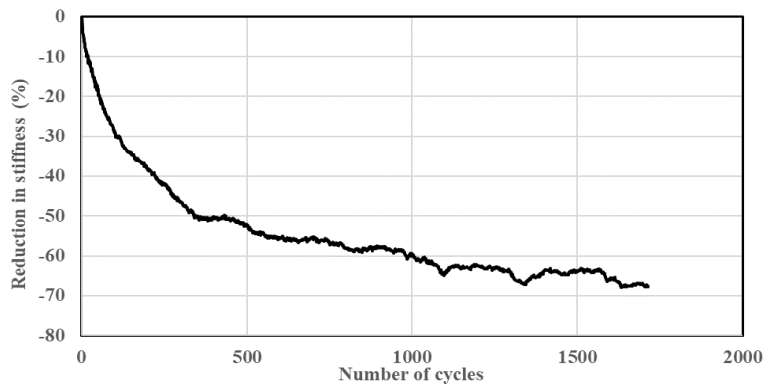
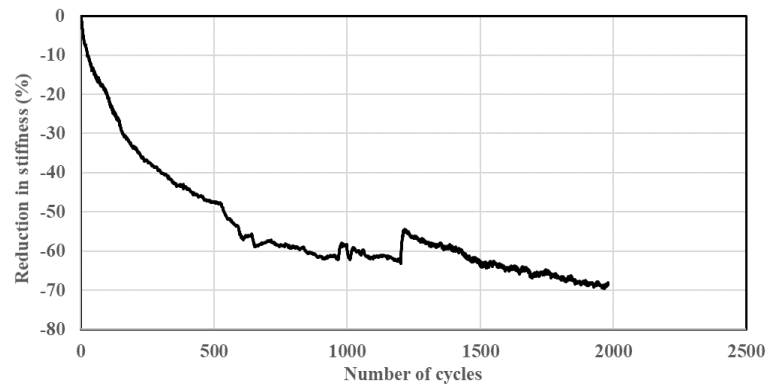


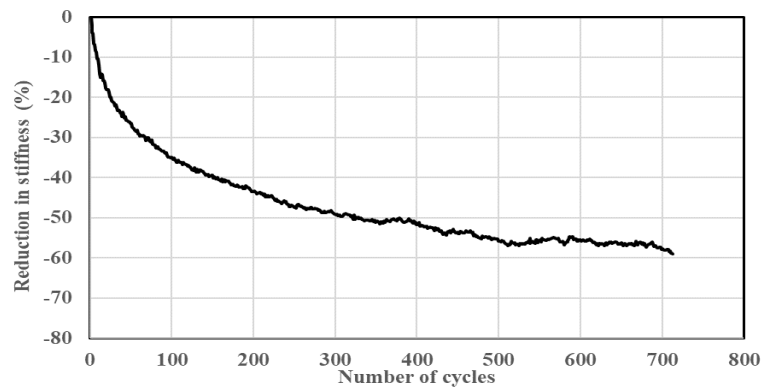
**Figure H**



### BFMAH5 (III)



### LCMAH0 (I)



### LCMAH0 (II)

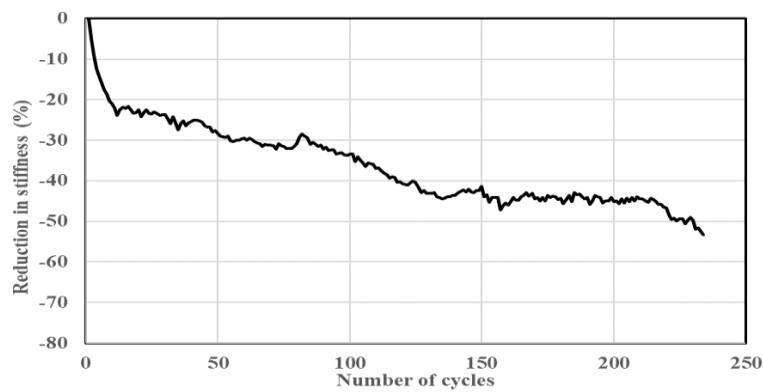
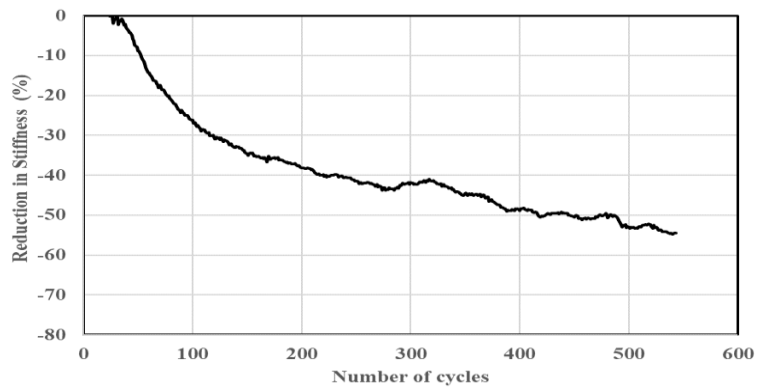
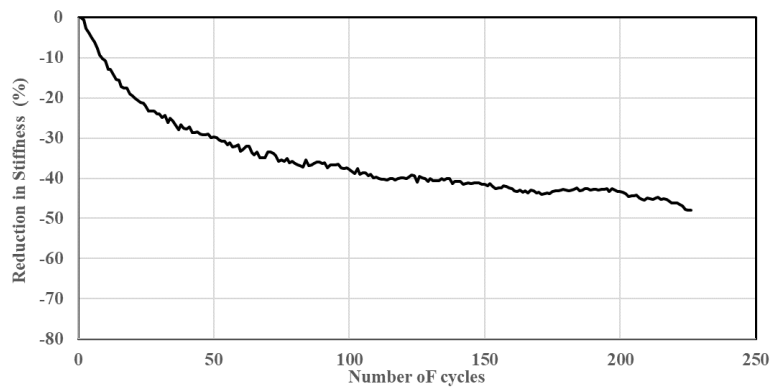


Figure H

### LCMAH0 (III)



### LCMUH5 (I)



### LCMUH5 (II)

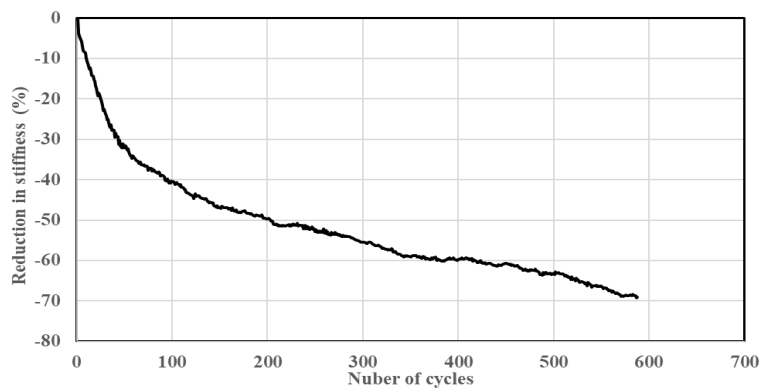
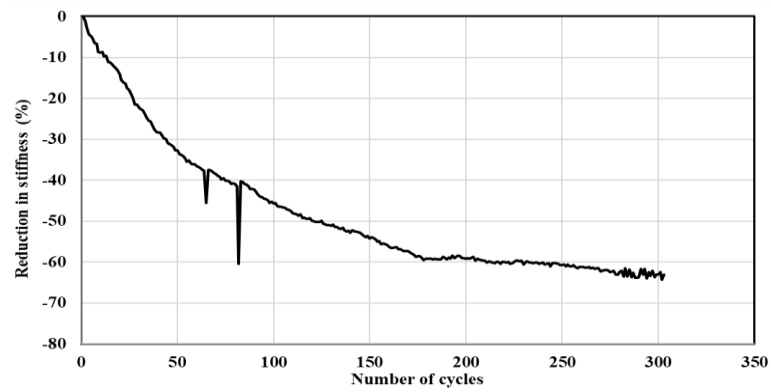
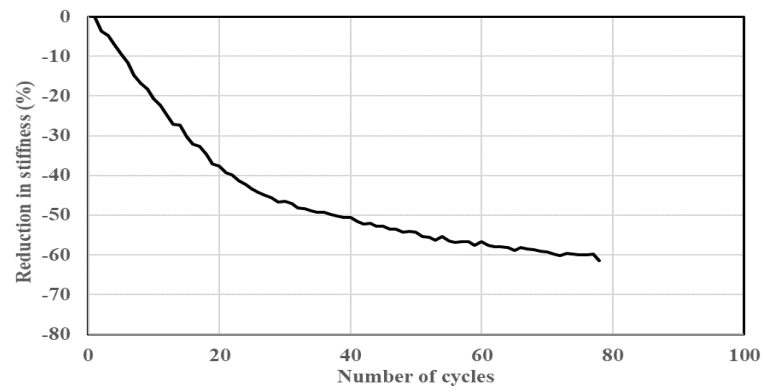


Figure H

### LCMUH5 (III)



### BFNUH0 (I)



### BFNUH0 (II)

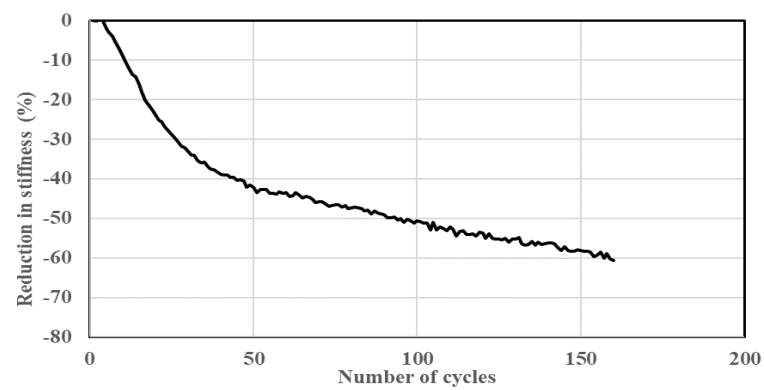
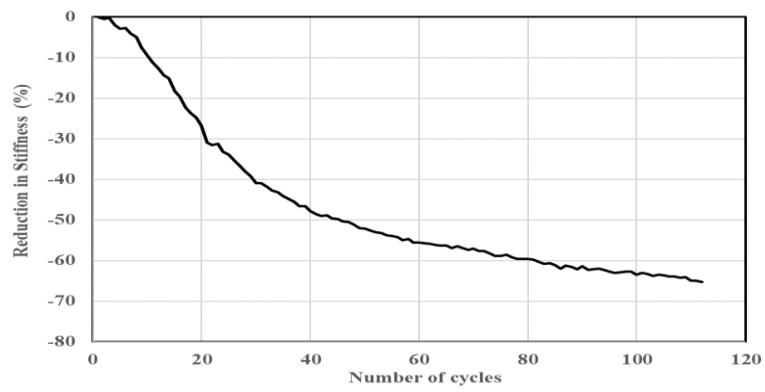
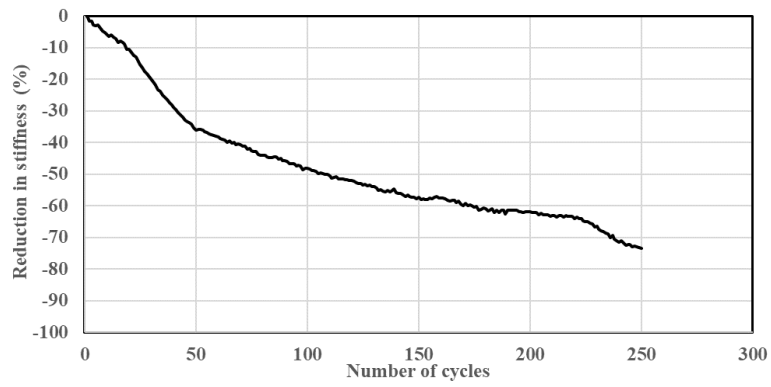


Figure H

### BFNUH0 (III)



### BFNAH5 (I)



### BFNAH5 (II)

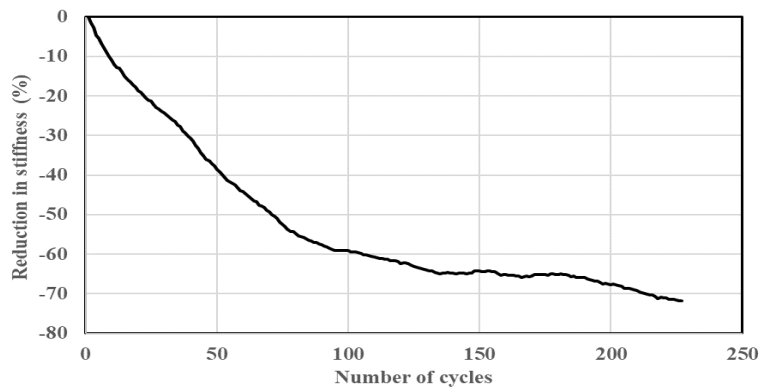
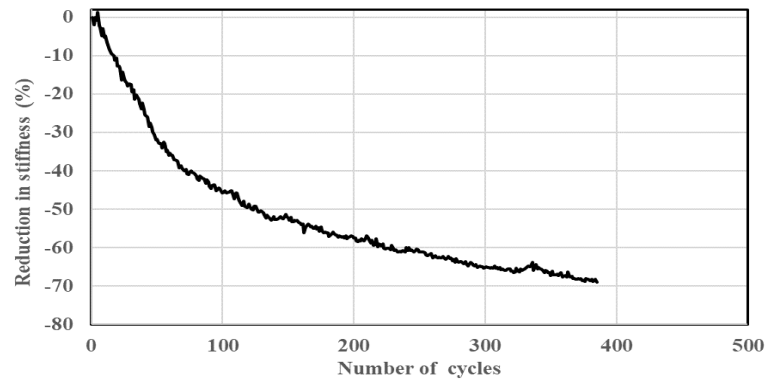
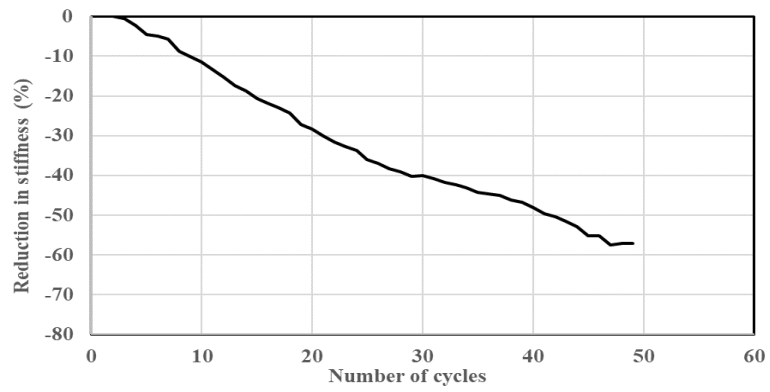


Figure H

### BFNAH5 (III)



### LCNAH10 (I)



### LCNAH10 (II)

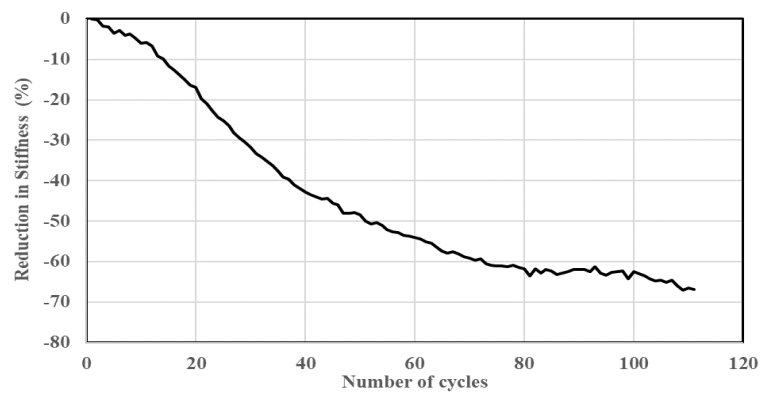
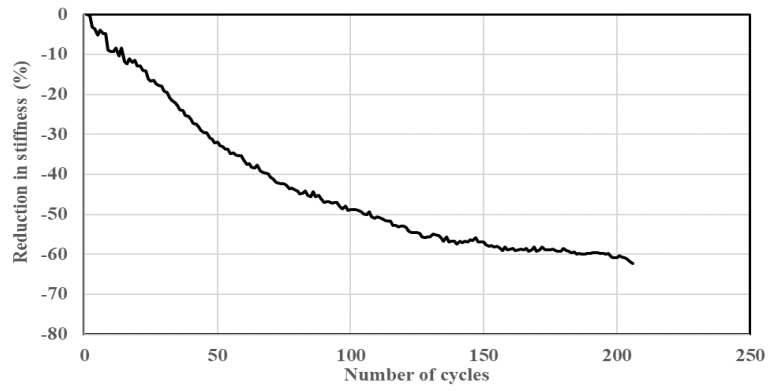
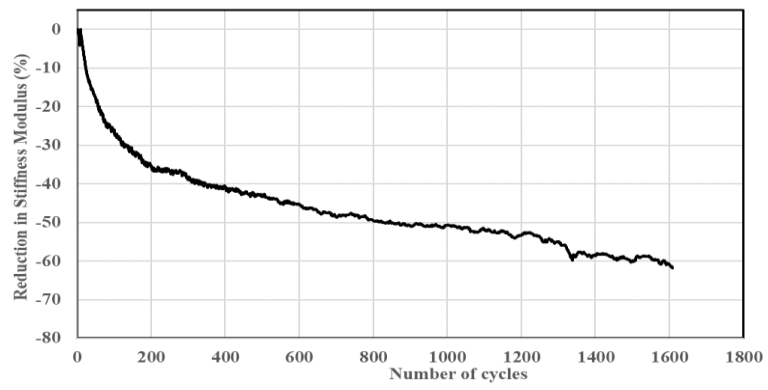


Figure H

### LCNAH10 (III)



### BFMUH0 (I)



### BFMUH0 (II)

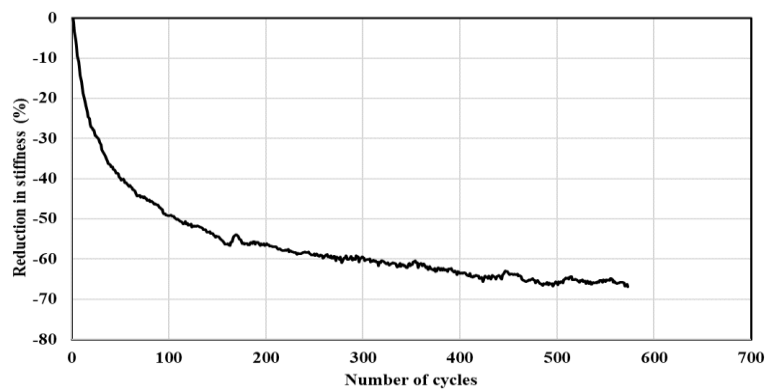
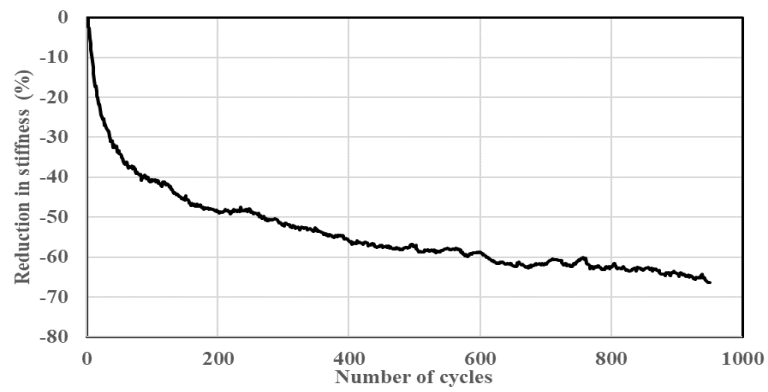
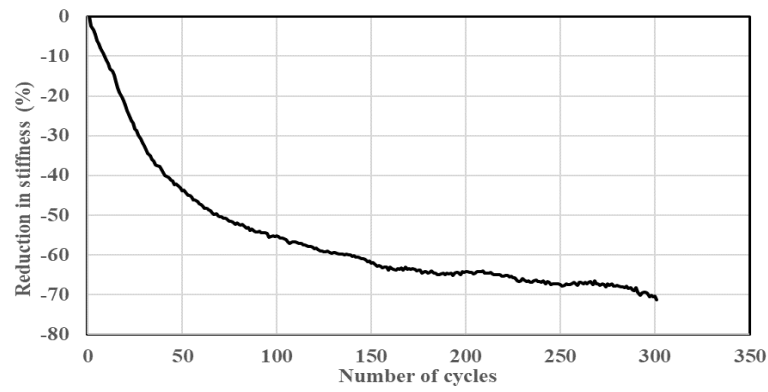


Figure H

**BFMUH0 (III)**



**BFNUH10 (I)**



**BFNUH10 (II)**

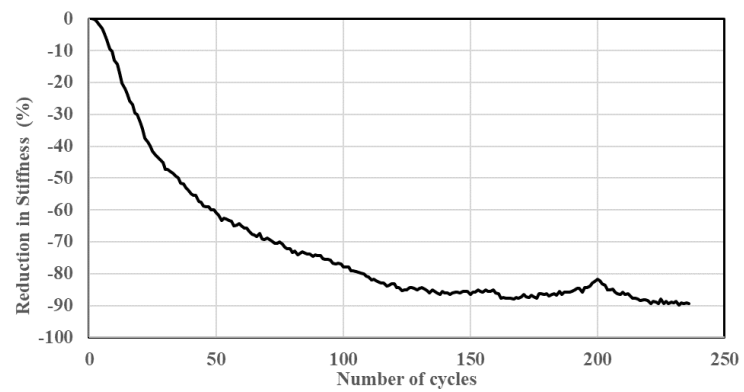
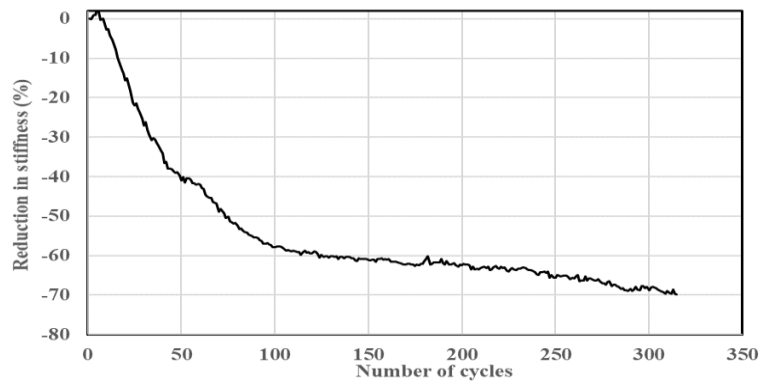
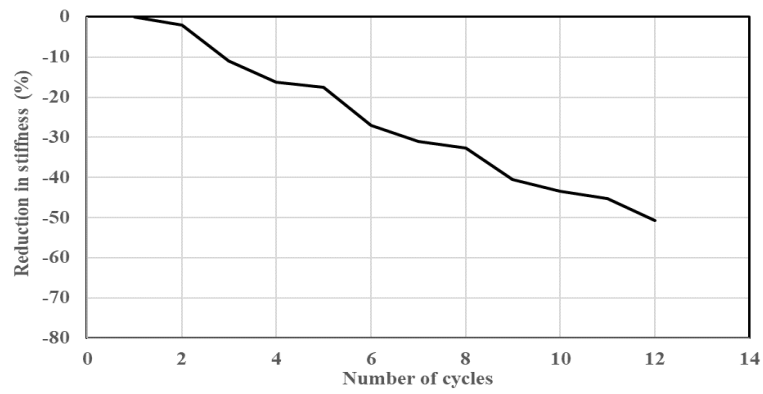


**Figure H**

### BFNUH10 (II)



### BCNAS0 (I)



### BCNAS0 (II)

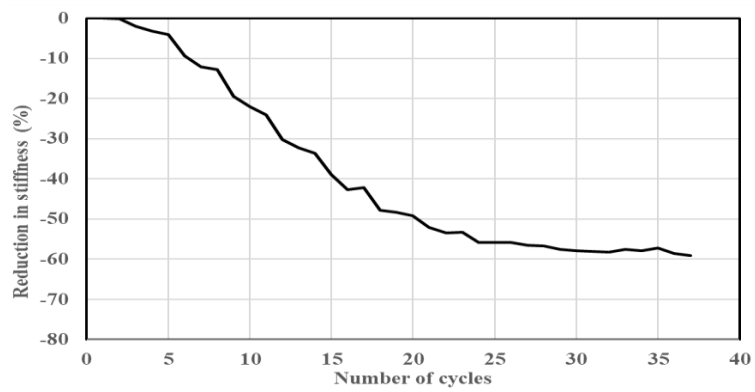
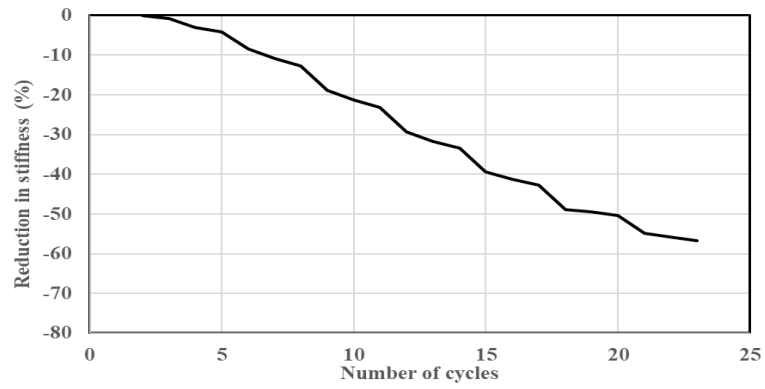


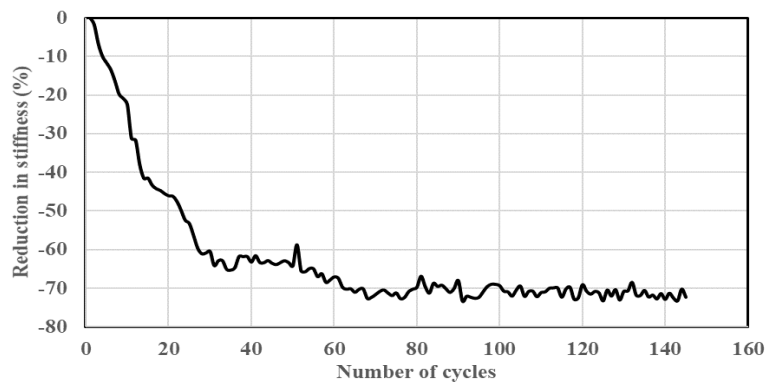
Figure H



### BCNAS0 (III)



### LFMUS0 (I)



### LFMUS0 (II)

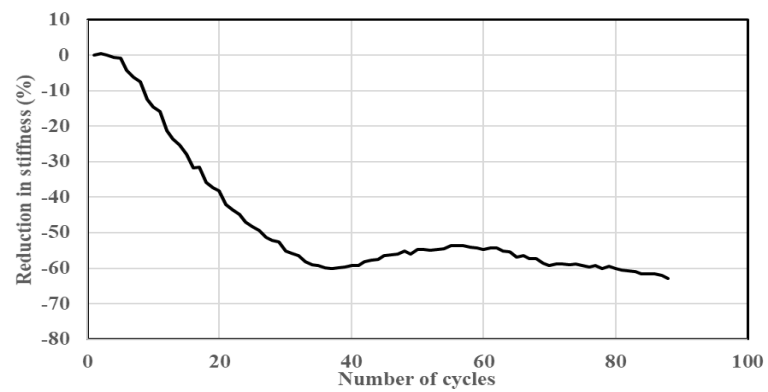
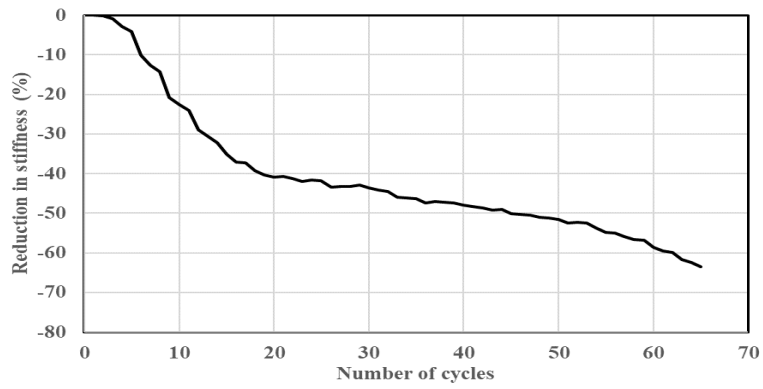
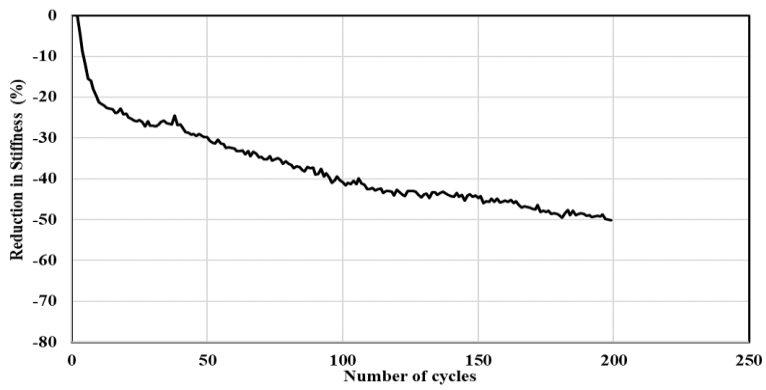


Figure H

**LFMUS0 (III)**



**BCMUS5 (I)**



**BCMUS5 (II)**

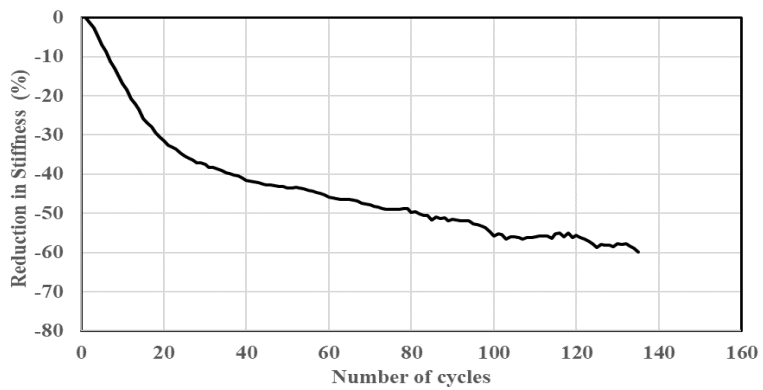
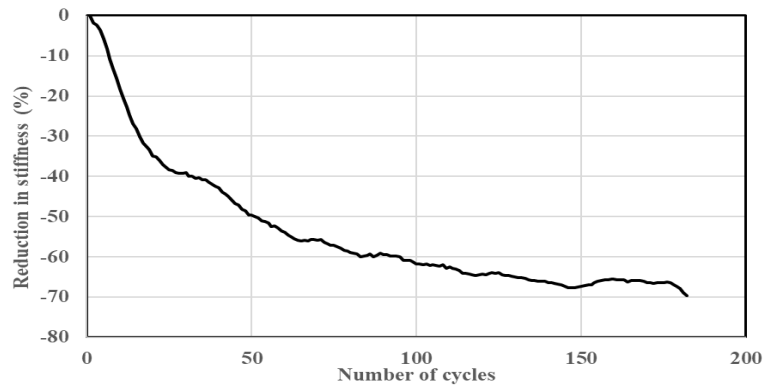
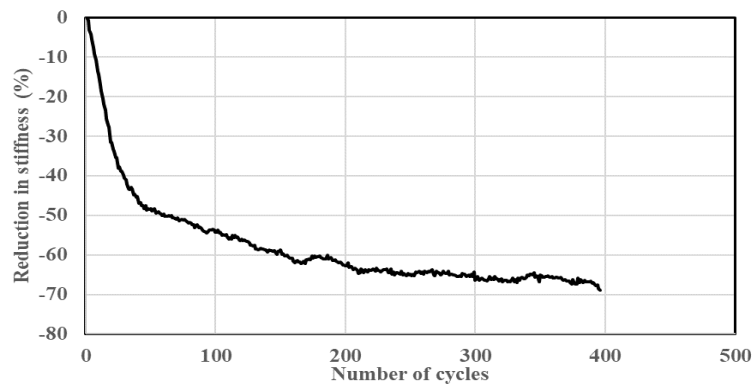


**Figure H**

### BCMUS5 (III)



### LCMUH0 (I)



### LCMUH0 (II)

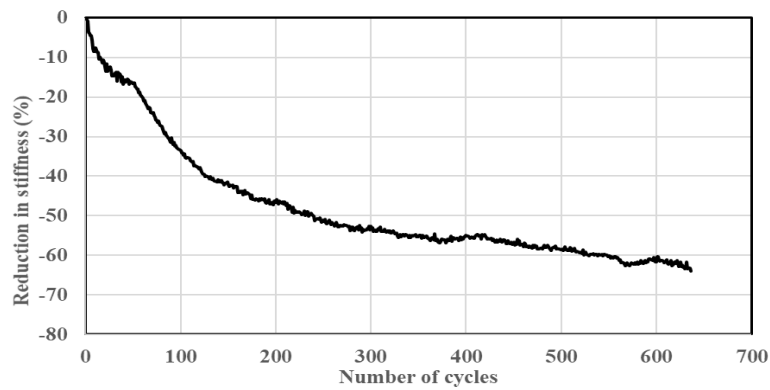
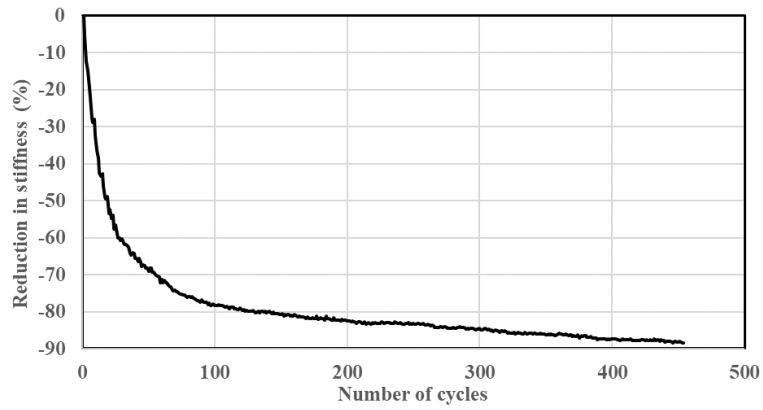
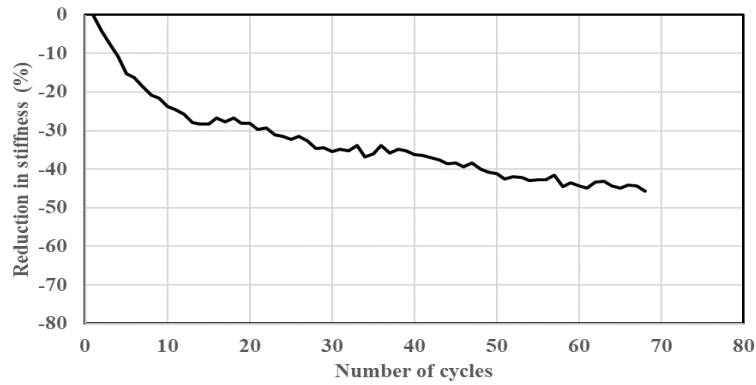


Figure H

### LCMUH0 (III)



### LFMUS10 (I)



### LFMUS10 (II)

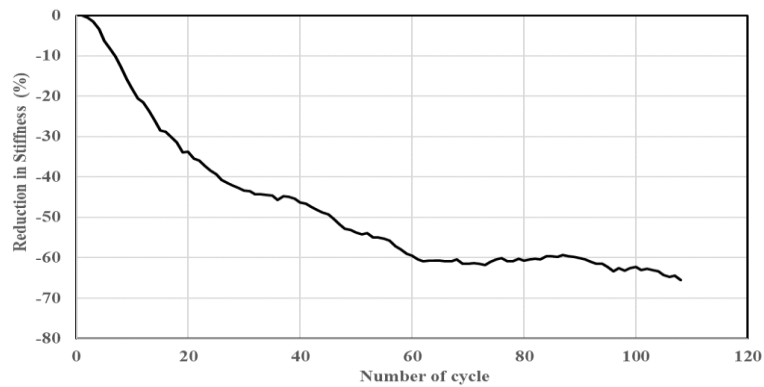
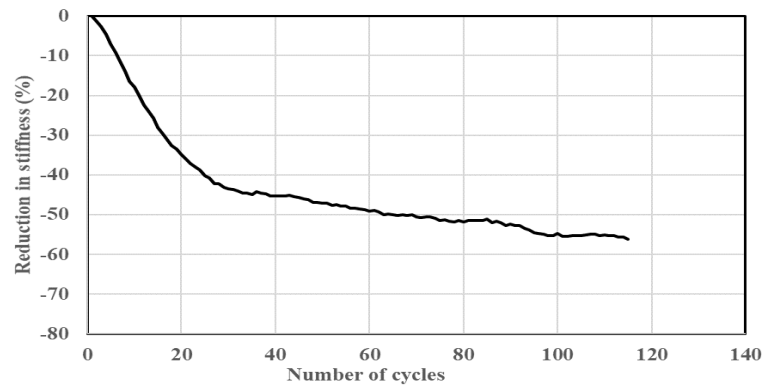
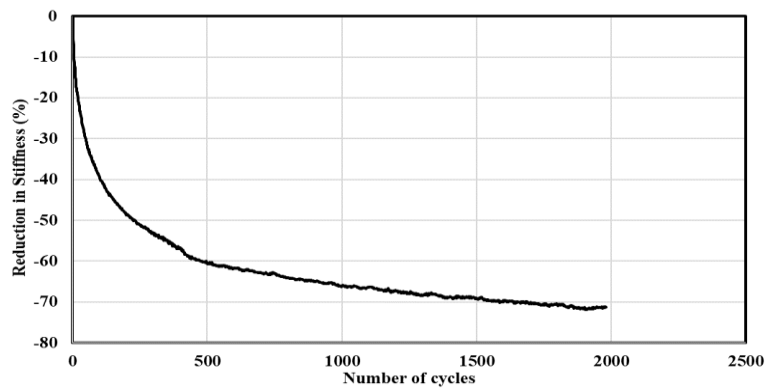


Figure H

### LFMUS10 (III)



### BFMUH10 (I)



### BFMUH10 (II)

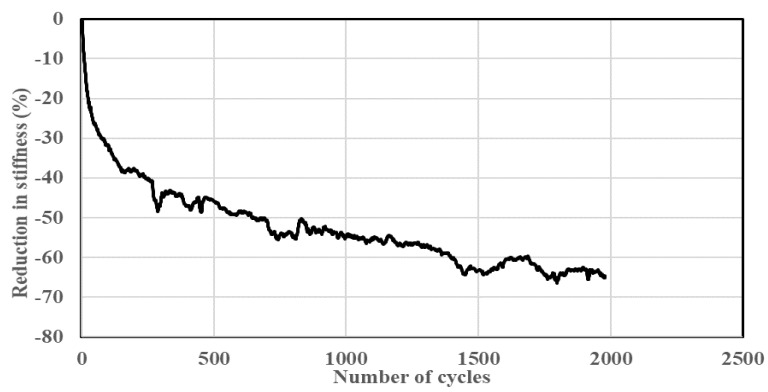
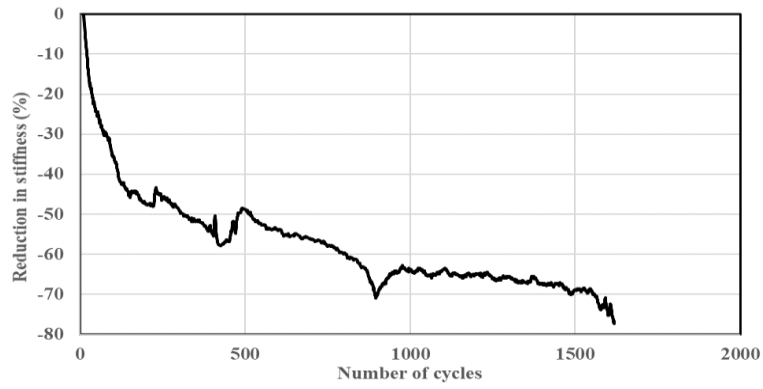
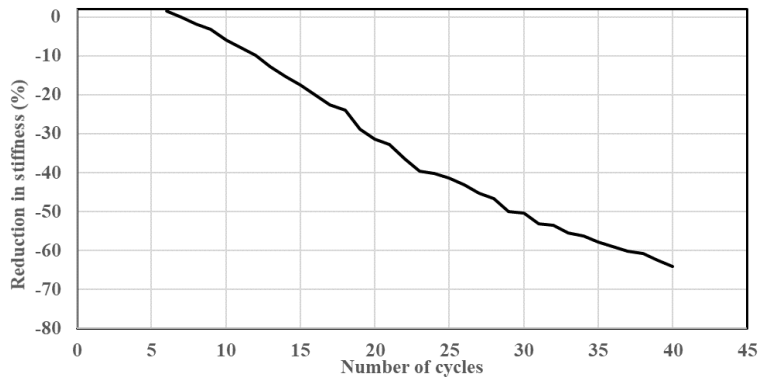


Figure H

### BFMUH10 (III)



### LCNUH0 (I)



### LCNUH0 (II)

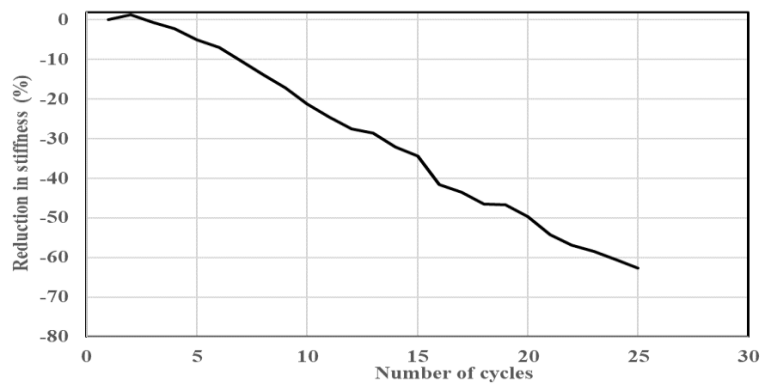
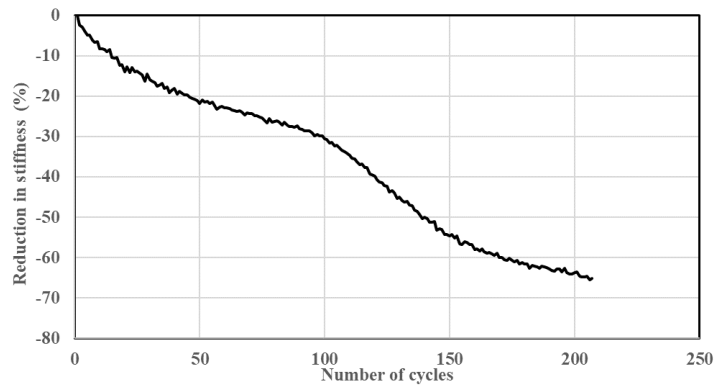
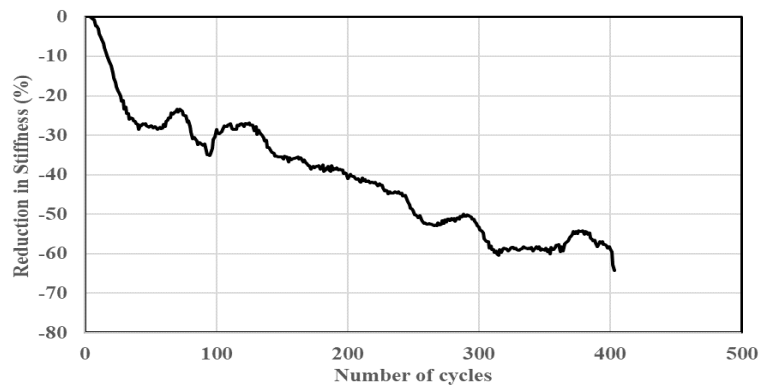


Figure H

**LCNUH0 (III)**



**LFMAS10 (I)**



**LFMAS10 (I)**

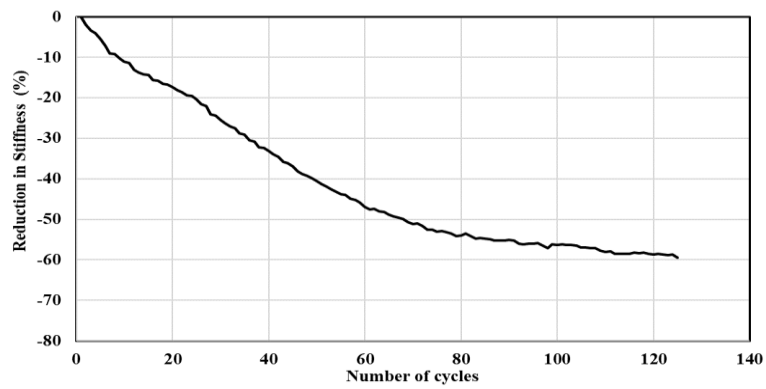
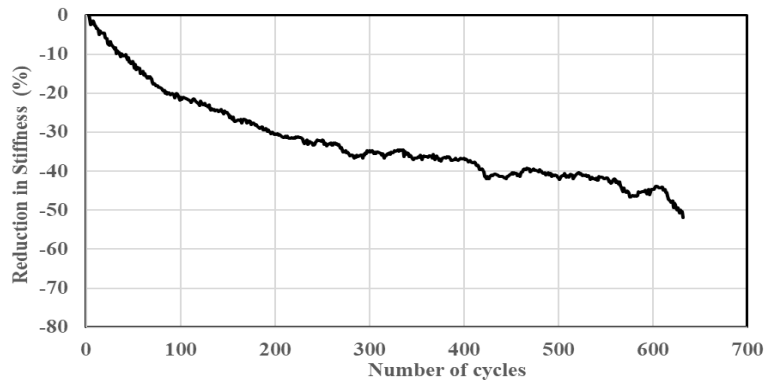
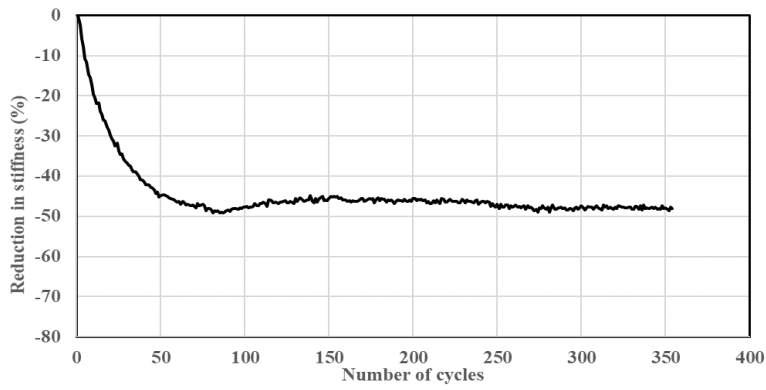


**Figure H**

**LFMAS10 (I)**



**LFMAS5 (I)**



**LFMAS5 (II)**

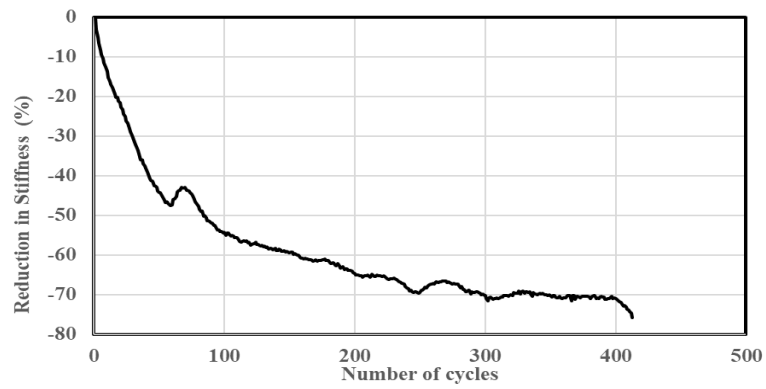
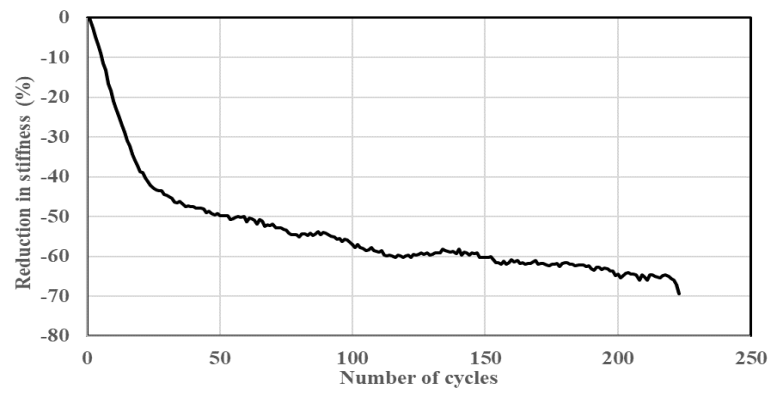


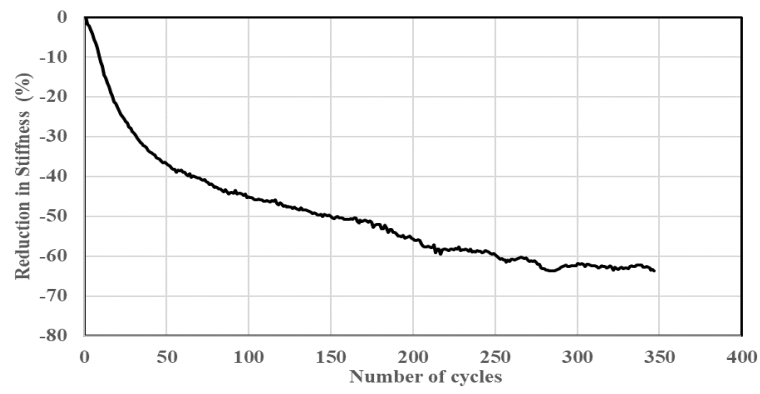
**Figure H**



### LFMAS5 (III)



### BCMAS0 (I)



### BCMAS0 (II)

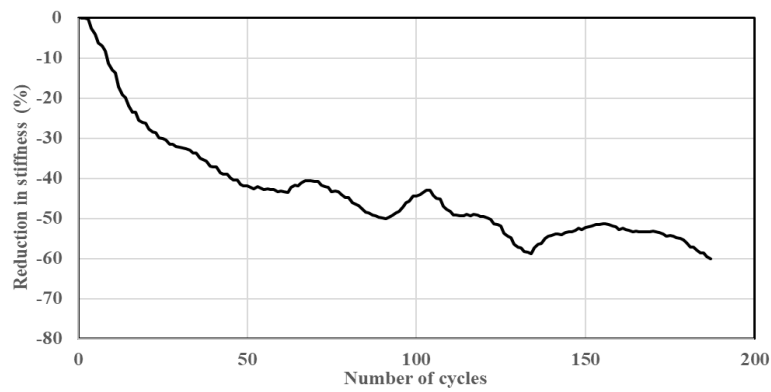
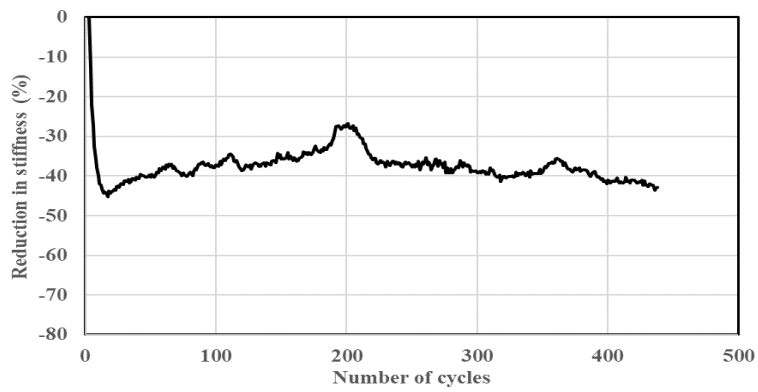
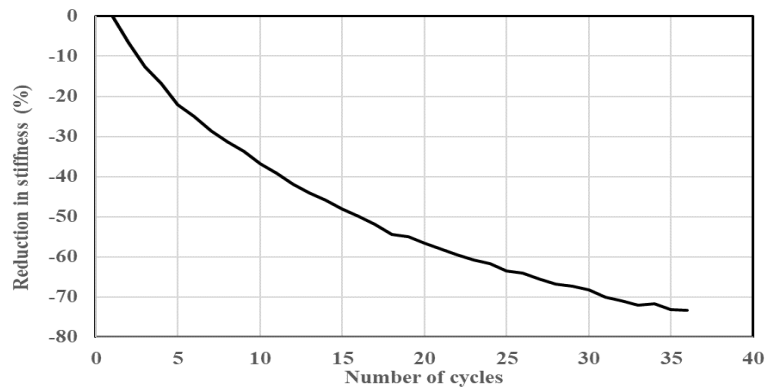


Figure H

### BCMAS0 (III)



### LFNAS5 (I)



### LFNAS5 (II)

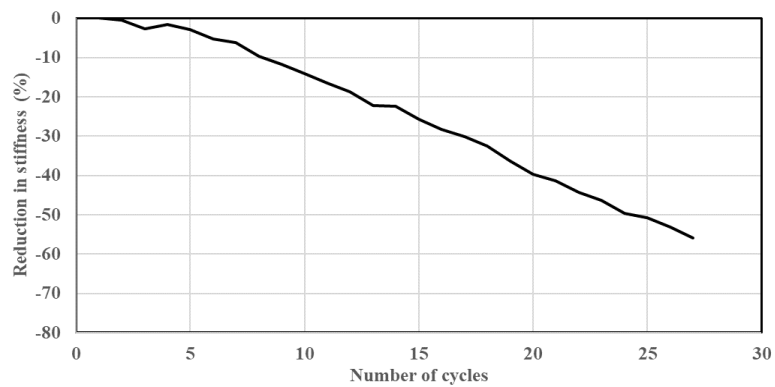
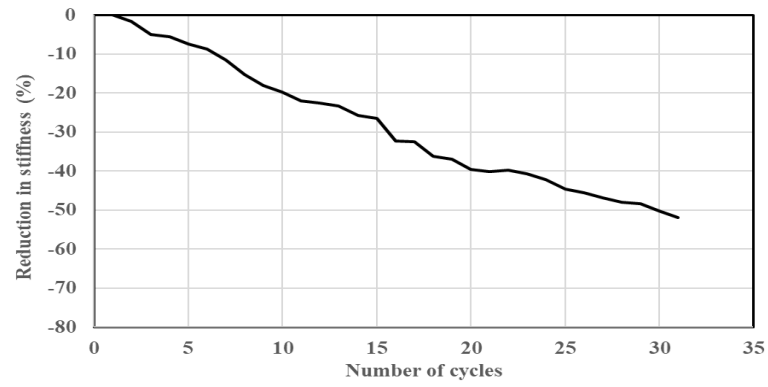
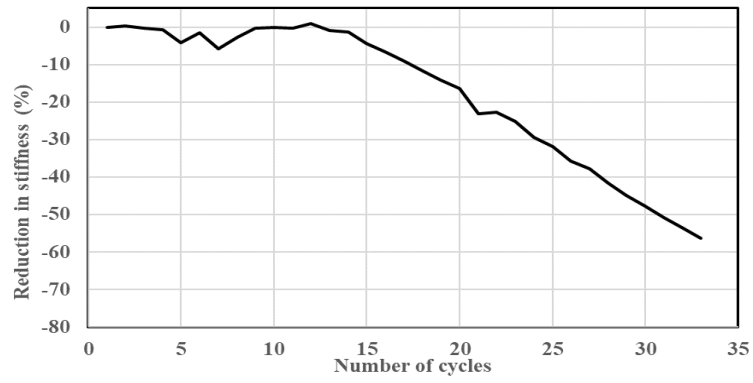


Figure H

**LFNAS5 (III)**



**LFNAS10 (I)**



**LFNAS10 (II)**

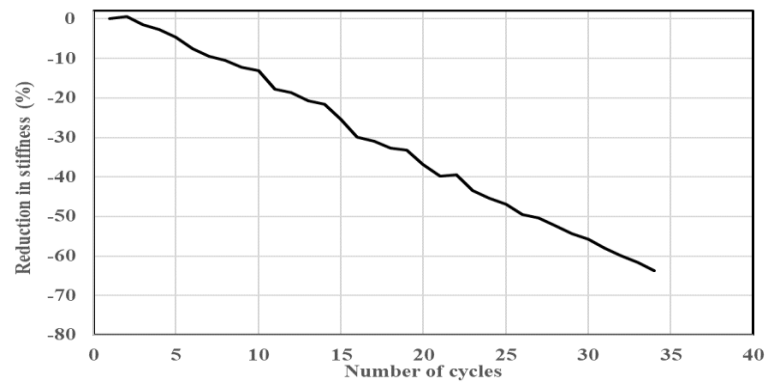
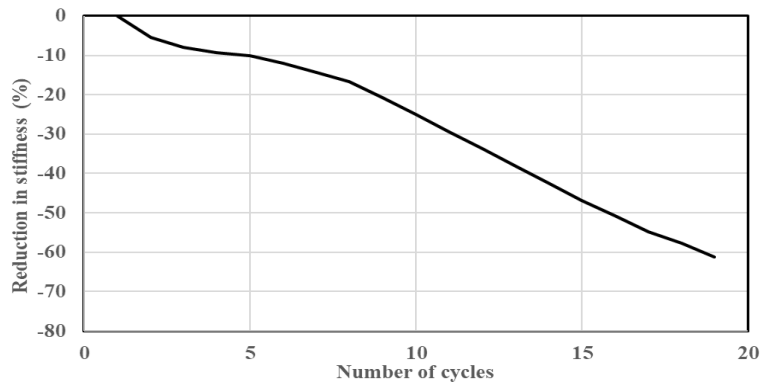
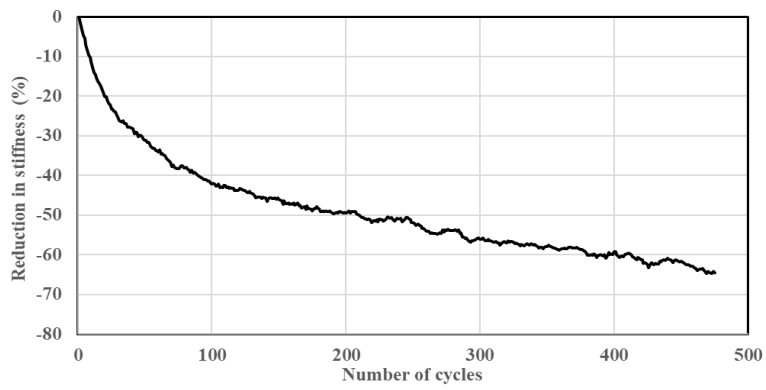


**Figure H**

**LFNAS10 (III)**



**LCNAH5 (I)**



**LCNAH5 (II)**

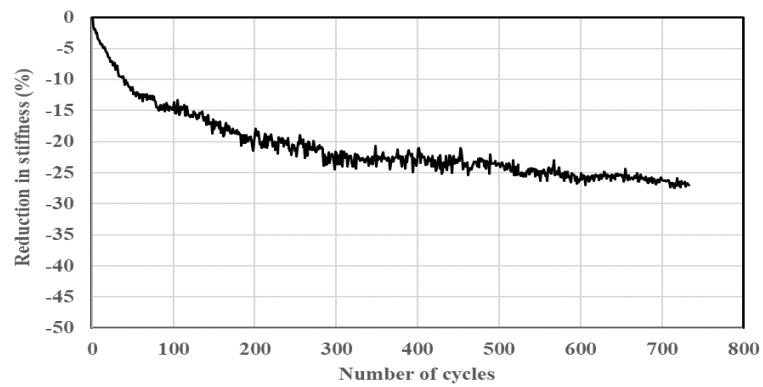


**Figure H**

### LCNAH5 (III)

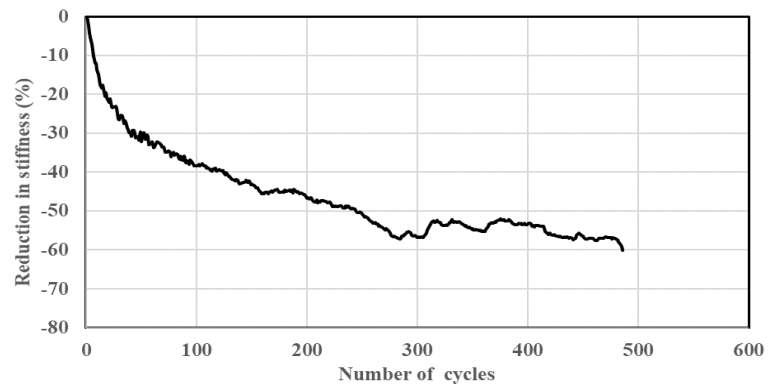


**Figure H**

**I. Stiffness from LLD**

**BCNAS10**

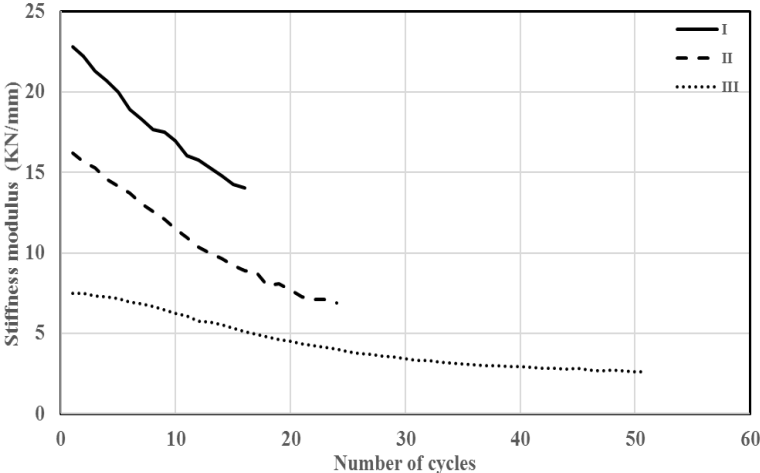
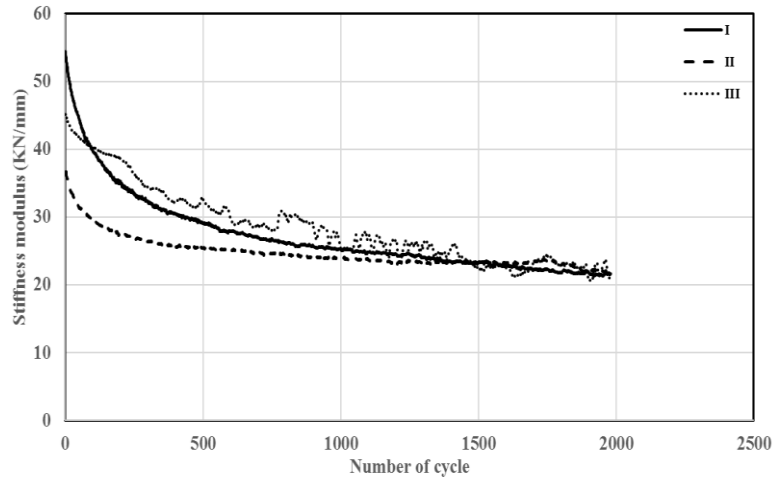


**Figure I. Stiffness versus cycle number, calculated from LLD**

### BFMAH10



### BFMAH10

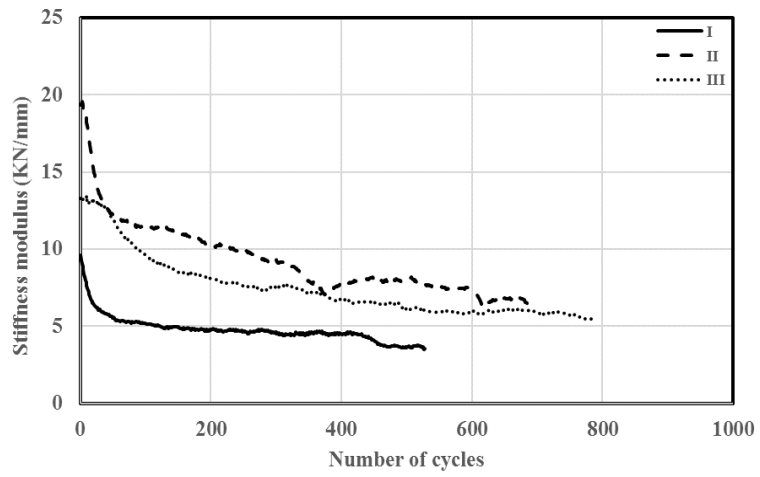
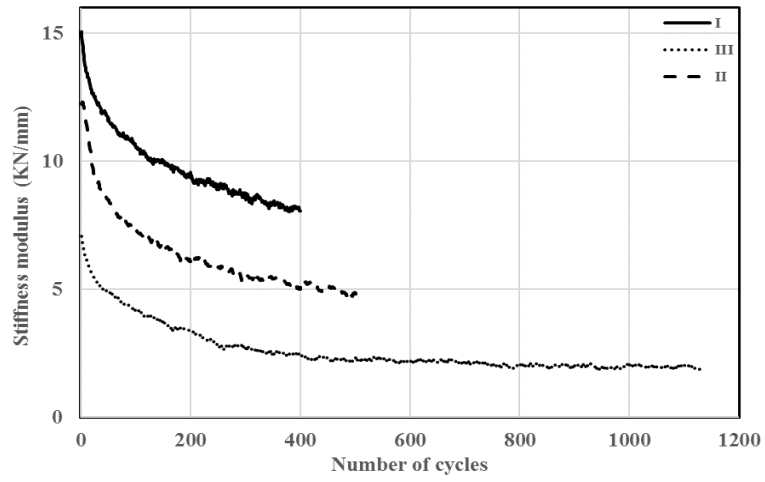


Figure I

### LCMAH0



### LCNUH10

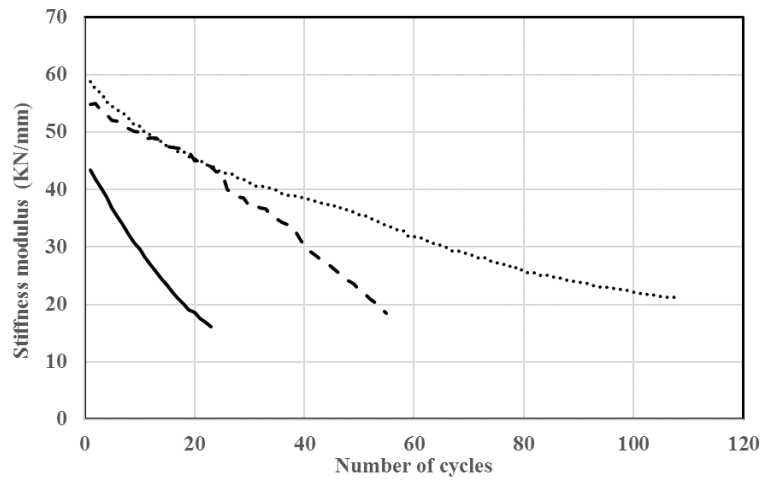
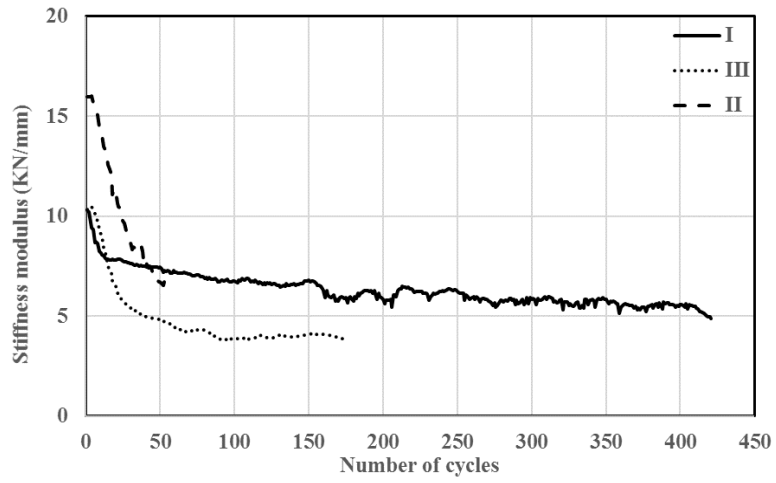


Figure I



### LFMAS0



### LFNUS10

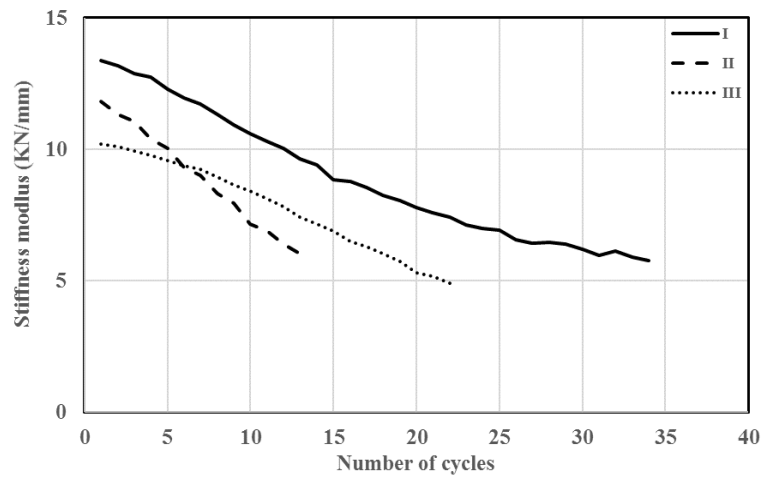
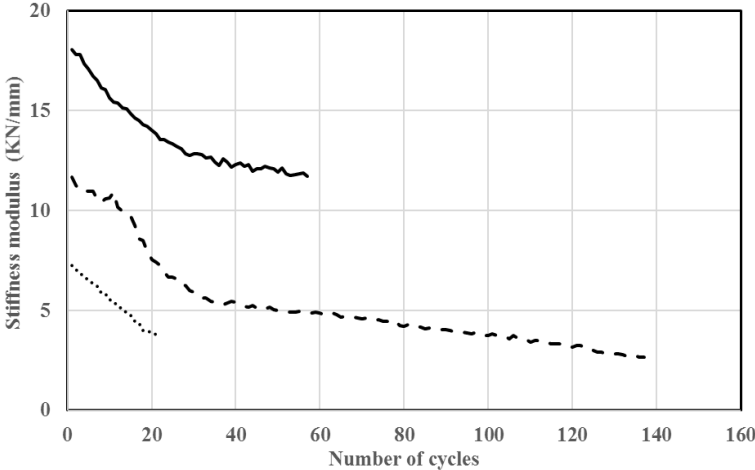
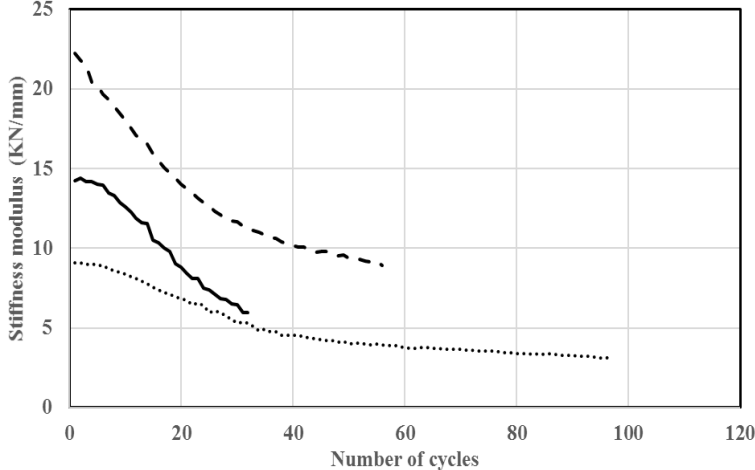


Figure I

**LCNUH5**

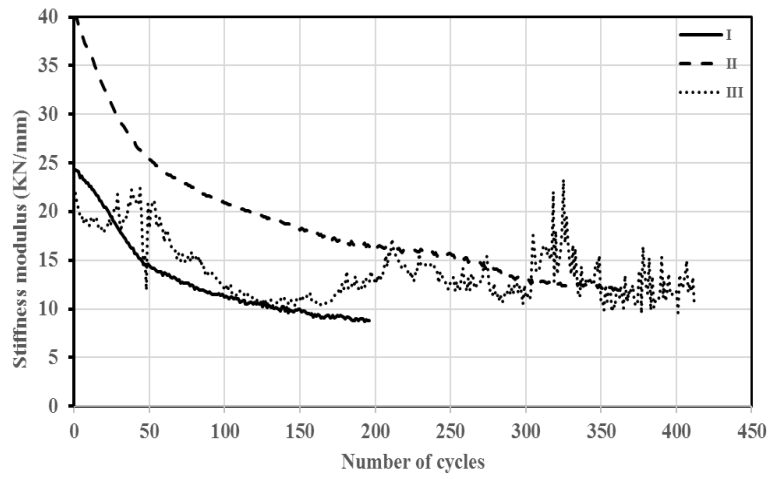


**LCNAH0**



**Figure I**

### BFNAH10



### LFNUS5

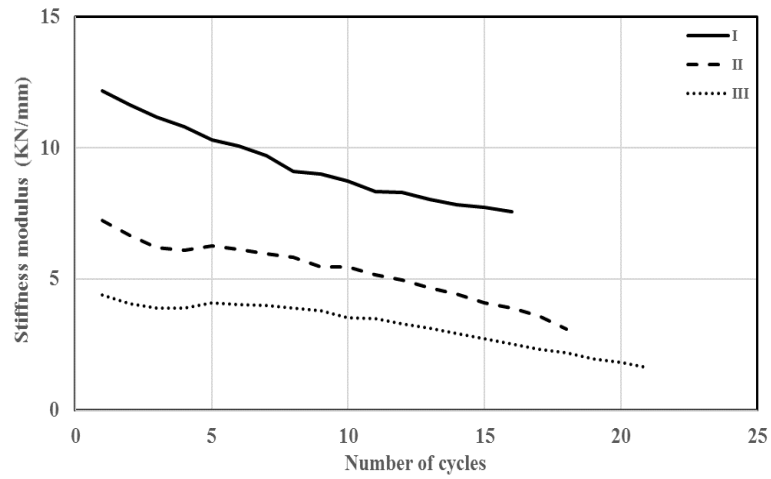
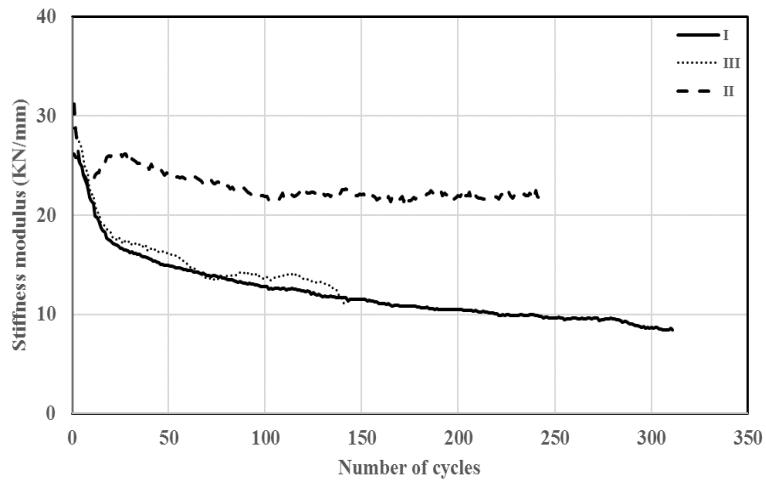


Figure I

### BCMUS0



### BCMAS10

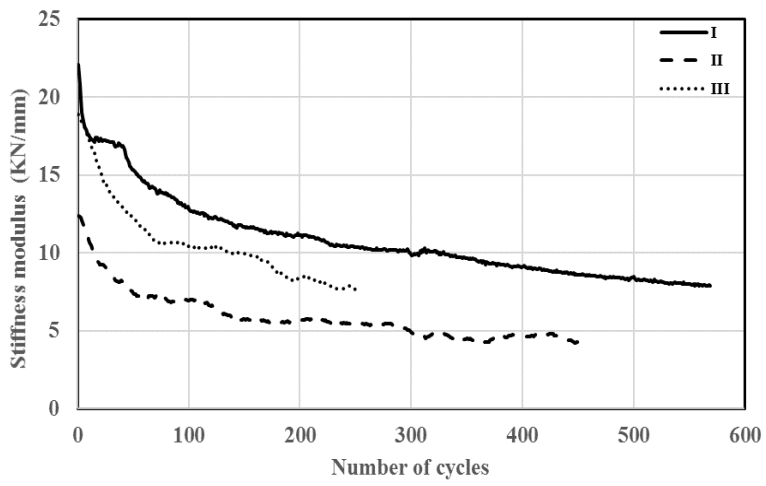
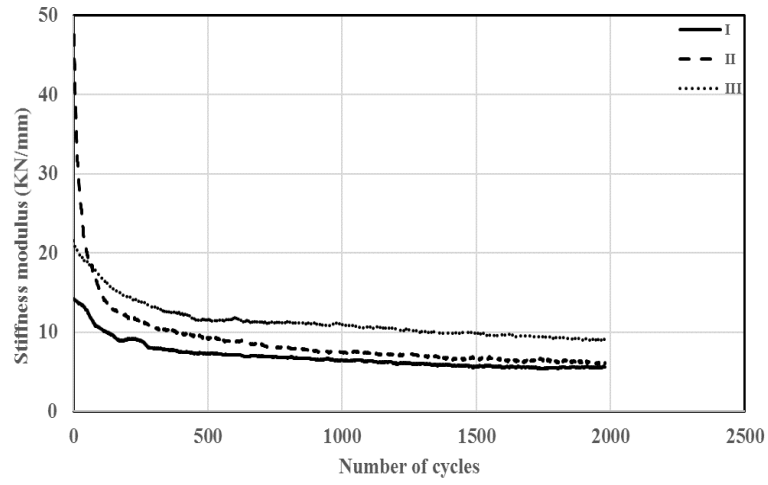


Figure I

### BFMAH0



### BCNAS5

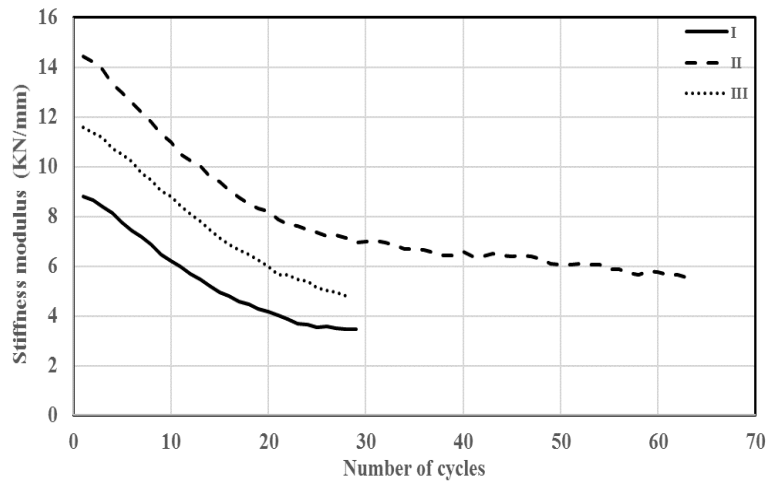
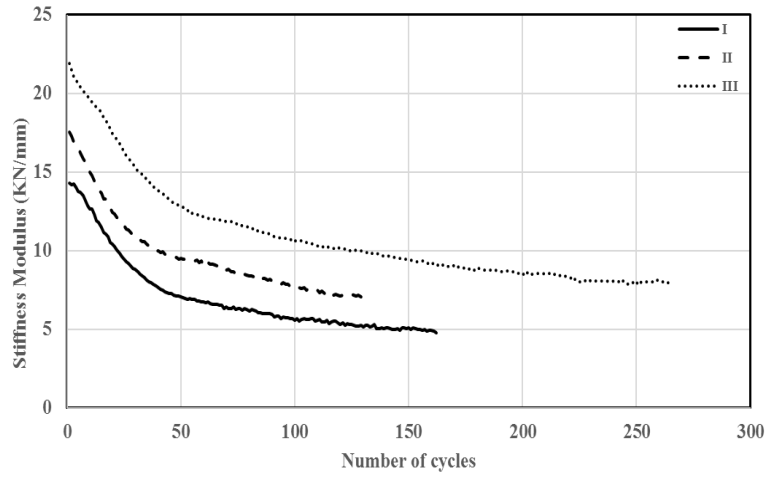


Figure I

### BFNAH0



### BFMUH5

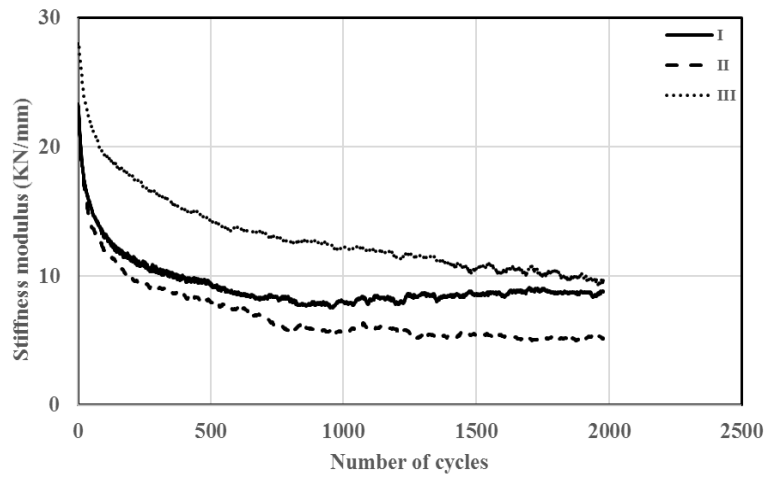
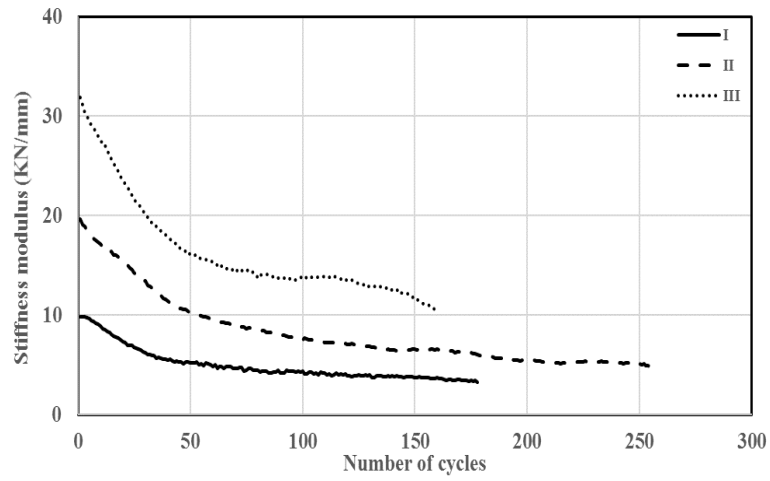


Figure I

### BFNUH5



### BCNUS10

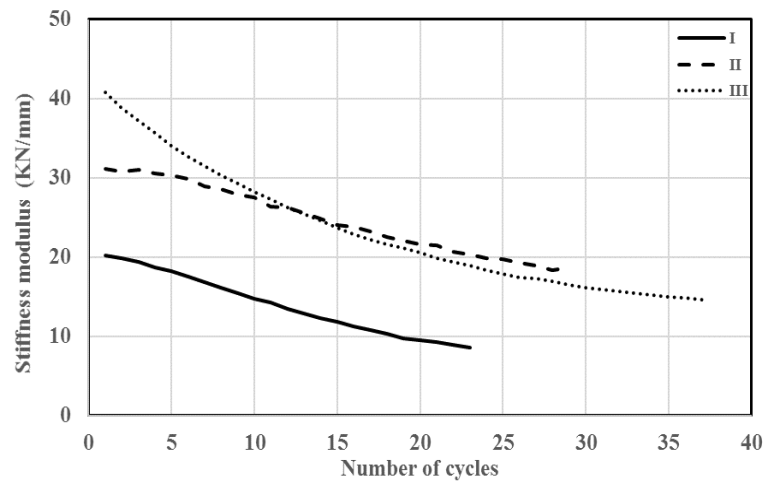
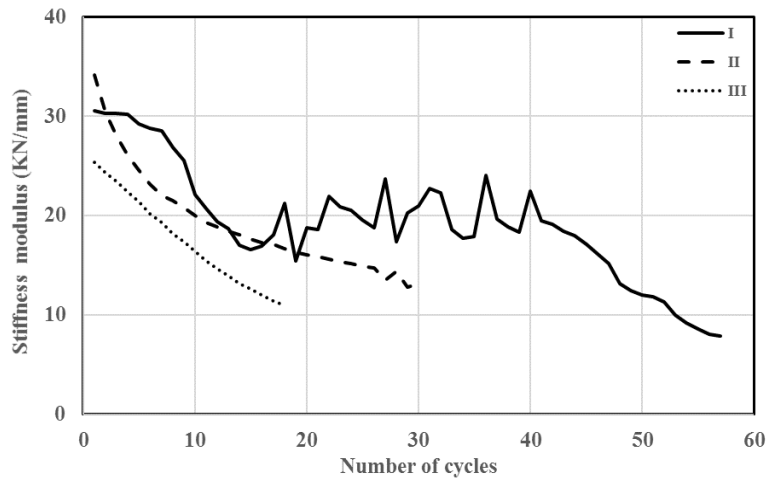


Figure I

### BCNUS5



### BCNUS0

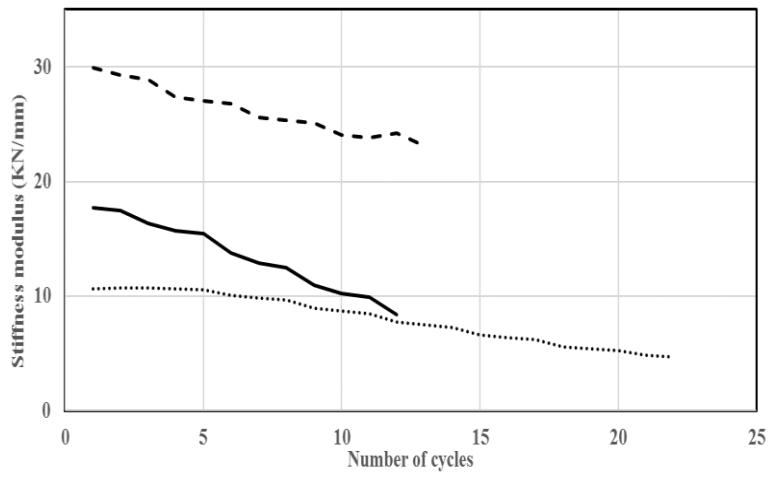
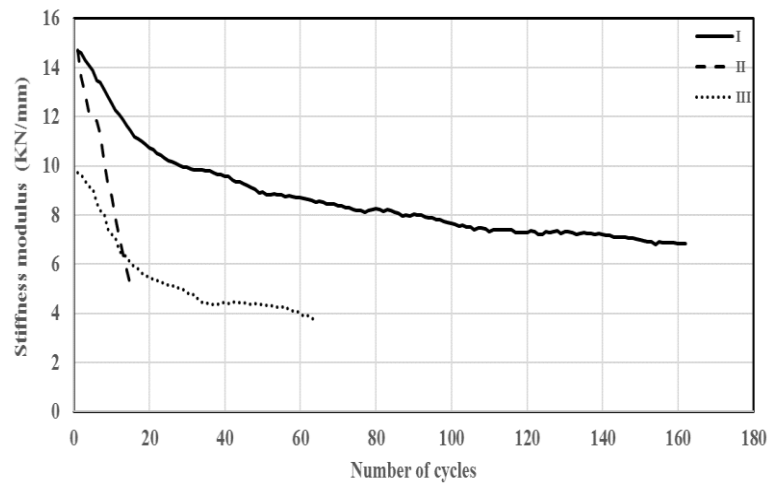


Figure I



### LFMUS5



### LFNAS0

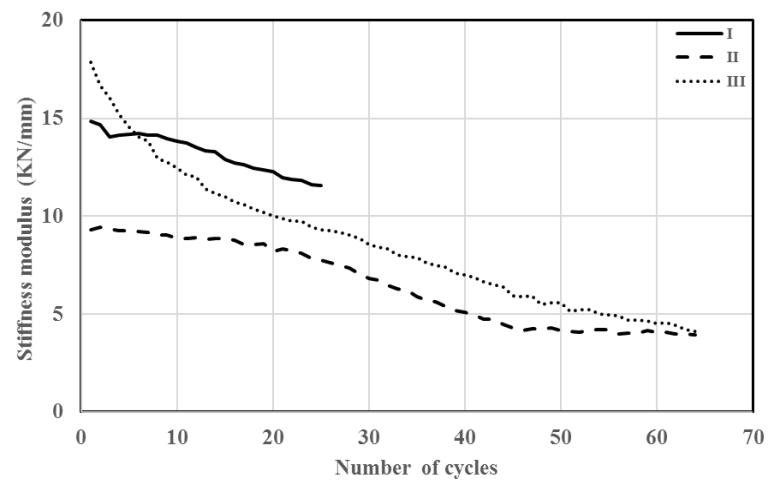
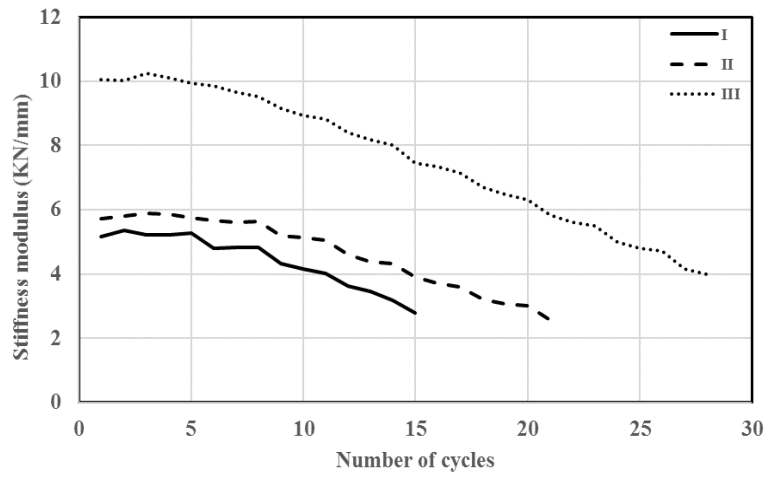


Figure I

### LFNUS0



### BCMUS10

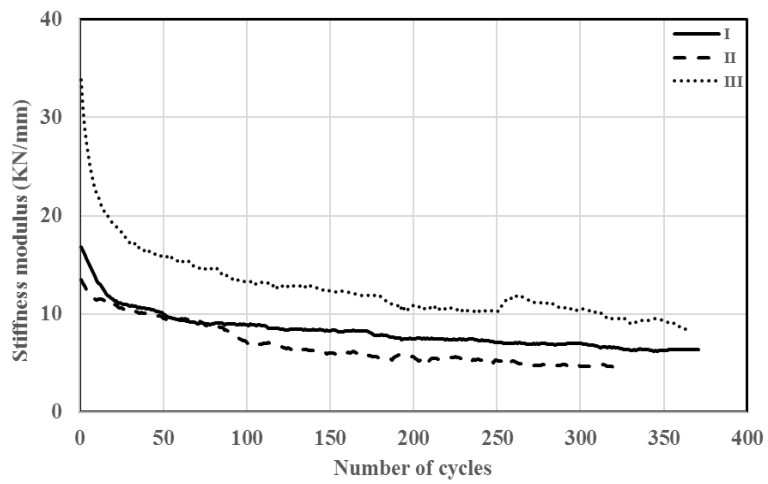
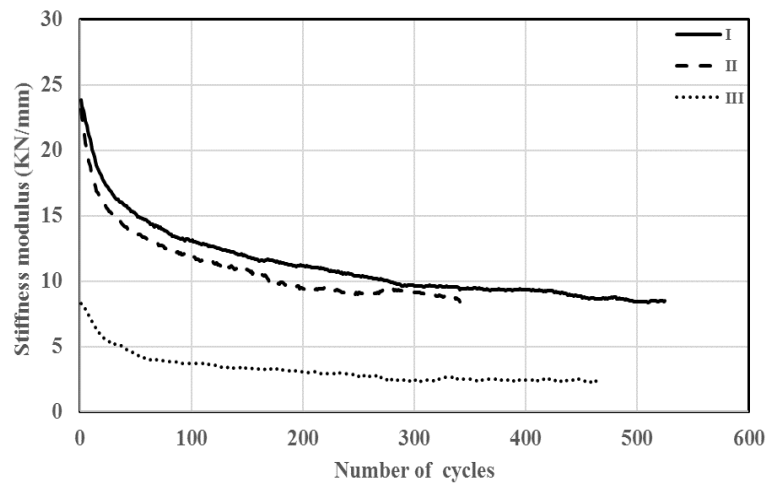


Figure I

### BCMAS5



### LCNUH5

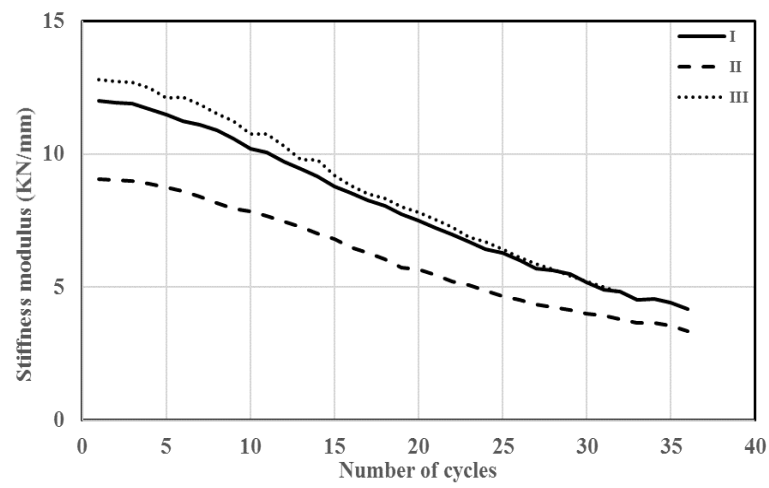
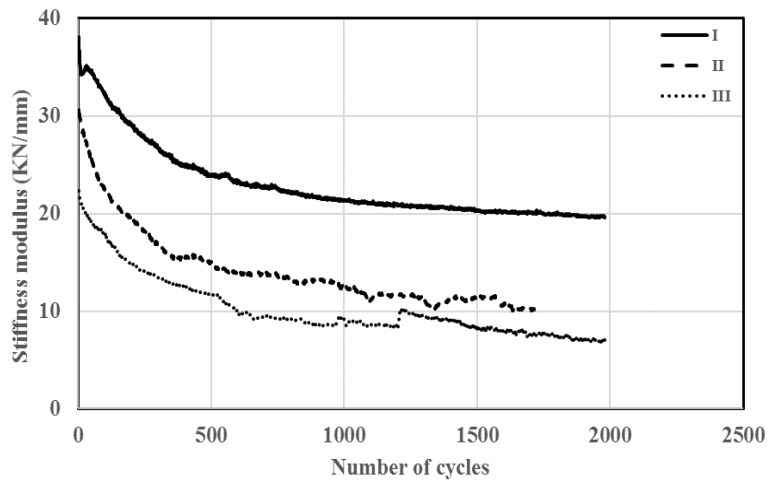


Figure I

### BFMAH5



### LCMAH10

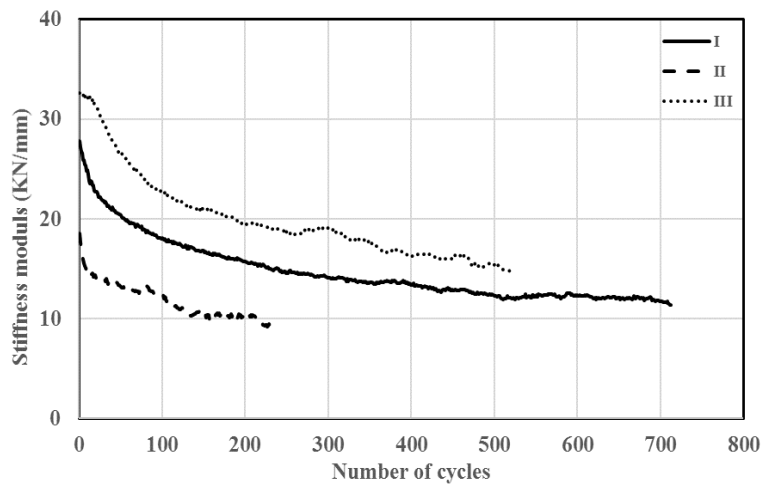
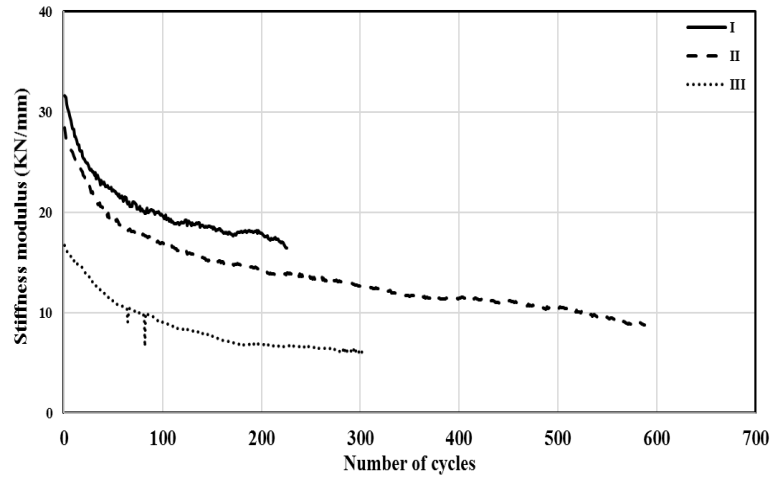


Figure I

### LCMUH5



### BFNUH0

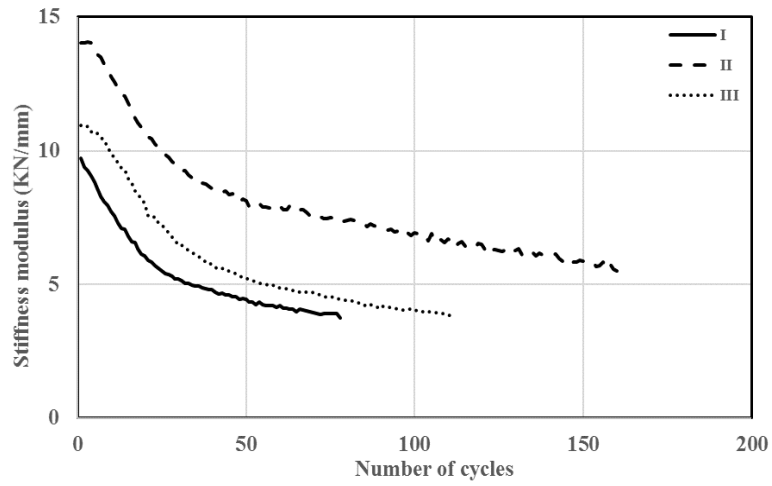
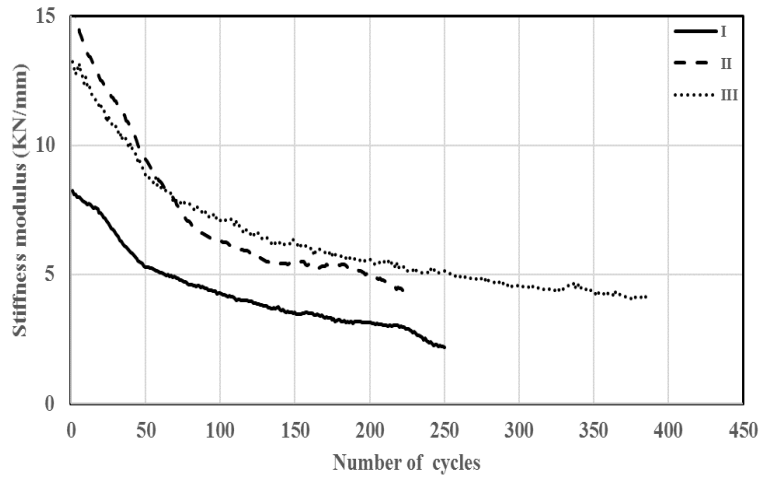


Figure I

### BFNAH5



### LCNAH10

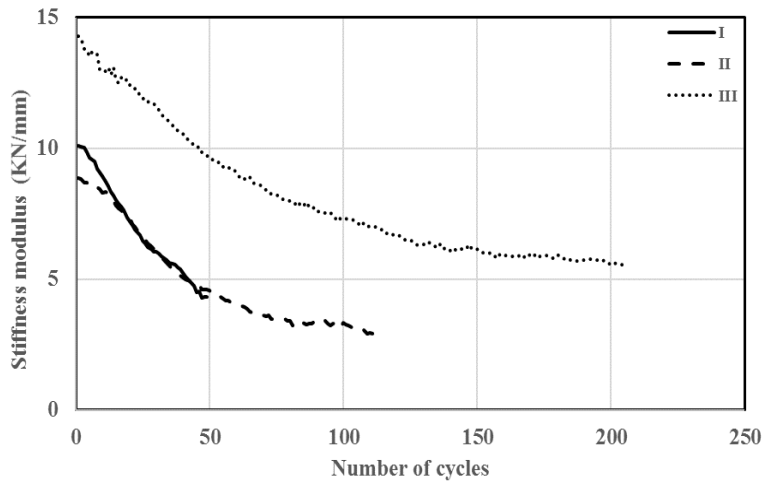
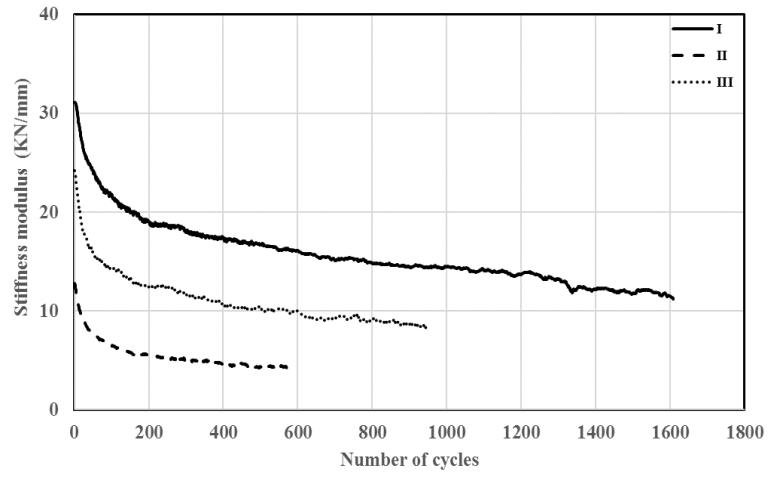


Figure I

### BFMUH0



### BFNUH10

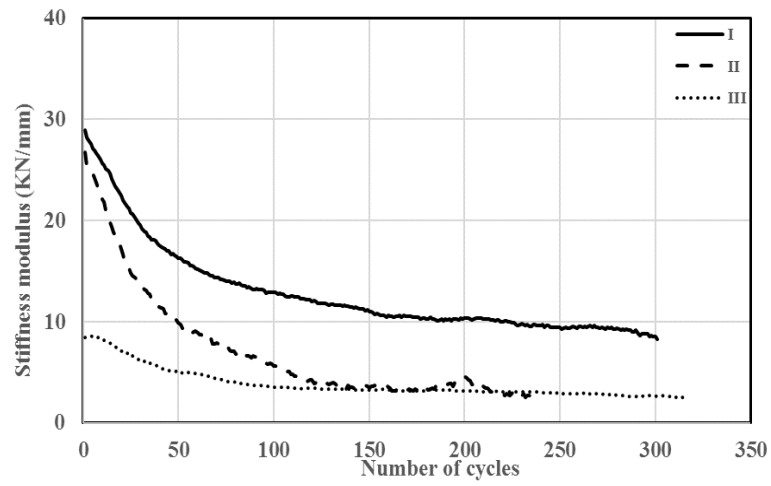
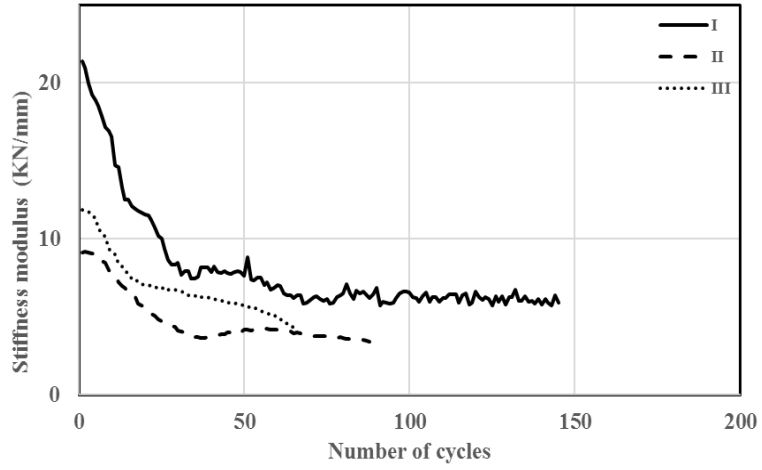


Figure I

### LFMUS0



### BCNAS0

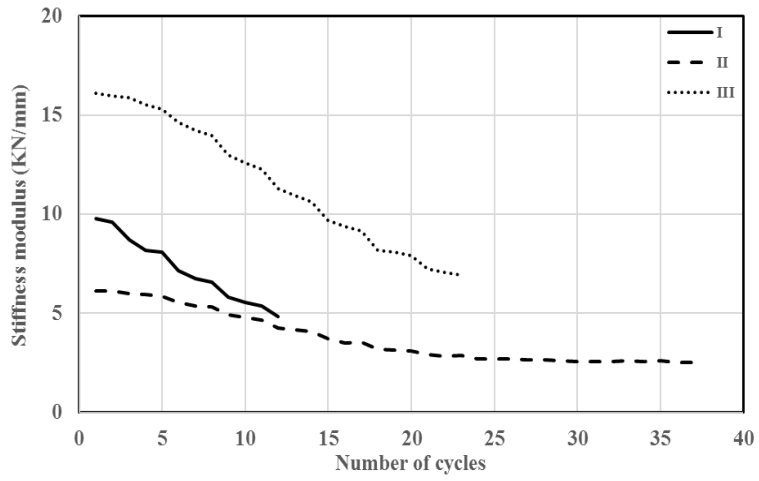
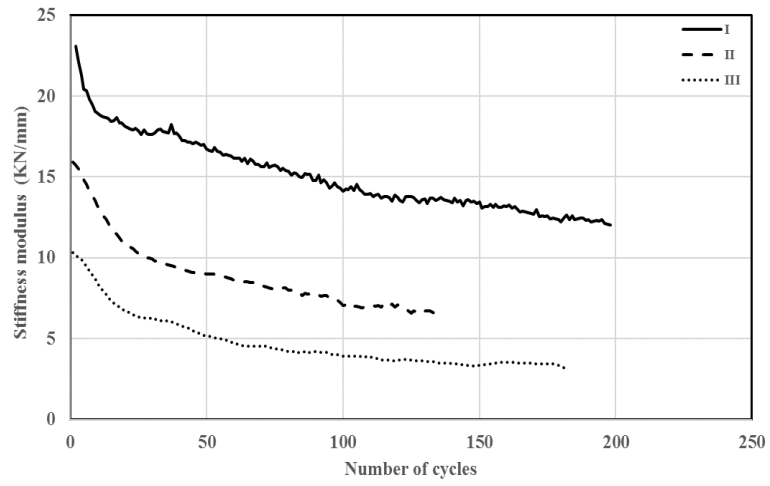


Figure I



### BCMUS5



### BCMAS0

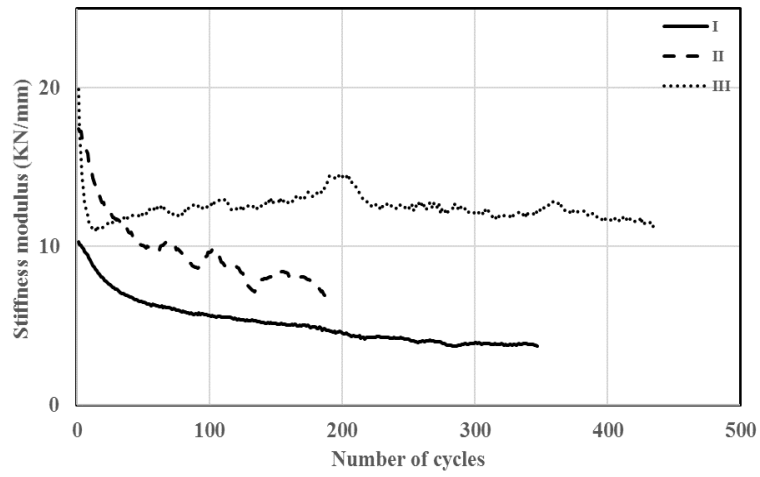
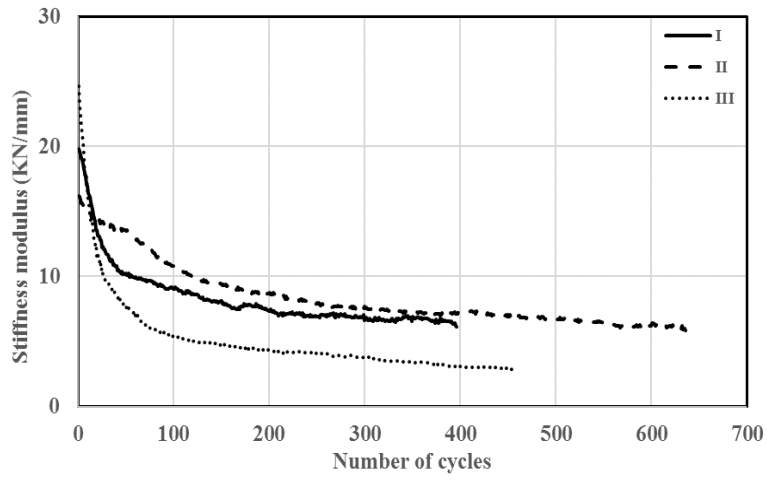


Figure I

### LCMUH0



### LFMUS10

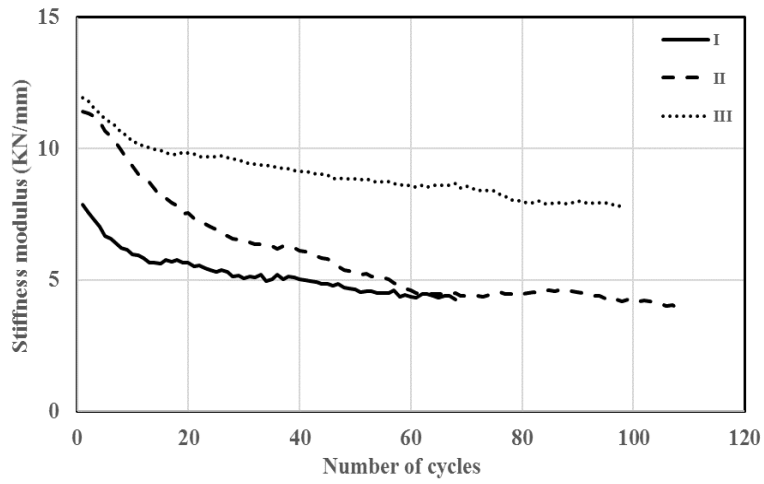
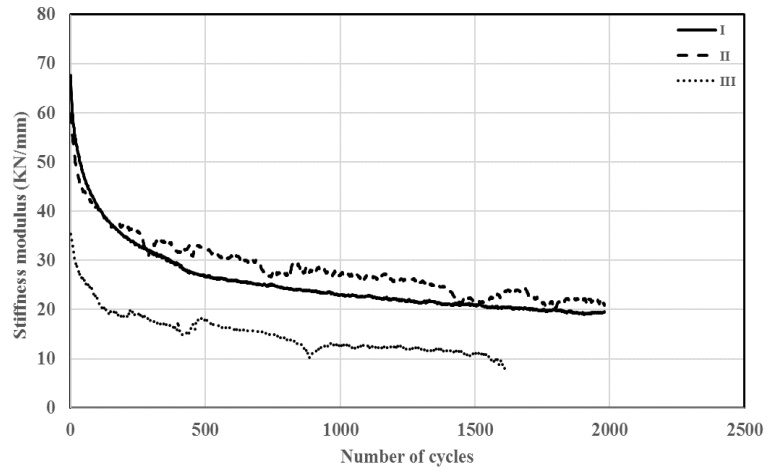


Figure I

### BFMUH10



### LCNUH0

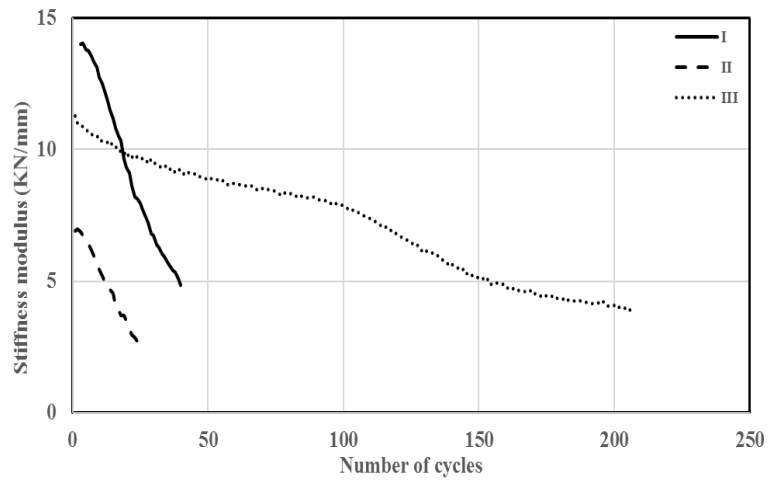
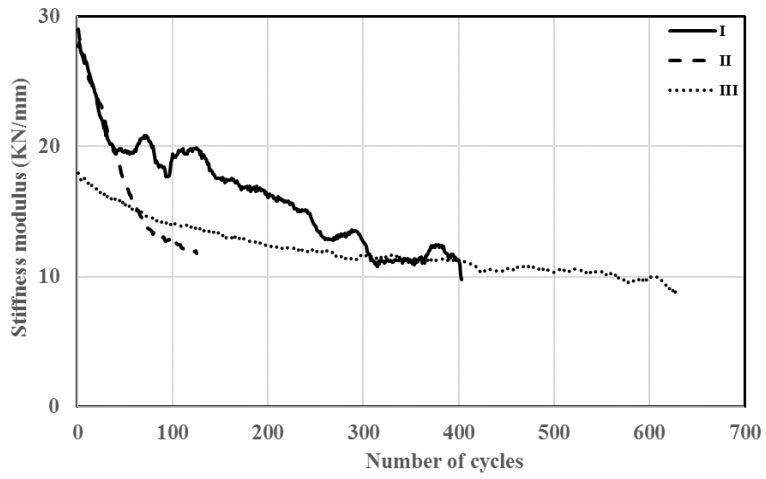


Figure I

### LFMAS10



### LFMAS5

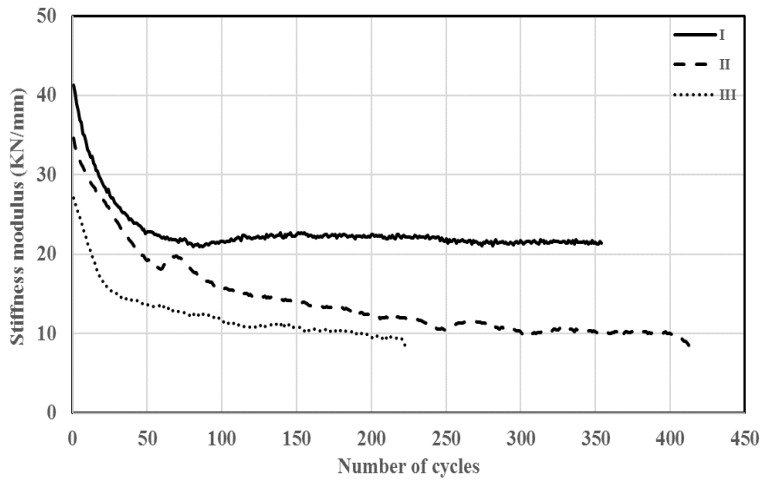
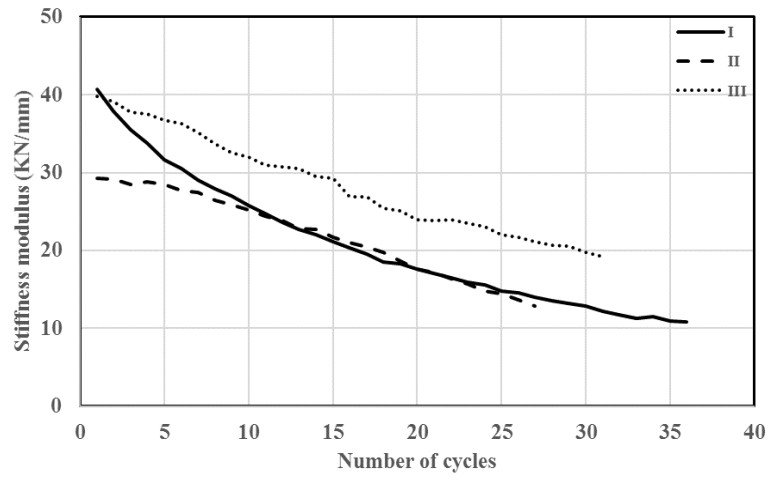


Figure I

### LFNAS5



### LFNAS10

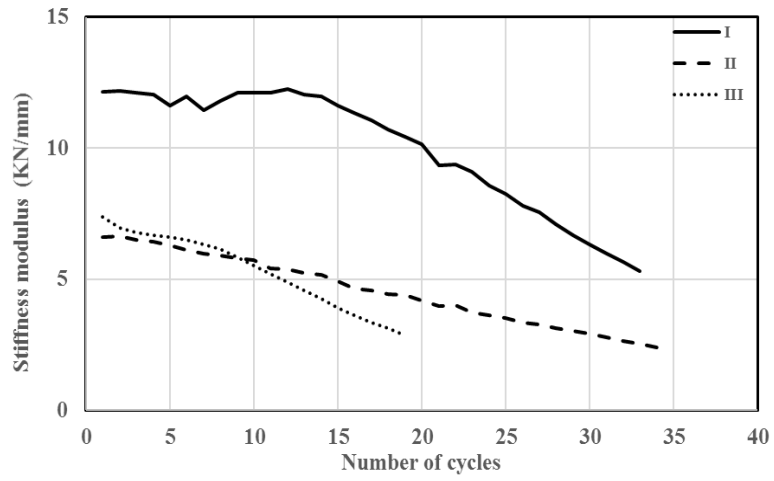


Figure I

### LCMAH5

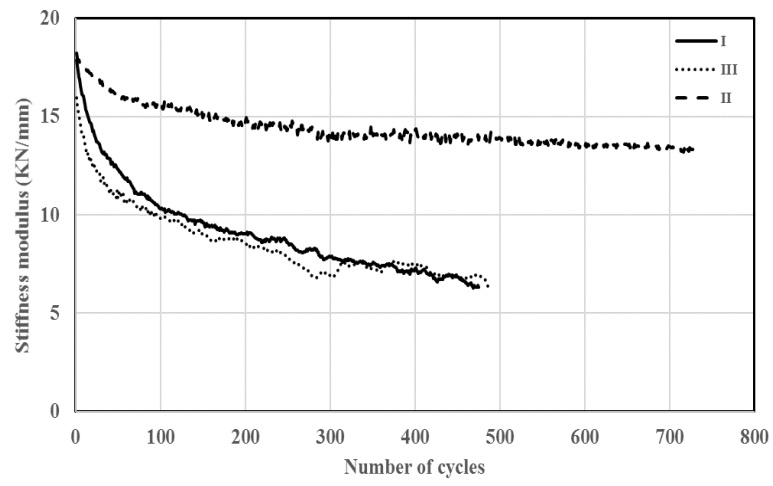


Figure I

## CURRICULUM VITAE

### PERSONAL INFORMATION

Surname, Name: Shabani, Reza  
Nationality: Iranian (IRIB)  
Date and Place of Birth: 20 September 1977, Ahvaz  
Marital Status: Single  
Email: rezashabani.1977@gmail.com

### EDUCATION

Degree	Institution	Year of Graduation
MS	Azad University, Tehran	2004
BS	Azad University, Tehran	2000
High School	Tazkieh High School, Tehran	1995

### WORK EXPERIENCE

Year	Place	Enrollment
2007-2012	Abad Rahan Pars Co. Tehran	Senior Estimator
2005-2006	Haraz Rah Co. Tehran	Design Engineer
2001-2003	Anchorage Co. Tehran	Tech Engineer

### FOREIGN LANGUAGES

Advanced English, Intermediate Turkish

## **PUBLICATIONS**

### **Journal Articles**

1. R. Shabani, M. Guler. Development of a New Testing Procedure to Measure Thermal Fatigue Performance of Asphalt Concrete
2. R. Shabani, E. Sengun, H.I. Ozturk, I.O. Yaman. The Effect of Mixture Variables on Surface characteristics of Roller Compacted Concrete, *Teknik Dergi*, 2020
3. E. Sengun a, B. Alam b, R. Shabani b, I.O. Yaman. The effects of compaction methods and mix parameters on the properties of roller compacted concrete mixtures, *Construction and Building Materials*, 2020
4. R. Shabani, E. Sengun, H.I. Ozturk, B. Alam, I.O. Yaman. Superpave gyratory Compactor as an Alternative Design Method for Roller Compacted Concrete (RCC) in Laboratory, *Journal of Materials in Civil Engineering*, 2020
5. E. Sengun a, B. Alam b, R. Shabani b, I.O. Yaman . Strength and Fracture Properties of Roller Compacted Concrete (RCC) Prepared by an In-situ Compaction Procedure, *Construction and Building Materials*, 2020

### **Conferences**

1. E. Sengun, R. Shabani, B. Alam, M.A. Aykutlu, I.O. Yaman. Comparison of Several Laboratory Compaction Practices Applied on Roller Compacted Concrete Pavements, 13th International Congress on Advances in Civil Engineering, 12-14 September 2018, Izmir/TURKEY (2018).
2. R. Shabani, E. Sengun, H.I. Ozturk, B. Alam, I.O. Yaman. Evaluation of Superpave Gyratory Compaction Method for Roller Compacted Concrete Mixture Design, *TRB Annual Meeting* (2019).
3. E. Sengun, R. Shabani, B. Alam, I.O. Yaman. The Effect of Set Retarding and Plasticizer Admixtures on the Fresh and Hardened Properties of Roller Compacted Concrete, 10th International Concrete Congress, Bursa/Turkey (2019).